Studies on the Thermal and Photo-Induced Electron-Transfer Properties of Entatic Copper Guanidine Quinoline Complexes

Von der Fakultät für Mathematik und Naturwissenschaften der RWTH Aachen University zur Erlangung des akademischen Grades eines Doktors der Naturwissenschaften genehmigte Dissertation

vorgelegt von

Tobias Seitz, M.Sc.
aus
Köln

Berichter:
Universitätsprofessorin Dr. Sonja Herres-Pawlis
Universitätsprofessor Dr. Jun Okuda

Tag der mündlichen Prüfung: 19.12.2025

Eidesstattliche Erklärung

Tobias Seitz
erklärt hiermit, dass diese Dissertation und die darin dargelegten Inhalte die eigenen sind und selbständig, als Ergebnis der eigenen originären Forschung, generiert wurden. Hiermit erkläre ich an Eides statt

1. Diese Arbeit wurde vollständig oder größtenteils in der Phase als Promovierender dieser Fakultät und Universität angefertigt;

2. Sofern irgendein Bestandteil dieser Dissertation zuvor für einen akademischen Abschluss oder eine andere Qualifikation an dieser oder einer anderen Institution verwendet wurde, wurde dies klar angezeigt;

3. Wenn immer andere eigene- oder Veröffentlichungen Dritter herangezogen wurden, wurden diese klar benannt;

4. Wenn aus anderen eigenen- oder Veröffentlichungen Dritter zitiert wurde, wurde stets die Quelle hierfür angegeben. Diese Dissertation ist vollständig meine eigene Arbeit, mit der Ausnahme solcher Zitate;

5. Alle wesentlichen Quellen von Unterstützung wurden benannt;

6. Wenn immer ein Teil dieser Dissertation auf der Zusammenarbeit mit anderen basiert, wurde von mir klar gekennzeichnet, was von anderen und was von mir selbst erarbeitet wurde;

7. Ein Teil oder Teile dieser Arbeit wurden zuvor veröffentlicht und zwar in:

T. Seitz, M. Walbeck, A. Hoffmann, S. Herres-Pawlis, *Dalton Trans.* **2025**, *54*, 957-965.
T. Seitz, A. Karabulut, R. M. Suzuki, J. Heck, A. Hoffmann, S. Herres-Pawlis, *Chem. Commun.* **2025**.

Ort, Datum

Unterschrift

Preface

List of Publications, Presentations and Posters

Publications

1. **T. Seitz**, M. Walbeck, A. Hoffmann, S. Herres-Pawlis, *Dalton Trans.* **2025**, *54*, 957-965.
2. **T. Seitz**, A. Karabulut, R. M. Suzuki, J. Heck, A. Hoffmann, S. Herres-Pawlis, *Chem. Commun.* **2025**.
3. D. Herrmann, P. Hodapp, M. Starman, P.-C. Huang, C.-L. Lin, L. B. Q. Le, T. G. Fischer, C. Bizzarri, P. Röse, N. Oppel, J. Klar, P. Tremouilhac, L. Holzhauer, S. Herres-Pawlis, A. Hoffmann, **T. Seitz**, A. Dorn, K. Zeitler, N. Jung, S. Bräse, *Chem. Sci.* **2025**, *16*, 4430-4441.

Presentations

1. 5. Ligandendesignworkshop, *Entatic Model Complexes of Tripodal Guanidine Ligands,* 2022, Cologne (Germany).
2. Tag der Chemie, *Kupferkomplexe für den biomimetischen Elektronentransfer*, 2023, Aachen (Germany).
3. 17. European Biological Inorganic Chemistry Conference, *Challenges of Modelling Active Sites of Type-0 Copper Proteins with Tripodal Triarylamine Ligands*, flash presentation, 2024, Münster (Germany).

Posters

1. 17. European Biological Inorganic Chemistry Conference, *Challenges of Modelling Active Sites of Type-0 Copper Proteins with Tripodal Triarylamine Ligands*, 2024, Münster (Germany).
2. 32. International Conference on Photochemistry, *Entatic State Model Systems in Copper Photochemistry*, 2025, Aachen (Germany).

Abstract

Copper represents a highly versatile redox-active metal whose facile Cu(I/II) interconversion is accompanied by distinct coordination geometries. Controlling the resulting structural reorganization through ligand architecture is the basis for increasing the efficiency of natural copper proteins. The steric restriction and rigid coordination sphere that results from this steric control is also known an entatic state. The guanidine quinolinyl ligands provide a suitable scaffold for such studies, as guanidine substituents allow systematic variation of steric bulk and donor strength while the quinolinyl backbone ensures structural rigidity. In the first part of this work, coordination-variant models using tripodal tetradentate guanidine quinolinyl ligands were studied. Their tetracoordinate Cu(I) complexes were found to adopt a rare umbrella distorted trigonal-pyramidal geometry that increases with guanidine substitution. The corresponding Cu(II) species were found to expand their coordination sphere, yielding penta-coordinate structures that were further investigated by DFT calculations. Cyclic voltammetry and stopped-flow measurements revealed quasi-reversible redox processes involving conformational changes and small self-exchange rate constants. The complexes follow an addition-oxidation pathway rather than the predominantly observed oxidation-addition sequence, indicating that the observed umbrella distortion in the Cu(I) state can be utilized to manipulate electron transfer mechanisms. The second part of the thesis focuses on coordination-invariant $[Cu(GUAqu)_2]^{+/2+}$ systems with sp^2-hybridized substituents. X-ray diffraction and computational analysis revealed several conformers of the phenyl-substituted $[Cu(TMG2Phqu)_2]^+$ complex, yet cyclic voltammetry showed similar redox potentials for both oxidation states, implying a common redox-active conformer. Correlation of charge-transfer energies with redox potentials demonstrated that structural rather than electronic factors dominate the redox behavior. Kinetic investigations confirmed that minimized internal reorganization in the phenyl-substituted complex affords the fastest self-exchange rate among comparable systems. The third part of the thesis extends the entatic concept to photoexcited states. DFT and transient XAFS studies established that increased steric bulk suppresses flattening distortions and prolongs triplet lifetimes. Electrochemical and spectroscopic data revealed highly negative redox potentials and short-lived but reactive excited states. All complexes exhibited measurable activity in atom transfer radical addition reactions, with yields scaling with expected lifetimes.

Kurzzusammenfassung

Kupfer stellt ein vielseitiges redoxaktives Metall dar, dessen Übergang zwischen den Oxidationsstufen +I und +II mit deutlichen Änderungen der Koordinationsgeometrie verbunden ist. Die resultierende Reorganisationsenergie kann durch gezieltes Ligandendesign minimiert werden, indem sterische Einflüsse die Koordinationsgeometrie beider Oxidationszustände einschränken. Die so entstehende starre, spannungsbehaftete Koordinationsumgebung wird als entatischer Zustand bezeichnet. Guanidin-Chinolinyl-Liganden sind dabei für Modellsysteme von Nutzen, da durch ihre sterischen und elektronischen Eigenschaften durch geeignete Substituenten angepasst werden können. Im ersten Teil der Arbeit wurden Kupferkomplexe mit koordinationsvariablen tripodalen, tetradentaten Guanidin-Chinolinyl-Liganden beschrieben. Röntgenstrukturanalysen der Cu(I)-Komplexe zeigten, dass diese über eine trigonal-pyramidale Struktur mit einer seltenen Regenschirmverzerrung verfügen, deren Ausprägung mit zunehmender Substitution von Guanidinresten stärker wird. Nach Oxidation entstehen pentakoordinate Cu(II)-Komplexe, die mittels DFT-Rechnungen eingehender untersucht wurden. Zyklovoltammetrische und zeitaufgelöste kinetische Untersuchungen ergaben quasi-reversible Redoxprozesse, die mit Konformationsänderungen und geringen Selbstaustauschraten verbunden sind. Der beobachtete Additions-Oxidations-Mechanismus, der von der üblichen Oxidations-Additions-Abfolge abweicht, weist darauf hin, dass die beobachtete Regenschirmverzerrung im Cu(I)-Zustand gezielt zur Steuerung von Elektronentransferprozessen genutzt werden kann. Im zweiten Teil der Arbeit wurden koordinationsinvariante $[Cu(GUAqu)_2]^{+/2+}$ Komplexe mit sp^2-hybridisierten Substituenten für den thermischen Elektronentransfer untersucht. Der Einfluss der strukturellen und sterischen Faktoren auf die Redoxpotentiale der untersuchten Systeme scheint dabei wichtiger zu sein als elektronische Faktoren, wie eine Korrelation von theoretisch erhaltenen Ladungstransferenergien mit den empirischen Redoxpotentialen nahelegt. Kinetische Untersuchungen bestätigten, dass die verringerte innere Reorganisationsenergie des phenylsubstituierten Redoxpaars $[Cu(TMG2Phqu)_2]^{+/2+}$ zur höchsten Selbstaustauschrate innerhalb der untersuchten Systeme führt. Im dritten Teil der Arbeit lag wurde das Konzept des entatischen Zustands auf die Cu-Photochemie übertragen. DFT- und zeitaufgelöste XAFS-Messungen zeigen, dass zunehmende sterischer Anspruch die Lebensdauer der angeregten Triplet-Zustände verlängert. Elektrochemische und spektroskopische Analysen ergaben stark negative Redoxpotentiale sowie kurzlebige, aber reaktive angeregte Zustände. Alle untersuchten Komplexe zeigten Aktivität in Atom-Transfer-Radikal-Additionen, deren Ausbeuten mit der Lebensdauer der angeregten Zustände korrelieren.

Danksagung

Mein Dank gebührt einer langen Liste von Leuten, ohne die diese Arbeit nicht möglich gewesen wäre.

Zuallererst möchte ich mich bei Frau Prof. Dr. Sonja Herres-Pawlis für die Möglichkeit bedanken, meine Dissertation in ihrem Arbeitskreis anzufertigen. Neben dem regen fachlichen Austausch möchte ich mich darüber hinaus auch noch für ihre stets gute Beratung und ihr stetes Vertrauen in mich herzlich bedanken! Die mir so eröffneten Freiheiten und Möglichkeiten haben dazu beigetragen, mein Wissen weiter zu vertiefen und die erfolgreiche Arbeit in diesem Arbeitskreis und dem Themenfeld des Elektronentransfers erst ermöglicht. Ich bin zudem dankbar für die Eindrücke, die ich auf mehreren Konferenzen sammeln konnte und die diese Arbeit mit neuen Impulsen bereichert haben.

Ich möchte mich zudem bei Herrn Prof. Dr. Okuda für die Übernahme des Zweitgutachtens dieser Arbeit bedanken.

Des Weiteren danke ich Dr. Alexander Hoffmann für die breit aufgestellte Unterstützung im Laboralltag, die zahlreichen Korrekturen wissenschaftlicher Arbeiten, das Lösen technischer Probleme und nicht zuletzt für Hilfe beim Lösen von Kristallstrukturen.

Weiterhin möchte ich mich auch bei Prof. Dr. Michael Rübhausen und seinen Mitarbeiter*innen von der Universität Hamburg und dem Center for Free-Electron Laser Science (CFEL), Dr. Tomke Glier, Malte van Heek, Patrick Klein und Mika Rerrer, für die exzellente Gastfreundschaft und die spannende und konstruktive Zusammenarbeit im Bereich der transienten Spektroskopie, sowie für das Messen der transienten XAFS-Spektren bedanken. Die gemeinsamen Messzeiten und der interdisziplinäre Austausch von Fachwissen waren mir eine große Freude und ein Privileg.

Mein Dank gilt auch allen technischen Angestellten des Instituts für Anorganische Chemie. Besonders möchte ich mich bei Herrn Dr. Gehard Fink und Frau Rachida Bomaharat für das Messen der NMR-Proben bedanken. Bei Frau Brigitte Pütz und der MS-Abteilung des IOC möchte ich mich für das Messen der ESI-MS Spektren bedanken.

Für das Messen der Kristallstrukturen möchte ich mich bei Dr. Henrika Hüppe, Felix Garg und Vitali Sidorin bedanken.

Claudia Nelleßen und Gwenda Golm danke ich für die organisatorische Unterstützung im Arbeitskreis sowie ihre stetige Hilfsbereitschaft und Hilfestellung bei Finanz- und Verwaltungsfragen.

Ein großer Dank gilt den in meiner Zeit aktiven Mitarbeiter*innen des gesamten Arbeitskreises Herres-Pawlis für eine angenehme und eine konstruktive Arbeitsatmosphäre. Speziell möchte ich mich bei meinen vielen Kolleg*innen aus Labor 003, Dr. Fabian Thomas, Fabian Fink, Dr. Konstantin Kröckert, Dr. Regina Schmidt, Dr. Henrika Hüppe, Dr. Joshua Heck, Dr. Larissa Laurini, Fangfang Nie, Leander Weinelt, sowie Aylin Karabulut bedanken. Ganz besonders möchte ich mich bei Matthias Oster und Dominik Steden bedanken für die zahlreichen fachlichen Gespräche, die Hilfestellung bei theoretischen Zusammenhängen, die gute Musik und die guten Abende.

Als mein ehemaliger Praktikant sei Aylin an dieser Stelle noch einmal zusammen mit meinen anderen Praktikanten Marcel Walbeck, Rafael Suzuki und David O'Hagan, sowie meiner HiWi Sonja Liu für die tatkräftige Unterstützung meiner Forschung gedankt. Dahingehend möchte ich auch gerne Niclas Neumann und Sandra Oden danken, die mir ebenfalls punktuell mit Synthesen und weiterer Laborarbeit unter die Arme gegriffen haben.

Für das Korrekturlesen meiner Arbeit danke ich Matthias Oster, Dominik Steden, Volkan Sahin und Andrea Weßels.

Für die moralische Unterstützung und die Geduld bezüglich meiner Chemie-lastigen Gespräche möchte ich meinen Freunden danken.

Meinen Eltern Manuela und Klaus, sowie meiner Schwester Ramona danke ich für die bedingungslose Unterstützung innerhalb und außerhalb der Uni.

Zuletzt möchte ich meiner Partnerin Andrea Weßels danken; neben dem Korrekturlesen großer Teile dieser Arbeit und fachlicher Hilfe vor allem für die Motivation in schwierigen Phasen. Danke, dass du immer da bist!

“The difference between screwing around and science is writing it down.”

-Adam Savage

Abbreviations

ATR	attenuated total reflectance (FTIR)
ATRA	atom transfer radical addition
ATRP	atom transfer radical polymerization
Br	broad resonance (NMR)
^{c}Hex	cyclohexyl
C	complex
CC	comparison complex
CN	coordination number
d	doublet (NMR)
D	doublet state (multiplicity)
DCM	dichloromethane
DFT	density functional theory
DMEG	dimethylethyleneguanidine
EPR	electron paramagnetic resonance
eq.	equivalent
ESI	electron spray ionization (HRMS)
Et	ethyl
et al.	*et alia* (and others)
EXAFS	extended X-ray absorption fine structure spectroscopy
Fc	ferrocene
FTIR	Fourier transform infrared spectroscopy
GD3BJ	D3 version of Grimme's dispersion with Becke-Johnson damping
Gua/GUA	guanidine
GUAqu	guanidine quinolinyl ligand
HRMS	high-resolution mass spectrometry
IC	internal conversion
IR	infrared
ISC	intersystem crossing
J	coupling constant (NMR)
LC	ligand centered
LF	ligand field
LMCT	ligand-to-metal charge-transfer
m	multiplet (NMR), medium (FTIR)
MC	metal centered
Me	methyl
MeCN	acetonitrile
Mee	methyl ester

MLCT	metal-to-ligand charge-transfer
MS	mass spectrometry
N_{Amine}	amine nitrogen donor
NBO	natural bond orbital (DFT)
N_{Gua}	guanidine nitrogen donor
NMR	nuclear magnetic resonance spectroscopy
N_{Qu}	quinoline nitrogen donor NTO natural transition orbital (DFT)
OQ	oxidative quenching
P	photo couple
PCM	polarizable continuum model (DFT)
Ph	phenyl
PXRD	powder X-ray diffraction
Qu/qu	quinoline
R	redox couple
R_f	retardation factor
RMSD	root-mean-square deviation
rt	room temperature
RQ	reductive quenching
s	singlet (NMR), strong (FTIR)
S	singlet state (multiplicity)
SCXRD	single-crystal X-ray diffraction
t	triplet (NMR) t Bu tert-butyl
T	tripet state (multiplicity)
TADF	thermally activated delayed fluorescence
TD	time-dependent (DFT)
THF	tetrahydrofuran
TMG	tetramethylguanidine
UV/Vis	ultraviolet/visible
vs	very strong (FTIR)
VS	Vilsmeier salt
vw	very weak (FTIR)
w	weak (FTIR)
XAFS	X-ray absorption fluorescence spectroscopy
XANES	X-ray absorption near-edge structure spectroscopy
XAS	X-ray absorption spectroscopy
Z	number of formula units per unit cell (SCXRD)

Lists of Compounds

List of Ligands

Ligand	Abbreviation (label)
2-(2-(Bis(2-methylquinolin-8-yl)amino)phenyl)-1,1,3,3-tetramethylguanidine	$N(QuMe)_2(PhTMG)$ (**$L1_{TMG}$**)*
N-(2-((1,3-dimethylimidazolidin-2-ylidene)amino)phenyl)-2-methyl-*N*-(2-methylquinolin-8-yl)quinolin-8-amine	$N(QuMe)_2(PhDMEG)$ (**$L1_{DMEG}$**)
2',2'-(((2-Methylquinolin-8-yl)azanediyl)bis(2,1-phenylene))bis(1,1,3,3-tetramethylguanidine)	$N(QuMe)(PhTMG)_2$ (**$L2_{TMG}$**)*
N,*N*-bis(2-((1,3-dimethylimidazolidin-2-ylidene)amino)phenyl)-2-methylquinolin-8-amine	$N(QuMe)(PhDMEG)_2$ (**$L2_{DMEG}$**)
2',2'',2''-(Nitrilotris(benzene-2,1-diyl))tris(1,1,3,3-tetramethylguanidine)	$TMG_3trphen$ (**$L3_{TMG}$**)#
Tris(2-((1,3-dimethylimidazolidin-2-ylidene)amino)phenyl)amine	$DMEG_3trphen$ (**$L3_{DMEG}$**)
Methyl 8-(di(quinolin-8-yl)amino)quinoline-2-carboxylate	$N(QuMee)(Qu)_2$ (**L4**)
2-(2-(Dimethylamino)quinolin-8-yl)-1,1,3,3-tetramethylguanidine	$TMG2NMe_2qu$ (**L5**)
1,1,3,3-Tetramethyl-2-(2-phenylquinolin-8-yl)guanidine	TMG2Phqu (**L6**)
2-(2-(1*H*-pyrrol-1-yl)quinolin-8-yl)-1,1,3,3-tetramethylguanidine	TMG2Pyqu (**L7**)
1,1,3,3-Tetramethyl-2-(quinolin-8-yl)guanidine	TMGqu (**L8**)#a
1,1,3,3-tetramethyl-2-(2-methylquinolin-8-yl)guanidine	TMG2Mequ (**L9**)#a
2-(2-Cyclohexylquinolin-8-yl)-1,1,3,3-tetramethylguanidine	$TMG2^cHexqu$ (**L10**)#a

*: Reported in the master thesis of Tobias Seitz and resynthesized for this work. #: Resynthesized, a: Synthesized and provided by coworkers.

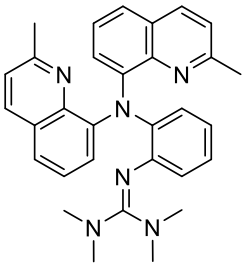

N(QuMe)$_2$(PhTMG)
(**L1$_{TMG}$**)

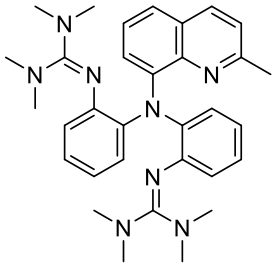

N(QuMe)(PhTMG)$_2$
(**L2$_{TMG}$**)

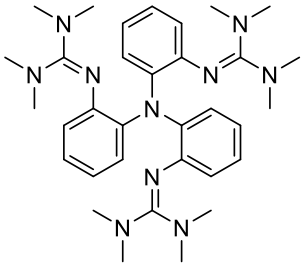

TMG$_3$trphen
(**L3$_{TMG}$**)

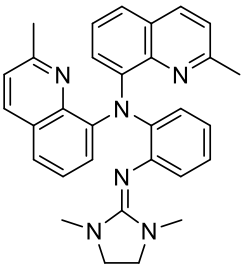

N(QuMe)$_2$(PhDMEG)
(**L1$_{DMEG}$**)

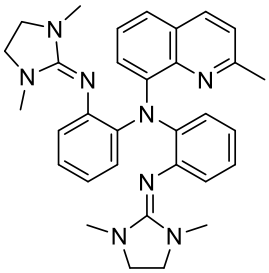

N(QuMe)(PhDMEG)$_2$
(**L2$_{DMEG}$**)

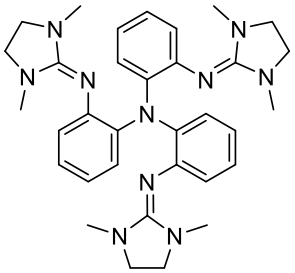

DMEG$_3$trphen
(**L3$_{DMEG}$**)

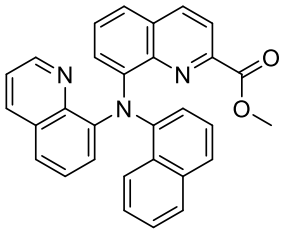

N(QuMee)(Qu)$_2$
(**L4**)

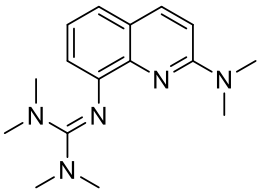

TMG2NMe$_2$qu (**L5**)

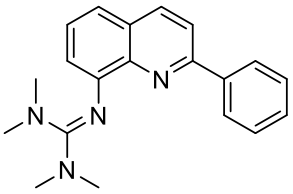

TMG2Phqu (**L6**)

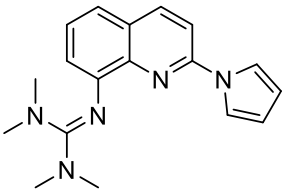

TMG2Pyqu (**L7**)

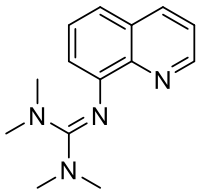

TMGqu (**L8**)

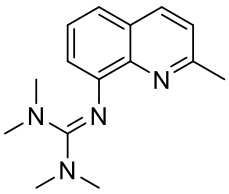

TMG2Mequ (**L9**)

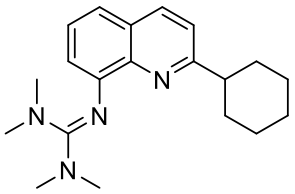

TMG2^{c}Hexqu (**L10**)

List of Complex Salts

Ligand (label)	Complex cation (label)	Complex salt (label)
$N(QuMe)_2(PhTMG)$ (**$L1_{TMG}$**)*	$[Cu\{N(QuMe)_2(PhTMG)\}]^+$ (**$C1_{TMG}$**)	$[Cu\{N(QuMe)_2(PhTMG)\}]PF_6$ (**$C1_{TMG}$–PF_6**)*
	$[Cu\{N(QuMe)_2(PhTMG)\}(MeCN)]^{2+}$ (**$C2_{TMG}$**)	-
$N(QuMe)_2(PhDMEG)$ (**$L1_{DMEG}$**)	$[Cu\{N(QuMe)_2(PhDMEG)\}]^+$ (**$C1_{DMEG}$**)	$[Cu\{N(QuMe)_2(PhDMEG)\}]PF_6$ (**$C1_{DMEG}$–PF_6**)
	$[Cu\{N(QuMe)_2(PhDMEG)\}(MeCN)]^{2+}$ (**$C2_{DMEG}$**)	-
$N(QuMe)(PhTMG)_2$ (**$L2_{TMG}$**)*	$[Cu\{N(QuMe)(PhTMG)_2\}]^+$ (**$C3_{TMG}$**)	$[Cu\{N(QuMe)(PhTMG)_2\}]PF_6$ (**$C3_{TMG}$–PF_6**)*
	$[Cu\{N(QuMe)(PhTMG)_2\}(MeCN)]^{2+}$ (**$C4_{TMG}$**)	-
$N(QuMe)(PhDMEG)_2$ (**$L2_{DMEG}$**)	$[Cu\{N(QuMe)(PhDMEG)_2\}]^+$ (**$C3_{DMEG}$**)	$[Cu\{N(QuMe)(PhDMEG)_2\}]PF_6$ (**$C3_{DMEG}$–PF_6**)
	$[Cu\{N(QuMe)(PhDMEG)_2\}(MeCN)]^{2+}$ (**$C4_{TMG}$**)	-
$TMG_3trphen$ (**$L3_{TMG}$**)	$[Cu(TMG_3trphen)]^+$ (**$C5_{TMG}$**)	$[Cu(TMG_3trphen)]PF_6$ (**$C5_{TMG}$–PF_6**)#
	$[Cu(TMG_3trphen)(MeCN)]^{2+}$ (**$C6_{TMG}$**)	-
$DMEG_3trphen$ (**$L3_{DMEG}$**)	$[Cu(DMEG_3trphen)]^+$ (**$C5_{DMEG}$**)	$[Cu(DMEG_3trphen)]PF_6$ (**$C5_{DMEG}$–PF_6**)
	$[Cu(DMEG_3trphen)(MeCN)]^{2+}$ (**$C6_{DMEG}$**)	-
$TMG2NMe_2qu$ (**L5**)	$[Cu(TMG2NMe_2qu)_2]^+$ (**C7**)	$[Cu(TMG2NMe_2qu)_2]PF_6$ (**C7–PF_6**)
	$[Cu(TMG2NMe_2qu)_2]^{2+}$ (**C8**)	$[Cu(TMG2NMe_2qu)_2](OTf)_2$ (**C8–OTf**)
TMG2Phqu (**L6**)	$[Cu(TMG2Phqu)_2]^+$ (**C9**)	$[Cu(TMG2Phqu)_2]PF_6$ (**C9–PF_6**)
	$[Cu(TMG2Phqu)_2]^{2+}$ (**C10**)	$[Cu(TMG2Phqu)_2](OTf)_2$ (**C10–OTf**)
TMGqu (**L8**)	$[Cu(TMGqu)_2]^+$ (**C11**)	$[Cu(TMGqu)_2]PF_6$ (**C11–PF_6**)#
	$[Cu(TMGqu)_2]^{2+}$ (**C12**)	-
TMG2Mequ (**L9**)	$[Cu(TMG2Mequ)_2]^+$ (**C13**)	$[Cu(TMG2Mequ)_2]PF_6$ (**C13–PF_6**)#
	$[Cu(TMG2Mequ)_2]^{2+}$ (**C14**)	-
$TMG2^cHexqu$ (**L10**)	$[Cu(TMG2^cHexqu)_2]^+$ (**C15**)	$[Cu(TMG2^cHexqu)_2]PF_6$ (**C15–PF_6**)#
	$[Cu(TMG2^cHexqu)_2]^{2+}$ (**C16**)	-

*: Reported in the master thesis of Tobias Seitz and resynthesized for this work. #: Resynthesized.

List of Labels for Crystallized Complexes

Precipitated complex salt (label)	Crystallized complex salt (label)
$[Cu\{N(QuMe)_2(PhTMG)\}]PF_6$ (**$C1_{TMG}$–PF_6**)	$[Cu\{N(QuMe)_2(PhTMG)\}]PF_6 \cdot MeCN$ (**$C1_{TMG}$–PF_6·MeCN**)*
$[Cu\{N(QuMe)_2(PhDMEG)\}]PF_6$ (**$C1_{DMEG}$–PF_6**)	$[Cu\{N(QuMe)_2(PhDMEG)\}]PF_6 \cdot MeCN$ (**$C1_{DMEG}$–PF_6·MeCN**)
$[Cu\{N(QuMe)(PhTMG)_2\}]PF_6$ (**$C3_{TMG}$–PF_6**)	$[Cu\{N(QuMe)(PhTMG)_2\}]PF_6 \cdot DCM \cdot C_5H_{12}$ (**$C3_{TMG}$–PF_6·DCM·C_5H_{12}**)*
$[Cu\{N(QuMe)(PhDMEG)_2\}]PF_6$ (**$C3_{DMEG}$–PF_6**)	$[Cu\{N(QuMe)(PhDMEG)_2\}]PF_6 \cdot DCM$ (**$C3_{DMEG}$–PF_6·DCM**)
$[Cu(DMEG_3trphen)]PF_6$ (**$C5_{DMEG}$–PF_6**)	$[Cu(DMEG_3trphen)]PF_6 \cdot DCM$ (**$C5_{DMEG}$–PF_6·DCM**)
$[Cu(TMG2NMe_2qu)_2]PF_6$ (**C7–PF_6**)	$[Cu(TMG2NMe_2qu)_2]PF_6 \cdot 2\ DCM$ (**C7–PF_6·DCM**)
$[Cu(TMG2NMe_2qu)_2](OTf)_2$ (**C8–OTf**)	$[Cu(TMG2NMe_2qu)_2](OTf)_2$ (**C8–OTf**)
$[Cu(TMG2Phqu)_2]PF_6$ (**C9–PF_6**)	$[Cu(TMG2Phqu)_2]PF_6 \cdot DCM$ (**C9–PF_6·DCM**)
$[Cu(TMG2Phqu)_2](OTf)_2$ (**C10–OTf**)	$[Cu(TMG2Phqu)_2](OTf)_2 \cdot 0.5\ H_2O$ (**C10–OTf·H_2O**)

*: Reported in the master thesis of Tobias Seitz.

List of Redox Couples

Ligand (label)	Constituting complex cations (label)	Redox couple label
$N(QuMe)_2(PhTMG)$ (**$L1_{TMG}$**)*	$[Cu\{N(QuMe)_2(PhTMG)\}]^+$ (**$C1_{TMG}$**) $[Cu\{N(QuMe)_2(PhTMG)\}(MeCN)]^{2+}$ (**$C2_{TMG}$**)	**$R1_{TMG}$**
$N(QuMe)_2(PhDMEG)$ (**$L1_{DMEG}$**)	$[Cu\{N(QuMe)_2(PhDMEG)\}]^+$ (**$C1_{DMEG}$**) $[Cu\{N(QuMe)_2(PhDMEG)\}(MeCN)]^{2+}$ (**$C2_{DMEG}$**)	**$R1_{DMEG}$**
$N(QuMe)(PhTMG)_2$ (**$L2_{TMG}$**)*	$[Cu\{N(QuMe)(PhTMG)_2\}]^+$ (**$C3_{TMG}$**) $[Cu\{N(QuMe)(PhTMG)_2\}(MeCN)]^{2+}$ (**$C4_{TMG}$**)	**$R2_{TMG}$**
$N(QuMe)(PhDMEG)_2$ (**$L2_{DMEG}$**)	$[Cu\{N(QuMe)(PhDMEG)_2\}]^+$ (**$C3_{DMEG}$**) $[Cu\{N(QuMe)(PhDMEG)_2\}(MeCN)]^{2+}$ (**$C4_{TMG}$**)	**$R2_{DMEG}$**
$TMG_3trphen$ (**$L3_{TMG}$**)	$[Cu(TMG_3trphen)]^+$ (**$C5_{TMG}$**) $[Cu(TMG_3trphen)(MeCN)]^{2+}$ (**$C6_{TMG}$**)	**$R3_{TMG}$**
$DMEG_3trphen$ (**$L3_{DMEG}$**)	$[Cu(DMEG_3trphen)]^+$ (**$C5_{DMEG}$**) $[Cu(DMEG_3trphen)(MeCN)]^{2+}$ (**$C6_{DMEG}$**)	**$R3_{DMEG}$**
TMG2NMe$_2$qu (**L5**)	$[Cu(TMG2NMe_2qu)_2]^+$ (**C7**) $[Cu(TMG2NMe_2qu)_2]^{2+}$ (**C8**)	**R4**
TMG2Phqu (**L6**)	$[Cu(TMG2Phqu)_2]^+$ (**C9**) $[Cu(TMG2Phqu)_2]^{2+}$ (**C10**)	**R5**
TMGqu (**L8**)	$[Cu(TMGqu)_2]^+$ (**C11**) $[Cu(TMGqu)_2]^{2+}$ (**C12**)	**R6**
TMG2Mequ (**L9**)	$[Cu(TMG2Mequ)_2]^+$ (**C13**) $[Cu(TMG2Mequ)_2]^{2+}$ (**C14**)	**R7**
TMG2^{c}Hexqu (**L10**)	$[Cu(TMG2^cHexqu)_2]^+$ (**C15**) $[Cu(TMG2^cHexqu)_2]^{2+}$ (**C16**)	**R8**

List of Photo Couples

Ligand (label)	Constituting complex cations (label)	State (abbreviation)	Redox couple label
TMGqu (**L8**)	$[Cu(TMGqu)_2]^+$ (**C11**)	Singlet ground state (S_0)	**P1**
	$[Cu(TMGqu)_2]^{+*}$	Triplet state (T_1)	
TMG2Mequ (**L9**)	$[Cu(TMG2Mequ)_2]^+$ (**C13**)	Singlet ground state (S_0)	**P2**
	$[Cu(TMG2Mequ)_2]^{+*}$	Triplet state (T_1)	
TMG2^{c}Hexqu (**L10**)	$[Cu(TMG2^cHexqu)_2]^+$ (**C15**)	Singlet ground state (S_0)	**P3**
	$[Cu(TMG2^cHexqu)_2]^{+*}$	Triplet state (T_1)	

List of Figures

List of Schemes

List of Tables

Table of Contents

1 Introduction

1.1 Bioinorganic and Bioinspired Chemistry

Many of the chemical processes inside organisms hinge on the properties of enzymes and other proteins to transport substances through the body or catalyze challenging reactions under mild conditions. While many of these biomolecules function exclusively without metals, a considerable number of proteins feature metal centers in their active site.[1] These so-called metalloproteins are studied in the field of bioinorganic chemistry, an interdisciplinary field between biochemistry and inorganic chemistry, concerning their reactions and possible structure-property relationships.

However, the study of proteins is challenging due to their large molecular masses and labile structures with high sensitivity towards fluctuations in pH and temperature.[2] While the steady increase of computing power and number of analytical methods help in this regard, bioinorganic chemists also use smaller molecules, so-called model systems, to replicate the properties of the active site.[3-4] These model systems are usually more resilient and can hence be analyzed by a wider array of analytic methods. They also enable the generalization of the highly selective reactivities of enzymes and proteins for technical or industrial applications. The increasingly frequent transfer of bioinorganic concepts and model systems to topics that are only distantly related to bioinorganic chemistry has led to the term of “bioinspired” chemistry to gain traction in literature.[5] Bioinspired chemistry might be more detached from the biochemical origin, the concepts and compounds it uses, but is nevertheless dependent on bioinorganic research on the behavior and properties of bound metals in metalloproteins. Due to bioavailability, the most common metals found in enzymes are generally iron, zinc or copper.[6]

1.2 Copper in Coordination and Bioinorganic Chemistry

Copper is the third most abundant metal found in the human body and one of the most abundant trace elements found in all living organisms, serving many different functions.[7] These stem from its special redox and coordination-chemical properties which arise from the electronic structures of its two most prevalent oxidation states, Cu(I) and Cu(II).[8-11]

Cu(I) is unstable in aqueous media, where it disproportionates into Cu(0) and Cu(II). However, this stability can be significantly enhanced by complexation of the Cu(I) cation. For example, adding ammonia to an aqueous solution of Cu(I) leads to the formation of the stable $[Cu(I)(NH_3)_2]^+$ complex.[12] This circumstance allows for a rich chemistry of Cu(I) in aqueous media. Cu(I) is a d^{10} ion, it therefore does not experience

ligand field stabilization energy.[11] This results in many different coordination geometries that have been reported for Cu(I) coordination compounds which mostly depend on the geometry and denticity of the ligands. Tetracoordinate Cu(I) complexes usually lie between a tetrahedral, a square planar or a trigonal pyramidal coordination geometry, depending on the steric strain and scaffolding of the employed ligands.[13] While pentacoordinate Cu(I) complexes are rare, there are examples for them, usually using chelate ligands.[14]

Cu(II), in turn, is a d^9 ion. It therefore exhibits geometric preferences based on the ligand field stabilization energy and thus usually adopts either axially distorted (bi)pyramidal or square planar geometries.[11-12] Despite this, steric strain and carefully crafted ligands can also enforce Cu(II) complexes with trigonal bipyramidal and tetrahedral geometries.[15-18]

Besides the different preferences concerning the coordination geometry of both oxidation states, they also show different donor-atom affinities according to the hard-soft-acid-base (HSAB) principle.[19-21] Cu(I), classified as a soft acid, interacts more favorably with softer donors like sulfur and phosphorus.[11, 20] Contrary to this, Cu(II), a borderline hard acid, slightly favors interactions with hard bases like oxygen.[11, 20] Nitrogen-donors and their corresponding ligands show to interact favorably with both oxidation states; N-donor chemistry therefore comprises a large part of the reported Cu(I) and Cu(II) coordination compounds.[11] This discrepancy between the preferred coordination geometries and donor atoms of both ions makes it possible to strongly influence the redox potential of a Cu(I/II) redox couple by constructing certain coordination geometries and ligand spheres that predominantly stabilize or destabilize one oxidation state.[10, 22-23] Due to its more strict geometric constraints and higher charge, Cu(II) is more sensitive towards changes in the coordination sphere than Cu(I).[10, 24] Therefore, geometries that are on average more tetrahedral and use softer donors enforce more oxidizing potentials.[10, 24] The two variables of coordination geometry and donor-preference result in the Cu(I/II) redox couple exhibiting a wide range of redox potentials from −0.66 to 0.89 V against a standard hydrogen electrode (SHE) to be known in aqueous media.[10, 24-25]

Next to these two oxidation states, Cu can also be found in the Cu(0) and Cu(III) state. While Cu(0) is largely unimportant in coordination or bioinorganic chemistry, the Cu(III) oxidation state can be stabilized with hard Lewis bases like O- or F-donors and adopts the square-planar and square-pyramidal coordination geometries typical for d^8 ions.[11-12] The characterization of Cu(III) as such is, however, not undisputed and usually considered to be formal.[26]

The versatile coordination chemistry of copper renders it a useful metal center not only for chemists but organisms as well. As such, copper containing metalloproteins are

important for the function of many biological processes, mostly using the Cu(I/II) redox pair and its variable redox potentials.[9, 27] They frequently serve as catalysts for redox reactions in oxidases and oxygenases, where the ion is bound in mononuclear centers with one or two labile aqua ligands.[28-30] Dinuclear copper centers can be found in hemocyanins that serve as dioxygen shuttles in arthropods and mollusks.[31-32] They are also found in the enzyme tyrosinase, where they play a central part in the synthesis of melanin by mediating the hydroxylation and subsequent oxidation of L-tyrosine to L-dopaquinone.[33-34] The mononuclear blue copper proteins like plastocyanin, on the other hand, are electron transfer proteins and serve as electron shuttles in photosynthesis, facilitating rapid electron transfer reactions.[35-38] The active site of these copper proteins is coordinated by two histidines, one cysteinate (Cys) and one distally coordinating methionine (Met) donor in the axial position (Figure 1.1). The resulting distorted tetrahedral coordination geometry is both unusual and very similar for both Cu(I) and Cu(II).[11, 36]

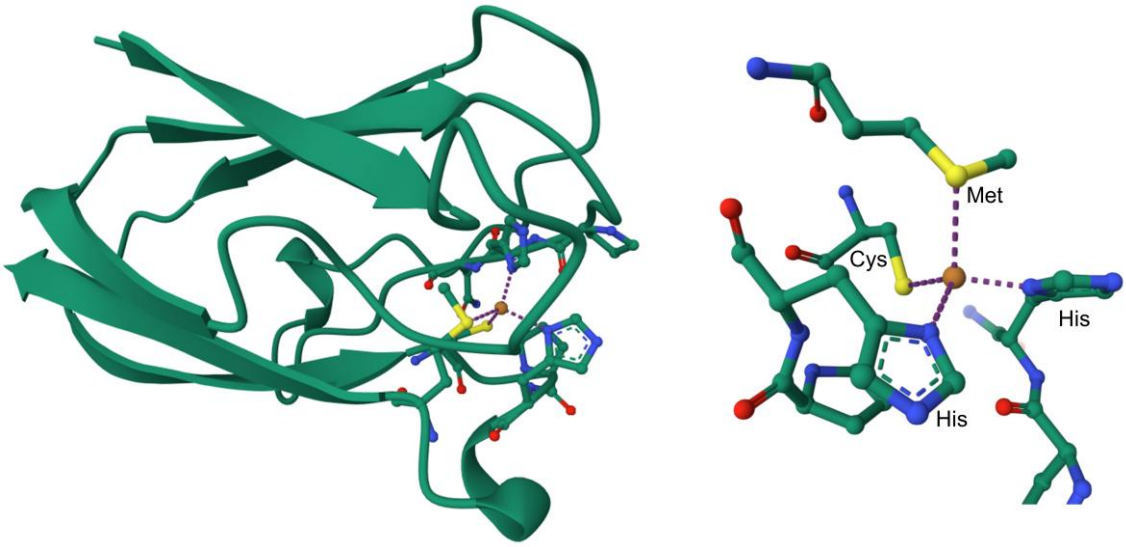

Figure 1.1: Solid state structure of plastocyanin (left) and the protein's active site (right).[39]

The peculiar geometry of the Cu(I/II) redox pair in blue copper proteins has been frequently cited as a reason for their rapid electron transfer rates and exhibit rate constants ranging from 10^3 to 10^6 M^{-1} s^{-1}.[35, 40-43] It is theorized that the distorted coordination environment exerts strain on both oxidation states, in turn minimizing the internal kinetic barrier for a redox reaction. This strained state the active site is found in is therefore often referred to as an entatic or rack-induced state.[44-46]

1.3 The Entatic State Concept

“Entasis” is a Greek term meaning “stretched” or “under tension” and originated in architecture over two millennia ago. It refers to an effect where columns with a convex curvature show improved stability due to an increased strength-to-weight ratio compared to parallel columns.[47] The transfer of the concept to bioinorganic chemistry was first done by Vallee and Williams in the 1950s; resulting in the creation of the term “entatic state” in 1968.[42-43] The original concept applies to any active site of a protein, metal or non-metal, that displays a distorted or energized state, even in the absence of substrate, that serves to increase the active site’s activity. Over time, this definition was narrowed down to bound metals in metalloproteins and complexes that catalyze electron transfer reactions where it shows most frequent use.[3, 42-43] The original notion of the entatic state by Vallee and Williams defines the entatic state by a rigid protein framework enforcing the distorted geometry of the active site, therefore minimizing geometric changes by the bound metal’s oxidation. An alternative mechanism of energization has been formulated by Malmström in the form of rack-induced bonding.[45-46] Here, the energization originates from the interplay between the protein matrix causing coordinative strain on the metal and *vice versa*; requiring a certain degree of flexibility from the protein matrix as opposed to a rigid coordination sphere. A more general definition was proposed by Comba, who defined the entatic state ‘‘as the energization due to a misfit” between ligands and metal ions or ‘‘between complex fragments and the corresponding substrate–catalyst complexes”.[48] This energization is occurring for both, the starting state and product state of the reaction, relative to the transition state, lowering the kinetic barrier (see Figure 1.2 for a visualization).

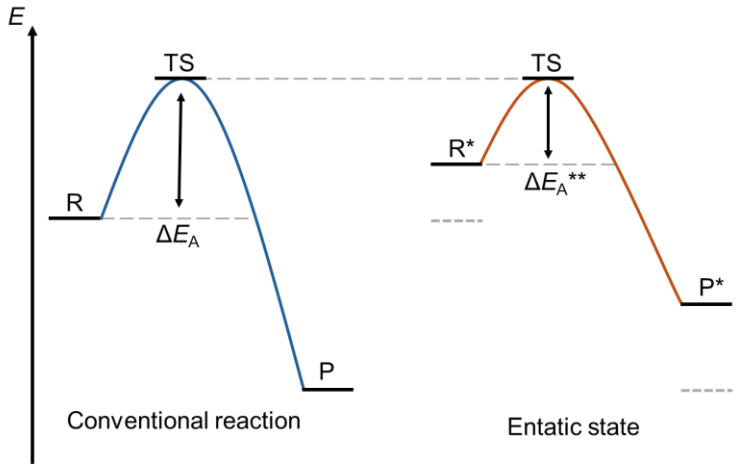

Figure 1.2: Schematic illustration of the energization in the entatic state. Entasis energizes the reagent (R) and product (P) state, lowering the activation barrier (DEA) without changing the energy of the transition state (TS).

A commonly used example for the entatic state is the aforementioned plastocyanin, a blue copper protein with a distorted coordination geometry of the active site. According

to the entatic state as discussed to this point, the protein's high activity stems from the distortion and rigidity of its coordination sphere. However, the necessary energization can also stem from other factors, since electronic influences can impact entasis as well. Solomon *et al.* investigated the impact of the methionine and cysteinate donors in blue copper proteins and found that the axial and weak Cu–S_{Met} bond of the methionine residue is compensated by a shortened Cu–S_{Cys} bond.[36, 49-50] The resulting strong covalency of the copper–thiolate bond leads to a preference for trigonal distorted geometries of Cu(II) and thus facilitates rapid electron transfer. This phenomenon was described by Rorabacher *et al*. as an electronic entatic state.[51-52] The influence of the S-donor is not a singular occurrence and other strong π-donors like guanidines can alter the preferred geometry of Cu-cations as well, as demonstrated by multiple groups theoretically and experimentally.[53-56] The electronic influences are, however, not necessary for entasis, as reported by Gray *et al.* The group describes artificial copper proteins whose sulfur binding sites were exchanged for O-donors and which still showed enhanced electron transfer properties.[35, 57]

Over the past decades, the entatic state concept has also received substantial criticisms that especially focus on electron transfer proteins. Concerning plastocyanin and other blue copper proteins, Frank and Benfatto showed that their peculiar Cu–S_{Cys} bond is independent of a rigid protein framework and they criticized the general notion of geometric strain in these proteins.[56] In light of similar criticisms, Hagen hypothesized that the entatic state might be of marginal existence in biological systems and proposed a wide distribution of possible coordination geometries, a so-called ecstatic state, to achieve the desired activity.[58] In agreement with this hypothesis, Aravena and Lemus *et al.* reported a group of copper complexes of tetradentate ligands whose reactivity increases with the flexibility of the ligand scaffolding.[59] Alternatively, building on previous work with Savéant *et al.*, Hureau *et al.* proposed an in-between state that can be referred to as a compromise between the ecstatic and entatic state (see Figure 1.3 for a comparison of all three models).[60-61]

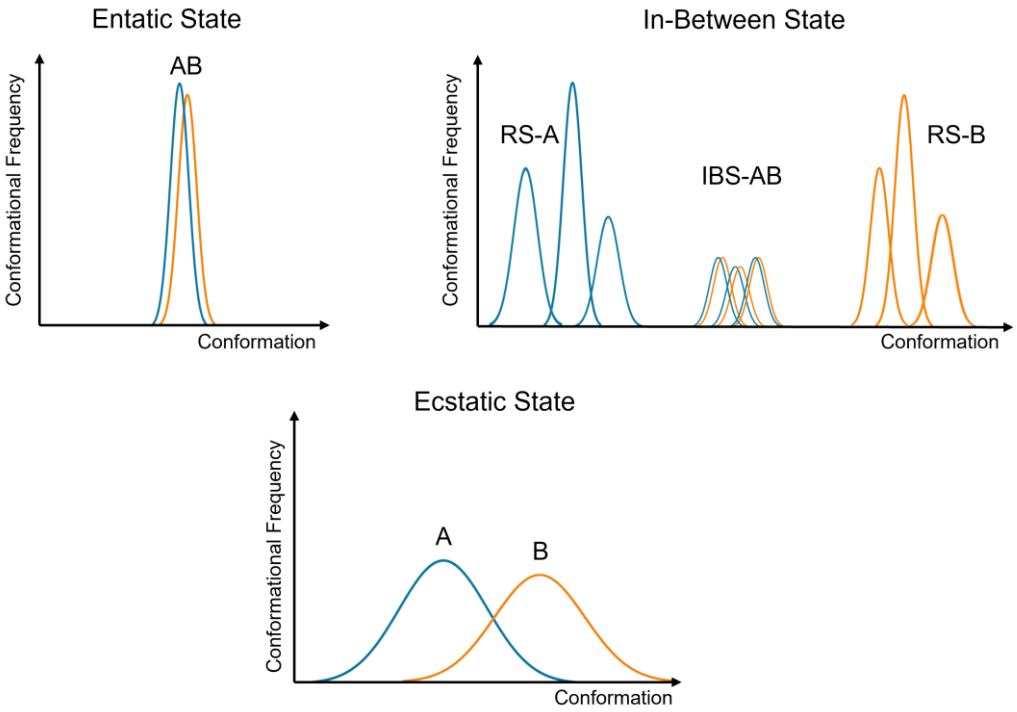

Figure 1.3: Comparison between the entatic state, ecstatic state and in-between state as plots of the conformational frequency vs. the conformation. Redox reaction from one state to the next can occur at the cross-sections of the curves. RS: Resting state, IBS: In-between state.[60]

With regard to blue copper proteins, charge delocalization also seems to affect electron transfer rates,[62] a finding that could be further demonstrated with complexes of redox-active ligands by Himmel *et al*.[63]

Partially due to these criticisms, the entatic state is less frequently used to describe the activity of electron transfer proteins. However, it is not obsolete and still applied in bioinorganic chemistry. In 2019, for example, Warren, Kräutler and co-workers reported that the B_{12} cofactors are in an entatic state that improves the reactivity of the bound Co(III) centers.[64] Crystallographic data of the free corrin ligand shows a distinct helical arrangement of the ring (Figure 1.4) that affects the donor-positions. This helicity is significantly less pronounced in the Co-bound structures and decreases from Co(I) to Co(III), implying increasing stress. The authors argue that this strain on the helical conformation functions like a spring, introducing strain to the Co(III)-bound corrins due to the metal's preference for octahedral coordination geometries. They infer that this strain weakens the metal center's axial positions and therefore aids the reactivity of B_{12}-dependent processes like homolytic Co–C bond cleavage.

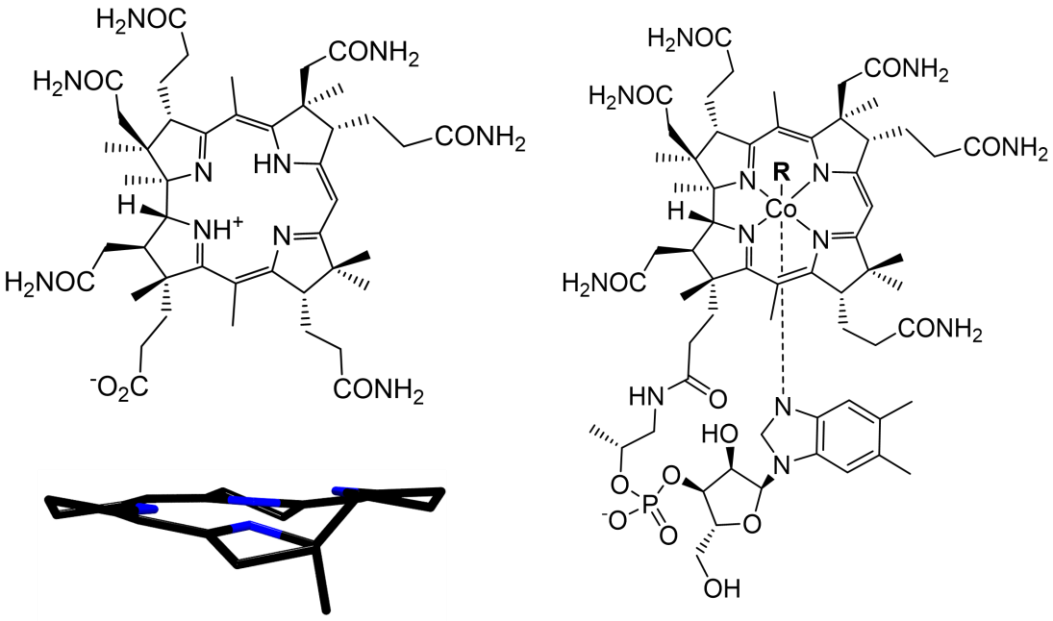

Figure 1.4: Left: Unbound corrin-ligand with a section of its solid-state structure that illustrates the donors' helical arrangement. Right: Co-bound corrin ligand. The previously visible helicity is not present in this complex.[64]

While the overall application of the entatic state concept in copper bioinorganic chemistry is receding, it remains popular in coordination chemistry, where it finds a broadening range of application.

1.4 The Entatic State in Model Systems and Coordination Compounds

To gather more insight into the entatic state in blue copper proteins, coordination compounds were used as model systems early on, as they are more resilient than proteins regarding changes in pH or temperature.[65] These models aim to bind Cu(I/II) in a geometry that is both rigid and not conforming to any of the ions' preferred geometries and by now constitute a vast library of structures.[37, 51, 66-70] The obtained copper complexes are evaluated on the basis of the achieved electron self-exchange rates k_{11} (more information on k_{11} in chapter 1.6), with the ideal rates ranging close to those of the blue copper proteins between 10^3 and 10^6 M^{-1} s^{-1}.[40-41] While the employed donors are usually limited to S-, N- and O-donors, the structural entasis is enforced by a wide variety of different ligand designs that can be roughly divided into coordination-variant and coordination-invariant (Figure 1.5 and 1.6, respectively).[4]

Rorabacher *et al.* have published a long list of coordination-variant blue copper protein models over the years, mostly focusing on macrocyclic and tripodal tetradentate ligand designs.[24, 51, 67, 70-74] These systems yield distorted structures for Cu(I) but tend to coordinate co-ligands from solution in Cu(II); a step that frequently leads to small k_{11} for many systems as well as deviating rates for the oxidation and reduction steps (Figure 1.5, for more info see Section 1.5).[70] These effects are, however, not

inherently linked to the change in coordination number (CN), as shown by Olshansky *et al.* They reported the $[CuCl(dpa^{SMe})]^{+/0}$ complex of a tripodal tetracoordinate ligand with a permanent chlorido co-ligand.[16] The central amine of the dpa^{SMe} ligand is a weak donor that allows a coordination-variant coordination sphere with marginal reorganization requirements. The obtained k_{11} on the order of 10^6 M^{-1} s^{-1} ranks it the fastest electron transfer system to date.

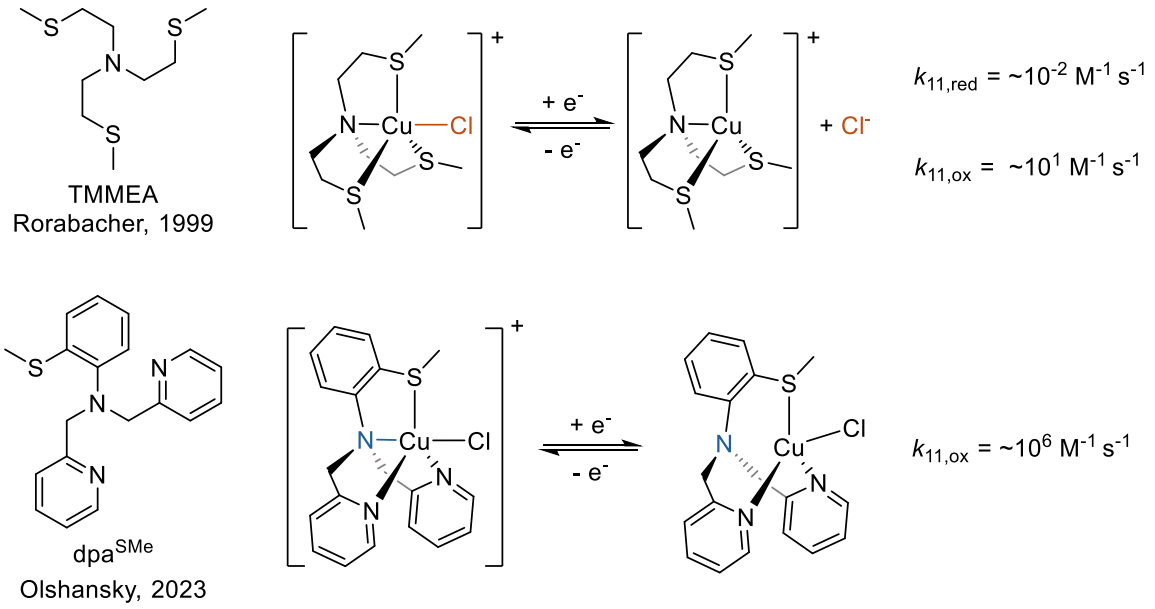

Figure 1.5: Illustration of two coordination-variant model systems, their coordination-variant behavior upon electron transfer as well as their reported self-exchange rates.[10, 16]

$[CuCl(dpa^{SMe})]^{+/0}$ is an effective yet atypical model system owing to its peculiar coordination-variant properties. Coordination-invariant model systems are more common in literature (Figure 1.6),[3, 75] as the conservation of the coordination number upon electron transfer simplifies the possible mechanistic steps and allows for structural comparison of both oxidation states via structural parameters like the τ_4 parameter.[76] This parameter serves to provide a simple estimate of whether a tetracoordinate structure is an ideal tetrahedron (τ_4 = 1), in an ideal square planar geometry (τ_4 = 0) or in-between. It is described via Equation 1.

$$\tau_4 = \frac{360° - \alpha - \beta}{141°} \quad (1)$$

Further information can be gained from comparing τ_4 between two oxidation states ($\Delta\tau_4$), indicating the degree of internal reorganization upon electron transfer.[77]

$$\Delta\tau_4 = \tau_4(\text{Cu(I)}) - \tau_4(\text{Cu(II)}) \quad (2)$$

An entatic redox pair should aim to have a small change in the observed structural parameter to indicate a low degree of internal reorganization. Next to τ_4 and its

derivatives there are further structural parameters, like the root mean square derivation of atomic positions (RMSD value), that can be used as well to provide a more nuanced evaluation of the entasis of model systems.

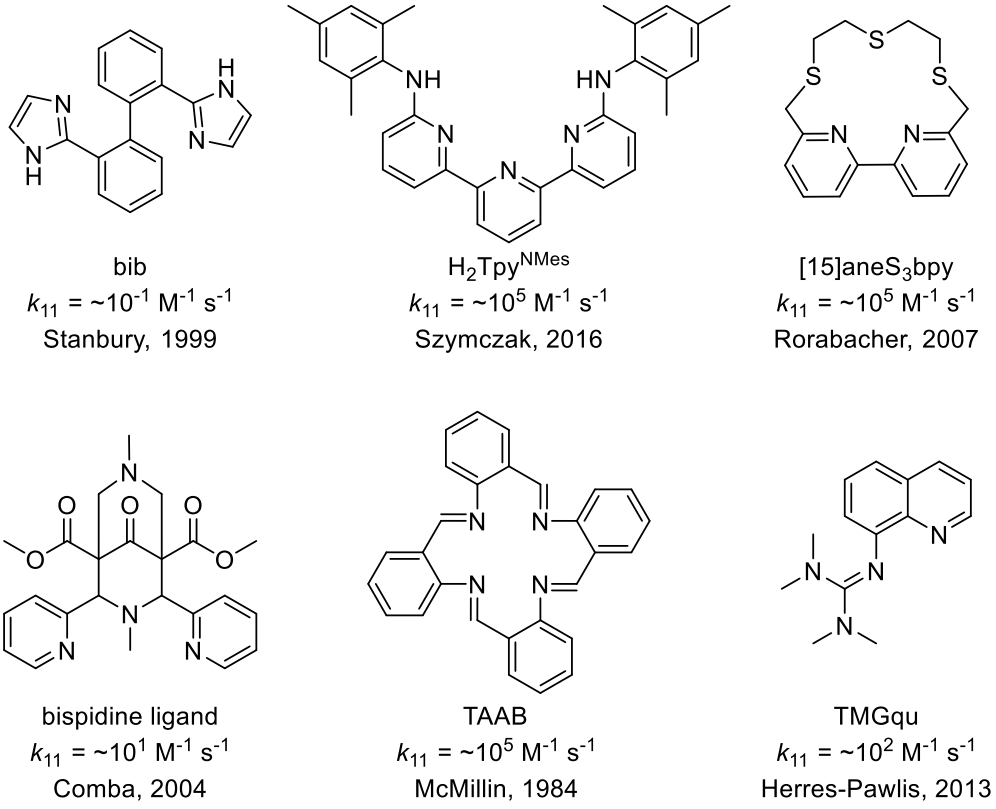

Figure 1.6: Examples of ligands of coordination-invariant systems as well as their self-exchange rates.[22, 51, 69, 78-81]

An example for coordination-invariant models is the Cu(I/II) redox pair of Stanbury's bib ligand.[78] It displays distorted geometries for both oxidation states, yet the self-exchange rate is orders of magnitude below that of blue copper proteins which can be explained by a relatively large internal reorganization barrier, indicated by a $\Delta\tau_4$ of 0.30.[82] Another example for a coordination-invariant entatic state model is the bispidine system by Comba *et al*.[83] The redox pair exhibits a rigid, preorganized coordination sphere with little internal reorganization, yet also low k_{11}. This is likely due to a large outer-reorganization energy of the solvent that is exacerbated by the elasticity of the coordination sheath. Szymczak *et al.* investigated the $[Cu(H_2Tpy^{NMes})Cl]^{0/+}$ redox pair featuring a tridentate pincer ligand containing additional anilines that function as hydrogen bond donor groups in the secondary coordination sphere, as well as a chlorido co-ligand.[79] The redox pair's structures are nearly isostructural, displaying an atypically flat Cu(I) coordination geometry with a τ_4 = 0.303. This pseudo-square-planar geometry is enforced by the hydrogen bonds that form between the anilines and the chlorido ligand and the resulting high structural accordance leads to an observed self-exchange rate on the order of 10^5 M^{-1} s^{-1},

rendering it one of the fastest reported coordination-invariant model systems. On the same order of magnitude is the redox pair of Rorabacher's macrocyclic [15]aneS$_3$bpy ligand.[51] It possesses five donors, giving rise to a pentacoordinate Cu-complex redox pair with very good structural accordance. This circumstance, as well as the electronic effects of the employed Cu–mercaptide bond, result in a high k_{11} on the order of 10^5 M^{-1} s^{-1}. Another model system with a self-exchange rate on the same order of magnitude is the [Cu(I/II)(TAAB)]$^{+/2+}$ system by McMillin *et al*.[81] It is notably one of the only pure N-donor complexes attaining such a high self-exchange rate, with the ligand being a tetradentate macrocyle. Due to minimal reported structural data, it cannot be definitively said whether the high self-exchange rates are due to high entasis. Lastly, a thoroughly studied family of model systems are the guanidine quinoline (GUAqu) systems. Their copper complexes are tetracoordinate, bis(chelate) N-donor systems, first reported by Herres-Pawlis *et al.* (Figure 6 depicts the archetypical TMGqu ligand).[22, 69, 77, 84-86] Their redox pairs generally display distorted, comparatively rigid geometries for both oxidation states with k_{11} between 10^1 and 10^3 M^{-1} s^{-1}.[22, 86]

Beyond copper proteins, several model systems of iron containing enzymes like a [Fe(S$_2$-o-xyl)$_2$]$^-$ compound that serves as a model for the active site of Fe–S$_4$ rubredoxin[87] or a number of model systems of Fe-only hydrogenases devised by Darensbourg *et al.*[26] have been reported that demonstrate active sites in an entatic state.

An interesting development is the application of entatic coordination compounds outside of modelling proteins. Examples of these bio-inspired applications include a study by Diógenes, León and Lemus *et al.* that leveraged the relation between the coordination geometry of copper complexes and their redox potentials to design anti-cancer metallodrugs.[88] They investigated the pentacoordinate copper 2,9-dimethylphenanthroline complex [Cu(dmp)$_2$(MeCN)]$^{2+}$. When the complex is dissolved in a solution of acetonitrile and water, the group reports an autoreduction of this species to [Cu(dmp)$_2$]$^+$ without the aid of external reductants. This behavior could not be observed for the analogous phenanthroline (phen) [Cu(phen)$_2$(MeCN)]$^{2+}$ complex. A structural analysis of both complexes yielded that the methyl substituents on dmp impose an entatic state on the pentacoordinate complex which in turn facilitates reduction and formation of the tetracoordinate species. The anticancer activity of the complex was successfully demonstrated in 2D and 3D *in-vitro* studies concerning the cytotoxicity and general anticancer properties.

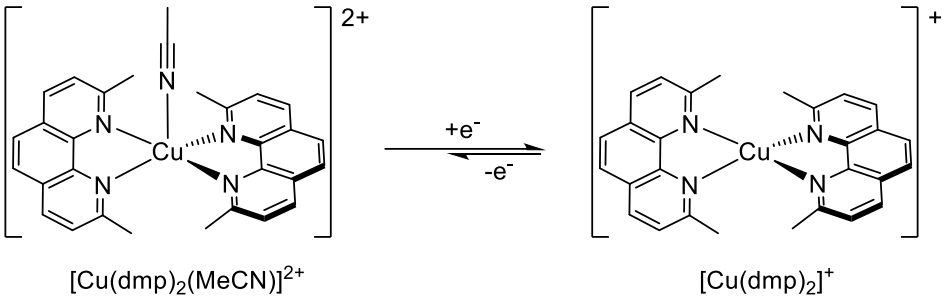

Scheme 1.1: Illustration of the water-mediated reduction $[Cu(dmp)_2(MeCN)]^{2+}$ experiences due to the entatic state imposed by the ligand.[88]

The entatic state can also be applied to catalysis, as Desage-El Murr and co-workers demonstrated.[89] They devised a ligand that combines redox-active iminosemiquinone (SQ) units, originally devised as galactose oxidase models, with an atropoisomeric 1,1'-2,2'-diamonphenyl (BINAP) backbone. Upon the complexation of Cu(II), the coordinative bonds result in an inward motion that conflicts with the outward strain of the atropoisomeric backbone, resulting in a strained coordination environment (Figure 1.8). The strained compound was employed as catalyst for aziridinations and cyclopropanations on styrene derivatives as well as deactivated or sterically hindered aliphates and olefines, where it gave improved yields compared to unstrained catalysts. Another application of entasis outside of model systems has turned out to be in copper photochemistry, which will be discussed herein at a later point (see chapter 1.10). Despite the expansion into other fields of chemistry, the entatic state concept remains strongly intertwined with redox processes. It can therefore be grasped at a more fundamental level by investigating electron transfer processes as well as the Marcus theory that describes them.

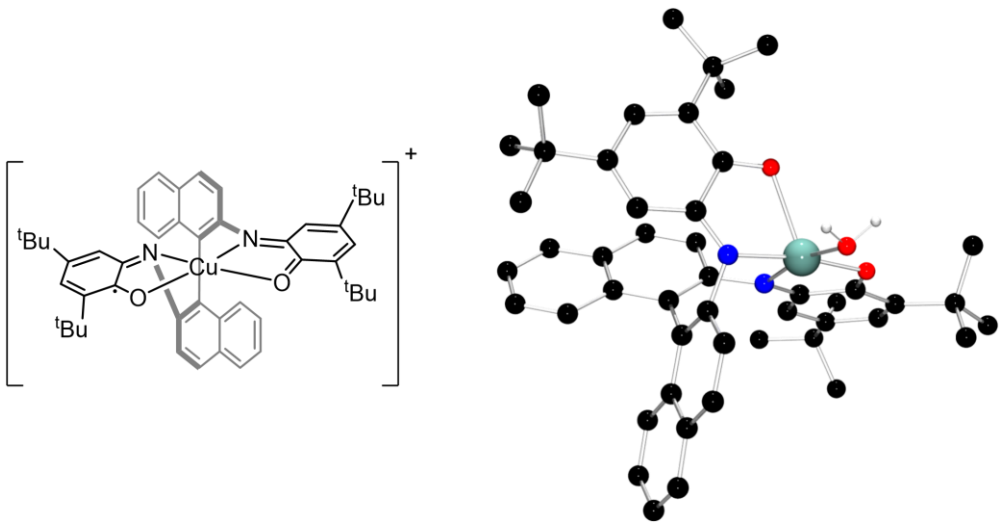

Figure 1.7: Left: Schematic illustration of the strained geometry of the Cu-SQBINAP complex. Right: Crystal structure of the Cu-SQBINAP complex with the additional water ligand.[89]

1.5 Electron Transfer Between Coordination Compounds

Redox reactions that occur between two metal complexes can follow two discrete electron transfer mechanisms: the outer-sphere and inner-sphere mechanism.[90-91] Both mechanisms depend on the formation of an adduct of both participating complexes and are differentiated based on the nature of that adduct.

The outer-sphere electron transfer describes a redox reaction that takes place without the cleavage or formation of a new chemical bond. The ligand spheres of both complexes are untouched by the reaction and the electron tunnels from one metal center to the other upon the formation of an outer-sphere complex (Scheme 1.2).[90-91]

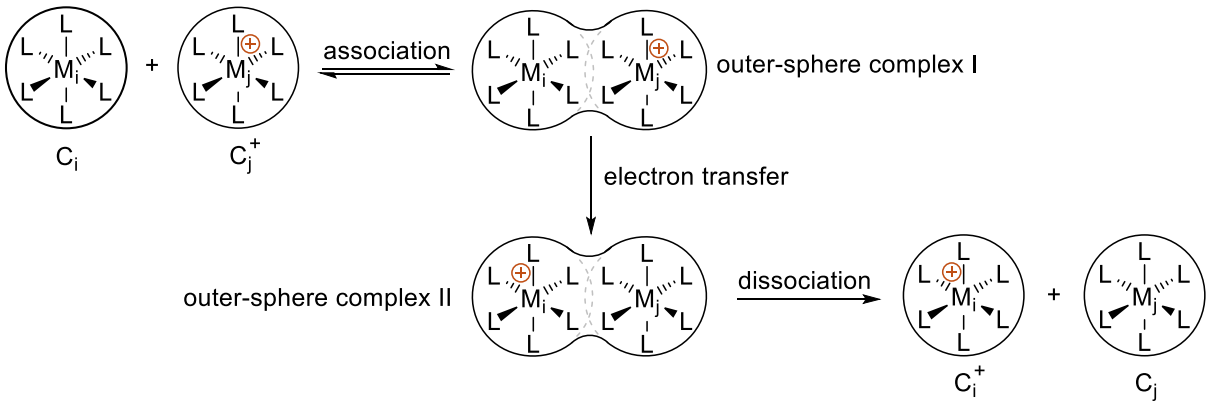

Scheme 1.2: Schematic representation of the inner-sphere electron transfer mechanism between two complexes.

Contrary to this, the inner-sphere electron transfer occurs via a bridging ligand (e.g. a halide). During an inner-sphere electron transfer, both metal complexes form one dinuclear complex, decaying upon termination of the reaction. The bridging ligand can be transferred as well (Scheme 1.3).[90-91]

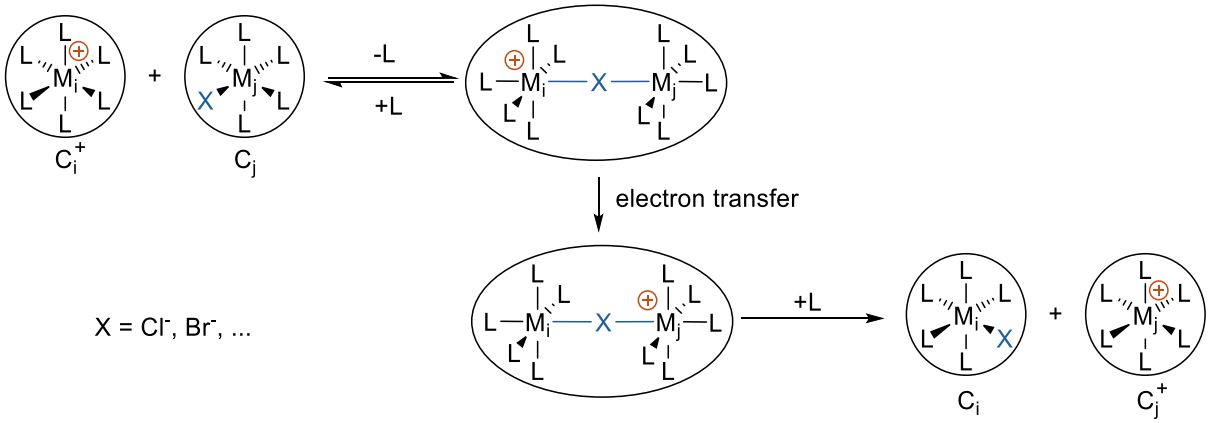

Scheme 1.3: Schematic representation of the outer-sphere electron transfer mechanism between two complexes.

Which mechanism is preferred is determined by the participating metal centers and ligands. Inner-sphere mechanisms are discouraged by inert metal centers as well as a

bulky and chemically inert ligand sphere, as they impede the formation of a dinuclear complex.[90]

Beyond these two mechanisms, some complexes require an activation step like a geometric rearrangement or the coordination of a co-ligand to participate in an electron transfer reaction, leading to the use of square-schemes that help to illustrate these additional mechanistic steps.[71, 92-93] An example of such a case are copper complexes of tetradentate tripodal ligands.[70] These show a change in coordination number between Cu(I) and Cu(II), meaning the reaction can either proceed via an addition-oxidation pathway (Pathway A) or an oxidation-addition pathway (Pathway B) via intermediates $\mathbf{I_A}$ or $\mathbf{I_B}$, respectively (Scheme 1.4).

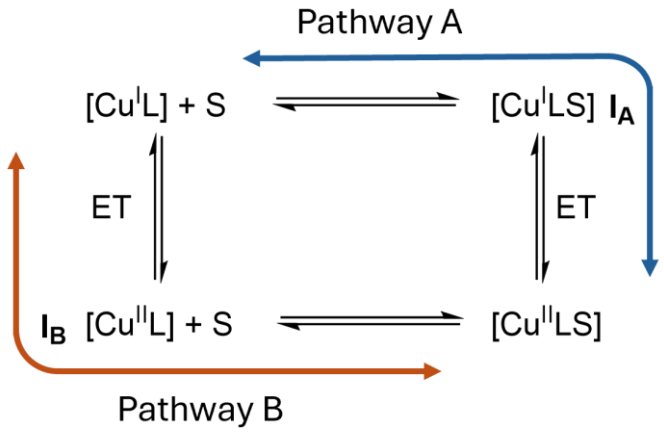

Scheme 1.4: Possible reaction pathways for coordination-variant copper complexes as proposed by Rorabacher *et al.* with S demarking the external co-ligand.[70]

Due to the additional kinetic barriers, such complexes usually exhibit low k_{11}. Accordingly, coordination-variant model systems can exhibit different rates for reduction and oxidation, as the corresponding Cu(I) and Cu(II) compounds do not necessarily follow a unitary pathway.[4, 70]

In general, the rapid electron transfer reactions in which copper proteins participate do follow an outer-sphere mechanism without additional mechanistic steps. The description of their electron transfer kinetics can therefore be performed via the Marcus cross-relation derived from the Marcus theory.

1.6 Marcus Theory and the Marcus Cross Relation

Marcus theory of electron transfer was devised in the 1960s by Rudolph A. Marcus. It is a semi-empirical theory that aims to describe the kinetics of an outer-sphere electron transfer reaction between two reactants.[94]

The general scheme for such a reaction is shown below (Scheme 1.5). If the reactants are different species ($i \neq j$), the reaction is called a cross reaction. If the reactants are identical ($i = j$), the reaction is referred to as a self-exchange reaction.[90]

$$C_i + C_j^+ \xrightarrow{k_{ij}} C_i^+ + C_j$$

Scheme 1.5: Electron transfer process of two cation reacting in an outer-sphere mechanism.

The reaction rate k_{ij} can be described using the following term:

$$k_{ij} = K_{A,ij} \cdot k_{ET,ij} \tag{3}$$

where $K_{A,ij}$ describes the formation constant of the outer-sphere complex and $k_{ET,ij}$ describes the electron transfer reaction rate between the two reactants of that complex, both representing the two most important kinetic hurdles of the reaction. $K_{A,ij}$ comprises the collision-number Z_{ij} of both reactants and an exponential term that includes the electronic work w_{ij} that must be invested for both reactants to come near each other.

$$K_{A,ij} = Z_{ij} \cdot \exp\left(-\frac{w_{ij}}{R \cdot T}\right) \tag{4}$$

R: Gasconstant, T: Absolute temperature

For the description of $k_{ET,ij}$, both the kinetic barrier of the electron transfer $\Delta G^{\ddagger}$ as well as the transmission coefficient κ_{ij} need to be considered.

$$k_{ET,ij} = \kappa_{ij} \cdot exp\left(-\frac{\Delta G_{ij}^{\ddagger}}{R \cdot T}\right) \tag{5}$$

The latter represents the probability of electron transfer between the reactants at the transition state and results from perturbation theory. For simplification, the coefficient is generally assumed as unity, yielding a simplified term.

$$k_{ET,ij} = exp\left(-\frac{\Delta G_{ij}^{\ddagger}}{R \cdot T}\right) \tag{6}$$

The activation energy $\Delta G_{ij}^{\ddagger}$ is also called the vibrational barrier of electron transfer reactions. Electron transfer processes are adiabatic and hence require the reactant and product state to be degenerate to proceed. The participating reactants (C_i/C_i^+ and C_j^+/C_j), however, have different ground state geometries and solvation spheres depending on their oxidation state, and thus varying ground state energies. Therefore, electron transfer reactions require a certain degree of deformation, also called reorganization, that functions as a kinetic barrier. This process of reorganization happens via thermal vibrations and can be described by modelling the Gibbs free enthalpy of the reactants $G_R(x)$ and products $G_P(x)$ jointly with the corresponding solvation spheres' Gibbs free enthalpy as harmonic oscillators. By only changing one vibrational mode over the reaction coordinate x, approximately quadratic equations for $G_R(x)$ and $G_P(x)$ are obtained (Figure 1.8).

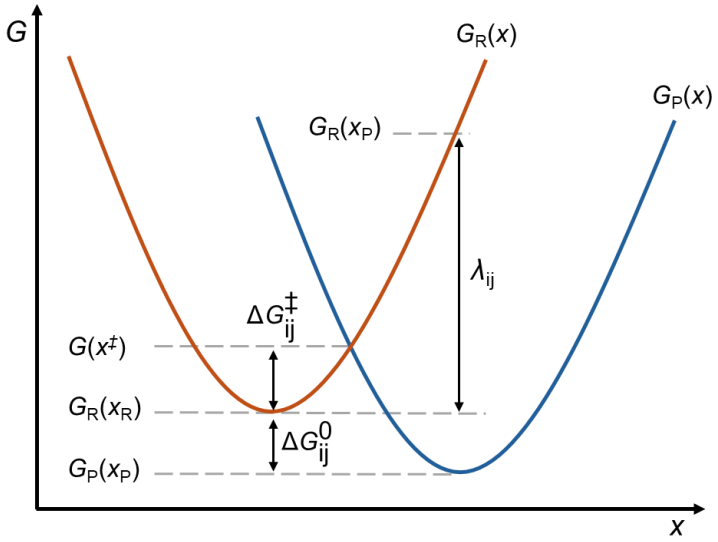

Figure 1.8: Schematic illustration of the Gibbs free energy of the reactant side R (orange) and the product side P (blue) versus the reaction coordinate *x*, as well as important Gibbs free enthalpy values.

This yields the reorganization energy λ_{ij} that is defined as the sum of the internal reorganization energy of the participating molecules ($\lambda_{ij,i}$) and the outer reorganization energy of the solvent sphere ($\lambda_{ij,s}$) (Eqn. 7).

$$\lambda_{ij} = \lambda_{ij,i} + \lambda_{ij,s} \tag{7}$$

It further yields the difference in Gibbs free enthalpy of the reactant and product side (ΔG_{ij}^{0}) that also drives the reaction rate. The reaction takes place at the minimal energy crossing point (MECP) of both parabolas ($x^{\ddagger}$) that can be reached by overcoming the activation barrier $\Delta G_{ij}^{\ddagger}$ described as follows.

$$\Delta G^{\ddagger} = \frac{\lambda_{ij}}{4} \cdot \left(1 + \frac{\Delta G_{ij}^{0}}{\lambda_{ij}}\right)^2 = \frac{(\lambda_{ij} + \Delta G_{ij}^{0})^2}{4\lambda_{ij}} \tag{8}$$

Using equations 3, 6 and 8, k_{ij} can be described as follows.

$$k_{ij} = K_{A,ij} \cdot \exp\left(-\frac{(\lambda_{ij} + \Delta G_{ij}^{0})^2}{4 \cdot \lambda_{ij} \cdot R \cdot T}\right) \tag{9}$$

This term is simplified for self-exchange reactions ($i = j$) where $\Delta G_{ij}^{0} = 0$. The reorganization energy of a self-exchange reaction can therefore be described via Equation 10.

$$\lambda_{ij} = 4 \cdot R \cdot T \cdot \ln\left(\frac{K_{A,ij}}{k_{ij}}\right) \tag{10}$$

For $i = j$

The vibrational barrier of a self-exchange reaction changes depending on the relative positions of $G_R(x)$ and $G_P(x)$, increasing with the displacement of the vertices and the parabolas' compression. The distortion imposed by the entatic state can therefore be understood as lowering the displacement of both parabolas, decreasing the vibrational barrier in the process. The expressions derived above can be used to obtain the Marcus cross relation for cross- and self-exchange reactions of the complexes C_1 and C_2 (Scheme 1.6).

$$C_1 + C_2^+ \xrightarrow{k_{12}} C_1^+ + C_2$$

$$C_2 + C_2^+ \xrightarrow{k_{22}} C_2^+ + C_2$$

$$C_1 + C_1^+ \xrightarrow{k_{11}} C_1^+ + C_1$$

Scheme 1.6: Possible self-exchange and cross reactions between complex C_1 and C_2.

While the cross reaction rate k_{12} is more difficult to describe due to $\Delta G_{ij}^0 \neq 0$, λ_{12} and $K_{A,12}$ can be approximated by the mean of their respective self-exchange parameters.

$$\lambda_{12} = \frac{1}{2}(\lambda_{11} + \lambda_{22}) = 2 \cdot R \cdot T \cdot \ln\left(\frac{K_{A,11} \cdot K_{A,22}}{k_{11} \cdot k_{22}}\right) \tag{11}$$

$$K_{A,12} = \sqrt{K_{A,11} \cdot K_{A,22}} \tag{12}$$

To describe the cross reaction rate k_{12} via the self-exchange reactions, the correction terms W_{12} and f_{12} must be implemented to correct for strong differences in charge, ionic radii and therefore changes in electrostatic work that are neglected in $K_{A,12}$. This leads to the Marcus cross relation being formulated as follows (Eqn. 15).

$$k_{12} = \sqrt{k_{11} \cdot k_{22} \cdot K_{12} \cdot f_{12}} \cdot W_{12} \tag{13}$$

$$f_{12} = \exp\left(\frac{\left(\ln\left(K_{12} + \frac{w_{12} - w_{21}}{R \cdot T}\right)\right)^2}{4 \cdot \left(\ln\left(\frac{k_{11} \cdot k_{22}}{Z_{11} \cdot Z_{22}}\right) + \frac{w_{11} + w_{22}}{R \cdot T}\right)}\right) \tag{14}$$

$$W_{12} = \exp\left(\frac{w_{11} + w_{22} - w_{12} - w_{21}}{2 \cdot R \cdot T}\right) \tag{15}$$

1.6.1 Marcus Normal and Marcus Inverse Processes

In reactions where $\Delta G_{ij}^{0} \neq 0$, the reaction rate is not only affected by the reorganization energy, but by the thermodynamic driving force as well.[94] This is a unique property of electron transfer reactions, not applicable to reactions described by Eyring's transition-state theory and comes with certain edge cases. One of such is the so-called Marcus normal region, where the thermodynamic driving force is smaller than the displacement of both minima ($\Delta G_{ij}^{0} < \Delta x_{ij}$), leading to an increased reaction rate with increased ΔG_{ij}^{0}. Inverting this relationship, however, results in the so-called Marcus inverted region ($\Delta G_{ij}^{0} > \Delta x_{ij}$). Here, an increased thermodynamic driving force will diminish the observed reaction rate.[95] These two regions can be visualized as shown in Figure 1.9.

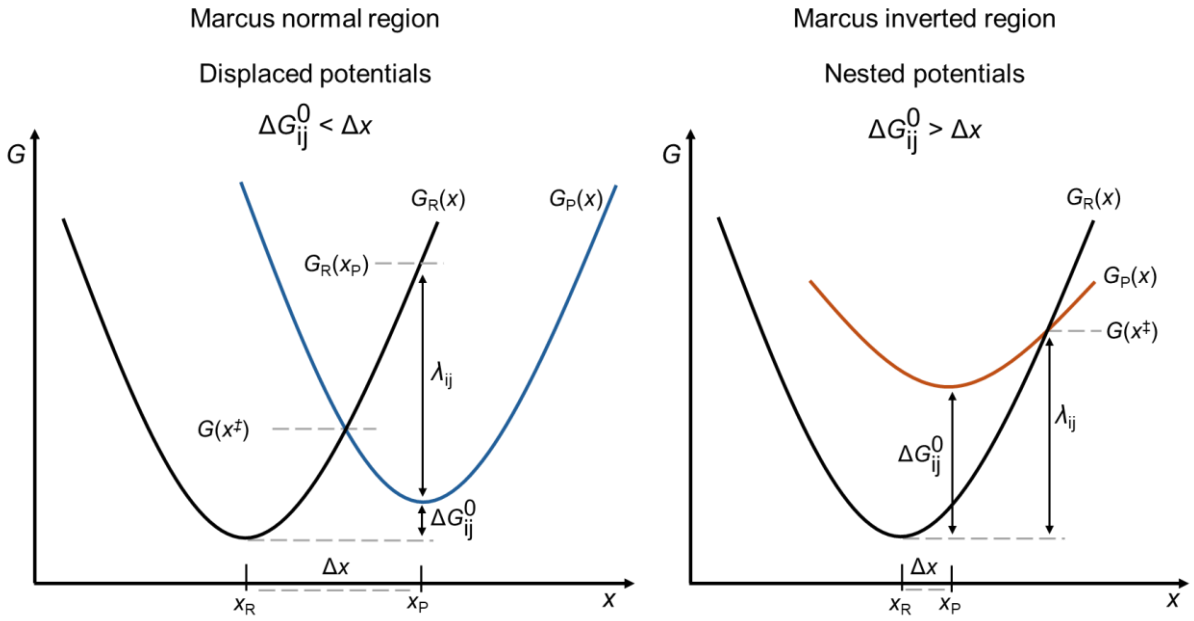

Figure 1.9: Schematic illustrations of the Marcus normal and Marcus inverted region as well as important Gibbs free enthalpy values.

While most thermal electron transfer reactions take place in the Marcus normal region and feature displaced potentials, the inverted region with its nested potentials is a common occurrence for photoinduced intramolecular charge transfer processes.[95-96]

1.7 Photo-Induced Processes in Coordination Compounds[97]

Excited states of molecules and coordination compounds are the result of a bound electron absorbing a photon of a certain energy to occupy an energetically elevated orbital. The nature of these transitions depend on the involved orbitals and the multiplicity of the molecules or complex in question. For coordination compounds, transitions can be classified as metal-centered (MC) inside the metal's ligand field,

ligand-centered (LC), a metal-to-ligand charge transfer (MLCT) from a metal-centered orbital to a ligand-centered orbital or a ligand-to-metal charge transfer (LMCT), from a ligand-centered orbital to a metal-centered one (Scheme 1.7).

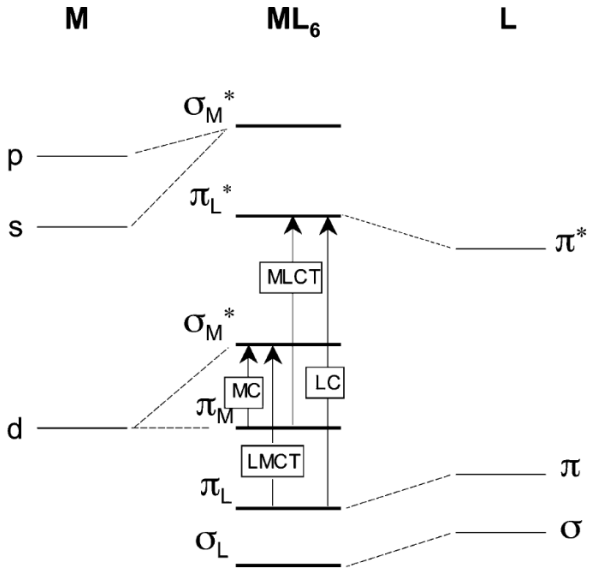

Scheme 1.7: Schematic illustration of important photo-induced transitions in a coordination compound and their denotations. From bottom to top: LMCT: Ligand-to-metal charge transfer, MC: Metal centered, LC: Ligand centered, MLCT: Metal-to-ligand charge transfer.[97]

The relative energetic order and availability of these transitions are dependent on the involved metal, its electron configuration and the involved ligands. MC and LMCT transitions for example are observed for open-shell transition metals but cannot be accessed by d^{10} ions. They are increasingly red shifted if the metal (MC) or ligand (LMCT) are easily reduced. Meanwhile, red shifted LC and MLCT transitions are mostly reliant on energetically low-lying, ligand-centered orbitals and are therefore most frequently observed for complexes of aromatic ligands with extended π and π^* systems. After a transition of any kind takes place, the resulting excited state can decay via various pathways, illustrated in Scheme 1.8 for a general molecule with singlet multiplicity in the ground state.

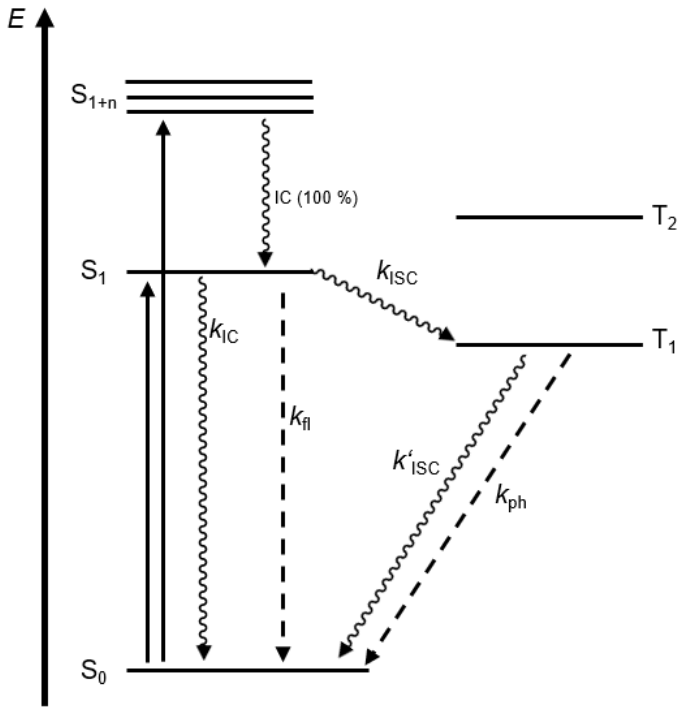

Scheme 1.8: Schematic Jablonski-diagram of the excited-state processes in a generic molecule. k_x: rate of process x. x = IC: internal conversion, ISC: Intersystem crossing, fl: Fluorescence, ph: Phosphorescence.

Quantum mechanics differentiates between allowed and formally forbidden transitions. Transitions between states of different multiplicity are forbidden, such as $S_1 \rightarrow T_1$ transitions. Allowed transitions include transitions where the multiplicity of the system is conserved, e.g. $S_0 \rightarrow S_n$ transitions in the energy diagram. The observed absorption bands in UV/vis spectra therefore correspond to spin-allowed transitions. Spin-forbidden transitions still occur via so-called intersystem crossing (ISC) processes, yet their forbidden nature renders them comparatively slow.

Once in an excited state, the molecule or complex is unstable and can either decay via intramolecular reactions or, more commonly, relax via radiative pathways or non-radiative pathways, also known as internal conversion (IC). Following Kasha's rule,[98] singlet excited states of high energy (S_{1+n}), also called "Franck-Condon states", usually decay very fast via efficient IC processes to the lowest spin-allowed excited state (S_1). This S_1 state can then decay either via fluorescence (k_{fl}) or internal conversion (k_{IC}) to the ground state or convert to the T_1 state via ISC (k_{ISC}). The T_1, in turn, can decay to the ground state via non-radiative IC (k'_{IC}) or via radiation in the form of phosphorescence (k'_{ph}). The ISC and phosphorescence pathways are relatively inefficient for organic molecules but are highly relevant for complexes containing heavy atoms. Lifetimes of excited states (τ) are described as the inverse of the sum of each competing deactivation pathway (Eqn. 16 and 17).

$$\tau(S_1) = \frac{1}{k_{IC} + k_{fl} + k_{ISC}} \quad (16)$$

$$\tau(T_1) = \frac{1}{k_{ph} + k'_{ISC}} \quad (17)$$

Additionally, the non-radiative decay rates often follow the kinetics of the Marcus theory in the Marcus inverted region;[23, 99] they therefore increase the smaller the energy gap (ΔE_{Gap}) between the two states in question becomes and *vice versa*. Excited state lifetimes can be measured via time-resolved methods such as transient emission spectroscopy that measures the decay of luminescence (fluorescence or phosphorescence). The charge separation that occurs during a photoexcitation gives excited states special reactivities that can be of interest for chemists, given sufficient τ.[100-101] Complexes that are able to interact with other substrates while in the excited state are generally categorized as photosensitizers.

1.8 Photosensitizers and Photoredox Catalysis

A photosensitizer is a compound that can absorb visible light to enter an excited state which can subsequently interact with a substrate in order to initiate or control reactivity.[100-101] The fundamental mechanism is the charge separation that occurs upon the absorption of a photon by an electron.[102] Once excited, the electron occupies a higher energy orbital than in the ground state and can thus participate in reactions as a strong reducing agent. Conversely, the generated electron hole can serve as a strong oxidizing agent. Among other applications, photosensitizers can be used for photodynamic therapy,[103] photoinduced hydrogen production from water[104] and for solar cells.[105] Additionally, they can be used as photoredox catalysts which absorb light to facilitate redox reactions under mild conditions that would otherwise not be possible.[106]

Further parameters for the use of photoredox catalysts are the photosensitizers' optical properties like their absorption maximum and the available transitions, and the redox potentials of the metal center as well as that of the ligands in the ground state and the excited state.[100-101]

The optical properties decide not only the wavelength required to excite the catalyst but also the nature of the transition. Most photoredox catalysts are based on usually intense charge transfer bands.[100] The energy of the excited state is further important for the reactivity of the photoredox catalyst that is linked to its redox potentials.[107] These decide the possible mechanisms the catalyst can participate in (*vide infra*) by limiting the substrates that can be activated. The redox waves of the S_0 state are

usually designated as E_{ox} and E_{red}, the former being the half-wave ($E_{1/2}$) potential of the metal and the latter that of the ligand. The excited state potentials $^*E_{ox}$ and $^*E_{red}$ can be derived from the ground state using the Rehm-Weller equations.[108-109]

$$^*E_{ox} = E_{ox} - E_{0\text{-}0} \quad (18)$$

$$^*E_{red} = E_{red} + E_{0\text{-}0} \quad (19)$$

where $E_{0\text{-}0}$ is the energy of the excited state in electron volts. It is usually obtained from the wavelength of the fluorescence emission maximum of the relevant excitation, although different methods such as the onset-wavelength of the absorption spectrum are also reported.[110] Ideally, the difference between the two ground state potentials is quite large, with E_{ox} sitting at strongly oxidizing ("positive") and E_{red} at strongly reducing ("negative") potentials.[102] This not only widens the substrate scope but further enables easy regeneration of the oxidized photocatalyst as a wider range of sacrificial donors are available.

Two essential catalytic cycles of photoredox catalysts are the reductive quenching (RQ) and oxidative quenching (OQ) which involve outer-sphere electron transfers and are depicted in Scheme 1.9.[106] The OQ cycle is the archetypical photocatalytic cycle. Here, the complex is first excited, then reduces a substrate before being regenerated by the reduction of another substrate or a sacrificial electron donor. The two most important potentials in this cycle are E_{ox} and $^*E_{ox}$. The RQ cycle utilizes the generated electron hole of the excited photocatalyst, reducing it via a substrate or sacrificial electron donor. The obtained reduced catalyst can then reduce a substrate and convert back to the ground-state species.

Frequently employed photocatalysts are coordination compounds of iridium and ruthenium. These have proven to be quite efficient, owing to their good absorption properties, strong excited state reduction potentials and long-lived excited states that are reported to reach up to several microseconds.[99-100] Attempts to substitute these metals for their lighter, cheaper and more common homologues in the periodic table proves to be challenging due to the differences in their electronic structure. While works on early transition metals like Co,[96] Fe[111] and Cr[112] based photosensitizers show potential, the open-shell nature of their ions pose an inherent limitation to their excited state lifetimes.[99, 101] Thus, the most promising metal center for early transition metal photosensitizers is the closed-shell Cu(I) ion.

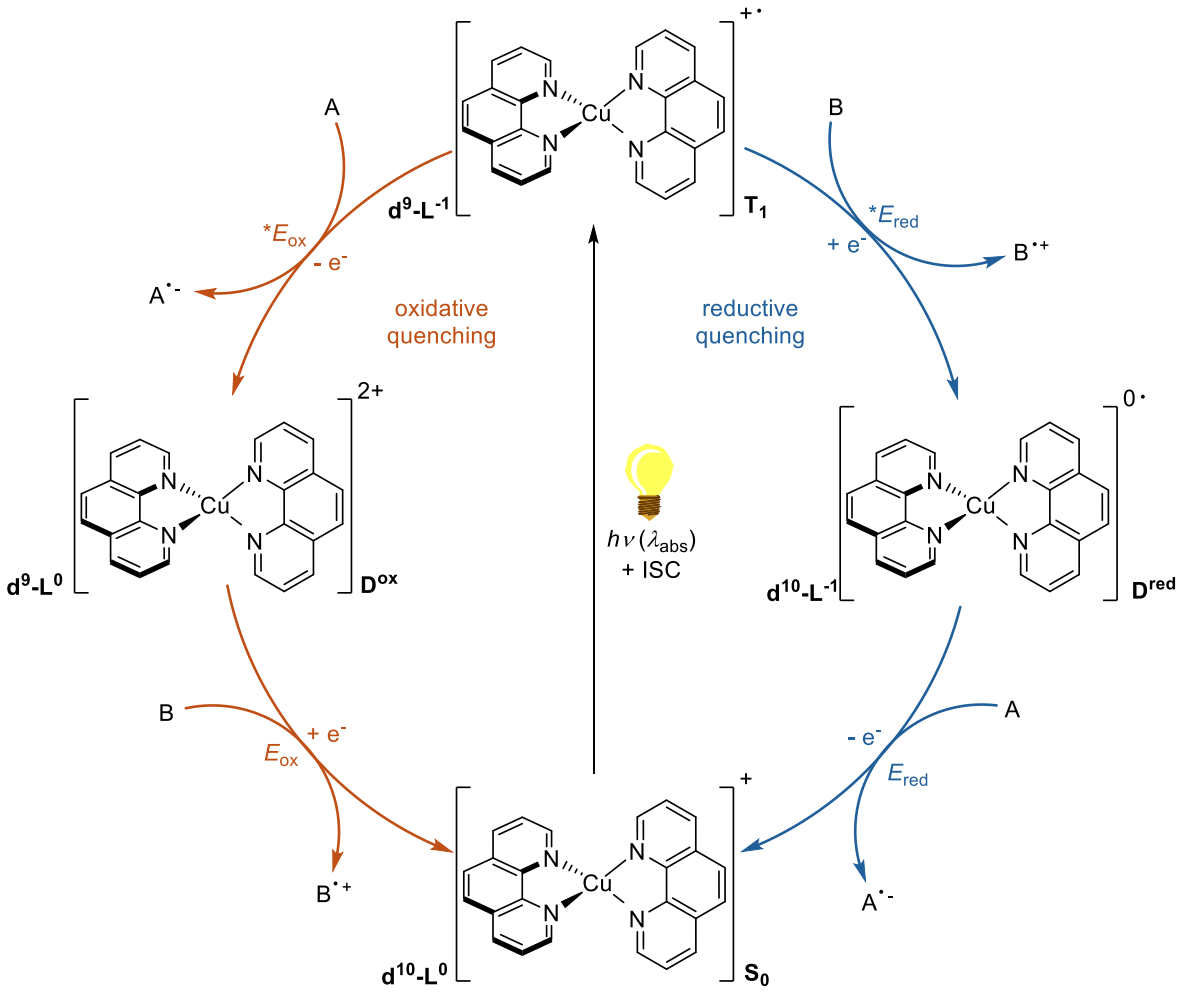

Scheme 1.9: Exemplary outer-sphere reductive quenching and oxidative quenching cycles of a photoredox catalytic reaction. The depicted catalyst $[Cu(phen)_2]^+$ is exemplary. Depicted are the participating catalyst species, their electron configurations and their denotations. Each step is further annotated with the redox potential that is required for it.[102]

1.9 Copper Photochemistry

In 1987, Sauvage *et al.* reported that the $[Cu(dap)_2]^+$ (dap = 2,9-bis(*p*-anisyl)-1,10-phenanthroline) complex was capable of benzyl bromide dimerization, reporting the first case of Cu-mediated photoredox catalysis.[113] Since then, and especially in the past decade, there has been an increasing interest in the photochemistry of Cu(I) complexes, with focus on tetra- or tricoordinate compounds.[102, 114] As Cu(I) possesses a closed d-shell, photophysical excitation of d-electrons can only occur via MLCT, requiring the presence of suited ligands that allow for MLCT bands in the visible regions. As a consequence, aromatic ligands with energetically low-lying π^*-orbitals like phenanthrolines haven become popular for this chemistry.[102] The lack of ligand-field transitions in Cu(I) complexes gives comparatively simple excited state dynamics that are mostly dominated by the behaviors of the S_1 and T_1 state. Since the MLCT corresponds to a photoinduced oxidation of the metal center, the excited states

experience the characteristic flattening distortion of Cu(II).[115] Depending on sterics, the degree of flattening and the presence of co-ligands, the longer-lived T_1 state can also form an exciplex with a solvent molecule or a co-ligand from the surrounding solution. A typical diagram of the photophysical processes in Cu(I) complexes is depicted in Scheme 1.10.

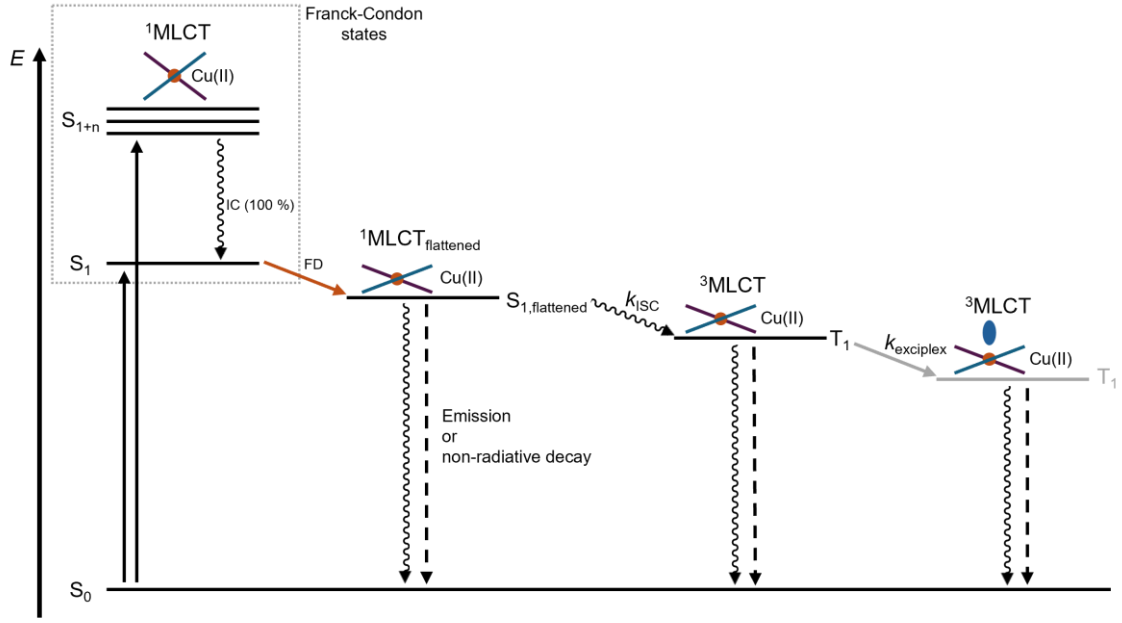

Scheme 1.10: Schematic general Jablonski-diagram of a tetracoordinate Cu-photosensitizer. The exciplex step is greyed out as its availability depends on the complex's sterics and the presence of suitable co-ligands. FD: Flattening distortion.[116]

The decay kinetics are described via the Marucs theory of the Marcus inverted region, the longevity is therefore strongly dependent on the energy gap between the S_0 and T_1 state.[99] A more pronounced flattening distortion as well as the formation of exciplexes are therefore detrimental, as they lower the T_1–S_0 energy gap (ΔE_{Gap}).[23] Hence, a large part of copper photochemistry is centered around the ligand design with the goal of mitigating the flattening distortion and maximizing ΔE_{Gap}. This concept has been coined "cooperative steric hindrance" by Castellano *et al*. in 2013, but recent publications also link the properties of these photosensitizers to the entatic state concept (*vide infra*).[117-118] Steric restriction of the flattening distortion has led to a drastic increase in the excited state lifetime from the order of picoseconds over to several microseconds.[23, 119-120]

While homoleptic complexes of diimine (N^N) donors have been the earliest examples of their class, their applicability is limited due to rather negative E_{ox}, which complicate catalyst regeneration, and comparatively short-lived excited states.[23, 114] Heteroleptic copper complexes consisting of one N^N ligand like phen and a chelate P-donor ligand (P^P) like bis[2-(diphenylphosphino)phenyl]ether) (POP) do alleviate both of these shortcomings and further enable better fine-tuning of their properties.[120-122] Due to

their heteroleptic nature, their performance suffers from unstable ligand spheres as they can participate in dynamic ligand exchange reactions to homoleptic complexes with inferior photophysical properties (Scheme 1.11 above).[123-124] This process can be suppressed, however, by using sterically very demanding ligands like HETPHEN that are unable to form homoleptic bis(chelate) complexes (Scheme 1.11 below).[121, 125-126]

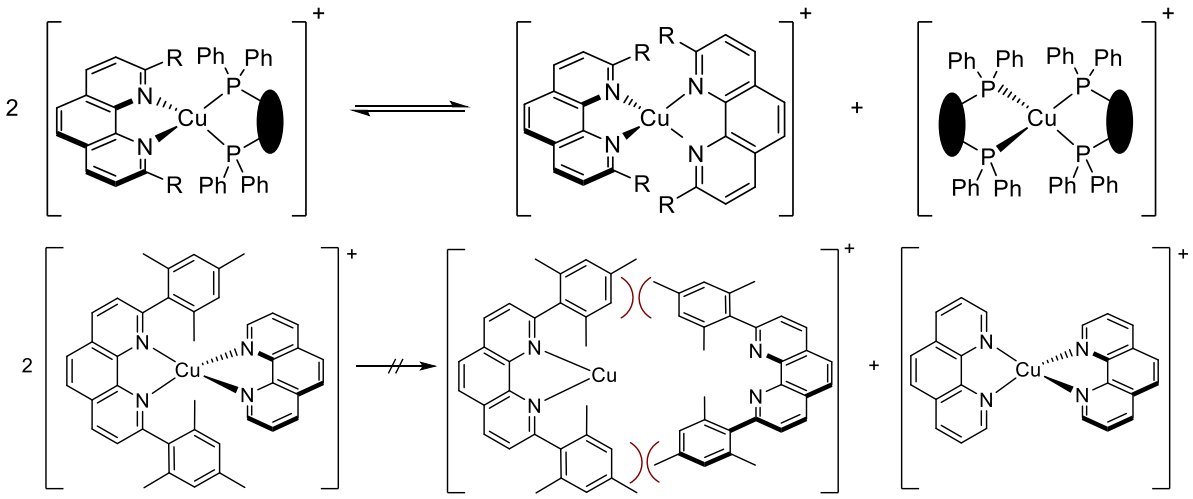

Scheme 1.11: Above: Example of a ligand exchange reaction of a heteroleptic Cu-photoredox catalyst.[123] Below: Schematic illustration behind the mechanism of the HETPHEN method that prevents ligand exchange reactions.[125-126]

Despite the extensive research regarding pseudo-tetrahedral Cu-photosensitizers with bis(chelate) N-, and P-donor ligands, there are plenty of photochemically viable Cu-complexes that deviate from this general motif.[110, 127-128] The thus available variety of suitable ligands together with mixed ligand design offers many avenues for tailoring Cu-photosensitizers to their desired applications, which has led to an extensive library of copper systems, some of which are shown in Figure 1.10.[110, 118, 120-122, 124, 127-132]

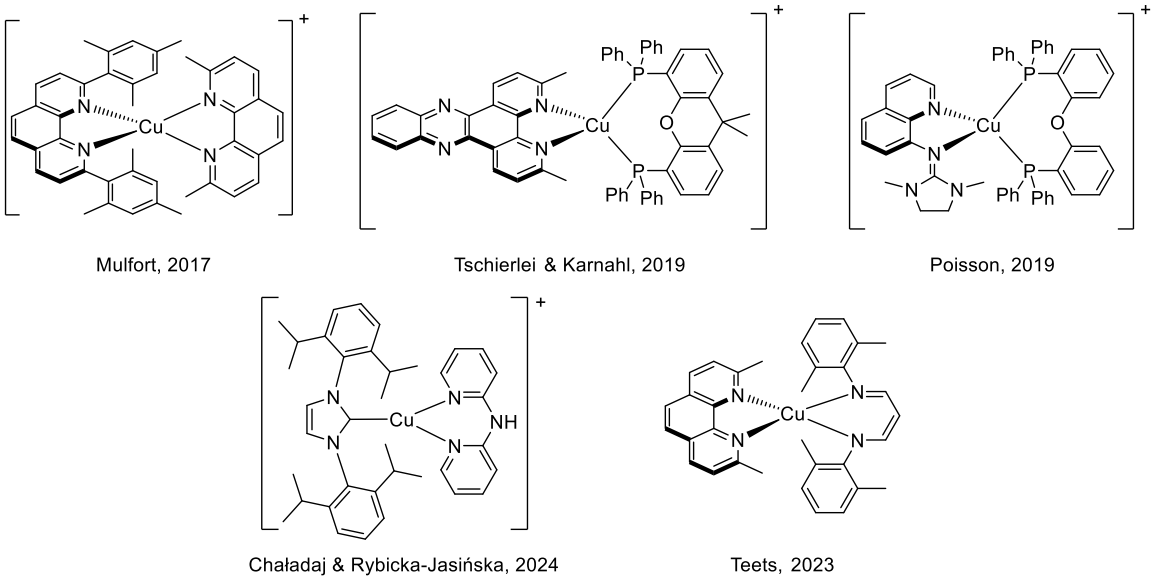

Figure 1.10: Examples of Cu-photoredox catalysts.[118, 120, 122, 128, 132]

In terms of reactivity, the discussed outer-sphere mechanisms (*vide supra*) are available, but copper photosensitizers can also participate in inner-sphere mechanisms, as illustrated by the atom transfer radical addition (ATRA) reaction that facilitates the addition of organohalides to an olefin (see Scheme 1.12).[133-135]

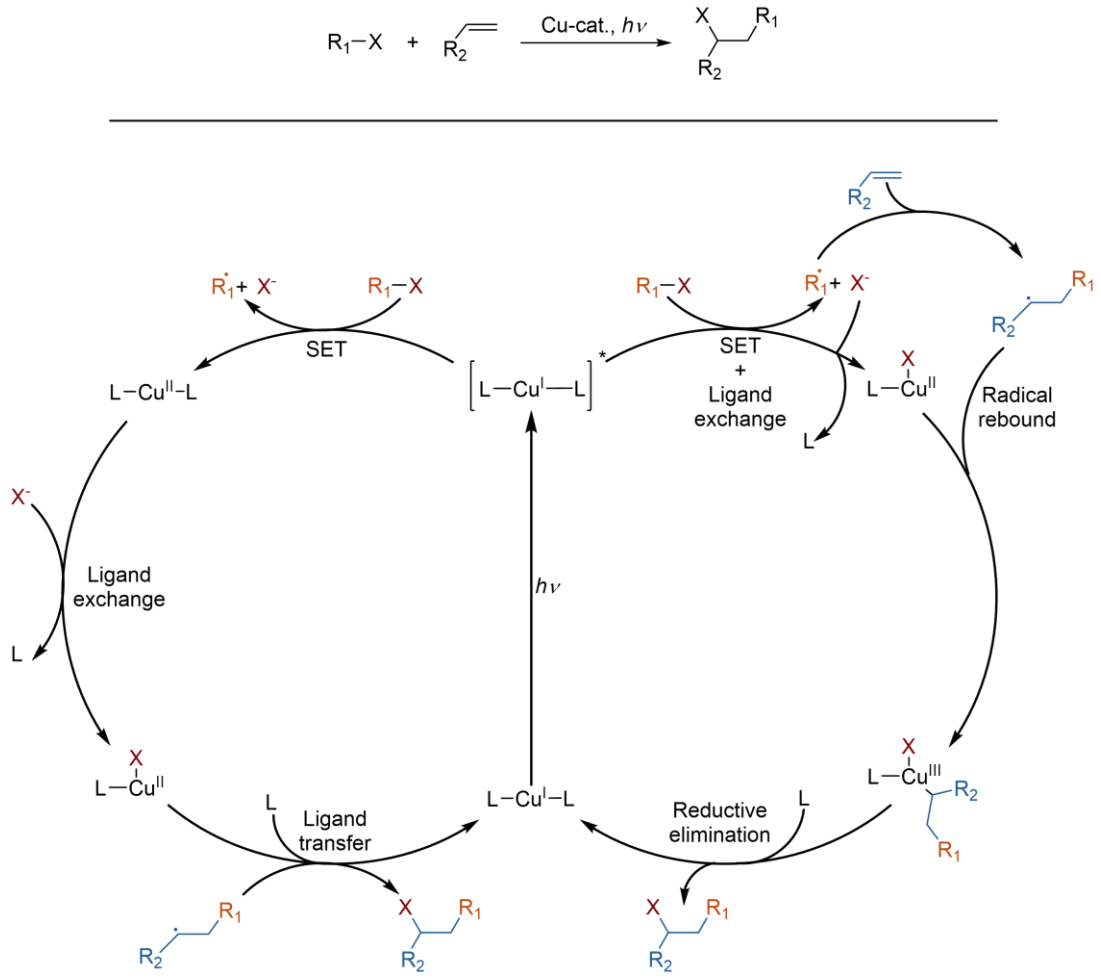

Scheme 1.12: Above: General reaction equation of an ATRA reaction. Below: Proposed mechanism of a Cu-catalyzed ATRA-reaction with inner-sphere steps.[102, 134]

This inner-sphere reactivity is owed to copper's propensity to expand its coordination sphere when oxidized as well as its affinity towards ligand exchange reactions.[134] In the case of the ATRA reaction, this reactivity circumvents the electrochemical problem of $[Cu(N\hat{}N)_2]^+$ catalysts' negative E_{ox} potentials by enabling a regeneration of the catalyst without requiring a strong sacrificial donor. It also enables reactivities pure outer-sphere photocatalysts cannot facilitate. For example, the addition of trifluoromethyl chlorosulfonate onto olefins will always proceed with an extrusion of SO_2 from the reaction when catalyzed with $[Ru(bpy)_3]Cl_2$, since the activated trifluoromethylsulfonyl radical decomposes (Scheme1.13).[136] The use of $[Cu(dap)_2]Cl$, however, allows to capture a chlorosulfonyl radical via inner-sphere reactivity, yielding trifluoromethyl-chlorosulfonylated olefin instead.[137]

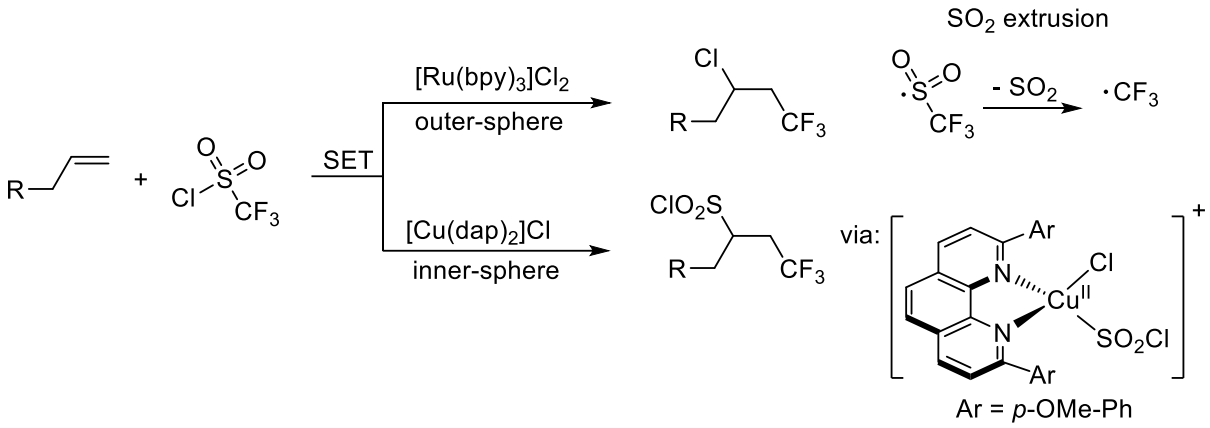

Scheme 1.13: Illustration of the different reactivity of an outer-sphere ATRA reaction and a Cu-catalyzed ATRA with inner-sphere steps.[134, 136-137]

1.10 The Entatic State in Photochemistry

Prolonged excited state lifetimes for Cu-photosensitizers can be achieved by increasing ΔE_{Gap} between the T_1 and S_0 state, mostly via steric strain imposed by ligands with bulky substituents that prohibit energy loss via flattening of the complex (Figure 1.11).

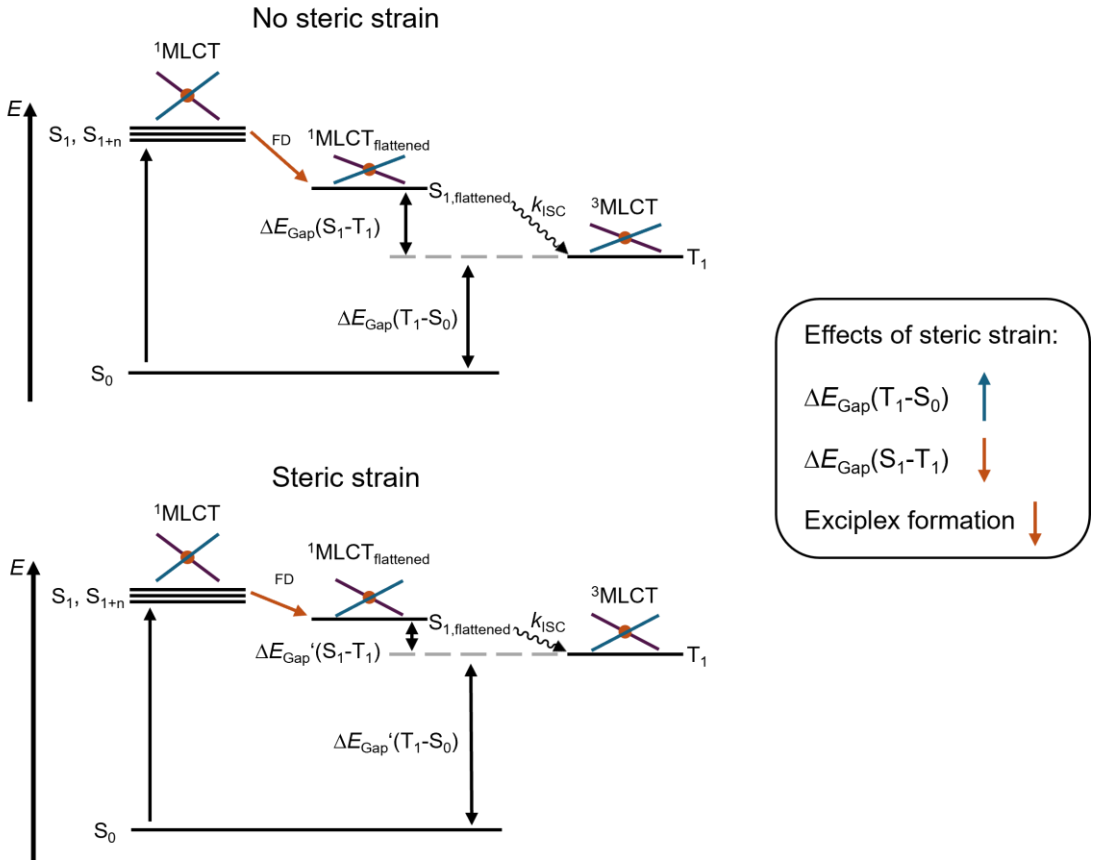

Figure 1.11: Schematic illustration of the effect of steric strain on the excited state dynamics of Cu-complexes. FD: Flattening distortion.

This destabilization of the excited state and its resulting energization is not dissimilar to Comba's definition of the entatic state (*vide supra*) which allows to transfer the entatic state concept from thermal electron transfer to photo-induced processes. While the improvement of photocatalytic properties through steric strain is common knowledge in Cu-photochemistry,[114, 117, 138] the transfer by name has only taken place in the past decade. The first work naming the entatic state in the context of photoexcited Cu-complexes was published in 2017 by Mulfort *et al.*[118] They were the first to describe the strain involved in preventing the flattening distortion and the resulting prolonged excited state lifetime of heteroleptic copper phenanthroline complexes as a result of entasis. This study was later expanded upon by Hadt *et al*. who reported a combined experimental and computational approach to quantify the entasis of tetracoordinate copper photosensitizers and its effect on the excited state lifetime.[23] They investigated a series of $[Cu(N\hat{}N)_2]^+$ compounds of 2,9-substituted phenanthroline ligands with excited state lifetimes τ that range across four orders of magnitude and correlated them with several thermodynamic and kinetic parameters (Figure 1.12). Important to highlight within the context of entasis are the correlations of τ with ΔE_{gap}, the ground-state reorganization energy λ and $E_{ox,}$ respectively. These show a connection between a rigid, tetrahedral coordination geometry, marked by a small λ and more positive E_{ox}, an increasingly large ΔE_{Gap}, and prolonged τ.

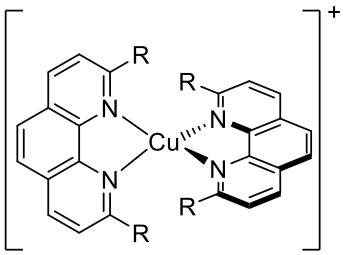

$[Cu(L)_2]^+$

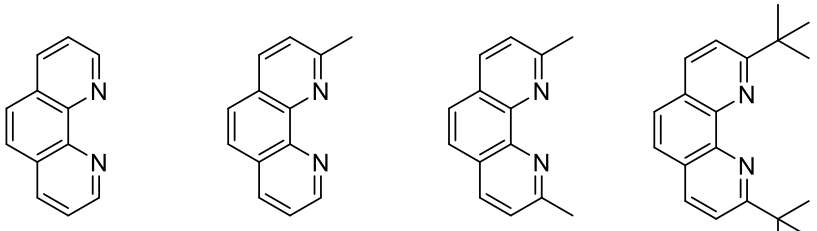

phen	**mmp**	**dmp**	**dtbp**
τ_{DCM} = 140 ps	τ_{DCM} = 2 ns	τ_{DCM} = 90 ns	τ_{DCM} = 3.3 µs
ΔE_{Gap} = 0.767 eV	ΔE_{Gap} = 1.03 eV	ΔE_{Gap} = 1.36 eV	ΔE_{Gap} = 1.89 eV
E_{ox} = 0.23 V	E_{ox} = 0.38 V	E_{ox} = 0.58 V	E_{ox} = 0.79 V
λ_{11} = 1.06 eV	λ_{11} = 0.763 eV	λ_{11} = 0.521 eV	λ_{11} = 0.183 eV

Figure 1.12: Ligands of the complexes studied by Hadt *et al.* as well as their corresponding excited state lifetime in DCM τ_{DCM}, the T_1-S_0 energy gap ΔE_{Gap} , the metal redox-potential E_{ox} (vs. Fc/Fc^+) and the ground state reorganization energy λ_{11}.[23]

While important, the effect of the entatic state on Cu-photosensitizers is not limited to the lifetime of the T_1 state but also extends to ISC as well as IC rates. Jha and Miller *et al*. utilized transient absorption measurements with femtosecond resolution to observe the structural dynamics of the pre-flattened $[Cu(dmp)_2]^+$ in the solid state and compared it to the behavior of the dissolved compound.[139] They found that the entatic state imposed by the crystal environment speeds up the complex's structural dynamics due to its pre-flattened geometry, reducing the lifetime of the Franck-Condon S_1 state from 730 fs (in solution) to 430 fs. The relaxed S_1 state further shows a faster ISC to the triplet T_1 state of 3.9 ps compared to 11.3 ps in solution. In parallel, a study of Zinth, Rübhausen and Herres-Pawlis *et al.* on the entatic state model system $[Cu(TMGqu)_2]^+$ fulfilled the transfer into photochemistry and reports even faster IC and ISC rates in solution with values of 0.2 ps and 1.3 ps, respectively.[116] These sped-up rates can be explained by the smaller energy gap between the excited states as well as their increased structural accordance (Figure 1.11).[140-141]

Entasis therefore has a profound impact on the excited state dynamics of Cu-photosensitizers, but it also affects their kinetics in photocatalytic outer-sphere steps. Since they are Marcus-normal electron transfer reactions, the outer-sphere electron transfer steps are also impacted by the resulting structural conformity of all states, as a computational study by Villagrán and Pinter *et al.* shows.[142] They computed the reorganization energies of all important outer-sphere electron transfer steps of photocatalytic mechanisms for $[Cu(N\text{^}N)_2]^+$ and $[Cu(N\text{^}N)(P\text{^}P)]^+$ systems with increasing steric strain. More rigid systems whose T_1 and D^{ox} states (see section 1.8, Scheme 1.9 for explanations of the abbreviations) changed less relative to the S_0 state yielded lower reorganization energies, especially for steps with metal-centered redox events like $T_1 \rightarrow D^{red}$ or $D^{ox} \rightarrow S_0$ (Figure 1.13).

The entatic state concept therefore finds multiple applications in photochemistry where it can serve as a model to understand and improve not only the photophysical properties of Cu-photosensitizers, but also their reactivity. As is the case in bioinorganic chemistry, the application of the entatic state in photochemistry is not limited to copper. Entatic states have been identified for the S_1 and T_1 states of $[Ag(Xantphos)(4,4'\text{-}(MeO)_2\text{-}2,2'\text{-bipy})]^+$ and Hadt *et al.* reported prolonged lifetimes for a structurally constrained Ni(II)−bpy aryl halide complex.[143-144]

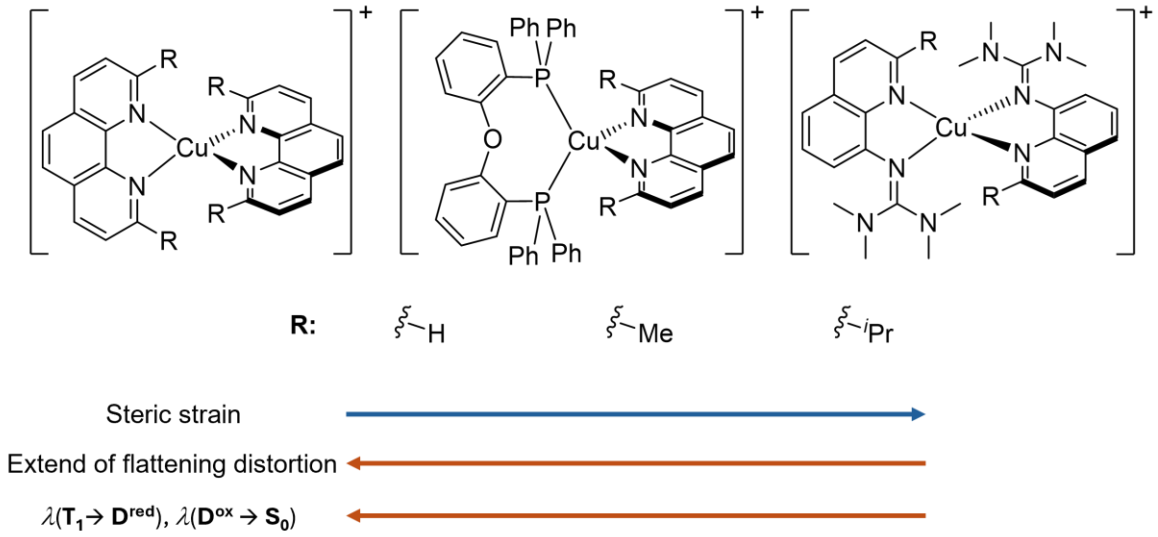

Figure 1.13: Studied complexes by Villagrán and Pinter *et al.* on the effects of rigid coordination spheres on excited state kinetics and the found negative correlations between the rigidity and reorganization energies.[142]

1.11 Pump-Probe Methods and Pump-Probe XAFS

As seen above, the detailed elucidation of the photophysical processes requires the use of time-resolved methods that are able to not only generate but also observe short-lived excited states. Pump-probe technology enables these observations, providing an extension of the experimental studies from ground state targets to excited states. The general setup of a pump-probe experiment is divided into two steps. First, the system under investigation is elevated into an excited state using a selected excitation called the “pump”. To observe excited states, this pump beam should be a laser with a wavelength λ_{pump} close to the desired transition. This pumped sample is subsequently investigated by a beam of particles referred to as the “probe”. The probe beam can constitute an optical laser, a particle beam, an X-ray or something else, depending on what ought to be studied.[145] Pump-probe measurements are thus very versatile and enable the measurement of transient UV/vis absorption spectra of triplet states, transient Raman spectra and even transient X-ray absorption spectroscopy (transient XAS).[116]

Transient XAS in particular is a useful spectroscopic method as it yields not only lifetimes but also structural information about the observed species. It is based on the ionization of an electron of the K shell of the examined metal center via high energy X-rays. This absorption can be quantified by comparing the incident beam’s intensity to that of the transmitted beam or by measuring the fluorescence given off by the excited atoms as an electron from a higher shell occupies the electron hole. After the absorption is determined for one energy of incident X-rays, the process is repeated for

a slightly altered energy. Repetition of this process for a series of energies gives rise to a spectrum.[146] The obtained XAS spectrum can be divided into two spectral regions (see Fig. 1.14).[147]

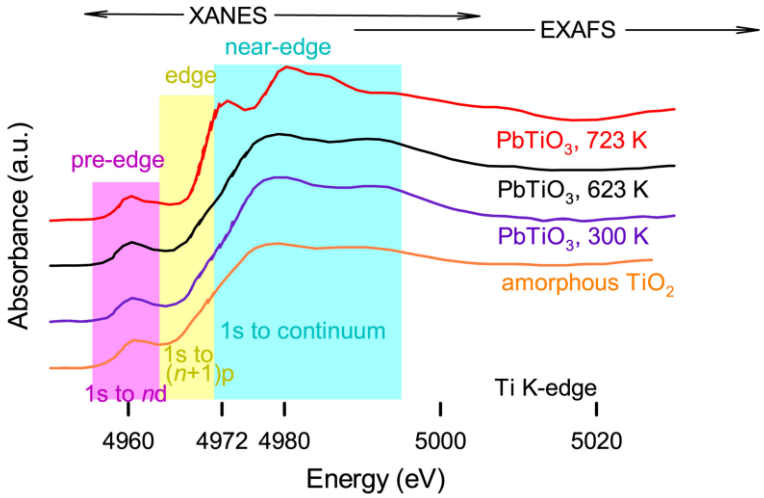

Figure 1.14: Exemplary XAS spectra and the corresponding segmentation into XANES and EXAFS regions as well as the pre-edge, edge and near-edge region.[147]

The X-ray absorption near-edge structure (XANES) depicts the absorption at low energies. In the XANES pre-edge region, the incident ray's energy is too small to excite the 1s electron to the continuum, so they populate higher orbitals instead. The pre-edge absorption, as well as the exact position of the K-edge, contain information about the oxidation state of the metal center. At higher energies, the extended X-ray absorption fine structure (EXAFS) region provides information about the type, number and distance of the nearest neighboring atoms. The fine structure is a result of the spreading wave of the emitted electron interfering with the nearest atoms. For certain energies, this interference causes back-scattering events where the detected signal lowers in intensity. This effect creates a characteristic interference pattern in the EXAFS spectrum that can be used to obtain direct information about the metal's coordination sphere.[22, 69]

In pump-probe XAS measurements, comparison of the pumped XANES region to the ground state one can be used to obtain information about the nature of the observed transition, to see whether it is an MLCT, an LMCT or something else. The pumped EXAFS can then be used to get more information about the geometry change between the ground state and the excited state. The XAS spectra of $[Cu(TMGqu)]^{+/2+}$ in the ground state and the triplet state are shown in Figure 1.15 as an example.[116] Pump-probe XAS is therefore a powerful toll for elucidating excited state dynamics and, when combined with additional time-resolved methods, can be used to construct the energy diagrams of studied compounds.[116, 148-149]

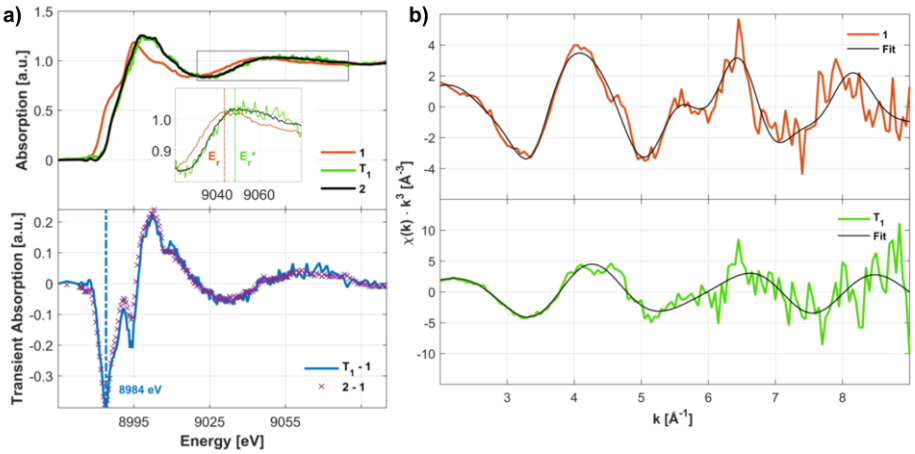

Figure 1.15: a) Above: XANES spectra of $[Cu(TMGqu)_2]^+$ (therein as **1**), $[Cu(TMGqu)_2]^{2+}$ (therein as **2**) and $[Cu(TMGqu)_2]^{+*}$ (therein as $\mathbf{T_1}$). It can be seen that the triplet state resembles a Cu(II) state due to the photo-induced oxidation from the MLCT. Below: corresponding difference spectra of the XANES region. b) EXAFS spectra of $[Cu(TMGqu)_2]^+$ and its corresponding triplet state.[116]

1.12 Guanidine Ligands and Their Copper Complexes

Guanidines are functional groups defined by their Y-shaped CN_3-group that is made up by a central carbon atom that is bound to one imine and two amine groups, which can further be functionalized by organic substituents (Figure 1.16).

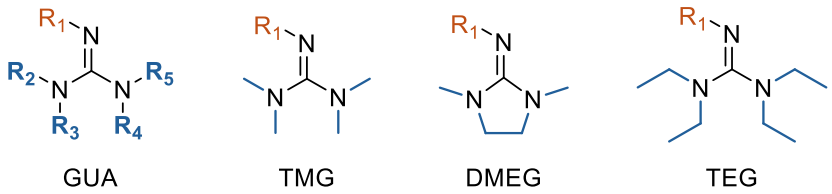

Figure 1.16: General guanidine motif and exemplary organic substituents on the amine groups.

One possible route to synthesize guanidines was reported by Kantlehner *et al.* and starts by synthesizing a so-called Vilsmeier salt from a reaction of a urea derivative with phosgene.[150]

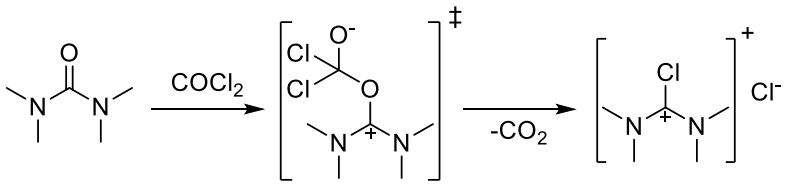

Scheme 1.14: Synthesis of a Vilsmeier salt (rightmost side) with phosgene starting from a urea derivative (leftmost side). The TMG substitution is exemplary.

The guanidine is obtained by a subsequent reaction of that Vilsmeier salt with an amine of choice via a nucleophilic substitution. Both the amine and the urea groups can be substituted; the amine specifically can link the guanidine moiety to a larger molecule like a ligand with further donor atoms.

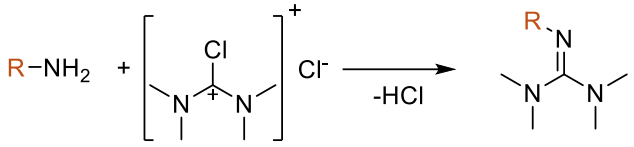

Scheme 1.15: Synthesis of a guanidine from a Vilsmeier salt.

Guanidines are considered one of the strongest neutral Brønsted bases with a pK_a of 13.6 close to that of the hydroxide ion.[151] This can be explained by the charge delocalization across the CN_3 unit that takes place upon protonation.

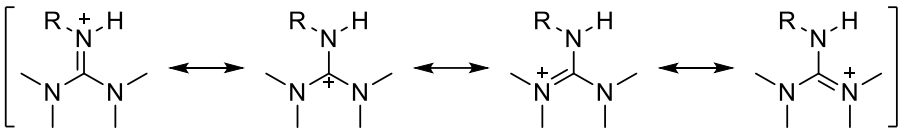

Scheme 1.16: Mesomeric structures of a protonated guanidine.

This basicity also translates to guanidines being potent Lewis acids that can form strong coordinative bonds to metal centers that exhibit σ- and π-contributions.[55, 152] Their strong donor properties have made guanidines popular in coordination chemistry and are frequently incorporated in ligands, a selection of which is shown in Figure 1.17.[69, 153-158]

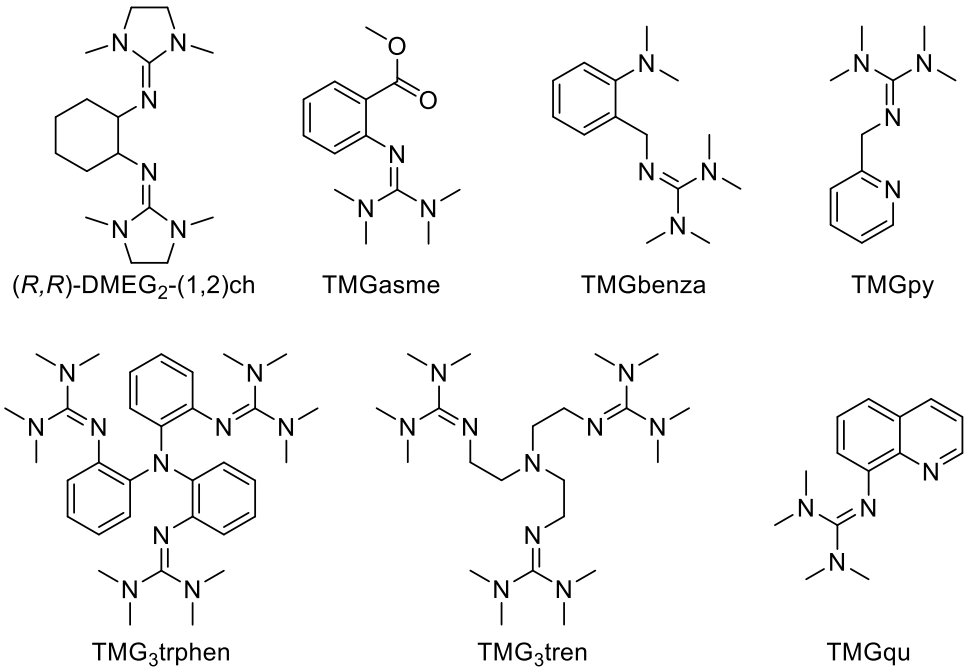

Figure 1.17: Selection of various guanidine ligands.[69, 153-158]

Zinc and iron complexes of guanidines can be employed for the ring-opening polymerization and co-polymerization of lactide, as well as the depolymerization of polylactide and other polyesters.[154-155, 159-161] Iron-guanidine complexes can further catalyze Atom transfer radical polymerization (ATRP) reactions.[162]

Cu-guanidine complexes have been used for catalytic C–N coupling reactions[156] and the guanidines' strong donor properties make them suitable to generate oxido complexes that can mimic the reactivity of tyrosinase in catalytic oxygenations.[157-158] When bound to Cu(II), the M–N_{Gua} bonds can lead to trigonal distortion of Cu(II) coordination geometries; an electronic effect caused by the guanidine's π-contributions similar to the Cu–S_{Cys} bond in blue copper proteins.[36, 54-55, 152] This distortion can be mitigated by removing π-electron density from the guanidine ligands, as demonstrated by Himmel *et al*.[55] This electronic entatic state, as well as their bulky substitution and modularity makes guanidine Cu-complexes suitable entatic state model systems. Examples include the GUAqu ligands by Herres-Pawlis *et al.* as well as the bis(chelating) bisguanidines by Himmel *et al.*[22, 63, 69, 77, 84, 86, 152, 163-164]

Next to distorted geometries, the entatic state models by Himmel *et al.* exhibit redox active properties that lead to valence tautomerism in their dicationic species. These exist in a temperature-dependent equilibrium of a Cu(I) and a Cu(II) form that can interconvert via intramolecular electron transfer between the ligand and the metal center (Scheme 1.18).[163] In a recent pair of studies, Himmel *et al*. discussed a series of mononuclear $[Cu(L)_2]^{+/2+}$ compounds of bisguanidine ligands and assessed their electron self-exchange rates.[63, 164] The obtained k_{ex} are between 10^4 and 10^6 M^{-1} s^{-1}, correlating with the degree of Cu(I) electromers in the dicationic species. The fast electron transfer is therefore rationalized as a result of the strong valence tautomerism and not a direct result of the systems' entasis.

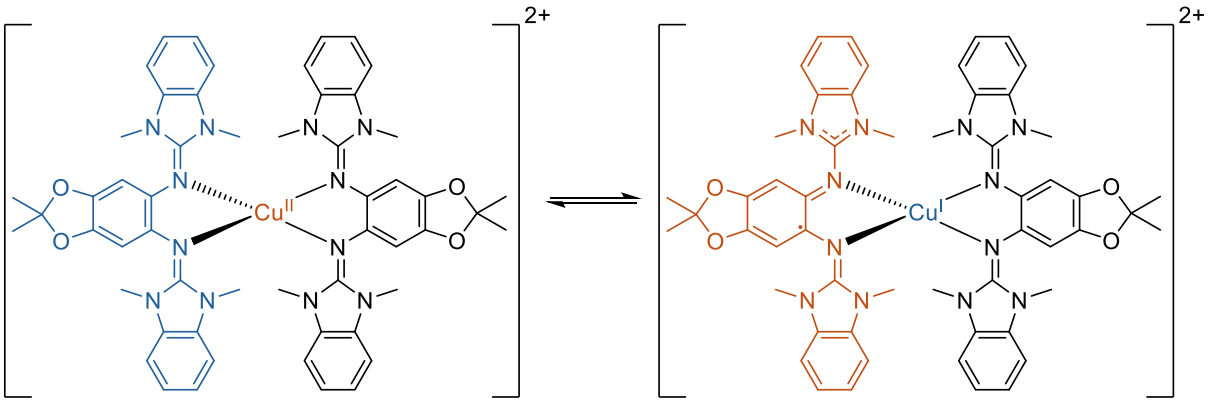

Scheme 1.17: Valence tautomerism exhibited by Cu-complexes of bisguanidine ligands.[163]

The entatic state models by Herres-Pawlis *et al.* do not exhibit valence tautomerism. Their distorted coordination geometries are partially caused by electronic factors, the substitution of the tetramethylguanidino (TMG) moiety in the TMGqu ligand with a more compact dimethylethyleneguanidino (DMEG) by Herres-Pawlis *et al*. resulted in an increase in $\Delta\tau_4$ and a decrease in k_{11} for the corresponding redox pairs. The electronic entatic state imposed by the guanidines should therefore be considered an additional

effect to steric restraints.[22, 84] In recent years, the number of GUAqu ligands used as entatic state models has grown significantly to study the influence of steric and electronic substituents in the 2-, 4-, and 6-position of the quinoline moiety (Figure 1.18).[22, 77, 84, 86, 165]

Studies of the electrochemical properties of the complexes show that substituents in the 6- and 4-position have a profound effect on the redox potential of the Cu(I/II) redox pair, yielding potentials between −0.34 to −0.64 V vs. Fc/Fc^+, depending on whether the substituent is electron donating or withdrawing in nature. However, the obtained k_{11} increase only marginally compared to the value of $[Cu(TMGqu)_2]^{+/2+}$ and are all on the order of magnitude of 10^2 M^{-1} s^{-1} or lower. Contrary to this, the 2-subtituted systems do not only show significant changes in their redox potentials, but their electron transfer rates as well. While the redox potentials skew to more positive values between −0.13 to −0.302 V vs. Fc/Fc^+, their k_{11} increase unanimously to 10^3 M^{-1} s^{-1}, one order of magnitude above $[Cu(TMGqu)_2]^{+/2}$. For the methyl- and cyclohexyl-substituted systems, both properties seem to originate from a more rigid coordination geometry that is also more tetrahedral on average than that of other GUAqu systems. Interestingly, the methyl ester substituent of the $[Cu(TMG2Meequ)_2]^{+/2+}$ pair leads to a change in the coordination motif from tetracoordinate in Cu(I) to a [4+2] coordination geometry in the Cu(II) complex due to additional O-donors. This renders the system coordination-variant and therefore an outlier to the otherwise coordination-invariant $[Cu(GUAqu)_2]^{+/2+}$ model systems. Overall, the conducted studies suggest that the entasis of the coordination-invariant systems is largely a function of steric strain and not of electron withdrawing or donating effects, reinforcing the notion of a rigid entatic state and the need for minimal internal reorganization between both oxidation states.

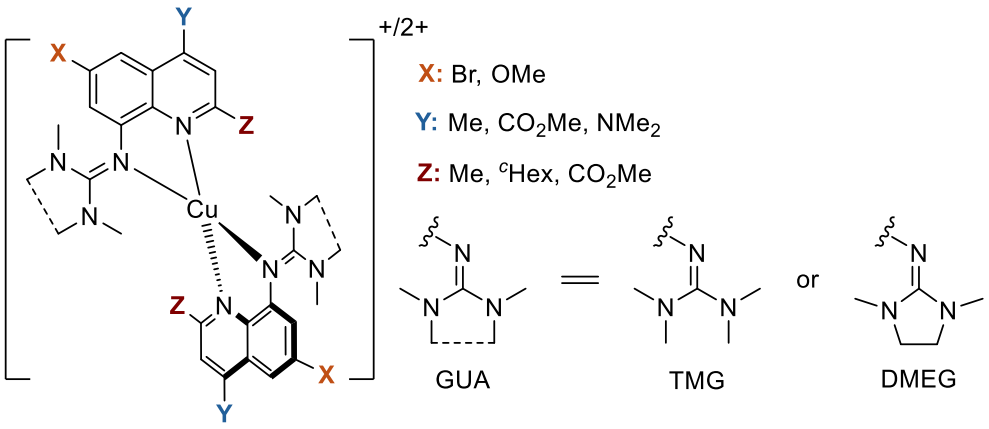

Figure 1.18: Studied organic substituents and their respective positions for GUAqu-model systems as well as studied guanidines. The ligands are mono-substituted.[22, 77, 84, 86, 165]

2 Objectives and Outline

2.1 Objectives

Several natural electron transfer processes in nature are mediated by copper proteins, which have long been modelled by transition metal complexes. These copper complexes have helped to better understand the nature of electron transfer mechanisms and how to improve their efficacy using ligand design. The main avenues of this research have focused on thermal electron transfer of coordination-variant and -invariant model systems, with the latter using the entatic state to increase the electron self-exchange rates. With the advent of copper photosensitizers, the entatic state concept has also found use in photoinduced electron transfer processes, mostly contained to intramolecular charge transfer processes.

The main objective of this thesis is to study electron transfer dynamics in all of these three main avenues using copper complexes of coordination-variant and -invariant guanidine quinolinyl ligands. Studied ligands include literature-known, but also mostly novel compounds that will be synthesized and characterized before studying their copper complexes. Studies of thermal electron transfer models will be conducted by utilizing single crystal X-ray diffraction (SCXRD) and density functional theory (DFT) to gain structural information on isolable, as well as metastable compounds, as well as cyclic voltammetry to assess their redox potentials and mechanistic details of reduction and oxidation steps. Lastly, the systems' electron-self exchange rate constants k_{11} will be determined using stopped-flow UV/vis spectroscopy and the Marcus cross relation and their reorganization energies will be computed via DFT to investigate the kinetics of the involved redox processes. This will allow for a holistic assessment of the structure-property relationships within the studied systems to inform future improvements in the ligand design.

For the photoinduced electron transfer, literature-known coordination-invariant model complexes of 2-substituted GUAqu ligands will be studied. The main objective of this part is to understand how the entatic state of thermal electron transfer models affects their photophysical and photochemical properties. Therefore, the structures of the complexes ground and excited states will be assessed using DFT to investigate the influence of steric bulk on the geometry changes upon excitation. The systems' excited state lifetimes will be measured using transient X-ray absorption and fluorescence spectroscopy (XAFS) and correlated with the obtained structural information to further assess the effect of entasis on excited state lifetimes. Lastly, the complexes' photochemical potential will be assessed using cyclic voltammetry and fluorescence

emission spectroscopy to find suitable reactions for them to function as potential photoredox catalysts.

2.2 Outline

This thesis' results are sub-divided into three parts.

The first part (chapter 3) investigates novel and literature-known tripodal tetradentate ligands with varying numbers of guanidine and quinolinyl moieties and aromatic backbones. Aim of this chapter is to understand the coordination-variant systems' electron transfer mechanism and to investigate how systematic changes in the ligand bulk and donor strength potentially affect this mechanism and subsequently the electron self-exchange rate. This is done by combining structural analysis via SCXRD and DFT with analysis of the systems' redox properties using cyclic voltammetry and stopped-flow UV/vis spectroscopy. The second part of the thesis (chapter 4) is concerned with thermal electron transfer of the well-established, coordination-invariant bis(chelate) copper complexes of guanidine quinolinyl (GUAqu) ligands that have already seen extensive study. Herein, the GUAqu ligands will be derivatized with sp^2-hybridized substituents in the 2-position to probe their effect on the structural, as well as thermodynamic and kinetic redox properties. The employed methodology largely follows the previous chapter but also includes EPR studies of the Cu(II) complexes as well as detailed time-dependent DFT (TD-DFT) simulations of the complexes' UV/vis spectra and transitions therein.

The final results chapter (chapter 5) focuses on the photophysical and photochemical properties of literature-known $[Cu(GUAqu)_2]^+$ complexes. This chapter includes structural analysis of the ground and excited states using DFT, XAFS measurements for the determination of excited state lifetimes. After photochemical assessment using cyclic voltammetry and fluorescence emission spectroscopy, several potential reaction systems were tested to verify the entatic state models' potential application as photoredox catalysts.

Chapter 6 summarizes these results and gives an outlook on future studies. Chapter 7 contains the experimental details and methods. Additional information is gathered in the Appendix (chapter 9), relevant sub-sections of which are referenced in the results section when necessary.

3 Tripodal Tetradentate Copper Guanidine Quinoline Model Systems

3.1 Motivations and Aim

Tripodal tetradentate ligand systems have been first studied by Rorabacher *et al*. and Yandell *et al*. under the lens of the rigid entatic state at the end of the last century.[10, 14, 70, 166] The ligands contain tertiary alkyl amines and three arms of with varying kinds of neutral donors. Those model systems are coordination-variant; changing coordination number (CN) upon oxidation by coordinating a previously dissociated halogenide or solvent molecule (Figure 3.1, above). Rorabacher *et al*. postulated that coordination-variant tripodal systems could undergo electron transfer following one of two possible pathways (Fig. 3.1).[70, 166]

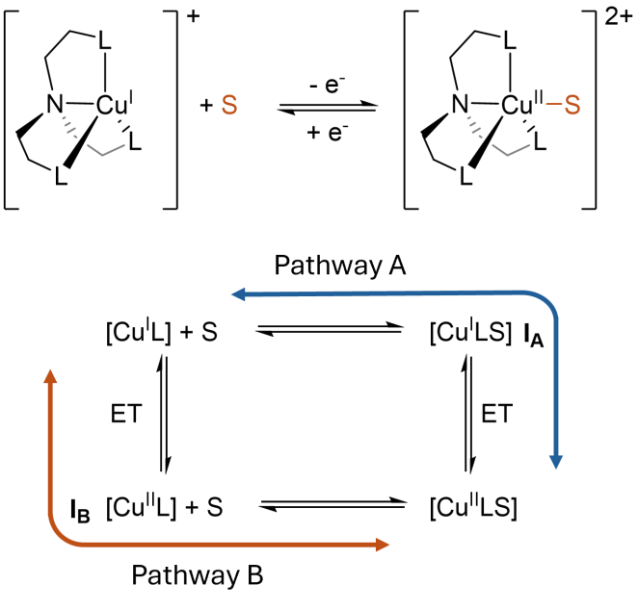

Figure 3.1: Above: Exemplary illustration of a CN-change upon reduction or oxidation of a coordination-variant model system. The co-ligand (S) in this case was chosen to be neutral. Below: Illustration of the square scheme of the reaction shown above.

Both discussed mechanisms involve an electron transfer and the change of CN as discrete chemical reactions. The change of CN in a Cu(I) system was regarded as too sterically demanding and Intermediate $\mathbf{I_A}$ as too unstable by Rorabacher *et al*. Therefore, the oxidation-addition mechanism of Pathway B was stated as preferred in the oxidation reaction for a majority of tripodal model systems. However, the nature of the kinetic barriers in these reactions remained elusive.[70]

By employing a previously overlooked tripodal scaffolding with a rigid aromatic backbone as well as significant steric bulk via employed guanidine substituents, this study aims to generate further insight into coordination-variant tripodal model systems and their mechanistic preferences. The steric bulk in these systems is varied by

changing both, the number of incorporated guanidine moieties and their bulk, by exchanging the bulky TMG moiety with the more compact DMEG moiety. This gives rise to six different ligands that were synthesized and complexed with Cu-salts to investigate the resulting complexes electron transfer rates and their mechanisms via DFT and cyclic voltammetry. The studied ligand systems are depicted in Figure 3.2.
A previously tested ligand system studied in the working group was the $N(2MeQu)_3$ system whose copper complexes were found to be unsuited for electron transfer studies due to electrochemical factors.[167]

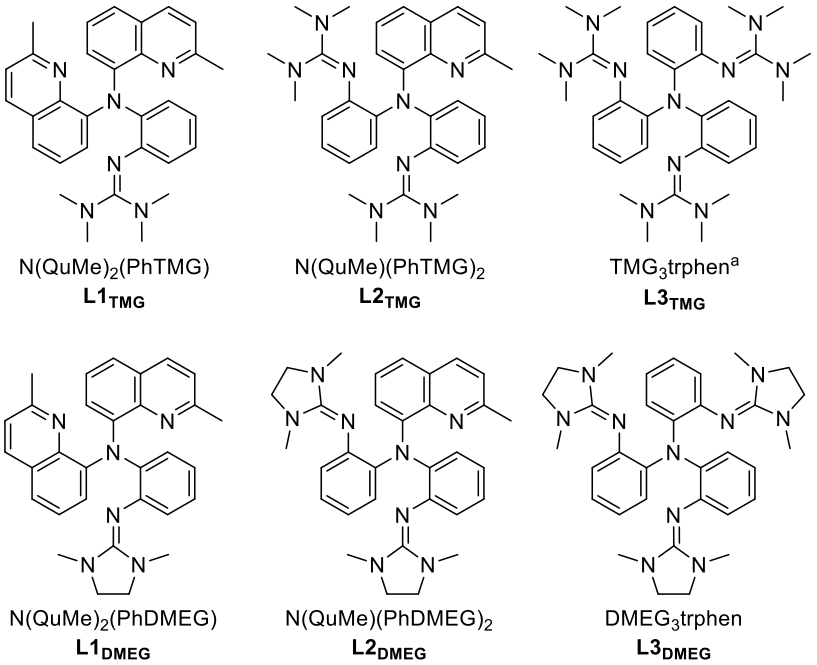

Figure 3.2: Structural formulas, names and abbreviations of the tripodal tetradentate triarylamine ligands covered in this chapter.

3.2 Ligand Synthesis

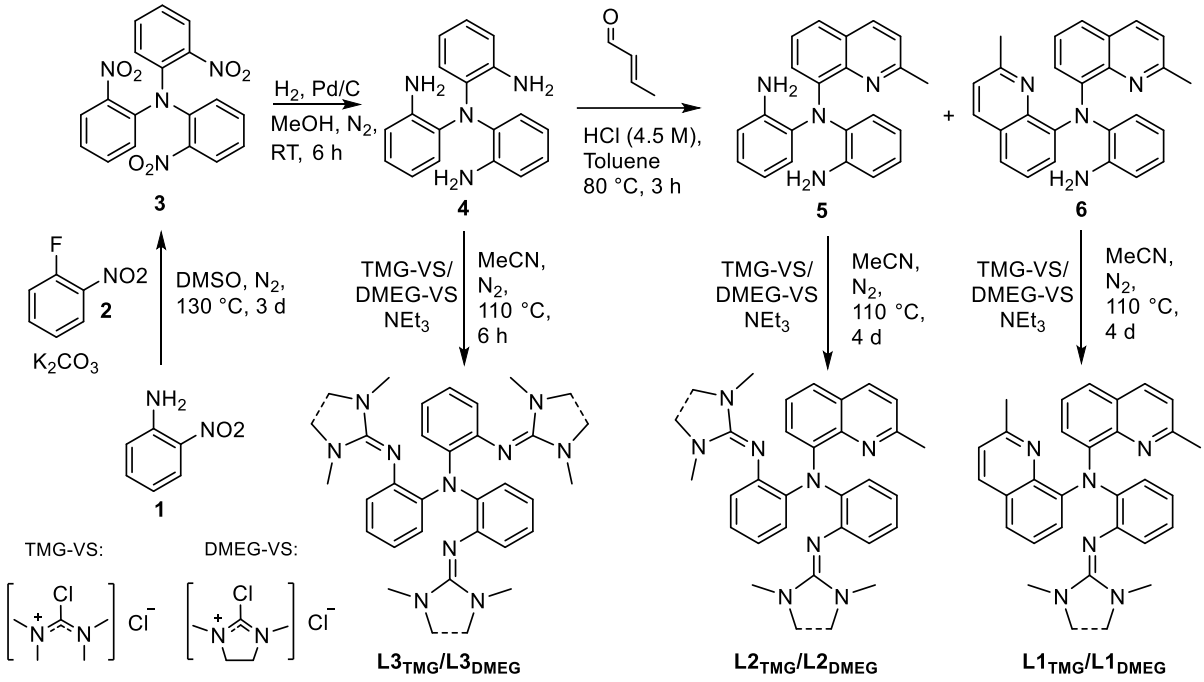

Scheme 3.1: Synthesis scheme of the ligand pairs **L1**, **L2** and **L3**.

All syntheses (Scheme 3.1) started with the S_NAr reaction of 2-nitroanilin (**1**) with 2 equivalents of 1-fluoro-2-nitrobenzene (**2**), yielding tris(nitrophenyl)amine (**3**). The reaction was inspired by a procedure from Gorvin.[168] The obtained nitro precursor **3** was then reduced following a modified procedure described by Stavropoulos and Cronin *et al.* to obtain N^1,N^1-bis(2-aminophenyl)benzene-1,2-diamine (**4**) as a white solid.[156] The amine was then combined with different Vilsmeier salts to obtain the corresponding ligand. To obtain pairs **L1** and **L2**, the amine precursor **4** was first subjected to a Doebner-Miller reaction in a procedure inspired by Dalko *et al*., followed by a separation of the products *via* gradient column-chromatography.[169] The Doebner-Miller reaction proved to be a bottleneck in the synthesis with inconsistent and comparatively low yields (10 to 25 %). Varying the amount of crotonaldehyde allowed for slight control of the preferred product but did not improve the yield. The amine precursor **4** and the cyclization products N^1-(2-aminophenyl)-N^1-(2-methylquinolin-8-yl)benzene-1,2-diamine (**5**) and N^1,N^1-bis(2-methylquinolin-8-yl)benzene-1,2-diamine (**6**) were subsequently functionalization with TMG- and DMEG-Vilsmeier salts after a procedure by Herres-Pawlis *et al.* to obtain the ligand pairs **L1, L2** and **L3**. The latter pair could be purified via repeated recrystallization from hot acetonitrile. **L1** and **L2** where first heated under vacuum to remove the remaining urea derivative and subsequently recrystallized from a mixture of THF and hexane. **L1$_{DMEG}$** could not be purified in the same way due the crude product separating off as an oil. A possible purification via filtration over alumina was tested but resulted in the complete

decomposition of all ligands. Due to the guanidines' basicity, the ligands were stored under inert conditions and handled in absolute solvents as they would otherwise protonate quickly.

3.3 Complex Synthesis and Characterization

3.3.1 Synthesis and Structural Characterization of the Cu(I) complexes

All six ligands were subsequently combined with $[Cu(MeCN)_4]PF_6$ in MeCN and precipitated with diethyl ether to yield complex pairs, $[Cu\{N(QuMe)_2(PhTMG)\}]PF_6$ (**C1$_{TMG}$–PF$_6$**) and $[Cu\{N(QuMe)_2(PhDMEG)\}]PF_6$ (**C1$_{DMEG}$–PF$_6$**), $[Cu\{N(QuMe)(PhTMG)_2\}]PF_6$ (**C3$_{TMG}$–PF$_6$**) and $[Cu\{N(QuMe)(PhDMEG)_2)\}]PF_6$ (**C3$_{DMEG}$–PF$_6$**) as well as $[Cu(TMG_3trphen)]PF_6$ (**C5$_{TMG}$–PF$_6$**)[156] and $[Cu(DMEG_3trphen)]PF_6$ (**C5$_{DMEG}$–PF$_6$**).

The solid-state structures of the **C1–PF$_6$** pair were crystallized by layering an acetonitrile solution with diethyl ether (Scheme 3.2).

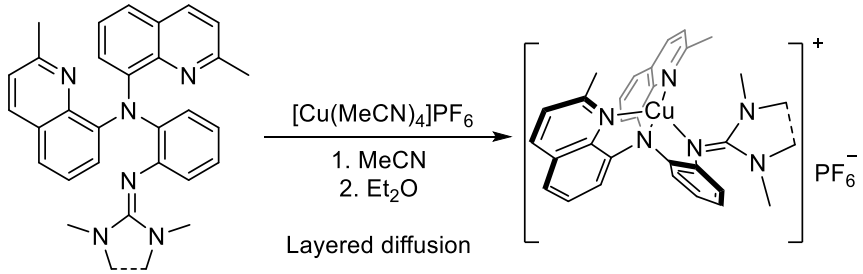

Scheme 3.2: Crystallization of the complex pair **C1–PF$_6$**.

The obtained structures for **C1$_{TMG}$–PF$_6$·MeCN** and **C1$_{DMEG}$–PF$_6$·MeCN** crystallized in the monoclinic space group *P*2/c and the triclinic space group *P*$\bar{1}$, respectively.

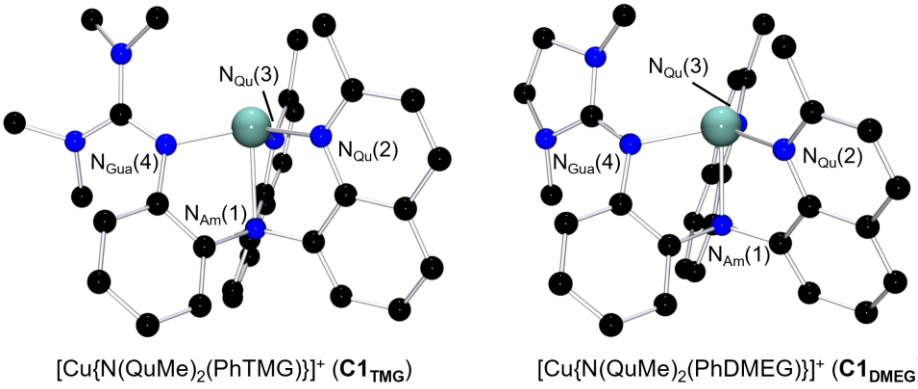

Figure 3.3: Molecular structures of the complex cations $[Cu\{N(QuMe)_2(PhTMG)\}]^+$ (**C1$_{TMG}$**, left) and $[Cu\{N(QuMe)_2(PhDMEG)\}]^+$ (**C1$_{DMEG}$**, right) in crystals of $[Cu\{N(QuMe)_2(PhTMG)\}]PF_6 \cdot$ MeCN (**C1$_{TMG}$–PF$_6$·MeCN**) and $[Cu\{N(QuMe)_2(PhDMEG)\}]PF_6 \cdot$ MeCN (**C1$_{DMEG}$–PF$_6$·MeCN**) (hydrogen atoms, non-coordinating anions and solvent molecules are omitted for clarity, important atoms are marked).

The solid state structures of **C3** were obtained in a similar fashion from a solution of dichloromethane layered with pentane.

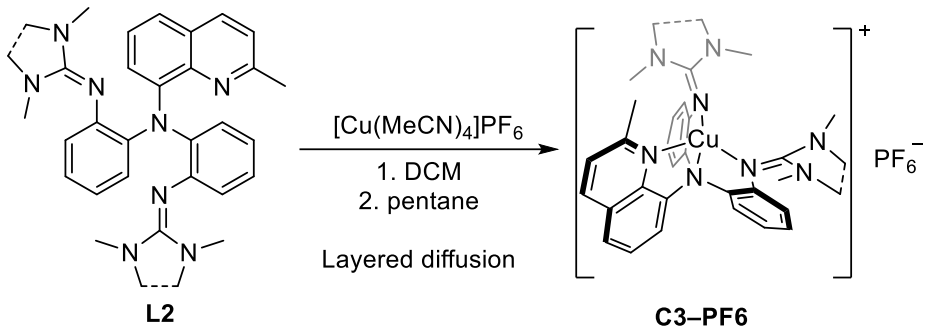

Scheme 3.3: Crystallization of the complex pair **C3–PF$_6$**.

The obtained structures for **C3$_{TMG}$–PF$_6$·DCM·C$_5$H$_{12}$** and **C3$_{DMEG}$–PF$_6$·DCM** crystallized in the monoclinic space group $P2_1/n$ and the triclinic space group $P\bar{1}$, respectively.

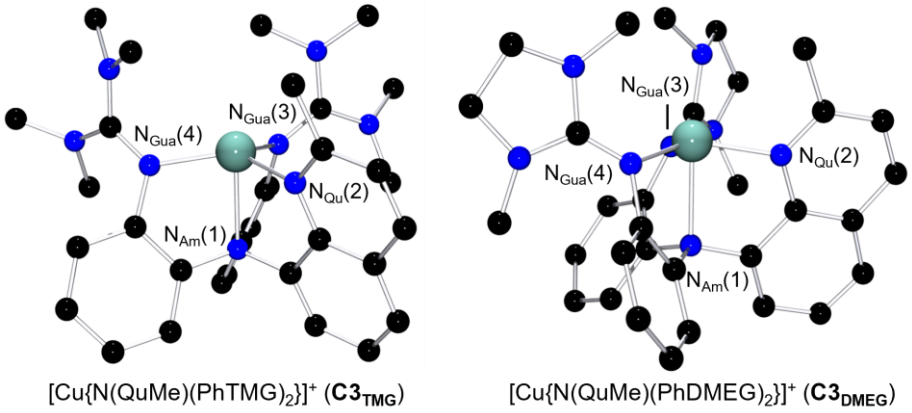

Figure 3.4: Molecular structures of the complex cations $[Cu\{N(QuMe)(PhTMG)_2\}]^+$ (**C3$_{TMG}$**, left) and $[Cu\{N(QuMe)(PhDMEG)_2\}]^+$ (**C3$_{DMEG}$**, right) in crystals of $[Cu\{N(QuMe)(PhTMG)_2\}]PF_6 \cdot DCM \cdot C_5H_{12}$ (**C3$_{TMG}$–PF$_6$·DCM·C$_5$H$_{12}$**) and $[Cu\{N(QuMe)(PhDMEG)_2\}]PF_6 \cdot DCM$ (**C3$_{DMEG}$–PF$_6$·DCM**) (hydrogen atoms, non-coordinating anions and solvent molecules are omitted for clarity, important atoms are marked).

The crystal structure for **C5$_{TMG}$** was already reported by Cronin and Stavropoulos *et al.*[156] The solid state structure of **C5$_{DMEG}$** was obtained analogously to **C1** by layered diffusion of diethyl ether into a solution of the complex in acetonitrile.

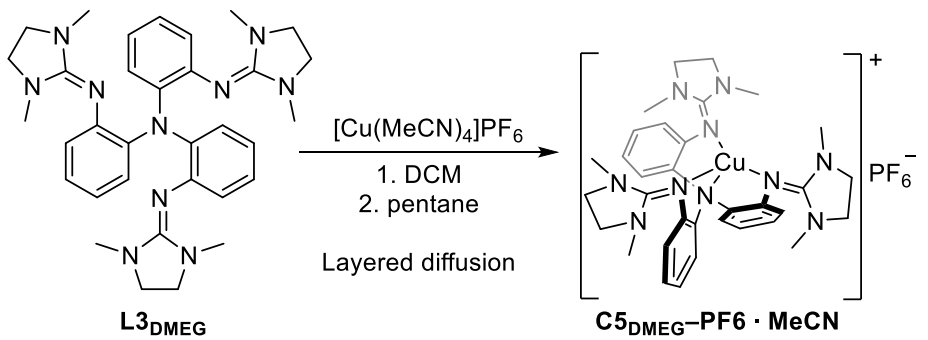

Scheme 3.4: Crystallization of the complex pair **C5$_{DMEG}$–PF$_6$·MeCN**.

The obtained structure for **C5$_{DMEG}$–PF$_6$·MeCN** crystallized in the triclinic space group $R\bar{3}c$.

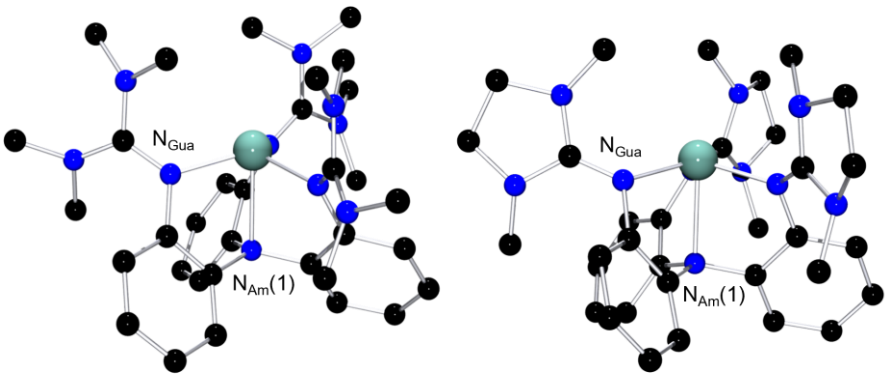

Figure 3.5: Molecular structures of the complex cations [Cu(TMG$_3$trphen)]$^+$ (**C5$_{TMG}$**, left) and [Cu(DMEG$_3$trphen)]$^+$ (**C5$_{DMEG}$**, right) in crystals of [Cu(TMG$_3$trphen)]PF$_6$ · MeCN (**C5$_{TMG}$–PF$_6$·DCM**) reported by Stavropoulos and Cronin *et al.* and [Cu(DMEG$_3$trphen)]PF$_6$ · MeCN (**C5$_{DMEG}$–PF$_6$·MeCN**) (hydrogen atoms, non-coordinating anions and solvent molecules are omitted for clarity, important atoms are marked).[156]

Selected bond lengths, angles, and structure parameters of the six structures are listed in Table 3-1. The Cu(I) complex cations display a four-coordinate coordination geometry best described as a distorted trigonal pyramid, a so-called umbrella-distortion, in which the copper ion is not positioned at the center, but slightly outside the face of the coordination polyhedron.[13] This distortion becomes more pronounced with an increasing number of guanidine donors, as can be seen by the lengthening Cu–N$_{Am}$ bonds and decreasing N(1)–Cu–N(X) angles. The SHAPE program by Alvarez *et al.* was applied to determine the coordination geometries' distortion away from the ideal square planar (D_{4h}), tetrahedral (T_d) or square pyramidal (C_{3v}) symmetries (Table 3-1). The coordination environments of all Cu(I)-structures display similar values, with strong distortions away from the T_d and D_{4h} symmetries and the least distortion away from C_{3v} symmetry. The umbrella distortion, as well as the asymmetric substitution of the equatorial donors, notably elevate the distortion values for this geometry as well. Comparing the complex cations' structures to those of the tetracoordinate [Cu(Me$_6$tren)]ClO$_4$ (**CC1**), [Cu(TMG$_3$tren)]PF$_6$ (**CC2**) and [Cu(N(QuMe)$_3$)]PF$_6$ (**CC3**) complexes shows that the umbrella distortion is more pronounced in all of the copper triarylamine complexes (**C1**, **C3**, **C5**, **CC3**) than in the aliphatic ones (**CC1** and **CC2**, Figure 3.6, Table 3-2).[153, 167, 170]

Table 3-1: Key bond lengths, bond angles and structural parameters of the Cu(I) complex cations **C1**, **C3** and **C5**.

	$C1_{TMG}$	$C1_{DMEG}$	$C3_{TMG}$	$C3_{DMEG}$	$C5_{TMG}$[a]	$C5_{DMEG}$
Bond Lengths [Å]						
Cu–N_{Am}(1)	2.254(2)	2.2608(16)	2.275(3)	2.282(2)	2.355(2)	2.3475(19)
Cu–N_{Gua}(2)					2.0129(15)	2.0299(11)
Cu–N_{Gua}(3)			2.051(3)	2.068(2)	2.0129(15)	2.0299(11)
Cu–N_{Gua}(4)	1.991(2)	2.0373(13)	1.974(3)	1.982(2)	2.0129(15)	2.0299(11)
Cu–N_{Qu}(2)	1.982(2)	1.9512(13)	1.971(3)	1.9735(19)		
Cu–N_{Qu}(3)	2.041(2)	2.0135(13)				
Bond Angles [°]						
N(1)–Cu–N(2)	83.29(9)	81.61(6)	82.24(12)	81.78(8)	78.54(4)	78.46(3)
N(1)–Cu–N(3)	80.28(9)	82.27(5)	79.22(13)	78.17(9)	78.54(4)	78.46(3)
N(1)–Cu–N(4)	81.49(9)	79.54(5)	87.87(12)	81.87(8)	78.54(4)	78.46(3)
N(2)–Cu–N(3)	111.92(9)	124.01(5)	131.67(13)	100.89(8)	116.15(3)	116.10(2)
N(2)–Cu–N(4)	129.68(10)	126.87(5)	113.22(13)	130.00(8)	116.15(3)	116.10(2)
N(3)–Cu–N(4)	112.23(9)	102.01(5)	107.48(14)	121.22(8)	116.15(3)	116.10(2)
Structural Parameters						
ρ [ ]	0.97	0.96	0.96, 0.97	0.96, 0.96	0.96, 0.96, 0.96	0.95, 0.95, 0.95
τ_4 [ ]	0.84	0.77	0.81	0.77	0.91	0.91
$S(T_d)$ [ ]	5.754	6.210	6.130	6.451	6.462	6.622
$S(D_{4h})$ [ ]	33.054	32.793	32.625	33.935	36.775	36.820
$S(C_{3v})$ [ ]	0.733	1.128	1.006	1.299	0.819	0.818

a: [156]

Noteworthy is that the aliphatic guanidine donors do not seem enforce an umbrella distortion, evident by **CC1** and **CC2** exhibiting an identical Cu–N_{Am} bond length, similar N(1)–Cu–N(X) angles and low $S(C_{3v})$ values. Only **CC3** exhibits signs of a distorted geometry, implying that the presence of an aromatic backbone is essential for its formation. While the umbrella distortion could therefore be considered a result of the aromatic scaffold's rigidity, electronic factors due to conjugation of the central amine with the ligand arms also requires consideration. Since a simple indicator for the degree of conjugation between two atoms is their corresponding bond length, all central amines' N_{Am}–R bonds of **C1**, **C3**, **C5** and **CC3** were investigated (Table 3-3).

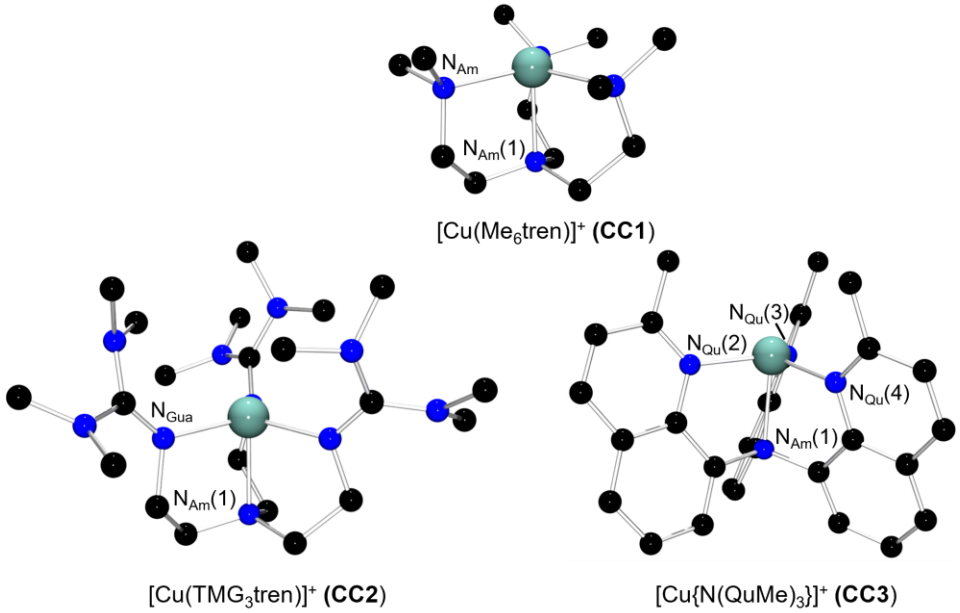

Figure 3.6: Molecular structures of the complex cations $[Cu(Me_6tren)]^+$ (**CC1**), $[Cu(TMG_3tren)]^+$ (**CC2**), $[Cu\{N(QuMe)_3\}]^+$ (**CC3**) (hydrogen atoms, non-coordinating anions and solvent molecules are omitted for clarity, important atoms are marked).[153, 167, 170]

Table 3-2: Key bond lengths, bond angles and structural parameters of the Cu(I) complex cations **CC1**, **CC2** and **CC3**.[153, 167, 170]

	$[Cu(Me_6tren)]$ ClO_4 (CC1)	**$[Cu(TMG_3tren)]$ PF_6 (CC2)**	**$[Cu(N(QuMe)_2]$ PF_6 (CC2)**
	x = Amine	x = Guanidine	x = Quinolinyl
Bond Lengths [Å]			
Cu–N_{Am}(1)	2.200(14)	2.200(2)	2.250(3)
Cu–N_x(2)	2.122(7)	2.053(2)	2.001(3)
Cu–N_x(3)	2.122(7)	2.053(2)	1.993(3)
Cu–N_x(4)	2.122(7)	2.053(2)	1.986(3)
Bond Angles [°]			
N(1)–Cu–N(2)	84.55(7)	84.1(1)	81.8(2)
N(1)–Cu–N(3)	84.55(7)	84.1(1)	82.8(2)
N(1)–Cu–N(4)	84.55(7)	84.1(1)	82.7(2)
N(2)–Cu–N(3)	119.11(2)	119.0(1)	115.8(2)
N(2)–Cu–N(4)	119.11(2)	119.0(1)	120.8(2)
N(3)–Cu–N(4)	119.11(2)	119.0(1)	118.4(2)
Structural Parameters			
ρ [ ]	-	0.95, 0.95, 0.95	-
τ_4 [ ]	0.86	0.87	0.86
$S(T_d)$ [ ]	5.139	5.070	5.212
$S(D_{4h})$ [ ]	35.677	35.755	35.498
$S(C_{3v})$ [ ]	0.174	0.210	0.385

Table 3-3: Cu–N_{Am} and N_{Am}–C bond lengths, as well as the average of the latter for **CC3**, **C1**, **C3** and **C5**.

	CC3	**$C1_{TMG}$**	**$C1_{DMEG}$**	**$C3_{TMG}$**	**$C3_{DMEG}$**	**$C5_{TMG}$[a]**	**$C5_{DMEG}$**
			Bond Lengths [Å]				
Cu–N_{Am}(1)	2.250(3)	2.254(2)	2.2608(16)	2.275(3)	2.282(2)	2.355(2)	2.3475(19)
N_{Am}–C_{Gua}(2)						1.434	1.4336(12)
N_{Am}–C_{Gua}(3)				1.443(5)	1.434(3)	1.434	1.4336(12)
N_{Am}–C_{Gua}(4)		1.458(3)	1.4468(17)	1.445(5)	1.458(3)	1.434	1.4336(12)
N_{Am}–C_{Qu}(2)	1.449(4)	1.439(4)	1.4464(17)	1.443(5)	1.448(3)		
N_{Am}–C_{Qu}(3)	1.455(4)	1.454(3)	1.4401(17)				
N_{Am}–C_{Qu}(3)	1.462(4)						
Average N_{Am}–C	1.455	1.450	1.444	1.444	1.447	1.434	1.434

While there are variations in each complex for the average N_{Am}–C and Cu–N_{Am} bond lengths, there is a correlation between both values. This correlation is indicative of the umbrella distortion being a result of conjugation of the central amine's lone pair and not exclusively due to the rigid aromatic backbone. An explanation for the shortening of N–C bonds with increasing number of guanidine moieties is the guanidine's connectivity within the ligand. Unlike the N_{Qu} donor, the N_{Gua} donor is not fixated by an aromatic ring which allows for greater rotation and thus a stronger planarization of the guanidine's "arm". Similar observations of weaker donation of the central amine in more planarized triarylamines have been reported by Krämer *et al*.[171]

Although the trigonal pyramidal geometry and the umbrella distortion of **C1**, **C3** and **C5** should allow for a fifth donor in form of a coordinating solvent molecule like acetonitrile, no signs of a predominantly pentacoordinate [Cu(L)(MeCN)] species were observed. This can be attributed to the steric bulk of the guanidines and the methyl groups of the quinolinyl units. Concerning other structural parameters, the obtained τ_4 parameters pinpoint rather tetrahedral geometries for all complexes that roughly increase with the number of guanidine units present. **$C1_{DMEG}$** and **$C3_{DMEG}$** both display the lowest τ_4 values. Given the Cu-center's position outside the coordination polyhedron, the τ_4 parameter's accuracy regarding these systems is questionable. The ρ parameter gives electronic information on the guanidines and denotes the level of delocalization of the electrons in each guanidine unit (Eqn. 20).

$$\rho = \frac{2a}{b + c} \tag{20}$$

a: length of C-N_{Imine} bond; b,c: lengths of C-N_{Amine} bond

The ρ values given in Table 3-1 show a minor difference between the delocalization of the TMG and DMEG groups, as expected in comparison to reported systems by Herres-Pawlis *et al*.[84]

3.3.2 Attempted Synthesis of the Cu(II) Complexes

Cronin and Stavropoulos *et al.* reported the solid-state structure of the Cu(II) salt [Cu(TMG$_3$trphen)(MeCN)](PF$_6$)$_2$ (**C6$_{TMG}$–PF$_6$**, Figure 3.7).[156]

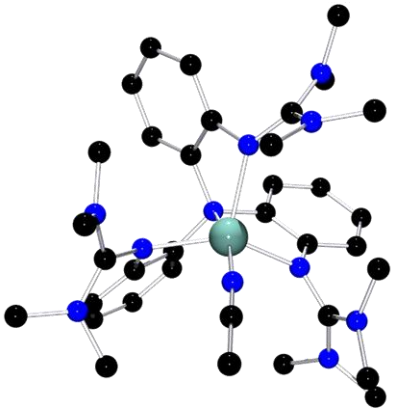

Figure 3.7: Molecular structure of the complex cation [Cu(TMG$_3$trphen)(MeCN)]$^{2+}$ (**C6$_{TMG}$**) as reported by Stavropoulos and Cronin *et al.* (hydrogen atoms, non-coordinating anions and solvent molecules are omitted for clarity).[156]

The structure shows the expansion of the coordination sphere to a pentacoordinate geometry with an acetonitrile co-ligand. Given the data on tripodal copper complexes, the increase in CN is to be expected and shows that the herein discussed systems are coordination-variant model systems. The solid-state structures of other Cu(II) complexes could not be obtained. Attempts to crystallize the analogous Cu(II) complex to **C6$_{TMG}$**, [Cu(DMEG$_3$trphen)(MeCN)](OTf)$_2$ (**C6$_{DMEG}$–OTf**) resulted in a black oil without the expected dark crystals. Similarly, the crystallization of the remaining Cu(II) complexes was attempted by combining the ligands with [Cu(II)(MeCN)$_4$](X)$_2$ (X = BF$_4$, OTf) but no crystalline Cu(II) compounds could be isolated. Instead, the crystallization attempts returned colorless crystals that XRD revealed to be [Cu(I)(MeCN)$_4$]X, without ligands (Figure 3.8) and black residue that could not be analyzed via XRD.

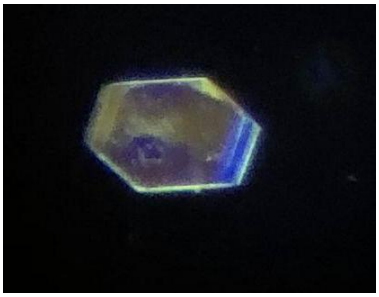

Figure 3.8: Obtained [Cu(MeCN)$_4$]BF$_4$ crystal from a crystallization batch initiated from [Cu(MeCN)$_2$](BF$_4$)$_2$ and **L2$_{TMG}$**.

The evident decomposition of the complexes could be considered a result of potential redox activity by the ligands, given the known redox active properties of Cu complexes with aromatic guanidine ligands.[55, 152, 164] These properties were not further investigated within this study. Since the main goal of the isolation of the Cu(II) compounds was to obtain their solid-state structures, further attempts to isolate them were discarded and the complexes were instead studied theoretically via DFT.

3.4 Theoretical Description of the Cu(I) and Cu(II) Complexes

DFT calculations of all compounds were performed using Gaussian 16, employing the functional TPSSh combined with the def2-TZV basis set for geometry optimization and single point.[172-177] Additionally, an implicit solvation model for MeCN using PCM and Grimme dispersion correction 3 with Becke-Johnson dampening were used.[178-180] The computations in this chapter focus on characterization of the structures and their electronic properties. Potential mechanistic steps of the electron transfer reactions were also calculated and are discussed in Sections 3.5.1 and 3.6.

3.4.1 Theoretical Description of the Cu(I) complexes

The obtained Cu(I) geometries are in good agreement with the solid-state structures, showing only minor deviations in the obtained angles and bond lengths as illustrated by RMSD values between 0.089 and 0.362 Å (Table 3-4).

Table 3-4: Key bond lengths, bond angles and structural parameters of the DFT optimized geometries of the Cu(I) complex cations **C1**, **C3** and **C5** (TPSSh-D3BJ/def2-TZVP+ PCM(MeCN) // TPSSh-D3BJ/def2-TZVP + PCM(MeCN)).

	$C1_{TMG}$	**$C1_{DMEG}$**	**$C3_{TMG}$**	**$C3_{DMEG}$**	**$C5_{TMG}$[a]**	**$C5_{DMEG}$**
Bond Lengths [Å]						
Cu–N_{Am}(1)	2.283	2.286	2.308	2.322	2.322	2.364
Cu–N_{Gua}(2)					2.030	2.034
Cu–N_{Gua}(3)			2.000	2.074	2.030	2.034
Cu–N_{Gua}(4)	2.026	2.040	2.063	2.006	2.030	2.034
Cu–N_{Qu}(2)	1.974	1.968	1.993	1.991		
Cu–N_{Qu}(3)	2.025	2.024				
Bond Angles [°]						
N(1)–Cu–N(2)	81.5	81.4	81.0	80.6	78.9	77.3
N(1)–Cu–N(3)	80.6	80.7	79.5	78.2	78.9	77.3
N(1)–Cu–N(4)	78.8	78.1	77.7	76.8	78.9	77.3
N(2)–Cu–N(3)	119.6	122.4	129.4	104.7	116.4	115.3
N(2)–Cu–N(4)	127.8	127.5	105.9	130.4	116.3	115.3
N(3)–Cu–N(4)	104.1	101.2	114.7	113.2	116.4	115.3
Structural Parameters						
ρ [ ]	0.97	0.96	0.97, 0.97	0.96, 0.96	0.97, 0.97, 0.97	0.96, 0.96, 0.96
τ_4 [ ]	0.80	0.78	0.82	0.83	0.90	0.91
RMSD (vs. SCXRD) [Å]	0.357	0.115	0.286	0.362	0.089	0.149

a: Solid-state structure published in [156]

3.4.2 Theoretical Description of the Cu(II) complexes

Given the good agreement of computational and experimental data for the Cu(I) structures, the Cu(II) structures were computed analogously. Since a pentacoordinate coordination of the Cu(II) systems is likely, their structures were optimized starting from the Cu(I) structures with an additional acetonitrile co-ligand. The substitution pattern of the ligands in combination with an additional co-ligand give rise to four different conformers of pentacoordinate Cu(II) complex cations (Figure 3.9).

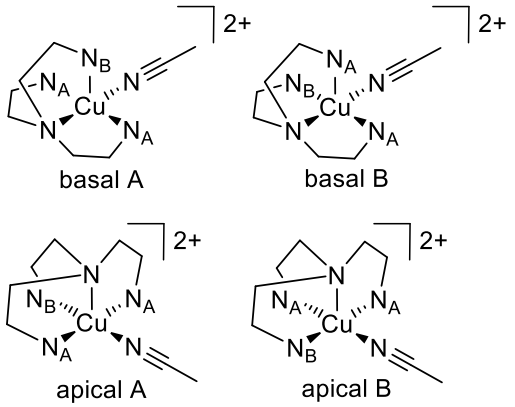

Figure 3.9: Schematic representation of the possible conformers for **C2**, **C4** and **C6**. For $\mathbf{C6_{TMG}}$ and $\mathbf{C6_{DMEG}}$, the corresponding A and B conformers are identical.

The shown four conformers can be divided into two separate pairs with either the aryl amine donor (N_{Am}) coordinating the metal center at the basal or the apical position of the resulting square pyramid. These basal and apical pairs can be subdivided further by the arrangement of the ligands' different arms relative to the co-ligand. Comparing Gibb's free enthalpies (Figure 3.10), it is noteworthy that the computations suggest the **C6** complex cations show either one basal conformer ($\mathbf{C6_{TMG}}$) or energetically prefer the basal conformer over the apical one by over 9 kJ mol^{-1} ($\mathbf{C6_{DMEG}}$). Contrary, the pairs of **C4** and **C2** seem to prefer the apical conformers over the basal conformation. The basal A conformers of **C2**, as well as the apical conformer of $\mathbf{C6_{TMG}}$, repeatedly interconverted during the course of the calculations into other conformers, indicating they are metastable. Relative to the most stable conformer within one set of conformers, the observed relative energy differences of the optimizable species are generally small with an overall range of 10.0 to 2.1 kJ mol^{-1}. An exception presents the apical A conformer of $\mathbf{C4_{TMG}}$ which is significantly higher in energy and therefore not statistically relevant. Given the otherwise relatively low energy differences within a set of conformers, a dynamic equilibrium between them is feasible. This equilibrium of varying structures could potentially explain the lack of measurable crystals. Given the number and overall similarity of the obtained Cu(II) structures, Table 3-5 shows only the $\mathbf{C4_{TMG}}$ conformers. For the sake of clarity, the donor labels do not correspond to their kind, but their position in relation to the acetonitrile co-ligand, as illustrated in Figure 3.11. The remaining structural data is listed in the Appendix, Section 9.6.

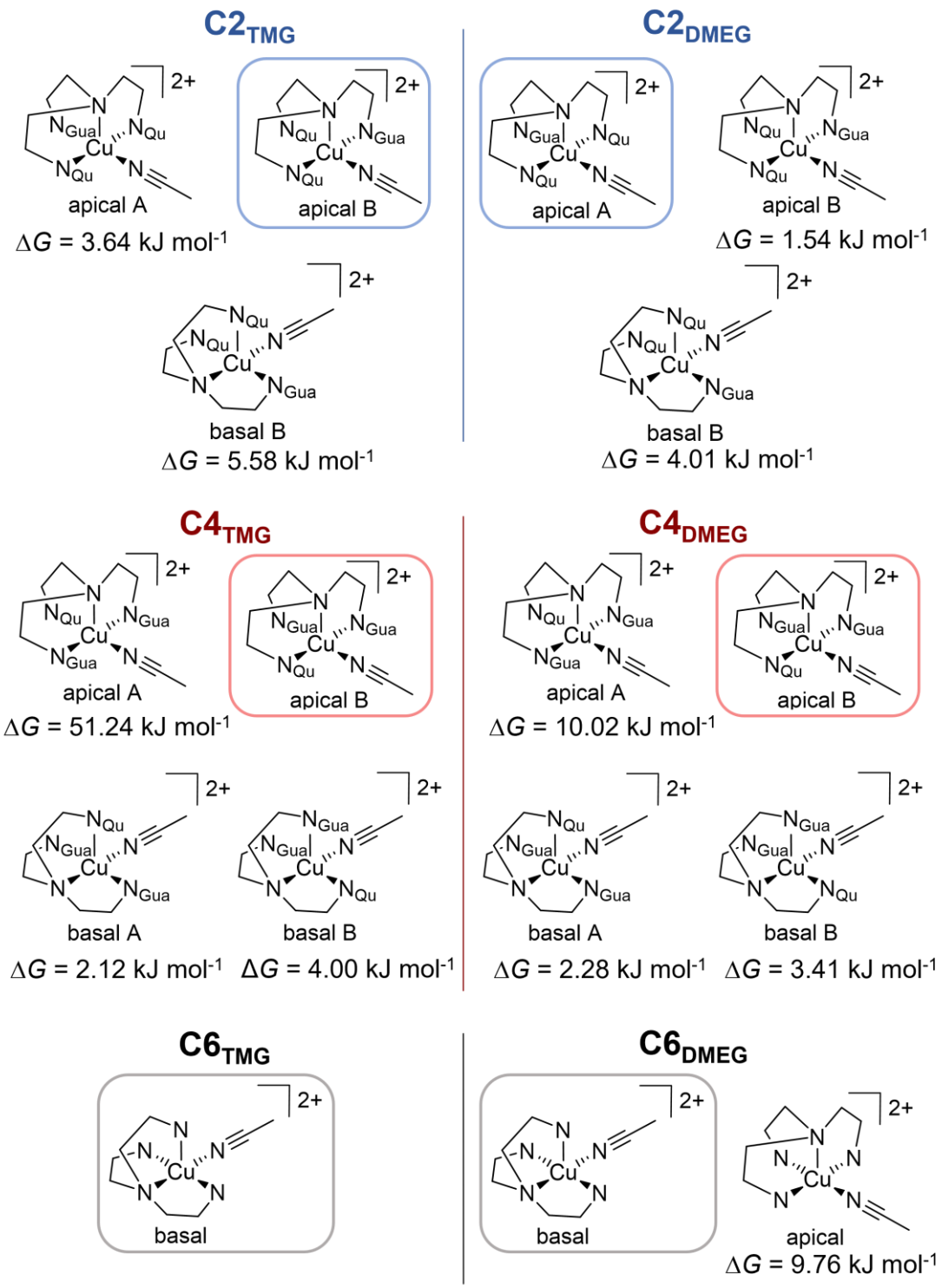

Figure 3.10: Schematic illustration of the conformer sets of each derivative of the complex cations **C2**, **C4** and **C6** via DFT structure optimization. The framed structures represent the lowest lying conformer of each species. The difference in energy (ΔG) of each other conformer relative to the framed one is noted below its schematic structure. If certain structures are not depicted, they could not be found via the employed methods (TPSSh-D3BJ/def2-TZVP+ PCM(MeCN) // TPSSh-D3BJ/def2-TZVP + PCM(MeCN)).

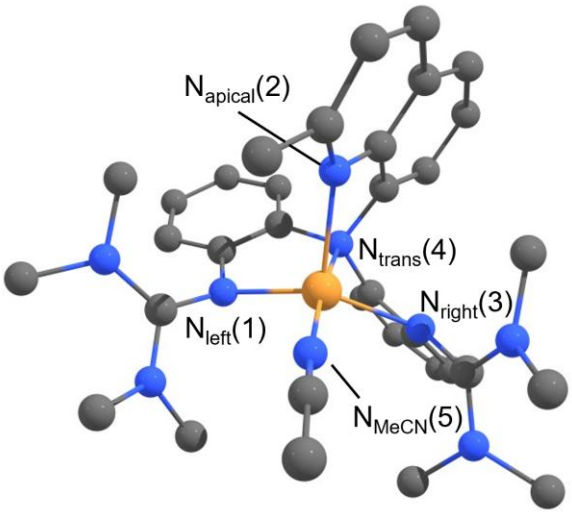

Figure 3.11: Exemplary numbering of the donors in the Cu(II) complexes. The positions are relative to the acetonitrile co-ligand and are consistent for every conformer.

Table 3-5: Key bond lengths, bond angles and structural parameters of the DFT optimized geometries for the conformers of the Cu(II) complex cation **$C4_{TMG}$** (TPSSh-D3BJ/def2-TZVP+ PCM(MeCN) // TPSSh-D3BJ/def2-TZVP + PCM(MeCN)).

	$C4_{TMG}$			
	Apical A	Apical B	Basal A	Basal B
Bond Lengths [Å]				
Cu–N_{left}(1)	2.069 (N_{Gua})	2.022 (N_{Qu})	2.015 (N_{Gua})	2.104 (N_{Qu})
Cu–N_{apical}(2)	2.200 (N_{Am})	2.260 (N_{Am})	2.224 (N_{Qu})	2.146 (N_{Gua})
Cu–N_{right}(3)	2.019 (N_{Gua})	2.029 (N_{Gua})	2.038 (N_{Gua})	2.002 (N_{Gua})
Cu–N_{trans}(4)	2.001 (N_{Qu})	2.017 (N_{Gua})	2.053 (N_{Am})	2.112 (N_{Am})
Cu–N_{MeCN}(5)	1.995	2.000	1.977	1.976
Bond Angles [°]				
N(1)–Cu–N(2)	77.8	81.6	102.5	105.1
N(1)–Cu–N(3)	160.9	156.3	141.7	141.5
N(1)–Cu–N(4)	43.7	91.7	83.5	77.5
N(2)–Cu–N(3)	83.4	77.5	107.7	103.1
N(2)–Cu–N(4)	84.0	80.2	79.8	130.4
N(3)–Cu–N(4)	90.6	95.7	79.5	113.2
N(5)–Cu–N(1)	91.4	87.3	101.0	79.9
N(5)–Cu–N(2)	99.1	108.7	102.2	120.6
N(5)–Cu–N(3)	88.2	88.9	95.1	97.2
N(5)–Cu–N(4)	176.6	170.8	174.5	158.8
Structural Parameters				
ρ [ ]	1.00, 0.99	0.98, 0.99	1.00, 1.00	0.98,1.00
τ_5 [ ]	0.26	0.24	0.55	0.29

The apical donor position seems to consistently exhibit the longest coordinative bond, which can be explained by the pseudo Jahn-Teller effect of Cu(II). Compared to **C3$_{TMG}$**, the Cu–N_{Am} bonds tend to be shortened, especially when the N_{Am} donor occupies a basal position in the coordination sphere. Additionally, the short N_{Am}-bonds of around 2.46 Å support the notion of electronic effects as one cause of the umbrella distortion. The geometry of the coordination sphere can be quantified via the τ_5 parameter that quantifies how much an investigated structure resembles an ideal square-pyramidal structure (τ_5 = 0) or a trigonal-bipyramidal one (τ_5 = 1, Equation 21).

$$\tau_5 = \frac{\alpha - \beta}{60°} \qquad (21)$$

a > b, largest angles

The τ_5 parameters of the Cu(II) complexes **C2**, **C4$_{DMEG}$** and **C6** are listed in Table 3-6. Computations show that a square-pyramidal geometry is generally more favored in apical conformers than in basal ones. Noteworthy is that the computed structures of cations with more guanidine moieties resemble neither a square-pyramidal nor a trigonal-bipyramidal structure, but intermediate structures indicated by a τ_5 parameter close to 0.5. This trend is exacerbated by the bulkier TMG substituents.

Table 3-6: τ_5 structural parameters of the DFT optimized geometries for the conformers of the Cu(II) complex cations of **C2**, **C4** and **C6** (TPSSh-D3BJ/def2-TZVP+ PCM(MeCN) // TPSSh-D3BJ/def2-TZVP + PCM(MeCN)).

Complex	Conformer	τ_5 [ ]	Complex	Conformer	τ_5 [ ]
C2$_{TMG}$	Apical A	0.15	**C2$_{DMEG}$**	Apical A	0.09
	Apical B	0.18		Apical B	0.14
	Basal B	0.51		Basal B	0.33
C4$_{TMG}$	Apical A	0.26	**C4$_{DMEG}$**	Apical A	0.05
	Apical B	0.24		Apical B	0.18
	Basal A	0.55		Basal A	0.75
	Basal B	0.29		Basal B	0.29
C6$_{TMG}$	Basal	0.54	**C6$_{DMEG}$**	Apical	0.24
				Basal	0.48

In conclusion, the number and type of guanidine units in the ligand seem to induce variance in the steric bulk, as initially intended. However, the guanidines also impose electronic effects on the complex cations of both oxidation states. To better understand these, NBO calculations were performed.

3.4.3 NBO analysis of the Complexes

The NBO studies were performed to gauge the impact of the guanidines on the electronics of the complex cations and to investigate how the TMG and DMEG units differentiate themselves electronically. For that purpose, the charge transfer energies E_{CT} of all nitrogen donors towards the copper center were calculated based on the obtained structures using NBO 6.0.[181-183] The charge transfer energies of the Cu(I) systems, which are split in σ and π contributions, are listed in Table 3-7.

Table 3-7: Charge transfer energies E_{CT} for the σ and π contributions of each donor in the complex cations of **C1**, **C3** and **C5** (Population analysis was performed using the NBO 6.0 package, based on the DFT structures calculated with the TPSSh-D3BJ/def2-TZVP+ PCM(MeCN) // TPSSh-D3BJ/def2-TZVP + PCM(MeCN) method).

	C1$_{TMG}$		**C1$_{DMEG}$**		**C3$_{TMG}$**		**C3$_{DMEG}$**		**C5$_{TMG}$**		**C5$_{DMEG}$**	
	E_{CT} [kcal mol^{-1}]											
	σ	π	σ	π	σ	π	σ	π	σ	π	σ	π
N_{Am}(1)→Cu	2.6	-	2.8	-	1.9	-	2.2	-	1.3	-	1.7	-
N_{Gua}(2)→Cu									20.1	0.4	22.9	0.6
N_{Gua}(3)→Cu					26.7	0.4	21.0	0.5	20.1	0.4	22.9	0.6
N_{Gua}(4)→Cu	25.5	0.4	24.3	1.0	20.2	0.4	28.2	0.4	20.1	0.4	22.9	0.6
N_{Qu}(2)→Cu	30.3	0.2	32.0	0.2	25.0	0.3	27.6	0.4				
N_{Qu}(3)→Cu	23.6	0.3	24.8	0.3								
Sum	82.9		85.5		74.7		80.3		62.8		72.2	

The obtained E_{CT} indicate that the amine donor's contributions are consistently the lowest, becoming weaker with the number of guanidine units present in the ligand scaffold. This trend correlates with the increasing Cu–N_{Am} bond length (Figure 3.12) and is therefore likely a result of the umbrella distortion.

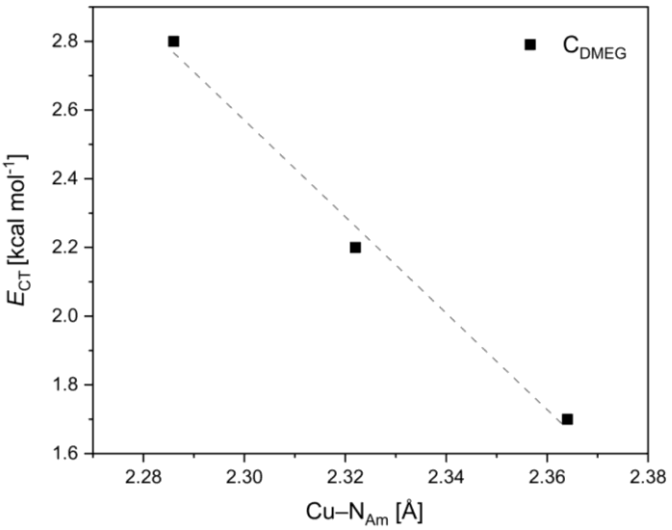

Figure 3.12: Correlation of the Cu–N_{Am} bond length with the central amines' E_{CT} values for the Cu(I) complexes of $\mathbf{L_{DMEG}}$ (TPSSh-D3BJ/def2-TZVP+ PCM(MeCN) // TPSSh-D3BJ/def2-TZVP + PCM(MeCN)).

The equatorial donors exhibit significantly higher E_{CT} that vary between 20 and 32 kcal mol^{-1}. Contrary to N_{Am}, the E_{CT} of the N_{Gua} and N_{Qu} donors exhibit additional π contributions to the typical σ contributions to the Cu(II) centers. This π contribution is more pronounced in the N_{Gua} donors than the N_{Qu} donors. Variations of E_{CT} between the same type of donor in a complex cation do correlate with the observed variations in bond length and are therefore likely a result of those. Noteworthy is that the sum of all E_{CT} contributions of all donors, as well as the individual values for each donor, are both decreasing with the number of guanidine units in the scaffold and are, further, consistently larger for DMEG than for TMG derivatives. This is counterintuitive as TMG units are considered to be stronger donors and complexes with TMG containing ligands consistently display shorter bonds and more negative redox potentials than their DMEG counterparts.[84, 184]

The E_{CT} of the Cu(II) complexes were also analyzed. Given the number of Cu(II) structures, Table 3-8 shows only the E_{CT} for all donors of $\mathbf{C4_{TMG}}$ as an example. The remaining data can be viewed in Section 9.7.

Table 3-8: Exemplary charge transfer energies E_{CT} for the σ and π contributions of each donor in all conformers of **C4$_{TMG}$** (Population analysis was performed using the NBO 6.0 package, based on the DFT structures calculated with the TPSSh-D3BJ/def2-TZVP+ PCM(MeCN) // TPSSh-D3BJ/def2-TZVP + PCM(MeCN) method).

C4$_{TMG}$								
	Apical A		Apical B		Basal A		Basal B	
	E_{CT} [kcal mol^{-1}]							
	σ	π	σ	π	σ	π	σ	π
$N_{left}(1)\rightarrow Cu$	36.6 (N_{Gua})	21.4	51.7 (N_{Qu})	-	39.0 (N_{Gua})	13.7	37.3 (N_{Qu})	0.6
$N_{apical}(2)\rightarrow Cu$	6.8 (N_{Am})	-	6.2 (N_{Am})	-	17.6 (N_{Qu})	0.2	23.6 (N_{Gua})	0.5
$N_{right}(3)\rightarrow Cu$	47.9 (N_{Gua})	15.3	54.9 (N_{Gua})	0.2	39.8 (N_{Gua})	8.7	47.8 (N_{Gua})	12.4
$N_{trans}(4)\rightarrow Cu$	47.9 (N_{Qu})	-	44.2 (N_{Gua})	9.4	40.7 (N_{Am})	-	33.4 (N_{Am})	-
$N_{MeCN}(5)\rightarrow Cu$	45.7	1.9	47.5	1.8	50.0	-	50.0	-
Sum	223.5		215.9		209.7		203.9	

The values for the Cu(II) complexes show much higher E_{CT} than those for Cu(I), with the apical conformers exhibiting the largest E_{CT} sum. Similarly to before, the charge transfer energies are strongly dependent on the bond length, as illustrated by the small E_{CT} of all donors in the apical position and the change in E_{CT} of the N_{Am} donor. Additionally, the π contributions of the N_{Gua} donors are much more pronounced for the oxidized cations, while those of the N_{Qu} donors seem to not be affected. Accordingly, the total N_{Gua} contributions exceed those of the N_{Qu} donors which implies that the π contributions of guanidines are more relevant for the description of bonding in Cu(II) species, likely due to changes in the ligand field symmetry.

To compare the influence of the charge transfer energies of the Cu(I) and Cu(II) systems, the averaged sums of the Cu(II) systems ($\bar{E}_{CT,Cu(II)}$) as well as the differences and ratios ($\Theta E_{CT,all}$) of these values to the sums of the Cu(I) systems. $\Theta E_{CT,all}$ was determined via Equation 22.

$$\Theta E_{CT,all} = \frac{\bar{E}_{CT,Cu(II)}}{E_{CT,Cu(I)}} \tag{22}$$

Cu(II) and Cu(I) refer to the corresponding redox pair.

Comparing the average of the E_{CT} of all Cu(II) complexes, there still seems to be a decrease in overall charge transfer energy with the number of guanidine units in the scaffold which is more pronounced for the Cu(I) complexes. The DMEG derivatives also retain their higher total amount of charge transfer contributions.

Table 3-9: The average of the sum of the Cu(II) complexes' charge transfer energies $\bar{E}_{CT,Cu(II)}$, the difference between E_{CT} of Cu(II) and Cu(I) and the ratio $\Theta E_{CT,total}$ with the corresponding Cu(I) complexes (Population analysis was performed using the NBO 6.0 package, based on the DFT structures calculated with the TPSSh-D3BJ/def2-TZVP+ PCM (MeCN) // TPSSh-D3BJ/def2-TZVP + PCM(MeCN) method).

Complex cation	$\bar{E}_{CT}$ [kcal mol^{-1}]	ΔE_{CT}(Cu(II)−Cu(I)) [kcal mol^{-1}]	$\Theta E_{CT,total}$ [ ]
C2$_{TMG}$	212.5	129.6	2.56
C2$_{DMEG}$	223.1	137.6	2.61
C4$_{TMG}$	213.3	138.8	2.85
C4$_{DMEG}$	220.2	139.9	2.74
C6$_{TMG}$	196.2	133.4	3.12
C6$_{DMEG}$	216.7	144.5	3.00

The differences between the sums of the Cu(II) and Cu(I) complexes' contributions generally increase, as do their ratios. The differences are larger for the DMEG derivatives. For the ratios, this trend reverses as they yield larger values for TMG derivatives. A larger ratio corresponds to a stronger relative donation of the ligand to Cu(II) than Cu(I). This fits the observed electrochemical behavior of copper guanidine complexes where TMG derivatives yield more negative redox potentials. In conclusion, complexes with DMEG donors do not seem to exhibit more reducing potentials because of worse donor properties, but because of their larger relative stabilization of the Cu(I) state.

3.5 Cyclic Voltammetry and Assessment of the Addition-Oxidation Mechanism

Cyclic voltammetry (CV) gives insights into the electrochemical behavior of the studied model systems; the technique can thus be used to gain information about the processes linked to the corresponding oxidation or reduction step. The obtained half-wave potentials $E_{1/2}$ are further necessary to calculate a models' self-exchange rates (see section 3.4.5). The cyclic voltammograms were measured at ambient conditions in acetonitrile and referenced against the Fc/Fc$^+$ couple as internal standard (Table 3-11).

Table 3-10: Redox pairs and corresponding Cu(I) and Cu(II) complexes.

Redox Pair	[Cu(I)L]$^+$	[Cu(II)L(MeCN)]$^{2+}$
R1$_{TMG}$ / R1$_{DMEG}$	**C1$_{TMG}$ / C1$_{DMEG}$**	**C2$_{TMG}$ / C2$_{DMEG}$**
R2$_{TMG}$ / R2$_{DMEG}$	**C3$_{TMG}$ / C3$_{DMEG}$**	**C4$_{TMG}$ / C4$_{DMEG}$**
R3$_{TMG}$ / R3$_{DMEG}$	**C5$_{TMG}$ / C5$_{DMEG}$**	**C6$_{TMG}$ / C6$_{DMEG}$**

The cyclic voltammograms of **R1$_{DMEG}$**, **R2$_{DMEG}$** and **R3$_{DMEG}$** are shown in Figure 3.13, the other three cyclic voltammograms are shown in Section 9.2.1.

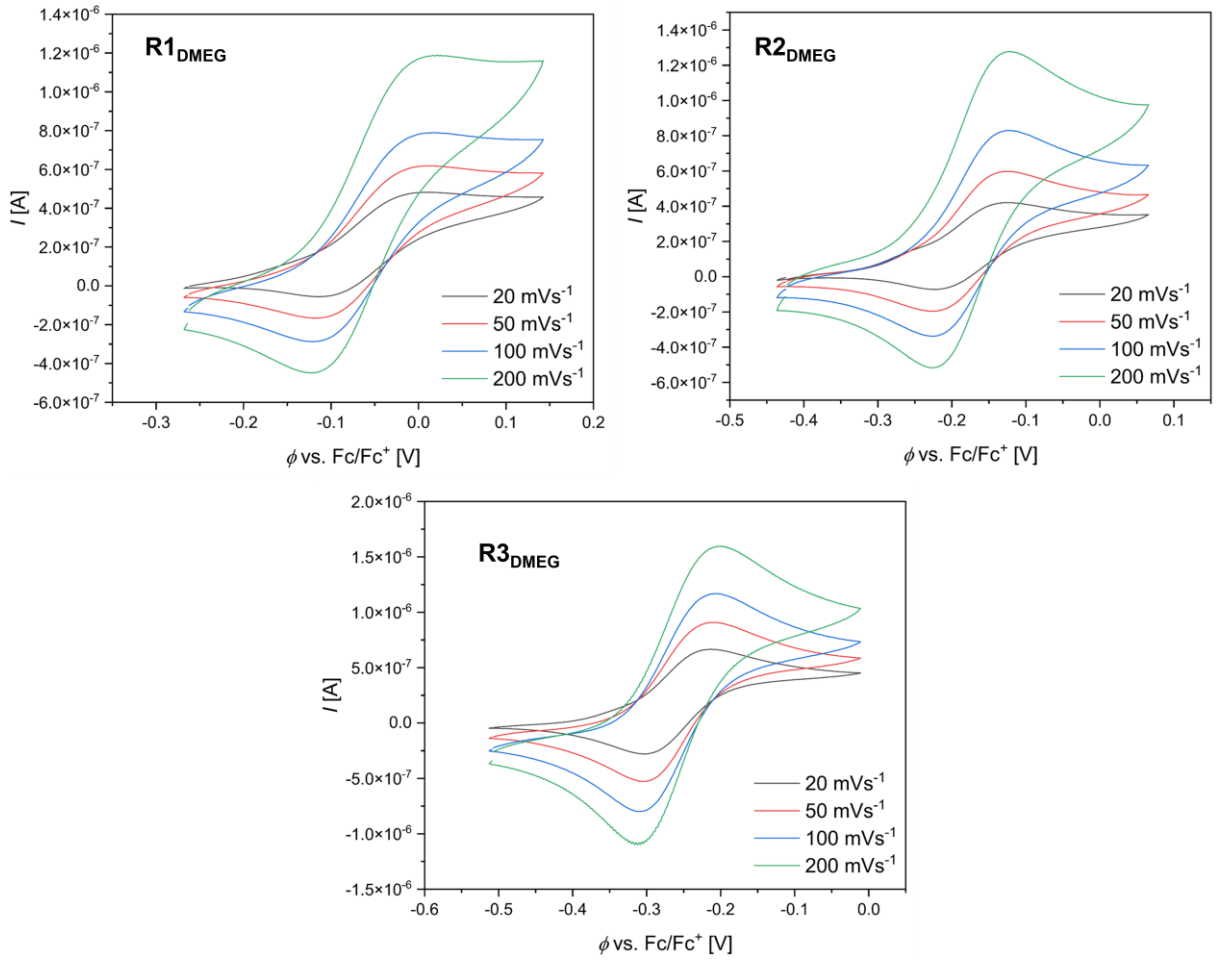

Figure 3.13: Cyclic voltammograms of **R1$_{DMEG}$**, **R2$_{DMEG}$** and **R3$_{DMEG}$** starting from the corresponding Cu(I) complex (c = 10^{-3} M) in MeCN with [NBu$_4$][PF$_6$] (c = 0.1 M).

Next to $E_{1/2}$, important data from the CV measurements are the peak-to-peak separation of the reduction and oxidation wave (ΔE_p), the ratio of their intensities (I_{red}/I_{ox}) and their change with the scan rate ν (Table 3-11).

Table 3-11: Key parameters of the cyclic voltammograms of **R1**, **R2** and **R3**.

Redox Pair	$E_{1/2}$ [V] *vs.* Fc/Fc$^+$	ΔE_P [mV] 20, 50, 100, 200 mV s^{-1}	Increase of ΔE_P [%]	I_{red}/I_{ox} [ ] 20, 50, 100, 200 mV s^{-1}	Increase of I_{red}/I_{ox} [%]
R1$_{TMG}$	−0.07	67, 70, 73, 77	15	1.11, 1.24, 1.29, 1.35	22
R1$_{DMEG}$	−0.06	77, 85, 89, 94	22	0.99, 1.18, 1.30, 1.42	43
R2$_{TMG}$	−0.20	76, 80, 87, 88	16	1.07, 1.12, 1.15, 1.19	11
R2$_{DMEG}$	−0.18	72, 77, 84, 85	18	0.91, 1.00, 1.03, 1.06	16
R3$_{TMG}$	−0.27	75, 82, 94, 103	37	1.08, 1.08, 1.09, 1.14	6
R3$_{DMEG}$	−0.26	75, 79, 85, 89	19	1.05, 1.08, 1.11, 1.14	9

The CV data show increasingly negative redox potentials with a higher number of guanidine units in the ligand scaffold, with TMG-containing systems showing slightly more negative values. Plotted against ΘE_{CT} (see Section 3.4.3), it can be seen that both values correlate well for both systems (Figure 3.14, left). Using the ΘE_{CT} of the energetically preferred Cu(II) conformers further yields good correlations for the isolated TMG and DMEG substituents (Figure 3.14, right).

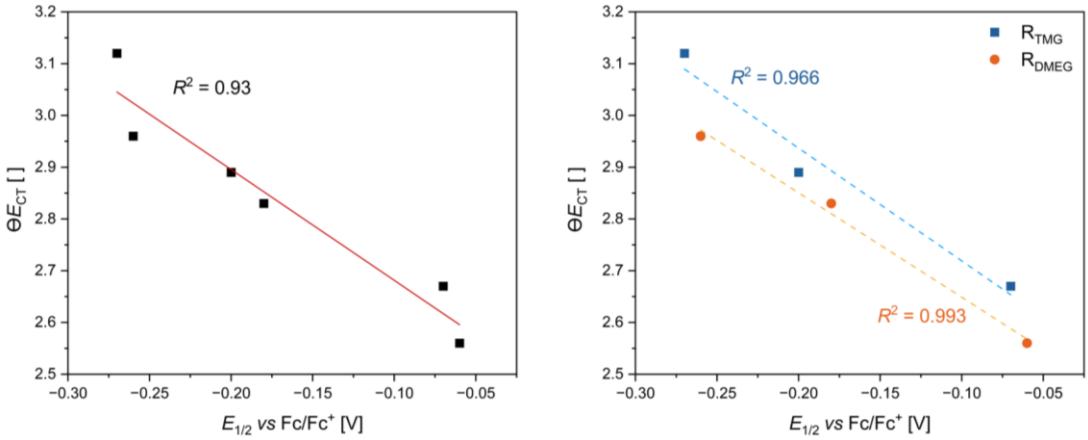

Figure 3.14: Left: Correlation of $\Theta E_{CT,all}$ *vs.* $E_{1/2}$ of all redox pairs. Right: Correlation of ΘE_{CT} *vs.* $E_{1/2}$ of all redox pairs with the $E_{CT,Cu(II)}$ of the energetically preferred conformer for each guanidine unit (TPSSh-D3BJ/def2-TZVP+ PCM(MeCN) // TPSSh-D3BJ/def2-TZVP + PCM(MeCN)).

This confirms that the obtained E_{CT} describe the electronic influence of the guanidine groups accurately and further shows that the E_{CT} ratio of two oxidation states can be used to estimate the redox potential of similar complexes relative to each other.

The cyclic voltammograms of all redox pairs exhibit quasi-reversible behavior, as can be seen by a dependence of the peak-to-peak separation and current ratio (I_{red}/I_{ox}) on the scan rate. This behavior diminishes with ligand bulk, with **R1$_{DMEG}$** displaying the most pronounced effects. The quasi-reversibility arises from chemical steps coupled to the redox events. For most systems, $I_{red}/I_{ox} > 1$ and increases with scan rate, suggesting that the oxidation of the Cu(I) species is preceded by a chemical reaction or structural rearrangement. Another indicator is the change of the current function, defined as $I_{ox}/\nu^{1/2}$ over ν, that better visualizes non-linear behavior in the change of I_{ox}. It is depicted in Figure 3.15 and shows a decrease with scan rate except for **R2$_{DMEG}$**.

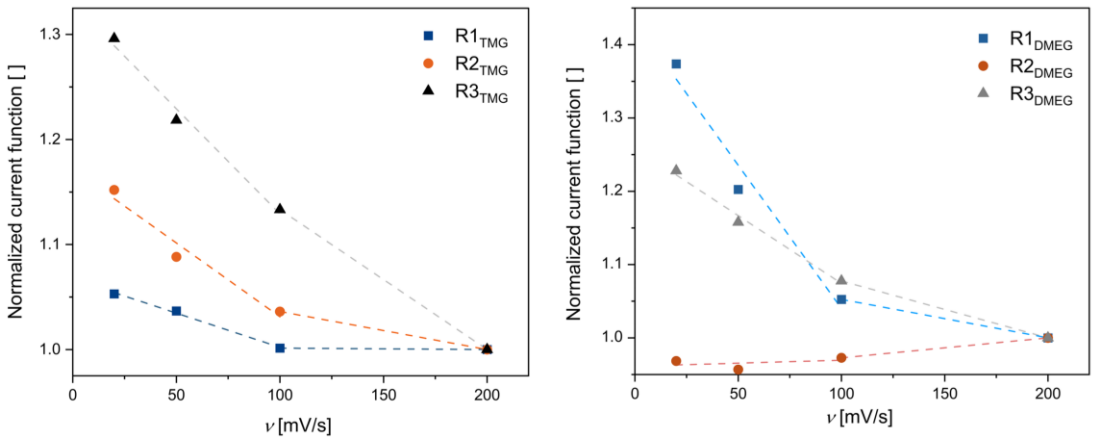

Figure 3.15: Normalized current functions of designated redox pairs plotted against the scan rate ν. The lines solely serve as guides to the eyes.

The decrease with scan rate is expected for a chemical reaction preceding a redox step, as the current function is elsewise expected to increase slightly.[185] This conclusion is further supported by the S-shaped oxidation wave of **R1$_{DMEG}$** and **R2$_{DMEG}$**, indicative of a fast pre-equilibrium favoring the reactant side (Scheme 3.5).

$$[Cu(I)L]^{+} + S \underset{}{\overset{K,\,k}{\rightleftharpoons}} [Cu(I)LS]^{+} \xrightarrow{ET} [Cu(II)LS]^{2+}$$

Scheme 3.5: Schematic illustration of the pre-equilibrium set before the actual electron transfer (ET), leading to the observed S-shape of redox processes in CV in the case of large *k* and small *K*.

The S-shape occurs because the high *k* enables to maintain a constant concentration of active species that, in turn, prevents the typical peak profile for the oxidation step.[185] While other systems lack this distinct S-shape, their elevated I_{red}/I_{ox} ratios still suggest a similar addition-oxidation mechanism. Absence of the S-shape likely results from smaller *k* which would be in agreement with the ligands' increased bulk compared to **L1$_{DMEG}$**.

R2$_{DMEG}$ represents a noteworthy deviation from the established behavior as its current ratio is initially <1. While this could potentially be indicative of a different mechanism, both the present S-shape and the increase of the current ratio with ν indicate accordance with the other systems. While there is no definitive explanation for the anomalous current ratio and current function, it is plausible that the previously stated decomposition of the Cu(II) species is particularly fast for **C4$_{DMEG}$**. This process would lower the amount of oxidized species in solution for slower scan rates but be less noticeable for faster ones, fitting the observed behavior.

To support the assumed addition-oxidation mechanism, isodesmic reactions for the CN-change of the Cu(I) species were simulated via DFT.

3.5.1 Isodesmic Reactions of the Cu(I) Complexes

Isodesmic reactions are reactions where the broken bonds in the reactant are the same as the formed bond in the product, e.g. the reversible association of an acetonitrile co-ligand to a Cu(I) complex (Scheme 3.6). They can be used to gauge which side of the equation is energetically preferred.

$$[Cu(I)L]^+ + MeCN \rightleftharpoons [Cu(I)L(MeCN)]^+$$

Scheme 3.6: Illustration of the investigated isodesmic reaction. The $[Cu(I)L(MeCN)]^+$ species was always set as product.

The isodesmic reactions of the acetonitrile association to the Cu(I) complexes **C1**, **C3** and **C5** were simulated with DFT calculations using the TPSSh-D3BJ/def2-TZVP + PCM(MeCN) // TPSSh-D3BJ/def2-TZVP + PCM(MeCN) method. The aim was to see whether the obtained complexes' Gibbs free reaction energies and equilibrium constants correspond to the results from the CV measurements. To obtain the $[Cu(I)L(MeCN)]^+$ species, an acetonitrile molecule was added to the coordination sphere of the tetracoordinate Cu(I) species, and the structures were geometry optimized. The process was repeated with an explicit acetonitrile molecule to obtain the reactant side (left side) of the reaction equation. The resulting Gibbs free reaction energies were obtained via Equation 23, the equilibrium constants $K_{A,DFT}$ via Equation 24.

$$\Delta G_{A,DFT} = G_{DFT,[Cu(I)L(MeCN)]^+} - G_{DFT,[Cu(I)L]^+} + MeCN \quad (23)$$

$$K_{A,DFT} = \exp\left(\frac{\Delta G_{A,DFT}}{R \cdot T}\right) \quad (24)$$

R: Gas constant, T: 298 K

Additionally, the transition state for the coordination of the acetonitrile were calculated. All obtained values, set with $[Cu(I)L(MeCN)]^+$ as product, are listed in Table 3-12. Interestingly, the obtained Gibbs free reaction energies indicate that the pentacoordinate structures are more stable than the tetracoordinate ones, with only **C5$_{TMG}$** favoring a tetracoordinate geometry. A predominantly pentacoordinate geometry would render the measured cyclic voltammograms reversible. Given that the CV measurements show quasi-reversible behavior that indicates a change of CN before oxidation, the obtained differences in Gibbs free energy likely stem from the used methods overestimating the pentacoordinate species' stability.

Table 3-12: Key thermodynamic and kinetic data obtained from the investigation of the isodesmic reactions (Equilibrium geometries: TPSSh-D3BJ/def2-TZVP+ PCM(MeCN) // TPSSh-D3BJ/def2-TZVP + PCM (MeCN).

	$\Delta G_{A,DFT}$ [kJ mol^{-1}]	$K_{A,DFT}$ [ ]	lg($K_{r,DFT}$) [ ]	$\Delta G^{‡}_{A,DFT}$ [kJ mol^{-1}]
C1$_{TMG}$	−11.6	1.1·10^{2}	2.0	28.0
C1$_{DMEG}$	−12.7	1.7·10^{2}	2.2	26.2
C3$_{TMG}$	−9.0	3.8·10^{1}	1.6	26.9
C3$_{DMEG}$	−9.3	4.3·10^{1}	1.6	28.3
C5$_{TMG}$	20.3	2.8·10^{-4}	−3.6	46.5
C5$_{DMEG}$	−1.8	2.1	3.2·10^{-1}	27.8

The obtained $K_{A,DFT}$ do decrease with the bulk of the ligand scaffold, implying that the guanidine units significantly destabilized the pentacoordinate species. While the found transition states all exhibit one comparatively low negative frequency between −40 and −63 cm^{-1}, they fit the expected molecular motion of a Cu(I)–N_{MeCN} bond formation or cleavage (see Section 9.9 for further information). Interestingly, the obtained activation barriers are comparatively small with energies between 26 to 28 kJ mol^{-1}, with the exception of **C5$_{TMG}$** with 47 kJ mol^{-1}. They show only a small incline with the number of guanidine units in the scaffold, which is not in agreement with the observed change in the S-shape character of the obtained cyclic voltammograms. This might be due to inaccuracies pf the employed level of theory.

The obtained $K_{A,DFT}$ and $\Delta G^{‡}_{A,DFT}$ should correlate with experimentally determined k_{11}. The self-exchange rates should therefore decrease from **R1** to **R3**, since the amount of the active pentacoordinate species, as well as its replenishment rate, diminish with ligand bulk. To verify this, the self-exchange rates were determined by stopped-flow UV/vis spectroscopy.

3.6 Determination of the Electron Self-Exchange Rates and Assessment of the Prevalent Mechanism

The electron self-exchange rates k_{11} were obtained via application of the Marcus cross relation (Eqn. 25), which is derived from the Marucs theory describing the outer-sphere mechanism of electron transfer reactions.[90, 94]

$$k_{11} = \frac{{k_{12}}^2}{k_{22} \cdot K_{12} \cdot f_{12} \cdot {W_{12}}^2} \tag{25}$$

k_{11} can be determined by observing the cross reaction of a complex C_1 with a counter complex C_2 with a known k_{22}. Calculating the cross reaction's equilibrium constant K_{12} from the complexes redox potentials. For the determination of the self-exchange rates

of **R1** to **R3**, $[Co(bpy)_3](PF_6)_3$ was chosen as counter complex as it is well-soluble in acetonitrile and its $E_{1/2}$ allows for the cross reaction to start from the stable Cu(I) complexes (Scheme 3.7).

Self-exchange reaction

$$[Cu(I)L]^+ + [Cu(II)L(MeCN)]^{2+} \overset{k_{11}}{\rightleftharpoons} [Cu(II)L(MeCN)]^{2+} + [Cu(I)L]^+$$

Cross reaction

$$[Cu(I)L]^+ + [Co(III)(bpy)_3]^{3+} \overset{k_{12}}{\rightleftharpoons} [Cu(II)L(MeCN)]^{2+} + [Co(II)(bpy)_3]^{2+}$$

Scheme 3.7: Investigated self-exchange reaction and cross reaction.

The k_{22} of $[Co(bpy)_3](PF_6)_3$ was used as reported by Rorabacher *et al.* in MeCN at room temperature.[67] The K_{12} of each reaction were obtained via Equation 26.

$$K_{12} = \exp\left(\frac{\Delta E \cdot n \cdot F}{R \cdot T}\right) \tag{26}$$

F: Faraday constant, R: Gas constant, T = 198 K

Where ΔE describes the difference between the redox potentials of C_1 and C_2, n describes the number of transferred electrons during the reaction (with n = 1). The used value for $E_{1/2}$ of the counter complex is −0.056 V *vs* Fc/Fc^+ as reported by Herres-Pawlis *et al*.[22] The obtained K_{12} are listed in Table 3-12 and show an exponential increase with ΔE.

The cross reaction rates k_{12} between the Cu(I) complexes and $[Co(bpy)_3]PF_6$ were determined via stopped-flow UV/vis spectroscopy in acetonitrile at 298 K for five distinct counter complex concentrations. The reactions were performed under pseudo-first order conditions, with each counter complex concentration in excess to the Cu(I) complexes present. For each concentration, the change in distinct absorption bands was plotted against time and fitted with a first-order decay function (Figure 3.16).

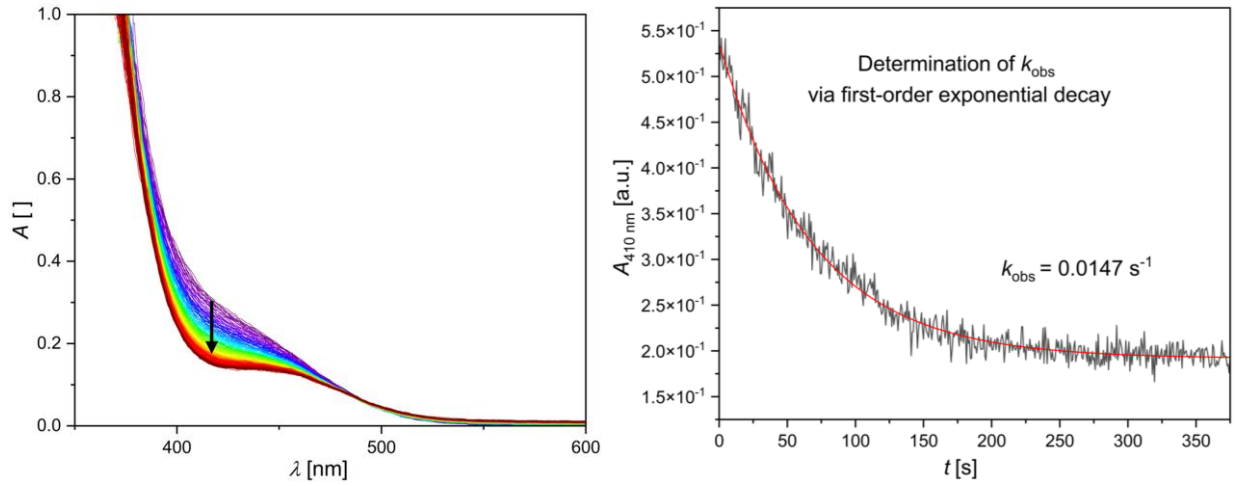

Figure 3.16: Left: Time-dependent change of the UV/vis spectrum of **R1$_{TMG}$** during the cross reaction of **C1$_{TMG}$** with $[Co(bpy)_3](PF_6)_3$ in MeCN solution at 298 K. Right: Exponential decay fit of the decrease of a Cu(I) absorption band from **R1$_{TMG}$** during the cross reaction at 410 nm.

The observed reaction rates were plotted against the counter complex concentration so that k_{12} was obtained as the slope of the linear regression from the resulting plot (shown exemplary for **R1$_{TMG}$** in Figure 3.17, remaining plots in Section 9.3.1). The relevant experimental data as well as the obtained cross reaction rates k_{12} for each redox pair are listed in Table 3-13. Lastly, the obtained values were used to obtain the self-exchange rate of every redox pair (Table 3-13).

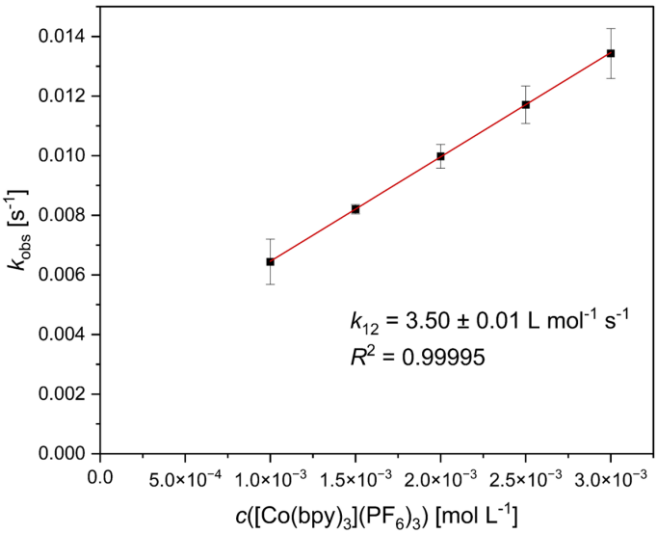

Figure 3.17: Plot of the reaction rates k_{obs} against the concentration of $[Co(bpy)_3]^{3+}$ for **R1$_{TMG}$**.

Table 3-13: Redox potentials $E_{1/2}$, differences between the redox potentials of the copper redox couple and the counter complex $\Delta E_{1/2}$, equilibrium constants K_{12}, reaction rates k_{12} and electron self-exchange rates k_{11} as well as the corresponding lg(k_{11}).

	$E_{1/2}$ *vs.* Fc/Fc$^+$ [V]	ΔE [V]	K_{12} [ ]	k_{12} [M^{-1} s^{-1}]	k_{11} [M^{-1} s^{-1}]	lg(k_{11}) [ ]
R1$_{TMG}$	−0.07	0.02	1.97	3.50 ± 0.01	4.26 ± 0.03	0.6
R1$_{DMEG}$	−0.06	0.01	1.16	$(1.03 \pm 0.64)\cdot10^{1}$	$(6.29 \pm 0.81)\cdot10^{1}$	1.8
R2$_{TMG}$	−0.20	0.14	$2.29\cdot10^{2}$	$(1.11 \pm 0.31)\cdot10^{1}$	$(4.03 \pm 0.23)\cdot10^{-1}$	−0.4
R2$_{DMEG}$[a]	−0.18	0.13	$1.83\cdot10^{2}$	$(1.54 \pm 0.13)\cdot10^{1}$	$(9.72 \pm 1.7)\cdot10^{-1}$	0.0
R3$_{TMG}$	−0.27	0.22	$4.29\cdot10^{3}$	$(3.82 \pm 0.12)\cdot10^{1}$	$(3.13 \pm 0.20)\cdot10^{-1}$	−0.5
R3$_{DMEG}$	−0.26	0.20	$2.83\cdot10^{3}$	$(1.30 \pm 0.05)\cdot10^{1}$	$(5.49 \pm 0.43)\cdot10^{-2}$	−1.3

a: k_{11} was obtained from a different set of counter complex concentrations. See section 7.3.11.1

The k_{11} range over four orders of magnitude, decreasing with the bulkiness of the ligands. **R1$_{DMEG}$** is the redox pair with the highest rate, located one magnitude above its TMG counterpart, whereas **R3$_{DMEG}$** displays the lowest k_{11}.

The comparison to other tripodal model systems requires the differentiation between the oxidation and reduction step, as each can follow either the oxidation-addition mechanism of pathway B or the addition-oxidation mechanism of Pathway A (Scheme 3.8).

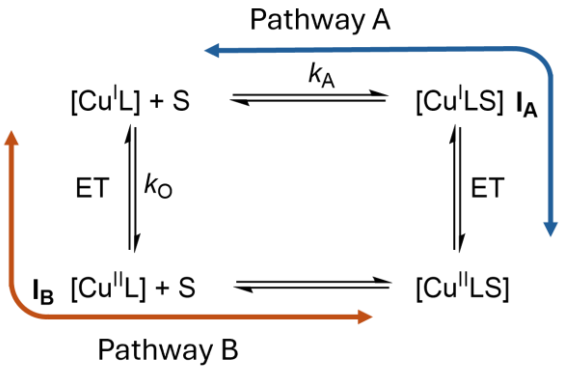

Scheme 3.8: General square scheme describing the possible reaction pathways of coordination-variant model systems in self-exchange reactions. k_A and k_O describe the reaction rates of the first two reaction steps of each mechanism starting at Cu(I).

While tripodal Cu(I) model systems usually oxidize via Pathway B to the pentacoordinate Cu(II) species, the reduction process is usually proposed to proceed via Pathway A. These two mechanisms can result in different k_{11}, which are therefore separated in $k_{11,red}$ and $k_{11,ox}$ for reduction and oxidation reactions, respectively (Figure 3.18).

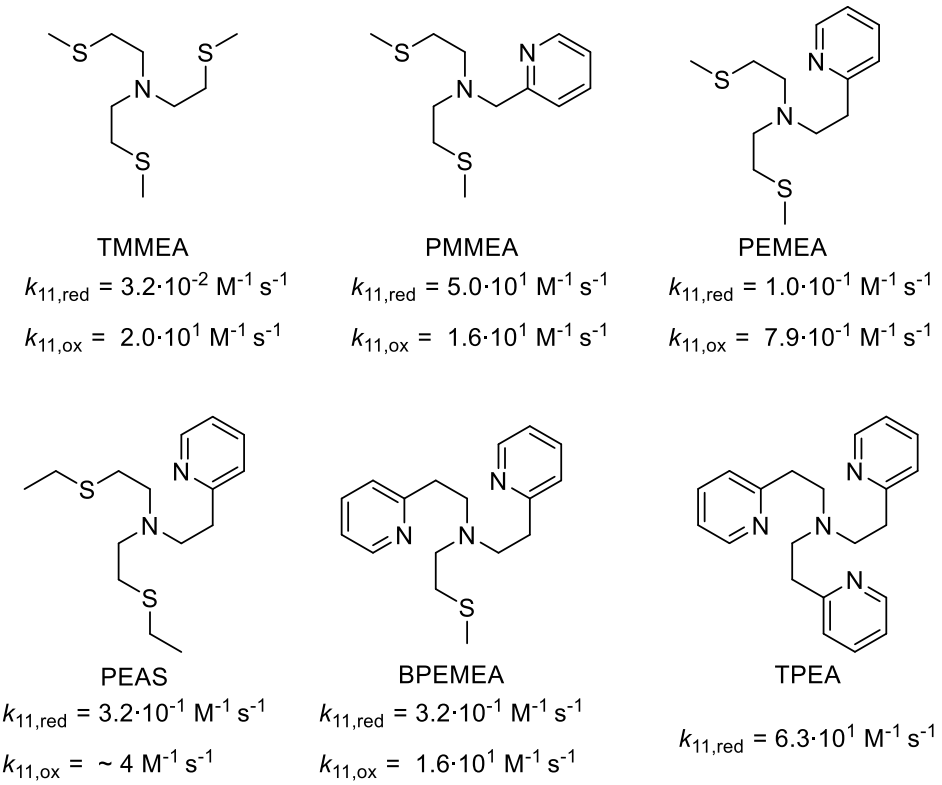

Figure 3.18: Tripodal ligands and the k_{11} of the model systems thereof reported in literature in aqueous solution at 298 K.[14, 70, 166]

Contrary to the redox pairs **R1** to **R3**, the systems reported by Yandell *et al.* and Rorabacher *et al.* were measured in aqueous solution, impacting the comparability of the data sets. While there is an overall similarity in the scale of the k_{11} obtained for **R1** to **R3** and those of the reported systems, the latter do not seem to follow a clear trend in the obtained self-exchange rates indicative of steric or electronic influence. Notably, **R1$_{DMEG}$** exhibits a k_{11} on the same order of magnitude as TPEA, the fastest of the reported systems. The observed trend in the determined k_{11} of the studied redox pairs is in agreement with the expected behavior of the addition-oxidation pathway discussed above. **R1** to **R3** display higher rate constants for systems that have less bulk, higher $K_{A,DFT}$ and lower activation barriers for CN change. Further, the k_{11} agree with the behavior of the cyclic voltammograms which also indicate a faster CN change for less bulky systems. Notably, the k_{11} of **R3$_{TMG}$** represents an exception from the observed trends. Since the obtained CV data imply that it also follows an addition-oxidation pathway, the unusually high k_{11} might be due to secondary effects, like the large driving force of the cross reaction, impacting the kinetics.

Two key parameters decide on the viability of the addition-oxidation pathway in the observed oxidation reactions. First, the conversion from Cu(I) to **I$_A$** is important, as it could be significantly faster than that for **I$_B$**, therefore yielding $k_A >> k_O$. Second is the stability of both intermediates. Pathway B will not be observed, even for a theoretically high k_O, if intermediate **I$_B$** is inherently unstable and therefore only present in negligible

concentrations. The oxidation-addition mechanism of pathway B was assessed by determining the oxidation steps reorganization energies.

3.6.1 Calculation of Inner and Outer Reorganization Energies and Conclusion of the Mechanistic Study

To understand why Pathway A is the preferred mechanism for the oxidation reaction of **R1, R2** and **R3**, the reorganization energies of the electron transfer reaction of Pathway B (Scheme 3.9) were calculated using the TPSSh-D3BJ/def2-TZVP+ PCM(MeCN) // TPSSh-D3BJ/def2-TZVP + PCM(MeCN) method and compared to the kinetic barriers of Pathway A.

$$[Cu(I)L]^{+} + [Cu(II)L]^{2+} \rightleftharpoons [Cu(II)L]^{2+} + [Cu(I)L]^{+}$$

Scheme 3.9: Self-exchange reaction of Pathway B for which the reorganization energies have been calculated.

The according tetracoordinate Cu(II) geometries were obtained by geometry optimization of the corresponding Cu(I) structures (See Appendix Section 9.6 for structural data). The total reorganization energy $\lambda_{11,T}$ of the depicted self-exchange reaction is divided into the internal reorganization energy $\lambda_{11,I}$ and the solvent reorganization energy $\lambda_{11,S}$ of the whole electron self-exchange (Eqn. 27).

$$\lambda_{11,T} = \lambda_{11,I} + \lambda_{11,S} \tag{27}$$

$\lambda_{11,I}$ was calculated using DFT calculations and Nelsen's four-point method. The computations of the reorganization energies were performed using the tetra-coordinate Cu(I) and Cu(II) geometries of the redox pairs **R1**, **R2** and **R3**.

The internal reorganization energy ($\lambda_{Cu(I),I}$ for Cu(I) and $\lambda_{Cu(II),I}$ for Cu(II)) of each complex is calculated based on its optimized ground state energy ($E_{Cu(I)L(I)}$ for Cu(I) and $E_{Cu(II)L(II)}$ for Cu(II)) and the energy of the complex with the same oxidation state but structure of the complementary complex ($E_{Cu(I)L(II)}$ for Cu(I) and $E_{Cu(II)L(I)}$ for Cu(II), Eqn. 28). The indices Cu(I) or Cu(II) represent the oxidation state and L(I) or L(II) represent the ground state complex structure of the appropriate oxidation state. In Figure 3.19 the energies $E_{Cu(I)}(x)$ and $E_{Cu(II)}(x)$ of the Cu(I) and Cu(II) complex are functions of the complex structure which are represented by the variable x_L.

$$\lambda_{11,I} = \lambda_{Cu(II),I} + \lambda_{Cu(I),I} = (E_{Cu(II)L(I)} - E_{Cu(II)L(II)}) + (E_{Cu(I)L(II)} - E_{Cu(I)L(I)}) \tag{28}$$

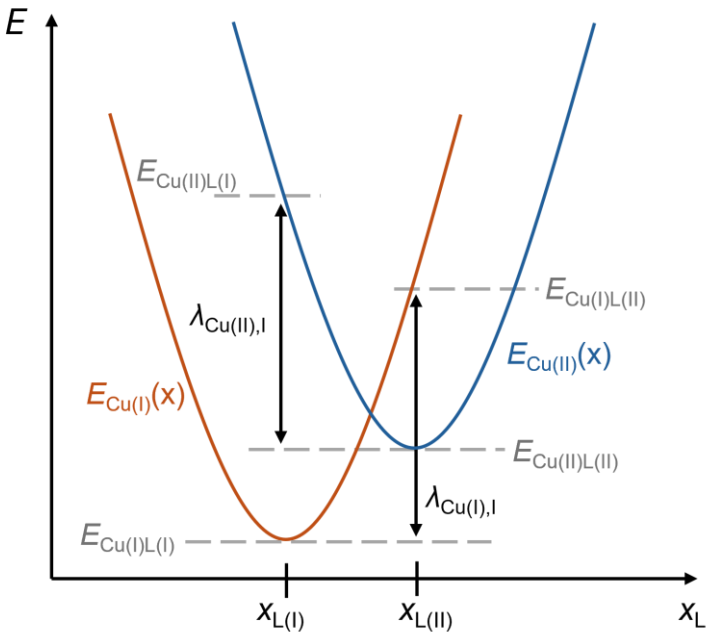

Figure 3.19: Schematic illustration of Nelsen's four-point method for the calculation of the internal reorganization energy $\lambda_{11,I}$.

The internal reorganization energies $\lambda_{11,I}$ have been determined for the electronic energies and are listed in Table 3-14.

While the solvent reorganization energy could be considered negligible, it can have a significant impact on the obtained self-exchange rates, as shown by the bispidine system of Comba *et al.*[83] $\lambda_{11,S}$ was obtained by using the continuum method, an alternative approach first described by Marcus and Sutin,[94] and employed as described by Solomon, Fukuzumi and Karlin *et al.*[186] It describes the outer sphere reorganization as a function of molecular radii, distance, transferred charge and the solvent's polarity as follows:

$$\lambda_{11,S,cont} = (\Delta e)^2 \cdot \left(\frac{1}{a_1} + \frac{1}{a_2} - \frac{1}{r}\right) \cdot \left(\frac{1}{D_{opt}} - \frac{1}{D_{Stat}}\right) \qquad (29)$$

$(\Delta e)^2$ = 1.439976 MeV fm, D_{opt} = 1.806 D_{stat} = 37.5

Where Δe is the change in charge upon the electron transfer, a_1 and a_2 are the molecular radii, determined by calculating the optimized geometries' collision diameters, r is the distance of both cations' centers. D_{opt} is the dynamic dielectric constant, approximated by the square of the refractive index, and D_{stat} is the normal dielectric constant of acetonitrile.[187-188]

$\lambda_{11,T}$ was obtained as the sum from $\lambda_{11,I}$ and $\lambda_{11,S}$. To allow comparison with the activation barriers from Section 3.4.4.1, $\lambda_{11,T}$ was converted into the activation barrier of the self-exchange reaction using Equation 30.[94] All obtained values are listed in Table 3-14.

$$\Delta E_B^{\ddagger} = \frac{\lambda_{11,T}}{4} \quad (30)$$

Table 3-14: Obtained values for the inner, outer and total reorganization energies as well as the derived activation barriers. The total reorganization energy was obtained as the sum of $\lambda_{11,I}$ and $\lambda_{11,S}$.

Cu(I) complex	$\lambda_{11,I}$ [kJ mol^{-1}]	$\lambda_{11,S}$ [kJ mol^{-1}]	$\lambda_{11,T}$ [kJ mol^{-1}]	$\Delta E_B^{\ddagger}$ [kJ mol^{-1}]
C1$_{TMG}$	53.8	65.1	118.9	29.7
C1$_{DMEG}$	65.7	65.2	130.9	32.7
C3$_{TMG}$	48.1	64.0	112.1	28.0
C3$_{DMEG}$	58.8	63.6	122.4	30.6
C5$_{TMG}$	54.4	61.8	116.2	29.1
C5$_{DMEG}$	64.3	60.6	124.9	31.2

The obtained values for the internal reorganization energies are similar to the ones obtained for the $[Cu(GUAqu)_2]^{+/2+}$ systems by Herres-Pawlis *et al.* that exhibit k_{11} up five orders of magnitude larger than the herein obtained rates.[22] Accordingly, the obtained activation barriers are decidedly smaller than those obtained for the CN-change of the Cu(I) systems discussed above. Furthermore, the observed change in the reorganization energies does not fit the observed trend of the k_{11}, with the former staying roughly the same or even decreasing with ligand bulk. The results therefore underscore the conclusion that **R1** to **R3** follow the addition-oxidation mechanism of Pathway A. It can hence be concluded that the discussed arylamine copper complexes adhere to a gated electron transfer pathway (Scheme 3.10) with the rate determining step likely being the formation of intermediate **I$_A$**.

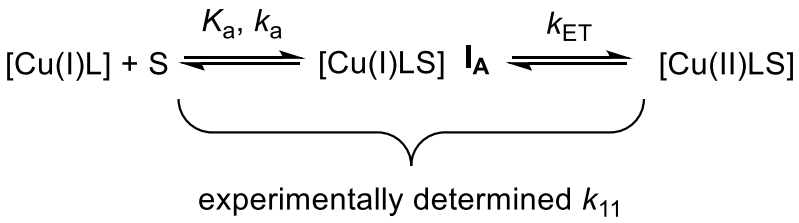

Scheme 3.10: Proposed general reaction equation followed by **R1** to **R3** for the herein discussed electron transfer reactions.

However, the obtained $\Delta E_B^{\ddagger}$ values indicate that k_O, the rate of oxidation of the Cu(I) species in Pathway B, would generally exceed the rate of CN-change. This leaves the inherent stability of the tetracoordinate Cu(II) species, intermediate **I$_B$**, as the cause for the unusual mechanistic properties of the discussed systems. The intermediate seems to be too destabilized to form in a significant margin for Pathway B to be followed. A possible explanation for this preference of a CN-change to intermediate **I$_A$** over a direct oxidation is found in the previously discussed umbrella distortion of the Cu(I) systems

(*vide supra*, Section 3.3.1). This distortion is the main distinction between the arylamine complexes and those with aliphatic tripodal ligand systems that seem to follow Pathway B. Based on the obtained charge-transfer energies of the Cu(I) systems, the elongation of N_{Am}–Cu bond also weakens it. Therefore, it is plausible that the resulting lack of charge donation in the distorted structures destabilizes the tetracoordinate $[Cu(II)L]^+$ intermediates of Pathway B and hinders their formation. Given that oxidations via Pathway B occur comparatively fast, this model for the observed reactivity could further explain the elevated k_{11} of **R3$_{TMG}$**. This is due to the large ΔE of its observed cross reaction, and therefore a strong driving force of the redox reaction on the one hand, and the strongly negative redox potential of **R3$_{TMG}$**, which is indicative of a strong relative stabilization of the Cu(II) state, on the other. These two factors could be sufficient for the participating Cu(I) complex to partially oxidize directly via Pathway B, slightly elevating the observed k_{11} relative to the expected value. This mixed mechanism would not be observable in the stopped-flow measurements as both pathways proceed via a first order decay. Changing the preferred pathway by increasing the redox reaction's driving force has already been proposed by Rorabacher *et al.*[70]

Furthermore, the umbrella distortion also seems to increase the affinity of Cu(I) systems to adopt a pentacoordinate geometry. This is not only implied by the gathered data herein but also by solid-state structures of the Cu(I) complex of the TDAPA ligand (**CC4**, Figure 3.20). It is the only other reported Cu(I) complex of a triarylamine ligand besides the herein reported systems and **CC3** and displays a fifth donor at the axial position as well as an extremely elongated axial Cu–N_{Am} bond of 2.37 Å.[189]

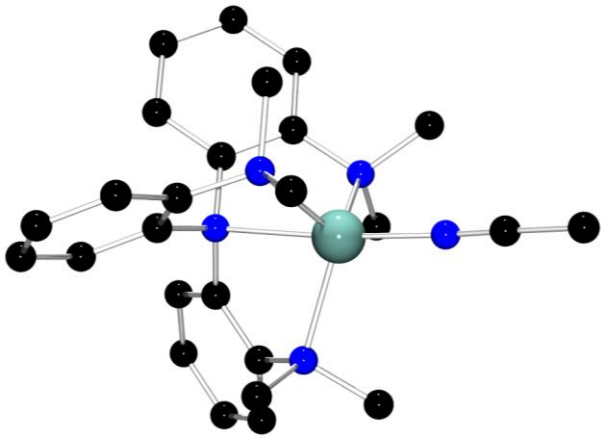

Figure 3.20: Molecular structure of $[Cu(I)(TDAPA)(MeCN)]^+$ (**CC4**, hydrogen atoms, non-coordinating anions and solvent molecules are omitted for clarity).

This tendency to expand the coordination sphere is not observed for the aliphatic model systems mentioned above and indicates an increased stability of the pentacoordinate Cu(I) species **I$_A$** for umbrella-distorted systems.[70, 166]

These results show that the chosen mechanism of coordination-variant electron transfer model systems can be controlled by molecular design, with the umbrella distortion in the Cu(I) systems seeming instrumental for this purpose. While coordination-variant model systems do not follow the entatic state concept, the reported behavior herein underscores that coordinative strain impacts the reactivity of these systems as well. With regards to possible improvements to said ligand design, the stark increase in k_{11} for less bulky systems indicates that the addition-oxidation mechanism is mainly limited by the association of the co-ligand. Therefore, it was attempted to synthesize a pentadentate tripodal arylamine ligand to see whether the elimination of the kinetic barrier of the co-ligand association would increase k_{11}.

3.7 Synthesis of a Pentadentate Arylamine Ligand

In order to eliminate the kinetic barrier of co-ligand association, the corresponding ligand was devised to be pentadentate and make use of the umbrella distortion. To obtain the latter, the system was based on the arylamine $N(QuMe)_3$ that was previously investigated in the working group. To obtain a pentadentate scaffold, a fifth donor was envisioned at the 2-position of one quinolinyl unit. As a possible ligand, $N(QuMee)(Qu)_2$ (**L4**, Figure 3.21) was devised, featuring a fifth donor in the form of a methyl ester group.

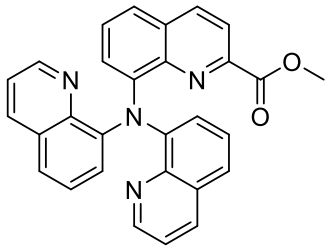

$N(QuMee)(Qu)_2$
L4

Figure 3.21: Lewis structure of the conceptualized tripodal pentadentate ligand $N(QuMee)(Qu)_2$.

The methyl ester donor was chosen because of synthetic limitations on the one hand, but also because Cu(I) has a low affinity for O-donors. This way, only Cu(II) should exhibit a pentacoordinate geometry and the coordination-variant nature of the system would be conserved (Scheme 3.11). This expected behavior is precedented in the TMGqu model system $[Cu(TMG2Meequ)_2]^{+/2+}$ that displays a methyl ester substituent in the 2-position and switches between tetracoordinate motif for Cu(I) and a [4+2] motif for Cu(II).[22]

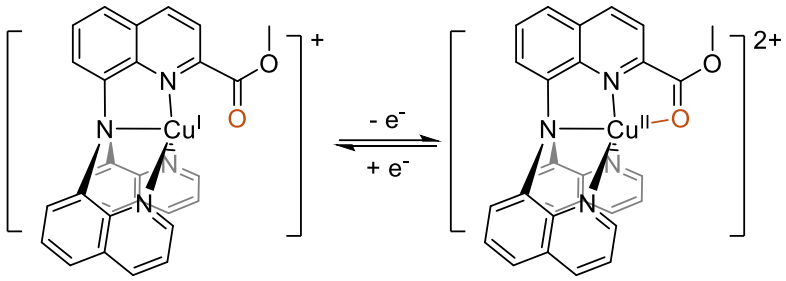

Scheme 3.11: Schematic representation of the conceptualized functionality of the fifth donor in the Cu-complexes of **L4**.

The synthesis of **L4** was done by first obtaining cyclization product **5** as shown in Scheme 3.11. **5** was subsequently combined with acrolein in a Doebner-Miller reaction to obtain the precursor 2-methyl-*N*,*N*-di(quinolin-8-yl)quinolin-8-amine (**7**, Scheme 3.12).

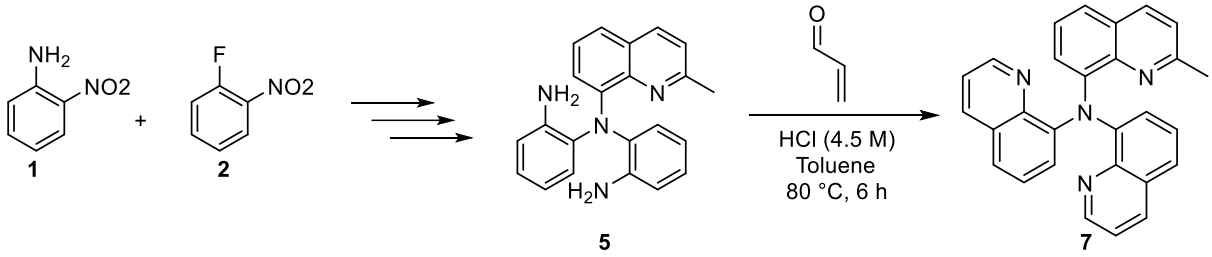

Scheme 3.12: Synthesis scheme to obtain the intermediate 2-methyl-*N*,*N*-di(quinolin-8-yl)quinolin-8-amine (**7**).

The reactivity of the acrolein lead to an improved yield compared to the cyclization reactions with crotonaldehyde. However, with values of up to 49 %, this subsequent cyclization represents a bottleneck as well. Following this step, the methyl group was converted into an aldehyde via a benzylic oxidation after a modified script by He and Fan *et al.* using SeO_2 to obtain 8-(di(quinolin-8-yl)amino)quinoline-2-carbaldehyde (**8**, Scheme 3.13).[190]

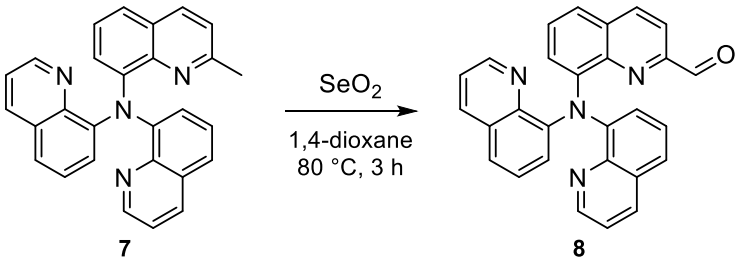

Scheme 3.13: Reaction scheme of the employed benzylic oxidation using SeO_2 to obtain the aldehyde 8-(di(quinolin-8-yl)amino)quinoline-2-carbaldehyde (**8**).

Conversion to the final product **L4** was initially attempted via oxidative esterification with thiamin hydrochloride as catalyst (Scheme 3.14). However, the reaction proved unsuccessful.

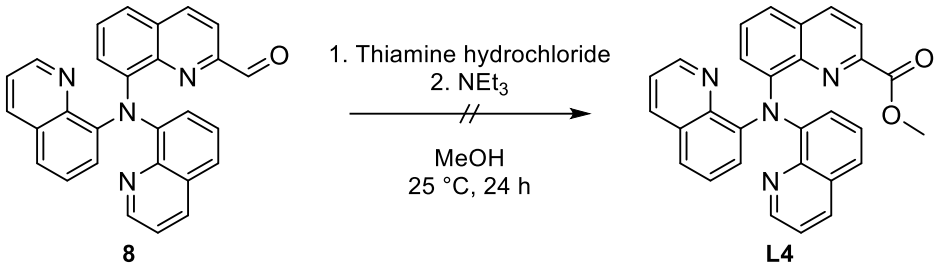

Scheme 3.14: Attempted oxidative esterification to obtain **L4** using thiamine hydrochloride.

Therefore, an alternative reaction after a procedure by Mori *et al.* was attempted using elemental iodine and K_2CO_3.[191] Small scale attempts with 0.21 mmol starting material yielded product with a yield of 31 %. However, up-scaling of the reaction to 0.73 mmol starting material lead to a steep reduction in yield to about 14 % (Scheme 3.15).

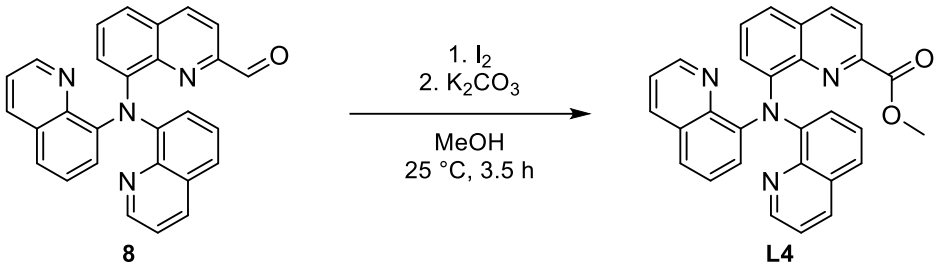

Scheme 3.15: Successful oxidative esterification of **8** to obtain **L4**.

The length and poor yields of the synthesis route made repeated attempts both time and material intensive, which is why further synthesis attempts were stopped. The obtained product was too little for studies beyond fundamental analytics.

Shortly after the project was halted, Olshansky *et al.* published a paper displaying two tripodal ligands with an arylamine each, dpa^{OMe} and dpa^{SMe}.[16] Their copper complexes display a non-dissociating chloride co-ligand in both oxidation states, however the central amine in $[CuCl(dpa^{SMe})]^0$ sits at a distance of 2.6 Å from the Cu(I) center and can therefore be considered dissociated. Therefore, similarly to the desired behavior of **L4** upon complexation, the system is still coordination-variant, yet the variable donor in the scaffold allows for CN-change with only minimal activation energy (Figure 3.22). This results in a high k_{11} of $2.21 \cdot 10^6$ M^{-1} s^{-1} for $[Cu(dpa^{SMe})Cl]^{+/0}$, among the highest for any reported model system to date. Given the herein discussed coordinative properties of tripodal arylamine ligands, the dissociation of the central amine can be considered the logical extreme of an umbrella distortion in the presence of a strong co-ligand.

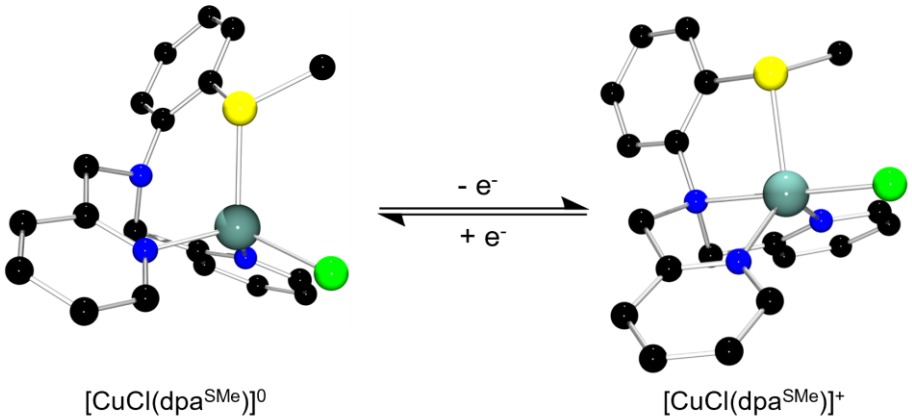

Figure 3.22: Solid state structures of $[Cu(Cl)(dpa^{SMe})]^{0/+}$ by Olshansky *et al.*[16]

Further studies of pentadentate tripodal arylamine ligands with varying numbers of aromatic arms and axial donors of varying strength could therefore be interesting candidates for novel coordination-variant model systems.

4 Thermal Electron Transfer Properties of Novel TMGqu-based Model Systems

4.1 Motivations and Aim

Guanidine quinoline, or GUAqu, ligands are bidentate N-donor ligands with one quinolinyl and one guanidine moiety each. In the absence of strongly coordinating anions, their bis(chelate) Cu(I) and Cu(II) complexes exhibit rigid, tetracoordinate and distorted coordination geometries that render them suitable as coordination-invariant entatic state model systems.

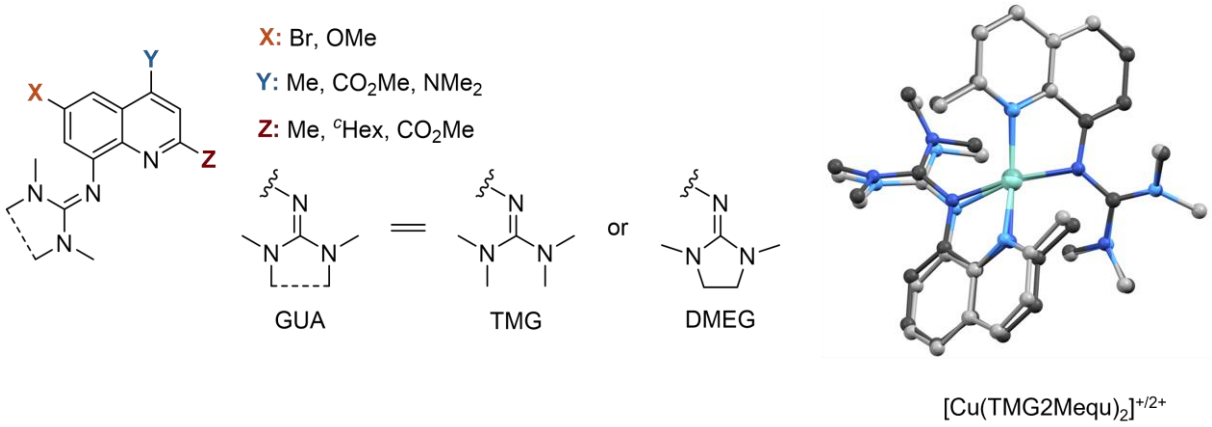

Figure 4.1: Left: Schematic illustration of a GUAqu ligand with reported substituents. Right: Overlay of the Cu GUAqu redox couple $[Cu(TMG2Mequ)_2]^{+/2+}$.[22, 69, 77, 85-86, 192]

Previous studies on these systems have resulted in a large number of GUAqu systems with different guanidines and a plethora of substituents in the 6-, 4- and 2-positions of the quinoline.[22, 69, 77, 85-86, 192] In the context of the entatic state, GUAqu systems with a TMG moiety (also referred to as TMGqu systems) and sterically demanding substituents in the quinolinyl's 2-position show more pronounced structural distortion and high k_{11} on the order of 10^3 M^{-1} s^{-1}.[22] To further enhance the electron transfer rates of the TMGqu complexes, novel 2-substituted TMGqu ligands were developed (Figure 4.2).

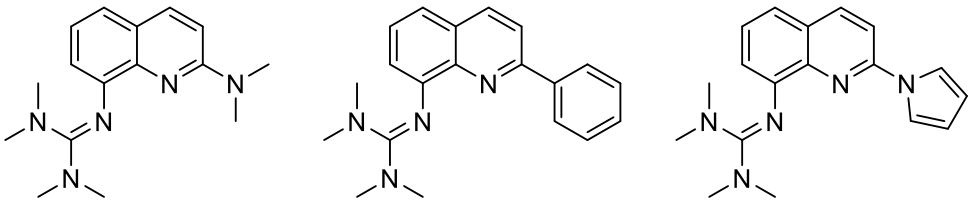

TMG2NMe$_2$qu (**L5**) TMG2Phqu (**L6**) TMG2Pyqu (**L7**)

Figure 4.2: Herein to be synthesized 2-substituted TMGqu ligands with sp^2-hybridized substituents.

The general commonality of these ligands is the sp^2-hybridized character of their substituents, something that has previously not been explored for 2-substituted TMGqu

systems. To study the effect of these substituents, the corresponding Cu(I) and Cu(II) complexes were synthesized and analyzed via single crystal X-ray diffraction (SCXRD), cyclic voltammetry, UV/vis- and EPR spectroscopy as well as theoretical DFT methods to simulate their geometries in solution. Lastly, the complexes' electron self-exchange rates k_{11} were determined using stopped-flow UV/vis spectroscopy to probe the substituents' effects on the entatic state.
The data was complemented by comparison to the other complexes of two other 2-substituted TMGqu ligands as well as those of the archetypical TMGqu ligand (Figure 4.3).

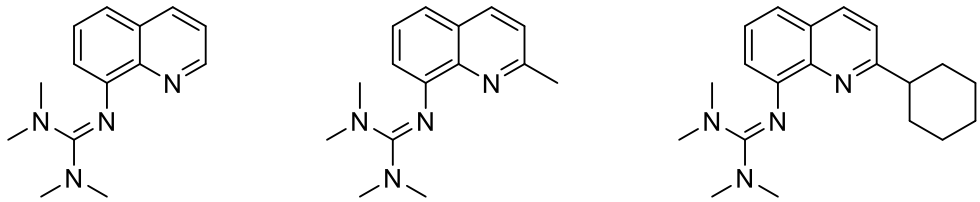

Figure 4.3: Ligands of the corresponding complexes for comparison.

The third reported 2-substituted TMGqu ligand, TMG2Meequ, was excluded from these comparisons due to the methyl ester groups resulting in a coordination-variant behavior of the redox couple.

4.2 Ligand Synthesis

4.2.1 Synthesis of TMG2NMe$_2$qu (L5)

The first step in the synthesis of ligand **L5** was the nitration of 2-cloroquinoline (**9**) using nitric acid and sulfuric acid following a procedure by Herres-Pawlis *et al.* (Scheme 4.1).[22]

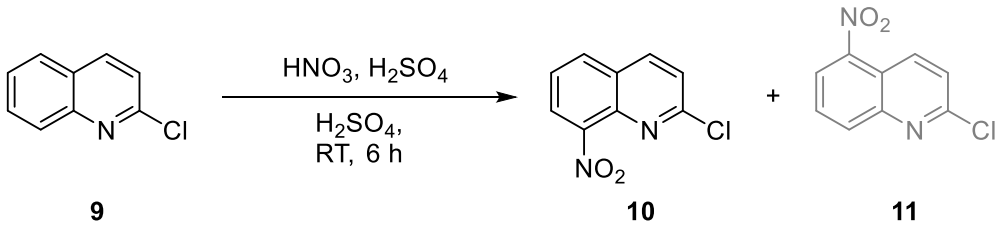

Scheme 4.1: Reaction scheme of the nitration of **9**.[22]

The reaction results in nitration of the 5- and 8-position of the quinoline, giving rise to two products, 2-chloro-8-nitroquinoline (**10**) and 2-chloro-5-nitroquinoline (**11**) that were separated via column chromatography. Later ligand syntheses either used **10** from this reaction or commercially available substrate. Subsequently, an S_NAr was performed with **10** and dimethylamine under increased pressure as reported by

Pozharskii *et al.* and Matyjaszewski *et al.* to yield 2-dimethylamine-8-nitroquinoline (**12**) as the nitro precursor in quantitative yield.[193-194] Reduction of the nitro group of **12** returned the diamine N^2,N^2-dimethylquinoline-2,8-diamine (**13**) in quantitative yields which was subsequently combined with TMG Vilsmeier salt (TMG-VS) to yield TMG2NMe2qu (**L5**).

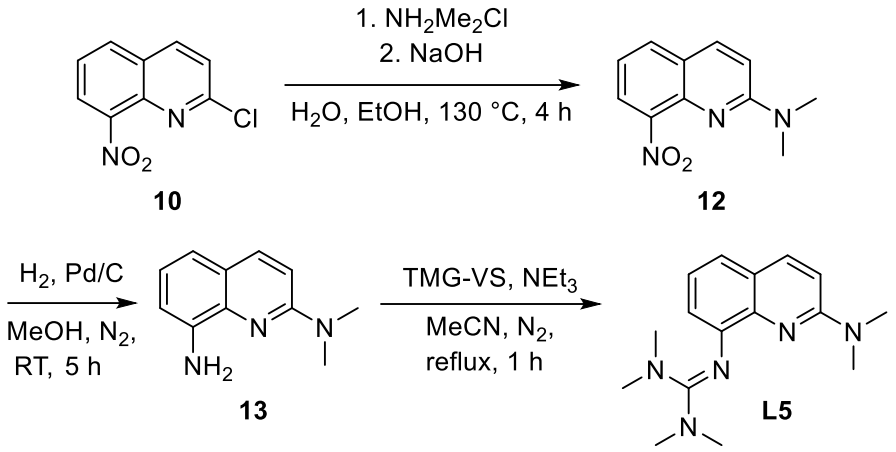

Scheme 4.2: Reaction schemes of the different steps of the synthesis of TMG2NMe2qu (**L5**) starting from intermediate **10**.[193-194]

4.2.2 Synthesis of TMG2Phqu (L6)

The first step in the synthesis of ligand **L6** was a Suzuki-Miyaura coupling reaction from **10** and phenylboronic acid after a modified procedure from Nahide *et al.*[195] The obtained product **14** was purified via column chromatography, subsequently reduced to 2-phenyl-8-nitroquinoline (**15**) which was finally combined with TMG Vilsmeier salt to yield TMG2Phqu (**L6**).

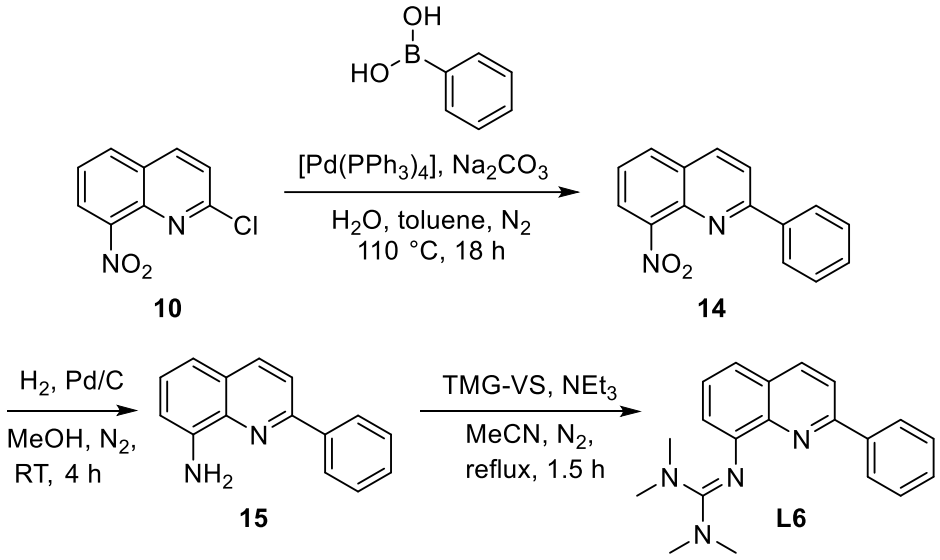

Scheme 4.3: Reaction schemes of the different steps of the synthesis of TMG2Phqu (**L6**) starting from intermediate **10**. [195]

4.2.3 Attempted Synthesis of TMG2Pyqu (L7)

An S_NAr was performed with **10** and a solution of sodium pyrrol-1-ide (**17**) that was prepared by deprotonation of pyrrole (**16**) with NaH at 0 °C in MeCN. While the reaction mixture showed strong discoloration to a dark solution and black precipitate forming, no product could be detected in mass spectrometry or NMR spectroscopy the following day. Repetition of the reaction with slower drop rate of **17** to the reaction mixture yielded less discoloration and no black precipitate, but the desired product 8-nitro-2-(1*H*-pyrrol-1-yl)quinoline (**18**) could not be detected in mass or NMR.

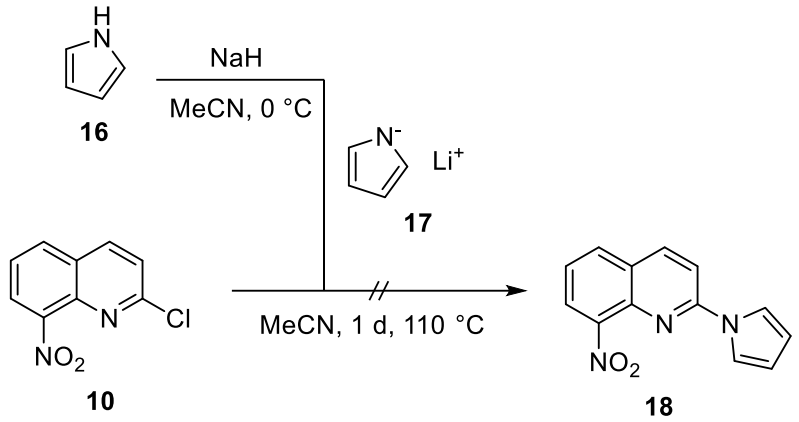

Scheme 4.4: Reaction scheme of the attempted synthesis of compound **18**.

Possible explanations for the lack of observed product are either insufficient nucleophilicity, or too demanding steric bulk of the anion of **17** for the sterically demanding S_NAr reaction to occur successfully. An alternative approach that was not tested is a recently reported palladium catalyzed cross-coupling reaction reported by Duan and Yu *et al*.[196]

The successfully obtained ligands were used to obtain the corresponding complexes.

4.3 Complex Synthesis and Characterization

The complex salts $[Cu(TMG2NMe_2qu)_2](OTf)_2$ (**C8–OTf**), $[Cu(TMG2Phqu)_2]PF_6$ and (**C9–PF_6**) $[Cu(TMG2Phqu)_2](OTf)_2$ (**C10–OTf**) were obtained by adding the corresponding precursor salts $[Cu(MeCN)_4]PF_6$ or $[Cu(MeCN)_4](OTf)_2$ to a solution of **L5** or **L6** in DCM under Schlenk conditions. The mixture was precipitated with pentane, and the resulting complex salt was filtered and stored under inert conditions to prevent oxidation and hydrolysis.

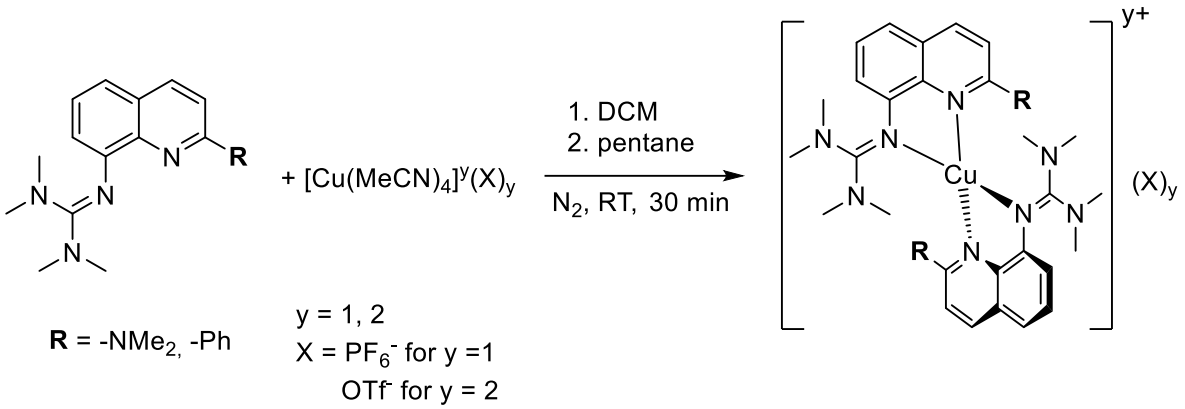

Scheme 4.5: General reaction scheme to obtain the compounds **C7–PF_6**, **C8–OTf**, **C9–PF_6** and **C10–OTf**. **C7–PF_6** was crystallized and not precipitated.

The solid-state structures of **C8–OTf**, **C9–PF_6** and **C10–OTf** were obtained by redissolving the complexes in a solvent and crystallizing them by layering the solution with a suitable anti-solvent.

Due to low yields by the method described above, **C7–PF_6** was obtained by dissolving TMG2NMe2qu (**L5**) and $[Cu(MeCN)_4]PF_6$ in DCM in a glovebox and slowly adding pentane via gaseous diffusion. This resulted in long, black, hexagonal columns of $[Cu(TMG2NMe_2qu)_2]PF_6 \cdot 2$ DCM (**C7–PF_6·DCM**). After single crystal analysis, these columns were dried *in-vacuo* to remove excess DCM, giving rise to the red-brown solid $[Cu(TMG2NMe_2qu)_2]PF_6$ (**C7–PF_6**).

C7–PF_6·DCM crystallized in the trigonal space group $P3_2$, the Cu(II) pendant **C8–OTf** in the triclinic space group $P\bar{1}$ (Figure 4.4, Table 4-1 for structural data). **C7–PF_6·DCM** was measured at 150 K instead of 100 K as the crystal decomposed at lower temperatures.

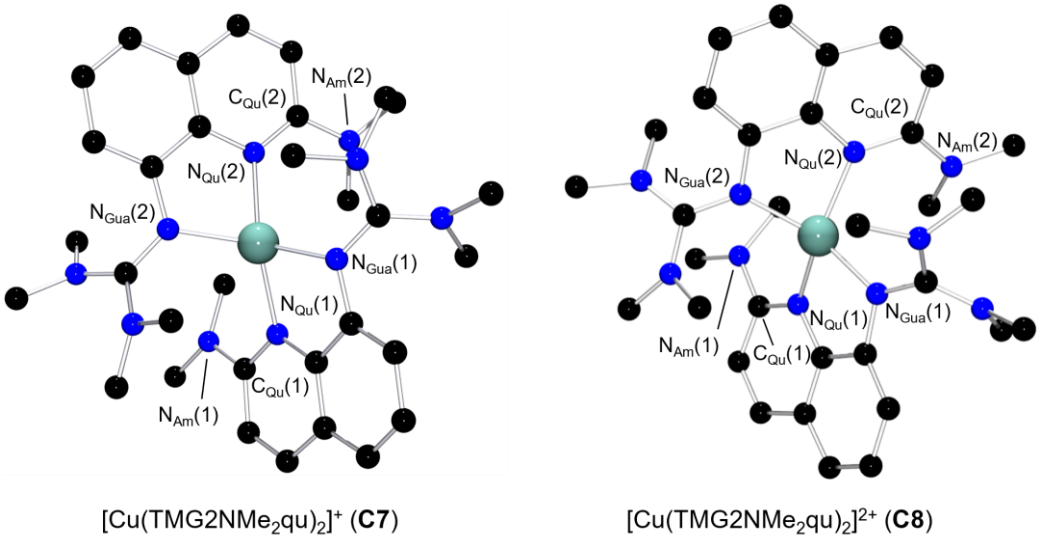

Figure 4.4: Molecular structure of the complex cations $[Cu(TMG2NMe_2qu)]^+$ (**C7**, left) and $[Cu(TMG2NMe_2qu)]^{2+}$ (**C8**, right) in the crystals of $[Cu(TMG2NMe_2qu)_2]PF_6 \cdot 2$ DCM (**C7–PF_6·DCM**) and $[Cu(TMG2NMe_2qu)_2](OTf)_2$ (**C8–OTf**) (hydrogen atoms, non-coordinating anions and solvent molecules are omitted for clarity, important atoms are marked).

The solid state structure of the Cu(I) complex $[Cu(TMG2Phqu)_2]PF_6 \cdot DCM$ (**C9–PF₆·DCM**) crystallizes in the monoclinic space group $P2_1/c$, the Cu(II) pendant $[Cu(TMG2Phqu)_2](OTf)_2 \cdot 0.5\ H_2O$ (**C10-OTf·H₂O**) in the orthorhombic space group *Pbcn* (Figure 4.4, Table 4-1 for structural data).

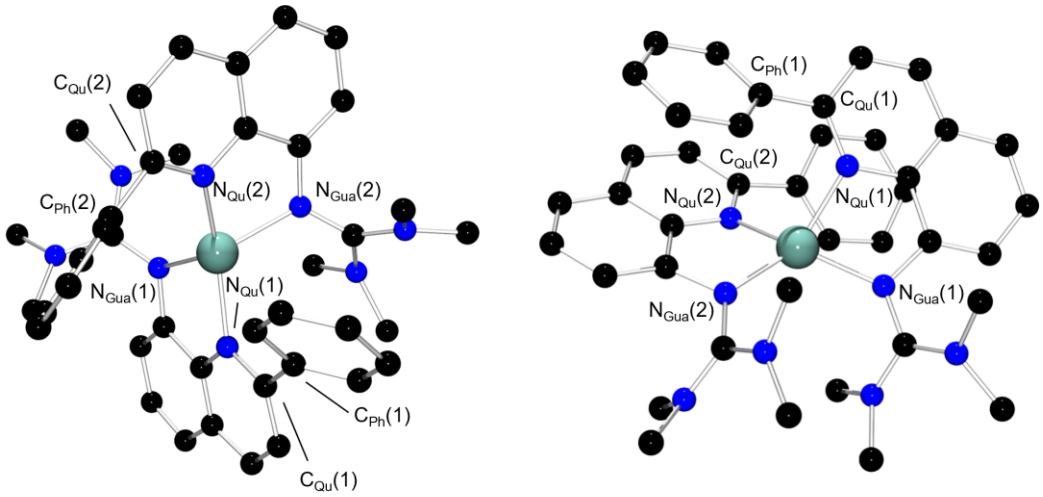

$[Cu(TMG2Phqu)_2]^+$ (**C9**) $[Cu(TMG2Phqu)_2]^{2+}$ (**C10**)

Figure 4.5: Molecular structure of the complex cations $[Cu(TMG2Phqu)]^+$ (**C9**, left) and $[Cu(TMG2Phqu)]^{2+}$ (**C10**, right) in the crystals of $[Cu(TMG2Phqu)_2]PF_6 \cdot DCM$ (**C9–PF₆·DCM**) and $[Cu(TMG2Phqu)_2](OTf)_2 \cdot 0.5\ H_2O$ (**C10-OTf·H₂O**) (hydrogen atoms, non-coordinating anions and solvent molecules are omitted for clarity, important atoms are marked).

Next to the τ_4 parameter, the plane angle $\measuredangle$ is used to evaluate the complex cations' molecular structures. It describes the angle between the planes the N_{Gua}–Cu–N_{Qu} units span for each ligand and yields smaller values for more flattened coordination geometries. As the entatic state is not only defined by the distortion of one geometry, but also by the degree of structural rearrangement between the oxidation states, the τ_4 parameter and plane angle of the corresponding structures are compared. Using τ_4, this can be quantified by determining both the difference $\Delta\tau_4$ (*vide supra*, Eqn. 2), as well as the average $\varnothing\tau_4$ of the τ_4 parameters of both oxidation states (Eqn. 32).

$$\varnothing\tau_4 = \frac{\tau_4\ (Cu(I)) + \tau_4\ (Cu(II))}{2} \qquad (32)$$

The plane angle is compared by determining the difference $\Delta\measuredangle$ of both oxidation states (Eqn. 33).

$$\Delta\measuredangle = \measuredangle(Cu(I)) - \measuredangle(Cu(II)) \qquad (33)$$

Since these values only describe the direct coordination geometry, the RMSD values of both redox pairs were determined as well to assess the change in the entire molecular structure between the oxidation states. An RMSD value of 0 corresponds to a perfect structural accordance between the structures.

An ideal entatic state in a coordination-invariant, tetracoordinate model systems has differences in structure close to zero for either the RMSD value, $\Delta\tau_4$ or $\Delta\measuredangle$ as well as a $\varnothing\tau_4$ of around 0.5, so that the structures are both distorted and rigid. The structures are compared to the previously reported systems $[Cu(TMGqu)_2]^+$ (**C11**), $[Cu(TMGqu)_2]^{2+}$ (**C12**), $[Cu(TMG2Mequ)_2]^+$ (**C13**), $[Cu(TMG2Mequ)_2]^{2+}$ (**C14**), $[Cu(TMG2^cHexqu)_2]^+$ (**C15**), $[Cu(TMG2^cHexqu)_2]^{2+}$ (**C16**) (Table 4-1).

Given the extremely elongated $Cu–N_{Qu}$ bonds of around 2.16 Å, the obtained structure for **C7** shows that the dimethylamine substituent exerts significant steric strain in the Cu(I) state. The $Cu–N_{Qu}$ bond is the longest coordinative bond found for all other 2-substituted $[Cu(GUAqu)_2]^{+/2+}$ systems (Table 4-1), followed by $[Cu(TMG2^cHexqu)_2]^+$ (**C15**) with a $Cu–N_{Qu}$ bond length of 2.08 Å.[22] This elongation is still present, if less pronounced, in **C8** which exhibits the longest $Cu–N_{Qu}$ bond of all Cu(II) systems with 2.01 Å. This strong steric influence of the dimethylamine group is likely due to the strong conjugation of the amine with the quinolinyl moiety, evidenced by the shortened $N_{Am}–C_{Qu}$ bond of 1.36 to 1.37 Å in both oxidation states compared to those of N–C single bonds with 1.47 Å.[197] This conjugation causes a co-planar orientation the NMe_2 substituent to the quinolinyl unit and restricts the rotation around the $N_{Am}–C_{Qu}$ axis, causing one methyl substituent to point towards the central ion. However, the overall change in geometry between **C7** and **C8** (jointly referred to as redox pair **R4**) is comparatively low. Both ions display distorted geometries with a τ_4 of 0.57 and 0.49, respectively, yielding a $\Delta\tau_4$ of 0.08, the second smallest of all $[Cu(GUAqu)_2]^{+/2+}$ systems next to **C15** and **C16** with a value of 0.06.[22] The difference between the plane angles of 0.08° and the RMSD value of 0.165 Å are each also either the smallest or the second smallest reported values, indicating a high structural agreement between the two complex cations (see Figure 4.6 for an overlay, Table 4-1 for comparison of structural parameters).

Table 4-1: Selected bond lengths, angles and structural parameters of the solid-state structures of **C7** to **C16**.

Redox Couple	**$[Cu(TMG2NMe_2qu)_2]^{+/2+}$ (R4)**		**$[Cu(TMG2Phqu)_2]^{+/2+}$ (R5)**		**$[Cu(TMGqu)_2]^{+/2+}$ (R6)**		**$[Cu(TMG2Mequ)_2]^{+/2+}$ (R7)**		**$[Cu(TMG2^cHexqu)_2]^{+/2+}$ (R8)**	
Complex Cation	**C7**	**C8**	**C9**	**C10**	**C11**[a]	**C12**[a]	**C13**[a]	**C14**[a]	**C15**[a]	**C16**[a]
Oxidation state	Cu(I)	Cu(II)	Cu(I)	Cu(II)	Cu(I)	Cu(II)	Cu(I)	Cu(II)	Cu(I)	Cu(II)
	Bond Lengths [Å]									
$Cu–N_{Gua}(1)$	1.995(4)	1.964(2)	2.097(4)	1.982(2)	2.068(3)	1.959(2)	2.091(3)	1.979(4)	2.018(3)	1.973(2)
$Cu–N_{Gua}(2)$	1.991(4)	1.961(2)	2.086(4)	1.982(2)	2.095(3)	1.964(2)	2.097(3)	1.978(4)	2.024(3)	1.973(2)
$Cu–N_{Qu}(1)$	2.164(4)	2.010(2)	2.042(4)	2.0010(19)	1.966(3)	1.976(2)	1.994(3)	1.987(4)	2.084(3)	1.988(2)
$Cu–N_{Qu}(2)$	2.155(4)	1.9922(19)	2.039(4)	2.0010(19)	1.999(3)	1.975(2)	1.994(3)	1.972(4)	2.081(3)	1.988(2)
$N_{Am}(1)–C_{Qu}(1)$	1.374(7)	1.360(3)	-	-	-	-	-	-	-	-
$N_{Am}(2)–C_{Qu}(2)$	1.371(7)	1.357(3)	-	-	-	-	-	-	-	-
$C_{Ph}–C_{Qu}(1)$	-	-	1.476(7)	1.469(4)	-	-	-	-	-	-
$C_{Ph}–C_{Qu}(2)$	-	-	1.497(7)	1.469(4)	-	-	-	-	-	-
	Bond Angles [°]									
$N_{Gua}(1)–Cu–N_{Gua}(2)$	141.04(14)	141.60(8)	118.29(15)	119.69(11)	129.1(2)	149.4(1)	126.0(2)	135.9(2)	135.0(2)	124.7(2)
$N_{Gua}(1)–Cu–N_{Qu}(2)$	112.85(15)	105.67(9)	119.50(16)	143.56(8)	108.2(2)	102.6(1)	111.7(2)	105.4(2)	128.7(2)	135.8(1)
$N_{Gua}(1)–Cu–N_{Qu}(1)$	81.33(15)	84.07(9)	81.69(16)	82.70(8)	82.6(2)	83.5(1)	81.7(2)	83.2(2)	81.2(2)	82.9(1)
$N_{Gua}(2)–Cu–N_{Qu}(1)$	111.86(15)	106.62(9)	112.17(15)	143.56(8)	114.1(2)	103.5(1)	113.2(2)	107.2(2)	127.9(2)	135.8(1)
$N_{Gua}(2)–Cu–N_{Qu}(2)$	81.90(15)	84.12(8)	81.65(16)	82.69(8)	82.1(2)	83.7(1)	81.6(2)	83.6(2)	81.3(2)	82.9(1)
$N_{Qu}(1)–Cu–N_{Qu}(2)$	138.81(14)	149.10(8)	146.72(16)	95.23(11)	149.0(2)	154.9(1)	149.9(2)	154.6(2)	104.9(2)	100.7(2)
	Structure Parameters									
τ_4 [ ]	0.57	0.49	0.67	0.52	0.58	0.40	0.60	0.49	0.68	0.63
$\Delta\tau_4$ [ ]	0.08		0.15		0.18		0.10		0.06	
$\varnothing\tau_4$ [ ]	0.53		0.60		0.49		0.54		0.65	
$\measuredangle$ [°]	63.25	53.02	77.59	52.27	65.1	42.5	68.2	54.7	78.1	65.5
$\Delta\measuredangle$ [°]	10.23		25.32		22.6		13.5		12.6	
ρ [ ]	0.97, 0.97	1.00, 1.00	0.96, 0.98	1.02, 1.02	0.97, 0.96	1.00, 0.99	0.97, 0.98	1.01, 1.00	0.99, 0.99	1.01, 1.01
RMSD [Å]	0.165		2.425		0.346		0.153		0.196	

a: data taken from [22].

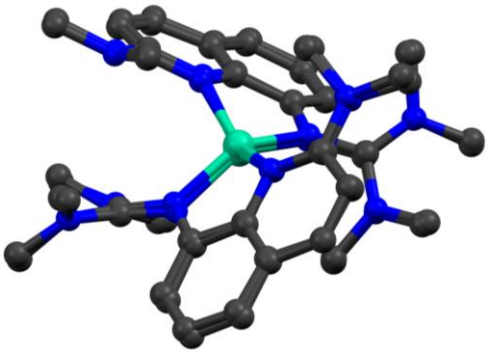

Figure 4.6: Overlap of the molecular structures of **C7** and **C8** from the redox couple **R4**.

With highly distorted geometries and little rearrangement between the oxidation states, the obtained structural values for **R4** are close to what can be considered an ideal entatic state for a tetracoordinate model system.

Conversely, **C9** and **C10** (jointly referred to as redox couple **R5**) represent conformational isomers of each other. While **C9** displays a conformation that is not unlike that of most other $[Cu(GUAqu)_2]^{+/2+}$ model systems, **C10** exhibits a flattened conformation that is also present in **C15** and **C16**. This conformer is characterized by the guanidines' co-facial orientation to each other and the stacked arrangement of the substituted quinolinyl moieties. The conformers can further be distinguished by their $N_{Qu}(1)$–Cu–$N_{Qu}(2)$ angle, which is 146.7° for **C9** and 95.2° for **C10**. **C9**'s conformation can therefore be described as a trans, and **C10**'s as a cis conformer (Figure 4.7).

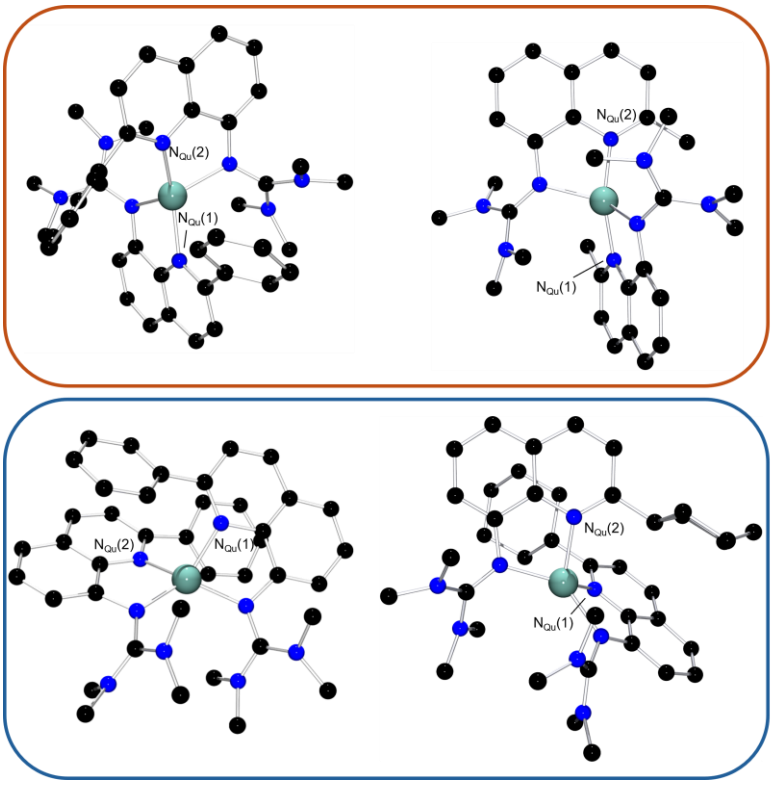

Trans conformer

- Guanidine co-facial to quinolinyl unit
- ∡($N_{Qu}(1)$–Cu–$N_{Qu}(2)$) around 140°

Cis conformer

- Guanidines co-facial to each other
- ∡($N_{Qu}(1)$–Cu–$N_{Qu}(2)$) around 100°

Figure 4.7: Illustration of the key differences between the trans and the cis conformers of $[Cu(GUAqu)_2]^{+/2+*}$ complexes.[22]

This conformational flexibility is likely possible because the phenyl-substituent does not exhibit a strong degree of conjugation with the quinolinyl moiety. This is supported by the C_{Ph}–C_{Qu} bond length that is between 1.47 and 1.50 Å and corresponds to the single-bond length between two sp^2 hybridized carbon atoms.[198-200] The bond can therefore rotate around its axis with little restriction which enables different conformations. Of further interest in **C10** are the distance and orientation of the two ligand planes from each other. The phenyl substituent of one ligand is oriented in a co-facial arrangement with the quinolinyl system of the other, separated by around 3.4 Å (Figure 4.8). This distance corresponds to about twice the van-der-Waals radius of carbon, pointing towards a possible intermolecular interaction between the two ligand units.[201]

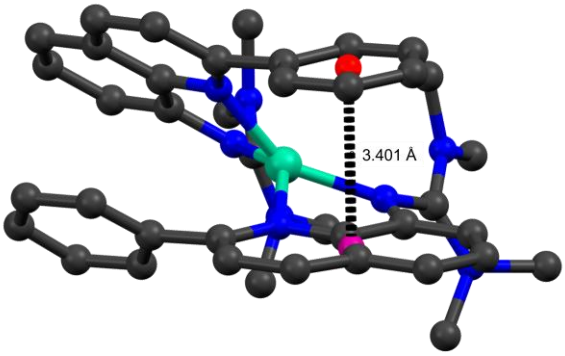

Figure 4.8: Illustration of the intermolecular distance between the center of the Ph substituent (red) and the center of the quinolinyl unit (purple).

Due to the two conformers, the comparability of **C9** and **C10** is limited, and the co-existence of both conformers for each oxidation in solution is plausible. Recrystallization of **C9–PF$_6$** was attempted in a different solvent system to potentially obtain a cis configured structure. An attempted layer-diffusion of Et_2O into a solution of **C9–PF$_6$** in MeCN yielded a crystal of poor quality. This structure exclusively shows different cis conformers with varying orientations of the phenyl-substituents in a large unit cell; yet the poor quality prevented an exact solution. Repeated attempts to recrystallize this structure remained unsuccessful, but the result indicates a possible conformational distribution of **C9–PF$_6$** in solution which was further investigated by DFT and CREST computations (Section 4.4.2).

4.4 Computational Assessment of the $[Cu(GUAqu)_2]^{+/2}$ Redox Couples

Similar to the triarylamine complexes, the $[Cu(GUAqu)_2]^{+/2}$ systems were optimized via the TPSSh-D3BJ/def2-TZVP + PCM(MeCN) // TPSSh-D3BJ/def2-TZVP + PCM(MeCN) method (**M1**), as it is known to yield reliable geometries and good electronic energies.[22, 86]

4.4.1 DFT Optimization of the $[Cu(TMG2NMe_2qu)_2]^{+/2+}$ Redox Pair (R4)

The geometries for **C7** and **C8** obtained via **M1** are in good agreement with the solid-state structures with RMSD values of 0.10 Å and 0.09 Å, respectively (Table 4-2).

Table 4-2: Key bond lengths, bond angles and structural parameters of the DFT optimized geometries of the complex cations **C7** and **C9** (TPSSh-D3BJ/def2-TZVP+ PCM(MeCN) // TPSSh-D3BJ/def2-TZVP + PCM(MeCN)).

Complex Cation	**C7**	**C7***	**C8**
Oxidation state	Cu(I)	Cu(I)	Cu(II)
		Bond Lengths [Å]	
$Cu–N_{Gua}(1)$	2.024	1.995	1.967
$Cu– N_{Gua}(2)$	2.024	1.991	1.967
$Cu–N_{Qu}(1)$	2.093	2.164	2.014
$Cu–N_{Qu}(2)$	2.094	2.155	2.014
$N_{Am}(1)–C_{Qu}(1)$	1.374	1.373	1.365
$N_{Am}(2)–C_{Qu}(2)$	1.374	1.373	1.365
		Bond Angles [°]	
$N_{Gua}(1)–Cu–N_{Gua}(2)$	135.6	141.0	140.3
$N_{Gua}(1)–Cu–N_{Qu}(2)$	112.5	113.2	106.9
$N_{Gua}(1)–Cu–N_{Qu}(1)$	82.3	81.3	83.9
$N_{Gua}(2)–Cu–N_{Qu}(1)$	112.9	113.1	106.9
$N_{Gua}(2)–Cu–N_{Qu}(2)$	82.3	81.6	83.9
$N_{Qu}(1)–Cu–N_{Qu}(2)$	141.2	137.1	148.4
		Structure Parameters	
τ_4 [ ]	0.59	0.58	0.51
$\Delta\tau_4$ (Cu(I) vs. Cu(II)) [ ]	0.08	0.07	-
$\varnothing\tau_4$ (Cu(I) vs. Cu(II)) [ ]	0.55	0.55	-
$\measuredangle$ [°]	65.5	64.9	54.7
$\Delta\measuredangle$ (Cu(I) vs. Cu(II)) [°]	10.8	10.2	-
ρ [ ]	0.97, 0.97	0.97, 0.97	1.00, 1.00
RMSD (vs. Cu(II)) [Å]	0.126	0.136	-
RMSD (vs. SCXRD) [Å]	0.100	0.092[a]	0.089

*Cu–N bond lengths were fixed from the solid-state structure. a: Comparability of the RMSD value is affected by the fixed bond lengths.

Notable, however, is a significant deviation in the $Cu–N_{Qu}$ bond lengths in **C7** that are drastically shortened for the DFT optimized geometry. Given the established accuracy of **M1** in the structural description of $[Cu(GUAqu)_2]^{+/2+}$ systems, these elongated bonds imply a possible complication of the theoretical description of **C7** due to the dimethylamine substituent in the 2-position. A possible reason for this might be the steric interactions of the substituent with its environment that causes the elongation. Due to the inaccuracies regarding the described $Cu–N_{Qu}$ bonds, **C7** was reoptimized via **M1** from the solid-state geometry with frozen Cu–N bond lengths, abbreviated as complex **C7***, the redox couple as **R4***, respectively. Compared to the unrestricted

optimization, **C7*** mostly deviates in the bond lengths with the angles and structural parameters being similar for both structures, albeit flipped for the angles between both guanidine and quinoline donors.

4.4.2 Conformational Analysis and DFT Optimization of $[Cu(TMG2Phqu)_2]^{+/2+}$

The conformational analysis of **R5** was conducted by running xtb/CREST on the gfn2 level of theory with the implicit solvent model ALPB for acetonitrile for both the cis and trans conformer under assumption of a Cu(I) oxidation state. Both computations resulted in seven unique conformers within the range of 12 kJ mol^{-1}, of which the previously discussed cis conformer was both times determined to be the most energetically favorable one. These seven conformers were subsequently optimized via DFT using **M1** for both Cu(I) and Cu(II) to assess the available conformational space of both oxidation states. The seven conformers can be grouped into four trans and three cis conformers that are further differentiated by the position of the phenyl-rings in relation to the quinolinyl moiety (Figure 4.9).

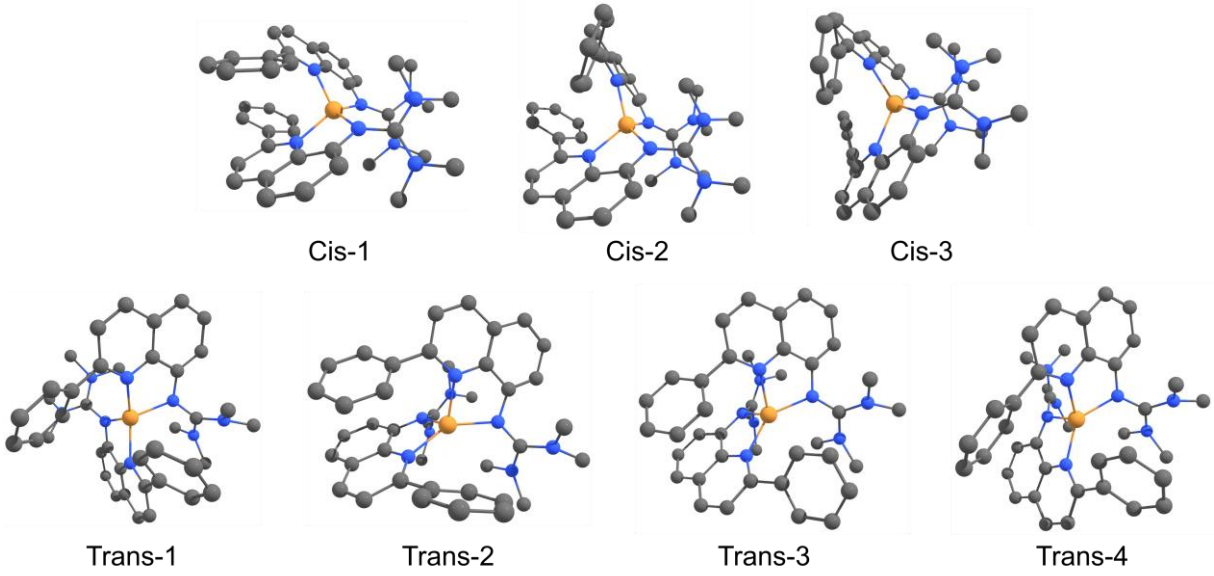

Figure 4.9: Molecular structures and labels of the found conformers of the complex cation **C7** using GFN2-xTB/ALPB(MeCN).

While the structural differences of the trans conformers are not as apparent, the cis conformers show a clear differentiation by the number of phenyl substituents that are co-facially orientated with the quinolinyl moiety of the second ligand. More in-depth structural analysis (Table 4-3) shows that both kinds of conformer express a range of τ_4 values between 0.55 and 0.77. The cis conformers' geometry become increasingly tetrahedral with the number of twisted phenyl substituents, going from τ_4 = 0.55 for cis-1 Cu(II) to 0.77 for cis-3 Cu(I).

Table 4-3: Key bond lengths, bond angles and structural parameters of the DFT optimized geometries of the conformers of the complex cation $[Cu(TMG2Phqu)_2]^+$ **C9** and $[Cu(TMG2Phqu)_2]^{2+}$ **C10** (TPSSh-D3BJ/def2-TZVP+ PCM(MeCN) // TPSSh-D3BJ/def2-TZVP + PCM(MeCN)).

Conformer	**Cis-1**		**Cis-2**		**Cis-3**		**Trans-1**		**Trans-2**		**Trans-3**		**Trans-4**	
Oxidation state	Cu(I)[a]	Cu(II)[a]	Cu(I)[c]	Cu(II)[c,d]	Cu(I)[c]	Cu(II)[c]	Cu(I)[b]	Cu(II)[b]	Cu(I)[c]	Cu(II)[c]	Cu(I)[c]	Cu(II)[c]	Cu(II)[c]	Cu(II)[c]
						Bond Lengths [Å]								
$Cu–N_{Gua}(1)$	2.073	1.999	2.087	-	2.050	1.971	2.076	1.994	2.065	1.948	2.124	2.012	2.046	2.018
$Cu–N_{Gua}(2)$	2.073	1.999	2.050	-	2.050	1.974	2.093	2.037	2.137	2.174	2.043	1.990	2.141	2.043
$Cu–N_{Qu}(1)$	2.039	1.999	2.041	-	2.075	2.054	2.024	1.999	2.067	2.028	2.002	1.981	2.071	1.974
$Cu–N_{Qu}(2)$	2.039	1.999	2.077	-	2.075	2.050	2.026	1.966	2.009	1.964	2.077	2.036	1.995	1.980
$C_{Ph}–C_{Qu}(1)$	1.475	1.471	1.478	-	1.477	1.472	1.477	1.476	1.477	1.477	1.477	1.472	1.477	1.475
$C_{Ph}–C_{Qu}(2)$	1.475	1.471	1.475	-	1.477	1.473	1.475	1.470	1.474	1.470	1.477	1.474	1.475	1.470
						Bond Angles [°]								
$N_{Gua}(1)–Cu–N_{Gua}(2)$	116.7	118.0	119.3	-	124.9	130.5	116.3	122.8	116.3	116.4	119.5	129.8	116.3	121.0
$N_{Gua}(1)–Cu–N_{Qu}(2)$	137.9	141.5	128.2	-	124.5	118.2	110.5	106.2	144.4	152.9	102.9	122.9	131.5	117.8
$N_{Gua}(1)–Cu–N_{Qu}(1)$	82.0	83.3	81.6	-	81.5	83.3	82.6	83.8	81.1	80.8	82.0	83.1	81.4	83.3
$N_{Gua}(2)–Cu–N_{Qu}(1)$	137.9	141.5	134.3	-	124.5	118.5	121.6	111.7	105.6	103.9	140.7	103.9	110.1	107.6
$N_{Gua}(2)–Cu–N_{Qu}(2)$	82.0	83.3	81.5	-	81.5	83.4	81.5	82.6	81.5	83.6	81.0	83.2	81.4	82.8
$N_{Qu}(1)–Cu–N_{Qu}(2)$	109.9	99.5	119.0	-	126.4	129.2	146.2	155.0	125.8	113.7	128.9	139.8	137.5	148.1
						Structure Parameters								
τ_4 [ ]	0.60	0.55	0.69	-	0.77	0.71	0.65	0.58	0.64	0.64	0.64	0.64	0.65	0.65
$\Delta\tau_4$ [ ]	0.05		-		0.06		0.07		0.00		0.00		0.00	
$\varnothing\tau_4$ [ ]	0.58		-		0.74		0.62		0.64		0.64		0.65	
$\measuredangle$ [°]	66.1	57.1	78.6	-	88.9	79.2	79.2	66.9	87.6	88.0	82.0	68.7	84.2	72.5
$\Delta\measuredangle$ [°]	9.0		-		9.7		12.3		−0.4		13.3		11.7	
ρ []	0.98, 0.98	1.00, 1.00	0.97, 0.97	-	0.98, 0.98	1.00, 1.00	0.98, 0.98	1.00, 1.00	0.98, 0.97	1.00, 1.00	0.97, 0.97	1.00, 1.00	0.98, 0.97	1.00, 1.00
RMSD [Å]	0.320		-		0.335		0.232		0.170		0.463		0.301	
RMSD (vs.SCXRD) [Å]	-	0.330	-	-	-	-	0.200	-	-	-	-	-	-	-

a: Optimized beginning from **C9–PF_6·DCM**; b: Optimized from **C10–PF_6·H_2O**; c: Optimized starting from geometry obtained via CREST; d: Geometry always interconverted into cis-1 upon optimization with **M1**.

Notably, both oxidation states of cis-1 show the most flattened geometry, with a $\varnothing\tau_4$ of 0.58. All of the computed redox pairs of one conformer show very little structural rearrangement between them. While the cis-1 and trans-1 conformer, each optimized from solid-state data, show minor structural differences with $\Delta\tau_4$ values of 0.05 and 0.07 respectively, the remaining trans conformers each display a $\Delta\tau_4$ = 0. For these conformers, the plane angles and RMSD values still show the presence of structural flattening. These changes are, however, minor relative to the obtained values for other 2-substituted $[Cu(GUAqu)_2]^{+/2+}$ systems (Table 4-1 for solid state data, Section 9.10 for DFT structural data).[22, 86] Apparent in many of the structures is that at least one phenyl substituent is oriented in either a co-facial or a perpendicular orientation towards another phenyl or quinolinyl moiety. These arrangements resemble the co-facial and edge-on arrangements observed in π-stacking and might point towards intermolecular interactions between the ligands (Figure 4.10).[202]

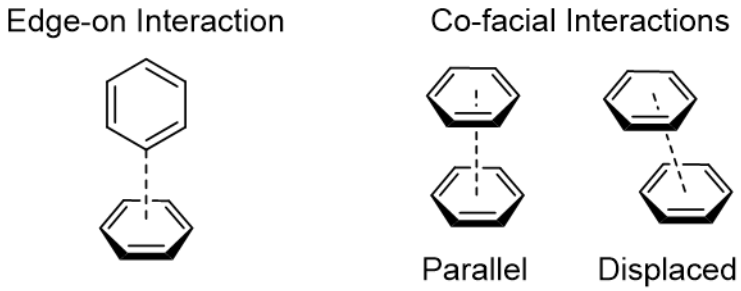

Figure 4.10: Schematic illustrations of typical π-π interactions.[202]

This feature is especially visible in the cis-1 and trans-1 conformers that exhibit co-facial and edge-on orientations, respectively. For cis-1, DFT predicts the distances between the phenyl and quinolinyl units to be 3.7 Å for Cu(I), shortening for Cu(II) where they are separated by 3.5 Å, similar to the observed separation of 3.4 Å in the solid-state structure (Figure 4.8). For trans-1, the edge-on separation is predicted to be 3.6 Å by **M1** for Cu(I) and 3.7 Å for Cu(II). These separations correspond to the van-der-Waals radius of carbon, although they are longer than the ideal predicted separation of 3.4 Å.[201] While these orientations could also be explained by simple steric effects and just resemble stable conformations, the potential presence of intermolecular interactions could account for the predicted rigidity of the conformers' coordination geometry between Cu(I) and Cu(II).

To discuss the effects of the obtained structures on the experimental data, the prevalent conformers in solution have to be identified which was done via the Boltzmann distribution (Eqn. 34).[203]

$$\text{Probability } (p_i) = \frac{\exp(\frac{G_j - G_i}{k_B T})}{\sum \exp(\frac{G_j - G_i}{k_B T})} \quad (34)$$

G_j: Gibb's free energy of compound; k_B = 8.3145·10^{-3} kJ K^{-1} mol^{-1}; T = 298.25 K

The lowest energy conformer was always chosen as reference G_j. Given the importance of the distribution to the interpretation of the gathered data further on, the Gibbs free energies obtained by method **M1** were controlled by calculations performed by reoptimizing all conformers with the MN15/def2-TZVP + PCM(MeCN) // MN15/def2-TZVP + PCM(MeCN) method (**M2**). While this method yielded a worse structural description of the complexes than **M1**, predicting elongated bonds (see Section 9.11), reported benchmarking showed that it gives better thermochemical descriptions of transition metal complexes than TPSSh.[204]

For more flexible Cu(I) state, the Gibbs free energy values obtained by **M1** suggest several present conformers in solution, with the trans-1 conformer as the most prevalent conformer in solution with a relative abundance of 86.4 % followed by cis-1 with 7.5 % (Figure 4.11, more details in Section 9.12).

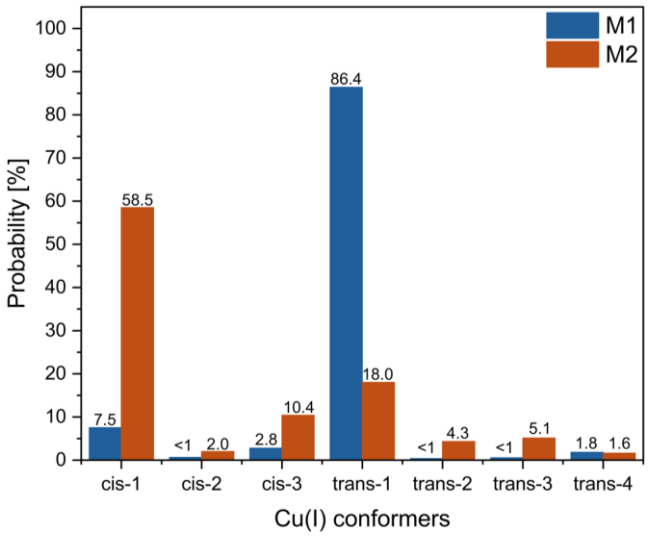

Figure 4.11: Bar graph showing the percentage of each Cu(I) conformer in solution at 298.15 K for the two employed DFT methods. **M1**: TPSSh-D3BJ/def2-TZVP+ PCM(MeCN) // TPSSh-D3BJ/def2-TZVP + PCM(MeCN); **M2**: MN15/def2-TZVP + PCM(MeCN) // MN15/def2-TZVP + PCM(MeCN).

Contrary to this, the data obtained by **M2** suggests a preference for cis-1 by Cu(I) with a relative abundance of 58.5 % in solution, followed by trans-1 with only 18.0 %. Notably, the cis-3 conformer is estimated to be the third most stable Cu(I) conformer by both methods with a relative abundance of 3 to 10 %.

In contrast, the results of both methods regarding Cu(II) are consistent in regard to the predicted conformational distribution, estimating the cis-1 conformer to be almost exclusively present in solution with a relative abundance of over 99 % (Figure 4.12).

This result is plausible as cis-1 is predicted to be the flattest conformer, therefore exhibiting the most favorable geometry for the d^9 Cu(II) ion. The preference for cis-1 is so strongly pronounced that both methods lead to an interconversion of conformer cis-2 into the more stable cis-1 upon optimization; it could therefore not be observed. This interconversion could further suggest low kinetic barriers between the cis conformers and could therefore indicate a dynamic equilibrium between the three conformers in the Cu(I) oxidation state. To gauge the accuracies of the two predicted distributions for Cu(I), the redox couples of the two most prevalent conformers, trans-1 (**R5$_{trans-1}$**) and cis-1 (**R5$_{cis-1}$**), were continually investigated in further computational assessment and used as reference for collected experimental data. For this purpose, the clear conformational preference of Cu(II) was utilized to control the initial conformer in CV measurements (Section 4.5) and electron transfer reactions (Section 4.8), as these measurements are sensitive to conformational changes.

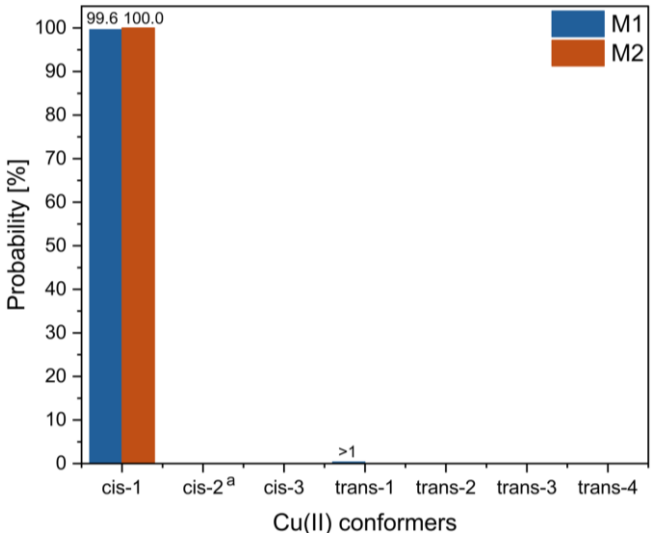

Figure 4.12: Bar graph showing the percentage of each Cu(II) conformer in solution at 298.15 K for the two employed DFT methods. **M1**: TPSSh-D3BJ/def2-TZVP+ PCM(MeCN) // TPSSh-D3BJ/def2-TZVP + PCM(MeCN); **M2**: MN15/def2-TZVP + PCM(MeCN) // MN15/def2-TZVP + PCM(MeCN).
a: Conformer cis-2 interconverted to conformer cis-1 upon optimization by both methods and was thus not observed.

4.4.3 NBO Analysis of the Cu TMGqu Redox Pairs

The complex cations of **R4**, **R5$_{cis-1}$** and **R5$_{trans-1}$** were further analyzed via NBO population analysis using **M1** and compared to the other 2-substituted $[Cu(GUAqu)_2)]^{+/2+}$ model systems $[Cu(TMGqu)_2]^{+/2+}$ (**C11**, **C12**, **R6**), $[Cu(TMG2Mequ)_2]^{+/2+}$ (**C13**, **C14**, **R7**) and $[Cu(TMG2^cHexqu)_2]^{+/2+}$ (**C15**, **C16**, **R8**). For that purpose, the charge transfer energies E_{CT} of the σ and π contributions of all redox pairs' donors were calculated based on the optimized structures using NBO 6.0 (Table 4-4).[181-183]

The charge transfer energies have previously been employed to investigate the influence of the different substituents, their positions and the coordination geometry on the donor properties of the ligands.[22, 84, 86] In these studies, it has been found that the change in overall charge transfer energy between Cu(II) and Cu(I), $\Delta E_{CT,total}$, is slightly dependent on the donor properties of substituents in the 4-position but most strongly correlates with substituents in the 2-positon. However, these works did not consider the contributions of possible π donation to the metal center, which is why the previously studied **R6**, **R7** a **R8** were re-investigated herein for this purpose. The obtained E_{CT} show the typical increase from Cu(I) to Cu(II) that has already been observed in previous studies and the tripodal model systems.[22, 86] Further, there is no clear trend for which donor, N_{Qu} or N_{Gua}, has stronger charge transfer properties; with the corresponding E_{CT} for each donor varying in relative strength from cation to cation. The individual contributions for each donor atom are usually identical for each cation with the exception of **C7***, **C9$_{trans-1}$** and **C10$_{trans-1}$** that show slight variations. Given the established correlation between bond length and charge transfer energy by Herres-Pawlis *et al.*,[86] these exceptions are very likely due to the unsymmetric bond lengths displayed by the cations in question. Interesting in that regard is that **R4***, possessing dimethylamine substituents with strong $^{+}$M-effects, does not seem to exhibit increased $E_{CT,total}$ for either oxidation state compared to the other complexes. This circumstance might also be connected to structural factors, as **C7*** especially displays severely elongated Cu–N_{Qu} bonds that should reduce the total amount of charge transfer energy of these donors. While this elongation is less pronounced in Cu(II), it can be assumed to still affect the overall donor properties. This is supported by the NBO calculations yielding comparatively small charge transfer energies for the N_{Qu} donors of both **C7*** and **C8**, while the sterically unhindered N_{Gua} donors exhibit comparatively high E_{CT} values. Also of note is that for **R5**, both conformers show near identical sums of all contributions, $E_{CT,total}$, for Cu(I) and Cu(II) each despite their strong structural differences. Contrary to this, the individual donor contributions vary strongly between the two conformers. Regarding the σ and π contributions, guanidine donors consistently show higher π charge transfer energies than quinolinyl donors, which is consistent with the observations for the tripodal model systems (*vide supra*). These contributions also show a strong variation from cation to cation, even for the different conformers of **R5**, and are significantly higher for Cu(II) than for Cu(I).

Table 4-4: Charge transfer energies E_{CT} for the σ and π contributions of each donor in the complex cations of **C7*** to **C15** (Population analysis was performed using the NBO 6.0 package, based on the DFT structures calculated with the TPSSh-D3BJ/def2-TZVP+ PCM(MeCN) // TPSSh-D3BJ/def2-TZVP + PCM(MeCN) method).

Complex (Redox Couple)	**C7* (R4*)**		**C9$_{trans-1}$ (R5$_{trans-1}$)**		**C9$_{cis-1}$ (R5$_{cis-1}$)**		**C11 (R6)**		**C13 (R7)**		**C15 (R8)**	
Ligand	**TMG2NMe$_2$qu**		**TMG2Phqu**		**TMG2Phqu**		**TMGqu**		**TMG2Mequ**		**TMG2^{c}Hexqu**	
Oxidation state	**Cu(I)**		**Cu(I)**		**Cu(I)**		**Cu(I)**		**Cu(I)**		**Cu(I)**	
						E_{CT} [kcal mol^{-1}]						
Component	σ	π	σ	π	σ	π	σ	π	σ	π	σ	π
$N_{Qu}(1)\rightarrow Cu$	15.3	0.3	21.3	0.2	18.5	0.2	29.6	0.2	26.7	0.2	17.8	0.1
$N_{Qu}(2)\rightarrow Cu$	15.5	0.3	22.6	0.1	18.5	0.2	29.6	0.2	26.7	0.2	17.8	0.1
$N_{Gua}(1)\rightarrow Cu$	27.7	0.7	15.9	0.4	19.0	0.6	20.3	1.3	18.4	0.9	21.0	0.7
$N_{Gua}(2)\rightarrow Cu$	27.8	0.7	15.4	0.9	19.0	0.6	20.3	1.3	18.4	0.9	21.0	0.7
$E_{CT,Qu}$	31.4		44.0		37.4		59.4		53.8		35.7	
$E_{CT,Gua}$	48.9		32.6		39.2		43.1		38.6		43.4	
$E_{CT,total}$	80.2		76.6		76.6		102.6		92.4		79.1	
Complex (Redox Couple)	**C8 (R4*)**		**C10$_{trans-1}$ (R5$_{trans-1}$)**		**C10$_{cis-1}$ (R5$_{cis-1}$)**		**C12 (R6)**		**C14 (R7)**		**C16 (R8)**	
Ligand	**TMG2NMe$_2$qu**		**TMG2Phqu**		**TMG2Phqu**		**TMGqu**		**TMG2Mequ**		**TMG2^{c}Hexqu**	
Oxidation state	**Cu(II)**		**Cu(II)**		**Cu(II)**		**Cu(II)**		**Cu(II)**		**Cu(II)**	
						E_{CT} [kcal mol^{-1}]						
Component	σ	π	σ	π	σ	π	σ	π	σ	π	σ	π
$N_{Qu}(1)\rightarrow Cu$	41.9	3.7	51.2	2.3	43.1	2.0	52.8	0.5	51.1	1.4	44.3	1.7
$N_{Qu}(2)\rightarrow Cu$	41.9	3.7	48.7	1.5	43.1	2.0	52.8	0.5	51.1	1.4	44.3	1.7
$N_{Gua}(1)\rightarrow Cu$	45.0	12.7	30.8	7.1	36.6	10.8	47.6	15.7	40.4	11.9	37.8	8.4
$N_{Gua}(2)\rightarrow Cu$	45.0	12.7	33.4	10.8	36.6	10.8	47.6	15.7	40.4	11.9	37.8	8.4
$E_{CT,Qu}$	91.2		103.6		90.1		106.7		104.9		92.0	
$E_{CT,Gua}$	115.4		82.1		94.7		126.6		104.6		92.4	
$E_{CT,total}$	206.5		185.8		184.8		233.2		209.5		184.4	
$\Delta E_{CT,total}$ [kcal mol^{-1}]	126.3		109.1		108.2		130.7		117.1		105.3	
$\Theta E_{CT,total}$ [ ]	2.57		2.42		2.41		2.27		2.27		2.33	

To investigate the interplay between the charge transfer energies and the complexes' coordination geometries, the difference in $E_{CT,total}$ between Cu(II) and Cu(I), $\Delta E_{CT,total}$ was correlated with the change and the average of the computationally obtained $\tau_{4,DFT}$ parameter, $\Delta\tau_{4,DFT}$ and $\varnothing\tau_{4,DFT}$ (Figure 4.13, Structural parameters listed in Tables 4-1 to 4-3).

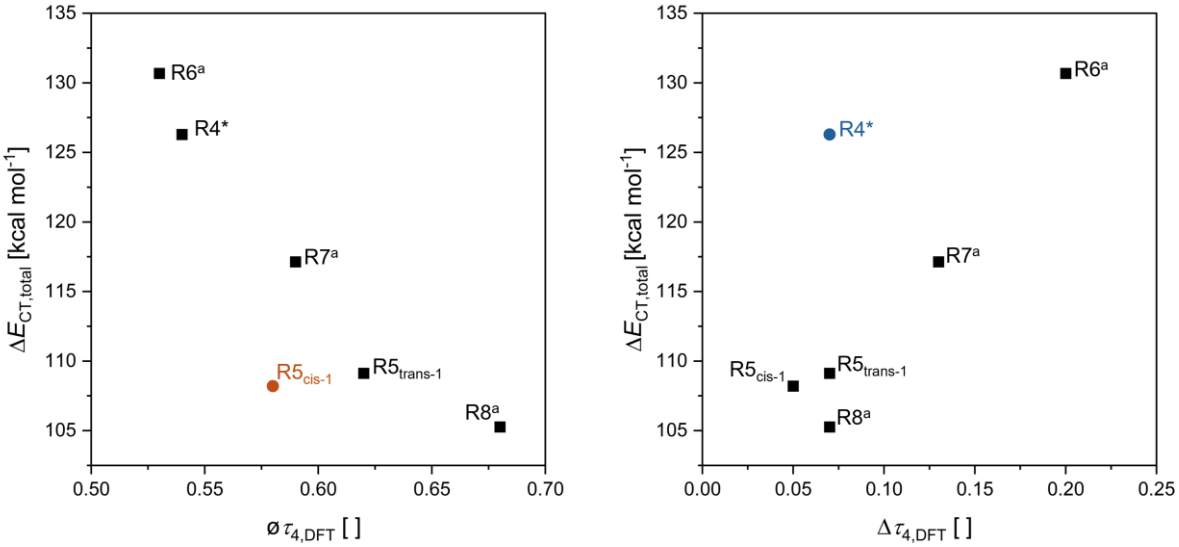

Figure 4.13: Left: Graph of $\Delta E_{CT,total}$ of all investigated redox couples against their mean τ_4 value. Right: Graph of $\Delta E_{CT,total}$ of all investigated redox couples against the corresponding difference in τ_4 value. a: Structural data taken from [22] (Population analysis was performed using the NBO 6.0 package, based on the DFT structures calculated with the TPSSh-D3BJ/def2-TZVP+ PCM(MeCN) // TPSSh-D3BJ/def2-TZVP + PCM(MeCN) method).

The data suggest that redox pairs with large structural flattening, like **R6** with a $\Delta\tau_{4,DFT}$ of 0.20, generally exhibit a larger $\Delta E_{CT,total}$ upon oxidation from Cu(I) to Cu(II) while less flexible systems like **R5$_{cis-1}$** with a $\Delta\tau_{4,DFT}$ of 0.05 experience less change in their electronic environment. This trend is mirrored for $\varnothing\tau_{4,DFT}$, where redox pairs with a flatter average geometry like **R6** with $\varnothing\tau_{4,DFT}$ of 0.53 exhibit a larger $\Delta E_{CT,total}$ compared to redox pairs with a more tetrahedral average geometry like **R8** with a $\varnothing\tau_{4,DFT}$ of 0.68. There are notable exceptions to both trends. As seen in Figure 4.13, the redox pair **R4*** displays an unexpectedly high change in charge transfer energy. This outlier behavior is likely because the significant contraction of the Cu–N_{Qu} bonds upon oxidation is not captured by the τ_4 parameter, which only considers donor angles. A possible explanation for the observed scattering at $\Delta\tau_{4,DFT}$ = 0.07 for **R5$_{trans-1}$** and **R8** is the influence of $\varnothing\tau_{4,DFT}$ on the charge transfer energies. Since **R8** is significantly more tetrahedral on average than **R5$_{trans-1}$**, the observed $\Delta E_{CT,total}$ of **R8** deviates from the expected value. In Figure 4.13, **R5$_{cis-1}$** exhibits a smaller change in charge transfer energy compared to other redox pairs. This deviation is likely the case because **R5$_{cis-1}$** has a $\Delta\tau_{4,DFT}$ of 0.05 that is significantly smaller than those of other redox pairs of

comparable average geometry, therefore lowering $\Delta E_{CT,total}$ beyond the observed trend. These two trends and their exceptions illustrate that the ligands' donor capabilities are dependent on the coordination geometry and the change thereof, with flatter and more flexible systems experiencing larger $\Delta E_{CT,total}$. Additionally, this does not only affect $\Delta E_{CT,total}$ but also the sum of the charge transfer energy of the Cu(II) systems ($E_{CT,total,Cu(II)}$) and the π contributions thereof ($E_{CT,total,Cu(II),\pi}$) that display higher values for flatter geometries (Figure 4.14).

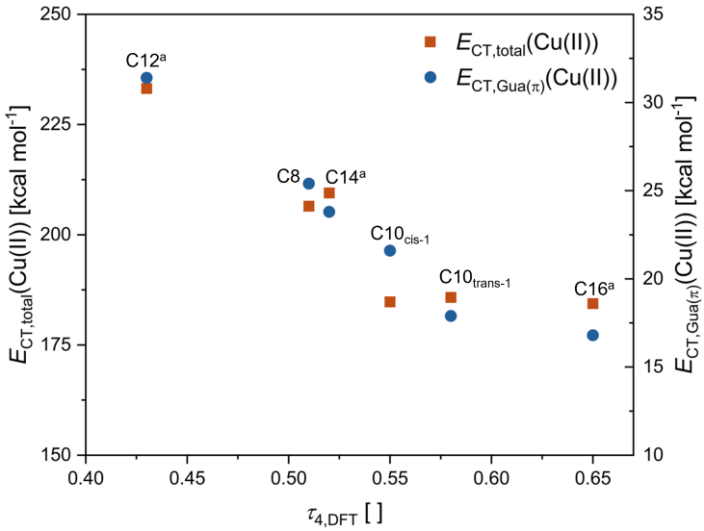

Figure 4.14: $E_{CT,total}$ and $E_{CT,Gua(\pi)}$ of the Cu(II) complex cations plotted against their respective τ_4 parameter. a: Structural data taken from [22] (Population analysis was performed using the NBO 6.0 package, based on the DFT structures calculated with the TPSSh-D3BJ/def2-TZVP+ PCM(MeCN) // TPSSh-D3BJ/def2-TZVP + PCM(MeCN) method).

In the context of ligand field theory (LFT), this can be explained by a better overlap between the ligand orbitals and the d-orbitals in a flatter geometry. The π contributions in particular depend on the structural flattening in order to properly overlap with d orbitals of corresponding symmetry (Scheme 4.6 illustrates this with the d_{xz} orbital as an example).

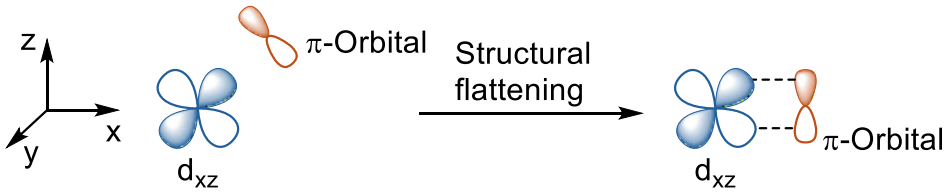

Scheme 4.6: Schematic illustration of the increased orbital overlap between π-bonding orbitals in a flattened coordination geometry.

The obtained differences in charge transfer energy therefore represent the change in electronic stabilization of the Cu(II) state with an increasingly tetrahedral coordination geometry and illustrate the influence of steric restriction on the electronic environment of the Cu(I/II) redox couple. This exact correlation for the $E_{CT,total}$ of Cu(I) against $\tau_{4,DFT}$

yields split trendlines that separate the redox couples with no or sp^3-hybridized substituents from those with sp^2-hybridized ones (Figure 4.15).

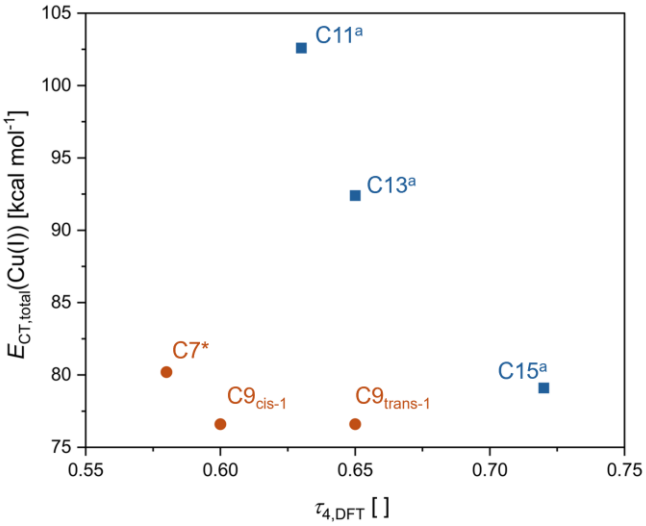

Figure 4.15: Graph of $\Delta E_{CT,total}$ of all investigated redox couples against the corresponding τ_4 value. blue: Complexes of TMGqu, TMG2Mequ and TMG2^{c}Hexqu, orange: Complexes of TMG2NMe_2qu and TMG2Phqu a: Structural data taken from [22] (Population analysis was performed using the NBO 6.0 package, based on the DFT structures calculated with the TPSSh-D3BJ/def2-TZVP+ PCM(MeCN) // TPSSh-D3BJ/def2-TZVP + PCM(MeCN) method).

While there still is a correlation between the planarity of a given compound and the total charge transfer energy, it is less pronounced than for Cu(II), especially for the sp^2-hybridized systems. The split trendlines are therefore a clear deviation from the observed behavior of the Cu(II) systems. Plotting the E_{CT} components of the N_{Qu} and N_{Gua} donors against their corresponding bond length obtained by DFT, non-linear correlations without split are observed (Figure 4.16).

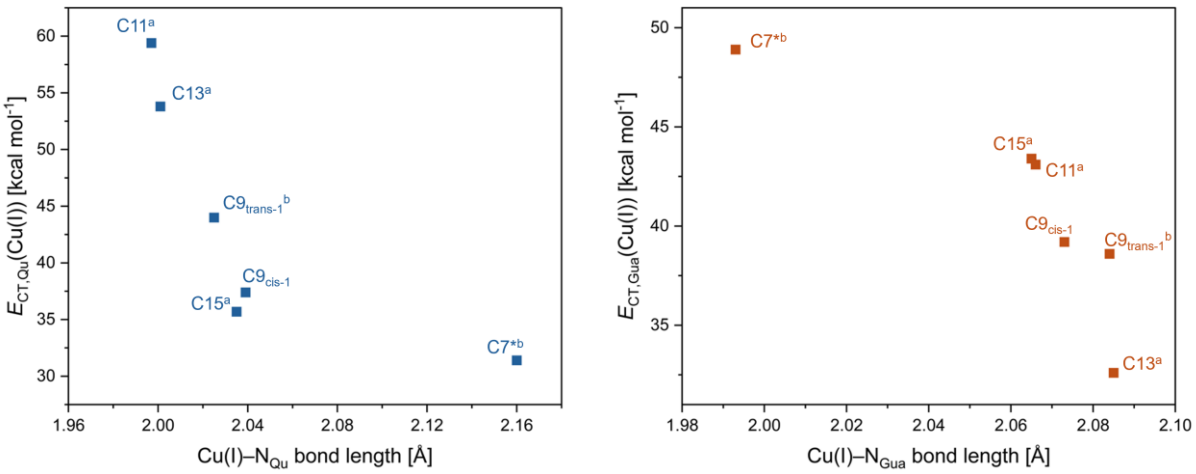

Figure 4.16: Left: Graph of $\Delta E_{CT,total}$ of all investigated Cu(I) complex cations against the corresponding Cu–N_{Qu} bond length. Right: Graph of $\Delta E_{CT,total}$ of all investigated Cu(I) complex cations against the corresponding Cu–N_{Gua} bond length. a: Structural data taken from [22], b: Value is average of two bond lengths (Population analysis was performed using the NBO 6.0 package, based on the DFT structures calculated with the TPSSh-D3BJ/def2-TZVP+ PCM(MeCN) // TPSSh-D3BJ/def2-TZVP + PCM(MeCN) method).

This suggests that the charge transfer energies in the investigated Cu(I) complexes are mostly dependent on the bond length and therefore the steric bulk of each substituent. The sp^2-hybdridized substituents of TMG2NMe$_2$qu (**L5**) and TMG2Phqu (**L6**) therefore seem to impose a different form of steric bulk compared to the non-substituted or alkyl-substituted ligands that alter the obtained geometries and bond lengths. The computational data imply that **L5** and **L6** induce flattened Cu(I) geometries with a smaller $\tau_{4,DFT}$ compared to TMG2Mequ (**L9**) and TMG2^{c}Hexqu (**L10**). In turn, likely due to steric strain induced by co-planar arrangements of the substituents with the quinolinyl moieties, the sp^2-hybridized substituents in **L5** and **L6** tend to elongate the Cu(I)–N_{Qu} bonds.

Notable is the ratio of E_{CT} of Cu(II) and Cu(I), $\Theta E_{CT,total}$. For the tripodal model systems (*vide supra*, Section 3.4.3), this ratio yielded good correlations with the number of present guanidine moieties as well as with the electrochemical potential. While the latter will be discussed at a later point for the systems herein (Section 4.5), it could be assumed that the ratio would also correlate with their $\Delta\tau_4$ and $\varnothing\tau_4$ parameters. As illustrated in Figure 4.17, however, this is not the case.

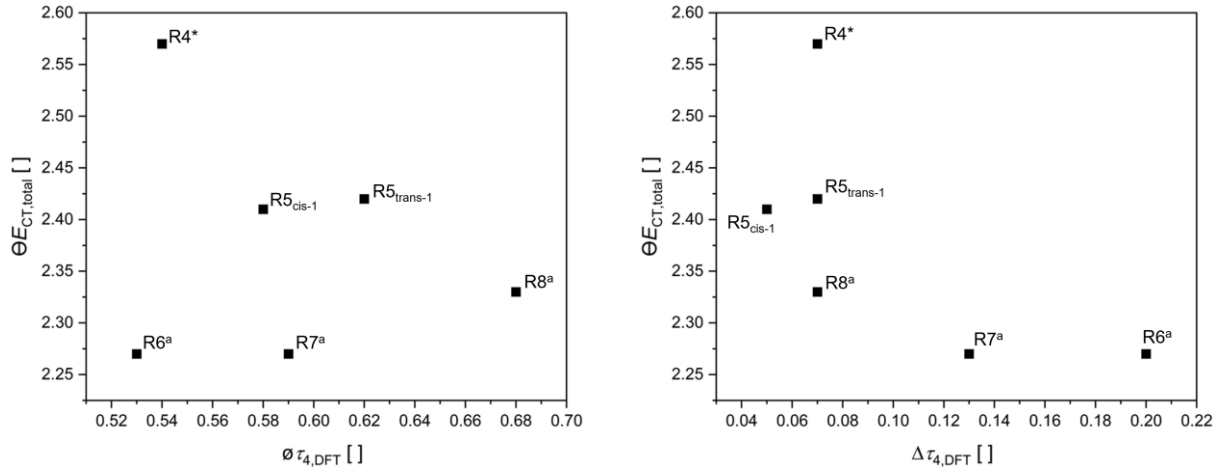

Figure 4.17: Left: Graph of $\Theta E_{CT,total}$ of all investigated redox couples against their mean τ_4 value. Right: Graph of $\Theta E_{CT,total}$ of all investigated redox couples against the corresponding difference in τ_4 value. a: Structural data taken from [22] (Population analysis was performed using the NBO 6.0 package, based on the DFT structures calculated with the TPSSh-D3BJ/def2-TZVP+ PCM(MeCN) // TPSSh-D3BJ/def2-TZVP + PCM(MeCN) method).

A possible explanation for this is that the general driving force in the tripodal model systems' redox potential were of electronic nature, i.e. the number of guanidine moieties present, while the $[Cu(GUAqu)_2]^{+/2+}$ systems are also influenced by steric factors. The ratio $\Theta E_{CT,total}$ could therefore be in indicator for one ligand's affinity to either oxidation state, with a larger number indicating an increased affinity for Cu(II), while ΔE_{CT} yields more information on orbital overlap and geometric influences on the redox potential.

The correlations discussed above illustrate the intricate link between the complexes' charge transfer energies, i.e. their electronic properties, and their coordination environment. The dependence of $\Delta E_{CT,total}$ on $\Delta\tau_4$ and $\varnothing\tau_4$ in particular indicates a worse stabilization of Cu(II) for increasingly tetrahedral geometries. Previous works have shown that this computationally observed behavior is linked to the experimentally obtained redox potentials which will be discussed in detail in section 4.5.[167]

4.5 Cyclic Voltammetry of the Redox Couples R4 and R5

The CV measurements of **R4** and **R5** were conducted to obtain the half-wave potentials $E_{1/2}$ which are required to determine the redox couples' corresponding electron self-exchange rates. Beyond that, the redox waves should yield information about any significant structural rearrangements that could impede the electron transfer process. This is especially important to **R5**, as the predicted conformational distributions for Cu(I) could indicate multiple redox waves or waves with a strong quasi-reversible character, similar to the tripodal model systems (Section 3.4.4). For this reason, **R5** was measured once starting from the conformationally variable Cu(I) salt **C9–PF$_6$**, and once from the Cu(II) salt **C10–OTf**, that the employed DFT methods predict to be exclusively present as the cis-1 conformer in solution. The cyclic voltammogram starting from **C10–OTf** should therefore be corresponding to the cis-1 conformer and serve as control to its Cu(I) counterpart that might exhibit more complex behavior. **R4** was only measured starting from **C7–PF$_6$**. All cyclic voltammograms were recorded at ambient conditions and referenced against the Fc/Fc$^+$ redox couple.

The CV of **R5** are depicted in Figure 4.18, the CV of **R4** can be viewed in the Appendix (Section 9.2.2), $E_{1/2}$ and other important data obtained from the CV are shown in Table 4-5.

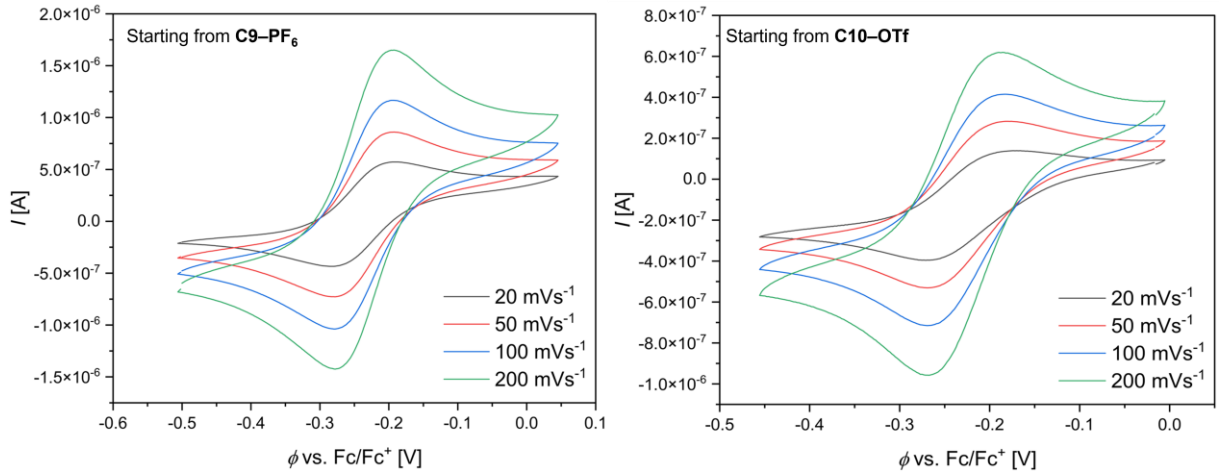

Figure 4.18: Cyclic voltammograms of **R5** starting from the corresponding Cu(I) salt **C9–PF$_6$** (left) and the Cu(II) salt **C10–OTf** (right) (c = 10^{-3} M) in MeCN with [NBu$_4$][PF$_6$] (c = 0.1 M).

Table 4-5: Key parameters of the cyclic voltammograms of **R4** and **R5**.

Sarting compound (redox couple)	$E_{1/2}$ [V] *vs.* Fc/Fc^+	ΔE_P [mV] 20, 50, 100, 200 mV s^{-1}	Increase of ΔE_P [%]	I_{red}/I_{ox} [ ] 20, 50, 100, 200 mV s^{-1}	Increase of I_{ox}/I_{red} [%]
C7–PF$_6$ (**R4**)	−0.34	72, 69, 71, 72	0	1.04, 1.04, 1.09, 1.10	6
C9–PF$_6$ (**R5**)	−0.24	72, 71, 69, 69	−4	1.09, 1.06, 1.05, 1.04	−5
C10–OTf (**R5**)	−0.22	67, 65, 65, 66	−1	1.27, 1.24, 1.23, 1.23	−4

The obtained CVs of all three measurements show good reversibility with peak-to-peak separations between 65 and 72 mV and no clear dependence on the scan rate. A similar behavior is seen for the current ratio of **R4** and the CV for **R5** started from **C9–PF$_6$**. While they reveal minor changes with scan rate, their ratios are consistently close to one. Conversely, the CV for **R5** starting from **C10–OTf** displays a current ratio that is consistently above 1.2.

The redox potentials are comparatively reducing, relative to the other 2-substituted $[Cu(GUAqu)_2]^{+/2+}$ systems, with only $[Cu(TMGqu)_2]^{+/2+}$ (**R6**) being more reducing than **R4** with a potential of −0.45 V *vs.* Fc/Fc^+.[22]

Notably, **R5** shows to have nearly identical redox potentials for each measurement, with the difference of 0.02 V likely resulting from different ionic strengths of the two solutions due to differing numbers and kinds of counter ions. Paired with the close-to-ideal ΔE_P of both cyclic voltammograms, this circumstance implies that the redox-active conformer in both measurements is the cis-1 conformer, undergoing minor conformational changes upon reduction and oxidation. These could potentially include interconversions into the cis-2 and cis-3 conformers, as they are structurally similar to cis-1, only requiring a rotation of the Ph substituents around the C_{Qu}–C_{Ph} bonds (Figure 4.9 for reference). Unexpected is the current ratio greater than 1.2 observed in the cyclic voltammogram of **C10–OTf**. This could be due to either the decay of the reduced species (**C9**) or its rapid conversion into a different conformer that is not redox-active within the scanned voltage range. However, since this behavior is not seen in the CV starting from the Cu(I) complex, a decay of the Cu(I) species is unlikely.

A more plausible explanation is that the cis-1 conformer, when reduced, undergoes conformational changes to form other species. The trans conformers, which are more tetrahedral in geometry than cis-1 in both oxidation states, likely have more positive redox potentials. As a result, these trans conformers do not participate in redox processes within the measured window and appear redox-inactive. When the measurement starts with **C9–PF$_6$**, the solution is already at equilibrium. Thus, the current ratio remains unaffected (see Scheme 4.7 for reference).

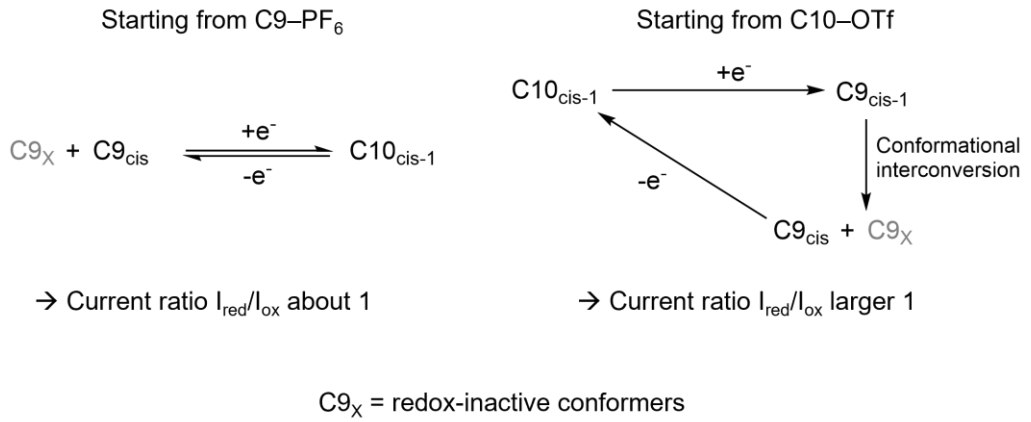

Scheme 4.7: Possible mechanisms behind the observed offset in current ratios in the cyclic voltammograms of $[Cu(TMG2Phqu)_2]^{+/2+}$ **R5**.

With an average I_{red}/I_{ox} of 1.24, the proposed scheme would therefore indicate a ratio of redox-active to redox-inactive conformers of around 4/1. This ratio is in overall agreement with the Boltzmann distribution obtained with the MN15/def2-TZVP + PCM(MeCN) // MN15/def2-TZVP + PCM(MeCN) method (**M2**), that predicted a general excess of all cis conformers of 71 % in solution. Conversely, the results obtained from the usually employed TPSSh-D3BJ/def2-TZVP + PCM(MeCN) // TPSSh-D3BJ/def2-TZVP + PCM(MeCN) method (**M1**) predicted the trans-1 conformer to be the dominant Cu(I) species in solution. **M1** does therefore seemingly not yield reliable thermal corrections for the studied $[Cu(GUAqu)_2]^{+/2+}$ systems.

The redox potentials of Cu(I/II) redox pairs are dependent on their coordination geometry and flexibility. Previous works have shown that more tetrahedral and more rigid $[Cu(GUAqu)_2]^{+/2+}$ systems yield significantly more positive values for $E_{1/2}$, supported by the NBO analysis provided herein (Section 4.3.4).[22] Correlations of the redox potentials of **R4** and **R5** with $\varnothing\tau_{4,DFT}$ and $\Delta E_{CT,total}$ each show that they also follow this trend (Figure 4.19).

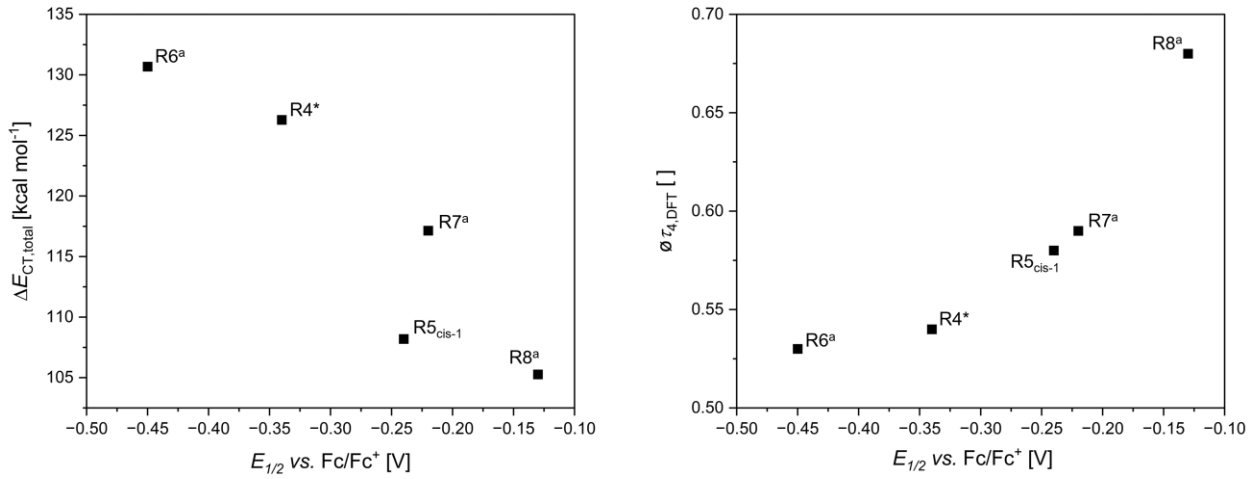

Figure 4.19: Left: Graph of $\Delta E_{CT,total}$ against the experimentally obtained $E_{1/2}$ *vs*. Fc/Fc⁺. Right: Graph of $\varnothing\tau_{4,DFT}$ against the experimentally obtained $E_{1/2}$ *vs*. Fc/Fc⁺. a: Structural data taken from [22] (Population analysis was performed using the NBO 6.0 package, based on the DFT structures calculated with the TPSSh-D3BJ/def2-TZVP+ PCM(MeCN) // TPSSh-D3BJ/def2-TZVP + PCM(MeCN) method).

These correlations support the notion that $\Delta E_{CT,total}$ and the complexes' entasis are connected, as smaller changes in E_{CT} and more tetrahedral geometries both correlate with increasingly positive redox potentials. The redox couple **R4** is especially interesting in this regard as the strongly electron donating dimethylamine group does not lead to a deviation from the observed structural dependence of $E_{1/2}$. It follows that the redox potentials of these systems are likely a primary result of geometric constraints imposed by the entatic state that appear to take precedent over the electronic influences of the substituents. A further indication of this structural bias for the complexes' redox potentials is Figure 4.20, showing the ratio of E_{CT}, $\Theta E_{CT,total}$, plotted against the redox potentials.

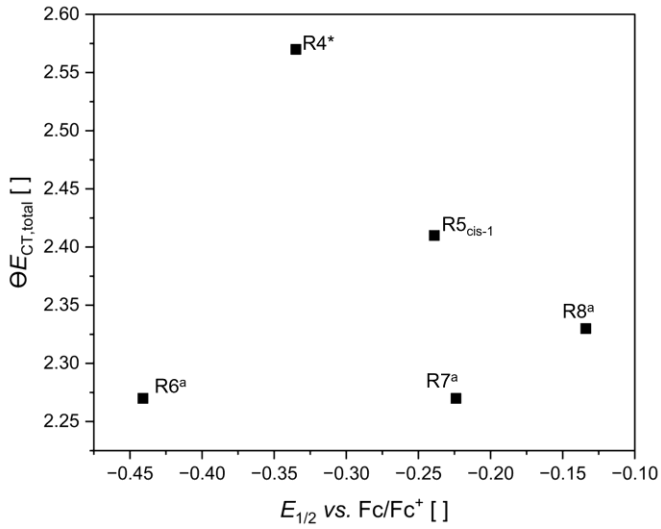

Figure 4.20: $\Theta E_{CT,total}$ of all investigated redox couples against the experimentally obtained $E_{1/2}$ *vs*. Fc/Fc⁺. a: Structural data taken from [22] (Population analysis was performed using the NBO 6.0 package, based on the DFT structures calculated with the TPSSh-D3BJ/def2-TZVP+ PCM(MeCN) // TPSSh-D3BJ/def2-TZVP + PCM(MeCN) method).

The plot shows a slight correlation between higher ratios and more reducing redox potentials, **R6** and **R7** however stand as outliers with a roughly identical $\Theta E_{CT,total}$ and widely varying redox potentials. This is a clear deviation from the previously established correlation between both parameters for the tripodal model systems (*vide supra*, Section 3.4.4). This observation further supports the explanation from Section 4.3.4 that ΘE_{CT} yields information about the preference of the ligand to either Cu oxidation state while ΔE_{CT} also incorporates structural factors like the entasis of a given complex. This would imply the redox potentials of 2-substituted $[Cu(GUAqu)_2]^{+/2+}$ to predominantly be a product of the structural restriction of the entatic state, while the redox potentials of the tripodal model systems are predominantly governed by their electronic preferences, i.e. their number of guanidine moieties.

4.6 Electron Paramagnetic Resonance Spectroscopy

While cyclic voltammetry serves to study the redox processes of a given redox couple, it does not yield information pertaining to the electronic states of the corresponding oxidation states. This can be achieved by electron paramagnetic resonance (EPR) spectroscopy that can directly probe the electronic structure of molecules or coordination compounds with unpaired electrons. The Cu(II) complexes $[Cu(TMG2NMe_2qu)](OTf)_2$ (**C8–OTf**) and $[Cu(TMG2Phqu)_2](OTf)_2$ (**C10–OTf**) were investigated via EPR dissolved in a frozen MeCN at 77 K (Figure 4.21), the spectra were fitted and analyzed via the EasySpin software (Table 4-6).[205]

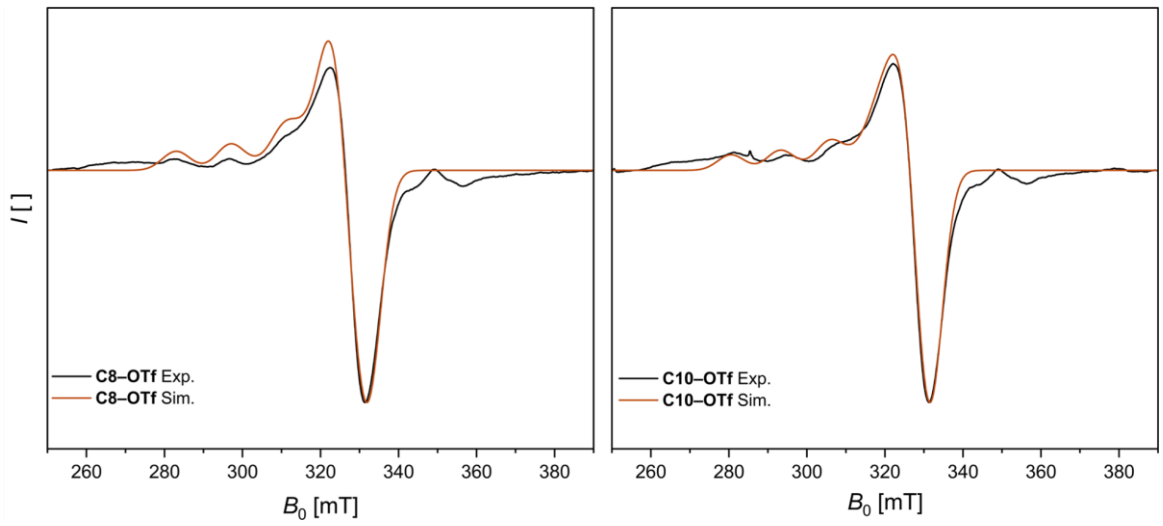

Figure 4.21: Experimental EPR spectrum of $[Cu(TMG2NMe_2qu)_2](OTf)_2$ (**C8−OTf**) and $[Cu(TMG2Phqu)_2](OTf)_2$ (**C10−OTf**) (*c* = 5 mM) in MeCN solution at 77 K (black) and simulated EPR spectrum (red).

Table 4-6: Determined *g* factors and *A* values of the Cu(II) complexes **C8−OTf**, **C10−OTf**, **C12−OTf**, **C14−OTf** and **C16−OTf** for the measurements in MeCN solution at 77 K.

Compound	$\tau_{4,XRD}$	$\tau_{4,DFT}$	$g_{\parallel}$ [ ]	$g_{\perp}$ [ ]	$A_{\parallel}$ [G]	$A_{\perp}$ [G]
$[Cu(TMGqu)_2](OTf)_2$[a] (**C12-OTf**)	0.40	0.43	2.213	2.060	158	10
$[Cu(TMG2NMe_2qu)_2](OTf)_2$ (**C8-OTf**)	0.49	0.51	2.217	2.065	150	8
$[Cu(TMG2Mequ)_2](OTf)_2$[a] (**C14-OTf**)	0.49	0.52	2.214	2.071	138	0
$[Cu(TMG2Phqu)_2](OTf)_2$ (**C10-OTf**)	0.52	0.55	2.249	2.058	138	10
$[Cu(TMG2^cHexqu)_2](OTf)_2$[a] (**C16-OTf**)	0.63	0.65	2.256	2.068	111	19

a: Values taken from [167].

Both the measured spectra and the referential data exhibit axial spectra. The obtained $g_{\parallel}$ and $g_{\perp}$ for **C9–OTf** and **C10–OTf** are very close to the other model systems with values that indicate a tetracoordinate N-donor environment of the central ion.[206] Further, all compounds exhibit the relation $g_{\parallel} > g_{\perp} > 2.0023$ that indicates a localization of the unpaired electron in the $d_{x^2-y^2}$ orbital.[206]

The EPR and τ_4 parameters of the Cu(II) complexes reveal two groups with relatively similar electronic structures, each. Group one encompasses **C8-OTf**, **C12-OTf** and **C14-OTf** and is demarked by a $g_{\parallel}$ of around 2.215 and a $g_{\perp}$ that increases with the $\tau_{4,DFT}$ parameter from 2.060 to 2.071. Likewise, the hyperfine coupling constant $A_{\parallel}$ decreases with a more tetrahedral geometry. The second group consists of **C10-OTf** and **C16-OTf** and is demarcated by a sharply increased $g_{\parallel}$ of around 2.25 and jumps in the trends for $g_{\perp}$ and $A_{\parallel}$. These still follow the same previously established patterns but are offset to the other group. The observed behavior for both groups is expected for tetracoordinate Cu(II) complexes with increasingly tetrahedral characteristics and are therefore generally in line with the obtained XRD and DFT data.[207-208]

A possible reason for the differences of both complex groups could be the cis conformation which could result in marginal electronic changes in the d-orbitals. In support of this hypothesis are the deviating donor properties in the form of low charge transfer energies which have already been observed for $\mathbf{R5_{cis\text{-}1}}$ (Section 4.3.4). These properties could potentially also be discernable via UV/vis spectroscopy.

4.7 UV/vis Spectra of the Redox Pairs R4 and R5

Previous works on $[Cu(GUAqu)_2]^{+/2+}$ systems included rigorous time-dependent density functional theory (TD-DFT) studies of the UV/vis spectra that provide insight into the nature of the observed transitions as well as the electronic structure of the Cu(I) and Cu(II) compounds known to literature.[167, 209-210] They further help to understand the complexes' charge transfer properties that are of potential interest for photophysical or photochemical experiments.[116] These works serve as basis for

further analysis of the bonding and general optical properties of **R4** and **R5** via a combined approach of static UV/vis spectroscopy and simulation of UV/vis spectra via TD-DFT. The spectra were measured in MeCN at ambient conditions.

The Cu(I) spectra of **C7–PF$_6$** and **C9–PF$_6$** show distinct differences from the spectrum of the unsubstituted [Cu(TMGqu)$_2$]PF$_6$ (**C11–PF$_6$**, Figure 4.22, Table 4-7).

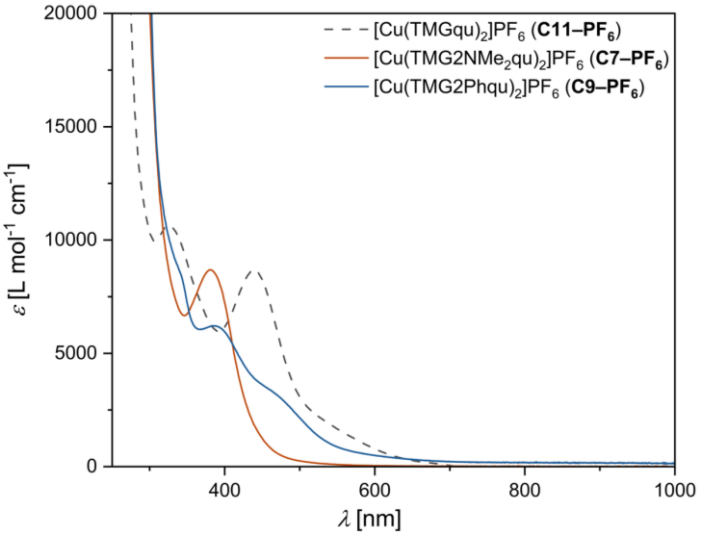

Figure 4.22: UV/vis spectra of **C7–PF$_6$** and **C9–PF$_6$** with that of **C11–PF$_6$** as comparison (c = 1 mM) in MeCN at ambient conditions.[167]

Table 4-7: Wavelengths and extinction coefficients for the absorption bands of **C7–PF$_6$** and **C9–PF$_6$** with that of **C11–PF$_6$** as comparison in MeCN at ambient conditions.

Complex		λ_{max} [nm]	ε_{max} [L mol^{-1} cm^{-1}]
[Cu(TMGqu)$_2$]PF$_6$ (**C11–PF$_6$**)[a]	Band 1:	440	$8.6 \cdot 10^3$
	Band 2:	325	$1.1 \cdot 10^4$
[Cu(TMG2NMe$_2$qu)$_2$]PF$_6$ (**C7–PF$_6$**)	Band 1:	380	$9.3 \cdot 10^3$
[Cu(TMG2Phqu)$_2$]PF$_6$ (**C9–PF$_6$**)	Band 1:	456	$3.5 \cdot 10^3$
	Band 2:	387	$6.2 \cdot 10^3$
	Band 3:	339	$8.7 \cdot 10^3$

a: Data taken from [22].

While **C11–PF$_6$** displays a prominent MLCT band at 440 nm and a band at 325 nm consisting of LCTs and MLCTs,[167] **C7–PF$_6$** only displays one band at 380 nm. Additionally, **C9–PF$_6$** displays two close-lying bands at 456 and 387 nm as well as a third band in the form of a shoulder at 339 nm. These differences to the archetypical [Cu(GUAqu)$_2$]$^+$ model system can be attributed to the electronic influence of both the dimethylamine and the phenyl substituents in the complexes. The blue shift for the band of **C7–PF$_6$** is likely due to an increased HOMO–LUMO gap caused by the electron donating effects of the dimethylamine substituent that elevate the ligands' π^*-orbitals relative to the occupied d-orbitals.[211] The additional band **C9–PF$_6$** exhibits is peculiar as it cannot be found in any other [Cu(GUAqu)$_2$]$^+$ system and could possibly be related to the additional π-system introduced by the phenyl substituent.

The Cu(II) spectra are more similar to **C12–OTf**, displaying one band at around 370-380 m that likely corresponds to an LMCT transition as well as one broad band between around 500-1000 nm that is characteristic for ligand-field (LF) transitions between d-orbitals within the d^9 configured metal center.[167]

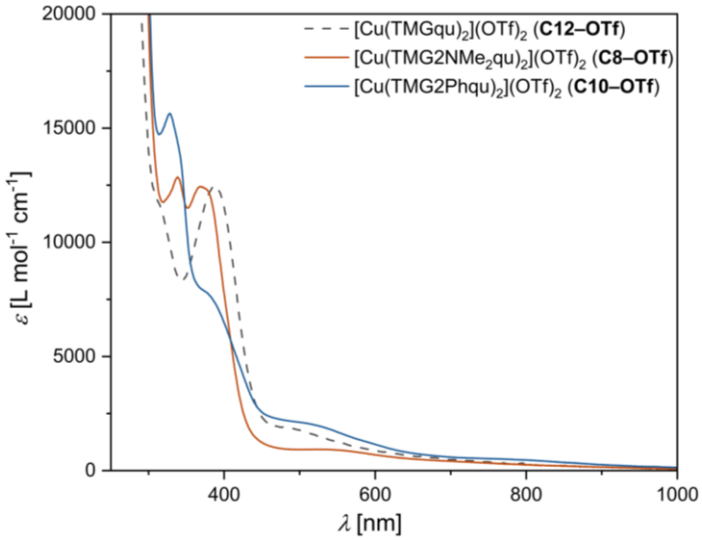

Figure 4.23: UV/vis spectra of **C8–OTf** and **C10–OTf** with that of **C12–OTf** as comparison (*c* = 1 mM) in MeCN at ambient conditions.[167]

Table 4-8: Wavelengths and extinction coefficients of the absorption bands **C8–OTf** and **C10–OTf** with that of **C12–OTf** as comparison in MeCN at ambient conditions.

Complex		λ_{max} [nm]	ε_{max} [L mol^{-1} cm^{-1}]
[Cu(TMGqu)$_2$]OTf (**C12–PF$_6$**)[a]	Band 1:	475-800	>1.9·10^3
	Band 2:	385	1.2·10^4
[Cu(TMG2NMe$_2$qu)$_2$]OTf (**C8–PF$_6$**)	Band 1:	485-1000	>1.0·10^3
	Band 2:	369	1.3·10^4
	Band 3:	339	1.0·10^4
[Cu(TMG2Phqu)$_2$]OTf (**C10–PF$_6$**)	Band 1:	457-1000	>2.4·10^3
	Band 2:	373	7.9·10^3
	Band 3:	328	1.6·10^3

a: Data taken from [167].

To investigate the nature of all observed bands, the complexes' spectra were simulated via TD-DFT using method **M1**, and their natural transition orbitals (NTOs) were visualized. The TD-DFT spectrum of **C7–PF$_6$** exhibits a red-shift of bands that is common for TD-DFT spectra but is in otherwise good agreement with the experimental data (Figure 4.24).[167, 210]

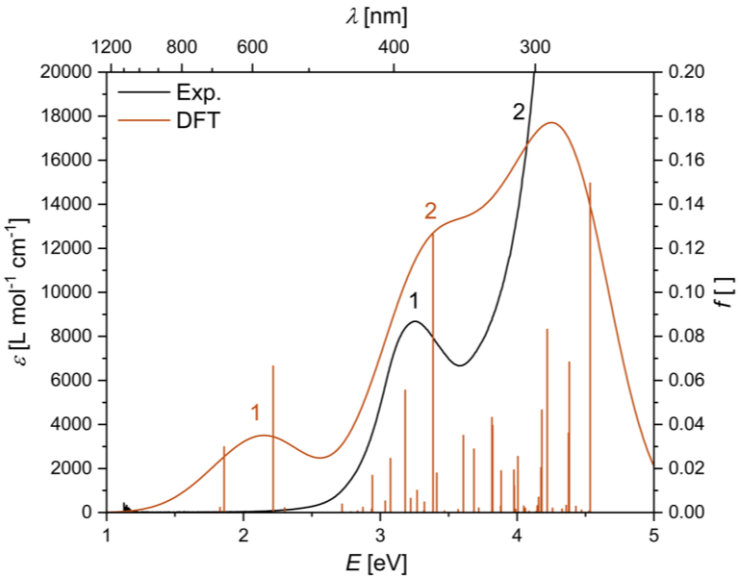

Figure 4.24: Experimental and calculated absorption spectra of $[Cu(TMG2NMe_2qu)_2]^+$ (**C7***) (TPSSh, def2-TZVP, GD3BJ, PCM (MeCN)) (TPSSh-D3BJ/def2-TZVP+ PCM(MeCN) // TPSSh-D3BJ/def2-TZVP + PCM(MeCN)).

The TD-DFT spectrum of **C7*** indicates that the "missing" band of the experimental spectrum is still present but significantly blue-shifted and of significantly increased intensity compared to other $[Cu(GUAqu)_2]^+$ systems.[167] The NTOs of the most prominent transitions show that band 1 likely consists of MLCT transitions (Figure 4.25) while band two consists of a mixture of MLCTs and LCTs (Figure 4.26).

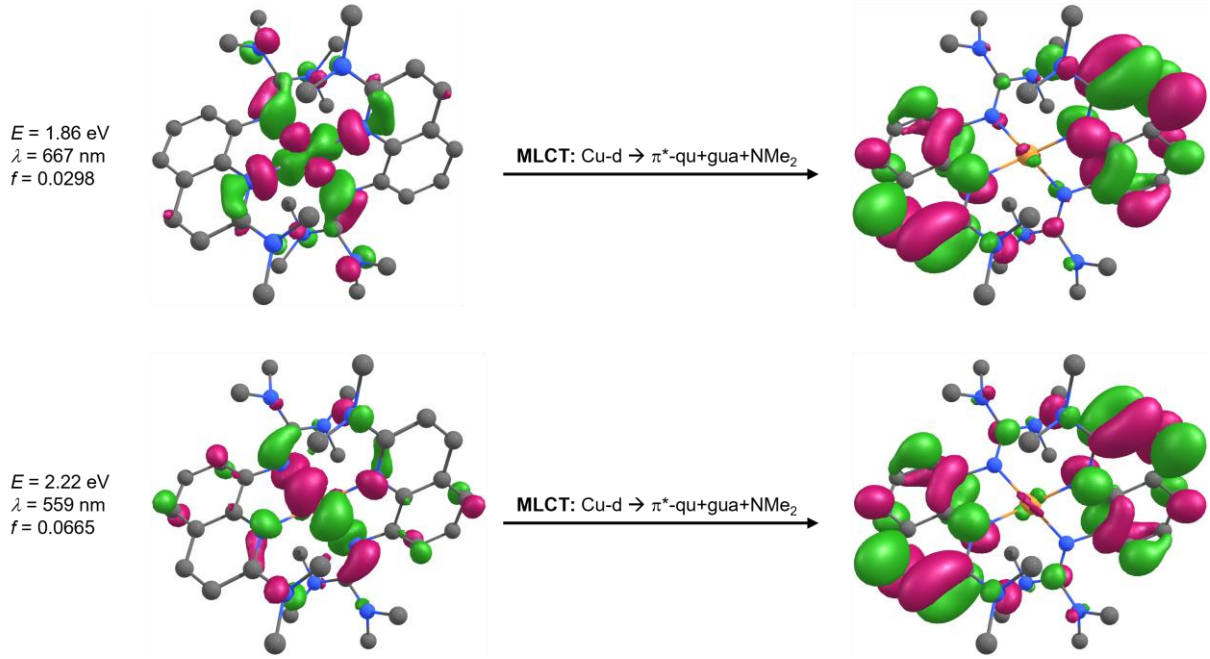

Figure 4.25: NTOs of the dominant transitions of $[Cu(TMG2NMe_2qu)_2]^+$ (**C7***) causing the absorption band at 380 nm (DFT: 613 nm) (TPSSh-D3BJ/def2-TZVP+ PCM(MeCN) // TPSSh-D3BJ/def2-TZVP + PCM(MeCN)).

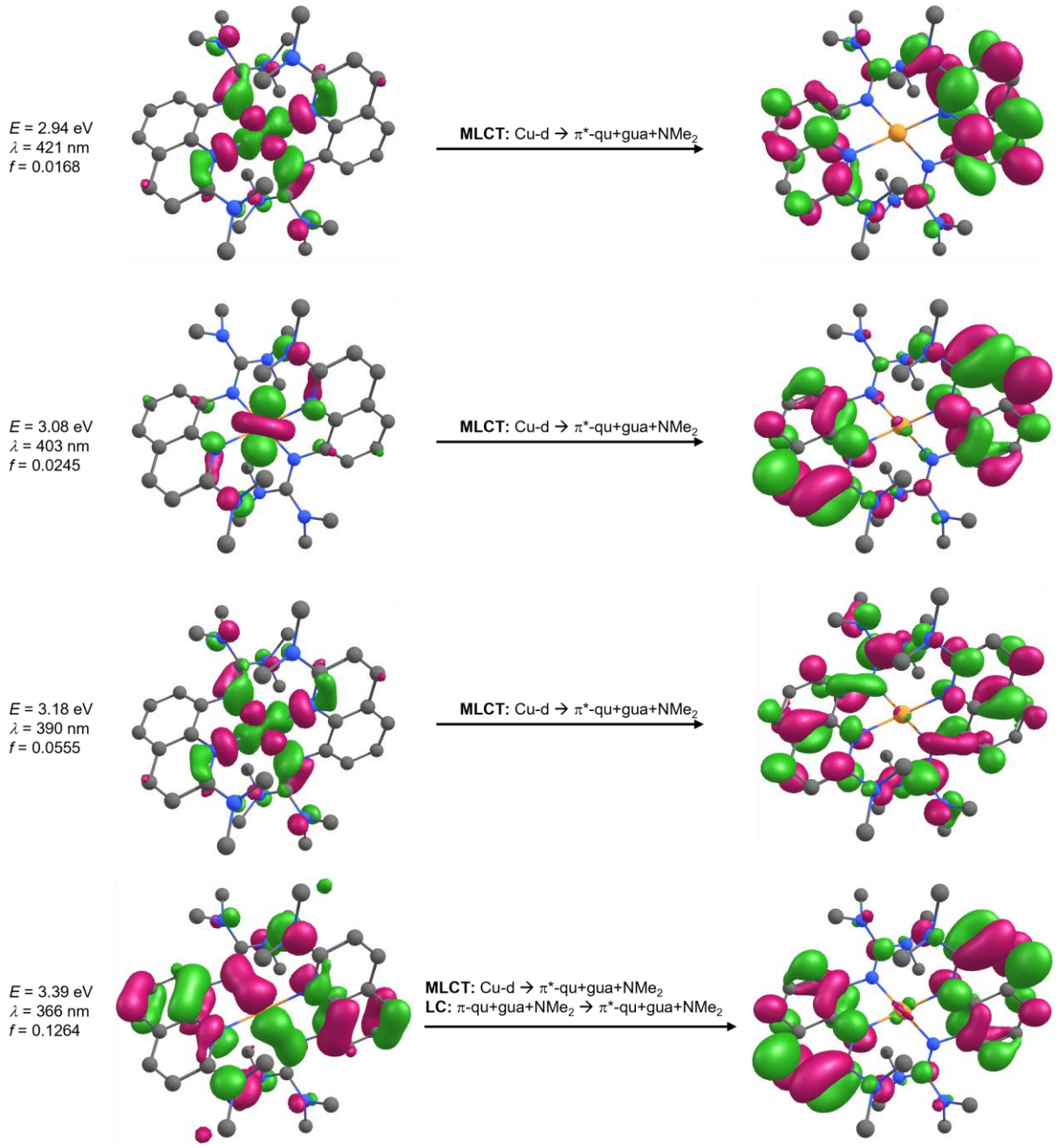

Figure 4.26: NTOs of the dominant transitions of $[Cu(TMG2NMe_2qu)_2]^+$ (**C7***) causing the shoulder at 300 nm (DFT: 366 nm) (TPSSh-D3BJ/def2-TZVP+ PCM(MeCN) // TPSSh-D3BJ/def2-TZVP + PCM(MeCN)).

The spectrum of **C9–PF$_6$** was simulated for both **C9$_{cis\text{-}1}$** and **C9$_{trans\text{-}1}$** (Figure 4.27, 4.28) with the former having the closest resemblance to the experimental spectrum as it also features the observed three bands instead of two. This is in general agreement with the conformational analysis and the CV data, further supporting **C9$_{cis\text{-}1}$** as the active species in solution.

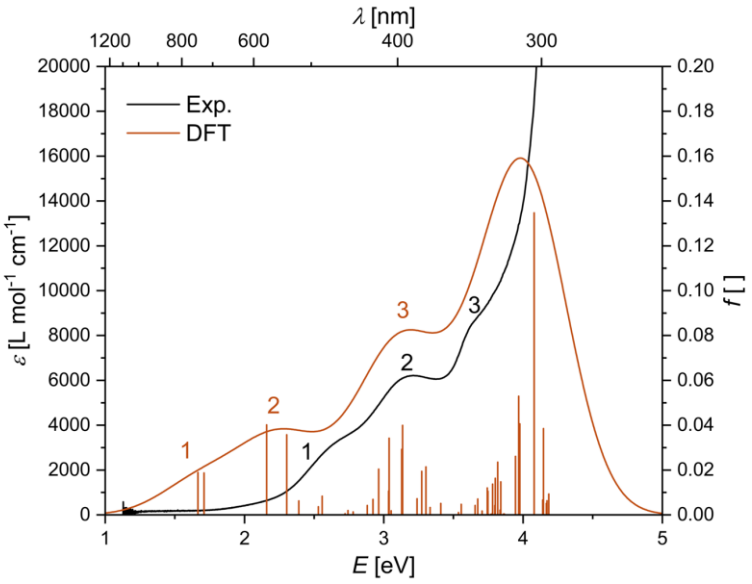

Figure 4.27: Experimental and calculated absorption spectra of the cis-1 conformer of $[Cu(TMG2Phqu)_2]^+$ (**C9$_{cis-1}$**) (TPSSh, def2-TZVP, GD3BJ, PCM (MeCN)) (TPSSh-D3BJ/def2-TZVP+ PCM(MeCN) // TPSSh-D3BJ/def2-TZVP + PCM(MeCN)).

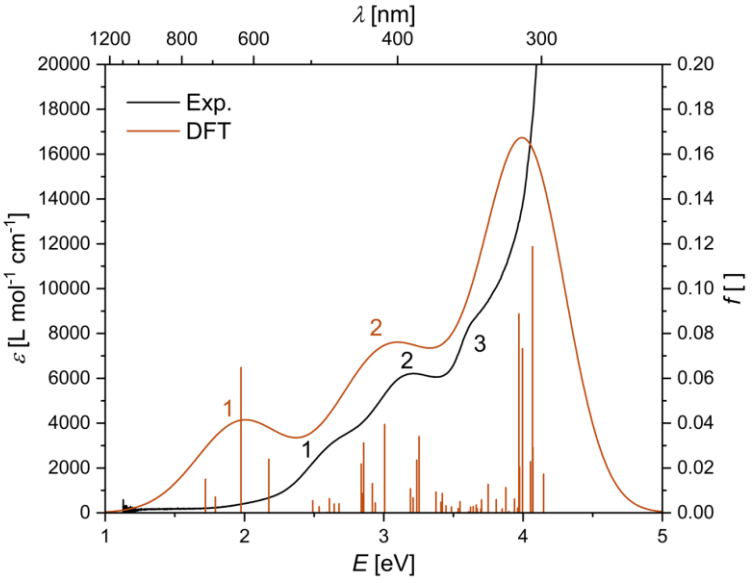

Figure 4.28: Experimental and calculated absorption spectra of the trans-1 conformer of $[Cu(TMG2Phqu)_2]^+$ (**C9$_{trans-1}$**) (TPSSh, def2-TZVP, GD3BJ, PCM (MeCN)) (TPSSh-D3BJ/def2-TZVP+ PCM(MeCN) // TPSSh-D3BJ/def2-TZVP + PCM(MeCN)).

Given the overall evidence in support of **C9$_{cis-1}$** as the active species in solution, only its TD-DFT data will be discussed in the following. The NTOs show that band 1 and 2 both likely consist of MLCT transitions from different d-Orbitals towards π* orbitals of the ligands that show clear participation of the phenyl-substituent as well as a binding π Ph–Qu component (Figure 4.29, 4.30).

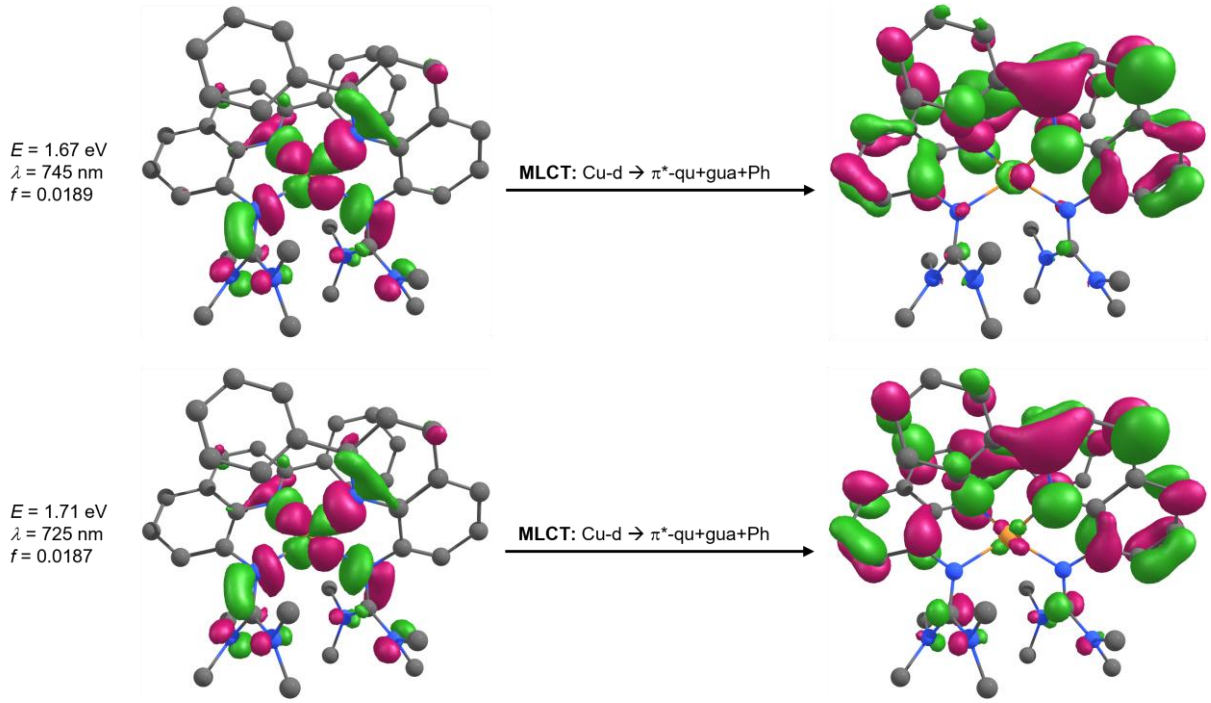

Figure 4.29: NTOs of the dominant transitions of the cis-1 conformer of $[Cu(TMG2Phqu)_2]^+$ ($\mathbf{C9_{cis\text{-}1}}$) causing the band at 456 nm (DFT: 730 nm) (TPSSh-D3BJ/def2-TZVP+ PCM(MeCN) // TPSSh-D3BJ/def2-TZVP + PCM(MeCN)).

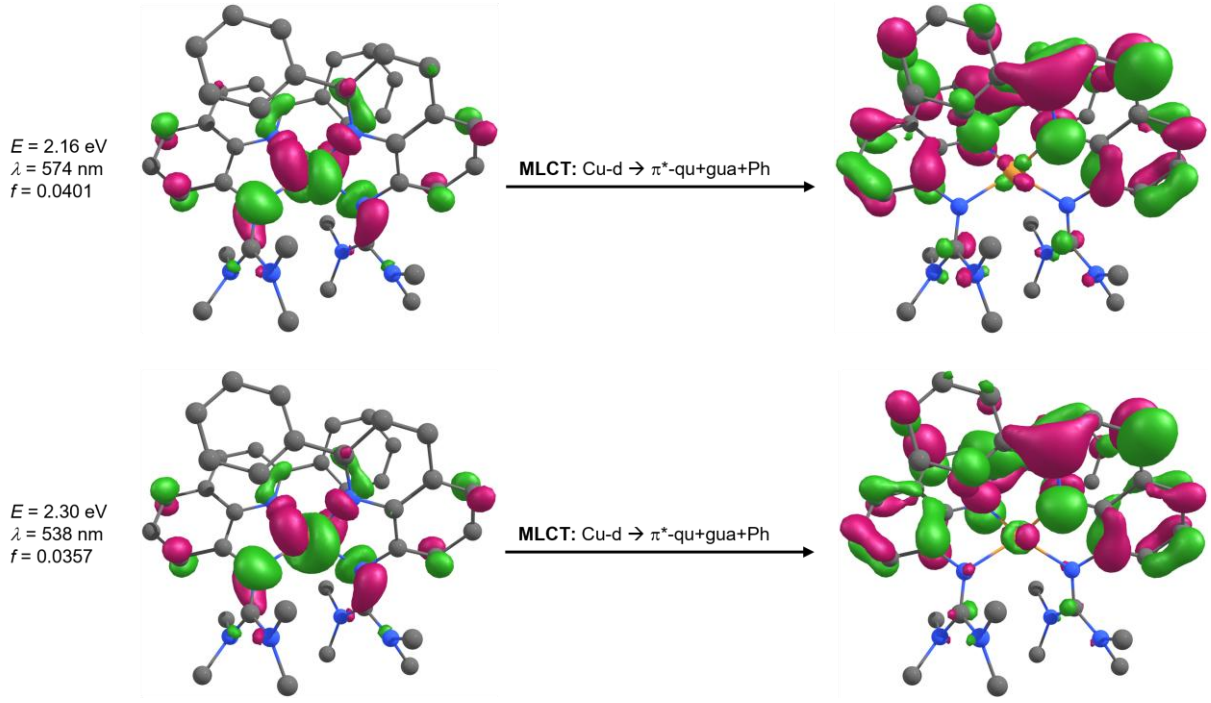

Figure 4.30: NTOs of the dominant transitions of the cis-1 conformer of $[Cu(TMG2Phqu)_2]^+$ ($\mathbf{C9_{cis\text{-}1}}$) causing the band at 387 nm (DFT: 556 nm) (TPSSh-D3BJ/def2-TZVP+ PCM(MeCN) // TPSSh-D3BJ/def2-TZVP + PCM(MeCN)).

Band 3 consists of a mixture of MLCT and LCT transitions which is similar to band 2 in **C7***, albeit the amount of LCTs is higher in comparison (Figure 4.31). Given that the simulated spectrum of $\mathbf{C9_{trans\text{-}1}}$ does not exhibit the three relatively distinct bands, the specific absorption spectrum of $\mathbf{C9–PF_6}$ is possibly caused by certain changes in the

electronic structure imposed by the cis configuration. This is further corroborated by the deviating charge-transfer energies for **C9$_{cis-1}$** and **C10$_{cis-1}$** discussed in Section 4.3.4 as well as the peculiarities in the EPR spectrum of **C10$_{cis-1}$** in Section 4.5.

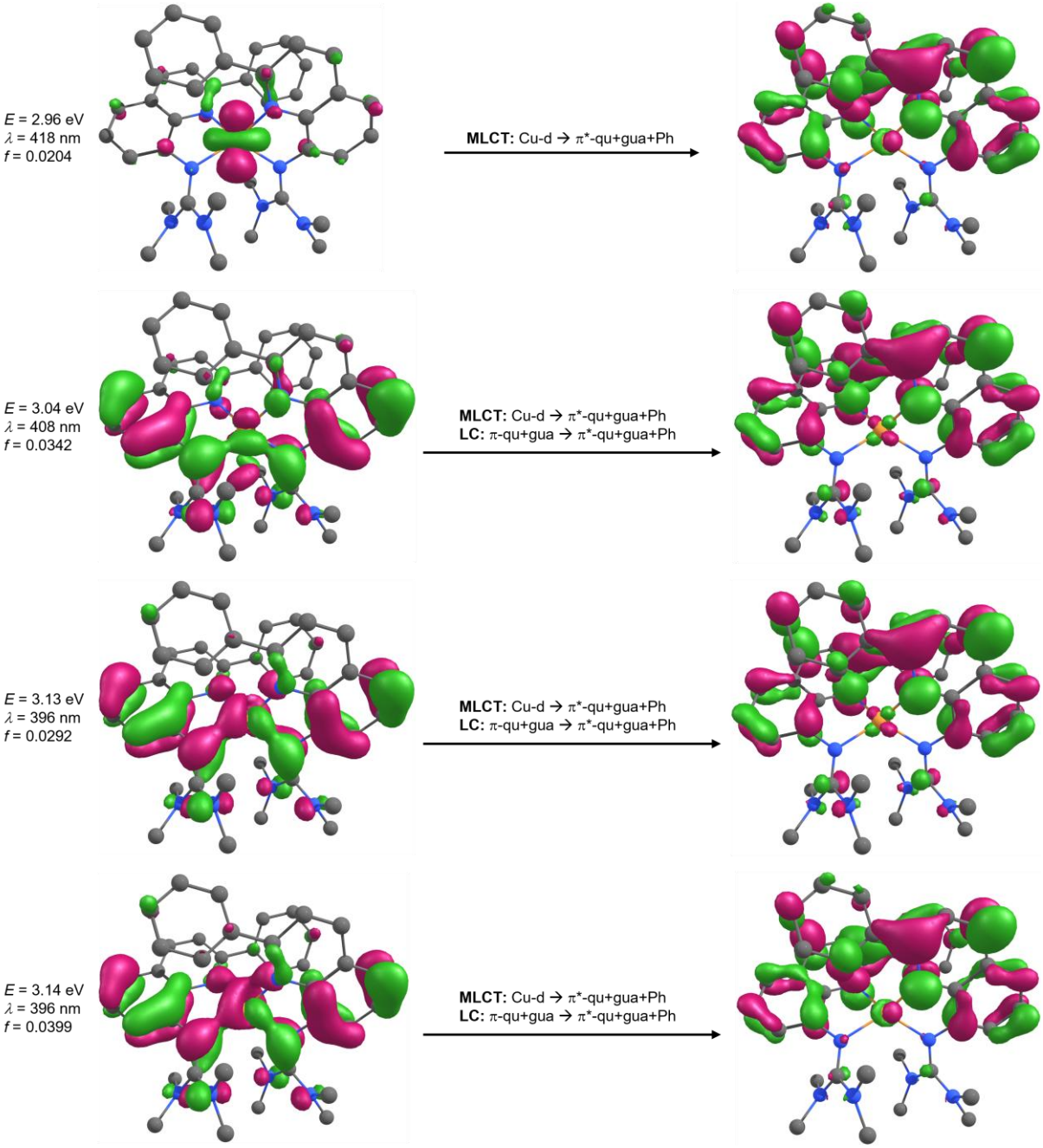

Figure 4.31: NTOs of the dominant transitions of the cis-1 conformer of $[Cu(TMG2Phqu)_2]^+$ (**C9$_{cis-1}$**) causing the band at 339 nm (DFT: 400 nm) (TPSSh-D3BJ/def2-TZVP+ PCM(MeCN) // TPSSh-D3BJ/def2-TZVP + PCM(MeCN)).

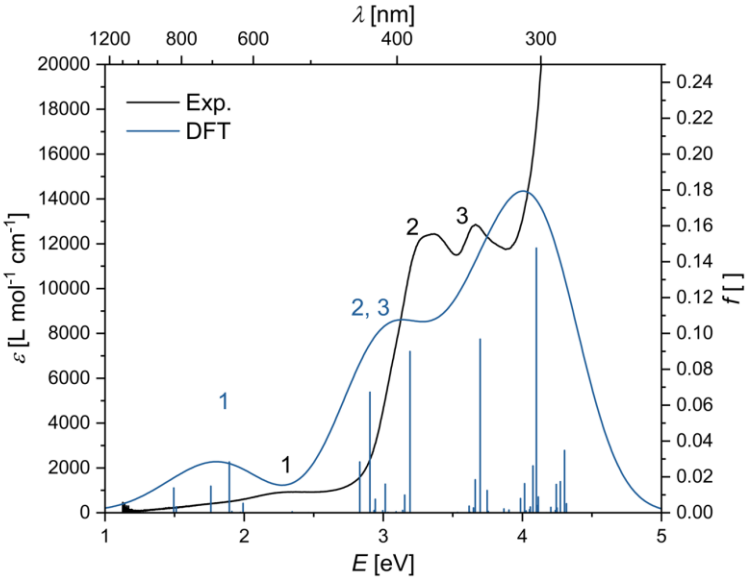

Figure 4.32: Experimental and calculated absorption spectra of $[Cu(TMG2NMe_2qu)_2]^{2+}$ (**C8**) (TPSSh, def2-TZVP, GD3BJ, PCM (MeCN)) (TPSSh-D3BJ/def2-TZVP+ PCM(MeCN) // TPSSh-D3BJ/def2-TZVP + PCM(MeCN)).

The TD-DFT spectrum of **C8–OTf** also gives blue shifted bands but is otherwise in accordance with the experimental data (Figure 4.32). However, it does not exhibit the distinct, sharp band observed at 339 nm, which might be caused by the line-broadening algorithm.

The NTO analysis of **C8** supports the EPR measurements, indicating that the absorption band at 485 nm is due to LF transitions from lower lying d-orbitals into the energetically elevated $d_{x^2-y^2}$ orbital, mixed with a small amount of LMCT contributions (Figure 4.33). Band 2 and 3, on the other hand, are mostly composed of LC and LMCT transitions, although the former dominate, which is typical for Cu(II) complexes of GUAqu ligands (Figure 4.34). While the experimental band 3 cannot be identified, it can be assumed to be the transition at 388 nm (3.19 eV), an LCT band, due to the relative distance to other transitions and the intensity.

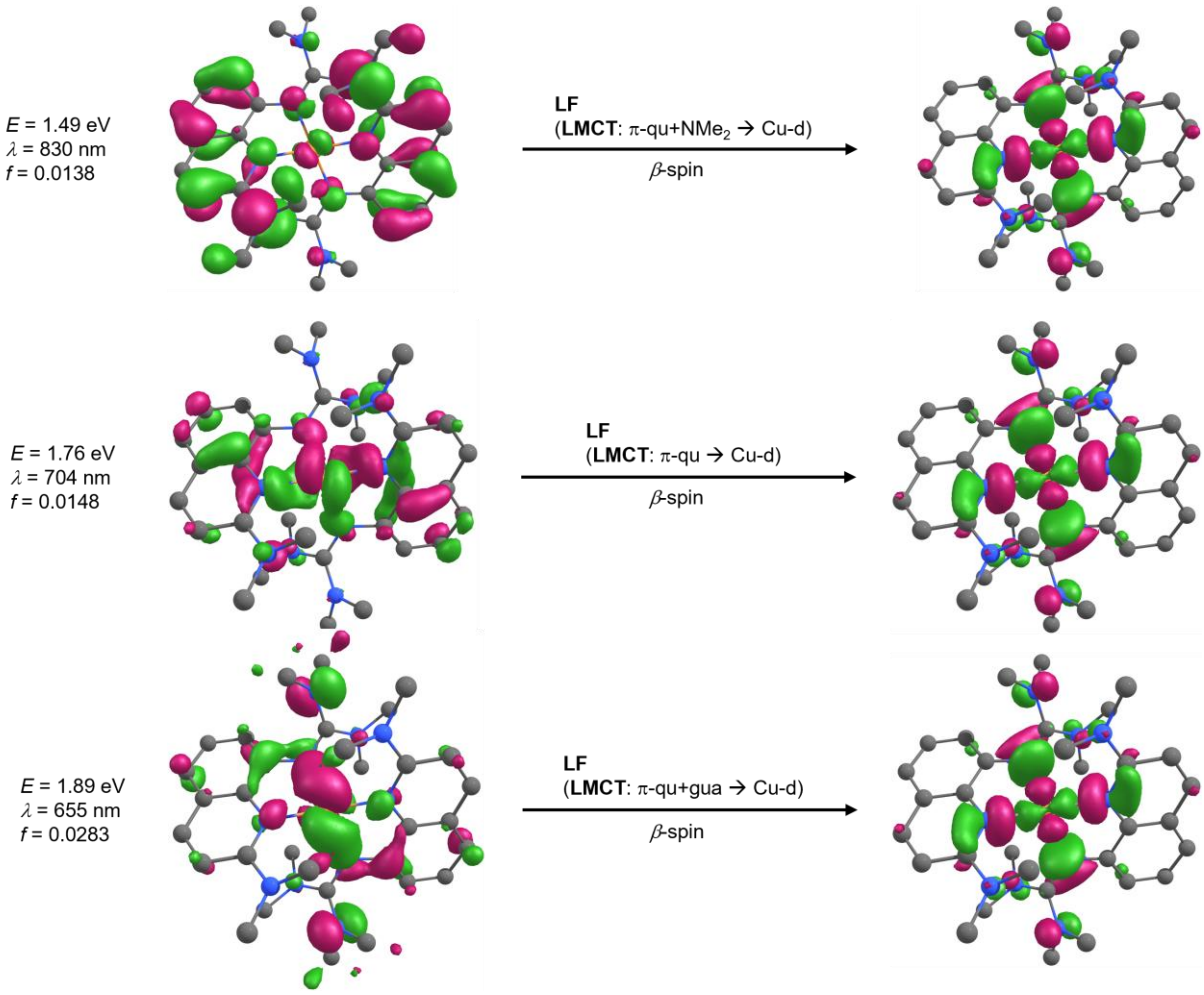

Figure 4.33: NTOs of the dominant transitions of $[Cu(TMG2NMe_2qu)_2]^{2+}$ (**C8**) causing the absorption band at 485 nm (DFT: 700 nm) (TPSSh-D3BJ/def2-TZVP+ PCM(MeCN) // TPSSh-D3BJ/def2-TZVP + PCM(MeCN)).

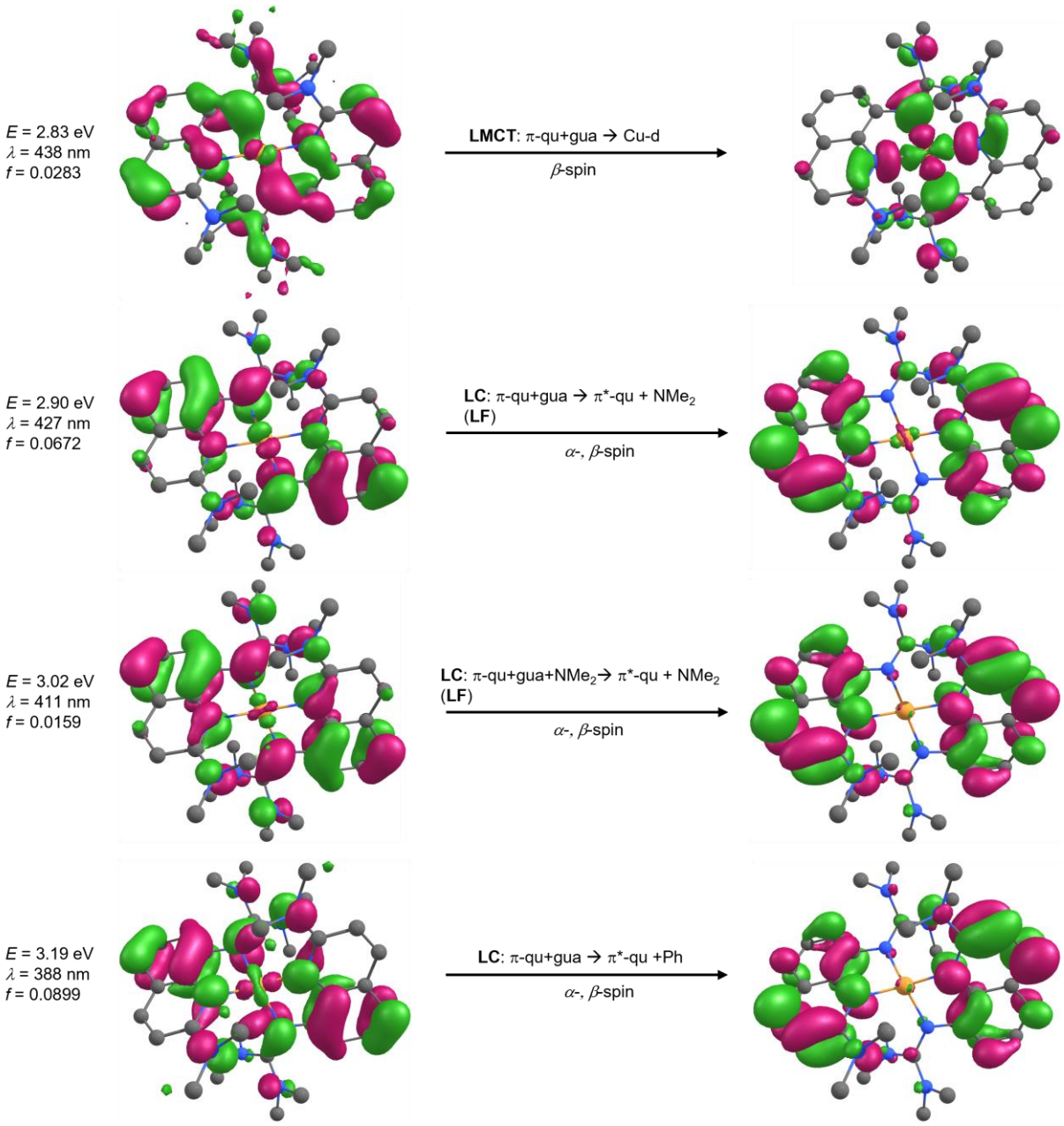

Figure 4.34: NTOs of the dominant transitions of $[Cu(TMG2NMe_2qu)_2]^{2+}$ (**C8**) causing the absorption band at 396 nm (DFT: 410 nm) (TPSSh-D3BJ/def2-TZVP+ PCM(MeCN) // TPSSh-D3BJ/def2-TZVP + PCM(MeCN)).

For **C10**, the simulated spectrum is also in general agreement with the experimental data yet also lacks the distinct band 3 (Figure 4.35).

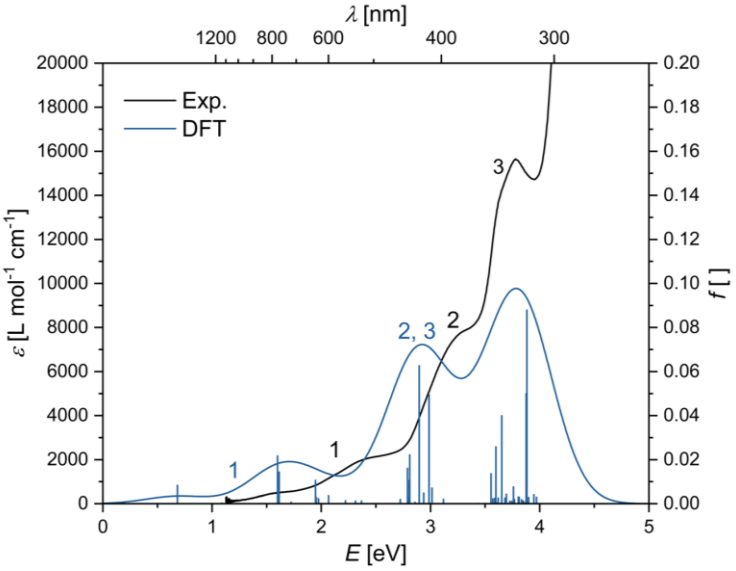

Figure 4.35: Experimental and calculated absorption spectra of the cis-1 conformer of $[Cu(TMG2Phqu)_2]^{2+}$ (**C10**$_{cis\text{-}1}$) (TPSSh, def2-TZVP, GD3BJ, PCM (MeCN)) (TPSSh-D3BJ/def2-TZVP+ PCM(MeCN) // TPSSh-D3BJ/def2-TZVP + PCM(MeCN)).

The obtained NTOs of band 1 are in agreement with the obtained EPR measurements, showing $d_{x^2-y^2}$ to be the orbital holding the unpaired electron (see Figure 4.36). The remaining band yields similar natural transition orbitals to **C8** and can therefore be viewed in the appendix (Section 9.13). The low intensity and visibility of the low-energy d-d bands in the experimental spectra and the unreliable energies of the TD-DFT spectra prohibit further analysis of the differences in electronic states observed for **C10–OTf** in the EPR. However, it can be said that the experimental Cu(II) spectra show less deviations from $[Cu(TMGqu)_2]^{2+}$ than the Cu(I) complexes to their Cu(I) archetype, which is overall supported by the obtained TD-DFT spectra and NTOs that show little differentiation of the novel complexes to their predecessors.[167, 209-210]

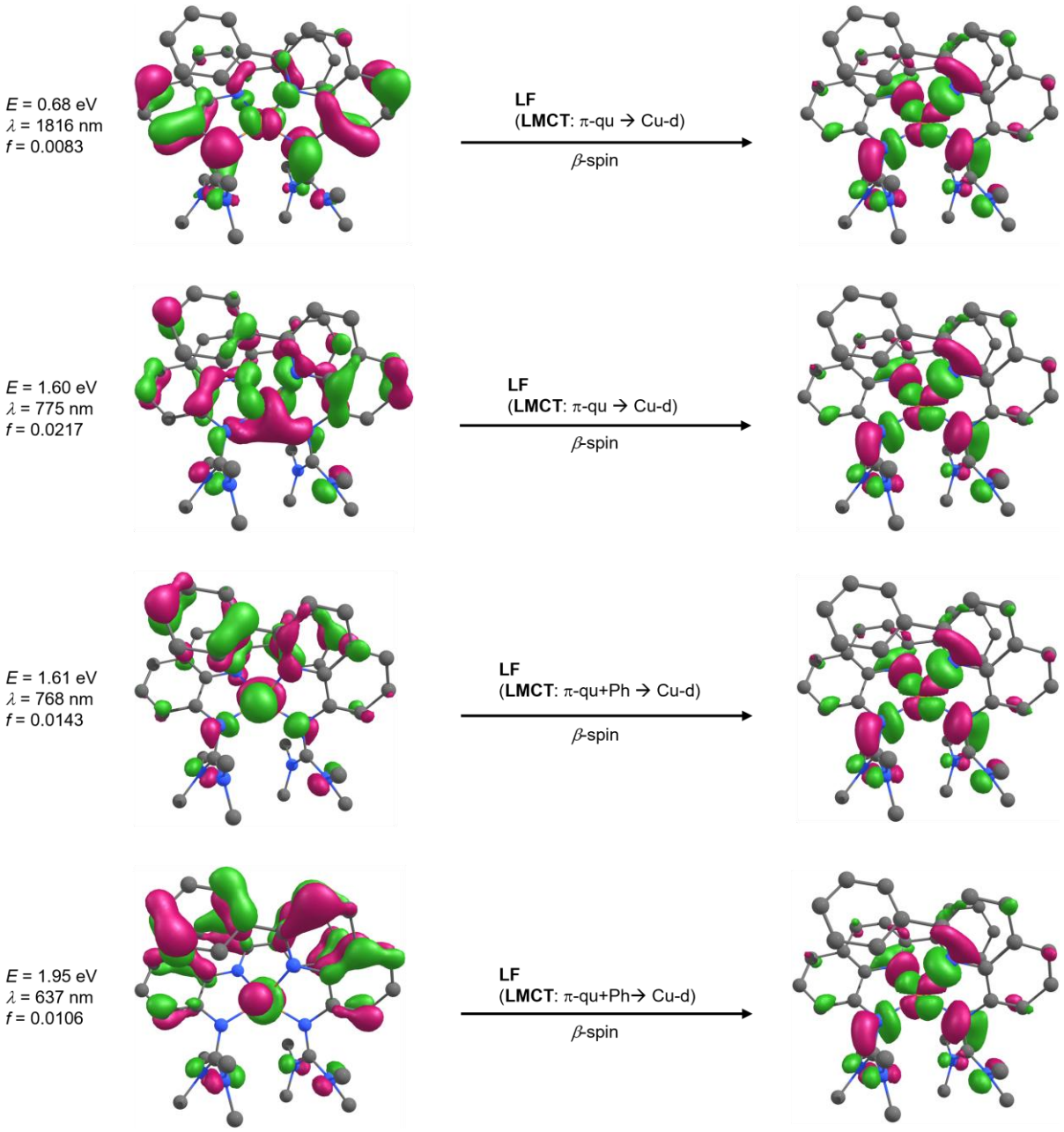

Figure 4.36: NTOs of the dominant transitions of the cis-1 conformer of $[Cu(TMG2Phqu)_2]^{2+}$ (**C10$_{cis-1}$**) causing the absorption band at 457 nm (DFT: 775 nm) (TPSSh-D3BJ/def2-TZVP+ PCM(MeCN) // TPSSh-D3BJ/def2-TZVP + PCM(MeCN)).

4.8 Determination of Electron Self-Exchange Rates

The electron self-exchange rates were obtained in the same fashion as for the tripodal model systems by employing stopped-flow UV/vis spectroscopy to determine the k_{12} of a given cross reaction that was then fed into the Marcus cross-relation (Eqn. 25) to return the desired k_{11} of the self-exchange reaction (Scheme 4.8).

$$[Cu(I)(GUAqu)_2]^+ + [Cu(II)(GUAqu)_2]^{2+} \overset{k_{12}}{\rightleftharpoons} [Cu(II)(GUAqu)_2]^{2+} + [Cu(I)(GUAqu)_2]^+$$

Scheme 4.8: Self-exchange reaction of a $[Cu(GUAqu)_2]^{+/2+}$ redox couple.

The electron self-exchange rates of the redox couples $[Cu(TMG2NMe_2qu)_2]^{+/2+}$ (**R4**) and $[Cu(TMG2Phqu)_2]^{+/2+}$ (**R5**) were determined starting from the corresponding Cu(I) salt with the counter complex $[Co(bpy)_3](PF_6)_3$ (Scheme 4.9).

$$[Cu(I)(GUAqu)_2]^+ + [Co(III)(bpy)_3]^{3+} \overset{k_{12}}{\rightleftharpoons} [Cu(II)(GUAqu)_2]^{2+} + [Co(II)(bpy)_3]^{2+}$$

Scheme 4.9: Cross reaction between a $[Cu(GUAqu)_2]^+$ complex cation and the $[Co(bpy)_3](PF_6)_3$ counter complex cation.

The k_{22}, $E_{1/2}$ and radius of $[Co(bpy)_3](PF_6)_3$ were employed as used for the tripodal model systems (Section 3.4.5). Additionally, the k_{11} of **R5** was not only determined starting from the Cu(I), but from the Cu(II) salt as well. This was done to rule out any adverse effects from possible conformation changes preceding the electron transfer step on the reaction rate constant, since **C10–OTf** does not exhibit a broad conformational distribution unlike **C9–PF$_6$**. A suitable counter complex for the according cross reaction must be able to reduce **C10–OTf** and should not interfere too strongly with the complex cation's UV/vis absorption. Both requirements are fulfilled by **C7–PF$_6$**, which was therefore chosen as counter complex yielding the below depicted cross reaction (Scheme 4.10).

$$[Cu(II)(TMG2Phqu)_2]^{2+} + [Cu(I)(TMG2NMe_2qu)_2]^+$$

$$\Big\Vert \; k_{12}$$

$$[Cu(I)(TMG2Phqu)_2]^+ + [Cu(II)(TMG2NMe_2qu)_2]^{2+}$$

Scheme 4.10: Cross reaction for the reduction of $[Cu(TMG2Phqu)_2]^{2+}$ (**C10**) using $[Cu(TMG2NMe_2qu)]PF_6$ (**C7–PF$_6$**) as counter complex.

To account for the different charges and radii of the "reductive" cross reaction compared to the usual oxidation reactions, the electrostatic terms w_{ij} (Eqn. 35) that influence the correction term f_{ij} and the work term W_{ij} in the Marcus cross relation (Equations 13 to 15) were changed accordingly (Table 4-9, all parameters listed in Section 7.3.11.2 in the experimental section).

$$w_{ij} = \frac{Z_i \cdot Z_j \cdot e^2 \cdot N_A}{\varepsilon \cdot (a_i + a_j) \cdot (1 + \beta \cdot (a_i + a_j) \cdot \sqrt{\mu})} \tag{35}$$

$$k_{12} = \sqrt{k_{11} \cdot k_{22} \cdot K_{12} \cdot f_{12}} \cdot W_{12} \tag{13}$$

$$f_{12} = \exp\left(\frac{\left(\ln\left(K_{12} + \frac{w_{12} - w_{21}}{R \cdot T}\right)\right)^2}{4 \cdot \left(\ln\left(\frac{k_{11} \cdot k_{22}}{Z_{11} \cdot Z_{22}}\right) + \frac{w_{11} + w_{22}}{R \cdot T}\right)} \right) \tag{14}$$

$$W_{12} = \exp\left(\frac{w_{11} + w_{22} - w_{12} - w_{21}}{2 \cdot R \cdot T}\right) \tag{15}$$

Table 4-9: Used Radii and w_{ij} parameters for determining the electron self-exchange rate using the Marcus cross relation.

Starting Complex (C)	**C7–PF_6**	**C9–PF_6**	**C10–OTf**
Counter complex (CC)	$[Co(bpy)_3]^{3+}$	$[Co(bpy)_3]^{3+}$	$[Cu(TMG2NMe_2qu)_2]^+$
r (C) [nm]	0.58	0.62	0.62
r (CC) [nm]	0.70	0.70	0.58
w_{11} [J mol^{-1}]	$6.63 \cdot 10^3$	$6.25 \cdot 10^3$	$6.25 \cdot 10^3$
w_{12} [J mol^{-1}]	$9.03 \cdot 10^3$	$8.79 \cdot 10^3$	$6.43 \cdot 10^3$
w_{21} [J mol^{-1}]	$1.20 \cdot 10^4$	$1.17 \cdot 10^4$	$6.43 \cdot 10^3$
w_{22} [J mol^{-1}]	$1.65 \cdot 10^4$	$1.65 \cdot 10^4$	$6.63 \cdot 10^3$

As before, the cross reaction rates k_{12} were determined via stopped-flow UV/vis spectroscopy in acetonitrile at 298 K for different counter complex concentrations. The reactions were performed under pseudo-first order conditions, with the counter complex concentration in excess. All reactions were carried out in duplicates. The change in absorption bands was plotted against time and fitted with a first-order decay function, and the observed reaction rates were plotted against the counter complex concentration so that k_{12} was obtained as the slope of the linear regression from the resulting plot (shown exemplary for **C7–PF_6** in Figure 4.37, see Section 9.2.2 for remaining plots).

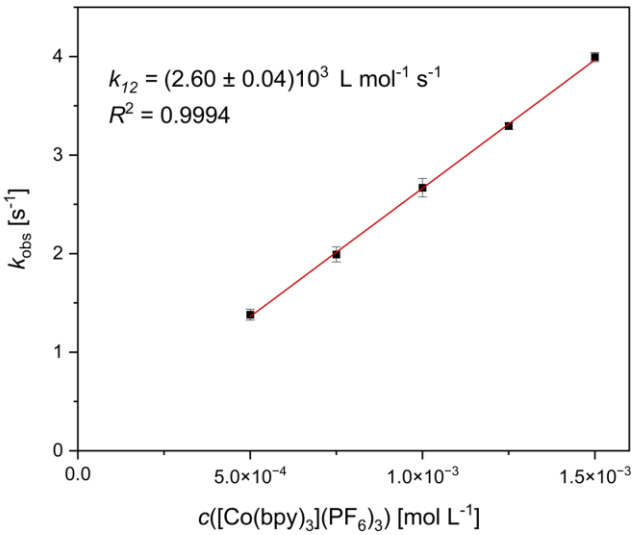

Figure 4.37: Plot of the reaction rates k_{obs} against the concentration of $[Co(bpy)_3]^{3+}$ for **R4**.

The self-exchange rates obtained via the Marcus cross relation are listed in Table 4-10.

Table 4-10: Employed counter complex, differences between the redox potentials of the starting compound and the counter complex $\Delta E_{1/2}$, equilibrium constants K_{12}, reaction rates k_{12} and self-exchange rates k_{11} of the given starting compound.

Starting compound (redox couple)	Counter complex	$\Delta E_{1/2}$ [V]	K_{12} [ ]	k_{12} [M^{-1} s^{-1}]	k_{11} [M^{-1} s^{-1}]
C7–PF$_6$ (**R4**)	[Co(bpy)$_3$](PF$_6$)$_3$	0.279	$4.88 \cdot 10^6$	$(2.60 \pm 0.04) \cdot 10^3$	$(1.64 \pm 0.05) \cdot 10^2$
C9–PF$_6$ (**R5**)	[Co(bpy)$_3$](PF$_6$)$_3$	0.183	$1.23 \cdot 10^3$	$(1.31 \pm 0.07) \cdot 10^4$	$(1.15 \pm 0.12) \cdot 10^5$
C10–OTf (**R5**)	**C7–PF$_6$**	0.115	$8.79 \cdot 10^1$	$(4.29 \pm 0.24) \cdot 10^4$	$(1.51 \pm 0.17) \cdot 10^5$

It can be seen that both redox couples have k_{11} that are three orders of magnitude apart, with **R4** on the lower end. Conversely, **R5** displays large k_{11} for both starting directions on the order of 10^5 M^{-1} s^{-1}, with the k_{11} of the cross reaction starting from **C10–OTf** being the larger of the two. Given variations in unaccounted for parameters that arise from swapping the counter complex (e.g. the outer-sphere formation constant, differences in ionic strength or potential changes in the transmission coefficient κ), the minor differences in k_{11} cannot be clearly associated with potential conformational effects. Therefore, only the limited conclusion can be drawn that the obtained k_{11} for **R5** indicate no significant kinetic hurdles that could impede the oxidation reaction of the Cu(I) complex and that both directions are likely to follow a unitary pathway. This is in agreement with the results from the cyclic voltammetry measurements, and, combined with the additional data from UV/vis, DFT and TD-DFT, points towards the cis-1 conformer likely being the active species for both oxidation states.

Comparing the obtained k_{11} and τ_4 parameters of the herein reported redox couples **R4** and **R5** to those of the other 2-substituted $[Cu(GUAqu)_2]^{+/2+}$ model systems (Table 4-11), the novel redox couples occupy the lower and higher end of the table, respectively.

Table 4-11: Electron self-exchange rates k_{11} and calculated $\varnothing\tau_{4,DFT}$ and $\Delta\tau_{4,DFT}$ parameters and $RMSD_{DFT}$ values of **R4*** to **R8** (TPSSh-D3BJ/def2-TZVP+ PCM(MeCN) // TPSSh-D3BJ/def2-TZVP + PCM(MeCN)).

Redox couple	k_{11} [M^{-1} s^{-1}]	$\Delta\tau_{4,DFT}$ [ ]	$\varnothing\tau_{4,DFT}$ [ ]	$RMSD_{DFT}$ [Å]
$[Cu(TMG2NMe_2qu)_2]^{+/2+}$ (**R4***)	$(1.64 \pm 0.05)\cdot10^2$	0.07	0.54	0.136
$[Cu(TMGqu)_2]^{+/2+,a}$ (**R6**)	$(2.81 \pm 0.18)\cdot10^2$	0.20	0.53	0.283
$[Cu(TMG2Mequ)_2]^{+/2+,a}$ (**R7**)	$(2.19 \pm 0.44)\cdot10^3$	0.13	0.59	0.191
$[Cu(TMG2^cHexqu)_2]^{+/2+,a}$ (**R8**)	$(1.15 \pm 0.15)\cdot10^3$	0.07	0.68	0.147
$[Cu(TMG2Phqu)_2]^{+/2+}$ (**$R5_{cis-1}$**)	$(1.15 \pm 0.12)\cdot10^5$, $(1.51 \pm 0.17)\cdot10^5$	0.05	0.58	0.320

a: Data taken from [22]. *: The Cu–N bonds were frozen for optimization (see Section 4.4.1).

The redox pair **R5** is therefore the $[Cu(GUAqu)_2]^{+/2+}$ model system with the highest k_{11} on record.[22, 77, 84-86] For **R5**, assuming the cis-1 conformer for both oxidation states, the increased k_{11} is in accordance with the mutual decrease in $\Delta\tau_4$ and $\varnothing\tau_4$ that likewise indicate a reduced reorganization energy. The k_{11} values of **R5** are not only the highest for the $[Cu(GUAqu)_2]^{+/2+}$ model systems but also in the range of the fastest reported model systems in general (Figure 4.38). While there are numerous model systems with a self-exchange rate of 10^5 M^{-1} s^{-1}, the k_{11} of **R5** is only surpassed in order of magnitude by two systems: the coordination-variant, mixed donor system $[CuCl(dpa^{SMe})]^{0/+}$ reported by Olshansky *et al*. and the N-donor system $[Cu(L7)_2]^{+/2+}$ from Himmel *et al*.[16, 63] The latter achieves this rate explicitly not due to an entatic or ecstatic state but because of strong electromerism induced by the bisguanidine ligands. **R5** is therefore among the fastest reported electron transfer systems and one of the fastest pure N-donor systems, which is likely a result of the redox couple's minute changes in geometry.

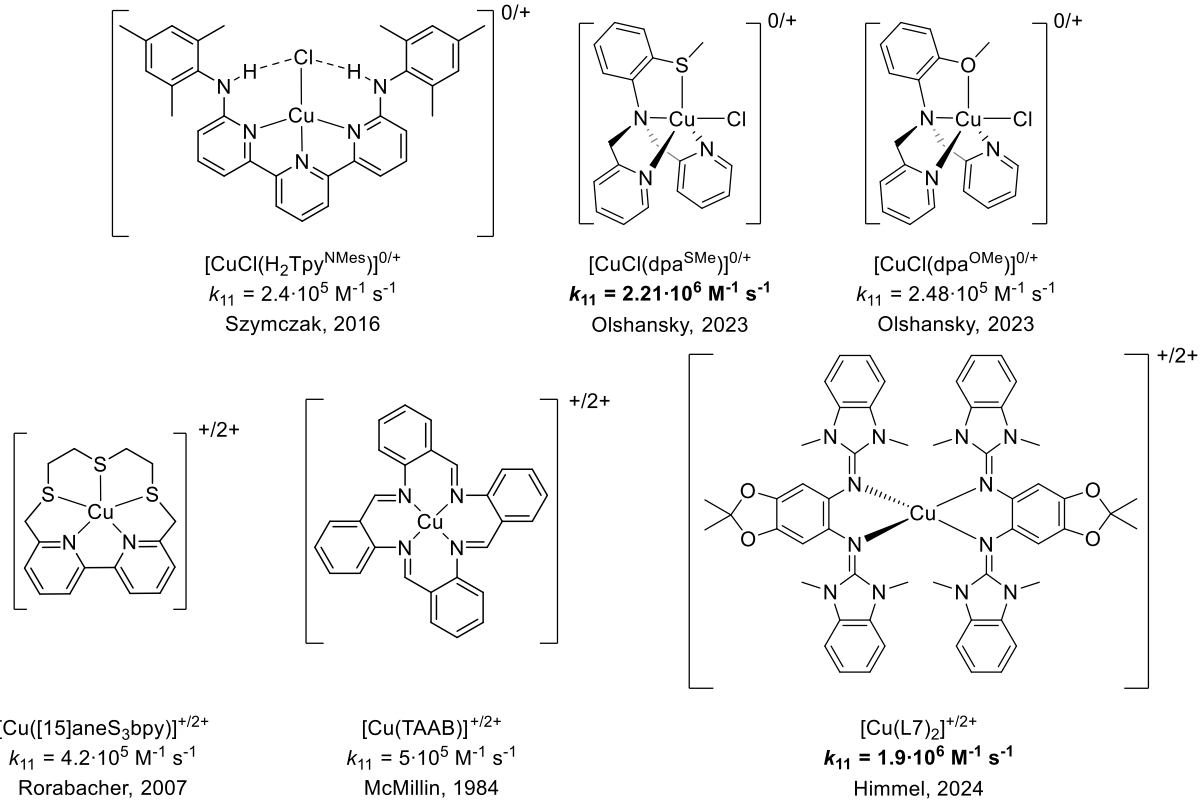

Figure 4.38: Lewis structures and k_{11} of prominent electron transfer model systems with self-exchange rates of 10^5 M^{-1} s^{-1} or above.[22, 77, 84-86]

Contrary to this is the small k_{11} of $[Cu(TMG2NMe_2qu)_2]^{+/2+}$ (**R4**) that contrasts with its ideal structural parameters. The redox couple exhibits strong structural accordance between both oxidation states, even the smallest $RMSD_{DFT}$ value of all listed $[Cu(GUAqu)_2]^{+/2+}$ redox couples. It would therefore be expected to exhibit a k_{11} at least one order of magnitude above the observed rate constant. This discrepancy implies that the employed structural parameters do not necessarily capture all structural changes of importance for this redox couple. To further investigate this, the reorganization energies of **R4** and **R5** were calculated in order to aim for a more holistic structural description.

4.8.1 Calculation of Inner and Outer Reorganization Energies of the Novel Model Systems

The reorganization energies were obtained as detailed in Section 3.6.1, using Nelsen's four-point method and method **M1** for the inner reorganization energies, and the continuum method for the outer reorganization energies (Table 4-12). To control for potential effects of the bond length contraction observed for **R4**, the reorganization energies were also calculated for the Cu(I) geometry optimized without restrictions (**R4$_{relaxed}$**, Section 4.3.2, Table 4-2). For **R5**, the two most important conformers, cis-1 and trans-1, were investigated to see whether the conformation affects the obtained reorganization energies. The inclusion of the trans-1 redox couple is only hypothetical,

as a potential corresponding redox wave has not been observed, possibly due the energetically unfavorable Cu(II) state.

Table 4-12: Total, inner and outer reorganization energies and selected structural parameters of the redox couples **R4***, **R4$_{relaxed}$**, **R5$_{cis-1}$**, **R5$_{trans-1}$** (TPSSh-D3BJ/def2-TZVP+ PCM(MeCN) // TPSSh-D3BJ/def2-TZVP + PCM(MeCN)).

Redox couple	$\lambda_{11,I}$ [kJ mol^{-1}]	$\lambda_{11,S}$ [kJ mol^{-1}]	$\lambda_{11,T}$ [kJ mol^{-1}]	$\Delta\tau_{4,DFT}$ [ ]	$\varnothing\tau_{4,DFT}$ [ ]	ΔCu–N$_{Qu,DFT}$ [Å]
[Cu(TMG2NMe$_2$qu)$_2$]$^{+/2+}$ (**R4***)	68.4	62.9	133.0	0.07	0.55	0.145
[Cu(TMG2NMe$_2$qu)$_2$]$^{+/2+}$ (**R4$_{relaxed}$**)	45.0	62.9	107.9	0.08	0.55	0.080
[Cu(TMG2Phqu)$_2$]$^{+/2+}$ (**R5$_{cis-1}$**)	45.6	61.1	106.5	0.05	0.58	0.040
[Cu(TMG2Phqu)$_2$]$^{+/2+}$ (**R5$_{trans-1}$**)	43.5	59.3	102.8	0.07	0.62	0.043

*: The Cu–N bonds were frozen for optimization (see Section 4.4.1).

The data yield a difference in $\lambda_{11,I}$ of 23 kJ mol^{-1} for **R4$_{relaxed}$**/**R4***, with only minimal changes in the structural parameters. This difference exceeds the span of $\lambda_{11,I}$ for all other investigated redox couples (*vide infra*, Table 4-13). This distinct difference renders **R4*** the redox couple with the largest $\lambda_{11,T}$ of the investigated systems, in line with the observed small k_{11}. Furthermore, the result suggests that the pronounced bond length contraction of **R4*** in particular imposes significant steric hindrance on the redox process. A correct structural description by DFT is therefore crucial for the accurate modeling of experimentally observed properties like k_{11}. Given that the elongated bonds in **C7** likely stem from intermolecular interactions, their correct description is therefore essential for an accurate structural description, especially for extreme examples like **R4**. In this context, the employed TPSSh-D3BJ/def2-TZVP + PCM(MeCN) // TPSSh-D3BJ/def2-TZVP + PCM(MeCN) method (**M1**), while accurately describing the remaining studied systems, seems unable to fully capture the experimentally observed bond lengths of **C7–PF$_6$**. The alternatively employed MN15/def2-TZVP + PCM(MeCN) // MN15/def2-TZVP + PCM(MeCN) method (**M2**) is also not suited for this purpose, as it tends to overestimate the Cu–N bond lengths in both oxidation states of all investigated systems (Section 9.11) These circumstances indicate a necessity for future investigations to find better suited theoretical methods that also encompass the accurate structural description of edge cases.

In the case of **R5**, both conformers exhibit a comparatively small $\lambda_{11,T}$ of around 105 kJ mol^{-1}. Furthermore, it can be seen that the conformation indeed affects the obtained reorganization rates, as **R5$_{trans-1}$** exhibits marginally smaller inner- and outer reorganization energies than the cis-1 conformer. For $\lambda_{11,S}$, this is sensible as the more tetrahedral trans conformation could likely result in a better charge shielding than the flat cis conformer. The decrease in $\lambda_{11,I}$, however, is unexpected. A possible reason for the marginally lower barrier for **R5$_{trans-1}$** could be the rotatable C$_{Qu}$–C$_{Ph}$ bond that might

grant the trans conformer higher structural flexibility. The small reorganization energy of **R5$_{cis-1}$** would therefore not be a result of the cis conformation and its deviating electronic structure, but the TMG2Phqu ligand and its unique scaffolding.

Concerning all investigated systems (Table 4-13), the reorganization energies $\lambda_{11,I}$ and $\lambda_{11,T}$ show a general decrease of over 20 kJ mol^{-1} from **R4*** to **R5$_{cis-1}$**, with either redox couple demarcating the largest and smallest values, respectively. This trend correlates with the obtained $\Delta\tau_4$ parameters, with the exception of **R4*** (Figure 4.39). The τ_4 parameter and its change therefore appear to be suitable for the description of most investigated model systems.

Table 4-13: Total, inner and outer reorganization energies and selected structural parameters of the redox couples **R4***, **R5$_{cis-1}$**, **R6**, **R7** and **R8** (TPSSh-D3BJ/def2-TZVP+ PCM(MeCN) // TPSSh-D3BJ/def2-TZVP + PCM(MeCN)).

	$\lambda_{11,I}$ [kJ mol^{-1}]	$\lambda_{11,S}$ [kJ mol^{-1}]	$\lambda_{11,T}$ [kJ mol^{-1}]	$\Delta\tau_{4,DFT}$ [ ]	ln(k_{11}) [ ]
[Cu(TMG2NMe$_2$qu)$_2$]$^{+/2+}$ **R4***	68.4	62.9	133.0	0.07	5.1
[Cu(TMGqu)$_2$]$^{+/2+}$ **R6**	66.6[a]	65.3	131.9	0.20[a]	5.6[b]
[Cu(TMG2Mequ)$_2$]$^{+/2+}$ **R7**	55.2[a]	63.8	119.0	0.13[a]	7.7[b]
[Cu(TMG2^{c}Hexqu)$_2$]$^{+/2+}$ **R8**	52.7[a]	60.6	113.3	0.07[a]	7.1[b]
[Cu(TMG2Phqu)$_2$]$^{+/2+}$ **R5$_{cis-1}$**	45.6	61.1	106.5	0.05	11.7[c]

a: Data taken from [22]. b: Data converted from k_{11} reported in [22]. c: k_{11} of oxidation reaction was chosen for better comparability. *: The Cu–N bonds were frozen for optimization (see Section 4.4.1).

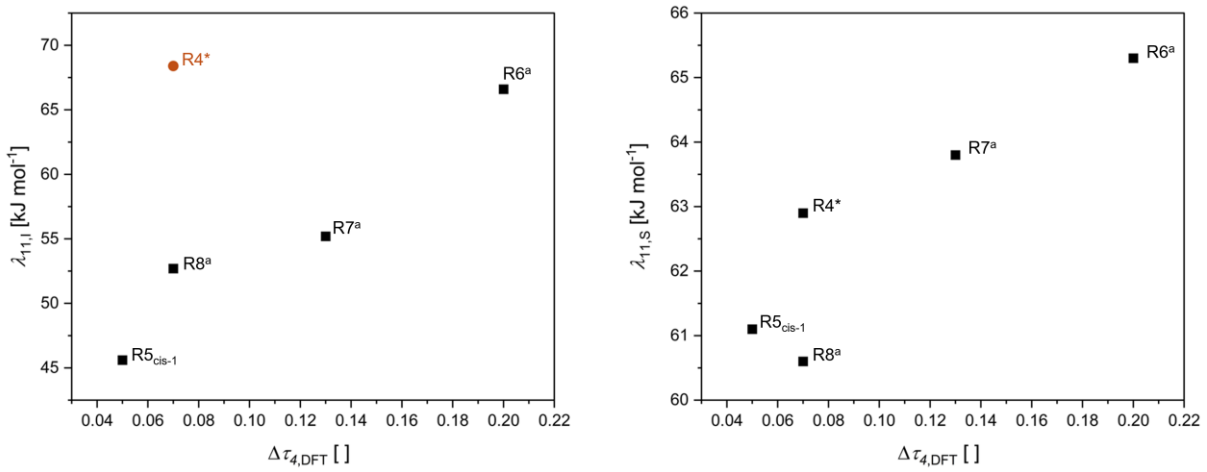

Figure 4.39: Left: Graph of the inner reorganization energy $\lambda_{11,I}$ against $\Delta\tau_{4,DFT}$ of all investigated redox couples. Right: Graph of the outer reorganization energy $\lambda_{11,S}$ against $\Delta\tau_{4,DFT}$ of all investigated redox couples. a: Structural data taken from [22] (TPSSh-D3BJ/def2-TZVP+ PCM(MeCN) // TPSSh-D3BJ/def2-TZVP + PCM(MeCN) method).

While the outer reorganization energy $\lambda_{11,S}$ follows a similar trend, this is most likely coincidental, as $\lambda_{11,S}$ is ought to represent the response of the solvent sphere to the change in dipole moment upon electron transfer.[90] The observed behavior is therefore better explained by the substituent's increasing bulk and the resulting charge shielding (H < Me < NMe$_2$ < Ph < ^{c}Hex) and not by structural restriction.

According to Marcus theory, the reorganization energy λ_{ij} and the electron transfer rate k_{ij} are connected via Equation 10.

$$\lambda_{ij} = 4 \cdot R \cdot T \cdot \ln\left(\frac{K_{A,ij}}{k_{ij}}\right) \tag{10}$$

The calculated reorganization energies should therefore be in a inversely proportional, linear relationship to the natural logarithm of the electron self-exchange rates, assuming T and $K_{A,11}$ to be the same for all complexes (Equation 36).

$$\lambda_{11} \propto -A \cdot \ln(k_{11}) \tag{36}$$

As seen in Figure 4.40, this correlation holds true, with the exception of $[Cu(TMG2^{c}Hexqu)_2]^{+/2+}$ (**R8**).

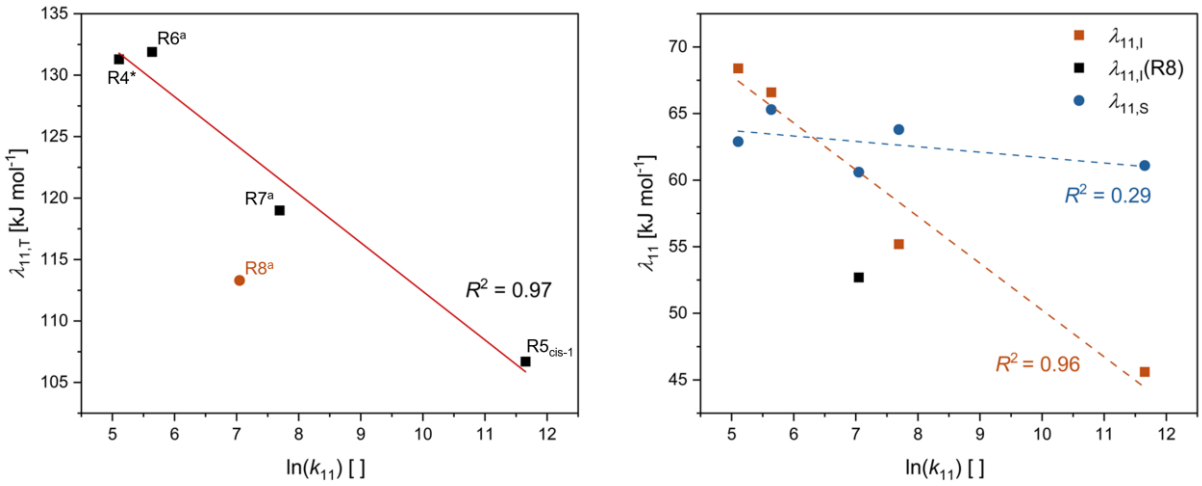

Figure 4.40: Left: Graph of the total reorganization energy $\lambda_{11,T}$ against $\ln(k_{11})$ of all investigated redox couples. Right: Graph of the inner reorganization energy $\lambda_{11,I}$ and the outer reorganization energy $\lambda_{11,S}$ against $\ln(k_{11})$ of all investigated redox couples. a: Structural data taken from [22] (TPSSh-D3BJ/def2-TZVP+ PCM(MeCN) // TPSSh-D3BJ/def2-TZVP + PCM(MeCN) method).

Separating the two components of the total reorganization energy shows that the correlation stems from the inner reorganization energy, with the outer reorganization energy only showing a weak correlation. The computations therefore suggest the central driving force behind increasing k_{11} is the inner reorganization energy. Possible reasons for the deviation of **R8** could be secondary factors in the self-exchange reaction that the given assumptions do not account for. Overall, however, it can be said that internal reorganization energies are in especially good agreement with the expected behavior. In turn, this means that $\lambda_{11,I}$ might be a suitable parameter for predicting the efficacy of future $[Cu(GUAqu)_2]^{+/2+}$ model systems, given an accurate simulation of their geometries.

Overall, the sp^2-hybridized substituents of the ligand TMG2NMe$_2$qu (**L5**) and TMG2Phqu (**L6**) exhibit a strong influence on the corresponding redox couples' electron self-exchange rates, similarly to other 2-substituted GUAqu ligands. However, the exact influence of a sp^2-hybridized substituent cannot be explained solely by its

bulk, as the resonance (or lack thereof) to the quinolinyl moiety, as well as intermolecular interactions, play a central role in determining the resulting complex's entasis. In the case of $[Cu(TMG2NMe_2qu)_2]^{+/2+}$ (**R4**), the NMe_2 substituents are strongly conjugated with their quinolinyl's π system; the resulting co-planarity leads to rigid configuration and, in turn, almost ideal entasis of the redox couple. However, due to the co-planarity, steric repulsion causes a drastic elongation of the Cu(I)–N_{Qu} bond, the contraction of which increases the otherwise small reorganization energy by a drastic amount, likewise lowering k_{11}.

In $[Cu(TMG2Phqu)_2]^{+/2+}$ (**R5**) on the other hand, the phenyl substituent is singly bonded to the remaining ligand scaffolding. The rotatable bond, in combination with the planar geometry of the substituent, leads to a number of different possible conformations in the Cu(I) complex. Ironically, this flexibility, and presumably $\pi-\pi$ interactions, allow the redox couple to adopt rigid geometries that show little geometrical change upon oxidation and therefore undergo rapid electron transfer. The assessment of sp^2-substituted ligand systems and their redox couples in modelling the entatic state is therefore more nuanced than for other systems, but especially aromatic substituents seem promising for possibly achieving even higher self-exchange rates.

5 Photochemical and Photophysical Properties of Copper Guanidine Quinolinyl Systems

5.1 Motivations and Aim

Due to their potential to achieve prolonged excited state lifetimes τ, Cu(I)-photosensitizers have seen increasing interest in study in recent years as a cheaper and more sustainable replacement for Ir and Ru based systems. Their propensity to flatten in structure in the excited state, however, tends to shorten these lifetimes drastically, limiting their potential applications. This flattening distortion can be mitigated by steric restriction in the form of ligand bulk, resulting in a rigid coordination geometry that is not unlike that of entatic state model systems.

While the photophysics of the $[Cu(TMGqu)_2]PF_6$ model system have been studied in the past, this is not the case for its photoredox catalytic properties. Investigation of the potential activity of $[Cu(GUAqu)_2]^+$ model systems in this field is therefore the aim of the following chapter. The lifetimes, as well as the excited state potentials and triplet energies of the three complexes $[Cu(TMGqu)_2]PF_6$ (**C11–PF$_6$**), $[Cu(TMG2Mequ)_2]PF_6$ (**C13–PF$_6$**) and $[Cu(TMG2^cHexqu)_2]PF_6$ (**C15–PF$_6$**) were characterized using X-ray absorption fluorescence spectroscopy (XAFS), cyclic voltammetry and fluorescence spectroscopy. The systems were further tested as catalysts in suitable photoreactions to investigate whether their photocatalytic activity changes depending on the systems' entasis.

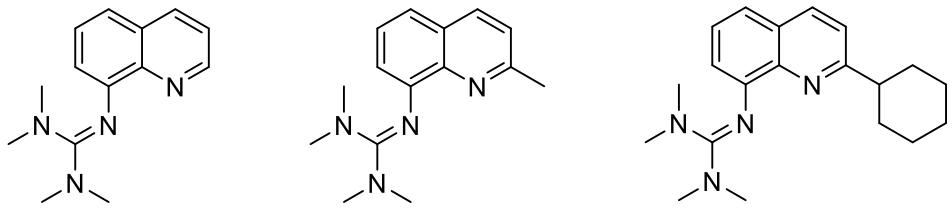

Figure 5.1: Ligands of the Cu(I) complexes investigated in this study.

These systems were chosen due to their similar electronic and structural properties on the one hand, as well as the accuracy of their DFT simulations on the other hand.[22] Their study should therefore provide a basis that will enable more in-depth studies with other $[Cu(GUAqu)_2]^+$ model systems in the future.

Discussion of the triplet (T_1) state is often coupled to the ground (S_0) state. The coupled S_0 and T_1 pairs will therefore be referred to as photo couples (**P**, Figure 5.2).

Photo couple:

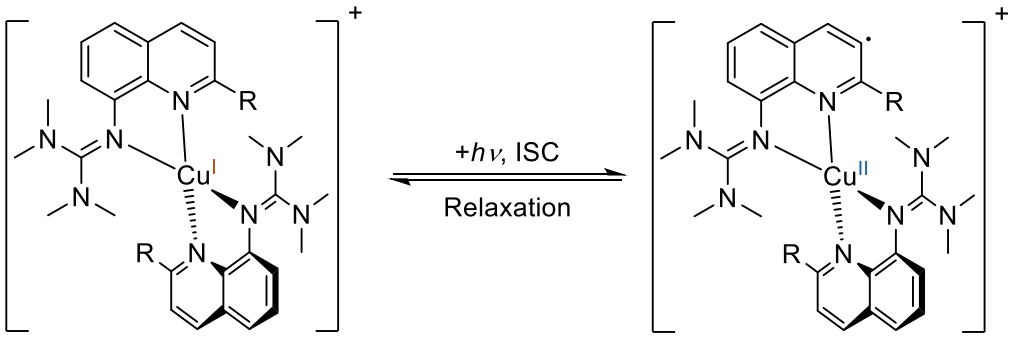

$[Cu(GUAqu)_2]^+$ S_0 $[Cu(GUAqu)_2]^{+*}$ T_1

Photo couples:

$[Cu(TMGqu)_2]^{+/+*}$ (**P1**) $[Cu(TMG2Mequ)_2]^{+/+*}$ (**P2**) $[Cu(TMG2^cHexqu)_2]^{+/+*}$ (**P3**)

Figure 5.2: Excitation and relaxation process that couples one S_0 state to its T_1 state as well as the photo couples discussed in this chapter.

5.2 UV/vis Spectra

The most important parameters for any photosensitizers are arguably their absorptive properties in the UV/vis range that allow excited states to form, as well as their corresponding lifetimes that enable interaction with other molecules. The UV/vis spectra of **C11**, **C13** and **C15** have been reported in previous works and are shown in Figure 5.3.[22] The three spectra are similar, with a band at 435 to 440 nm that TD-DFT studies indicate to be MLCT transitions (Table 5-1).[22, 178] This similarity allows for easy comparison of the photo couples. A notable difference between the spectra is a decreased tailing of the MLCT bands from **P1** to **P3** which suggests an increasingly similar excited state geometry to the corresponding ground state.[212]

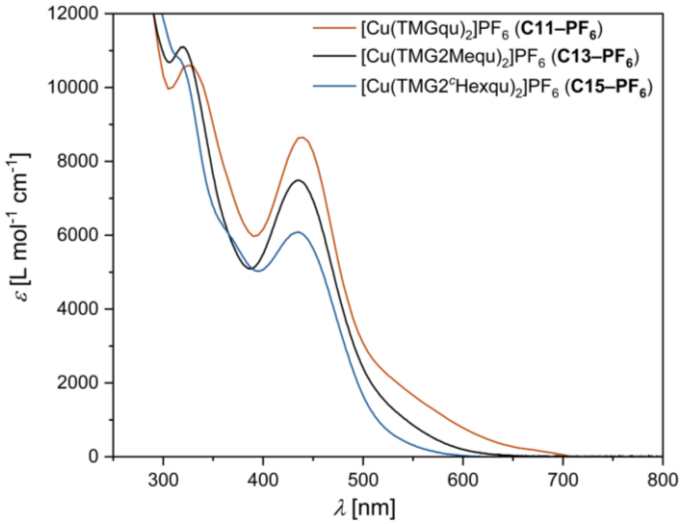

Figure 5.3: Reported UV/vis spectra of the complexes **C11–PF_6**, **C13–PF_6** and **C15–PF_6**.[22, 69]

Table 5-1: Molar extinction coefficients and wavelengths of the reported bands of **C11–PF$_6$**, **C13–PF$_6$** and **C15–PF$_6$**.[22, 69, 167]

Complex		λ_{max} [nm]	ε_{max} [L mol^{-1} cm^{-1}]
[Cu(TMGqu)$_2$]PF$_6$ (**C11–PF$_6$**)	Band 1:	440	$8.6 \cdot 10^3$
	Band 2:	325	$1.1 \cdot 10^4$
[Cu(TMG2Me$_2$qu)$_2$]PF$_6$ (**C13–PF$_6$**)	Band 1:	435	$7.5 \cdot 10^3$
	Band 2:	320	$1.1 \cdot 10^4$
[Cu(TMG2^{c}Hexqu)$_2$]PF$_6$ (**C15–PF$_6$**)	Band 1:	435	$6.1 \cdot 10^3$
	Band 2:	314	$1.1 \cdot 10^4$

The lifetimes of the excited MLCT states can be determined by time-resolved methods like pump-probe fluorescence-, UV/vis or X-ray absorption (XAS) spectroscopy. These methods have been applied to **P1** in the past,[116] and have additionally been conducted for [Cu(TMG2Mequ)$_2$]$^{+/*}$ (**P2**) (discussed in Section 5.4). However, a cost-efficient method to assess the relative expected triplet state lifetimes $\tau(T_1)$ is via DFT and the energy gap between the computationally obtained S_1 and T_1 states.

5.3 Computational Assessment of Triplet Geometries and Energy Gap Law

The relevant ground state (S_0) and triplet (T_1) geometries of the photo couples **P1** to **P3** were obtained via the TPSSh-D3BJ/def2-TZVP + PCM(MeCN) // TPSSh-D3BJ/def2-TZVP + PCM(MeCN) method (**M1**) (Table 5-2).

The triplet states all exhibit shortened bonds compared to the S_0 states, as well as the expected structural flattening. These changes in geometry result in a close similarity between the T_1 states and their corresponding Cu(II) ground state (D_0). Therefore, the observed trends in τ_4 and the plain angle are near identical to the structural changes observed for the standard redox couples, with the flattening distortion decreasing from **P1** to **P3**. The decreasing flattening distortion between the S_0 and T_1 states is in line with the previously discussed decrease in trailing of the UV/vis data. Besides the structural changes, the energy gap between the T_1 and S_0 states increases with the redox couple's entasis, being the largest for **P3** with 1.75 eV. The complexes' flattening distortion is linked to the excited state lifetime via Marcus theory (see Section 1.6.1).

Table 5-2: Key bond lengths, angles and structural parameters for the simulated structures of **P1**, **P2** and **P3** (TPSSh-D3BJ/def2-TZVP + PCM(MeCN) // TPSSh-D3BJ/def2-TZVP + PCM(MeCN) method).

Photo couple	$[Cu(TMGqu)_2]^{+/+*}$ **(P1)**		$[Cu(TMG2Mequ)_2]^{+/+*}$ **(P2)**		$[Cu(TMG^cHexqu)_2]^{+/+*}$ **(P3)**	
State	S_0	T_1	S_0	T_1	S_0	T_1
			Bond Lengths [Å]			
$Cu–N_{Gua}(1)$	2.066	1.987	2.084	2.000	2.053	2.015
$Cu–N_{Gua}(2)$	2.066	1.987	2.084	2.010	2.053	2.001
$Cu–N_{Qu}(1)$	1.997	1.948	2.001	1.940	2.035	2.008
$Cu–N_{Qu}(2)$	1.997	1.948	2.001	1.990	2.035	1.945
			Bond Angles [°]			
$N_{Gua}(1)–Cu–N_{Gua}(2)$	129.3	147.1	124.6	132.8	131.1	123.5
$N_{Gua}(1)–Cu–N_{Qu}(2)$	114.3	104.4	115.8	107.6	128.0	136.6
$N_{Gua}(1)–Cu–N_{Qu}(1)$	82.3	83.6	81.9	83.9	81.5	82.2
$N_{Gua}(2)–Cu–N_{Qu}(1)$	114.3	104.4	115.8	109.0	128.0	131.8
$N_{Gua}(2)–Cu–N_{Qu}(2)$	82.3	83.6	81.9	82.6	81.5	83.7
$N_{Qu}(1)–Cu–N_{Qu}(2)$	142.2	152.0	143.1	151.6	111.0	105.1
			Structure Parameters			
τ_4 [ ]	0.63	0.43	0.65	0.54	0.72	0.65
$\Delta\tau_4$ [ ]	0.20		0.12		0.07	
$\varnothing\tau_4$ [ ]	0.53		0.60		0.67	
$\measuredangle_a$ [°]	70.3	46.5	74.4	59.6	81.5	69.8
$\Delta\measuredangle_a$ [°]	23.8		14.8		11.7	
ρ [ ]	0.98, 0.98	1.00, 1.00	0.97, 0.97	1.00, 1.00	0.98, 0.98	1.00, 1.00
RMSD [Å]	0.267		0.167		0.167	
RMSD (vs.$Cu(II)_{DFT}$) [Å]	0.283	0.056	0.191	0.050	0.147	0.067
$\Delta E_{Gap}(T_1\text{-}S_0)$ [eV]	1.33		1.58		1.75	

The excited state dynamics of Cu photosensitizers usually follow the rules of the Marcus inverted region, which means the excited state lifetime of the T_1 state $\tau(T_1)$ increases exponentially with the T_1-S_0 energy gap (Eqn. 36).

$$\tau(T_1) = \frac{1}{k'_{ISC}} \propto \exp(\Delta E_{Gap}(T_1 - S_0)) \qquad (36)$$

This relationship is also referred to as the energy gap law. Previous theoretical works by Hadt *et al.* have already demonstrated a strong correlation between the energy gap and structural restriction of the photo couples. The energy gap thereby increases with an increasing structural similarity of the S_0 and T_1 states.[23] A similar correlation can be observed between the energy gap and $\Delta\tau_4$ (Figure 5.4).

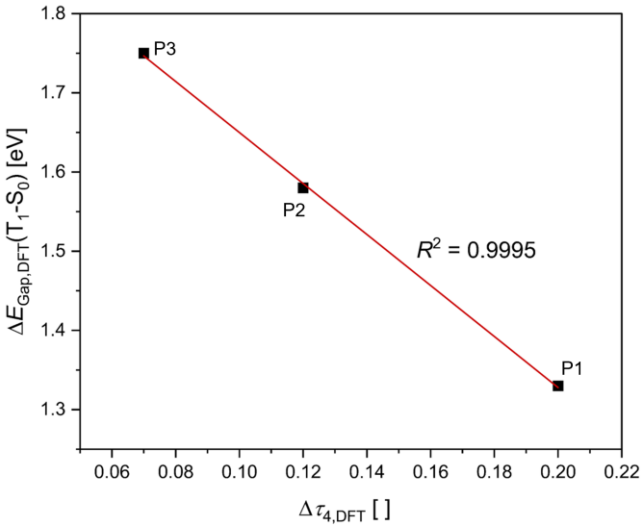

Figure 5.4: Graph of the T_1-S_0 energy gap against the computed changes in τ_4 value of the two states' geometries (TPSSh-D3BJ/def2-TZVP+ PCM(MeCN) // TPSSh-D3BJ/def2-TZVP + PCM(MeCN) method).

While precise predictions of $\tau(T_1)$ are beyond this method, the exponential correlation of Equation 36 implies this increase to be significant. However, it has to be considered that the excited states can theoretically be quenched by the formation of exciplexes; associations of the T_1 states with co-ligands like solvent molecules. While such an exciplex has been found to exist for **P1** in the form of the pentacoordinate $[Cu(TMGqu)_2(MeCN)]^{+*}$,[116] exciplex computations for **P2** and **P3** with acetonitrile as co-ligand yielded nearly identical geometries to the tetracoordinate T_1 states with the acetonitrile located more than 4 Å away from the central ion. Exciplex formation of **P2** and **P3** can therefore be regarded as unlikely, which can be explained by the increased steric bulk of the Me substituents as well as the less pronounced flattening distortion of the photo couple (the Appendix Section 9.14).
Experimental determination of the lifetimes can be achieved via various methods. In this work, the triplet state lifetimes of **P2** were assessed via pump-probe XAFS.

5.4 Pump-Probe XAFS Measurements of $[Cu(TMG2Mequ)_2]PF_6$

Pump-probe XAFS measurements were performed to obtain information about the T_1 state of $[Cu(TMG2Mequ)_2]^{+/+*}$ **P2**, its lifetime and possible intersystem crossing rates and exciplex formations. **C13–PF_6** was synthesized by dissolving the ligand TMG2Mequ (**L9**) and $[Cu(MeCN)_4]PF_6$ in DCM and precipitating the complex using pentane (Scheme 5.1).

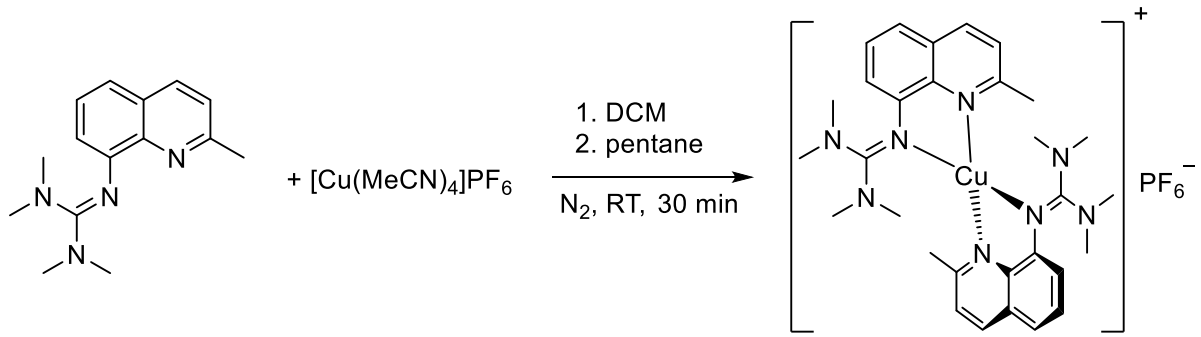

Scheme 5.1: Synthesis scheme for $[Cu(TMG2Mequ)_2]PF_6$ (**C13–PF$_6$**).

The XAFS measurements were performed by the Rübhausen group. The spectra were measured in acetonitrile at various concentrations of **C13–PF$_6$** in nitrogen atmosphere in a flow-chamber. The pump-beam was set to λ_{pump} = 435 nm using an optical parametric amplifier (OPA) laser system. The delay between pump and probe beams was optimized to yield maximum transient intensity at about 8990 eV (for information on the method, *vide supra*, Section 1.11). One of the obtained transients is shown in Figure 5.5.

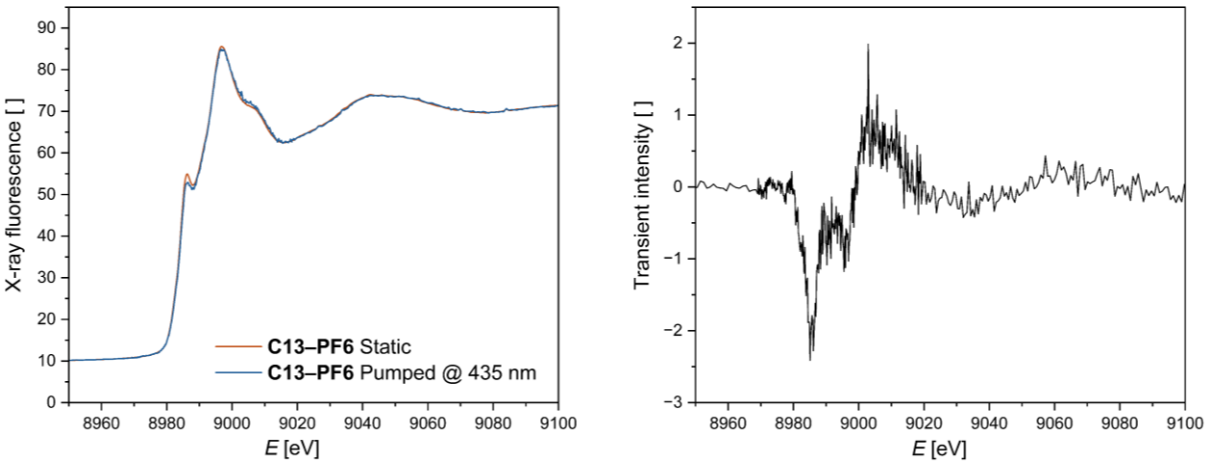

Figure 5.5: Left: Overlay of the static XAFS and the pumped XAFS spectrum of **C13–PF$_6$**. Right: Transient spectrum of the two spectra.

The XAFS spectrum of the complex cation changes in subtle way upon excitation, most prominently seen in the shrinking of the pre-edge feature, a characteristic of Cu(I) XAFS spectra, at 8986 eV. The excited transition at 435 nm is assigned to be an MLCT, the obtained transient should therefore show similar characteristics to the difference spectrum of the static XAFS spectra of **C13–PF$_6$** and **C14–OTf** (Figure 5.6).

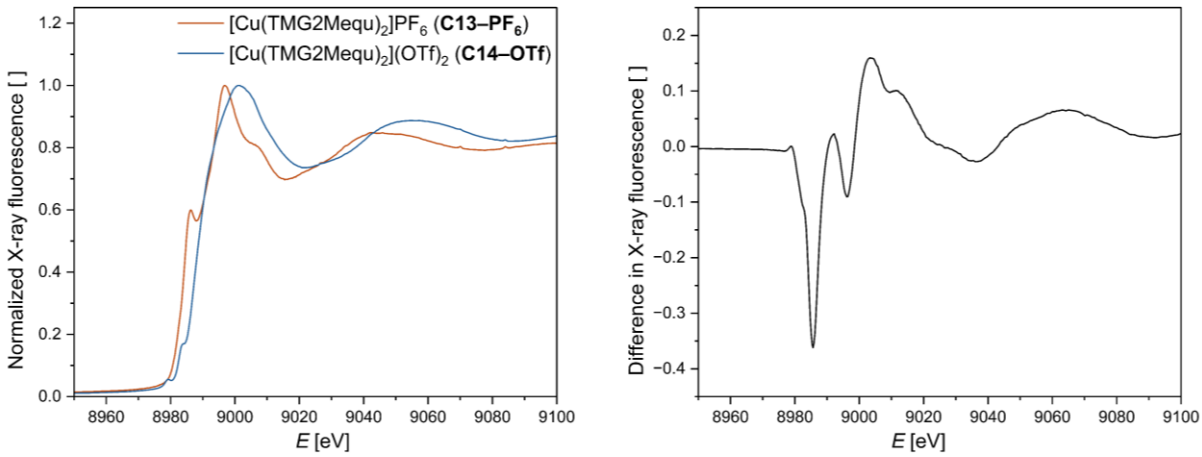

Figure 5.6: Left: Overlay of the static XAFS spectra of **C13–PF$_6$** and **C14–OTf**. Right: Difference spectrum of the two spectra. **C14–OTf** was taken from the laboratory stock.

The evident similarities between the transient and the difference spectrum underscore the MLCT character of the band at 435 nm. Observing the decay of the transient signal at 8990 eV and fitting the resulting delay scans allows to determine the excitation's constituent time constants (exemplary for c = 1.5 mmol L^{-1}, Figure 5.7, remaining delay scans in the Appendix, Section 9.5).

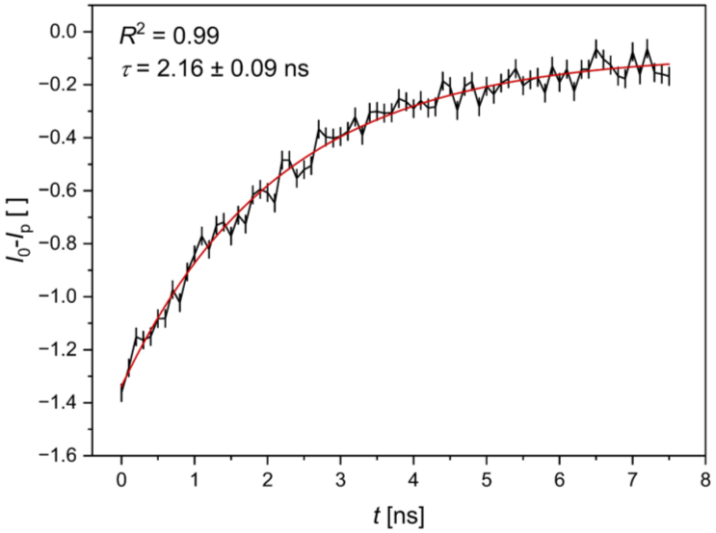

Figure 5.7: Baseline-corrected delay scan of **C13–PF$_6$** after pump at 435 nm at 1.5 mmol L^{-1} with first-order decay fit and time constant τ.

The excited state decay is well described by a first-order decay function and thus by one time constant τ, indicating that only one decay process is observed for **P2**. Previous transient XAFS measurements conducted with [Cu(TMGqu)$_2$]$^{+/+*}$ **P1** yielded decay functions with multiple time constants that could be associated with the decay of the triplet state as well as the formation and decay of an [Cu(TMGqu)$_2$(MeCN)]$^{+*}$ exciplex.[116] The absence of further time constants therefore indicates no detectable exciplex formation, which is in accordance with the DFT simulations that predict this process to be disfavored.

Further, the delay scans show no time constant that could be associated with the intersystem crossing from the S_1 to the T_1 state. This is in accordance with the previous measurements of **P1** in which S_1 was determined via transient IR and UV/vis spectroscopic methods to be very short lived with a τ_{ISC} of around 2 ps.[116] Determining the intersystem crossing rate for **P2** would therefore require additional experiments with higher temporal resolution.

Therefore, the observed decay of **P2** can be associated with the decay of the T_1 state. The obtained time constants τ for this decay show no significant change with concentration (Figure 5.8), indicating no concentration-dependent quenching processes in the measured range.

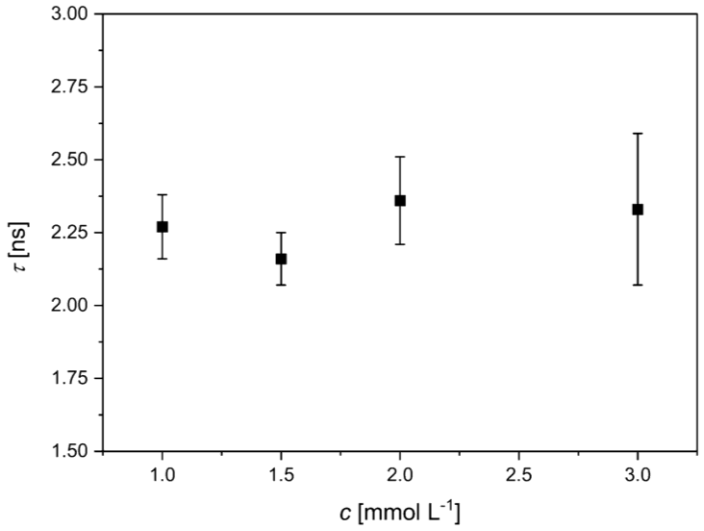

Figure 5.8: Time constants of the delay scans with errors plotted against the concentrations the delay scans were measured at.

All four obtained time constants result in a weighted average triplet state lifetime $\tau(T_1)$ = 2.24 ± 0.06 ns.

This presents a significant increase in the triplet state lifetime over that of **P1** with 120 ps.[116] Given the increase in $\Delta E_{Gap}(T_1\text{-}S_0)$ from **P1** to **P2**, this observation is in agreement with the energy gap law (Eqn. 36); the excited state dynamics of the $[Cu(GUAqu)_2]^+$ model systems therefore likely follow the Marcus inverted region. This, in turn, means that the systems' entasis increases the T_1 lifetimes, highlighting the mutual design principles behind entatic state model systems and Cu photosensitizers.

Due to time constraints, similar measurements of the excited state dynamics of $[Cu(TMG2^cHexqu)_2]^{+/+*}$ **P3** were not possible. However, the positive correlation between τ and $\Delta E_{Gap}(T_1\text{-}S_0)$ suggests that **P3** could potentially exhibit the longest T_1 lifetime of the investigated $[Cu(GUAqu)_2]^+$ systems.

Compared to the phenanthroline-based $[Cu(phen)_2]^+$ systems, the most prominent class of homoleptic Cu photosensitizers,[102, 114] the entatic state models display

significantly shorter lifetimes in relation to their computationally determined energy gaps (Figure 5.9).[23]

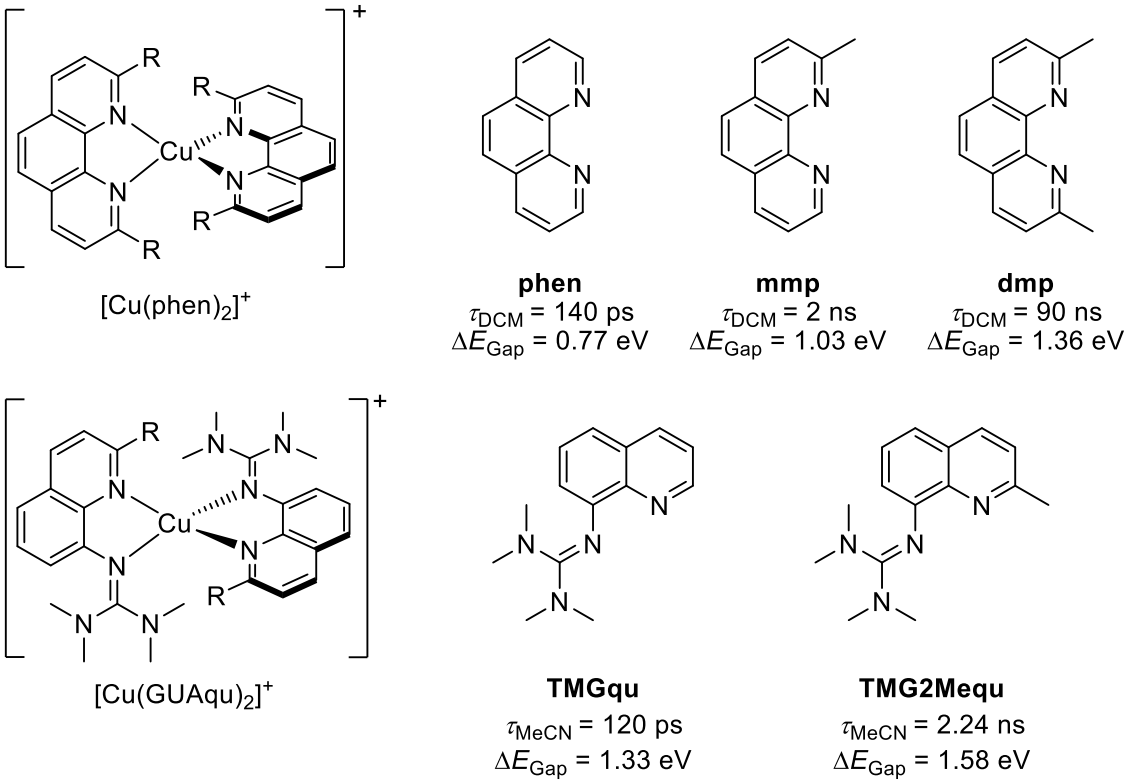

Figure 5.9: Triplet state lifetimes and T_1-S_0 energy gaps of different phenanthroline- and GUAqu-based systems.[23, 116]

The reason for this discrepancy is not clear. While electronic influences of the guanidine donors could be a factor, they would stabilize the triplet state, thus lowering the energy gap. It could also be possible that the GUAqu systems allow for more effective non-radiative decay pathways than phen-based systems. However, a definitive answer for the observed behavior was not possible within the scope of this thesis and requires further study.

5.5 Photoredox Catalytic Benchmarking of the Photo Couples

Next to the absorptive properties and the excited state lifetimes, the reactivity of photoredox catalysts is dependent on their redox potentials of the ground state E_{ox} and E_{red} and those of the excited states $^*E_{ox}$ and $^*E_{red}$. The latter can be approximated using the Rehm-Weller equations (Eqn. 18, 19, Section 1.8 for more detail).

$$^*E_{ox} = E_{ox} - E_{0\text{-}0} \tag{18}$$

$$^*E_{red} = E_{red} + E_{0\text{-}0} \tag{19}$$

One way to obtain excited state energy $E_{0\text{-}0}$ is from the fluorescence emission maximum. Therefore, to assess the reactivity of the complexes $[Cu(TMGqu)_2]PF_6$ (**C11–PF$_6$**), $[Cu(TMG2Mequ)_2]PF_6$ (**C13–PF$_6$**) and $[Cu(TMG2^cHexqu)_2]PF_6$ (**C15–PF$_6$**), the redox potentials E_{ox} and E_{red} are required, as well as the fluorescence emission of the Cu(I) complexes. **C11–PF$_6$** and **C15–PF$_6$** were synthesized according to Scheme 5.1.

5.5.1 Cyclic Voltammetry of the Entatic State Models

While cyclic voltametric measurements of the studied model systems have been reported before, these were limited to the metal-centered $[Cu(GUAqu)_2]^{+/2+}$ redox waves that constitute the E_{ox} potential.[22, 69, 77, 85-86, 192] For Cu photosensitizers, the additional redox potential E_{red} is defined as the ligand-centered $[Cu(GUAqu)_2]^{+/0\cdot}$ redox wave that involves the reduction and oxidation of the ligands according to Scheme 5.2.

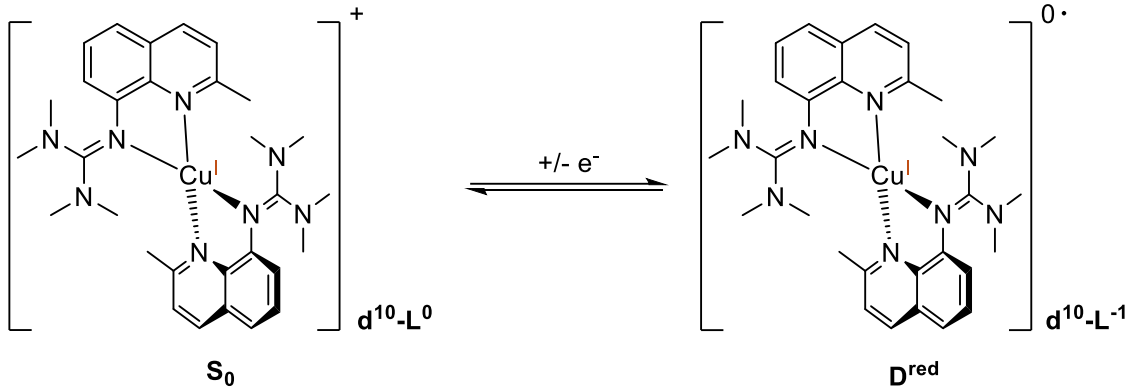

Scheme 5.2: Scheme of the reaction that constitutes the E_{red} potential. The redox process is ligand centered and does therefore not affect the Cu oxidation state.

The product of the ligand reduction, the neutrally charged $[Cu(GUAqu)_2]^{0\cdot}$ complex **D^{red}**, is the reactive intermediate in the reductive quenching (RQ) pathway. Due to the radical character of **D^{red}**, the cyclic voltammetry experiments were conducted within a glove box to exclude potential adverse effects of oxygen or water on the reversibility of the E_{red} waves. The initial experiments were carried out in acetonitrile. However, these measurements exhibit artifacts (Figure 5.10 as illustration).

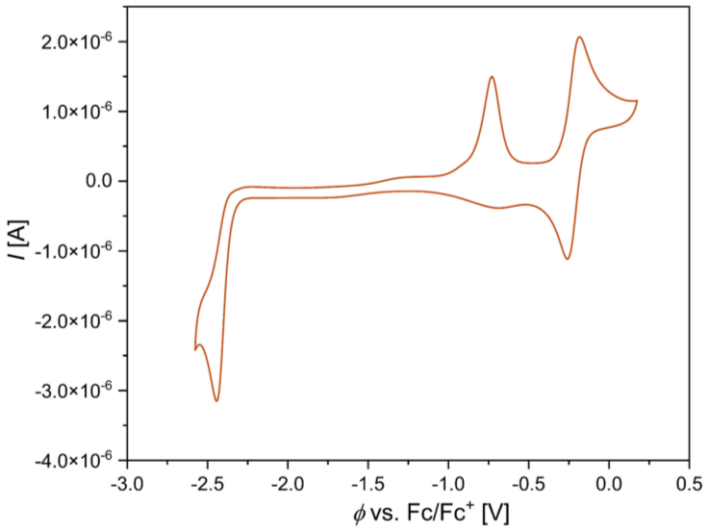

Figure 5.10: Cyclic voltammogram of **C13–PF$_6$** (c = 10^{-3} M) in MeCN with [NBu$_4$][PF$_6$] (c = 0.1 M) under inert conditions at 100 mV s^{-1}.

These artifacts could be attributed to either unintended reactivity of the **D^{red}** species or a breakdown of impurities or the acetonitrile itself due to the applied negative potentials of over −2 V *vs.* Fc/Fc$^+$. To rule out the former, the measurements were repeated in THF under otherwise identical conditions (Figure 5.11, Table 5-3).

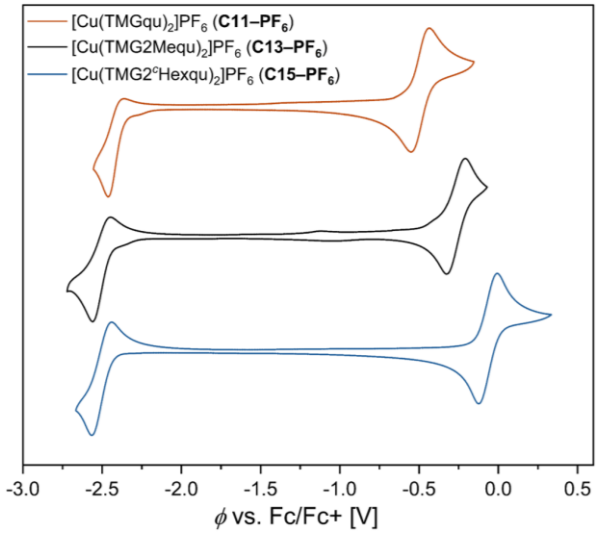

Figure 5.11: Cyclic voltammogram of **C11–PF$_6$**, **C13–PF$_6$** and **C15–PF$_6$** (c = 10^{-3} M) in THF with [NBu$_4$][PF$_6$] (c = 0.1 M) under inert conditions at 100 mV s^1.

Table 5-3: Key parameters of the E_{ox} and E_{red} redox waves of **C11–PF$_6$**, **C13–PF$_6$** and **C15–PF$_6$** obtained from the cyclic voltammograms

Sarting compound	E_{ox} [V] *vs.* Fc/Fc$^+$	ΔE_P [mV]	I_{red}/I_{ox} [ ]	E_{red} [V] *vs.* Fc/Fc$^+$	ΔE_P [mV]	I_{red}/I_{ox} [ ]
C11–PF$_6$	−0.49	109	1.29	−2.41	76	1.31
C13–PF$_6$	−0.27	98	1.37	−2.50	102	1.05
C15–PF$_6$	−0.07	112	1.23	−2.51	108	1.17

The obtained E_{ox} display values that get increasingly more positive, which is in agreement with the reported values in acetonitrile.[22] Conversely, the peak-to-peak separation as well as the current ratios display worse reversibility, making the measured E_{ox} waves quasi-reversible. This behavior is likely linked to the change in solvent, given that the measurements in acetonitrile yield values similar to the ones reported in literature (see Section 9.2.3)

The ligand-centered E_{red} waves get increasingly more negative from **C11–PF$_6$** to **C15–PF$_6$**, likely due to the inductive effects of the alkyl substituents. The ligand-centered waves also show quasi-reversible behavior, with the oxidation wave getting increasingly pronounced from **C11–PF$_6$** to **C15–PF$_6$**, indicating an increased stability of the reduced ligand for the substituted ligands. The dependency of both waves on the scan rate was tested for **C11–PF$_6$** (Figure 5.12), revealing that the oxidation wave of E_{red} is less pronounced for slow scan rates. This suggests the reduced ligands are meta-stable and decay over time.

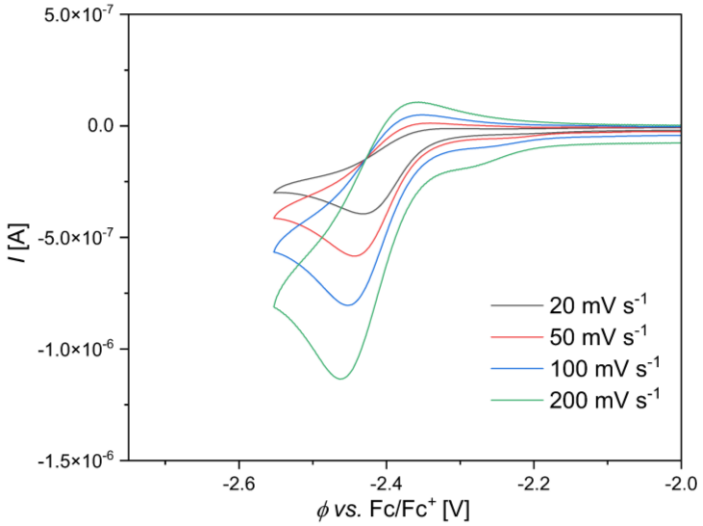

Figure 5.12: Cyclic voltammogram of the E_{red} redox wave of **C11–PF$_6$** (c = 10^{-3} M) in THF with [NBu$_4$][PF$_6$] (c = 0.1 M) under inert conditions.

5.5.2 Fluorescence Spectroscopy of the Entatic State Model Systems

The emission of the MLCT transition is required to obtain the excited state redox potentials $^*E_{ox}$ and $^*E_{red}$. These measurements were conducted at ambient conditions in degassed THF for consistency with the electrochemical measurements. Selecting excitation wavelengths close to the MLCT band at 440 nm for **C13–PF$_6$** gives a weak emission at 563 nm that increases with intensity the closer the emission wavelength gets to the absorption band. This weak emission is initially hidden beneath the fluorescence of the ligand that is significantly more intense (see Appendix, Section 9.4). To verify this emission as the MLCT emission, excitation spectra were measured with the wavelength varying around the detected emission band, likewise showing a

correlation between the emission wavelength and an excitation band at 440 nm (Figure 5.13).

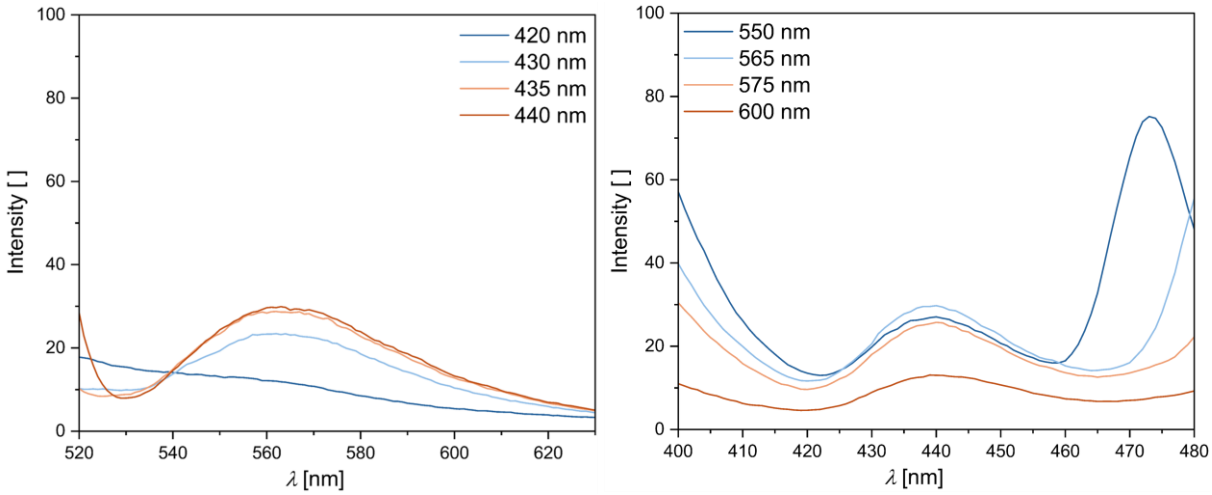

Figure 5.13: Fluorescence emission (left) and excitation (right) spectra of $[Cu(TMG2Mequ)_2]PF_6$ (**C13–PF$_6$**) in degassed THF at ambient conditions at different wavelengths (c = 10 µmol L^{-1}). The maximum at 470 nm for the excitation spectrum at 550 nm is an artifact of the light source.

The emission band is therefore most likely the corresponding emissive decay of the MLCT transition that can also be found for the other two photo couples (Figure 5.14).

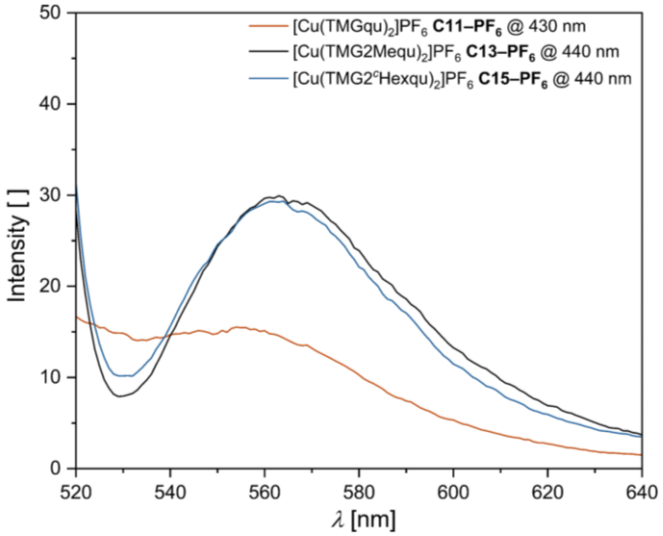

Figure 5.14: Fluorescence emission spectra of $[Cu(TMGqu)_2]PF_6$ (**C11–PF$_6$**), $[Cu(TMG2Mequ)_2]PF_6$ (**C13–PF$_6$**) and $[Cu(TMG2^cHexqu)_2]PF_6$ (**C15–PF$_6$**) in degassed THF at ambient conditions at the wavelength of the most intense emission (c = 10 µmol L^{-1}).

The emission maxima can be converted into $E_{0\text{-}0}$ by simply converting the wavelength into electronvolts (Table 5-4). A reason for the low-intensity emissions might be the high k_{ISC} of the complexes that occur due to the small $\Delta E_{Gap}(S_1\text{-}T_1)$ discussed in Section 5.4. It facilitates a fast depopulation of the S_1 state into the T_1 state and, combined with the latter's spin-forbidden emissive decay, effectively quenches the fluorescence of the complexes. This phenomenon is also known as thermally activated

delayed fluorescence (TADF) and can be verified using temperature-dependent fluorescence emission spectroscopy.[213] Unfortunately, this method was not available over the course of this work; this hypothesis could therefore not be tested. Using the Rehm-Weller equations, the obtained emission maxima, together with the ground state redox potentials, give the additional information required for an assessment of the entatic state models in photoredox catalysis.

Table 5-4: Key parameters for the assessment of the photocatalytic activity of the complexes $[Cu(TMGqu)_2]PF_6$ (**C11–PF$_6$**), $[Cu(TMG2Mequ)_2]PF_6$ (**C13–PF$_6$**) and $[Cu(TMG2^cHexqu)_2]PF_6$ (**C15–PF$_6$**).

	λ_{abs} [nm]	λ_{em} [nm]	E_{0-0} [eV]	ΔE_{Stokes} [eV]	E_{ox} [V]	E_{red} [V]	$^*E_{ox}$ [V]	$^*E_{red}$ [V]	τ [ns]
$[Cu(TMGqu)_2]PF_6$	440	557	2.23	0.59	−0.49	−2.41	−2.72	−0.18	0.12[a,b]
$[Cu(TMG2Mequ)_2]PF_6$	435	563	2.20	0.65	−0.27	−2.50	−2.47	−0.30	2.24[b]
$[Cu(TMG2^cHexqu)_2]PF_6$	435	563	2.20	0.65	−0.07	−2.51	−2.27	−0.31	-

An additional value ΔE_{Stokes} in Table 5-4 is the Stokes shift (Eqn. 37) that serves as a measure for the loss of energy between absorption and emission of a photon by a given system.

$$\Delta E_{Stokes} = \lambda_{abs}\,[eV] - \lambda_{em}\,[eV] = \lambda_{abs}\,[eV] - E_{0\text{-}0} \qquad (37)$$

The data shows that the excited state potentials are close to identical to the opposite ground state potentials and even exceed them in the case of **C11–PF$_6$**. A general comparison of the values in Table 5-4 to homoleptic phenanthroline-based Cu photosensitizers (Figure 5.15, Table 5-5) shows that the lifetimes of the herein studied systems are significantly shorter, and all redox potentials significantly more negative. Both circumstances impede the potential application of the entatic state systems in oxidative quenching cycles (see Section 1.8), with the significantly more reducing E_{ox} being especially limiting as they prohibit a regeneration of the Cu(II) state via organic sacrificial donors.[114]

Notable, however, are the comparatively small Stokes-shifts and large excited state energies $E_{0\text{-}0}$ of the $[Cu(GUAqu)_2]^+$ systems compared to the listed phenanthroline-based complexes that indicate a generally small structural change of the entatic state model systems upon excitation. A direct consequence of this is that their ground- and excited-state redox potentials are closely matched overall ($E_{red} \approx {}^*E_{ox}$ and ${}^*E_{red} \approx E_{ox}$). On the one hand, this means that both the reductive and oxidative quenching cycles have about the same reactivity. Combined with the required 0.3 V overpotential for a sacrificial donor, however, these similarities render it unlikely to selectively target either the oxidative or reductive pathway for all complexes.[107]

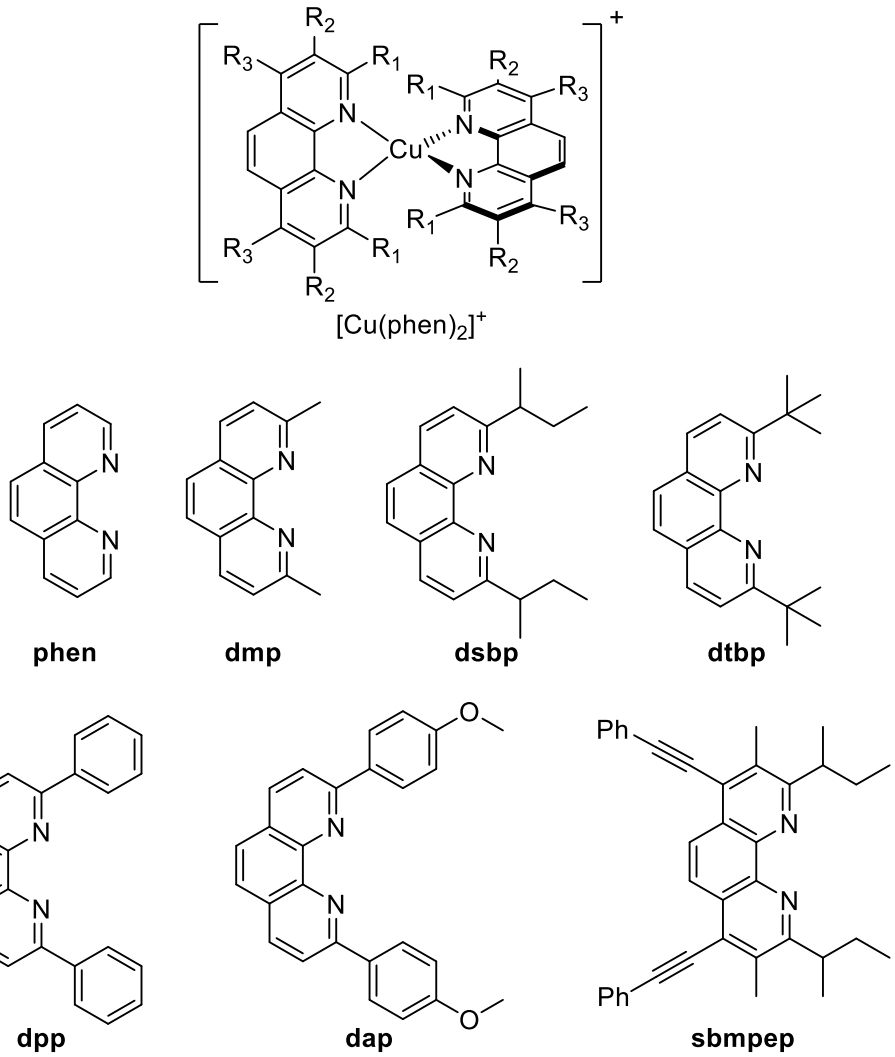

Figure 5.15: Ligands of corresponding phenanthroline-based copper photosensitizers used for comparison.[113, 214-220]

Table 5-5: Key parameter of several phenanthroline-based copper photosensitizers used for comparison.[113, 214-220]

	λ_{abs} [nm]	λ_{em} [nm]	E_{0-0} [eV]	ΔE_{Stokes} [eV]	E_{ox} [V]	E_{red} [V]	$^*E_{ox}$ [V]	$^*E_{red}$ [V]	τ [ns]	Source
$[Cu(phen)_2]PF_6$[a]	458	-	-	-	0.14	-	-	-	0.14	[214-215]
$[Cu(dmp)_2]PF_6$[a]	454	740	1.68	1.05	0.59	-	−1.45	-	90	[214]
$[Cu(dsbp)_2]PF_6$[b]	452	670	1.85	0.89	0.50	−2.19	−1.35	−0.34	130	[217]
$[Cu(dtbp)_2]SbF_6$[a]	425	599	2.07	0.85	0.60	-	−1.76	-	$1.9 \cdot 10^3$	[218]
$[Cu(dpp)_2]PF_6$[a]	443	672	1.98	0.82	0.37	−1.33	−1.48	0.65	239	[216]
$[Cu(dap)_2]BF_4$[b]	436	710	1.75	1.10	0.22	-	−1.83	-	260	[113, 219]
$[Cu(sbmpep)_2]PF_6$[a]	491	687	1.81	0.72	0.75	−1.92	−1.30	0.14	216	[220]

a: Recorded in DCM, b: Recorded in MeCN

5.6 Photoredox Catalysis

The tests for photoredox catalytic activity of the $[Cu(GUAqu)_2]^+$ systems were carried out under inert conditions in an EvoluChem PhotoRedOx Box™ using a 450 nm LED, the yields were quantified via ^{1}H-NMR spectroscopy with nitromethane as internal standard (for more information see Section 7.4).

The primary aim of these tests was to prove the activity of the employed entatic state model systems; the conditions and compositions of the reaction systems were therefore not optimized for yield. Initially, reactions were selected that are proposed to proceed via outer-sphere mechanisms that are characteristic for photoredox catalytic reactions. The first reaction tested was a hydrodehalogenation reaction, proposed to proceed via the reductive quenching cycle (*vide supra*, Section 1.8).

Next to a sacrificial donor that reduces the catalyst, the reaction requires a proton source to protonate the substrate. Therefore, commonly used donors are benzimidazolines like BIH that release protons upon oxidation. With a comparatively positive E_{ox} = −0.07 V *vs.* Fc/Fc^+, however, BIH cannot function as an electron donor for the investigated $[Cu(GUAqu)_2]^+$ systems.[221-222] Therefore, all screened substrates were also combined with different electron donors and, if necessary, tetraethylammonium chloride as proton source. $HNEt_3Cl$ was selected as the triethylammonium cation is proposed to serve as proton donor in various reductive and oxidative quenching mechanisms.[107, 114] For an overview of the used substrates and electron donors for the hyrodehalogenation, see Scheme 5.3. Iodo- and bromo aryl compounds were chosen as substrates since their corresponding X–C bonds are readily reduced.

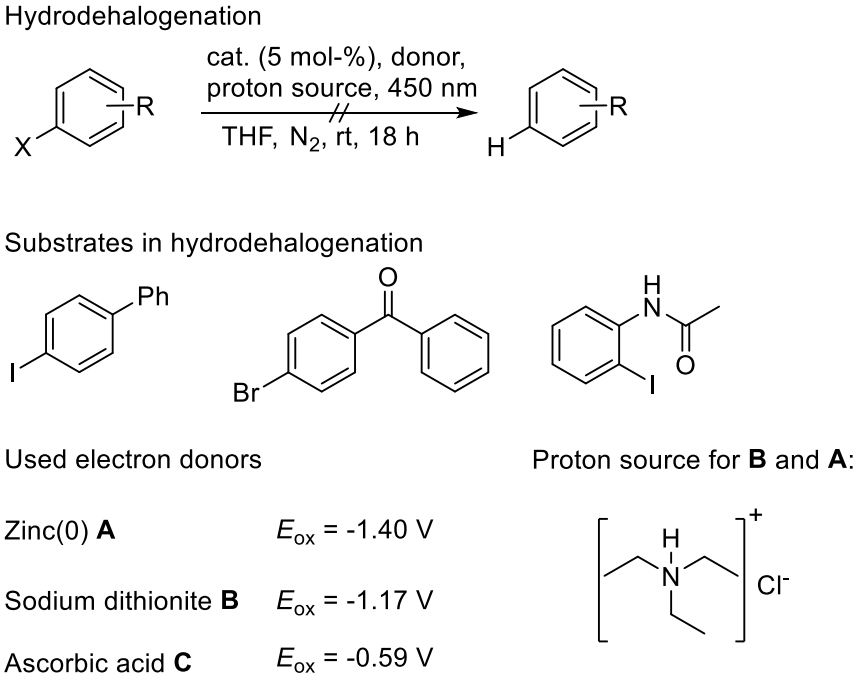

Scheme 5.3: Reaction scheme of the tested hydrodehalogenation, as well as tested substrates and electron donors. Screened catalysts were $[Cu(TMGqu)_2]PF_6$ (**C11–PF$_6$**), $[Cu(TMG2Mequ)_2]PF_6$ (**C13–PF$_6$**) and $[Cu(TMG2^cHexqu)_2]PF_6$ (**C15–PF$_6$**).

Unfortunately, no tested reaction system resulted in observable product in either ^{1}H-NMR spectra or ESI-mass spectra. The reason for the lack of observed activity is unclear, given that the donors' redox potentials all indicate compatible reactivity with the catalysts. While this could be explained by a lack of activity on the catalysts' side, problems with the electron donors and the proton source are also likely, as all tested compounds showed poor solubility. For a systematic reduction of the reaction system's complexity, a reductive coupling of benzyl bromide was attempted with different electron donors as it does not require additional proton donors (Scheme 5.4). However, this reaction also yielded no detectable product for any of the chosen electron donors.

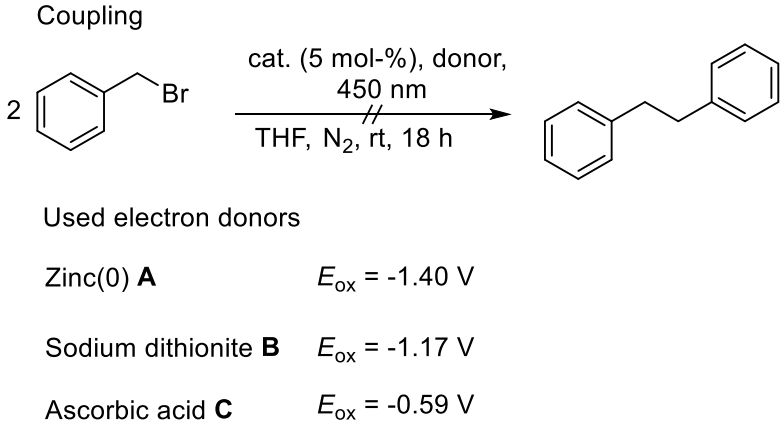

Scheme 5.4: Reaction scheme of the tested hydrodehalogenation, as well as tested substrates and electron donors. Screened catalysts were $[Cu(TMGqu)_2]PF_6$ (**C11–PF$_6$**), $[Cu(TMG2Mequ)_2]PF_6$ (**C13–PF$_6$**) and $[Cu(TMG2^cHexqu)_2]PF_6$ (**C15–PF$_6$**).

Lastly, to forego the necessity of an electron donor, an atom transfer radical addition (ATRA) reaction was tested. ATRA reactions follow atypical mechanisms in copper photochemistry as they are proposed to involve a combination of outer-sphere and inner-sphere reactivities.[134] The additional inner-sphere reactivity circumvents the electrochemical complication of the catalysts' negative E_{ox} potentials by enabling a regeneration of the catalyst without requiring a strong sacrificial donor (further information in Section 1.9).[134] The tested reaction (Scheme 5.5), was conducted following a modified procedure by Reiser *et al*.[223]

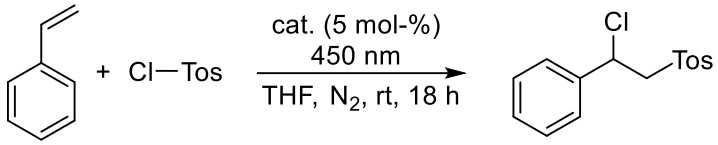

Scheme 5.5: Reaction scheme of the tested ATRA reactions. Screened catalysts were $[Cu(TMGqu)_2]PF_6$ (**C11–PF$_6$**), $[Cu(TMG2Mequ)_2]PF_6$ (**C13–PF$_6$**) and $[Cu(TMG2^cHexqu)_2]PF_6$ (**C15–PF$_6$**).[223]

^{1}H-NMR measurements show the desired product using the combination of any complex and irradiation of light, while the absence of any of the two resulted in no or only traces of product (Table 5-6). The complexes are therefore demonstrably able to perform as photoredox catalysts. The lack of activity in the reactions above is therefore likely due to inadequate choice of electron donors.

Table 5-6: Catalysts, wavelengths and yields of the tested ATRA reactions and the corresponding controls.

	Catalyst	λ [nm]	Yield (NMR) [%]
1	**C11–PF$_6$**	450	11
2	**C13–PF$_6$**	450	30
3	**C15–PF$_6$**	450	30
4[a]	**C15–PF$_6$**	-	-
5[b]	**C15–PF$_6$**	-	-
6	-	450	-

a: Vial was located outside of photoreactor for the duration of the reaction. b: Vial was located inside photoreactor and darkened with aluminum foil.

The obtained yields are rather low, ranging from 11 to 30 % from **C11–PF$_6$** to **C15–PF$_6$**, as compared to up to 96 % for $[Cu(dap)_2Cl]$ reported by Reiser *et al*.[223] While the yields roughly scale with the expected excited state lifetime of the complex cations, the kinetics are obscured by the inner-sphere steps and thus prohibit a direct correlation of the lifetime to the yields. A possible way to achieve a better understanding of this correlation would be a mechanistic investigation of the ATRA reaction to assess the

main kinetic barriers in the mechanism. An investigation of this scale is beyond the scope of this thesis but could potentially be subject of future research in this field.
Overall, the $[Cu(GUAqu)_2]^+$ systems were successfully employed as photoredox catalysts in an ATRA reaction. DFT computations of the singlet and triplet geometries, as well as the experimentally obtained small Stokes shifts suggest the complexes' rigid coordination geometry also applies in the excited state. However, their comparatively low lifetimes and highly reducing redox potentials limit the range of possible applications of the tested catalysts outside of ATRA reactions. The comparatively low yields from these reactions show that there is potential for the optimization of reaction conditions as well as improvement of ligand design focused on increasing the excited state lifetime of the $[Cu(GUAqu)_2]^{+/2+}$ systems.

6 Conclusion and Outlook

6.1 Conclusion

Within this thesis, three distinct electron transfer dynamics of Cu complexes with guanidine quinolinyl models were explored, focusing on structure-property relationships and their electron transfer mechanisms.

In the first part of the thesis, novel and literature-known Cu complexes of tetradentate tripodal guanidine quinolinyl ligands were synthesized and examined with respects to their coordination geometries, redox properties and electron transfer mechanism. The ligands **L1** to **L3** were equipped with either TMG or DMEG units to investigate the effects of their different steric impact on the electron transfer kinetics and coordination chemistry.

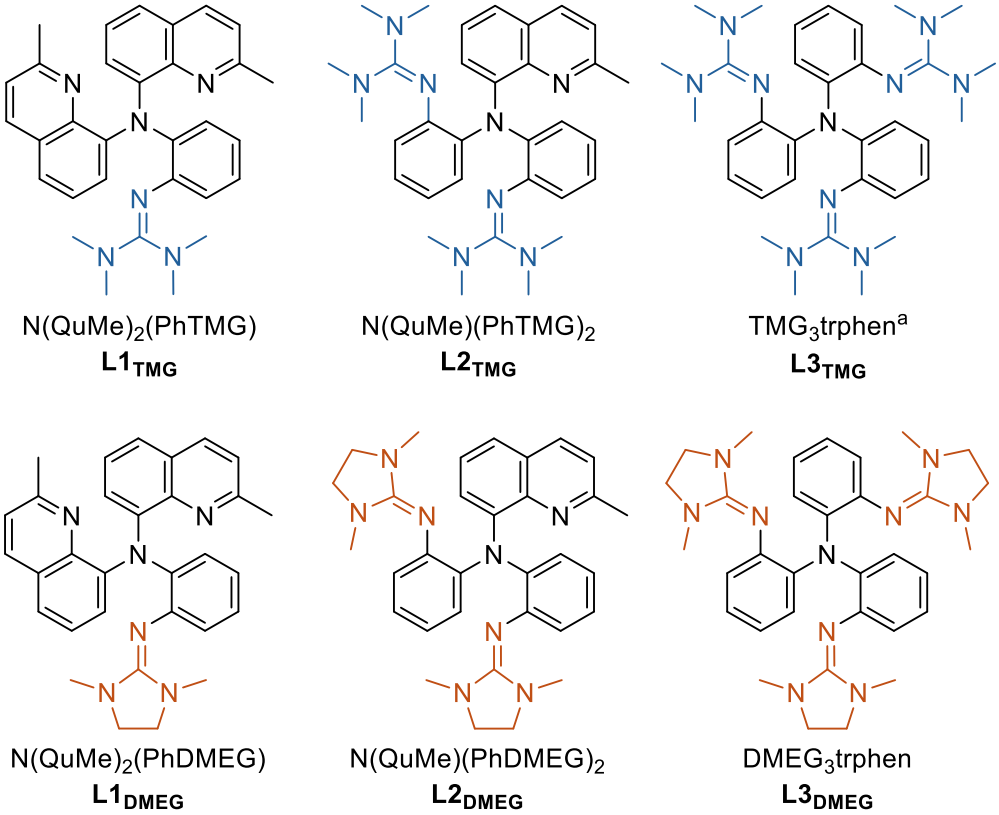

Figure 6.1: Scheme of the herein synthesized and investigated tripoda, tetradentate ligands. a: First reported by Cronin and Stavropoulos *et al.*[156]

The Cu(I) complexes exhibit unusual umbrella distortions, characterized by elongated N_{Am}–Cu(I) bonds, leading to distorted trigonal pyramidal coordination geometries. These distortions become increasingly pronounced for higher numbers of guanidine moieties in the ligand scaffolding, which is likely due to electronic effects between the aromatic backbone and the central amine.

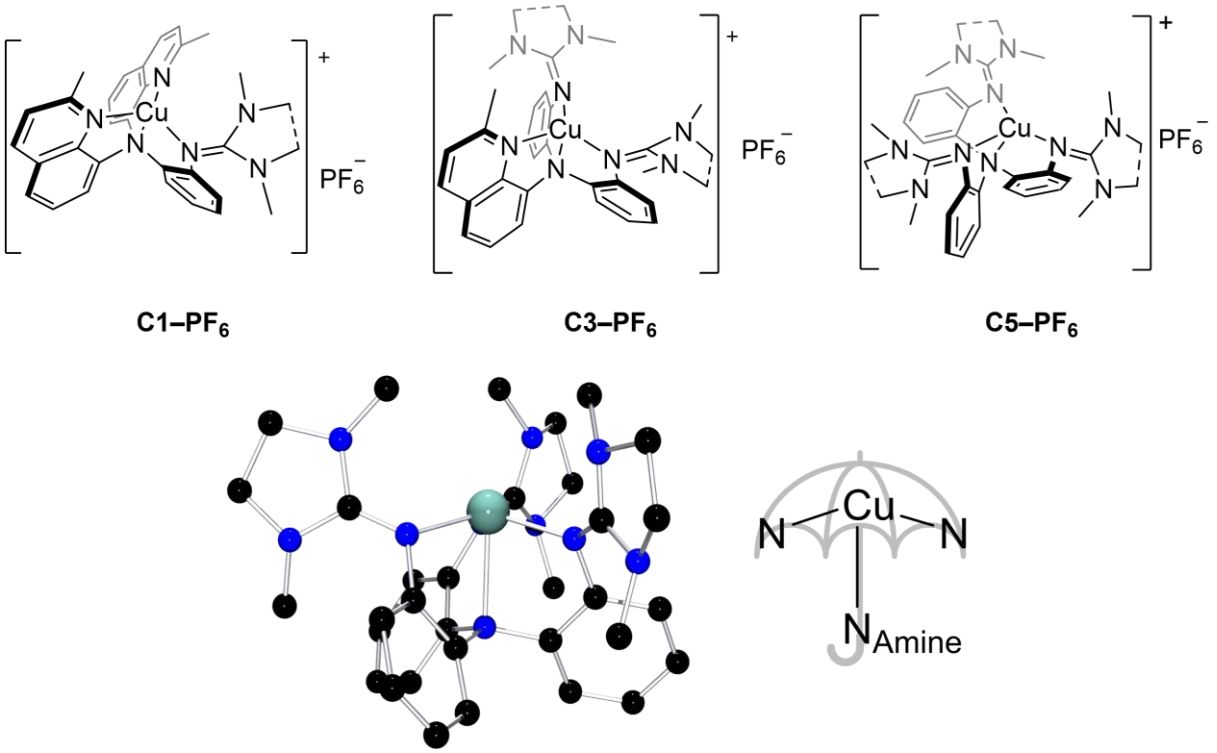

Figure 6.2: The herein studied Cu(I) complexes of the tripodal, tetradentate copper complexes exhibit an uncommon umbrella distortion characterized by an elongated N_{Am}–Cu(I) bond.

Within literature, the herein reported complex pairs **C1**, **C3** and **C5** represent rare cases of tetracoordinate umbrella distorted systems without an additional co-ligand, likely due to the steric bulk of the guanidine moieties. The Cu(II) complexes could not be isolated as they were found to be unstable, owing to possible redox active properties of the ligands. However, DFT simulations suggest them to expand their coordination number to five, coordinating an acetonitrile co-ligand from solution and rendering the model systems coordination-variant. Conformational analysis of these Cu(II) complexes further suggests them to exist in a dynamic equilibrium of up to four conformers.

Electron transfer analysis via cyclic voltammetry revealed quasi-reversible redox processes that are preceded by a reaction step, most likely a change of coordination number by association of an acetonitrile co-ligand. Most notable is the pronounced S-shape in the oxidative wave exhibited by the DMEG-substituted complexes that is consistent with fast pre-equilibrium structural reorganizations. Kinetic studies of self-exchange reactions further showed that the electron transfer rates increase significantly with decreasing steric bulk, spanning four orders of magnitude. Computational modeling supported this observation by linking steric hindrance to inhibited ligation of acetonitrile co-ligands. Interestingly, the complex pairs **C1** to **C3** therefore uniformly follow an addition-oxidation pathway (Pathway A, Figure 6.3), an uncommon mechanism as most Cu(I) systems in literature reportedly follow the opposite oxidation-addition pathway (Pathway B, Figure 6.3).

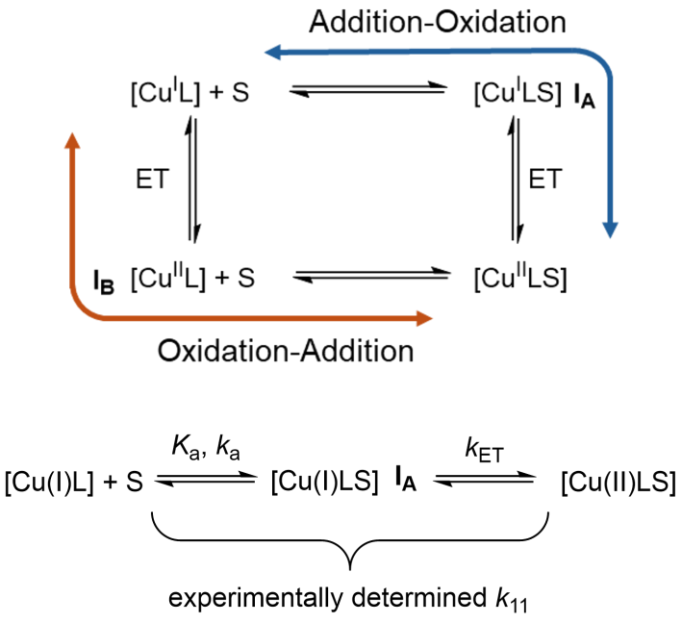

Figure 6.3: The herein studied coordination-variant electron transfer models follow the atypical addition-oxidation mechanism that results in a gated electron transfer.

Further, this mechanistic deviation corresponds to the presence of the umbrella distortion in the Cu(I) complexes that is absent in the reported complexes of other tripodal tetracoordinate electron-transfer models. The investigated complexes **C1** to **C3** therefore demonstrate that molecular design can alter the electron transfer mechanism of coordination-variant model systems. While the studied tripodal systems do not follow the common definition of the entatic state, the umbrella distortion could be seen as an example of the effects of coordinative strain on Cu(I) ions in coordination-variant model systems.

In the second part of the thesis, the electron transfer properties coordination-invariant Cu-complexes of GUAqu ligands with sp^2-hybridized substituents were investigated. For this purpose, the ligands TMG2NMe$_2$qu (**L5**) and TMG2Phqu (**L6**) were synthesized and characterized. Reactions of these ligands with Cu(I) and Cu(II) salt with weakly coordinating anions yielded the novel bis(chelate) Cu(I) and Cu(II) complex cations **C7**-**C10** that were investigated in the solid state via X-ray diffraction. The solid-state structures of **C7** and **C8** (redox couple **R4**) show strongly distorted coordination geometries with high structural accordance. Notable are the strongly elongated N_{Qu}-Cu(I) bonds in **C7** of over 2.15 Å that imply significant steric strain of the dimethylamine substituents on the coordination sphere. The solid-state structures of **C8** and **C9** (redox couple **R5**) display two different conformations that can be classified as a trans and a cis conformer, with the latter being notably flattened compared to the trans conformer.

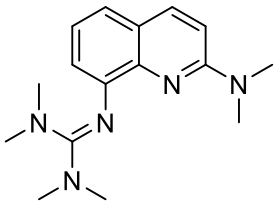

TMG2NMe$_2$qu (**L5**)

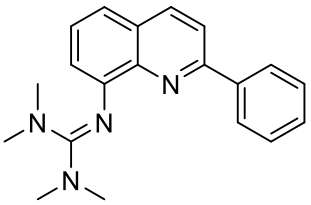

TMG2Phqu (**L6**)

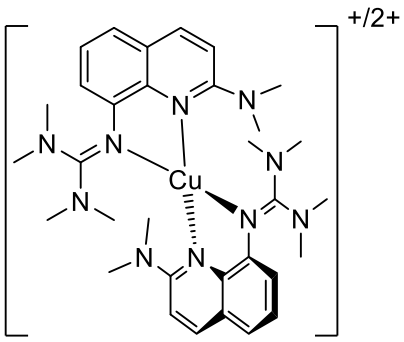

[Cu(TMG2NMe$_2$qu)$_2$]$^{+/2+}$ (**C7**, **C8**, **R4**)

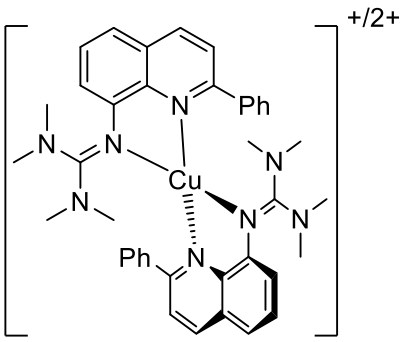

[Cu(TMG2Phqu)$_2$]$^{+/2+}$ (**C9**, **C10**, **R5**)

Figure 6.4: Novel GUAqu ligands and their redox couples investigated in this thesis.

DFT simulations of all complex cations are generally in good agreement with the solid-state data, however the elongated bond lengths of **C7** could not be accounted for by DFT without freezing bonds, which is likely due to the poor consideration of dispersion interactions by DFT. The conformational space of **C9** and **C10** was investigated via xtb and CREST, yielding seven distinct conformers. The calculated Boltzmann distributions of these conformers reveal that the two conformers found in the solid state are likely the prominent species in solution for the Cu(I) state, while those for the Cu(II) state exclusively prefer the cis-1 conformer initially found in the solid-state structure of the Cu(II) complex salt **C10–OTf**. Investigation of the redox properties of **R4** and **R5** via cyclic voltammetry show reversible redox waves similar to those of other [Cu(GUAqu)$_2$]$^{+/2+}$ systems. For **R5**, the redox potential was recorded once starting from **C9–PF$_6$** as well as **C10–OTf** to investigate potential conformational interconversions and their influences on the electrochemical properties. Since the two redox potentials show no significant differences, the prevalent and redox active conformer for both oxidation states of **R5** is likely to be the cis-1 conformer.

The calculated charge transfer energies show a strong correlation between $\Delta E_{CT,total}$ of the redox couples **R4** to **R8** and their corresponding redox potentials, with the differences in $E_{CT,total}$ increasing with more negative redox potentials. Contrary to the tripodal model systems, the ratio of charge transfer energy $\Theta E_{CT,total}$ does not seem to correlate with the redox potentials. This difference in both systems was linked to the dominating electronic factors in the redox potentials of the tripodal model systems as

compared to the structural factors that dominate the electrochemical behavior of the 2-substituted $[Cu(GUAqu)_2]^{+/2+}$ systems.

Lastly, electron transfer kinetics of **R4** and **R5** were investigated by determining their k_{11} and their reorganization energies λ_{11}. Together, these parameters reveal that the bond contraction of the Cu–N_{Qu} bond of **R4** imposes a significant kinetic barrier on the redox reaction, resulting in a small k_{11} despite otherwise ideal entasis of the redox couple. **R5**, on the other hand, displays a k_{11} on the order of 10^5 M^{-1} s^{-1}, the highest of any $[Cu(GUAqu)_2]^{+/2+}$ model reported prior that was linked to the low amount of internal reorganization energy that arises from the marginal structural differences between the Cu(I) and Cu(II) complex cations (Figure 6.5). The studies on novel GUAqu ligands and complexes herein therefore show that sp^2-hybridized substituents in the 2-position have nuanced effects on the coordination geometry and preferred conformations of the complexes and are prone to intramolecular interactions that highlight the necessity of accurate structural description. Hence, **R5** balances all structural and electronic effects identified earlier in an ideal way to provide very high k_{11}.

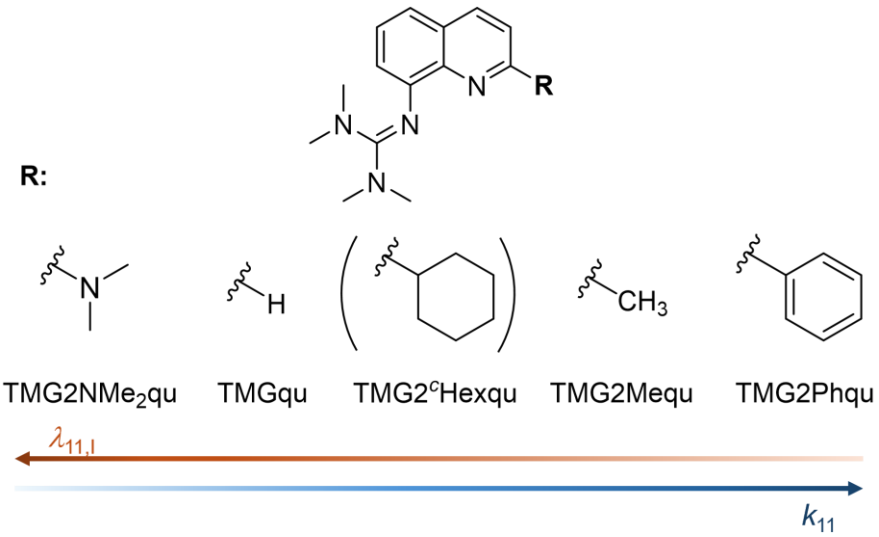

Figure 6.5: Observed correlation between the internal reorganization energy $\lambda_{11,I}$, and k_{11} of the studied 2-sbstituted $[Cu(GUAqu)_2]^{+/2+}$ systems. The bracketed ligand represents an outlier to this trend.

The third part of this thesis focused on investigating the photochemical properties of the complex cations $[Cu(TMGqu)_2]^+$ (**C11**), $[Cu(TMG2Mequ)_2]^+$ (**C13**) and $[Cu(TMG2^cHexqu)_2]^+$ (**C15**). DFT optimized geometries of the ground state and triplet states suggest that the increased steric bulk of the substituent leads to a reduction in the amount of structural flattening in the triplet state that is overall comparable to that between the Cu(I) and the Cu(II) state. Transient XAFS measurements further show that the triplet state lifetime of **C13** increases relative to **C11** according to the computationally obtained energy gap between the triplet and the ground state. Compared to phenanthroline-based copper photosensitizers, the obtained triplet lifetimes are short lived despite a large energy gap, for as of now unknown reasons.

Additionally, cyclic voltammograms of the complexes in THF show that the complexes have overall strongly negative redox potentials, while the ligands exhibit meta-stable properties under the applied conditions. Fluorescence emission spectroscopy yielded low-intensity emission of the MLCT at around 550 nm, with small Stokes shifts and high excited state redox potentials for all three complexes that become apparent when compared to phenanthroline-based copper photosensitizers. These small Stokes shifts and high excited state energies highlight the small structural changes of the studied $[Cu(GUAqu)_2]^+$ systems upon excitation, underscoring their entatic state.
Lastly, the complexes' activity in photoredox catalytic reactions were tested. While classical reductive and oxidative quenching pathways did not lead to any detectable product, all three complexes showed photoredox catalytic activity in an ATRA reaction with yields that increase with the expected excited state lifetimes of the complexes. While the studied guanidine quinoline systems do not reach comparable activity to phenanthroline-based systems, this study provided a proof of concept concerning the use of the entatic state concept to tune and improve the properties of copper photosensitizers.

6.2 Outlook

Future studies regarding the tripodal model systems could focus on investigating the tripodal pentacoordinate ligand scaffolding that could not be successfully isolated in this study. Since the concept demonstrably does not require a weak methyl ester donor to achieve high self-exchange rates,[16] a potential ligand could include another N-donor in the form of a pyridinyl substituent in 2-position of the quinolinyl moiety. This N-donor would serve to facilitate a better synthesis and also increase the ligand's chemical stability. This concept could be connected with a varying number of aromatic arms that could further probe the influence of the umbrella distortion on the electron transfer mechanism (Figure 6.6).

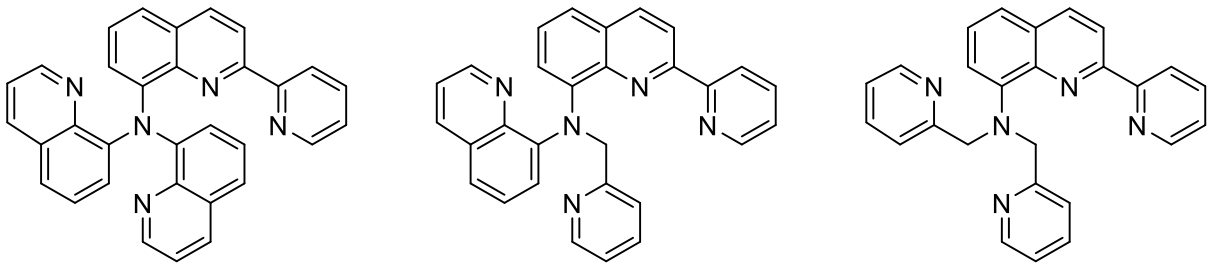

Figure 6.6: Potential ligand frameworks that could be used in future studies of coordination-variant tripodal electron transfer models.

Regarding the thermal electron transfer properties of the $[Cu(GUAqu)_2]^{+/2+}$ systems, the GUAqu ligand scaffolding could be further decorated to potentially increase the

self-exchange rates even further. The TMG2Phqu ligand represents a good basis for investigations in this regard, as the cis conformation and its change upon oxidation or reduction is possibly influenced by intermolecular interactions. Therefore, interesting novel GUAqu ligand system could include substituents in meta or para position of the phenyl moiety with the goal of increasing these intermolecular interactions, potentially increasing the structural accordance between the Cu(I) and Cu(II) state. Potential substituents include methyl-substituents that increase the dispersion interactions between the two ligands, but also F-, CF_3-groups that should increase the π-π interactions (Figure 6.7).

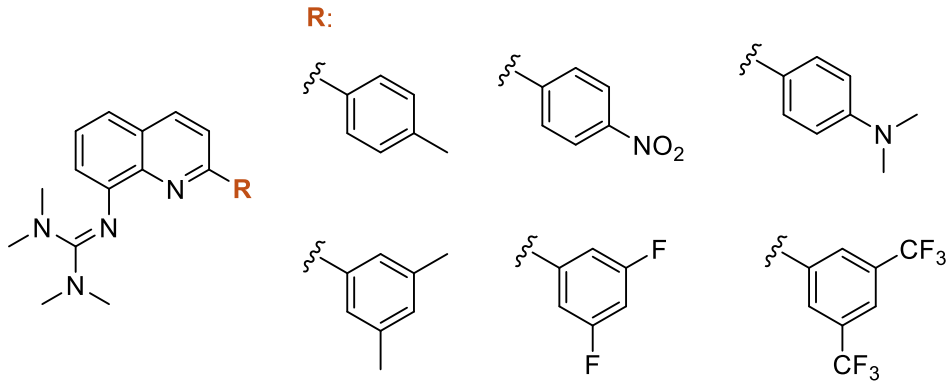

Figure 6.7: Potential substituents in ortho- and meta-position of the phenyl ring in the quinolinyl's 2-position.

To improve the understanding of entasis and structural flattening, the photophysical properties of the $[Cu(GUAqu)_2]^{+/2+}$ systems could be further investigated by conducting transient XAFS studies of $[Cu(TMG2^cHexqu)_2]PF_6$ as well as the herein reported **C7** and **C9**. These would serve to obtain the triplet lifetimes of the systems as well as help to understand the structural changes the complexes undergo upon excitation. These experiments could be augmented by further transient analytics, including pump-probe Raman spectroscopy that have higher temporal resolution to also investigate the effects of the systems' entasis on their intersystem crossing rates and further excited state dynamics.

Future photoredox catalytic studies could potentially look into the ATRA activity of the 2-substituted model systems, mostly focused on substrate scope. An additional point of interest would be mechanistic investigations of the ATRA reactions, as these are presently underrepresented in literature and mechanistic proposals often include Cu(III) as a potential participating species.

7 Experimental Section

7.1 Data Availability

Parts of chapter 3 and chapter 4 of this thesis were previously published. The data is available via the Chemotion repository and RADAR4Chem.

Chapter 3:
The obtained analytical Stopped-Flow and cyclic voltammetry data, as well as the optimized coordinates from DFT computations are provided in the RADAR4Chem repository: https://www.radar-service.eu/radar/en/dataset/snmphx276tt041sa?token=QwPxHaoRvtRHZDfFgQFZ

Experimental data like NMR-, mass- and IR-spectra can be viewed in the Chemotion repository: https://dx.doi.org/10.14272/collection/ToS_2024-10-09

Chapter 4:
The obtained analytical Stopped-Flow and cyclic voltammetry data, as well as the optimized coordinates from DFT computations are provided in the RADAR4Chem repository: DOI:10.22000/ab0bmuwhdgfs0tqq

Experimental data like NMR-, mass- and IR-spectra can be viewed in the Chemotion repository: https://dx.doi.org/10.14272/collection/ToS_2024-11-28

7.2 General Aspects, Chemicals and Solvents

All reactions and manipulations that require inert conditions were carried out under nitrogen atmosphere (99.999 %), with the nitrogen gas being purified by passage through a column filled with SICAPENT®. If necessary, the solvents were purified by standard literature procedures and degassed by three circles of freeze pump thaw.[224] The Vilsmeier salts chloro-*N*,*N*,*N*',*N*'-tetramethylformamidinium chloride (TMG-VS) and *N*,*N*'-dimethylethylenechloroformamidinium chloride (DMEG-VS) were synthesized according to the literature.[225-226] The ligands TMGqu, TMG2Mequ and TMG2^{c}Hexqu, as well as $[Co(bpy)_3](PF_6)_3$ and the copper salts $[Cu(II)(MeCN)_4](OTf)_2$ and $[Cu(II)(MeCN)_4](BF_4)_2$ were previously synthesized by coworkers. All other chemicals were purchased from commercial suppliers and used without further purification.

Table 7-1: List of purchased chemicals.

Compound (purity)	Supplier
Acetone (99.8 %)	Acros
Acetonitrile (≥ 99.8 %)	Fisher Chemical
Acetonitrile-d_3 (≥ 99.8 %)	Sigma Aldrich
Acrolein (90 %)	Sigma Aldrich
Ascorbic acid	Sigma Aldrich
Bromobenzene (>98 %)	TCI
1-Bromo-2-nitrobenzene	abcr
(4-bromophenyl)(phenyl)methanone (99.63 %)	BLDpharm
Chloroform-d_1 (≥ 99.9 %)	Sigma Aldrich
2-Chloro-8-nitroquinoline (98 %)	Angene
2-Chloroquinoline (99.93 %)	BLDpharm
Dichloromethane (≥ 99.8 %)	Fisher Chemical
Dichloromethane-d_2 (≥ 99.8 %)	Sigma Aldrich
Diethylammonium chloride (99 %)	Acros
Diethyl ether (≥ 99.5 %)	Fisher Chemical
1,4-Dioxane (99 %)	abcr
Ethyl acetate (≥ 99.8 %)	Fisher Chemical
Ferrocene	Not specified
1-Fluoro-2-nitrobenzene	Fluorochem
Hydrochloric acid (37 %)	VWR
Hydrogen (≥ 99.999 %)	Westfalen AG
Iodine (≥ 99.8 %)	ACS reagent
4-iodo-1,1'-biphenyl (97.5 %)	BLDpharm
Magnesium sulfate, anhydrous	Grüssing
Methanol (≥ 99.9 %)	Fisher Chemical
4-methylbenzenesulfonyl chloride (>99 %)	Fluka
2-Methyl-8-nitroquinoline (≥ 98.0 %)	TCI
N-(2-iodophenyl)acetamide (98 %)	BLDpharm
Nitric acid, fuming (99 %)	Sigma Aldrich
n-Hexane (≥ 95 %)	Fisher Chemical
n-Pentane (≥ 99 %)	Fisher Chemical
Potassium carbonate (99.5 %)	Grüssing
Potassium hydroxide (85 %)	Grüssing
Phenylboronic acid (98 %)	abcr
Palladium on acitvated charcoal (10 % Pd)	Sigma Aldrich
Palladium tetrakis(triphenylphosphine) (99.9 %)	Sigma Aldrich
Pyrazole (98 %)	abcr
Selenium dioxide	Not specified
SICAPENT®	Merck
Sodium bicarbonate (99.5 %)	Grüssing
Sodium dithionite	Merck
Sodium hydroxide (99 %)	Grüssing
Sodium sulfate, anhydrous (99.5 %)	Fisher Chemical

Sodium thiosulfate pentahydrate (99.5 %)	Grüssing
Sulfuric acid (≥ 95 %)	Fisher Chemical
Tertbutylammonium hexafluorophosphate (99.9 %)	Sigma Aldrich
Tetrahydrofuran (100 %)	VWR
Tetrakis(acetonitrile)copper(I) hexafluorophosphate (97 %)	Sigma Aldrich
trans-Crotonaldehyde (≥ 99 %)	Sigma Aldrich
Thiamine hydrochloride (99 %)	Fluka
Toluene (≥ 99.9 %)	Grüssing
Triethylamine (≥ 99.5 %)	Sigma Aldrich
Triethylammonium chloride	Not specified
Zinc (powder)	Not specified

7.3 Analytics and Compound Purification

7.3.1 Nuclear Magnetic Resonance Spectroscopy

The nuclear magnetic resonance (NMR) spectra were recorded on a Bruker Avance III HD 400 or a Bruker Avance II 400 nuclear resonance spectrometer at 25 °C. The 1H NMR spectra were referenced to the solvent residual resonance, and the 13C{H} NMR spectra were referenced to the solvent resonance. The solvent resonances in the 1H and 13C{H} NMR spectra were defined relative to the external standard tetramethylsilane (TMS) as reported in the literature.[227] Data in the 1H and 13C NMR spectra are stated as follows: chemical shift (δ in ppm) (multiplicity, coupling constant (*J* in Hz), integration). To describe the multiplicity of the resonances the following abbreviations are used: s = singlet, d = doublet, t = triplet, q = quartet, m = multiplet or combinations thereof. The chemical shifts of the compounds were assigned with the use of two-dimensional NMR spectroscopic experiments (COSY, HSQC, HMBC, APT). Hydrogen and carbon atoms of all molecules are consecutively numbered for a clear and simple classification. For the Bruker Avance III HD 400, the software Topspin (Version 3.5 pl 7) from Bruker Corporation and for the Bruker Avance II 400, the software TopSpin (Version 2.1) from Bruker Corporation were used for data acquisition. For visualization and examination of the NMR spectra the software MestReNova (Version 12.0.1-20560) from Mestrelab Research was used. Selected NMR spectroscopic data were deposited as original data in the Chemotion Repository and are published under an Open Access model.[228-229]

7.3.2 Electron Spray Ionization High Resolution Mass Spectrometry

The electron spray ionization (ESI) high-resolution (HR) mass spectra were performed and recorded on an UHR-TOF Bruker Daltonik maXis II or a ThermoFisher Scientific LTQ Orbitrap XL. Detection was in positive mode. The mass spectrometer was

calibrated subsequently to every experiment via direct infusion of a L-proline sodium salt solution, which provided a *m*/*z* range of singly charged peaks up to 3000 Da in both ion modes. For the ThermoFisher Scientific LTQ Orbitrap XL the source voltage was 4.49 kV and the capillary temperature was 299.54 °C. The tube lens voltage was set between 110 and 130 V. For the Bruker Daltonik maXis II, the software otofControl (Version 6.3, Build 0.5) and Compass DataAnalysis (Version 5.3, Build 556.396.6383) from Bruker Corporation and for the ThermoFisher Scientific LTQ Orbitrap XL, the software Thermo Xcalibur (Version 4.5.445.18) were used for data acquisition and examination. Selected ESI-HRMS data were deposited as original data in the Chemotion Repository and are published under an Open Access model.[228-229]

7.3.3 Fourier Transform Infrared Spectroscopy

The Fourier transform infrared (FTIR) spectra were recorded on a Shimadzu IRTracer 100 using a CsI beam splitter in combination with an attenuated total reflectance (ATR) unit (Quest model from Specac utilising a robust monolithic crystalline diamond) in a resolution of 2 cm^{-1}. For data acquisition, the software LabSolution IR (Version 2.15) from Shimadzu Corporation was used. The obtained IR data are stated as reciprocal wave numbers of the absorption (cm^{-1}). The vibration bands of the spectra are characterized based on the Würzburger Model as follows: vw = very weak, w = weak, m = medium, s = strong and vs = very strong. Selected FTIR spectroscopic data were deposited as original data in the Chemotion Repository and are published under an Open Access model.[228-229]

7.3.4 Thin Layer Chromatography

Thin layer chromatography (TLC) was performed with TLC sheets from MACHEREY-NAGEL pre-coated with a layer of silica gel 60 with a thickness of 0.20 mm and a fluorescent indicator.

7.3.5 Column Chromatography

Column chromatography was performed with Geduran® Si 60 (40-63 µm) from Merck.

7.3.6 Single-Crystal X-Ray Diffraction

The ellipsoid plots and crystallographic data of all reported molecular structures in the solid state are listed in Section 9.1.The data were collected with a four-circle goniometer Stoe Stadivari with Dectris Pilatus3 R 200 K hybrid pixel detector using

GeniX 3D high flux Mo-K_α radiation (λ = 0.71073 Å) at 150 K for **C9–PF_6·DCM** and at 100 K for every other compound. The temperature was controlled by an Oxford Cryostream 800. Crystals were mounted on cryoloops with perfluorinated oil. Data were collected with X-Area Pilatus,[230] indexed with X-Area Recipe[231] and integrated with X-Area Integrate.[232] A spherical absorption correction was performed with STOE X-Red32 followed by a multi-scan absorption correction and scaling of reflections with X-Area LANA.[233]

The structures were solved by intrinsic phasing (ShelXT[234]) or direct methods (ShelXS[235]) and refined against F^2 with the full-matrix least-square method of ShelXL[236] using the graphical user interface ShelXle.[237] Non-hydrogen atoms were refined with anisotropic displacement parameters. All hydrogen atoms were localized at idealized positions and refined with isotropic displacement parameters. All methyl groups were allowed to rotate but not to tip.

In **C10–OTf·H_2O** and **$C3_{TMG}$–PF_6·DCM,** it was not possible to model the disordered solvent molecules in an adequate manner, and the data set was treated with the SQUEEZE routine as implemented in PLATON.[238-239] **C7–PF_6·DCM** is a twin and the data set was treated with the TwinRotMat routine as implemented in platon (rotation axis in reciprocal space (2 -1 0) and twin law 1 0 0 -1 -1 0 0 0 -1).[238-239]

Full crystallographic data of **$C1_{TMG}$–PF_6·MeCN**, **$C1_{DMEG}$–PF_6·MeCN**, **$C3_{TMG}$–PF_6·DCM**, **$C3_{DMEG}$–PF_6·DCM**, **$C5_{DMEG}$–PF_6·MeCN**, **C7–PF_6·DCM**, **C8–PF_6**, **C9–PF_6·DCM** and **C10–OTf·H_2O** have been deposited with the Cambridge Crystallographic Data Centre as supplementary no. CCDC – 2382530 for **$C1_{TMG}$–PF_6·MeCN**, CCDC – 2382531 for **$C1_{DMEG}$–PF_6·MeCN**, CCDC – 2382528 for **$C3_{TMG}$–PF_6·DCM**, CCDC – 2382529 for **$C3_{DMEG}$–PF_6·DCM**, CCDC – 2382527 for **$C5_{DMEG}$–PF_6·MeCN**, CCDC – 2401618 for **C7–PF_6·DCM**,CCDC – 2401619 for **C8–PF_6**, CCDC – 2401616 for **C9–PF_6·DCM** and CCDC – 2401617 for **C10–OTf·H_2O**. Copies of the data can be obtained free of charge on application to CCDC, 12 Union Road, Cambridge CB2 1EZ, UK (fax: (+44)1223-336-033; e-mail: deposit@ccdc.cam.ac.uk).

7.3.7 Powder Diffraction (PXRD)

PXRD experiments were performed at ambient conditions on flat samples using a STOE STADI P diffractometer with Debye-Scherrer geometry (Cu-$K_{\alpha1}$, λ = 1.540598 Å, STOE image plate detector IP-PSD).

7.3.8 Cyclic Voltammetry

7.3.8.1 Cyclic Voltammetry under Aerobic Conditions

The measurements were performed at room temperature with a METROHM AUTOLAB PGSTAT 101 potentiostat using a three-electrode arrangement with a Pt disc working electrode (1 mm diameter), a Pt wire as counter electrode and an Ag/AgCl (in saturated ethanolic LiCl) reference electrode. The measurements were performed in MeCN and 100 mmol/L NBu_4PF_6 with a sample concentration of 1 mmol/L at room temperature. Ferrocene was added as an internal standard after the measurements of the sample and all potentials are referenced relative to the Fc/Fc^+ potential. Cyclic voltammograms were measured with sweep rates of 200 mV s^{-1}, 100 mV s^{-1}, 50 mV s^{-1} and 20 mV s^{-1}. For data acquisition and examination, the software NOVA 2.1.5 (Build 7691) from Metrohm Autolab was used. For visualization of the cyclic voltammograms the software OriginPro 2021b (Version 9.8.5.212) from OriginLab was used.

7.3.8.2 Cyclic Voltammetry under Inert Conditions

Cyclic voltammetric measurements were performed at room temperature with a METROHM AUTOLAB PGSTAT 101 potentiostat with a three-electrode arrangement with a Pt disc working electrode (1mm diameter), an Ag wire pseudo reference electrode and a glassy-carbon counter electrode under inert conditions. Before starting the measurement of the sample, a test measurement only with solvent and conducting salt was performed to check the setup. The samples were prepared with a 1 mmol/L concentration of analyte and 100 mmol/L NBu4PF6 as supporting electrolyte in absolute and degassed solvent (acetonitrile or THF). Ferrocene was added as internal standard after each measurement. All potentials are referenced relative to the Fc/Fc+ couple. The cyclic voltammograms were measured with sweep rates of 20, 50, 100 and 200 mVs^{-1}. For data acquisition and examination, the software NOVA 2.1.5 (Build 7691) from Metrohm Autolab was used. For visualization of the cyclic voltammograms the software OriginPro 2021b (Version 9.8.5.212) from OriginLab was used.

7.3.9 Electron Paramagnetic Resonance Spectroscopy (EPR)

The electron paramagnetic resonance (EPR) spectroscopic measurements were performed with a Magnettech Miniscope MS 400. The setup included the Resonator Rectangular TE102 and a microwave frequency counter Magnettech FC. The solutions of the Cu(II) complexes were prepared as a 5 mM solution in MeCN. The measurements were performed in EPR tubes, closed with Critoseal® wax, at 77 K. The

experiments were carried out using a microwave frequency of 9.428 ± 0.001 GHz, a B_0 field of 328 mT, a B_0 sweep of 180 mT and a modulation amplitude of 0.40 mT. For data acquisition, the software MiniscopeCtrl (Version 1.0.0.1542) from magnettech GmbH was used. The spectra were simulated with the Matlab tool EasySpin to obtain further information about the spin system.[205] The applied simulation function was "pepper", a function for solid state continuous wave EPR with an arbitrary number of spins. For visualization of the EPR spectra, the software OriginPro 2021b (Version 9.8.5.212) from OriginLab was used.

7.3.10 UV/vis Spectroscopy

The UV/vis spectra were recorded with a Cary 60 spectrophotometer from Agilent Technologies in combination with quartz glass cuvettes (1 mm, QS) at room temperature. The solutions (c = 1 mM) were prepared from the corresponding complexes. For data acquisition, the software Cary WinUV (Version 5.1.3.1042) from Agilent Technologies was used. For visualization of the UV/vis spectra, the software OriginPro 2021b (Version 9.8.5.212) from OriginLab was used.

7.3.11 Stopped-Flow UV/vis Spectroscopy

7.3.11.1 Stopped-Flow UV/vis Spectroscopy of Tripodal Model Systems

The stopped-flow spectroscopic measurements were performed with a HI-TECH Scientific SF-61SX2 device with a diode array detector. The optical light path for transmission of the quartz glass cuvette was 10 mm. The mixing time is given by HI-TECH to amount to 2 ms. UV/vis spectra in a wavelength range of 300 nm to 800 nm were detected with a maximum temporal resolution of 375 s. The analyses were carried out with the TgK Scientific program Kinetic Studio 4.0.8.18533. For visualization and examination of the results the software OriginPro 2021b (Version 9.8.5.212) from OriginLab was used.

The cross reactions of the Cu(I) complexes with the counter complex $[Co(bpy)_3](PF_6)_3$ were monitored. To measure the kinetic of the cross reaction a solution of each Cu(I) complex (0.4 mM) in MeCN was mixed with five differently concentrated solutions (with reactant in excess) of $[Co(bpy)_3](PF_6)_3$ complex (2 mM, 3 mM, 4 mM, 5 mM and 6 mM), corresponding to 5, 7.5, 10, 12.5 and 15 equivalents relative to the employed Cu(I) complex. For every concentration of $[Co(bpy)_3](PF_6)_3$ 5 measurements were performed. Each measurement for each Cu(I) complex was repeated twice.

For $[Cu(I)\{N(QuMe)(PhDMEG)_2\}]PF_6$ (**$C3_{DMEG}$–PF_6**), a jump in the k_{obs}-values was observed between $[Co(bpy)_3](PF_6)_3$ concentrations of 3 mM and 4 mM (see Fig. 9.19,

Section 9.3.1) that was apparent in both separately conducted measurements. The Cu(I) complex has a comparatively weak absorbance in a similar range where the employed counter-complex is active as well (see Section 9.3.1.1), rendering an interference of the counter-complex at higher concentrations a likely cause. Since only the relative position and not the slope seems to be affected, the cross-reaction rate k_{12} was evaluated from 3 mM to 6 mM to remain in the pseudo-first order regime. Two additional data points were collected with $[Co(bpy)_3](PF_6)_3$ concentrations of 4.5 mM and 5.5 mM.

Due to the five differently concentrated solutions of the counter complex, the ionic strength was not the same for all analyzed cross reactions and varied for every solution of the counter complex with a specific concentration. The ionic strength influences the activity coefficients of the reactants. However, the influence on the activity coefficient is not significant for the determination of k_{12}. Therefore, for simplification the concentrations the activity coefficients were not considered for the determination of k_{12}. The resulting plots are depicted in Section 9.3.1. All additional parameters used for the Marcus cross relation can be viewed in Table 7-2.

Table 7-2: Used counter complex, constants and parameters for obtaining k_{11} for the tripodal model systems.

Complex/paramaters used	
Counter complex (CC)	$[Co(bpy)_3](PF_6)_3$
r(C) [nm]	0.57
r(CC) [nm]	0.70
$E_{1/2}$ (CC) [V] vs Fc/Fc^+	−0.056
k_{22} [L mol^{-1} s^{-1}]	0.645
β [$m^{0.5}$ mol^{-1}]	$4.88 \cdot 10^{-6}$
w_{11} [J mol^{-1}]	$6.78 \cdot 10^{3}$
w_{12} [J mol^{-1}]	$9.13 \cdot 10^{3}$
w_{21} [J mol^{-1}]	$1.22 \cdot 10^{4}$
w_{22} [J mol^{-1}]	$1.65 \cdot 10^{4}$
W_{12} [ ]	1.51
k_B [J K^{-1}]	$1.38 \cdot 10^{-23}$
E_{MeCN} [C V^{-1} m^{-1}]	$3.97 \cdot 10^{-9}$
μ [mol m^{-3}]	1.60

7.3.11.2 Stopped-Flow UV/vis Spectroscopy of TMGqu Model Systems

The stopped-flow spectroscopic measurements were performed with a HI-TECH Scientific SF-61SX2 device with a diode array detector. The optical light path for transmission of the quartz glass cuvette was 10 mm. The mixing time is given by HI-TECH to amount to 2 ms. UV/vis spectra in a wavelength range of 300 nm to 800 nm were detected with temporal resolutions of 0.75 to 7.5 s. The analyses were carried out with the TgK Scientific program Kinetic Studio 4.0.8.18533. UV/vis spectra (300–800 nm) were detected. For visualization and examination of the results the software OriginPro 2021b (Version 9.8.5.212) from OriginLab was used.

The cross reactions starting from $[Cu(TMG2Phqu)_2]PF_6$ (**C9–PF$_6$**) and $[Cu(TMG2NMe_2qu)_2]PF_6$ (**C7–PF$_6$**) were conducted using the counter complex $[Co(bpy)_3](PF_6)_3$. The cross reactions starting from $[Cu(TMG2Phqu)_2](OTf)_2$ (**C10–OTf**) were conducted using the counter complex **C7–PF$_6$**. To measure the kinetics of the cross-reaction, a solution of the measured complex (0.2 mM) in MeCN was mixed with up to five differently concentrated solutions (with reactant in excess) of employed counter complex and the increase of the solutions' absorptions at a constant wavelength were observed. Every measurement was performed twice. Employed concentrations are listed in Table 7-3.

Due to the differently concentrated solutions of the counter complexes, the ionic strength was not the same for all analyzed cross reactions and varied for every solution of the counter complex with a specific concentration. The ionic strength influences the activity coefficients of the reactants. However, the influence on the activity coefficient is not significant for the determination of k_{12}. Therefore, for simplification of the concentrations the activity coefficients were not considered for the determination of k_{12}. The resulting plots are depicted in Section 9.3.2. All additional parameters used for the Marcus cross relation can be viewed in Table 7-4.

Table 7-3: Employed counter complex-concentrations for each reported stopped-flow measurement.

Measured Complex	$[Cu(TMG2NMe_2qu)_2]PF_6$ (**C7–PF$_6$**)	$[Cu(TMG2Phqu)_2]PF_6$ (**C9–PF$_6$**)	$[Cu(TMG2Phqu)_2](OTf)_2$ (**C10–OTf**)*
Counter Complex	$[Co(bpy)_3](PF_6)_3$	$[Co(bpy)_3](PF_6)_3$	**C7–PF$_6$**
c_1 [mmol/L]	1.0	1.0	1.0
c_2 [mmol/L]	1.5	1.5	1.67
c_3 [mmol/L]	2.0	2.0	2.34
c_4 [mmol/L]	2.5	2.5	3.0
c_5 [mmol/L]	3.0	3.0	-

*__C10__−__OTf__ was measured against 4 concentrations to conserve the amount of available **C7–PF$_6$**.

Table 7-4: Used constants and parameters for obtaining k_{11} for the GUAqu model systems.

Complex (C)	$[Cu(TMG2NMe_2qu)_2]PF_6$ (**C7–PF$_6$**)	$[Cu(TMG2Phqu)_2]PF_6$ (**C9–PF$_6$**)	$[Cu(TMG2Phqu)_2](OTf)_2$ (**C10–OTf**)*
Counter complex (CC)	$[Co(bpy)_3](PF_6)_3$	$[Co(bpy)_3](PF_6)_3$	$[Cu(TMG2NMe_2qu)_2]PF_6$
r(C) [nm]	0.58	0.62	0.62
r(CC) [nm]	0.70	0.70	0.58
$E_{1/2}$ (CC) [V] vs Fc/Fc^+	−0.056	−0.056	−0.335
k_{22} [L mol^{-1} s^{-1}]	0.645	0.645	164
β [m$^{0.5}$ mol^{-1}]	$4.88 \cdot 10^{-6}$	$4.88 \cdot 10^{-6}$	$4.88 \cdot 10^{-6}$
w_{11} [J mol^{-1}]	$6.63 \cdot 10^{3}$	$6.25 \cdot 10^{3}$	$6.25 \cdot 10^{3}$
w_{12} [J mol^{-1}]	$9.03 \cdot 10^{3}$	$8.79 \cdot 10^{3}$	$6.43 \cdot 10^{3}$
w_{21} [J mol^{-1}]	$1.20 \cdot 10^{4}$	$1.17 \cdot 10^{4}$	$6.43 \cdot 10^{3}$
w_{22} [J mol^{-1}]	$1.65 \cdot 10^{4}$	$1.65 \cdot 10^{4}$	$6.63 \cdot 10^{3}$
W_{12} [ ]	1.53	1.59	1.00
k_B [J K^{-1}]	$1.38 \cdot 10^{-23}$	$1.38 \cdot 10^{-23}$	$1.38 \cdot 10^{-23}$
E_{MeCN} [C V^{-1} m^{-1}]	$3.97 \cdot 10^{-9}$	$3.97 \cdot 10^{-9}$	$3.97 \cdot 10^{-9}$
μ [mol m^{-3}]	1.60	1.60	1.60
f_{12} [ ]	0.531	0.747	0.839

7.3.12 Fluorescence Spectroscopy

The fluorescence spectroscopic measurements were performed with an FL-2500 Fluorescence Spectrophotometer from Hitachi High-Technology Corporation. The solutions of the Cu(I)complexes (**C11−PF$_6$**, **C13−PF$_6$**, **C15−PF$_6$**) (c = 10 µM) in THF were prepared inside a glovebox, where they were also transferred into quartz glass cuvettes (1 cm, QS). The measurements where conducted under ambient conditions, The signal amplification was achieved by a photomultiplier tube with a voltage of 700 V. Before the measurements, the integrated function of the fluorimeter to measure the instrumental response on the excitation and emission side was applied to obtain corrected excitation and emission spectra. The instrumental response on the excitation and emission side was measured within a wavelength range of 220 to 600 nm and the photomultiplier tube was automatically set to a voltage of 400 V. The measurement of the instrumental response on the excitation side was performed with a standardized rhodamine B solution in a triangular cell in combination with a cut filter.

The triangular cell was set in the cell holder so that the excitation light hits the diagonal side of the triangular cell and the diagonal side of the triangular cell faces away from

the detector. The cut filter was set between the triangular cell and the detector. Afterward, the measurement of the instrumental response on the emission side was performed with a quartz diffuser in combination with an attenuator. After the measurement of the instrumental response on the excitation and emission side, the direct measurement of corrected excitation and emission spectra is possible. For data acquisition, the software FL Solutions (Build 190) from Hitachi High-Technology Corporation was used. For visualization of the fluorescence spectra, the software OriginPro 2021b (Version 9.8.5.212) from OriginLab was used.

7.3.13 Transient X-ray Absorption Spectroscopy

The measurements were done by the Rübhausen Group of Hamburg University during a beamtime in April 2025. PETRA III served as X-Ray source. To make use of stable timing, the measurements were conducted in the timed 40-bunch mode. The pump light source was installed permanently adjacent to P64 and synchronized with the synchrotron as described below. For the shown measurements, the OPA output of the source was used. The samples were dissolved in acetonitrile and is delivered to the Jet via an automated sample delivery system which ensures inert atmosphere.
The electron beam of Petra III operates at 6GeV and the used 40-bunch mode.
The monochromator used was a Si the double crystal monochromator. The laser system used at the PETRA III beamline P64 consists of two parts, a fiber-laser and an optical parametric oscillator (OPA). The fiber-laser (UFFL_39_150_1030_300_REPLOCK, Active Fiber Systems GmbH, Jena, Germany) produces a fundamental output of 1030 nm with up to 48 W average power and a pulse duration of 200 fs. The repetition rate of the system is tunable between 5.2 MHz and 150 kHz and is synchronized to PETRA III. For the experiments presented in this work, a repetition rate of 273 kHz was chosen in order to decrease noise. The OPA installed at P64 is an AVUS system (ORIGAMI IRO CONFIGURATION: Standard + IR ext. + Bypass + SHG output, APE Angewandte Physik und Elektronik GmbH, Berlin, Germany) with a spectral range from 210 nm to 2.6 µm and an output power from 100 mW up to 1.6 W, depending on the wavelength. Pump-probe measurements were conducted at 320 nm, 350 nm, 368 nm, 385 nm, 400 nm, 435 nm and 465 nm.
From the external laser hutch, the beam is guided onto the sample via a set of mirrors and focused with a fused silica lens (d= 25.4 mm, f=1000 mm, Thorlabs GmbH, Bergkirchen, Germany) onto the jet. Focus and spatial overlap of the beam with the X-ray can be controlled via motorized translation stages. The overlap of the two beams is observed via two cameras that are looking into the jet-cage from the side and from the front. The spot-size of the laser was determined using a camera (LaserCam-HR,

Coherent Corp., Saxonbourg, USA) at the sample position. The spot sizes were chosen to correspond to the jet-diameter of 300 µm and to be larger than the X-ray-spot size of 230 µm. The temporal overlap at the sample position was observed via a UV/Vis and X-ray sensitive photodiode.

The samples were solutions of **C13–PF_6** in acetonitrile, which were jetted in inert atmosphere via a PEEKsil nozzle with (300+-5)µm inner diameter. The samples were prepared with a concentration of 3 mmol/L that was varied between 1 and 3 mmol/L using absolute reserve solvent during the measurements. The samples were kept under nitrogen atmosphere, stored in glass bottles and transferred with PTFE tubing. The funnel which caught the jet was made of stainless steel.

XAS Measurements were done in fluorescence mode of the beamline, Using single pixel solid state detectors with maximal count rates up to 1M photons/s.

Measurements were done with few-photon-counting intensities from which the intensities were reconstructed via poisson correction. Fluorescence photons were filtered with capton protected nickel filters with 5µm/15µm thickness. Pump- and probe signal were differentiated on the hardware level.

The data was exported in beamline specific formats which were preprocessed and averaged with software provided by M. Naumova and A. Kalink.

7.4 Photoredox Catalytic Transformations

All photoredox catalytic transformations were carried out inside a EvoluChem PhotoRedOx Box™ photoreactor equipped with an EvoluChem™ LED with a 450 nm emission wavelength. The photoreactor was additionally equipped with a custom-made light protection to prevent potential eye damage. The reactor was mounted on a stirring plate and fixed using a clamp (Figure 7.1).

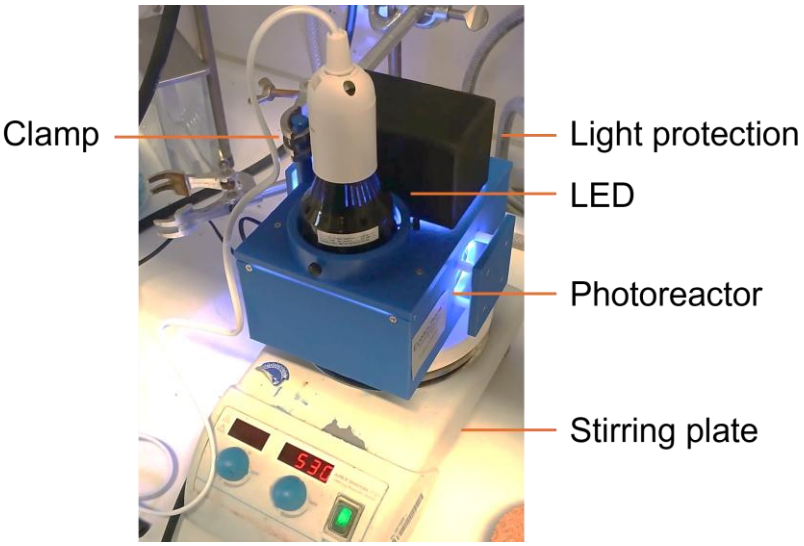

Figure 7.1: Used setup for the photoredox catalytic conversions.

The stem solutions of the reaction mixtures were prepared under inert conditions and then divided into three 3 mL screw cap vials each. To prevent any intrusion of oxygen for the time of the reaction, the vials' threads were fitted with Teflon tape before being put into the photoreactor outside the glovebox. The reactions were ran for various time frames at 450 to 550 rpm. No additional heating was applied to the reaction, but Bergonzini and König *et al.*[240] report that the temperature inside the chosen photoreactor sits slightly above room temperature at around 30 °C. The reaction mixtures were analyzed via ^{1}H-NMR spectroscopy. Present product was quantified using nitromethane as internal standard with its resonance at 4.31 ppm in $CDCl_3$.

7.4.1 General Procedure for Performed Hydrodehalogenations

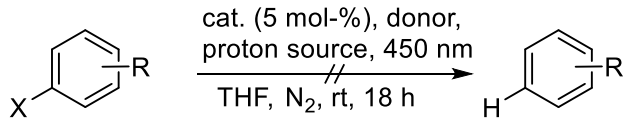

Substrates in hydrodehalogenation

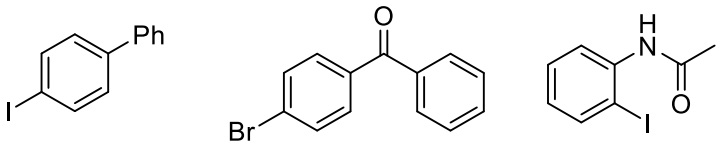

Used electron donors

Zinc(0) **A**	E_{ox} = -1.40 V
Sodium dithionite **B**	E_{ox} = -1.17 V
Ascorbic acid **C**	E_{ox} = -0.59 V

Proton source for **B** and **A**:

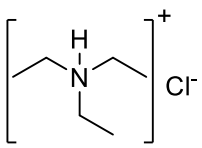

A solution of substrate (0.06 mmol, 1 eq.), electron donor (0.12 mmol, 2 eq.), a proton source (0.06 mmol, 1 eq.) and copper catalyst (5 mol%) in THF_{abs} (7.5 mL) was prepared under inert conditions. The reaction mixture was transferred into three 3 mL screw cap vial (2.5 mL each), placed in the photoreactor and irradiated for 18 hours. Afterwards, the reaction mixture was concentrated under reduced pressure, and the residue characterized via ^{1}H-NMR spectroscopy with no discernable product reonances. Additional ESI-MS measurements also yielded no peaks that could be associated with product.

7.4.2 General Procedure for Performed Reductive Couplings

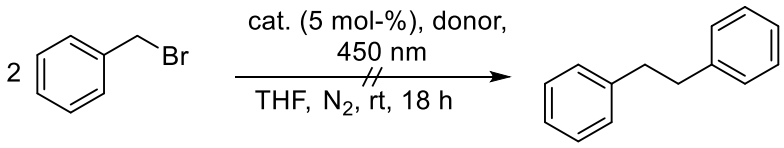

Used electron donors

Zinc(0) **A**	E_{ox} = -1.40 V
Sodium dithionite **B**	E_{ox} = -1.17 V
Ascorbic acid **C**	E_{ox} = -0.59 V

A solution of benzyl bromide (0.06 mmol, 10.2 mg, 1 eq.), electron donor (0.12 mmol, 2 eq.) and copper catalyst (5 mol%) in THF_{abs} (7.5 mL) was prepared under inert conditions. The reaction mixture was transferred into three 3 mL screw cap vial (2.5 mL each), placed in the photoreactor and irradiated for 18 hours. Afterwards, the reaction mixture was concentrated under reduced pressure, and the resulting residue was characterized via ^{1}H NMR spectroscopy with no discernable product resonances. Additional ESI-MS measurements also yielded no peaks that could be associated with product.

7.4.3 General Procedure for Performed ATRA Reactions

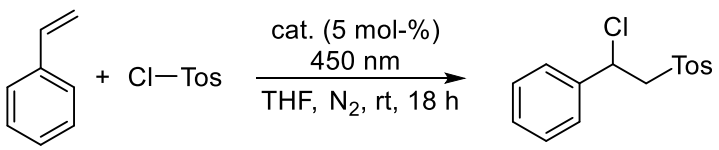

A solution of styrene (0.06 mmol, 6.9 µL, 1 eq.), tosyl chloride (0.06 mmol, 11.4 mg, 1 eq.), and copper catalyst (5 mol%) in THF_{abs} (7.5 mL) was prepared under inert conditions. The reaction mixture was transferred into three 3 mL screw cap vial (2.5 mL each), placed in the photoreactor and irradiated for 18 hours. Afterwards, the reaction mixture was concentrated under reduced pressure, and the resulting residue was

characterized in $CDCl_3$ by ^1H NMR. The product of the reaction, 1-((2-chloro-2-phenylethyl)sulfonyl)-4-methylbenzene, could be identified and quantified using nitromethane as internal standard.
The product's ^1H NMR spectrum is in agreement with the literature.[241]

^{1}H NMR (400 MHz, $CDCl_3$) δ [ppm] = 7.62 (d, J = 8.4 Hz, 2H, H-f), 7.29 – 7.18 (m, 7H, H-a, H-b, H-c, H-g), 5.31 (t, J = 6.9 Hz, 1H, H-d), 3.97 – 3.79 (m, 2H, H-e), 2.40 (s, 3H, H-h).

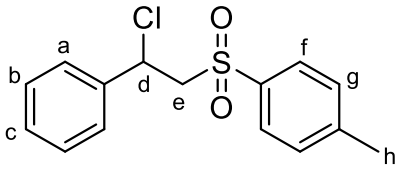

7.5 Synthetic Procedures of Tripodal Ligands and corresponding Complexes

7.5.1 Resynthesis of Tris(2-nitrophenyl)amine

This molecule has been synthesized before and the synthesis was performed following a modified version of a literature-known procedure.[168]

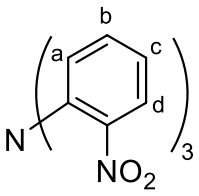

$C_{18}H_{12}N_4O_6$
380.32 g/mol

2-Nitroaniline (25.00 g, 181.0 mmol, 1 eq.), 1-fluoro-2-nitrobenzene (76.6 g, 57.3 mL, 543 mmol, 3 eq.) and K_2CO_3 (150 g, 1086 mmol, 6 eq.) were combined in DMSO (140 mL). The mixture was heated to 130 °C under stirring for 3.5 d. After cooling to room temperature, water (500 mL) was given into the flask. The orange-brown precipitate was filtered off and washed with water (5x 100mL) and methanol (5x 100 mL), then dissolved in dichloromethane. Then, the solution was filtered over a small column filled with SiO_2, the solvent was evaporated under reduced pressure. Afterwards, the orange solid was suspended in methanol (500 mL), cooked in it for 1 h and filtered off under reduced pressure. The procedure was repeated twice. The product tris(2-nitrophenyl)amine (40.0 g, 105 mmol, 58 % yield) was obtained as an orange solid.

^{1}H NMR (400 MHz, $CDCl_3$) δ [ppm] = 7.82 (dd, J = 8.2, 1.6 Hz, 3H, H-d), 7.53 (ddd, J = 8.2, 7.4, 1.7 Hz, 3H, H-b), 7.30 (ddd, J = 8.2, 7.3, 1.3 Hz, 3H, H-c), 7.21 (dd, J = 8.2, 1.3 Hz, 3H, H-a).

7.5.2 Resynthesis of Tris(2-aminophenyl)amine

This molecule has been synthesized before and the synthesis was performed following a modified version of a literature-known procedure.[169]

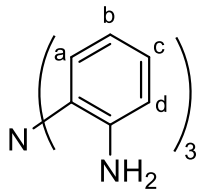

$C_{18}H_{18}N_4$
290.37 g/mol

Tris(2-nitrophenyl)amine (8.00 g, 21.0 mmol, 1.00 eq.) and palladium on activated charcoal (600 mg, 5.64 mmol, 0.268 eq.) were given into a round bottom flask which was subsequently evacuated and flushed with nitrogen three times. Methanol (250 mL) was added to the flask, which was then evacuated to the solvent's boiling point, then flushed with nitrogen for three times. The flask's atmosphere was substituted with molecular hydrogen and the reaction was stirred at room temperature for 16 hours. Afterwards, the grey precipitate was filtered off and suspended in degassed dichloromethane (300 mL) under nitrogen atmosphere. The suspension was filtered again under nitrogen atmosphere to remove the catalyst. The solvent was removed under reduced pressure, giving rise to the crude product in form of an off-white solid. The solid was then placed in a Büchner funnel and washed dropwise with cooled DCM (−30 °C) under reduced pressure to remove any remaining catalyst. After removal of remaining solvent in vacuo, the product tris(2-aminophenyl)amine (4.75 g, 16.4 mmol, 78 % yield) was obtained in form of a colorless solid.

^{1}H NMR (400 MHz, $CDCl_3$) δ [ppm] = 6.99 (td, J = 7.6, 1.6 Hz, 3H, H-c), 6.91 (dd, J = 7.9, 1.5 Hz, 3H, H-a), 6.74 – 6.66 (m, 6H, H-b, H-d), 3.21 (s, 6H, H-N).

7.5.3 Resynthesis of N^1,N^1-bis(2-methylquinolin-8-yl)benzene-1,2-diamine

This molecule has been synthesized before and the synthesis was performed following a modified version of a literature-known procedure.[169]

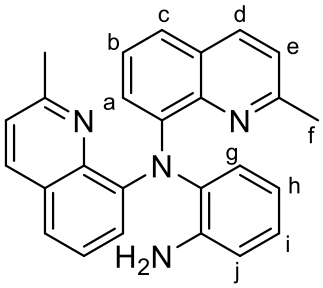

$C_{26}H_{22}N_4$
390.49 g/mol

Tris(2-aminophenyl)amine (2.80 g, 9.64 mmol, 1.00 eq.) was given into a round bottom flask and dissolved in HCl (6 M, 70 mL). The dissolution was heated to 80 °C, during which the crotonaldehyde (2.03 g, 2.40 mL, 28.9 mmol, 3.00 eq.) was dissolved in toluene (20 mL) in parallel. The dissolved aldehyde was then added to the heated HCl-solution via syringe and the reaction mixture was stirred at 80 °C for 3 hours. Afterwards, 100 mL of air were added to the solution via syringe, the heat was turned off and the flask was allowed to slowly cool to room temperature for an additional hour. The flask and its contents were subsequently cooled to 0 °C and KOH in water (50 % w/w) was added until a pH of 14 could be registered. The crude product was extracted from the aqueous layer with dichloromethane (3x 300 mL). The combined organic layers were dried over $MgSO_4$ and the solvent was removed under reduced pressure. The resulting crude product appeared as a black tar that was further purified via gradient elution column-chromatography (hexane:EtOAc 4:1 -> 3:2, R_f = 0.42 for hexane/EtOAc 3:2). The product was obtained as a pale yellow solid (730 mg, 2.14 mmol, 17 % yield).

^{1}H NMR (400 MHz, $CDCl_3$): δ [ppm] = 7.91 (d, J = 8.2 Hz, 2H, H-d), 7.39 (dd, J = 7.7 Hz, 1.5 Hz, 2H, H-c), 7.28-7.24 (m, 2H, H-b), 7.16 (dd, J = 7.7 Hz, 1.5 Hz, 1H, H-g), 7.11 (dd, J = 7.5 Hz, 1.3 Hz, 2H, H-a), 7.07-7.03 (m, 3H, H-2, H-i), 6.83 (dd, J = 7.9 Hz, 1.4 Hz, 1H, H-j), 6.69 (td, J = 7.6 Hz, 1.4 Hz, 1H, H-h), 4.63 (s, 2H, H-N), 2.14 (s, 6H, H-f).

7.5.4 Resynthesis of N^1-(2-aminophenyl)-N^1-(2-methylquinolin-8-yl)benzene-1,2-diamine

This molecule has been synthesized before and the synthesis was performed following a modified version of a literature-known procedure.[169]

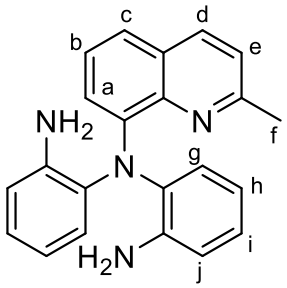

$C_{22}H_{20}N_4$
340.43 g/mol

Tris(2-aminophenyl)amine (3.53 g, 12.2 mmol, 1.00 eq.) was dissolved in aqueous HCl (6 M, 73 mL) and heated to 80 °C. Crotonaldehyde (1.27 g, 1.50 mL, 18.1 mmol, 1.49 eq.), dissolved in toluene (21mL), was added and the reaction heated for 6 h with air (ca 100 mL) being injected after 3.5 h and after 6 h. In an ice bath 50 % w/w aqueous NaOH was added until a pH of 14 was reached. The mixture was diluted with water (300 mL) and extracted with DCM (4x 300 mL). The combined washings were dried with $MgSO_4$, filtered and the solvent was removed under reduced pressure. After drying on high vacuum, a black tar was obtained which was purified by column chromatography (hexane:EtOAc 4:1 -> 3:2) yielding N^1-(2-aminophenyl)-N^1-(2-methylquinolin-8-yl)benzene-1,2-diamine (1.00 g, 2.94 mmol, 24 % yield, R_f = 0.25 for hexane:EtOAc 3:2) as a yellow solid.

^{1}H NMR (400 MHz, $CDCl_3$): δ [ppm] = 7.95 (d, J = 8.4 Hz, 1H, H-d), 7.47 (dd, J = 8.1 Hz, J1.4 Hz, 1H, H-c), 7.33 (t, J = 7.8 Hz, 1H, H-b), 7.22 (dd, J = 7.5 Hz, 1.4 Hz, 1H, H-6), 7.17 (d, J = 8.2 Hz, 1H, H-e), 6.96 (td, J = 7.6 Hz, 1.5 Hz, 2H, H-i), 6.89 (dd, J = 7.8 Hz, 1.5 Hz, 2H, H-g), 6.75 (dd, J = 7.8 Hz, 1.4 Hz, 2H, H-j), 6.63 (td, J = 7.6 Hz, 1.4 Hz 2H, H-h), 3.64 (s, 4H, H-N), 2.47 (s, 3H, H-f).

7.5.5 Synthesis of 2-methyl-*N*,*N*-di(quinolin-8-yl)quinolin-8-amine

This molecule was synthesized following a procedure by Dunkel *et al.*[169]

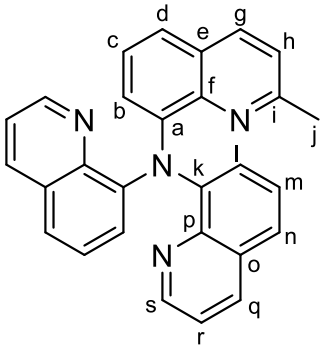

$C_{28}H_{20}N_4$
412.50 g/mol

N^1-(2-aminophenyl)-N^1-(2-methylquinolin-8-yl)benzene-1,2-diamine (1.00 g, 2.94 mmol, 1.00 eq.) was dissolved in 6 M HCl (70.0 mL) and heated to 80 °C. A solution of acrolein (0.78 mL, 11.8 mmol, 3.99 eq.) in toluene (20.0 mL) was added and the mixture was stirred at 80 °C for 4 h. After 2 h, air (ca. 100 mL) was led through the mixture. After letting the mixture cool to 25 °C, NaOH in water (50 % w/w) was added until a pH of 14 was reached. The mixture was diluted with water (250 mL) and extracted with DCM (5x 100 mL). The combined organic layers were dried with $MgSO_4$, filtered and the solvent was removed yielding an orange oil which was purified by column chromatography (hexane:EtOAc 1:4, R_f = 0.29). 2-methyl-*N*,*N*-di(quinolin-8-yl)quinolin-

8-amine (600 mg, 1.45 mmol, 49% yield) was obtained as a yellow solid. Full characterization was outside the scope of this thesis.

^{1}H NMR (400 MHz, CD_2Cl_2) δ [ppm] = 8.51 (dd, *J* = 4.1, 1.9 Hz, 2H, H-s), 8.18 (dd, *J* = 8.3, 1.8 Hz, 2H, H-q), 7.99 (d, *J* = 8.4 Hz, 1H, H-g), 7.60 (dd, *J* = 8.2, 1.4 Hz, 2H, H-l), 7.46 (dd, *J* = 8.2, 1.4 Hz, 1H, H-b), 7.37 – 7.28 (m, 4H, H-m, H-r), 7.25 – 7.18 (m, 3H, H-c, H-n), 7.10 (d, *J* = 8.4 Hz, 1H, H-h), 7.02 (dd, *J* = 7.7, 1.4 Hz, 1H, H-d), 2.03 (s, 3H, H-j).

^{13}C NMR (101 MHz, CD_2Cl_2) δ [ppm] = 156.56 (i, 1C), 148.83 (s, 2C), 148.66 (a, 1C), 148.12 (k, 2C), 144.14 (p, 2C), 142.33 (f, 1C), 136.15 (q, 2C), 136.07 (g, 1C), 130.10 (o, 2C), 128.14 (e, 1C), 126.71 (m, 2C), 125.66 (c, n, 3C), 123.36 (l, d, 3C), 122.12 (b, 1C), 121.55 (h, 1C), 121.08 (r, 2C), 25.05 (j, 1C).

HR-ESI-MS (m/z (%) $[M+H]^+$, M+H = $C_{28}H_{21}N_4$) found: 413.1756 (100), 414.1788 (31), 415.1821 (5). Calculated: 413.1761 (100) $[^{12}C_{28}{}^{1}H_{21}{}^{14}N_4]^+$, 414.1791 (32) $[^{12}C_{27}{}^{13}C^{1}H_{21}{}^{14}N_4]^+$, 415.1828 (5) $[^{12}C_{26}{}^{13}C_2{}^{1}H_{21}{}^{14}N_4]^+$.

7.5.6 Synthesis of 8-(di(quinolin-8-yl)amino)quinoline-2-carbaldehyde

The molecule was synthesized following a procedure by He and Fan *et al*.[190]

SeO_2 (453 mg, 4,05 mmol, 3.3 eq.) was stirred in 1,4-dioxane (30 mL) at 80 °C for 30 min. 2-methyl-*N*,*N*-di(quinolin-8-yl)quinolin-8-amine (560 mg, 1.36 mmol, 1.00 eq.) was added and the solution stirred at 80 °C for 3 h. The reaction mixture was filtered through celite with DCM after letting cool to 25 °C. The solvent was removed under reduced pressure and the residue dissolved in DCM. The solution was filtered over silica and the solvent removed under reduced pressure. The product 8-(di(quinolin-8-yl)amino)quinoline-2-carbaldehyde (557 mg, 1.31 mmol, 96% yield) was obtained as a red-orange solid.

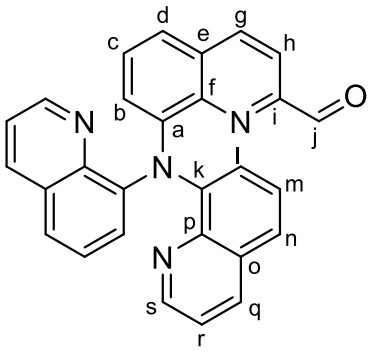

$C_{28}H_{18}N_4O$
426.48 g/mol

The NMR resonances could not be assigned due to strong overlap of key resonances. Full characterization was outside the scope of this thesis.

^{1}H NMR (400 MHz, $CDCl_3$) δ [ppm] = 8.78 (s, 1H), 8.71 (s, 2H), 8.18 (ddd, *J* = 15.4, 8.5, 1.4 Hz, 3H), 7.74 (d, *J* = 8.5 Hz, 1H), 7.65 (dd, *J* = 7.9, 1.6 Hz, 2H), 7.50 – 7.30 (m, 8H), 7.03 (dd, *J* = 7.7, 1.4 Hz, 1H).

^{13}C NMR (101 MHz, $CDCl_3$) δ [ppm] = 193.83, 180.74, 149.73, 149.44, 137.20, 131.55, 129.81, 129.55, 126.93, 124.48, 121.30, 121.08, 116.68, 60.54, 21.20.

ESI-MS (m/z (%) $[M+H]^+$, M+H = $C_{28}H_{19}N_4O$) found: 427.1489 (100), 428.1521 (31), 429.1552 (5). Calculated: 427.1553 (100) $[^{12}C_{28}{}^{1}H_{19}{}^{14}N_4{}^{16}O]^+$, 428.1584 (32) $[^{12}C_{27}{}^{13}C^{1}H_{19}{}^{14}N_4{}^{16}O]^+$, 429.1614 (5) $[^{12}C_{26}{}^{13}C_2{}^{1}H_{19}{}^{14}N_4{}^{16}O]^+$.

7.5.7 Synthesis of methyl 8-(di(quinolin-8-yl)amino)quinoline-2-carboxylate (L4)

This compound's synthesis was attempted by two different methods.

Method A: This synthesis was attempted following a modified protocol by Zeitler and Connon *et al.*[242] 8-(di(quinolin-8-yl)amino)quinoline-2-carbaldehyde (156 mg, 366 µmol, 1.00 eq.) and thiamine hydrochloride (18.5 mg, 54.9 µmol, 0.150 eq.) were dissolved in MeOH (5 mL) and NEt_3 (0.13 mL, 0.515 mmol, 2.5 eq.) was added. The reaction mixture was stirred under air overnight. No product formation could be detected by TLC.

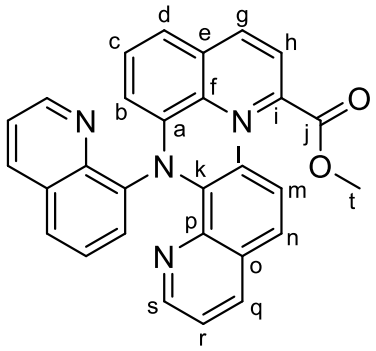

$C_{29}H_{20}N_4O_2$
456.51 g/mol

Method B: The molecule was synthesized following a protocol by Mori *et al.*[191] 8-(di(quinolin-8-yl)amino)quinoline-2-carbaldehyde (89.0 mg, 209 µmol, 1.00 eq.) was dissolved in MeOH (1 mL) and I_2 (63 mg, 0.25 mmol, 1.2 eq.) and K_2CO_3 (87 mg, 0.63 mmol, 3 eq.) were added. The mixture was stirred at 25 °C for 3.5 h at which point full conversion was detected by TLC. A saturated aqueous solution of $Na_2S_2O_3$ (0.5 mL) and water (20 mL) were added and extracted with DCM (3x 10 mL). The combined organic layers were dried with $MgSO_4$, filtered and the solvent was removed. The residue was purified by column chromatography (acetone:DCM 3:2, R_f = 0.30) yielding methyl 8-(di(quinolin-8-yl)amino)quinoline-2-carboxylate (**L4**) (31.0 mg, 67.9 µmol, 33% yield) as a yellow solid. Full characterization was outside the scope of this thesis.

^{1}H NMR (400 MHz, CD_2Cl_2) δ [ppm] = 8.52 (s, 2H), 8.17 (dd, J = 8.3, 1.8 Hz, 3H), 7.89 (d, J = 8.8 Hz, 1H), 7.61 (dd, J = 8.1, 1.6 Hz, 2H), 7.47 (d, J = 7.7 Hz, 1H), 7.37 – 7.28 (m, 6H), 7.25 (d, J = 7.9 Hz, 2H), 6.99 (d, J = 7.5 Hz, 1H), 3.36 (s, 3H).

ESI-MS (m/z (%) $[M+H]^+$, M+H = $C_{29}H_{21}N_4O_2$) found: 457.16592 (<5). Calculated: 457.16590 (100) $[^{12}C_{29}{}^{1}H_{21}{}^{14}N_4{}^{16}O_2]^+$.
$[M+Na]^+$ (M+Na = $C_{29}H_{20}N_4O_2Na$) found: 479.14810 (20). Calculated: 479.14840 (100) $[^{12}C_{29}{}^{1}H_{20}{}^{14}N_4{}^{16}O_2{}^{23}Na]^+$.
$[M+K]^+$ (M+K = $C_{29}H_{20}N_4O_2K$) found: 495.12161 (100). Calculated: 495.12233 (100) $[^{12}C_{29}{}^{1}H_{20}{}^{14}N_4{}^{16}O_2{}^{39}K]^+$.

7.5.8 Synthesis of N(QuMe)$_2$(PhTMG) (L1$_{TMG}$)

The guanidine synthesis was performed following a slightly modified procedure of Herres-Pawlis *et al.* which itself is based on the procedure of Kantlehner *et al*.[150, 226]

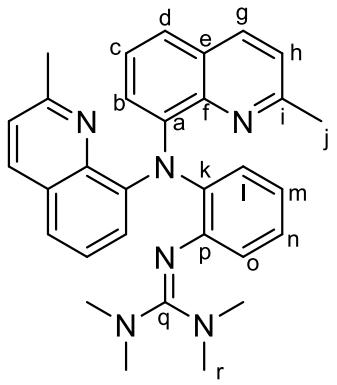

$C_{31}H_{32}N_6$
488.64 g/mol

N^1,*N*^{1}-bis(2-methylquinolin-8-yl)benzene-1,2-diamine (509 mg, 1.3 mmol, 1.0 eq.), TMG-VS (325 mg, 1.9 mmol, 1.5 eq.), and triethylamine (0.4 mL, 3.0 mmol, 2.3 eq.) were added in a preheated flask under a nitrogen counterflow and dissolved in absolute acetonitrile (80 mL). The reaction mixture was connected to a reflux condenser and refluxed under a nitrogen atmosphere for five days. Subsequently, the reaction mixture was cooled to room temperature and treated with potassium hydroxide solution (100 mL, 1:1 w/w). The aqueous phase was extracted with diethyl ether (3 x 100 mL), and the combined organic phases were dried over $MgSO_4$. The solvent was removed under reduced pressure. The resulting orange oil was then heated under vacuum (<10^{-1} mbar), starting at 100 °C and rising to 250 °C, to remove any remaining urea derivative. The remaining crude product was recrystallized in THF/hexane until no side product could be detected via NMR spectroscopy. N(QuMe)$_2$(PhTMG) (**L1$_{TMG}$**) was obtained as an orange solid (334 mg, 0.68 mmol, 52 %) and stored under a nitrogen atmosphere.

^{1}H NMR (400 MHz, CD_2Cl_2) *δ* [ppm] = 7.93 (d, *J* = 8.4 Hz, 2H, H-g), 7.41 (dd, *J* = 7.9, 1.6 Hz, 2H, H-d), 7.30 (t, *J* = 7.8 Hz, 2H, H-c), 7.21 (dd, *J* = 7.6, 1.6 Hz, 2H, H-b), 7.12 – 7.00 (m, 4H, H-h, H-m, H-o), 6.77 (td, *J* = 7.4, 1.6 Hz, 1H, H-n), 6.61 (dd, *J* = 7.9, 1.6 Hz, 1H, H-l), 2.36 (s, 12H, H-r), 2.11 (s, 6H, H-j).

^{13}C NMR (101 MHz, CD_2Cl_2) *δ* [ppm] = 157.2 (q, 1C), 155.4 (i, 2C), 147.6 (k, 1C), 146.8 (a, 2C), 143.2 (f, 2C), 141.7 (p, 1C), 135.9 (g, 2C), 128.5 (o, 1C), 127.8 (e, 2C), 125.6 (c, 2C), 124.5 (m, 1C), 123.7 (b, 2C), 123.1 (l, 1C), 121.0 (h, 2C), 121.0 (d, 2C), 120.3 (n, 1C), 39.7 (r, 4C), 24.9 (j, 2C).

HR-ESI-MS (m/z (%) $[M+H]^+$, M+H = $C_{31}H_{33}N_6$) found: 489.27558 (100), 490.27873 (35), 491.28194 (6), calculated: 489.27667 (100) $[^{12}C_{31}{}^{1}H_{33}{}^{14}N_6]^+$, 490.28002 (33) $[^{12}C_{30}{}^{13}C^{1}H_{33}{}^{14}N_6]^+$, 491.28337 (5) $[^{12}C_{29}{}^{13}C_2{}^{1}H_{33}{}^{14}N_6]^+$.

IR (ATR, $\tilde{\nu}$) = 3050 (m), 3009 (m), 2923 (s), 2880 (m), 2800 (m), 1610 (vs), 1599 (vs), 1579 (vs), 1556 (vs), 1501 (vs), 1483 (vs), 1459 (vs), 1428 (vs), 1369 (vs), 1336 (vs), 1331 (vs), 1273 (vs), 1236 (vs), 1219 (s), 1197 (s), 1134 (vs), 1114 (vs), 1064 (s), 1060 (s), 1015 (vs), 966 (m), 926 (s), 851 (m), 831 (vs), 800 (s), 791 (vs), 749 (vs), 745 (vs), 702 (s), 666 (vs), 632 (s), 620 (s), 591 (m), 583 (m), 543 (m), 511 (m), 493 (m), 490 (m), 479 (m) cm^{-1}.

7.5.9 Synthesis of N(QuMe)$_2$(PhDMEG) (L1$_{DMEG}$)

The guanidine synthesis was performed following a slightly modified procedure of Herres-Pawlis *et al.* which itself is based on the procedure of Kantlehner *et al*.[150, 226]

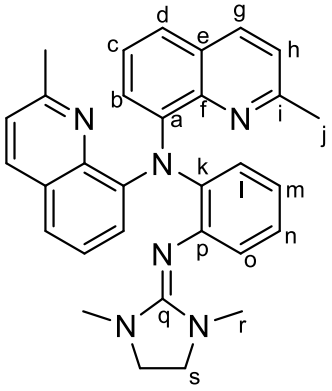

$C_{31}H_{30}N_6$
486.62 g/mol

N^1,N^1-bis(2-methylquinolin-8-yl)benzene-1,2-diamine (786 mg, 2.0 mmol, 1.0 eq.), DMEG-VS (442 mg, 2.6 mmol, 1.3 eq.), and triethylamine (0.6 mL, 4.0 mmol, 2.0 eq.) were added in a preheated flask under a nitrogen counterflow and dissolved in absolute acetonitrile (80 mL). The reaction mixture was connected to a reflux condenser and refluxed under a nitrogen atmosphere for five days. Subsequently, the reaction mixture was treated with a potassium hydroxide solution (100 mL, 1:1 w/w). The aqueous phase was extracted with diethyl ether (3 x 100 mL), and the combined organic phases were dried over $MgSO_4$. The solvent was removed under reduced pressure. The resulting orange oil was then heated under vacuum (<10^{-1} mbar), starting at 150 °C and rising to 250 °C, to remove any remaining urea derivative. Recrystallizations of the crude product in THF/hexane mixtures as well as acetonitrile were attempted but proved unsuccessful due to the crude product separating off as an oil. N(QuMe)$_2$(PhDMEG) (**L1$_{DMEG}$**) was obtained as an orange solid (548 mg, 1.1 mmol, 56 %) and stored under a nitrogen atmosphere.
Since purification of the crude product was unsuccessful, it was not possible to obtain NMR spectra of a purer substance.

^{1}H NMR (400 MHz, CD_2Cl_2) δ [ppm] = 7.90 (d, J = 8.4 Hz, 2H, H-g), 7.36 (dd, J = 7.9, 1.5 Hz, 2H, H-b), 7.26 (t, J = 7.7 Hz, 2H, H-c), 7.19 (dd, J = 7.7, 1.5 Hz, 2H, H-d), 7.09 (dd, J = 7.8, 1.6 Hz, 1H, H-o), 7.03 – 6.94 (m, 3H, H-h, H-m), 6.81 – 6.74 (m, 2H, H-l, H-n), 2.75 (s, 4H, H-s), 2.12 – 2.09 (m, 12H, H-r, H-j).

^{13}C NMR (101 MHz, CD_2Cl_2) δ [ppm] = 155.6 (i, 2C), 152.9 (q, 1C), 147.5 (a, 2C), 143.2 (k, 1C), 142.6 (f,p, 3C), 135.9 (g, 2C), 129.1 (b, 2C), 127.8 (e, 2C), 125.7 (c, 2C), 124.4 (n, 1C), 124.3 (l, 1C), 123.9 (d, 2C), 121.0 (h, 2C), 121.0 (o, 1C), 120.7 (m, 1C), 48.3 (s, 2C), 34.7 (r, 2C), 25.0 (j, 2C).

HR-ESI-MS (m/z (%) $[M+H]^+$, M+H = $C_{31}H_{31}N_6$) found: 487.25956 (100), 488.26265 (35), 489.26772 (6), calculated: 487.26102 (100) $[^{12}C_{31}{}^{1}H_{31}{}^{14}N_6]^+$, 488.26437 (34) $[^{12}C_{30}{}^{13}C^{1}H_{31}{}^{14}N_6]^+$, 491.28337 (5) $[^{12}C_{29}{}^{13}C_2{}^{1}H_{31}{}^{14}N_6]^+$.

IR (ATR, $\tilde{\nu}$) = 3043 (m), 2927 (s), 2854 (s), 1701 (s), 1649 (vs), 1594 (s), 1586 (vs), 1557 (s), 1502 (vs), 1477 (vs), 1460 (vs), 1428 (vs), 1396 (vs), 1368 (s), 1336 (vs), 1277 (vs), 1237 (vs), 1162 (s), 1132 (s), 1112 (s), 1071 (s), 1031 (vs), 993 (m), 970

(s), 933 (m), 830 (vs), 801 (s), 793 (s), 752 (vs), 702 (s), 665 (s), 649 (s), 630 (s), 595 (s), 581 (s), 520 (s), 488 (s), 447 (s) cm^{-1}.

7.5.10 Synthesis of N(QuMe)(PhTMG)$_2$ (L2$_{TMG}$)

The guanidine synthesis was performed following a slightly modified procedure of Herres-Pawlis *et al.* which itself is based on the procedure of Kantlehner *et al*.[150, 226]

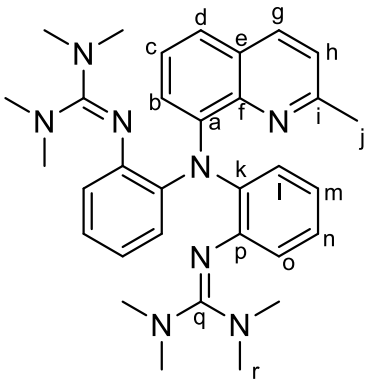

$C_{32}H_{40}N_8$
536.73 g/mol

In a preheated round-bottom flask, *N*^{1}-(2-aminophenyl)-*N*^{1}-(2-methylquinolin-8-yl)benzene-1,2-diamine (603.0 mg, 1.77 mmol, 1.0 eq.), TMG-VS (696 mg, 4.07 mmol, 2.30 eq.), and triethylamine (0.73 mL, 5.3 mmol, 3.0 eq.) were added under a nitrogen counterflow and dissolved in absolute acetonitrile (60 mL). The reaction mixture was connected to a reflux condenser and refluxed under a nitrogen atmosphere for five days. Subsequently, the reaction mixture was treated with an aqueous potassium hydroxide solution (100 mL, 1:1 w/w). The aqueous phase was extracted with diethyl ether (3 x 100 mL), and the combined organic phases were dried over $MgSO_4$. The solvent was removed under reduced pressure. The resulting orange oil was then heated under vacuum (<10^{-1} mbar), starting at 150 °C and rising to 250 °C, to remove any remaining urea derivative. The crude product was purified by repeated recrystallization in acetonitrile. N(QuMe)(PhTMG)$_2$ (**L2$_{TMG}$**) was obtained in the form of a bright yellow solid (342 mg, 0.64 mmol, 36 %).

^{1}H NMR (400 MHz, CD_2Cl_2) δ [ppm] = 7.88 (d, *J* = 8.4 Hz, 1H, H-g), 7.36 (dd, *J* = 7.8, 1.6 Hz, 1H, H-d), 7.25 (t, *J* = 7.7 Hz, 1H, H-c), 7.18 (dd, *J* = 7.5, 1.5 Hz, 1H, H-b), 7.07 (d, *J* = 8.4 Hz, 1H, H-h), 6.97 (dd, *J* = 7.9, z1.6 Hz, 2H, h-O), 6.84 (td, *J* = 7.5, 1.6 Hz, 2H, H-m), 6.67 (td, *J* = 7.9, 1.6 Hz, 2H, H-n), 6.36 (dd, *J* = 7.8, 1.7 Hz, 2H, H-l), 2.34 – 2.24 (m, 27H, H-j, H.r).

^{13}C NMR (101 MHz, CD_2Cl_2) δ [ppm] = 156.5 (q, 2C), 155.7 (i, 1C), 146.7 (a, 1C), 145.6 (k, 2C), 144.2 (f, 1C), 141.6 (p, 2C), 136.0 (g, 1C), 127.8 (e, 1C), 127.1 (o, 2C), 125.6 (c, b, 2C), 122.8 (m, 2C), 122.2 (l, 2C), 121.4 (d, 1C), 121.1 (h, 1C), 120.0 (n, 2C), 39.7 (r, 8C), 25.0 (j, 1C).

HR-ESI-MS (m/z (%) $[M+H]^+$, M+H = $C_{32}H_{41}N_8$) found: 537.34536 (100), 538.34790 (70), 539.35083 (12), calculated: 537.34541 (100) $[^{12}C_{32}{}^{1}H_{41}{}^{14}N_8]^+$, 538.34877 (36) $[^{12}C_{31}{}^{13}C^{1}H_{41}{}^{14}N_8]^+$, 539.34580 (2) $[^{12}C_{30}{}^{13}C_2{}^{1}H_{41}{}^{14}N_8]^+$.

IR (ATR, $\tilde{\nu}$) = 3050 (m), 3009 (m), 2922 (s), 2887 (s), 2880 (s), 2847 (s), 2803 (m), 1687 (m), 1609 (vs), 1601 (vs), 1574 (vs), 1563 (vs), 1497 (vs), 1482 (vs), 1459 (vs),

1450 (vs), 1425 (vs), 1367 (vs), 1328 (vs), 1278 (vs), 1271 (vs), 1235 (vs), 1206 (s), 1133 (vs), 1117 (vs), 1065 (s), 1058 (s), 1013 (vs), 925 (s), 922 (s), 917 (s), 853 (s), 849 (s), 841 (s), 827 (s), 795 (s), 772 (vs), 736 (vs), 713 (s), 702 (s), 674 (s), 671 (s), 666 (s), 630 (s), 624 (s), 618 (s), 584 (s), 563 (s), 552 (s), 546 (s), 538 (s) cm^{-1}.

7.5.11 Synthesis of N(QuMe)(PhDMEG)$_2$ (L2$_{DMEG}$)

The guanidine synthesis was performed following a slightly modified procedure of Herres-Pawlis *et al.* which itself is based on the procedure of Kantlehner *et al*.[150, 226] In a preheated round-bottom flask, N^1-(2-aminophenyl)-N^1-(2-methylquinolin-8-yl)benzene-1,2-diamine (1.14 g, 3.35 mmol, 1.0 eq.), DMEG-VS (1.30 g, 7.70 mmol, 2.30 eq.), and triethylamine (1.4 mL, 10.1 mmol, 3.0 eq.) were added under a nitrogen counterflow and dissolved in absolute acetonitrile (100 mL). The reaction mixture was connected to a reflux condenser and refluxed under a nitrogen atmosphere for four days. Subsequently, the reaction mixture was cooled to room temperature and treated with an aqueous potassium hydroxide solution (100 mL, 1:1 w/w). The aqueous phase was extracted with diethyl ether (3 x 100 mL), and the combined organic phases were dried over $MgSO_4$. The solvent was removed under reduced pressure. The resulting brown oil was then heated under vacuum (<10^{-1} mbar), starting at 150 °C and rising to 250 °C, to remove any remaining urea derivative. The crude product was purified by repeated recrystallization in THF/hexane. N(QuMe)(PhDMEG)$_2$ (**L2$_{DMEG}$**) was obtained in the form of a yellow solid (374 mg, 0.70 mmol, 21 %).

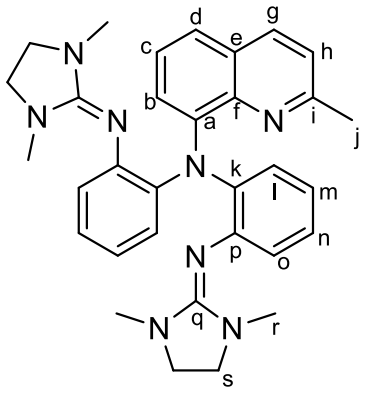

$C_{32}H_{36}N_8$
532.70 g/mol

^{1}H NMR (400 MHz, CD_2Cl_2) δ [ppm] = 7.86 (d, J = 8.3 Hz, 1H, H-g), 7.26 – 7.14 (m, 4H, H-b, H-c, H-l), 7.02 (d, J = 8.4 Hz, 1H, H-h), 6.97 (dd, J = 7.6, 1.6 Hz, 1H, H-d), 6.87 (td, J = 7.5, 1.7 Hz, 2H, H-m), 6.77 (td, J = 7.4, 1.7 Hz, 2H, H-n), 6.67 (dd, J = 7.7, 1.7 Hz, 2H, H-o), 2.73 (s, 8H, H-s), 2.32 (s, 3H, H-j), 2.01 (s, 12H, H-r).

^{13}C NMR (101 MHz, CD_2Cl_2) δ [ppm] = 155.0 (q, 2C), 152.5 (i, 1C), 146.5 (a, 1C), 145.6 (k, 2C), 143.6 (f, 1C), 142.6 (p, 2C), 135.8 (g, 1C), 128.9 (e, 1C), 127.9 (b, 1C), 125.6 (c, 1C), 124.1 (o, 2C), 123.5 (m, 2C), 123.0 (d, 1C), 120.8 (h, 1C), 120.6 (n, 2C), 119.7 (l, 2C), 48.4 (s, 4C), 34.6 (r, 4C), 25.1 (j, 1C).

HR-ESI-MS (m/z (%) $[M+H]^+$, M+H = $C_{32}H_{37}N_8$) found: 533.31315 (100), 534.31612 (37), 535.31871 (7), calculated: 533.31411 (100) $[^{12}C_{32}{}^{1}H_{37}{}^{14}N_8]^+$, 534.31747 (35) $[^{12}C_{31}{}^{13}C^{1}H_{37}{}^{14}N_8]^+$, 535.31450 (1) $[^{12}C_{30}{}^{13}C_2{}^{1}H_{37}{}^{14}N_8]^+$.

IR (ATR, $\tilde{\nu}$) = 3055 (w), 2928 (w), 2861 (w), 1654 (vs), 1651 (vs), 1608 (vs), 1596 (s), 1577 (vs), 1560 (s), 1480 (vs), 1437 (vs), 1430 (s), 1420 (s), 1391 (m), 1368 (w), 1327 (w), 1313 (w), 1274 (vs), 1236 (s), 1160 (w), 1110 (w), 1081 (w), 1069 (w), 1038 (m), 1032 (s), 979 (w), 970 (m), 849 (w), 841 (w), 802 (w), 781 (w), 763 (s), 756 (vs), 742 (vs), 698 (m), 691 (s), 673 (w), 652 (m), 629 (w), 619 (m), 599 (w), 593 (m), 591 (m), 585 (w), 547 (m), 534 (m), 524 (m), 513 (m), 489 (m), 471 (m), 450 (m), 428 (m) cm^{-1}.

7.5.12 General Procedure for the (Re-)Synthesis of Ligand Pair L3

Both syntheses (TMG_3trphen and $DMEG_3$trphen) were performed following a modified version of a literature-known procedure that was reported for TMG_3trphen (**L3$_{TMG}$**) by Stavropoulos and Cronin *et al*.[156]

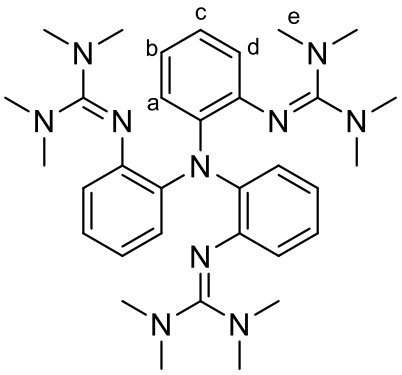

$C_{33}H_{48}N_{10}$
584.82 g/mol

Tris(2-aminophenyl)amine (1.00 g, 3.44 mmol, 1.00 eq.), together with the corresponding Vilsmeier salt (TMG-VS: 1.89 g, 11.02 mmol, 3.2 eq. or DMEG-VS: 2.04 g, 12.05 mmol, 3.5 eq.) and triethylamine (3.3 eq.) were placed into a preheated round-bottom flask and dissolved in absolute acetonitrile (100 mL) under nitrogen counterflow. The reaction mixture was refluxed under a nitrogen atmosphere for 6 hours. Subsequently, the mixture was cooled to room temperature and treated with sodium hydroxide solution (100 mL, 1:1 w/w). The product was extracted with ethyl acetate (3 x 100 mL) from the aqueous phase, the combined organic phases were dried over $MgSO_4$, and the solvent was removed under reduced pressure. For purification, the product was recrystallized five times in acetonitrile. The product was stored under an inert atmosphere to avoid protonation. TMG_3trphen (**L3$_{TMG}$**) was obtained in the form of colorless crystals (0.430 g, 0.74 mmol, 21 %).

^{1}H NMR (400 MHz, $CDCl_3$) δ [ppm] = 7.00-6.89 (m, 3H, H-a), 6.80-6.89 (m, 3H, H-c), 6.64-6.60 (m, 3H, H-b), 6.27-6.20 (m, 3H, H-d), 2.44 (s, 36H, H-e).

DMEG$_3$trphen (**L3$_{DMEG}$**) was obtained in the form of light purple crystals (0.870 g, 1.50 mmol, 44 %).

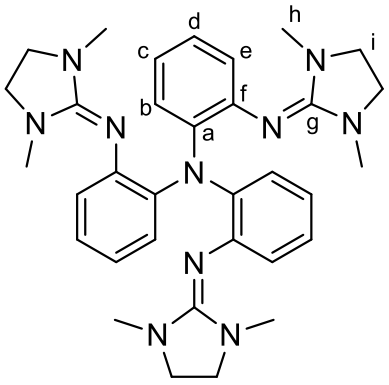

$C_{33}H_{42}N_{10}$
578.77 g/mol

^{1}H NMR (400 MHz, CD_2Cl_2) δ [ppm] = 6.84 (dd, *J* = 7.7, 1.6 Hz, 3H, H-b), 6.74 (td, *J* = 7.5, 1.7 Hz, 3H, H-d), 6.65 – 6.57 (m, 6H, H-e, H-c), 3.03 (s, 12H, H-i), 2.37 (s, 18H, H-h).

^{13}C NMR (101 MHz, CD_2Cl_2) δ [ppm] = 152.7 (g, 3C), 144.5 (a, 3C), 141.3 (f, 3C), 127.3 (b, 3C), 123.2 (c, 3C), 121.9 (d, 3C), 119.6 (e, 3C), 48.8 (i, 6C), 35.2 (h, 6C).

HR-ESI-MS (m/z (%) $[M+H]^+$, M+H = $C_{33}H_{43}N_{10}$) found: 579.3572 (100), 580.3600 (38), 581.3629 (7), calculated: 579.3672 (100) $[^{12}C_{33}{}^{1}H_{42}{}^{14}N_{10}]^+$, 580.3705 (36) $[^{12}C_{32}{}^{13}C^{1}H_{42}{}^{14}N_{10}]^+$, 581.3676 (1) $[^{12}C_{31}{}^{13}C_2{}^{1}H_{43}{}^{14}N_{10}]^+$.

IR (ATR, $\tilde{\nu}$) = 3047 (w), 3018 (w), 2971 (w), 2940 (w), 2867 (w), 2845 (w), 2767 (w), 2224 (w), 2201 (w), 2162 (w), 2158 (w), 2117 (w), 2087 (w), 2051 (w), 2029 (w), 1980 (w), 1973 (w), 1651 (vs), 1579 (vs), 1476 (vs), 1432 (vs), 1417 (m), 1394 (s), 1389 (s), 1309 (m), 1296 (m), 1281 (vs), 1278 (vs), 1260 (s), 1239 (s), 1201 (m), 1173 (w), 1154 (w), 1142 (m), 1121 (w), 1113 (m), 1105 (m), 1077 (w), 1074 (w), 1044 (m), 1033 (vs), 992 (w), 969 (s), 941 (w), 930 (w), 917 (m), 871 (w), 854 (w), 844 (w), 833 (w), 766 (m), 761 (m), 753 (m), 742 (s), 735 (vs), 720 (m), 712 (s), 697 (m), 687 (w), 650 (m), 643 (w), 628 (w), 619 (m), 598 (w), 587 (w), 560 (w), 545 (w), 536 (w), 530 (w), 529 (w), 507 (m), 485 (m), 472 (m), 462 (m), 445 (w), 429 (w), 426 (w), 405 (w), 398 (w), 385 (w), 366 (w), 357 (w) cm^{-1}.

7.5.13 Synthesis of [Cu(I){N(QuMe)$_2$(PhTMG)}]PF$_6$ (C1$_{TMG}$–PF$_6$)

A preheated Schlenk tube was charged with $[Cu(MeCN)_4]PF_6$ (163 mg, 432 µmol, 1.00 eq.) and N(QuMe)$_2$(PhTMG) (234 mg, 478 µmol, 1.11 eq.) in a nitrogen counterflow. The solids were dissolved in acetonitrile (5.00 mL) and stirred for 30 min at 30 °C. Afterwards, diethyl ether was added to the mixture and the resulting yellow precipitate was filtered off under reduced pressure. The product was washed with diethyl ether (3x 10 mL) and dried *in vacuo*. [Cu(I){N(QuMe)$_2$(PhTMG)}]PF$_6$ (**C1$_{TMG}$–PF$_6$**) was obtained as a yellow powder (216 mg, 310 µmol, 72 % yield).

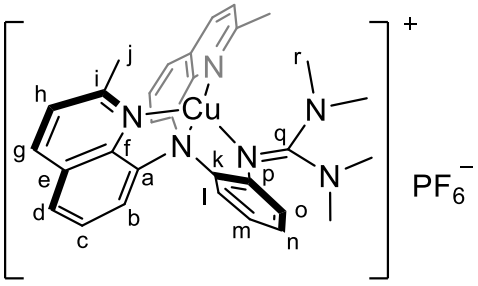

$C_{31}H_{32}N_6CuPF_6$
697.15 g/mol

^{1}H NMR (400 MHz, CD_3CN) *δ* [ppm] = 8.28 (d, *J* = 8.5 Hz, 2H, H-g), 7.78 (d, *J* = 8.1 Hz, 2H, H-d), 7.69 (d, *J* = 7.6 Hz, 2H, H-b), 7.55 – 7.41 (m, 4H, H-h, H-c), 7.35 (dd, *J*

= 8.0, 1.5 Hz, 1H, H-o), 7.11 (td, *J* = 7.6, 1.6 Hz, 1H, H-m), 6.89 (td, *J* = 7.5, 1.6 Hz, 1H, H-n), 6.61 (dd, *J* = 8.0, 1.5 Hz, 1H, H-l), 3.11 – 2.12 (m, *J* = 140.6 Hz, 18H, H-j, H-r).

^{13}C NMR (101 MHz, CD_3CN) *δ* [ppm] = 164.6 (q, 1C), 159.0 (i, 2C), 149.1 (k, 1C), 145.5 (a, 2C), 144.0 (f, 2C), 139.8 (p, 1C), 138.4 (g, 2C), 129.5 (b,o, 3C), 129.4 (e, 2C), 128.1 (m, 1C), 126.9 (c, 2C), 126.8 (d, 2C), 124.2 (h, 2C), 122.8 (l, 1C), 122.4 (n, 1C), 40.1 (r, 4C), 27.4 (j, 2C).

HR-ESI-MS (m/z (%) $[M]^+$, M = $C_{31}H_{32}N_6Cu$) found: 551.1979 (100), 552.2010 (33), 553.1967 (41), 554.1994 (15), 555.2023 (4), calculated: 551.1979 (100) $[^{12}C_{31}{}^{1}H_{32}{}^{14}N_6{}^{63}Cu]^+$, 552.2013 (34) $[^{12}C_{30}{}^{13}C^{1}H_{32}{}^{14}N_6{}^{63}Cu]^+$, 553.1961 (45) $[^{12}C_{31}{}^{1}H_{32}{}^{14}N_6{}^{65}Cu]^+$, 554.1995 (15) $[^{12}C_{30}{}^{13}C^{1}H_{32}{}^{14}N_6{}^{65}Cu]^+$, 555.2028 (2) $[^{12}C_{29}{}^{13}C_2{}^{1}H_{32}{}^{14}N_6{}^{65}Cu]^+$.

IR (ATR, $\tilde{\nu}$) = 3321 (w), 3302 (m), 3244 (w), 3159 (w), 2924 (w), 1636 (s), 1598 (s), 1532 (w), 1425 (w), 1376 (s), 1342 (vs), 1304 (vs), 1281 (vs), 1266 (vs), 1159 (w), 1146 (w), 1100 (vs), 1059 (vs), 1045 (s), 1032 (w), 1020 (w), 1012 (w), 989 (s), 867 (w), 826 (vs), 792 (w), 750 (m), 590 (w), 553 (s), 515 (w) cm^{-1}.

XRD: Section 9.1.1

7.5.14 Synthesis of [Cu(I){N(QuMe)$_2$(PhDMEG)}]PF$_6$ (C1$_{DMEG}$–PF$_6$)

A Schlenk tube was charged with $[Cu(MeCN)_4]PF_6$ (200 mg, 531 µmol, 1.00 eq.) and N(QuMe)$_2$(PhDMEG) (340 mg, 699 µmol, 1.32 eq.) in a nitrogen counterflow. The solids were dissolved in acetonitrile (1.50 mL) and stirred for 30 min at 30 °C. Afterwards, diethyl ether was added to the mixture and the resulting yellow precipitate was filtered off under reduced pressure. The product was washed with diethyl ether (3x 5 mL) and dried *in vacuo*. [Cu(I){N(QuMe)$_2$(PhDMEG)}]PF$_6$ (**C1$_{DMEG}$–PF$_6$**) was obtained as a yellow powder (279 mg, 401 µmol, 75 % yield).

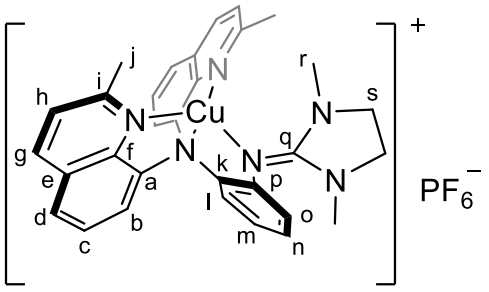

$C_{31}H_{30}N_6CuPF_6$
695.13 g/mol

^{1}H NMR (400 MHz, CD_3CN) *δ* [ppm] = 8.28 (d, *J* = 8.5 Hz, 2H, H-g), 7.78 (dd, *J* = 8.1, 1.4 Hz, 2H, H-d), 7.60 (dd, *J* = 7.5, 1.3 Hz, 2H, H-b), 7.52 – 7.40 (m, 4H, H-c, H-h), 7.19 (dd, *J* = 8.0, 1.5 Hz, 1H, H-o), 7.11 – 7.02 (m, 1H, H-m), 6.91 (dd, *J* = 8.1, 1.6 Hz, 1H, H-l), 6.88 – 6.76 (m, 1H, H-n), 3.20 (s, 4H, H-s), 2.67 (s, 6H, H-j), 2.56 (s, 6H, H-r).

^{13}C NMR (101 MHz, CD_3CN) *δ* [ppm] = 163.4 (q, 1C), 159.0 (i, 2C), 147.5 (k, 1C), 145.4 (a, 2C), 143.7 (f, 2C), 139.9 (p, 1C), 138.4 (g, 2C), 129.3 (e, 2C), 128.8 (o, 1C),

128.9 (b, 2C), 127.5 (m, 1C), 126.9 (c, 2C), 126.6 (d, 2C), 124.2 (h, 2C), 123.7 (l, 1C), 122.0 (n, 1C), 48.9 (s, 2C), 35.9 (r, 2C), 27.2 (j, 2C).

HR-ESI-MS (m/z (%) $[M]^+$, M = $C_{31}H_{30}N_6Cu$) found: 549.1737 (100), 550.1769 (34), 551.1727 (47), 552.1752 (16), 553.1782 (3), calculated: 549.1828 (100) $[^{12}C_{31}{}^{1}H_{30}{}^{14}N_6{}^{63}Cu]^+$, 550.1891 (35) $[^{12}C_{30}{}^{13}C^{1}H_{30}{}^{14}N_6{}^{63}Cu]^+$, 551.1810 (45) $[^{12}C_{31}{}^{1}H_{30}{}^{14}N_6{}^{65}Cu]^+$, 552.1843 (15) $[^{12}C_{30}{}^{13}C^{1}H_{30}{}^{14}N_6{}^{65}Cu]^+$, 553.1876 (2) $[^{12}C_{29}{}^{13}C_2{}^{1}H_{30}{}^{14}N_6{}^{65}Cu]^+$.

IR (ATR, $\tilde{\nu}$) = 3050 (m), 2925 (s), 2868 (s), 2847 (s), 1695 (s), 1652 (vs), 1636 (vs), 1614 (s), 1596 (vs), 1586 (vs), 1557 (s), 1500 (vs), 1478 (vs), 1460 (vs), 1429 (vs), 1396 (vs), 1368 (s), 1338 (vs), 1325 (vs), 1276 (vs), 1250 (s), 1238 (vs), 1205 (s), 1162 (s), 1136 (s), 1111 (s), 1106 (s), 1075 (s), 1030 (vs), 990 (m), 969 (s), 927 (m), 863 (m), 830 (vs), 800 (s), 791 (s), 752 (vs), 701 (s), 667 (s), 647 (s), 631 (s), 620 (s), 593 (s), 579 (s), 541 (m), 533 (m), 519 (s), 505 (s), 484 (s), 477 (s), 468 (s), 447 (s), 437 (s), 368 (s) cm^{-1}.

XRD: Section 9.1.1

7.5.15 Synthesis of [Cu(I){N(QuMe)(PhTMG)$_2$}]PF$_6$ (C3$_{TMG}$–PF$_6$)

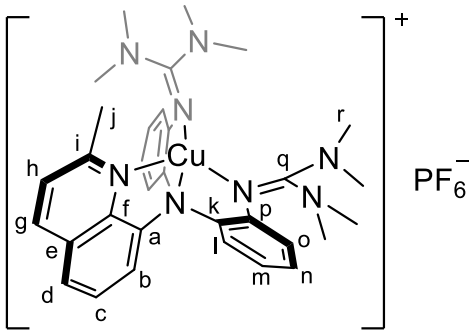

$C_{32}H_{40}N_8CuPF_6$
745.24 g/mol

A preheated Schlenk tube was charged with [Cu(MeCN)$_4$]PF$_6$ (220 mg, 584 µmol, 1.00 eq.) and N(QuMe)(PhTMG)$_2$ (313 mg, 584 µmol, 1.00 eq.) in a nitrogen counterflow. The solids were dissolved in acetonitrile (5.00 mL) and stirred for 30 min at 30 °C. Afterwards, diethyl ether was added to the mixture, and the resulting orange precipitate was filtered off under reduced pressure. The product was washed with diethyl ether (3x 10 mL) and dried in vacuo. [Cu(I){N(QuMe)(PhTMG)$_2$}]PF$_6$ (**C3$_{TMG}$–PF$_6$**) was obtained as an orange powder (364 mg, 489 µmol, 84 % yield).

^{1}H NMR (400 MHz, CD_3CN) δ [ppm] = 8.27 (d, J = 8.6 Hz, 1H H-g), 7.79 – 7.76 (m, 2H, H-b, H-d), 7.52 (t, J = 7.8 Hz, 1H, H-c), 7.46 (d, J = 8.4 Hz, 1H, H-h), 7.28 (d, J = 7.9 Hz, 2H, H-o), 7.04 (td, J = 7.5, 1.6 Hz, 2H, H-m), 6.84 (t, J = 6.8 Hz, 2H, H-n), 6.54 (dd, J = 8.0, 1.5 Hz, 2H, H-l), 3.27 – 1.61 (m, 27H, H-j, H-r).

^{13}C NMR (101 MHz, CD_3CN) δ [ppm] = 164.2 (q, 2C), 158.4 (i, 1C), 149.4 (k, 2C), 144.2 (f, 1C), 144.1 (a, 1C), 138.2 (g, 1C), 131.0 (b, 1C), 129.5 (e, p, 3C), 129.3 (o, 2C), 127.3 (m, 2C), 126.9 (c, 1C), 126.7 (d, 1C), 124.2 (h, 1C), 122.6 (l, 2C), 121.9 (n, 2C), 39.8 (r, 8C), 28.1 (j, 1C).

HR-ESI-MS (m/z (%) $[M]^+$, M = $C_{32}H_{40}N_8Cu$) found: 599.2673 (100), 600.2704 (37), 601.2661 (49), 602.2688 (18). calculated: 599.2666 (100) $[^{12}C_{32}{}^{1}H_{40}{}^{14}N_8{}^{63}Cu]^+$, 600.2700 (34) $[^{12}C_{31}{}^{13}C^{1}H_{40}{}^{14}N_8{}^{63}Cu]^+$, 601.2648 (45) $[^{12}C_{32}{}^{1}H_{40}{}^{14}N_8{}^{65}Cu]^+$, 602.2687 (15) $[^{12}C_{31}{}^{13}C^{1}H_{40}{}^{14}N_8{}^{65}Cu]^+$, 603.2715 (3) $[^{12}C_{30}{}^{13}C_2{}^{1}H_{40}{}^{14}N_8{}^{65}Cu]^+$.

IR (ATR, $\tilde{\nu}$) = 3065 (m), 2941 (m), 2880 (m), 2803 (m), 1599 (m), 1534 (vs), 1476 (s), 1441 (s), 1425 (s), 1411 (s), 1394 (vs), 1341 (m), 1326 (m), 1317 (m), 1279 (m), 1267 (m), 1237 (s), 1211 (m), 1155 (s), 1144 (m), 1111 (m), 1064 (m), 1026 (s), 926 (m), 876 (m), 831 (vs), 798 (s), 751 (vs), 741 (s), 718 (m), 703 (m), 691 (m), 674 (s), 636 (m), 629 (m), 624 (m), 556 (vs), 531 (m), 486 (s) cm^{-1}.

XRD: Section 9.1.1

7.5.16 Synthesis of [Cu(I){N(QuMe)(PhDMEG)$_2$}]PF$_6$ (C3$_{DMEG}$–PF$_6$)

A preheated Schlenk tube was charged with $[Cu(MeCN)_4]PF_6$ (105 mg, 278 µmol, 1.00 eq.) and $N(QuMe)(PhDMEG)_2$ (178 mg, 334 µmol, 1.20 eq.) in a nitrogen counterflow. The solids were dissolved in acetonitrile (5.00 mL) and stirred for 30 min at 30 °C. Afterwards, diethyl ether was added to the mixture and the resulting orange precipitate was filtered off under reduced pressure. The product was washed with diethyl ether (3x 10 mL) and dried *in vacuo*. [Cu(I){N(QuMe)(PhDMEG)$_2$}]PF$_6$ (**C3$_{DMEG}$–PF$_6$**) was obtained as an orange powder (65.0 mg, 87.7 µmol, 31 % yield).

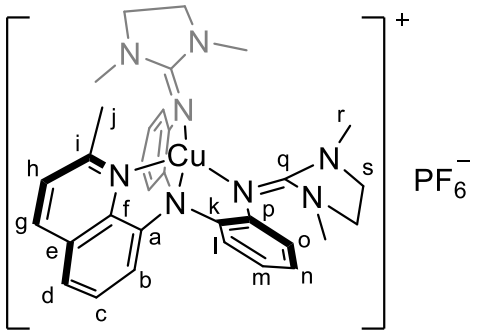

$C_{32}H_{36}N_8CuPF_6$
741.21 g/mol

^{1}H NMR (400 MHz, CD_2Cl_2) δ [ppm] = 8.30 (d, J = 8.4 Hz, 1H, H-g), 7.80 (d, J = 8.1 Hz, 1H, H-d), 7.73 (d, J = 7.4 Hz, 1H, H-b), 7.54 (t, J = 7.8 Hz, 1H, H-c), 7.48 (d, J = 8.5 Hz, 1H, H-h), 7.15 (d, J = 7.9 Hz, 2H, H-o), 7.03 (t, J = 6.9 Hz, 2H, H-m), 6.91 – 6.76 (m, 4H, H-l, H-n), 3.18 (s, 8H, H-s), 2.81 (s, 3H, H-j), 2.45 (s, 12H, H-r).

^{13}C NMR (101 MHz, CD_3CN) δ [ppm] = 162.92 (q, 2C), 158.8 (i, 1C), 147.5 (k, 2C), 144.1 (f, 1C), 143.5 (a, 1C), 140.7 (p, 2C), 138.5 (g, 1C), 131.5 (b, 1C), 129.6 (e, 1C), 128.4 (o, 2C), 127.0 (c, 1C), 126.8 (d, 1C), 126.7 (m, 2C), 124.2 (h, 1C), 123.7 (l, 2C), 121.9 (n, 2C) , 48.9 (s, 4C), 35.7 (r, 4C), 28.2 (j, 1C).

HR-ESI-MS (m/z (%) $[M]^+$, M = $C_{32}H_{36}N_8Cu$) found: 595.2270 (100), 596.2300 (37), 597.2260 (48), 598.2285 (17), 599.2314 (3). calculated: 595.2358 (100) $[^{12}C_{32}{}^{1}H_{36}{}^{14}N_8{}^{63}Cu]^+$, 596.2392 (35) $[^{12}C_{31}{}^{13}C^{1}H_{36}{}^{14}N_8{}^{63}Cu]^+$, 597.2340 (45) $[^{12}C_{32}{}^{1}H_{36}{}^{14}N_8{}^{65}Cu]^+$, 598.2374 (15) $[^{12}C_{31}{}^{13}C^{1}H_{36}{}^{14}N_8{}^{65}Cu]^+$, 599.24079 (3) $[^{12}C_{30}{}^{13}C_2{}^{1}H_{36}{}^{14}N_8{}^{65}Cu]^+$.

IR (ATR, $\tilde{\nu}$) = 2861 (w), 1697 (w), 1602 (w), 1566 (w), 1506 (w), 1479 (w), 1451 (w), 1413 (w), 1396 (w), 1288 (w), 1264 (w), 1238 (w), 1140 (w), 1117 (w), 1109 (w), 1076 (w), 1038 (w), 973 (w), 937 (w), 875 (w), 834 (s), 794 (w), 777 (w), 750 (w), 737 (w), 700 (w), 677 (w), 653 (w), 629 (w), 608 (w), 556 (m), 544 (w), 529 (w), 517 (w), 499 (w), 489 (w), 481 (w), 472 (w), 438 (w), 433 (w), 431 (w), 425 (w), 423 (w) cm^{-1}.

XRD: Section 9.1.1

7.5.17 Resynthesis of [Cu(I){TMG$_3$trphen}]PF$_6$ (C5$_{TMG}$–PF$_6$)

This molecule has been synthesized before.[156]

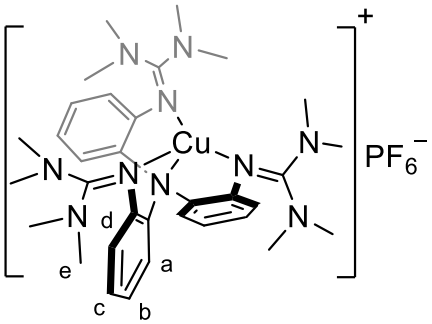

$C_{33}H_{48}N_{10}CuPF_6$
793.33 g/mol

A preheated Schlenk tube was charged with [Cu(MeCN)$_4$]PF$_6$ (40.7 mg, 108 µmol, 1.00 eq.) and TMG$_3$trphen (63.9 mg, 109 µmol, 1.01 eq.) in a nitrogen counterflow. The solids were dissolved in acetonitrile (2.5 mL) and stirred for 30 min at 30 °C. Afterwards, diethyl ether was added to the mixture and the resulting colorless precipitate was filtered off under reduced pressure. The product was washed with diethyl ether (3x 5 mL) and dried *in vacuo*. [Cu(I){TMG$_3$trphen}]PF$_6$ (**C5$_{TMG}$–PF$_6$**) was obtained as a colorless powder (69.8 mg, 88.0 µmol, 81 % yield).

^{1}H NMR (400 MHz, CD_2Cl_2) δ [ppm] = 7.24 (dd, J = 7.8, 1.6 Hz, 3H, H-a), 7.05 – 6.95 (m, 3H, H-c), 6.82 (td, J = 7.5, 1.5 Hz, 3H, H-b), 6.42 (dd, J = 7.9, 1.5 Hz, 3H, H-d), 3.35 – 2.36 (m, 27H, H-e, H-e'), 1.52 (s, 9H, H-e'').

7.5.18 Synthesis of [Cu(I){DMEG$_3$trphen}]PF$_6$ (C5$_{DMEG}$–PF$_6$)

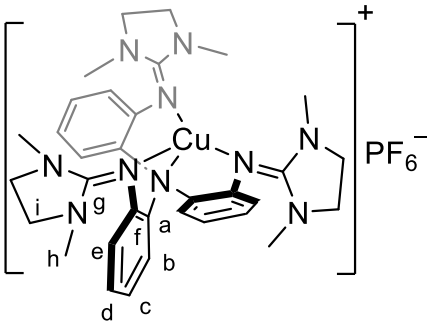

$C_{33}H_{42}N_{10}CuPF_6$
787.28 g/mol

A preheated Schlenk tube was charged with [Cu(MeCN)$_4$]PF$_6$ (111 mg, 295 µmol, 1.00 eq.) and DMEG$_3$trphen (63.1 mg, 109 µmol, 1.00 eq.) in a nitrogen counterflow. The solids were dissolved in acetonitrile (2.5 mL) and stirred for 30 min at 30 °C. Afterwards, diethyl ether was added to the mixture and the resulting colorless precipitate was filtered off under reduced pressure. The product was washed with diethyl ether (3x 5 mL) and dried *in vacuo*. [Cu(I){DMEG$_3$trphen}]PF$_6$ (**C5$_{DMEG}$–PF$_6$**) was obtained as a colorless powder (49.1 mg, 62.4 µmol, 57 % yield).

^{1}H NMR (400 MHz, CD_3CN) δ [ppm] = 7.12 (dd, J = 7.8, 1.7 Hz, 3H, H-b), 7.07 – 6.97 (m, 3H, H-d), 6.91 – 6.78 (m, 6H, H-c, H-e), 3.28 (s, 12H, H-i), 2.48 (s, 18H, H-h).

^{13}C NMR (101 MHz, CD_3CN) δ [ppm] = 163.5 (g, 3C), 147.5 (a, 3C), 140.2 (f, 3C), 129.2 (b, 3C), 126.1 (d, 3C), 123.6 (e, 3C), 121.7 (c, 3C), 48.9 (i, 6C), 35.8 (h, 6C).

HR-ESI-MS (m/z (%) $[M]^+$, M = $C_{33}H_{42}N_{10}Cu$) found: 641.2789 (100), 642.2819 (39), 643.2781 (49), 644.2804 (18), 645.2832 (3). calculated: 641.2889 (100) $[^{12}C_{33}{}^{1}H_{42}{}^{14}N_{10}{}^{63}Cu]^+$, 642.2923 (36) $[^{12}C_{32}{}^{13}C^{1}H_{42}{}^{14}N_{10}{}^{63}Cu]^+$, 643.2871 (45) $[^{12}C_{33}{}^{1}H_{42}{}^{14}N_{10}{}^{65}Cu]^+$, 644.2905 (16) $[^{12}C_{32}{}^{13}C^{1}H_{42}{}^{14}N_{10}{}^{65}Cu]^+$, 645.2938 (3) $[^{12}C_{31}{}^{13}C_2{}^{1}H_{42}{}^{14}N_{10}{}^{65}Cu]^+$.

IR (ATR, $\tilde{\nu}$) = 2974 (w), 2963 (w), 2960 (w), 1772 (w), 1602 (m), 1588 (w), 1574 (m), 1564 (m), 1506 (w), 1480 (m), 1465 (w), 1448 (w), 1442 (w), 1419 (w), 1398 (w), 1384 (w), 1287 (m), 1250 (w), 1235 (w), 1222 (w), 1198 (w), 1170 (w), 1151 (w), 1140 (w), 1108 (w), 1098 (w), 1071 (w), 1038 (w), 990 (w), 922 (w), 878 (w), 838 (vs), 797 (w), 754 (w), 747 (m), 738 (w), 722 (w), 704 (w), 649 (w), 622 (w), 607 (w), 592 (w), 557 (m), 545 (w), 533 (w), 494 (w), 481 (w), 479 (w), 469 (w), 462 (w), 449 (w), 419 (w) cm^{-1}.

XRD: Section 9.1.1

7.6 Syntheses of TMGqu Ligands and their corresponding Complexes

7.6.1 Resynthesis of 2-chloro-8-nitroquinoline

This molecule has been synthesized before.[243] The synthesis was performed following a procedure by Herres-Pawlis *et al*.[22]

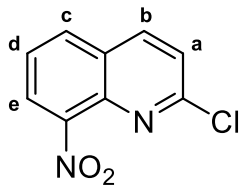

208.60 g/mol

2-chloroquinoline (24.9 g, 152 mmol, 1.00 eq.) was dissolved in conc. sulfuric acid (115 mL) and cooled to 0 °C. Fuming nitric acid (22.2 mL, 532 mmol, 3.50 eq.) was then added drop wise under stirring and the ice bath was removed afterwards. The reaction mixture was stirred at 25 °C for 4 hours and then poured on ice water. The solution was neutralized using saturated, aqueous solutions of $NaHCO_3$ and K_2CO_3. The resulting solid was filtered off, dissolved in DCM (200 mL) and washed with water (2x 250 mL). The organic phases were separated, dried over $MgSO_4$ and filtered off. The remaining solvent was removed under reduced pressure. The resulting pale yellow solid was purified using column chromatography (Hex/EtOAc 3:1, R_f = 0.23). The product 2-chloro-8-nitroquinoline was obtained as a pale yellow solid (10.6 g, 50.6 mmol, 33 % yield).

^{1}H NMR (400 MHz, $CDCl_3$) δ [ppm] = 8.21 (d, J = 8.6 Hz, 1H, H-c), 8.11 – 8.02 (m, 2H, H-c, H-e), 7.68 – 7.61 (m, 1H, H-d), 7.53 (d, J = 8.8 Hz, 1H, H-a).

7.6.2 Attempted Synthesis of 8-nitro-2-(1*H*-pyrrol-1-yl)quinoline

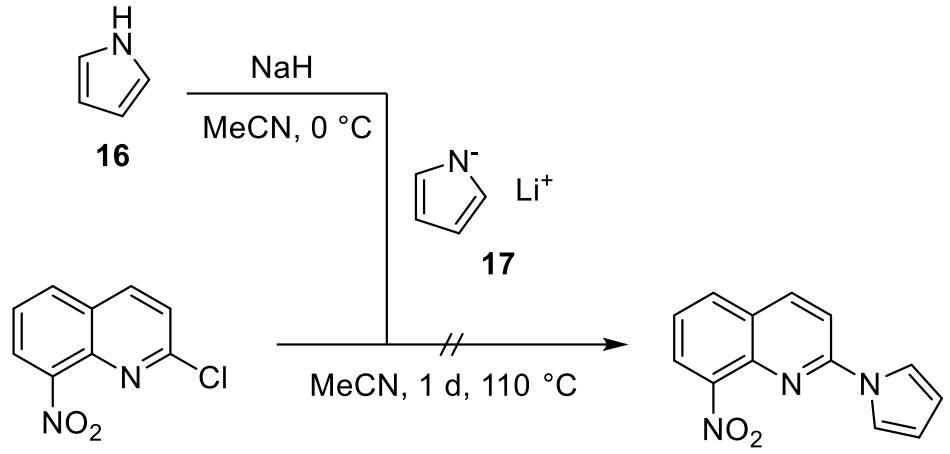

Sodium hydride (115 mg, 4.79 mmol, 1.00 eq.) was added to preheated Schlenk flask under nitrogen counterflow and dissolved in absolute acetonitrile (100 mL) at 0 °C. Pyrrole (322 mg, 333 µL, 4.79 mmol, 1.00 eq.) was slowly added to the solution via syringe and the reaction mixture was stirred at 0 °C. The cooling was removed after no gas formation could be observed and the mixture was allowed to heat to 25 °C. 2-chloro-8-nitroquinoline (1.00 g, 4.79 mmol, 1.00 eq.) was added under nitrogen counterflow and the reaction mixture was heated to reflux for 18 hours. The resulting dark red mixture was allowed to cool to 25 °C, then water (50 mL) was added to the mixture, and the organic solvent was removed under reduced pressure. The remaining solution was extracted with DCM (3x 50 mL) and the organic phases were separated and dried over $MgSO_4$ and filtered off. The remaining solvent was removed under reduced pressure, resulting in an unidentifiable red solid. No product could be detected.

7.6.3 Synthesis of 8-nitro-2-dimethylaminequinoline

The synthesis was performed following a modified procedure by Herres-Pawlis *et al*.[22]

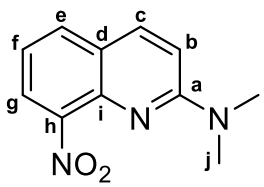

217.23 g/mol

A pressure flask (100 mL) was charged with 2-chloro-8-nitroquinoline (8.00 g, 38.4 mmol, 1.00 eq.), *N*-methylmethanamine hydrochloride (18.8 g, 230 mmol, 6.00 eq.), water (37.0 mL) and ethanol (7.30 mL). Subsequently, sodium hydroxide (9.20 g, 230 mmol, 6.00 eq.) was added to the mixture and the flask was sealed tight. The reaction mixture was then stirred and heated to 130 °C; a blast-panel placed in front of the reaction as a safety measure. After 4 hours, the initial yellow reaction had turned red and was allowed to cool to room temperature. The aqueous phase was extracted with dichloromethane (4x 50 mL), the organic phase was separated and dried over Na_2SO_4, and the remaining solvent was reduced under

reduced pressure. The remaining solution was subsequently filtered over alumina and the remaining solvent was removed under reduced pressure. The remaining yellow solid was dried *in-vacuo* and the product 8-nitro-2-dimethylaminequinoline (8.30 g, 38.2 mmol, 100 % yield) was obtained as a yellow solid without further purification. The product needs to be stored under inert conditions to prevent decomposition.

^{1}H NMR (400 MHz, $CDCl_3$) δ [ppm] = 7.91 – 7.81 (m, 2H, H-c, H-g), 7.71 (dd, J = 7.9, 1.5 Hz, 1H, H-e), 7.13 (t, J = 7.8 Hz, 1H, H-f), 6.93 (d, J = 9.3 Hz, 1H, H-b), 3.22 (s, 6H, H-j).

^{13}C NMR (101 MHz, $CDCl_3$) δ [ppm] = 158.1 (a, 1C), 145.4 (h, 1C), 140.2 (i, 2C), 137.0 (c, 1C), 131.6 (e, 1C), 124.5 (g, 1C), 123.9 (d, 1C), 119.4 (f, 1C), 110.5 (b, 1C), 37.9 (j, 2C).

HR-ESI-MS $[M+H]^+$ (m/z (%) $[M+H]^+$, M+H = $C_{11}H_{12}N_3O_2$) found: 218.09157 (100), 219.09471 (13), 220.09705 (1). Calculated: 218.09240 (100) $[^{12}C_{11}{}^{1}H_{12}{}^{14}N_3{}^{16}O_2]^+$, 219.09576 (12) $[^{12}C_{10}{}^{13}C^{1}H_{12}{}^{14}N_3{}^{16}O_2]^+$, 220.09665 (1) $[^{12}C_9{}^{13}C_2{}^{1}H_{12}{}^{14}N_3{}^{16}O_2]^+$.

IR (ATR, $\tilde{\nu}$) = 3075 (vw), 3046 (vw), 3007 (vw), 2936 (w), 2887 (vw), 2880 (vw), 2797 (vw), 1620 (vs), 1609 (s), 1520 (vs), 1489 (m), 1443 (m), 1427 (s), 1402 (w), 1387 (vs), 1352 (vs), 1333 (vs), 1236 (m), 1215 (w), 1179 (w), 1157 (vs), 1105 (w), 1070 (w), 1063 (w), 1026 (w), 1011 (vw), 978 (m), 961 (w), 922 (vw), 874 (m), 862 (m), 827 (vs), 802 (s), 795 (s), 768 (vs), 735 (m), 673 (w), 656 (s), 598 (vw), 552 (vw), 530 (w), 513 (w), 505 (w), 455 (w) cm^{-1}.

7.6.4 Synthesis of 2-*N*,2-*N*-dimethylquinoline-2,8-diamine

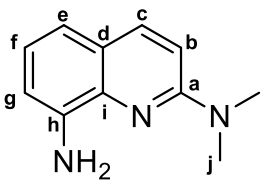

187.25 g/mol

A 500 mL Schlenk-flask was flushed with nitrogen and evacuated three times in a row. Afterwards, 2-chloro-8-nitroquinoline (5.00 g, 23.0 mmol, 1.00 eq.) and palladium on charcoal (141 mg, 10 wt%, 1.32 mmol, 0.0576 eq.) were added in nitrogen counterflow. After the flask was evacuated and flushed with nitrogen three times, the powder in the flask was allowed to settle before methanol (230 mL) was slowly added under nitrogen counterflow. The pressure inside was reduced until the solvent started to boil and then flushed with nitrogen. Then, the nitrogen atmosphere was substituted with hydrogen using balloons. Afterwards, the reaction was stirred at room temperature for 5 hours with the hydrogen balloons attached. Afterwards, the solvent was removed under reduced pressure, the crude product was dissolved in dichloromethane (100 mL) and filtered through silica to remove the catalyst. The remaining solvent was removed under reduced pressure and after drying *in-vacuo*, 2-*N*,2-*N*-dimethylquinoline-2,8-diamine (4.17 g, 22.3 mmol, 97 %

yield) was obtained as a yellow solid without further purification. The product needs to be stored under inert conditions to prevent decomposition.

^{1}H NMR (400 MHz, $CDCl_3$) δ [ppm] = 7.82 (d, J = 9.1 Hz, 1H, H-c), 7.06 – 6.98 (m, 2H, H-e, H-g), 6.92 – 6.83 (m, 2H, H-b, H-f), 4.70 (s, 2H, H-N), 3.21 (s, 6H, H-j).

^{13}C NMR (101 MHz, $CDCl_3$) δ [ppm] = 156.3 (a, 1C), 141.6 (i, 1C), 137.7 (h, 1C), 137.5 (c, 1C), 122.3 (C-d), 122.1 (e/g, 1C), 116.3 (e/g, 1C), 111.0 (f, 1C), 109.3 (b, 1C), 38.3 (j, 2C).

HR-ESI-MS $[M+H]^+$ (m/z (%) $[M+H]^+$, M+H = $C_{11}H_{14}N_3$) found: 188.11782 (100), 189.12108 (11). Calculated: 188.11822 (100) $[^{12}C_{11}{}^{1}H_{14}{}^{14}N_3]^+$, 189.12158 (12) $[^{12}C_{10}{}^{13}C^{1}H_{14}{}^{14}N_3]^+$, 190.12493 (1) $[^{12}C_9{}^{13}C_2{}^{1}H_{14}{}^{14}N_3]^+$.

IR (ATR, $\tilde{\nu}$) = 3412 (w), 3316 (w), 3049 (w), 3021 (vw), 2924 (w), 2841 (w), 2187 (vw), 2160 (vw), 2039 (vw), 1919 (vw), 1883 (vw), 1736 (vw), 1618 (vs), 1605 (vs), 1560 (s), 1514 (vs), 1499 (vs), 1491 (s), 1447 (s), 1427 (vs), 1402 (w), 1377 (vs), 1344 (m), 1335 (s), 1279 (s), 1242 (m), 1186 (w), 1171 (w), 1148 (s), 1132 (w), 1076 (w), 1059 (w), 978 (m), 961 (w), 856 (w), 818 (vs), 795 (m), 741 (vs), 704 (m), 662 (m), 557 (w), 548 (w), 517 (w), 474 (w), 467 (w), 424 (vw), 415 (vw) cm^{-1}.

7.6.5 Synthesis of TMG2NMe$_2$qu (L5)

The guanidine synthesis was performed following a slightly modified procedure of Herres-Pawlis et al. which bases on the procedure of Kantlehner *et al*.[150, 226]

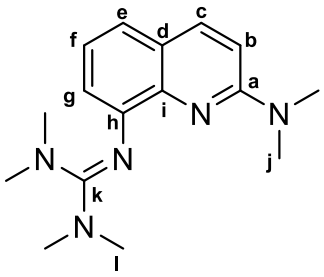

285.40 g/mol

2-*N*,2-*N*-dimethylquinoline-2,8-diamine (3.78 g, 20.2 mmol, 1.00 eq.) and TMG-VS (3.85 g, 22.5 mmol, 1.11 eq.) were dissolved in acetonitrile (80.0 mL) and triethylamine (5.68 g, 7.78 mL, 56.1 mmol, 2.78 eq.) was added. The reaction mixture was heated to reflux for 1 hour under stirring and subsequently allowed to cool to room temperature. An aqueous KOH solution (70 mL, 50 wt-%) was added to the reaction mixture and the aqueous phase was extracted with acetonitrile (3x 50 mL). The organic layer was separated, dried over Na_2SO_4 and the remaining solvent was removed under reduced pressure. The remaining brown oil was then dissolved in small amounts of DCM and filtered through alumina with DCM as eluent, after which the solvent was removed under reduced pressure. The resulting oil was then heated under vacuum (<10^{-1} mbar), starting at 100 °C and rising to 250 °C, to remove any remaining urea derivative. TMG2NMe$_2$qu (**L5**) (5.00 g, 17.5 mmol, 87 % yield) was obtained as a brown oil that slowly solidifies in several weeks. The product needs to be stored under inert conditions to avoid protonation.

^{1}H NMR (400 MHz, $CDCl_3$) δ [ppm] = 7.79 (d, J = 9.0 Hz, 1H, H-c), 7.10 – 7.04 (m, 3H, H-e, H-f, H-g), 6.78 (d, J = 9.0 Hz, 1H, H-b), 3.10 (s, 6H, H-j), 2.64 (s, 12H, H-l).

^{13}C NMR (101 MHz, $CDCl_3$) δ [ppm] = 162.0 (k, 1C), 156.6 (a, 1C), 147.7 (h, 1C), 141.3 (i, 1C), 137.6 (c, 1C), 123.0 (d, 1C), 122.4 (e/f/g, 1C), 120.8 (e/f/g, 1C), 118.5 (e/f/g, 1C), 108.1 (b, 1C), 39.5 (l, 4C), 37.8 (j, 2C).

HR-ESI-MS $[M+H]^+$ (m/z (%) $[M+H]^+$, M+H = $C_{16}H_{24}N_5$) found: 286.20252 (100), 287.20553 (18), 288.20857 (2). Calculated: 286.20262 (100) $[^{12}C_{16}{}^{1}H_{24}{}^{14}N_5]^+$, 287.20598 (17) $[^{12}C_{15}{}^{13}C^{1}H_{24}{}^{14}N_5]^+$, 288.20933 (1) $[^{12}C_{14}{}^{13}C_2{}^{1}H_{24}{}^{14}N_5]^+$.

IR (ATR, $\tilde{\nu}$) = 3048 (vw), 2997 (vw), 2926 (w), 2874 (w), 2847 (w), 2816 (w), 2789 (vw), 1611 (vs), 1570 (vs), 1553 (vs), 1501 (vs), 1462 (s), 1454 (s), 1437 (vs), 1423 (vs), 1400 (s), 1375 (vs), 1360 (vs), 1323 (m), 1306 (m), 1275 (w), 1225 (m), 1215 (s), 1177 (m), 1140 (vs), 1109 (w), 1080 (m), 1061 (m), 1053 (s), 1011 (vs), 974 (m), 959 (w), 945 (vw), 926 (w), 881 (w), 856 (w), 831 (s), 826 (vs), 806 (w), 799 (s), 752 (vs), 745 (vs), 712 (w), 681 (m), 665 (m), 621 (w), 569 (w), 519 (w), 501 (vw), 459 (w) cm^{-1}.

7.6.6 Synthesis of 8-nitro-2-phenylquinoline

The procedure was inspired by Ortíz-Alvarado, Chacón-García and Solorio-Alvarado *et al.*[195]

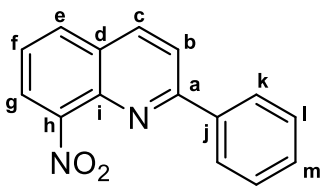

250.26 g/mol

A Schlenk-flask was evacuated and flushed with nitrogen gas three times. Under nitrogen counterflow, it was charged with 2-chloro-8-nitroquinoline (2.00 g, 9.59 mmol, 1.00 eq.), phenylboronic acid (1.40 g, 11.5 mmol, 1.20 eq.), palladium triphenylphosphane (295 mg, 255 µmol, 0.027 eq.) and sodium carbonate (1.21 g, 11.4 mmol, 1.19 eq.). The flask was again evacuated and flushed with nitrogen three times, then toluene (20.0 mL) and water (4.00 mL) were added under nitrogen counterflow. The flask was connected to a reflux condenser under inert conditions and left stirring at 110 °C for 18 h. Afterwards, the reaction mixture was allowed to cool to room temperature, and the mixture was extracted with DCM (3x 20 mL). The combined organic phases were dried over $MgSO_4$, and the remaining solvent was removed under reduced pressure. The resulting red oil was purified using column chromatography (pentane/EtOAc = 3/2, R_f = 0.46), the solvent was removed under reduced pressure, and the product was dried *in-vacuo*. 8-nitro-2-phenylquinoline (1.52 g, 6.07 mmol, 63 % yield) was obtained as a yellow solid.

^{1}H NMR (400 MHz, $CDCl_3$) δ [ppm] = 8.29 (d, J = 8.8 Hz, 1H, H-c), 8.24 – 8.18 (m, 2H, H-k), 8.05 – 7.97 (m, 3H, H-b, H-e, H-g), 7.58 – 7.49 (m, 4H, H-f, H-l, H-m).

^{13}C NMR (101 MHz, $CDCl_3$) δ [ppm] = 159.0 (a, 1C), 148.8 (h, 1C), 139.6 (i, 1C), 138.5 (j, 1C), 137.2 (c, 1C), 131.9 (e/g, 1C), 130.7 (m, 1C), 129.3 (l, 2C), 128.4 (d, 1C), 128.0 (k, 2C), 125.2 (f, 1C), 124.0 (e/g, 1C), 120.5 (b, 1C).

HR-ESI-MS $[M+H]^+$ (m/z (%) $[M+H]^+$, M+H = $C_{15}H_{11}N_2O_2$) found: 251.08116 (100), 252.08442 (17), 253.08664 (2). Calculated: 251.08150 (100) $[^{12}C_{15}{}^{1}H_{11}{}^{14}N_2{}^{16}O_2]^+$, 252.08486 (16) $[^{12}C_{14}{}^{13}C^{1}H_{11}{}^{14}N_2{}^{16}O_2]^+$, 253.08821 (1) $[^{12}C_{13}{}^{13}C_2{}^{1}H_{11}{}^{14}N_2{}^{16}O_2]^+$.

IR (ATR, $\tilde{\nu}$) = 3094 (vw), 3055 (vw), 2955 (vw), 2920 (vw), 2870 (vw), 2855 (vw), 1622 (w), 1612 (vw), 1599 (m), 1582 (w), 1564 (vw), 1553 (w), 1520 (vs), 1506 (vs), 1489 (s), 1458 (w), 1443 (m), 1423 (w), 1377 (w), 1354 (vs), 1323 (s), 1310 (w), 1287 (m), 1223 (w), 1215 (w), 1207 (w), 1182 (w), 1157 (w), 1146 (w), 1103 (vw), 1074 (w), 1049 (vw), 1022 (w), 1001 (vw), 993 (vw), 980 (w), 924 (w), 881 (m), 858 (w), 845 (vs), 818 (vw), 795 (s), 760 (vs), 731 (w), 702 (m), 691 (vs), 658 (vs), 619 (vw), 604 (w), 565 (vw), 550 (w), 513 (w), 501 (w), 457 (vw), 442 (vw), 432 (w) cm^{-1}.

7.6.7 Synthesis of 2-phenylquinolin-8-amine

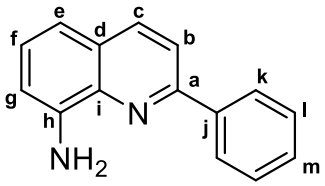

220.28 g/mol

A Schlenk-flask was evacuated and flushed with nitrogen three times. 8-nitro-2-phenylquinoline (2.69 g, 10.7 mmol, 1.00 eq.) and palladium on charcoal (60.0 mg, 10 wt-% Pd, 56 µmol, 0.00525 eq. Pd) were added under nitrogen counterflow; the flask was subsequently evacuated and flushed with nitrogen three times. The powder in the flask was allowed to settle before methanol (120 mL) was slowly added under nitrogen counter flow. The pressure inside was reduced until the solvent started to boil and then flushed with nitrogen. Then, the nitrogen atmosphere was substituted with hydrogen gas using balloons. Afterwards, the reaction was stirred at room temperature for 4 hours with the hydrogen balloons attached. The solvent was removed under reduced pressure, the crude product was dissolved in ethyl acetate (100 mL) and filtered through silica to remove the catalyst, the solvent was subsequently removed under reduced pressure. The resulting red solid was further purified using column chromatography (Hexane/EtOAc = 3/1, R_f = 0.35), after which the solvent was removed under reduced pressure and the product was dried *in-vacuo*. 2-phenylquinolin-8-amine (1.88 g, 8.54 mmol, 79 % yield) was obtained as a yellow solid and stored under inert conditions to avoid decomposition.

^{1}H NMR (400 MHz, CD_2Cl_2) δ [ppm] = 8.22 (dd, J = 8.4, 1.3 Hz, 2H, H-k), 8.16 (d, J = 8.6 Hz, 1H, H-c), 7.90 (d, J = 8.6 Hz, 1H, H-b), 7.58 – 7.51 (m, 2H, H-l), 7.50 – 7.44 (m, 1H, H-m), 7.33 (t, J = 7.9 Hz, 1H, H-f), 7.17 (dd, J = 8.1, 1.3 Hz, 1H, H-g), 6.95 (dd, J = 7.5, 1.3 Hz, 1H, H-e), 5.14 (s, 2H, H-N).

^{13}C NMR (101 MHz, CD_2Cl_2) δ [ppm] = 154.3 (a, 1C), 144.8 (h, 1C), 139.9 (j, 1C), 138.3 (i, 1C), 137.2 (c, 1C), 129.5 (m, 1C), 129.1 (l, 2C), 128.2 (d, 1C), 127.7 (f, 1C), 127.6 (k, 2C), 119.2 (b, 1C), 115.8 (g, 1C), 110.3 (e, 1C).

HR-ESI-MS $[M+H]^+$ (m/z (%) $[M+H]^+$, M+H = $C_{15}H_{13}N_2$) found: 221.10713 (100), 222.11041 (17), 223.11365 (1). Calculated: 221.10733 (100) $[^{12}C_{15}{}^{1}H_{13}{}^{14}N_2]^+$, 222.11068 (16) $[^{12}C_{14}{}^{13}C^{1}H_{13}{}^{14}N_2]^+$, 223.11404 (1) $[^{12}C_{13}{}^{13}C_2{}^{1}H_{13}{}^{14}N_2]^+$.
$[M+Na]^+$ (m/z (%) $[M+Na]^+$, M+Na = $NaC_{15}H_{12}N_2$) found: 243.08912 (100), 244.09238 (16), 245.11479 (6). Calculated: 243.08927 (100) $[^{23}Na^{12}C_{15}{}^{1}H_{12}{}^{14}N_2]^+$, 244.09262 (16) $[^{23}Na^{12}C_{14}{}^{13}C^{1}H_{12}{}^{14}N_2]^+$, 245.08966 (1) $[^{23}Na^{12}C_{13}{}^{13}C_2{}^{1}H_{12}{}^{14}N_2]^+$.
$[M+K]^+$ (m/z (%) $[M+K]^+$, M+K = $KC_{15}H_{12}N_2$) found: 259.06310 (100), 260.06633 (17), 261.06195 (7). Calculated: 259.06321 (100) $[^{39}K^{12}C_{15}{}^{1}H_{12}{}^{14}N_2]^+$, 260.06656 (16) $[^{39}K^{12}C_{14}{}^{13}C^{1}H_{12}{}^{14}N_2]^+$, 261.06133 (7) $[^{41}K^{12}C_{13}{}^{13}C^{1}H_{12}{}^{14}N_2]^+$, 261.06992 (1) $[^{41}K^{12}C_{13}{}^{13}C_2{}^{1}H_{12}{}^{14}N_2]^+$.

IR (ATR, $\tilde{\nu}$) = 3431 (w), 3310 (w), 3051 (w), 3036 (w), 1614 (m), 1589 (s), 1578 (m), 1560 (w), 1553 (w), 1508 (s), 1491 (vs), 1470 (vs), 1443 (w), 1429 (s), 1375 (vs), 1342 (s), 1337 (s), 1302 (w), 1298 (w), 1285 (m), 1273 (m), 1227 (w), 1155 (vw), 1128 (m), 1103 (w), 1086 (w), 1076 (w), 1055 (vw), 1020 (w), 999 (vw), 972 (vw), 966 (w), 959 (vw), 918 (vw), 891 (vw), 881 (w), 843 (w), 831 (vs), 810 (vw), 760 (vs), 750 (vs), 723 (w), 689 (vs), 644 (w), 588 (w), 569 (w), 550 (w), 534 (w), 525 (w), 501 (w), 484 (w), 463 (w), 422 (vw) cm^{-1}.

7.6.8 Synthesis of TMG2Phqu (L6)

The guanidine synthesis was performed following a slightly modified procedure of Herres-Pawlis *et al.* which itself is based on the procedure of Kantlehner *et al*.[150, 226]

A preheated Schlenk-flask was charged with 2-phenylquinolin-8-amine (700 mg, 3.18 mmol, 1.00 eq.) and TMG-VS (650 mg, 3.80 mmol, 1.20 eq.) and acetonitrile (abs., 30 mL) under nitrogen counterflow. Triethylamine (639 mg, 880 µL, 6.31 mmol, 1.99 eq.) was added under nitrogen counterflow and the reaction mixture was heated to reflux for 90 minutes under stirring and subsequently allowed to cool to room temperature. An aqueous KOH solution (25 mL, 50 wt-%) was added to the reaction mixture and the aqueous phase was extracted with acetonitrile (3x 50 mL). The organic layer was separated, dried over Na_2SO_4 and the remaining solvent was removed under reduced pressure. The resulting brown oil was then dissolved in small amounts of DCM and filtered over alumina with DCM as eluent, after which the solvent was removed under reduced pressure. The resulting yellow oil was then heated under vacuum (<10^{-1} mbar), starting at 100 °C and rising to 250 °C, to remove any remaining urea derivative. TMG2Phqu

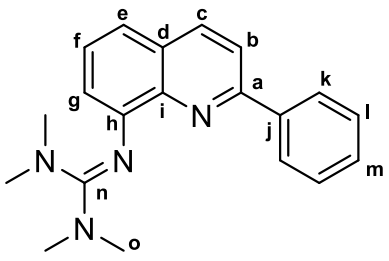

318.42 g/mol

(**L6**) (710 mg, 2.23 mmol, 70 % yield) was obtained as a yellow, wax-like solid. The product needs to be stored under inert conditions to avoid protonation.

^{1}H NMR (400 MHz, CD_2Cl_2) δ [ppm] = 8.23 – 8.18 (m, 2H, H-k), 8.15 (d, *J* = 8.7 Hz, 1H, H-c), 7.86 (d, *J* = 8.6 Hz, 1H, H-b), 7.52 – 7.46 (m, 2H, H-l), 7.45 – 7.36 (m, 2H, H-f, H-m), 7.26 (dd, *J* = 8.1, 1.5 Hz, 1H, H-e), 7.09 (dd, *J* = 7.5, 1.5 Hz, 1H, H-g), 2.64 (s, 12H, H-o).

^{13}C NMR (101 MHz, CD_2Cl_2) δ [ppm] = 162.8 (n, 1C), 154.0 (a, 1C), 151.5 (h, 1C), 142.2 (i, 1C), 140.1 (j, 1C), 137.2 (c, 1C), 129.2 (m, 1C), 128.9 (l, 2C), 128.5 (d, 1C), 127.8 (f, 1C), 127.3 (k, 2C), 120.1 (g, 1C), 117.9 (e, 1C), 117.8 (b, 1C), 39.7 (o, 4C).

HR-ESI-MS $[M+H]^+$ (m/z (%) $[M+H]^+$, M+H = $C_{20}H_{23}N_4$) found: 319.19151 (100), 320.19466 (22), 321.19780 (2). Calculated: 319.19172 (100) $[^{12}C_{20}{}^{1}H_{23}{}^{14}N_4]^+$, 320.19508 (22) $[^{12}C_{19}{}^{13}C{}^{1}H_{23}{}^{14}N_4]^+$, 321.19843 (2) $[^{12}C_{18}{}^{13}C_2{}^{1}H_{23}{}^{14}N_4]^+$.

IR (ATR, $\tilde{\nu}$) = 3055 (w), 3046 (w), 3019 (w), 3015 (w), 2990 (w), 2930 (w), 2876 (w), 2864 (w), 2845 (w), 2814 (vw), 2806 (vw), 2791 (w), 1618 (w), 1584 (s), 1564 (vs), 1541 (vs), 1506 (vs), 1487 (vs), 1472 (s), 1456 (vs), 1429 (vs), 1420 (vs), 1400 (m), 1381 (vs), 1366 (vs), 1348 (s), 1319 (m), 1302 (w), 1285 (m), 1234 (w), 1223 (s), 1186 (w), 1161 (w), 1140 (vs), 1109 (w), 1090 (m), 1061 (m), 1013 (vs), 999 (m), 957 (w), 939 (w), 924 (w), 889 (w), 853 (w), 839 (vs), 820 (w), 779 (vs), 766 (vs), 756 (vs), 710 (s), 698 (s), 677 (s), 638 (vw), 627 (w), 619 (w), 583 (vw), 573 (w), 552 (w), 532 (vw), 505 (w), 476 (w), 467 (vw), 457 (w), 420 (w) cm^{-1}.

7.6.9 Synthesis of $[Cu(TMG2NMe_2qu)_2]PF_6$ ($C7–PF_6$)

Inside a glove box, a 20 mL vial was charged with $TMG2NMe_2qu$ (1.00 g, 3.50 mmol, 2.10 eq.) and $[Cu(MeCN)_4]PF_6$ (622 mg, 1.67 mmol, 1.00 eq.). The solids were dissolved in dichloromethane (4 mL) and pentane was allowed to diffuse into the solution for a week. Afterwards, black column-like crystals could be filtered off and dried *in vacuo*. $[Cu(TMG2NMe2qu)_2]PF_6$ (**$C7–PF_6$**) (1.30 g, 1.62 mmol, 97 % yield, 97 % purity) was obtained in the form of brown crystals.

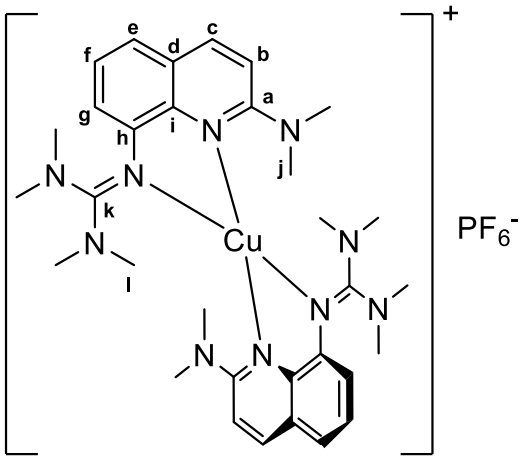

779.30 g/mol

^{1}H NMR (400 MHz, CD_3CN) δ]ppm] = 7.96 (d, *J* = 8.6 Hz, 2H, H-c), 7.26 (dd, *J* = 7.9, 1.4 Hz, 2H, H-e), 7.11 (t, *J* = 7.7 Hz, 2H, H-f), 7.02 (br. s, 2H, H-g), 6.63 (d, *J* = 7.5 Hz, 2H, H-b), 3.26 (s, 12H, H-j), 2.41 (s, 24H, H-l).

^{13}C NMR (101 MHz, CD_3CN) δ [ppm] = 164.3 (k, 2C), 157.5 (a, 2C), 145.6 (h, 2C), 142.2 (i, 2C), 138.8 (c, 2C), 124.3 (d, 2C), 123.3 (f, 2C), 121.0 (e, 2C), 119.6 (b, 2C), 111.8 (g, 2C), 40.0 (C-j, C-l, 12C).

HR-ESI-MS $[Cu(TMG2NMe_2qu)_2]^+$ (m/z (%) $[M]^+$, M = $C_{32}H_{46}N_{10}Cu$) found: 633.32126 (100), 634.32478 (35), 635.31935 (46), 636.32294 (15), 637.32662 (1). Calculated: 633.31974 (100) $[^{12}C_{32}{}^{1}H_{46}{}^{14}N_{10}{}^{63}Cu]^+$, 634.32310 (35) $[^{12}C_{31}{}^{13}C^{1}H_{46}{}^{14}N_{10}{}^{63}Cu]^+$, 635.31793 (45) $[^{12}C_{32}{}^{1}H_{46}{}^{14}N_{10}{}^{65}Cu]^+$, 636.32129 (15) $[^{12}C_{31}{}^{13}C^{1}H_{46}{}^{14}N_{10}{}^{65}Cu]^+$, 637.32464 (3) $[^{12}C_{30}{}^{13}C_2{}^{1}H_{46}{}^{14}N_{10}{}^{63}Cu]^+$.
$[Cu(TMG2NMe_2qu)_2{-}C_{16}H_{23}N_5]^+$ (m/z (%), $[M]^+$, M = $C_{16}H_{23}N_5Cu$) found: 348.12544 (100), 349.12848 (17), 350.12350 (47), 351.12648 (5), 352.12955 (<1). Calculated: 348.12440 (100) $[^{12}C_{16}{}^{1}H_{23}{}^{14}N_5{}^{63}Cu]^+$, 349.13067 (17) $[^{12}C_{15}{}^{13}C^{1}H_{23}{}^{14}N_5{}^{63}Cu]^+$, 350.12260 (45) $[^{12}C_{16}{}^{1}H_{23}{}^{14}N_5{}^{65}Cu]^+$, 351.12594 (8) $[^{12}C_{15}{}^{13}C^{1}H_{23}{}^{14}N_5{}^{65}Cu]^+$, 352.12930 (1) $[^{12}C_{14}{}^{13}C_2{}^{1}H_{23}{}^{14}N_5{}^{65}Cu]^+$.

IR (ATR, $\tilde{\nu}$) = 3049 (vw), 3003 (vw), 2928 (vw), 2886 (vw), 2878 (vw), 2868 (vw), 2803 (vw), 2374 (vw), 2166 (vw), 2029 (vw), 2018 (vw), 1981 (vw), 1616 (w), 1599 (w), 1522 (vs), 1518 (vs), 1489 (w), 1470 (m), 1441 (m), 1422 (s), 1408 (m), 1391 (s), 1383 (s), 1364 (m), 1348 (w), 1339 (m), 1271 (w), 1236 (w), 1223 (w), 1180 (w), 1153 (m), 1111 (vw), 1082 (vw), 1065 (w), 1018 (m), 980 (w), 930 (vw), 876 (w), 833 (vs), 791 (m), 752 (m), 710 (w), 694 (w), 673 (vw), 638 (w), 575 (w), 555 (vs), 523 (w) cm^{-1}.

XRD: Section 9.1.2

7.6.10 Synthesis of $[Cu(TMG2NMe_2qu)_2](OTf)_2$ (C8–OTf)

To a solution of $TMG2NMe_2qu$ (31.0 mg, 109 µmol, 2.20 eq.) in DCM (1 mL) a solution of $[Cu(MeCN)_4](OTf)_2$ (26.0 mg, 49.4 µmol, 1.00 eq.) in MeCN (1 mL) was added, resulting in an immediate blackening of the mixture. By slow diffusion of Et_2O, the compound $[Cu(TMG2NMe_2qu)_2](OTf)_2$ (**C8–OTf**) crystallized after a few days in the form of black crystals.

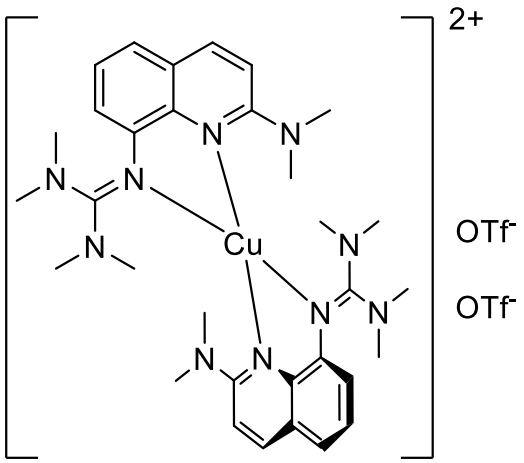

932.46 g/mol

XRD: Section 9.1.2

EPR: Section 4.6

7.6.11 Synthesis of $[Cu(TMG2Phqu)_2]PF_6$ ($C9–PF_6$)

A preheated Schlenk flask was charged with $[Cu(MeCN)_4]PF_6$ (250 mg, 671 µmol, 1.00 eq.) and TMG2Phqu (450 mg, 1.41 mmol, 2.11 eq.) in a nitrogen counterflow. The solids were dissolved in dichloromethane (3 mL) and stirred for 30 min at 28 °C. Afterwards, pentane was added to the mixture and the resulting black precipitate was filtered off under reduced pressure. The product was washed with pentane (3x 10 mL) and dried *in-vacuo*. $[Cu(TMG2Phqu)_2]PF_6$ (**$C9–PF_6$**) (390 mg, 461 µmol, 69 % yield) was obtained as a brown powder.

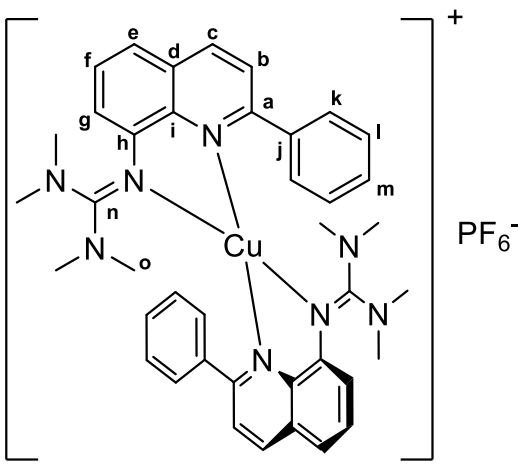

845.35 g/mol

Due to the broad resonances, the NMRs could not be completely assigned.

^{1}H NMR (400 MHz, CD_3CN) δ [ppm] = 8.32 (d, J = 6.1 Hz, 2H, H-c), 7.94 – 7.64 (m, 6H, H-e/H-l), 7.49 – 7.40 (m, 4H, H-f/H-m), 7.19 – 6.87 (m, 6H, H-g/H-k), 6.72 (d, J = 6.9 Hz, 2H, H-b), 2.41 (s, 24H, H-o).

^{13}C NMR (101 MHz, CD_3CN) δ [ppm] = 163.8 (n, 2C), 156.0 (C_q), 148.7 (C_q), 142.4 (C_q), 141.4 (C_q), 138.4 (c, 2C), 129.8 (g/k), 129.5 (g/k), 128.8 (f/m), 128.5 (e/l, d) , 123.4 (e/l), 119.5 (f/m), 119.1 (b, 2C), 39.8 (o, 8C).

HR-ESI-MS M^+ (m/z (%) $[M]^+$, M = $C_{40}H_{44}N_8Cu$) found: 699.29711 (100), 700.29982 (45), 701.29611 (50), 702.29792 (20). Calculated: 699.29794 (100) $[^{12}C_{40}{}^{1}H_{44}{}^{14}N_8{}^{63}Cu]^+$, 700.301297 (43) $[^{12}C_{39}{}^{13}C^{1}H_{44}{}^{14}N_8{}^{63}Cu]^+$, 701.29613 (45) $[^{12}C_{40}{}^{1}H_{44}{}^{14}N_8{}^{65}Cu]^+$, 702.29949 (19) $[^{12}C_{39}{}^{13}C^{1}H_{44}{}^{14}N_8{}^{65}Cu]^+$.

IR (ATR, $\tilde{\nu}$) = 3055 (vw), 2930 (vw), 2886 (vw), 2870 (vw), 2801 (vw), 2160 (vw), 2035 (vw), 1736 (vw), 1595 (vw), 1578 (vw), 1524 (s), 1489 (w), 1470 (w), 1454 (m), 1422 (m), 1406 (m), 1393 (s), 1369 (w), 1341 (w), 1323 (w), 1285 (w), 1273 (w), 1231 (w), 1153 (w), 1107 (vw), 1094 (w), 1084 (w), 1065 (w), 1016 (w), 926 (vw), 899 (vw), 876 (w), 831 (vs), 766 (m), 756 (m), 696 (m), 642 (w), 617 (vw), 584 (vw), 555 (vs), 525 (w), 478 (w), 463 (w), 459 (w), 444 (w), 430 (vw), 424 (vw), 419 (vw), 409 (vw) cm^{-1}.

XRD: Section 9.1.2

7.6.12 Synthesis of $[Cu(TMG2Phqu)_2](OTf)_2$ (C10–OTf)

A vial was charged with TMG2Phqu (261 mg, 820 µmol, 2.09 eq.) and $[Cu(MeCN)_4](OTf)_2$ (206 mg, 392 µmol, 1.00 eq.) and dissolved in absolute dichloromethane (5 mL). The solution was stirred at 28 °C for 10 minutes, after which the complex was precipitated via hexane. The resulting precipitate was filtered off and dissolved in DCM (2 mL) and pipetted into a beaker of pentane (50 mL), the resulting powder was filtered off under reduced pressure and dried *in-vacuo*. $[Cu(TMG2Phqu)_2](OTf)_2$ (**C10–OTf**) (109 mg, 109 µmol, 28 % yield) was obtained as a black powder.

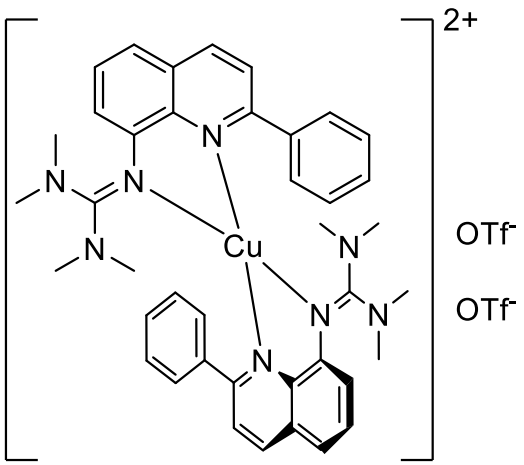

998.52 g/mol

HR-ESI-MS $[TMG2Phqu-NMe_2]^+$ ((m/z (%) $[M]^+$, M = $C_{18}H_{16}N_3$) found: 274.13437. Calculated: 274.13387 $[^{12}C_{18}{}^{1}H_{16}{}^{14}N_3]^+$

$[TMG2Phqu+H]^+$ ((m/z (%) $[M+H]^+$, M+H = $C_{20}H_{23}N_4$) found: 319.19138. Calculated: 319.19151 $[^{12}C_{20}{}^{1}H_{23}{}^{14}N_4]^+$.

$[\{Cu(TMG2Phqu)\}OTf]^+$ ((m/z (%) $[M]^+$, M = $C_{21}H_{22}CuF_3N_4O_3S$) found: 530.06647 (100), 531.07007 (20), 532.06549 (45), 533.06802 (10). Calculated: 530.06552 (100) $[^{12}C_{21}{}^{1}H_{22}{}^{14}N_4{}^{19}F_3{}^{63}Cu^{16}O_3{}^{32}S]^+$, 531.06888 (23) $[^{12}C_{20}{}^{13}C^{1}H_{22}{}^{14}N_4{}^{19}F_3{}^{63}Cu^{16}O_3{}^{32}S]^+$, 532.06371 (45) $[^{12}C_{21}{}^{1}H_{22}{}^{14}N_4{}^{19}F_3{}^{65}Cu^{16}O_3{}^{32}S]^+$, 533.06707 (10) $[^{12}C_{20}{}^{13}C_2{}^{1}H_{22}{}^{14}N_4{}^{19}F_3{}^{65}Cu^{16}O_3{}^{32}S]^+$.

$[Cu(TMG2Phqu)_2]^+$ (m/z (%) $[M]^+$, M = $C_{40}H_{44}N_8Cu$) found: 699.29958 (100), 700.30306 (45), 701.29728 (50), 702.30110 (20). Calculated: 699.29794 (100) $[^{12}C_{40}{}^{1}H_{44}{}^{14}N_8{}^{63}Cu]^+$, 700.301297 (43) $[^{12}C_{39}{}^{13}C^{1}H_{44}{}^{14}N_8{}^{63}Cu]^+$, 701.29613 (45) $[^{12}C_{40}{}^{1}H_{44}{}^{14}N_8{}^{65}Cu]^+$, 702.29949 (19) $[^{12}C_{39}{}^{13}C^{1}H_{44}{}^{14}N_8{}^{65}Cu]^+$.

$[\{Cu(TMG2Phqu)_2\}OTf]^+$ (m/z (%) $[M]^+$, M = $C_{41}H_{44}CuF_3N_8O_3S$) found: 848.25230 (100), 849. 25579 (43), 850.24961 (43), 851.25329 (18), 852.25845 (5). Calculated: 848.24997 (100) $[^{12}C_{41}{}^{1}H_{44}{}^{14}N_8{}^{19}F_3{}^{63}Cu^{16}O_3{}^{32}S]^+$, 849.25332 (44) $[^{12}C_{40}{}^{13}C^{1}H_{44}{}^{14}N_8{}^{19}F_3{}^{63}Cu^{16}O^{32}S]^+$, 850.24816 (45) $[^{12}C_{41}{}^{1}H_{44}{}^{14}N_8{}^{19}F_3{}^{65}Cu^{16}O^{32}S]^+$, 851.25151 (20) $[^{12}C_{40}{}^{13}C^{1}H_{44}{}^{14}N_8{}^{19}F_3{}^{65}Cu^{16}O^{32}S]^+$, 852.25487 (4) $[^{12}C_{39}{}^{13}C_2{}^{1}H_{44}{}^{14}N_8{}^{19}F_3{}^{65}Cu^{16}O^{32}S]^+$.

$[\{Cu(TMG2Phqu)_2\}_2(OTf)_3]^+$ ((m/z (%) $[M]^+$, M = $C_{83}H_{88}Cu_2F_9N_{16}O_9S_3$) found: 1845.45567 (60), 1846.45870 (65), 1847.45565 (100), 1848.45756 (80), 1849.45636 (50), 1850.45673 (27), 1851.45718 (14). Calculated: 1845.45207 (74), 1846.45535 (72), 1847.45306 (100), 1848.45448 (81), 1849.45405 (54), 1850.45362 (32), 1851.45504 (15), 1852.45460 (6).

IR (ATR, ṽ) = 2926 (vw), 2183 (vw), 2160 (vw), 2039 (vw), 1626 (vw), 1582 (m), 1558 (w), 1520 (m), 1510 (m), 1491 (w), 1476 (w), 1460 (m), 1435 (w), 1427 (w), 1404 (s), 1385 (w), 1339 (w), 1319 (w), 1260 (vs), 1225 (vs), 1152 (vs), 1144 (vs), 1099 (w), 1084 (w), 1061 (vw), 1028 (vs), 1001 (w), 922 (vw), 918 (vw), 897 (vw), 864 (w), 833 (w), 808 (vw), 756 (s), 710 (w), 696 (m), 637 (vs), 571 (w), 544 (vw), 515 (m), 482 (w), 424 (vw), 419 (w) cm^{-1}.

XRD: Section 9.1.2

PXRD: Section 9.1.3

EPR: Section 4.6

7.6.13 Resynthesis of $[Cu(TMGqu)_2]PF_6$ (C11–PF_6)

This compound has been synthesized before.[69]

A preheated Schlenk flask was charged with $[Cu(MeCN)_4]PF_6$ (540.5 mg, 1.45 mmol, 1.0 eq.) and TMGqu (734.2 mg, 3.03 mmol, 2.1 eq.) in a nitrogen counterflow. The solids were dissolved in dichloromethane (5 mL) and stirred for 30 min at 28 °C. Afterwards, pentane was added to the mixture, and the resulting black precipitate was filtered off under reduced pressure. The product was washed with pentane (3x 10 mL) and dried *in-vacuo*. $[Cu(TMGqu)_2]PF_6$ (**C11–PF_6**) (845.7 mg, 1.22 mmol, 84 % yield) was obtained as a black crystalline powder.

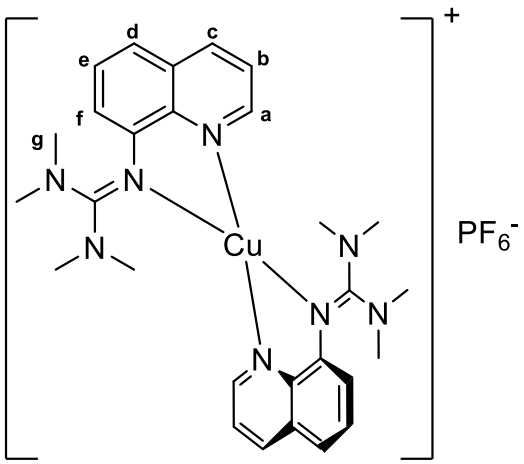

693.16 g/mol

^{1}H NMR (400 MHz, CD_3CN) δ [ppm] = 8.52 (dd, J = 4.5, 1.6 Hz, 2H, H-a), 8.35 (dd, J = 8.4, 1.6 Hz, 2H, H-c), 7.60 – 7.44 (m, 6H, H-d, H-e, H-f), 6.90 (dd, J = 7.4, 1.3 Hz, 2H, H-b), 2.49 (s, 24H, H-g).

7.6.14 Resynthesis of [Cu(TMG2Mequ)$_2$]PF$_6$ (C13–PF$_6$)

This compound has been synthesized before.[22]

A preheated Schlenk flask was charged with [Cu(MeCN)$_4$]PF$_6$ (540.5 mg, 1.45 mmol, 1.0 eq.) and TMG2Mequ (776.7 mg, 3.03 mmol, 2.1 eq.) in a nitrogen counterflow. The solids were dissolved in dichloromethane (5 mL) and stirred for 30 min at 28 °C. Afterwards, pentane was added to the mixture, and the resulting black precipitate was filtered off under reduced pressure. The product was washed with pentane (3x 10 mL) and dried *in-vacuo*. [Cu(TMG2Mequ)$_2$]PF$_6$ (**C13–PF$_6$**) (805.2 mg, 1.12 mmol, 77 % yield) was obtained as a red crystalline powder.

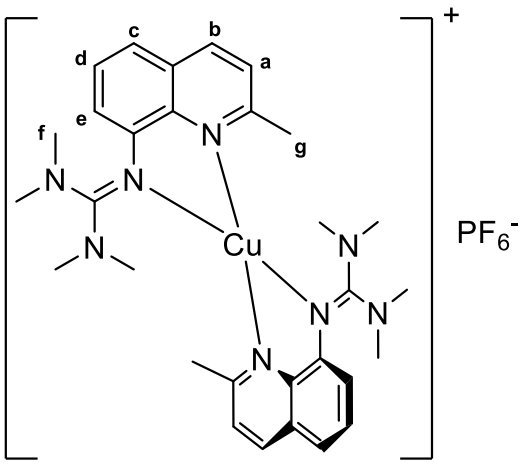

721.22 g/mol

^{1}H NMR (400 MHz, CD$_3$CN) δ [ppm] = 8.26 (d, J = 8.5 Hz, 2H, H-b), 7.52 – 7.39 (m, 6H, H-c, H-d, H-e), 6.84 (dd, J = 7.1, 1.8 Hz, 2H, H-a), 2.80 (s, 8H, H-f), 2.57 (s, 6H, H-g), 2.39 (s, 16H, H-f).

7.6.15 Resynthesis of [Cu(TMG2^{c}Hexqu)$_2$]PF$_6$ (C15–PF$_6$)

This compound has been synthesized before.[22]

A preheated Schlenk flask was charged with [Cu(MeCN)$_4$]PF$_6$ (540.5 mg, 1.45 mmol, 1.0 eq.) and TMG2^{c}Hexqu (983.1 mg, 3.03 mmol, 2.1 eq.) in a nitrogen counterflow. The solids were dissolved in dichloromethane (5 mL) and stirred for 30 min at 28 °C. Afterwards, pentane was added to the mixture, and the resulting black precipitate was filtered off under reduced pressure. The product was washed with pentane (3x 10 mL) and dried *in-vacuo*. [Cu(TMG2^{c}Hexqu)$_2$]PF$_6$ (**C15–PF$_6$**) (895.2 mg, 1.04 mmol, 72 % yield) was obtained as an orange powder.

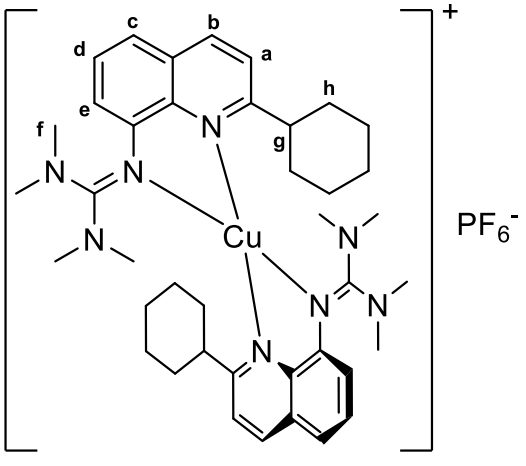

857.45 g/mol

^{1}H NMR (400 MHz, CD_3CN) δ [ppm] = 8.20 (d, J = 8.5 Hz, 2H, H-b), 7.51 – 7.45 (m, 2H, H-d), 7.41 (dd, J = 8.1, 1.4 Hz, 2H, H-c), 7.32 (d, J = 8.9 Hz, 2H, H-a), 6.90 (d, J = 7.5 Hz, 2H, H-e), 2.90 (s, 20H, H-f, H-g), 2.43 (s, 6H, H-f), 1.66 – 0.76 (m, 20H, H-h).

7.7 Theoretical Calculations

7.7.1 General

Density functional theory (DFT) calculations were performed with Gaussian 16, Revision B.01 using the default UltraFine grid (a 99,590 grid).[172] The geometry optimizations of each conformer were started from the corresponding molecular structure in the solid state and conducted using the TPSSh functional[173-174] and with the Ahlrichs type basis set def2-TZVP[175-177] as implemented in Gaussian 16, Revision B.01. As solvent model, the Polarizable Continuum Model (PCM) was used as implemented in Gaussian 16. As empirical dispersion correction, the D3 dispersion with Becke–Johnson damping was used as implemented in Gaussian 16, Revision B.01.[178-180] Frequency calculations did not show imaginary values. For visualization and extraction of the calculated structural information Chemcraft (Version 1.8) was used.

To confirm the preferred conformers of **C9** and **C10** in solution, additional computations were carried out using the same basis set with MN15 as functional.[204, 244] For this, the structures were re-optimized from the solid state data as described above. The dispersion correction was omitted for these calculations.

7.7.2 NBO Calculations

NBO calculations were accomplished using the program NBO 6.0 delivering the NBO charges and the charge-transfer energies E_{CT} by second-order perturbation theory.[181, 183] For visualization and extraction of the charge transfer energies, Chemcraft (Version 1.8) was used. The $CHOOSE command was used to assign one lone pair to each donor and to ensure that the Cu–N bonds were interpreted as dative bonds by the program. All contributions of a given donor atom's lone pair (LP), as well as their N–C double bonds (BD(2)) towards the lone valence (LV) orbitals of the central ion were considered and added together, all contributions involving Rydberg (RY) orbitals were discarded.

7.7.3 Transition State Calculations

The transition states were optimized using the same level of theory as the standard geometry optimizations with the opt=TS command starting from an initial guess. All

states show one imaginary frequency. Their structures and energies are shown in Section 9.9.

7.7.4 Conformer-rotamer ensemble sampling tool calculations

To verify the results of the DFT optimization calculations, conformer-rotamer ensemble sampling tool (CREST) calculations were performed.[245] The applied theory level was GFN2-xTB.[246]

8 Bibliography

[1] J. M. Berg, J. L. Tymoczko, *Stryer biochemie, Vol. 8*, Springer, **2018**.
[2] D. Sadava, D. M. Hillis, H. C. Heller, S. D. Hacker, *Purves biologie*, Springer-Verlag, **2019**.
[3] P. Comba, *Coord. Chem. Rev.* **2000**, *200-202*, 217-245.
[4] D. B. Rorabacher, *Chem. Rev.* **2004**, *104*, 651-697.
[5] A. Das, C. Hessin, Y. Ren, M. Desage-El Murr, *Chem. Soc. Rev.* **2020**, *49*, 8840-8867.
[6] I. Kostova, *Inorganics* **2023**, *11*, 56.
[7] W. Maret, *Metallomics* **2010**, *2*, 117-125.
[8] A. F. Holleman, N. Wiberg, *Grundlagen und Hauptgruppenelemente*, Walter de Gruyter GmbH & Co KG, **2016**.
[9] A. Cass, H. Hill, in *Ciba Foundation Symposium 79-Biological Roles of Copper*, Wiley Online Library, **1980**, pp. 71-91.
[10] E. A. Ambundo, M. Deydler, A. J. Grall, N. Aguera-Vega, L. T. Dressel, T. H. Cooper, M. J. Heeg, L. A. Ochrymowycz, D. B. Rorabacher, *Inorg. Chem.* **1999**, *38*, 4233-4242.
[11] R. R. Conry, in *Encyclopedia of Inorganic Chemistry*, **2005**.
[12] E. Riedel, *Allgemeine und anorganische Chemie*, de Gruyter, **2010**.
[13] J. Cirera, P. Alemany, S. Alvarez, *Chem.* **2004**, *10*, 190-207.
[14] K. Karlin, J. Yandell, *Inorg. Chem.* **1984**, *23*, 1184-1188.
[15] P. J. Griffin, M. J. Dake, A. D. Remolina, L. Olshansky, *Dalton Trans.* **2023**, *52*, 8376-8383.
[16] P. J. Griffin, L. Olshansky, *J. Am. Chem. Soc.* **2023**, *145*, 20158-20162.
[17] L. Garcia, F. Cisnetti, N. Gillet, R. Guillot, M. Aumont-Nicaise, J. P. Piquemal, M. Desmadril, F. Lambert, C. Policar, *J. Am. Chem. Soc.* **2015**, *137*, 1141-1146.
[18] P. R. Raithby, G. P. Shields, F. H. Allen, W. D. S. Motherwell, *Acta Crystallogr. Sect. B* **2000**, *56*, 444-454.
[19] R. G. Pearson, *J. Am. Chem. Soc.* **1963**, *85*, 3533-3539.
[20] R. G. Pearson, *J. Chem. Educ.* **1968**, *45*, 581.
[21] R. G. Pearson, *J. Chem. Educ.* **1968**, *45*, 643.
[22] J. Heck, F. Metz, S. Buchenau, M. Teubner, B. Grimm-Lebsanft, T. P. Spaniol, A. Hoffmann, M. A. Rubhausen, S. Herres-Pawlis, *Chem. Sci.* **2022**, *13*, 8274-8288.
[23] G. D. Stroscio, R. D. Ribson, R. G. Hadt, *Inorg. Chem.* **2019**, *58*, 16800-16817.
[24] M. M. Bernardo, M. J. Heeg, R. R. Schroeder, L. Ochrymowycz, D. Rorabacher, *Inorg. Chem.* **1992**, *31*, 191-198.
[25] C. P. Kulatilleke, *Polyhedron* **2007**, *26*, 1166-1172.
[26] I. M. DiMucci, J. T. Lukens, S. Chatterjee, K. M. Carsch, C. J. Titus, S. J. Lee, D. Nordlund, T. A. Betley, S. N. MacMillan, K. M. Lancaster, *J. Am. Chem. Soc.* **2019**, *141*, 18508-18520.
[27] E. I. Solomon, D. E. Heppner, E. M. Johnston, J. W. Ginsbach, J. Cirera, M. Qayyum, M. T. Kieber-Emmons, C. H. Kjaergaard, R. G. Hadt, L. Tian, *Chem. Rev.* **2014**, *114*, 3659-3853.
[28] J. Jin, E. Wong, *Encyclopedia of inorganic and bioinorganic chemistry, Vol. 1*, Wiley Online Library, **2011**.
[29] W. Kaim, J. Rall, *Angew. Chem. Int. Ed.* **1996**, *35*, 43-60.
[30] I. S. MacPherson, M. E. Murphy, *Cell. Mo. Life Sci.* **2007**, *64*, 2887-2899.
[31] J. Markl, *Biochim. Biophys. Acta* **2013**, *1834*, 1840-1852.

[32] S. Kato, T. Matsui, C. Gatsogiannis, Y. Tanaka, *Biophys. Rev.* **2018**, *10*, 191-202.
[33] E. I. Solomon, U. M. Sundaram, T. E. Machonkin, *Chem. Rev.* **1996**, *96*, 2563-2606.
[34] J. L. Muñoz-Muñoz, F. Garcia-Molina, R. Varon, P. A. Garcia-Ruíz, J. Tudela, F. Garcia-Cánovas, J. N. Rodríguez-López, *IUBMB Life* **2010**, *62*, 539-547.
[35] H. B. Gray, B. G. Malmström, R. J. P. Williams, *J. Biol. Inorg. Chem.* **2000**, *5*, 551-559.
[36] E. I. Solomon, R. G. Hadt, *Coord. Chem. Rev.* **2011**, *255*, 774-789.
[37] P. L. Holland, W. B. Tolman, *J. Am. Chem. Soc.* **2000**, *122*, 6331-6332.
[38] S. Yanagisawa, C. Dennison, *J. Am. Chem. Soc.* **2004**, *126*, 15711-15719.
[39] T. Inoue, H. Sugawara, S. Hamanaka, H. Tsukui, E. Suzuki, T. Kohzuma, Y. Kai, *Biochemistry* **1999**, *38*, 6063-6069.
[40] C. Dennison, *Coord. Chem. Rev.* **2005**, *249*, 3025-3054.
[41] R. B. King, *Encyclopedia of inorganic chemistry, Vol. 10*, Wiley Online Library, **2005**.
[42] B. L. Vallee, R. J. P. Williams, *Proc. Natl. Acad. Sci. U.S.A.* **1968**, *59*, 609-614.
[43] R. J. P. Williams, *Eur. J. Biochem.* **1995**, *234*, 363-381.
[44] R. J. P. Williams, *Inorg. Chim. Acta Rev.* **1971**, *5*, 135-155.
[45] B. G. Karlsson, R. Aasa, B. G. Malmström, L. G. Lundberg, *FEBS Lett.* **1989**, *253*, 99-102.
[46] B. G. Malmstrom, *Eur. J. Biochem.* **1994**, *223*, 711-718.
[47] P. Thompson, E. Papadopoulou, E. Vassiliou, *Spat. Vis.* **2007**, *20*, 531-543.
[48] P. Comba, *Coord. Chem. Rev.* **2003**, *238-239*, 21-29.
[49] E. I. Solomon, M. D. Lowery, J. A. Guckert, L. B. LaCroix, in *Electron Transfer Reactions*, American Chemical Society, **1997**, pp. 317-330.
[50] M.-L. Tsai, R. G. Hadt, N. M. Marshall, T. D. Wilson, Y. Lu, E. I. Solomon, *Proc. Natl. Acad. Sci.* **2013**, *110*, 14658-14663.
[51] G. Chaka, J. L. Sonnenberg, H. B. Schlegel, M. J. Heeg, G. Jeaeger, T. J. Nelson, L. A. Ochrymowycz, D. B. Rorabacher, *J. Am. Chem. Soc.* **2007**, *129*, 5217-5227.
[52] S. Herres-Pawlis, P. Klüfers, *Bioanorganische Chemie: Metalloproteine, Methoden und Modelle*, John Wiley & Sons, **2017**.
[53] U. Ryde, M. H. M. Olsson, B. O. Roos, A. C. Borin, *Theor. Chem. Acc.* **2001**, *105*, 452-462.
[54] U. Ryde, M. H. M. Olsson, K. Pierloot, B. O. Roos, *J. Mol. Biol.* **1996**, *261*, 586-596.
[55] S. Wiesner, A. Wagner, E. Kaifer, H. J. Himmel, *Dalton Trans.* **2016**, *45*, 15828-15839.
[56] P. Frank, M. Benfatto, *J. Phys. Chem. B* **2021**, *125*, 10779-10795.
[57] K. M. Lancaster, S. D. George, K. Yokoyama, J. H. Richards, H. B. Gray, *Nat. Chem.* **2009**, *1*, 711-715.
[58] W. R. Hagen, *Metallomics* **2019**, *11*, 1768-1778.
[59] L. Llanos, C. Vera, A. Vega, D. Aravena, L. Lemus, *Inorg. Chem.* **2020**, *59*, 15061-15073.
[60] E. Falcone, C. Hureau, *Chem. Soc. Rev.* **2023**, *52*, 6595-6600.
[61] V. Balland, C. Hureau, J.-M. Savéant, *Proc. Natl. Acad. Sci.* **2010**, *107*, 17113-17118.
[62] S. Mitra, S. R. K. Ainavarapu, J. Dasgupta, *J. Phy. Chem. B* **2022**, *126*, 5390-5399.

[63] S. Holzmann, J. Osterbrink, O. Hübner, M. Schulz, A. Poddelskii, E. Kaifer, H.-J. Himmel, *Eur. J. Inorg. Chem.* **2024**, e202400597.
[64] C. Kieninger, E. Deery, A. D. Lawrence, M. Podewitz, K. Wurst, E. Nemoto-Smith, F. J. Widner, J. A. Baker, S. Jockusch, C. R. Kreutz, K. R. Liedl, K. Gruber, M. J. Warren, B. Kräutler, *Angew. Chem. Int. Ed.* **2019**, *58*, 10756-10760.
[65] J. H. Timmons, J. W. L. Martin, A. E. Martell, P. R. Rudolf, A. Clearfield, *Inorg. Chem.* **1988**, *27*, 1638-1640.
[66] D. K. Coggin, J. A. González, A. M. Kook, C. Bergman, T. D. Brennan, W. R. Scheldt, D. M. Stanbury, L. J. Wilson, *Inorg. Chem.* **1991**, *30*, 1125-1134.
[67] B. C. Dunn, L. Ochrymowycz, D. Rorabacher, *Inorg. Chem.* **1995**, *34*, 1954-1956.
[68] D. F. Schrempp, S. Leingang, M. Schnurr, E. Kaifer, H. Wadepohl, H. J. Himmel, *Chem. Eur. J.* **2017**, *23*, 13607-13611.
[69] A. Hoffmann, S. Binder, A. Jesser, R. Haase, U. Flörke, M. Gnida, M. Salomone Stagni, W. Meyer-Klaucke, B. Lebsanft, L. E. Grünig, S. Schneider, M. Hashemi, A. Goos, A. Wetzel, M. Rübhausen, S. Herres-Pawlis, *Angew. Chem. Int. Ed.* **2013**, *53*, 299-304.
[70] E. A. Ambundo, Q. Yu, L. A. Ochrymowycz, D. B. Rorabacher, *Inorg. Chem.* **2003**, *42*, 5267-5273.
[71] M. J. Martin, J. F. Endicott, L. Ochrymowycz, D. Rorabacher, *Inorg. Chem.* **1987**, *26*, 3012-3022.
[72] A. M. Vande Linde, K. L. Juntunen, O. Mols, M. B. Ksebati, L. Ochrymowycz, D. Rorabacher, *Inorg. Chem.* **1991**, *30*, 5037-5042.
[73] A. M. Vande Linde, B. C. Westerby, L. Ochrymowycz, D. Rorabacher, *Inorg. Chem.* **1993**, *32*, 251-257.
[74] K. Krylova, C. P. Kulatilleke, M. J. Heeg, C. A. Salhi, L. Ochrymowycz, D. Rorabacher, *Inorg. Chem.* **1999**, *38*, 4322-4328.
[75] J. Stanek, A. Hoffmann, S. Herres-Pawlis, *Coord. Chem. Rev.* **2018**, *365*, 103-121.
[76] L. Yang, D. R. Powell, R. P. Houser, *Dalton Trans.* **2007**, *9*, 955-964.
[77] J. Stanek, M. Konrad, J. Mannsperger, A. Hoffmann, S. Herres-Pawlis, *Eur. J. Inorg. Chem.* **2018**, *2018*, 4997-5006.
[78] B. Xie, T. Elder, L. J. Wilson, D. M. Stanbury, *Inorg. Chem.* **1999**, *38*, 12-19.
[79] E. W. Dahl, N. K. Szymczak, *Angew. Chem. Int. Ed.* **2016**, *55*, 3101-3105.
[80] P. Comba, *Coord. Chem. Rev.* **1999**, *182*, 343-371.
[81] E. J. Pulliam, D. R. McMillin, *Inorg. Chem.* **1984**, *23*, 1172-1175.
[82] S. Knapp, T. P. Keenan, X. Zhang, R. Fikar, J. A. Potenza, H. J. Schugar, *J. Am. Chem. Soc.* **1990**, *112*, 3452-3464.
[83] P. Comba, M. Kerscher, A. Roodt, *Eur. J. Inorg. Chem.* **2004**, *2004*, 4640-4645.
[84] A. Hoffmann, J. Stanek, B. Dicke, L. Peters, B. Grimm-Lebsanft, A. Wetzel, A. Jesser, M. Bauer, M. Gnida, W. Meyer-Klaucke, M. Rübhausen, S. Herres-Pawlis, *Eur. J. Inorg. Chem.* **2016**, *2016*, 4731-4743.
[85] J. Stanek, N. Sackers, F. Fink, M. Paul, L. Peters, R. Grunzke, A. Hoffmann, S. Herres-Pawlis, *Chem. Eur. J.* **2017**, *23*, 15738-15745.
[86] J. Heck, A. Kucenko, A. Hoffmann, S. Herres-Pawlis, *Dalton Trans.* **2024**, *53*, 12527-12542.
[87] R. W. Lane, J. A. Ibers, R. B. Frankel, R. H. Holm, *Proc. Nat. Acad. Sci. USA* **1975**, *72*, 2868-2872.

[88] P. Levín, M. C. Ruiz, A. I. B. Romo, O. R. Nascimento, A. L. Di Virgilio, A. G. Oliver, A. P. Ayala, I. C. N. Diógenes, I. E. León, L. Lemus, *Inorg. Chem. Front.* **2021**, *8*, 3238-3252.
[89] Y. Ren, J. Forte, K. Cheaib, N. Vanthuyne, L. Fensterbank, H. Vezin, M. Orio, S. Blanchard, M. Desage-El Murr, *iScience* **2020**, *23*, 100955.
[90] L. H. Gade, *Koordinationschemie*, John Wiley & Sons, **2012**.
[91] C. Janiak, H.-J. Meyer, D. Gudat, P. Kurz, *Riedel Moderne Anorganische Chemie*, Walter de Gruyter GmbH & Co KG, **2018**.
[92] E. Laviron, L. Roullier, *J. Electroanal. Chem.* **1985**, *186*, 1-15.
[93] J. Jacq, *J. Electroanal. Chem.* **1971**, *29*, 149-180.
[94] R. A. Marcus, N. Sutin, *Biochim. Biophys. Acta* **1985**, *811*, 265-322.
[95] A. Y. Chan, A. Ghosh, J. T. Yarranton, J. Twilton, J. Jin, D. M. Arias-Rotondo, H. A. Sakai, J. K. McCusker, D. W. C. MacMillan, *Science* **2023**, *382*, 191-197.
[96] A. Ghosh, J. T. Yarranton, J. K. McCusker, *Nat. Chem.* **2024**, *16*, 1665-1672.
[97] V. Balzani, G. Bergamini, S. Campagna, F. Puntoriero, *Photochemistry and photophysics of coordination compounds: overview and general concepts*, Springer, **2007**.
[98] M. Kasha, *Discussions of the Faraday Society* **1950**, *9*, 14-19.
[99] J. K. McCusker, *Science* **2019**, *363*, 484-488.
[100] D. M. Arias-Rotondo, J. K. McCusker, *Chem. Soc. Rev.* **2016**, *45*, 5803-5820.
[101] G. Morselli, C. Reber, O. S. Wenger, *J. Am. Chem. Soc.* **2025**, *147*, 11608-11624.
[102] C. Sandoval-Pauker, G. Molina-Aguirre, B. Pinter, *Polyhedron* **2021**, *199*.
[103] J. F. Lovell, T. W. B. Liu, J. Chen, G. Zheng, *Chem. Rev.* **2010**, *110*, 2839-2857.
[104] S. Jasimuddin, T. Yamada, K. Fukuju, J. Otsuki, K. Sakai, *Chem. Commun.* **2010**, *46*, 8466-8468.
[105] M. R. Narayan, *Renewable and sustainable energy reviews* **2012**, *16*, 208-215.
[106] C. K. Prier, D. A. Rankic, D. W. C. MacMillan, *Chem. Rev.* **2013**, *113*, 5322-5363.
[107] L. Gimeno, C. Queffélec, K. Mall Haidaraly, E. Blart, Y. Pellegrin, *Catal. Sci. Technol.* **2021**, *11*, 6041-6047.
[108] D. Rehm, A. Weller, *Isr. J. Chem.* **1970**, *8*, 259-271.
[109] A. A. Vlcek, E. S. Dodsworth, W. J. Pietro, A. B. P. Lever, *Inorg. Chem.* **1995**, *34*, 1906-1913.
[110] P. Chaibuth, N. Chuaytanee, J. Hojitsiriyanont, K. Chainok, S. Wacharasindhu, O. Reiser, M. Sukwattanasinitt, *New J. Chem.* **2022**, *46*, 12158-12168.
[111] L. H. M. de Groot, A. Ilic, J. Schwarz, K. Wärnmark, *J. Am. Chem. Soc.* **2023**, *145*, 9369-9388.
[112] J.-R. Jiménez, M. Poncet, B. Doistau, C. Besnard, C. Piguet, *Dalton Trans.* **2020**, *49*, 13528-13532.
[113] J.-M. Kern, J.-P. Sauvage, *J. Chem. Soc., Chem. Commun.* **1987**, 546-548.
[114] J. Beaudelot, S. Oger, S. Perusko, T. A. Phan, T. Teunens, C. Moucheron, G. Evano, *Chem. Rev.* **2022**, *122*, 16365-16609.
[115] C. Förster, K. Heinze, *Chem. Soc. Rev.* **2020**, *49*, 1057-1070.
[116] B. Dicke, A. Hoffmann, J. Stanek, M. S. Rampp, B. Grimm-Lebsanft, F. Biebl, D. Rukser, B. Maerz, D. Gories, M. Naumova, M. Biednov, G. Neuber, A. Wetzel, S. M. Hofmann, P. Roedig, A. Meents, J. Bielecki, J. Andreasson, K. R. Beyerlein, H. N. Chapman, C. Bressler, W. Zinth, M. Rubhausen, S. Herres-Pawlis, *Nat. Chem.* **2018**, *10*, 355-362.
[117] C. E. McCusker, F. N. Castellano, *Inorg. Chem.* **2013**, *52*, 8114-8120.

[118] L. Kohler, R. G. Hadt, D. Hayes, L. X. Chen, K. L. Mulfort, *Dalton Trans.* **2017**, *46*, 13088-13100.
[119] M. W. Mara, K. A. Fransted, L. X. Chen, *Coord. Chem. Rev.* **2015**, *282*, 2-18.
[120] R. Giereth, I. Reim, W. Frey, H. Junge, S. Tschierlei, M. Karnahl, *Sustain. Energy Fuels* **2019**, *3*, 692-700.
[121] M. Sandroni, M. Kayanuma, M. Rebarz, H. Akdas-Kilig, Y. Pellegrin, E. Blart, H. Le Bozec, C. Daniel, F. Odobel, *Dalton Trans.* **2013**, *42*, 14628-14638.
[122] A. Nitelet, D. Thevenet, B. Schiavi, C. Hardouin, J. Fournier, R. Tamion, X. Pannecoucke, P. Jubault, T. Poisson, *Chem.* **2019**, *25*, 3262-3266.
[123] A. Kaeser, M. Mohankumar, J. Mohanraj, F. Monti, M. Holler, J.-J. Cid, O. Moudam, I. Nierengarten, L. Karmazin-Brelot, C. Duhayon, B. Delavaux-Nicot, N. Armaroli, J.-F. Nierengarten, *Inorg. Chem.* **2013**, *52*, 12140-12151.
[124] Y. Zhang, M. Schulz, M. Wächtler, M. Karnahl, B. Dietzek, *Coord. Chem. Rev.* **2018**, *356*, 127-146.
[125] M. Schmittel, A. Ganz, *Chem. Commun.* **1997**, 999-1000.
[126] S. De, K. Mahata, M. Schmittel, *Chem. Soc. Rev.* **2010**, *39*, 1555-1575.
[127] G. Chakkaradhari, A. A. Belyaev, A. J. Karttunen, V. Sivchik, S. P. Tunik, I. O. Koshevoy, *Dalton Trans.* **2015**, *44*, 13294-13304.
[128] K. Grudzień, Z. Szeptuch, H. Kubiszewski, W. Chaładaj, K. Rybicka-Jasińska, *J. Org. Chem.* **2024**, *89*, 8546-8550.
[129] L. Gimeno, E. Blart, J. N. Rebilly, M. Coupeau, M. Allain, T. Roisnel, A. Quarre de Verneuil, C. Gourlaouen, C. Daniel, Y. Pellegrin, *Chem.* **2020**, *26*, 11887-11899.
[130] R. Giereth, A. K. Mengele, W. Frey, M. Kloß, A. Steffen, M. Karnahl, S. Tschierlei, *Chem. Eur. J.* **2020**, *26*, 2675-2684.
[131] M. Knorn, T. Rawner, R. Czerwieniec, O. Reiser, *ACS Catalysis* **2015**, *5*, 5186-5193.
[132] D. Kim, M. C. Rosko, V. Q. Dang, F. N. Castellano, T. S. Teets, *Inorg. Chem.* **2023**, *62*, 16759-16769.
[133] S. Engl, O. Reiser, *Eur. J. Org. Chem.* **2020**, *2020*, 1523-1533.
[134] S. Engl, O. Reiser, *Chem. Soc. Rev.* **2022**, *51*, 5287-5299.
[135] S. K. Pagire, S. Paria, O. Reiser, *Org. Lett.* **2016**, *18*, 2106-2109.
[136] S. H. Oh, Y. R. Malpani, N. Ha, Y.-S. Jung, S. B. Han, *Org. Lett.* **2014**, *16*, 1310-1313.
[137] D. B. Bagal, G. Kachkovskyi, M. Knorn, T. Rawner, B. M. Bhanage, O. Reiser, *Angew. Chem. Int. Ed.* **2015**, *54*, 6999-7002.
[138] L. Gimeno, B. T. Phelan, E. A. Sprague-Klein, T. Roisnel, E. Blart, C. Gourlaouen, L. X. Chen, Y. Pellegrin, *Inorg. Chem.* **2022**, *61*, 7296-7307.
[139] V. Tiwari, M. Gallagher-Jones, H. Hwang, H.-G. Duan, A. I. Kirkland, R. J. D. Miller, A. Jha, *ACS Physical Chemistry Au* **2024**, *4*, 660-668.
[140] V. Ferraro, C. Bizzarri, S. Bräse, *Adv. Sci.* **2024**, *11*, 2404866.
[141] Y.-J. Gao, Z.-R. Wang, W.-K. Chen, W.-H. Fang, G. Cui, *Chem. Phys.* **2018**, *515*, 692-703.
[142] C. Sandoval-Pauker, G. Molina-Aguirre, D. Villagrán, B. Pinter, *Inorg. Chem. Front.* **2024**, *11*, 4019-4031.
[143] J. M. Carbonell-Vilar, E. Fresta, D. Armentano, R. D. Costa, M. Viciano-Chumillas, J. Cano, *Dalton Trans.* **2019**, *48*, 9765-9775.
[144] D. Bím, K. M. Luedecke, D. A. Cagan, R. G. Hadt, *Inorg. Chem.* **2024**, *63*, 4120-4131.
[145] F. J. Wuilleumier, M. Meyer, *J. Phys. B: At. Mol. Opt. Phys.* **2006**, *39*, R425.
[146] S. Calvin, *XAFS for Everyone*, CRC press, **2024**.

[147] A. Iglesias-Juez, G. L. Chiarello, G. S. Patience, M. O. Guerrero-Pérez, *The Canadian Journal of Chemical Engineering* **2022**, *100*, 3-22.
[148] Y. Kim, R. Ma, J. Lee, J. Harich, D. Nam, S. Kim, M. Kim, M. Ochmann, I. Eom, N. Huse, J. H. Lee, T. K. Kim, *J. Phys. Chem. Lett.* **2021**, *12*, 12165-12172.
[149] R. M. Jay, M. R. Coates, H. Zhao, M.-O. Winghart, P. Han, R.-P. Wang, J. Harich, A. Banerjee, H. Wikmark, M. Fondell, E. T. J. Nibbering, M. Odelius, N. Huse, P. Wernet, *J. Am. Chem. Soc.* **2024**, *146*, 14000-14011.
[150] W. Kantlehner, E. Haug, W. W. Mergen, P. Speh, T. Maier, J. J. Kapassakalidis, H. J. Bräuner, H. Hagen, *Liebigs Ann. Chem.* **1984**, *1984*, 108-126.
[151] S. Angyal, W. Warburton, *Journal of the Chemical Society (Resumed)* **1951**, 2492-2494.
[152] D. F. Schrempp, S. Leingang, M. Schnurr, E. Kaifer, H. Wadepohl, H. J. Himmel, *Chem.* **2017**, *23*, 13607-13611.
[153] K. W. Kröckert, F. Garg, J. Heck, M. V. Heinz, J. Lange, R. Schmidt, A. Hoffmann, S. Herres-Pawlis, *Dalton Trans.* **2024**, *53*, 2973-2990.
[154] T. Langletz, P. M. Grande, J. Viell, D. Wolters, J. Tonn, H. Klose, S. G. Schriever, A. Hoffmann, A. Jupke, T. Gries, S. Herres-Pawlis, *Adv. Energy Sustainability Res.* **2024**, *5*, 2300187.
[155] T. Becker, A. Hermann, N. Saritas, A. Hoffmann, S. Herres-Pawlis, *ChemSusChem* **2024**, *17*, e202400933.
[156] V. Bagchi, P. Paraskevopoulou, P. Das, L. Chi, Q. Wang, A. Choudhury, J. S. Mathieson, L. Cronin, D. B. Pardue, T. R. Cundari, G. Mitrikas, Y. Sanakis, P. Stavropoulos, *J. Am. Chem. Soc.* **2014**, *136*, 11362-11381.
[157] L. Laurini, A. Béteille, G. Fink, S. Herres-Pawlis, K. Loubière, *Chem. Eng. Technol.* **2023**, *46*, 1664-1672.
[158] L. Laurini, S. M. Conte, K. Hüser, P. R. F. Cordero, H. M. Núñez Ponce, S. Zimmer, L. Lauterbach, S. Herres-Pawlis, *Eur. J. Inorg. Chem.* **2024**, *27*, e202300700.
[159] L. Burkart, A. Eith, A. Hoffmann, S. Herres-Pawlis, *Chem.: Asian J.* **2023**, *18*, e202201195.
[160] C. Conrads, L. Burkart, S. Soerensen, S. Noichl, Y. Kara, J. Heck, A. Hoffmann, S. Herres-Pawlis, *Catal. Sci. Technol.* **2023**, *13*, 6006-6021.
[161] M. Fuchs, P. M. Schäfer, W. Wagner, I. Krumm, M. Walbeck, R. Dietrich, A. Hoffmann, S. Herres-Pawlis, *ChemSusChem* **2023**, *16*, e202300192.
[162] R. D. Rittinghaus, A. Karabulut, A. Hoffmann, S. Herres-Pawlis, *Angew. Chem. Int. Ed.* **2021**, *60*, 21795-21800.
[163] J. Osterbrink, P. Walter, S. Leingang, H. Pfisterer, E. Kaifer, H. J. Himmel, *Chem. Eur. J.* **2023**, *29*, e202300514.
[164] J. Osterbrink, F. Dos Santos, E. Kaifer, H.-J. Himmel, *Eur. J. Inorg. Chem.* **2024**, *27*, e202400070.
[165] J. Stanek, N. Sackers, F. Fink, M. Paul, L. Peters, R. Grunzke, A. Hoffmann, S. Herres-Pawlis, *Chem.* **2017**, *23*, 15738-15745.
[166] E. A. Ambundo, L. Ochrymowycz, D. Rorabacher, *Inorg. Chem.* **2001**, *40*, 5133-5138.
[167] J. Heck, Dissertation thesis, RWTH Aachen (Aachen), **2023**.
[168] J. H. Gorvin, *J. Chem. Soc., Perkin Trans. 1* **1988**, 1331-1335.
[169] P. Dunkel, M. Petit, H. Dhimane, M. Blanchard-Desce, D. Ogden, P. I. Dalko, *ChemistryOpen* **2017**, *6*, 660-667.
[170] M. Becker, F. W. Heinemann, S. Schindler, *Chem. Eur. J.* **1999**, *5*, 3124-3129.
[171] S. Worl, D. Hellwinkel, H. Pritzkow, M. Hofmann, R. Kramer, *Dalton Trans.* **2004**, 2750-2757.

[172] M. J. Frisch, G. W. Trucks, H. B. Schlegel, G. E. Scuseria, M. A. Robb, J. R. Cheeseman, G. Scalmani, V. Barone, G. A. Petersson, H. Nakatsuji, M. C. X. Li, A. V. Marenich, J. Bloino, B. G. Janesko, R. Gomperts, B. Mennucci, H. P. Hratchian, J. V. Ortiz, A. F. Izmaylov, J. L. Sonnenberg, Williams, F. Ding, F. Lipparini, F. Egidi, J. Goings, B. Peng, A. Petrone, T. Henderson, D. Ranasinghe, V. G. Zakrzewski, J. Gao, N. Rega, G. Zheng, W. Liang, M. Hada, M. Ehara, K. Toyota, R. Fukuda, J. Hasegawa, M. Ishida, T. Nakajima, Y. Honda, O. Kitao, H. Nakai, T. Vreven, K. Throssell, J. A. Montgomery Jr., J. E. Peralta, F. Ogliaro, M. J. Bearpark, J. J. Heyd, E. N. Brothers, K. N. Kudin, V. N. Staroverov, T. A. Keith, R. Kobayashi, J. Normand, K. Raghavachari, A. P. Rendell, J. C. Burant, S. S.Iyengar, J. Tomasi, M. Cossi, J. M. Millam, M. Klene, C. Adamo, R. Cammi, J. W. Ochterski, R. L. Martin, K. Morokuma, O. Farkas, J. B. Foresman, D. J. Fox, *Gaussian 16*, Gaussian Inc., Wallington CT, **2016**.
[173] V. Staroverov, G. Scuseria, J. Tao, J. Perdew, *J. Chem. Phys.* **2003**, *119*, 12129-12137.
[174] J. Tao, J. P. Perdew, V. N. Staroverov, G. E. Scuseria, *Phys. Rev. Lett.* **2003**, *91*, 146401.
[175] A. Schäfer, H. Horn, R. Ahlrichs, *J. Chem. Phys.* **1992**, *97*, 2571-2577.
[176] K. Eichkorn, F. Weigend, O. Treutler, R. Ahlrichs, *Theor. Chem. Acc.* **1997**, *97*, 119-124.
[177] F. Weigend, R. Ahlrichs, *Phys. Chem. Chem. Phys.* **2005**, *7*, 3297-3305.
[178] A. Hoffmann, R. Grunzke, S. Herres-Pawlis, *J. Comput. Chem.* **2014**, *35*, 1943-1950.
[179] L. Goerigk, S. Grimme, *Phys. Chem. Chem. Phys.* **2011**, *13*.
[180] S. Grimme, S. Ehrlich, L. Goerigk, *J. Comput. Chem.* **2011**, *32*, 1456-1465.
[181] E. D. Glendening, C. R. Landis, F. Weinhold, *J. Comput. Chem.* **2013**, *34*, 1429-1437.
[182] F. Weinhold, C. R. Landis, *Valency and bonding: a natural bond orbital donor-acceptor perspective*, Cambridge University Press, **2005**.
[183] E. Glendening, J. Badenhoop, A. Reed, J. Carpenter, J. Bohmann, C. Morales, C. Landis, F. Weinhold, *Theoretical Chemistry Institute, University of Wisconsin, Madison, WI* **2013**.
[184] O. Bienemann, R. Haase, A. Jesser, T. Beschnitt, A. Döring, D. Kuckling, I. dos Santos Vieira, U. Flörke, S. Herres-Pawlis, *Eur. J. Inorg. Chem.* **2011**, *2011*, 2367-2379.
[185] P. Zanello, N. G. Connelly, *Inorganic Electrochemistry*, The Royal Society of Chemistry, **2003**.
[186] R. Cao, C. Saracini, J. W. Ginsbach, M. T. Kieber-Emmons, M. A. Siegler, E. I. Solomon, S. Fukuzumi, K. D. Karlin, *J. Am. Chem. Soc.* **2016**, *138*, 7055-7066.
[187] A. A. Maryott, E. R. Smith, *Table of dielectric constants of pure liquids, Vol. 514*, US Government Printing Office, **1951**.
[188] T. M. Aminabhavi, B. Gopalakrishna, *J. Chem. Eng. Data* **1995**, *40*, 856-861.
[189] W. T. Eckenhoff, A. B. Biernesser, T. Pintauer, *Inorg. Chem.* **2012**, *51*, 11917-11929.
[190] Y. Chen, Y. Pan, Y.-M. He, Q.-H. Fan, *Angew. Chem. Int. Ed.* **2019**, *58*, 16831-16834.
[191] N. Mori, H. Togo, *Tetrahedron* **2005**, *61*, 5915-5925.
[192] T. Seitz, M. Walbeck, A. Hoffmann, S. Herres-Pawlis, *Dalton Trans.* **2025**, *54*, 957-965.
[193] T. G. Ribelli, M. Fantin, J.-C. Daran, K. F. Augustine, R. Poli, K. Matyjaszewski, *J. Am. Chem. Soc.* **2018**, *140*, 1525-1534.

[194] O. V. Dyablo, E. A. Shmoilova, A. F. Pozharskii, V. A. Ozeryanskii, O. N. Burov, Z. A. Starikova, *Org. Lett.* **2012**, *14*, 4134-4137.
[195] P. D. Nahide, C. Alba-Betancourt, R. Chávez-Rivera, P. Romo-Rodríguez, M. Solís-Hernández, L. A. Segura-Quezada, K. R. Torres-Carbajal, R. Gámez-Montaño, M. A. Deveze-Álvarez, M. A. Ramírez-Morales, *Bioorg. Med. Chem. Lett.* **2022**, *63*, 128649.
[196] Y. Yin, Y. Xiao, X. Yang, H. Li, J. Du, W. Duan, L. Yu, *Organic & Biomolecular Chemistry* **2025**, *23*, 1581-1587.
[197] H. Takeuchi, T. Kojima, T. Egawa, S. Konaka, *J. Phys. Chem.* **1992**, *96*, 4389-4396.
[198] M. Dewar, H. Schmeising, *Tetrahedron* **1959**, *5*, 166-178.
[199] D. W. J. Cruickshank, R. Sparks, *Proc. R. Soc. London, Ser. A* **1960**, *258*, 270-285.
[200] J. Trotter, *Acta Crystallogr.* **1961**, *14*, 1135-1140.
[201] A. v. Bondi, *J. Phys. Chem.* **1964**, *68*, 441-451.
[202] K. Carter-Fenk, J. M. Herbert, *Phys. Chem. Chem. Phys.* **2020**, *22*, 24870-24886.
[203] A. Turksoy, A. Weßels, K. Deckers, C. D. T. Nielsen, F. Schoenebeck, *Org. Lett.* **2025**, *27*, 2908-2912.
[204] S. Y. Haoyu, X. He, S. L. Li, D. G. Truhlar, *Chem. Sci.* **2016**, *7*, 5032-5051.
[205] S. Stoll, A. Schweiger, *J. Magn. Reson.* **2006**, *178*, 42-55.
[206] B. Bennett, J. M. Kowalski, *Methods Enzymol.* **2015**, *563*, 341-361.
[207] D. S. Marlin, M. M. Olmstead, P. K. Mascharak, *Inorg. Chem.* **2001**, *40*, 7003-7008.
[208] A. Winter, K. Thiel, A. Zabel, T. Klamroth, A. Pöppl, A. Kelling, U. Schilde, A. Taubert, P. Strauch, *New J. Chem.* **2014**, *38*, 1019-1030.
[209] A. Jesser, M. Rohrmüller, W. G. Schmidt, S. Herres-Pawlis, *J. Comput. Chem.* **2014**, *35*, 1-17.
[210] A. Hoffmann, M. Rohrmueller, A. Jesser, I. dos Santos Vieira, W. G. Schmidt, S. Herres-Pawlis, *J. Comput. Chem.* **2014**, *35*, 2146-2161.
[211] P. Gayen, U. Das, S. Banerjee, *J. Phys. Chem. A* **2020**, *124*, 4654-4665.
[212] P. W. Atkins, J. De Paula, *Physikalische Chemie*, John Wiley & Sons, **2006**.
[213] L. E. Burmeister, L. J. Groth, P. R. Meinhold, J. P. Zurwellen, D. Bockfeld, R. Frank, M. Karnahl, M. Tamm, S. Tschierlei, *JACS Au* **2025**, *5*, 2792-2801.
[214] M. Ruthkosky, F. N. Castellano, G. J. Meyer, *Inorg. Chem.* **1996**, *35*, 6406-6412.
[215] J. V. Lockard, S. Kabehie, J. I. Zink, G. Smolentsev, A. Soldatov, L. X. Chen, *J. Phys. Chem. B* **2010**, *114*, 14521-14527.
[216] K. K. Chen, S. Guo, H. Liu, X. Li, Z. M. Zhang, T. B. Lu, *Angew. Chem. Int. Ed.* **2020**, *59*, 12951-12957.
[217] M. K. Eggleston, D. R. McMillin, K. S. Koenig, A. J. Pallenberg, *Inorg. Chem.* **1997**, *36*, 172-176.
[218] O. Green, B. A. Gandhi, J. N. Burstyn, *Inorg. Chem.* **2009**, *48*, 5704-5714.
[219] A. K. Gushurst, D. R. McMillin, C. O. Dietrich-Buchecker, J. P. Sauvage, *Inorg. Chem.* **1989**, *28*, 4070-4072.
[220] S. Garakyaraghi, C. E. McCusker, S. Khan, P. Koutnik, A. T. Bui, F. N. Castellano, *Inorg. Chem.* **2018**, *57*, 2296-2307.
[221] E. Hasegawa, S. Takizawa, T. Seida, A. Yamaguchi, N. Yamaguchi, N. Chiba, T. Takahashi, H. Ikeda, K. Akiyama, *Tetrahedron* **2006**, *62*, 6581-6588.
[222] N. G. Connelly, W. E. Geiger, *Chem. Rev.* **1996**, *96*, 877-910.
[223] A. Hossain, S. Engl, E. Lutsker, O. Reiser, *ACS Catalysis* **2019**, *9*, 1103-1109.
[224] A. J. Niestroj, M. E. Maier, *Angew. Chem.* **1997**, *109*, 1854-1854.

[225] H. Eilingsfeld, G. Neubauer, M. Seefelder, H. Weidincer, *Chem. Ber.* **1964**, *97*, 1232-1245.
[226] S. Herres-Pawlis, A. Neuba, O. Seewald, T. Seshadri, H. Egold, U. Flörke, G. Henkel, *Eur. J. Org. Chem.* **2005**, *2005*, 4879-4890.
[227] G. R. Fulmer, A. J. M. Miller, N. H. Sherden, H. E. Gottlieb, A. Nudelman, B. M. Stoltz, J. E. Bercaw, K. I. Goldberg, *Organometallics* **2010**, *29*, 2176-2179.
[228] P. Tremouilhac, C. L. Lin, P. C. Huang, Y. C. Huang, A. Nguyen, N. Jung, F. Bach, R. Ulrich, B. Neumair, A. Streit, S. Brase, *Angew. Chem. Int. Ed.* **2020**, *59*, 22771-22778.
[229] P. Tremouilhac, P. C. Huang, C. L. Lin, Y. C. Huang, A. Nguyen, N. Jung, F. Bach, S. Bräse, *Chemistry–Methods* **2020**, *1*, 8-11.
[230] *X-Area Pilatus3_SV 1.31. 170.0* **2020**, *STOE*.
[231] *X-Area Recipe 1.33.0.0* **2015**, *STOE*.
[232] *X-Area Integrate 1.71.0.0* **2016**, *STOE*.
[233] *X-Area LANA 1.83.8.0* **2020**, *STOE*.
[234] G. Sheldrick, *Acta Crystallogr. Sect. A* **2015**, *71*, 3-8.
[235] G. M. Sheldrick, *Acta Crystallogr. Sect. A* **2008**, *64*, 112-122.
[236] G. M. Sheldrick, *Acta Crystallogr. Sect. C* **2015**, *71*, 3-8.
[237] C. B. Hübschle, G. M. Sheldrick, B. Dittrich, *J. Appl. Crystallogr.* **2011**, *44*, 1281-1284.
[238] A. Spek, P. A. M. C. Tool, **2008**, *65*.
[239] A. L. Spek, *Acta Crystallogr. Sect. D. Biol. Crystallogr.* **2009**, *65*, 148-155.
[240] T. D. Svejstrup, A. Chatterjee, D. Schekin, T. Wagner, J. Zach, M. J. Johansson, G. Bergonzini, B. König, *ChemPhotoChem* **2021**, *5*, 808-814.
[241] J. Saavedra-Olavarría, P. Hermosilla-Ibáñez, I. Almodóvar, E. G. Pérez, *Eur. J. Org. Chem.* **2022**, *2022*, e202101526.
[242] E. G. Delany, C. L. Fagan, S. Gundala, A. Mari, T. Broja, K. Zeitler, S. J. Connon, *Chem. Commun.* **2013**, *49*, 6510-6512.
[243] A. R. Todorov, S. Aikonen, M. Muuronen, J. Helaja, *Org. Lett.* **2019**, *21*, 3764-3768.
[244] H. S. Yu, X. He, D. G. Truhlar, *J. Chem. Theory Comput.* **2016**, *12*, 1280-1293.
[245] P. Pracht, F. Bohle, S. Grimme, *Phys. Chem. Chem. Phys.* **2020**, *22*, 7169-7192.
[246] C. Bannwarth, S. Ehlert, S. Grimme, *J. Chem. Theory Comput.* **2019**, *15*, 1652-1671.

9 Appendix

9.1 Crystallographic Data

9.1.1 Crystallographic Data of Tripodal Complexes

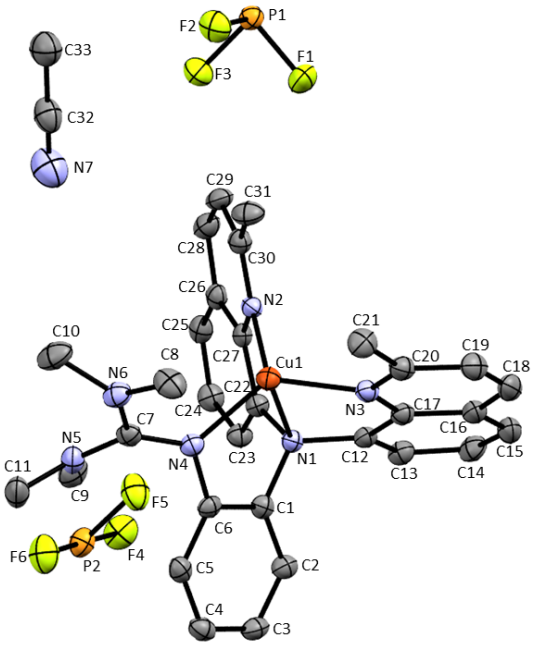

Figure 9.1: Molecular structure of [Cu{N(QuMe)$_2$(PhTMG)}]PF_6 · MeCN (**$C1_{TMG}$–PF_6·MeCN**) in the solid state (50 % probability, asymmetric unit, H atoms are omitted for clarity).

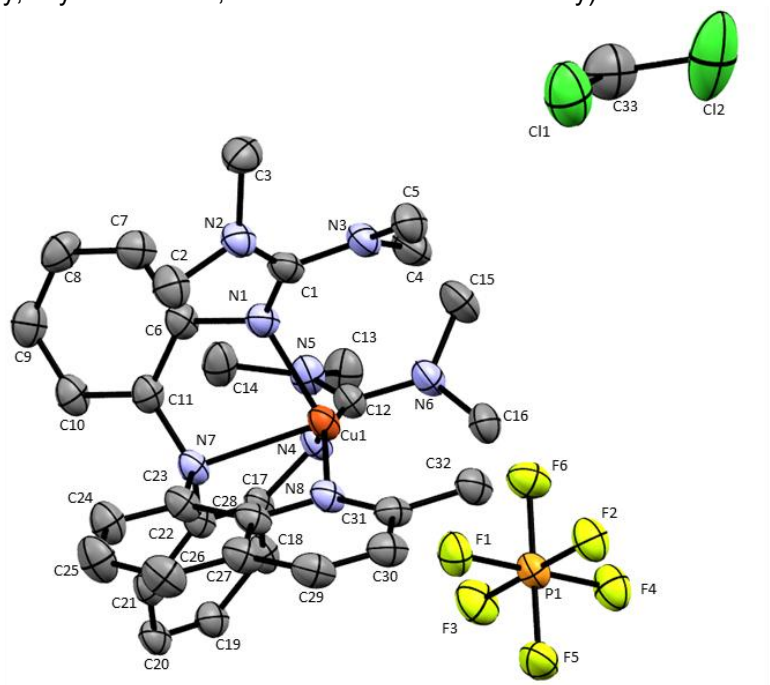

Figure 9.2: Molecular structure of [Cu{N(QuMe)(PhTMG)$_2$}]PF_6 · DCM · C_5H_{12} (**$C3_{TMG}$–PF_6·DCM·C_5H_{12}**) in the solid state (ellipsoids drawn at 50 % probability level, asymmetric unit, H atoms are omitted for clarity). A strongly disordered molecules of pentane was removed via SQUEEZE.

Table 9-1: Crystallographic data of [Cu{N(QuMe)$_2$(PhTMG)}]PF_6 · MeCN (**$C1_{TMG}$–PF_6·MeCN**) and [Cu{N(QuMe)(PhTMG)$_2$}]PF_6·DCM·C_5H_{12} (**$C3_{TMG}$–PF_6·DCM·C_5H_{12}**). In **$C3_{TMG}$–PF_6·DCM·C_5H_{12}**, it was not possible to model the disordered molecule pentane per asymmetric unit adequately and the data sets were treated with the SQUEEZE routine as implemented in PLATON.

	$C1_{TMG}$–PF_6·MeCN	**$C3_{TMG}$–PF_6·DCM·C_5H_{12}**
Empirical formula	$C_{33}H_{35}CuF_6N_7P$	$C_{33}H_{42}Cl_2CuF_6N_8P$ [+C_5H_{12}]
Formular weight [g mol^{-1}]	738.19	830.15
Crystal size [mm]	0.220 x 0.150 x 0.070	0.320 x 0.310 x 0.280
Crystal system	monoclinic	monoclinic
Space group	*P2/c*	*P*2$_1$/*n*
a [Å]	15.796(3)	10.622(2)
b [Å]	11.950(2)	28.710(6)
c [Å]	18.191(4)	13.779(3)
α [°]	90	90
β [°]	108.23(3)	103.09(3)
γ [°]	90	90
V [Å^3]	3261.4(13)	4092.9(15)
Z	4	4
ρ [g cm^{-1}]	1.503	1.347
μ [mm^{-1}]	0.790	0.764
Wavelength[Å]	0.71073	0.71073
T [K]	100	100
F(000)	1520	1712
hkl range	-15 ≤ *h* ≤ 20, -15 ≤ *k* ≤ 15, -22 ≤ *l* ≤ 23	-12 ≤ *h* ≤ 12, -17 ≤ *k* ≤ 34, -16 ≤ *l* ≤ 16
Reflections collected	49202	67893
Independent reflections	7117	7615
$R_{int.}$	0.0736	0.1157
Number of parameters	441	469
Goodness-of-fit für F^2	0.956	1.059
R_1 [$I > 2\sigma(I)$]	0.0516	0.0641
wR_2 (all data)	0.1371	0.1642
Largest diff. Peak, hole [e Å^{-3}]	0.877, -0.610	1.475, -1.391

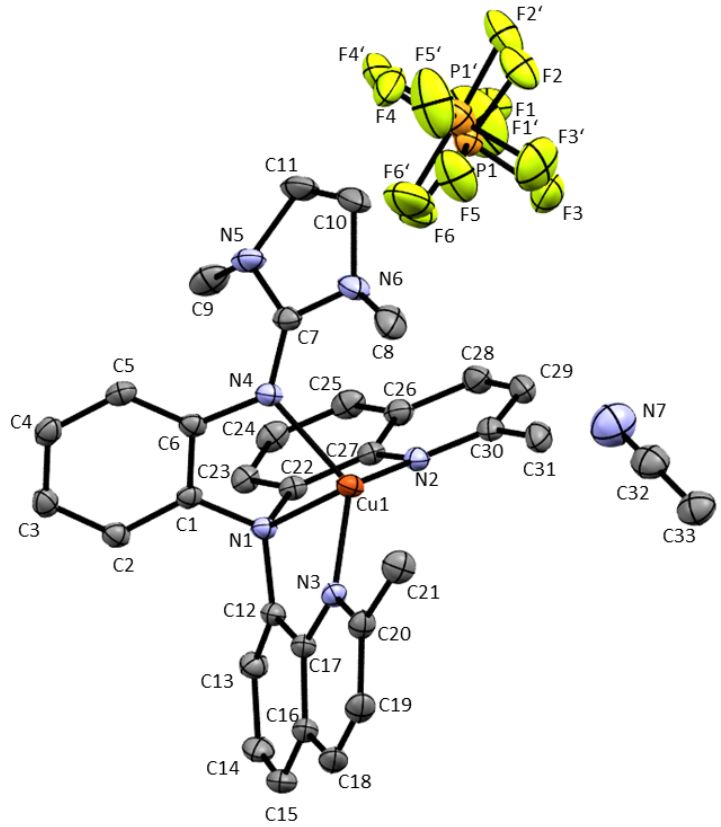

Figure 9.3: Molecular structure of [Cu{N(QuMe)$_2$(PhDMEG)}]PF_6 · MeCN (**$C1_{DMEG}$–PF_6·MeCN**) in the solid state (50 % probability, asymmetric unit, H atoms are omitted for clarity).

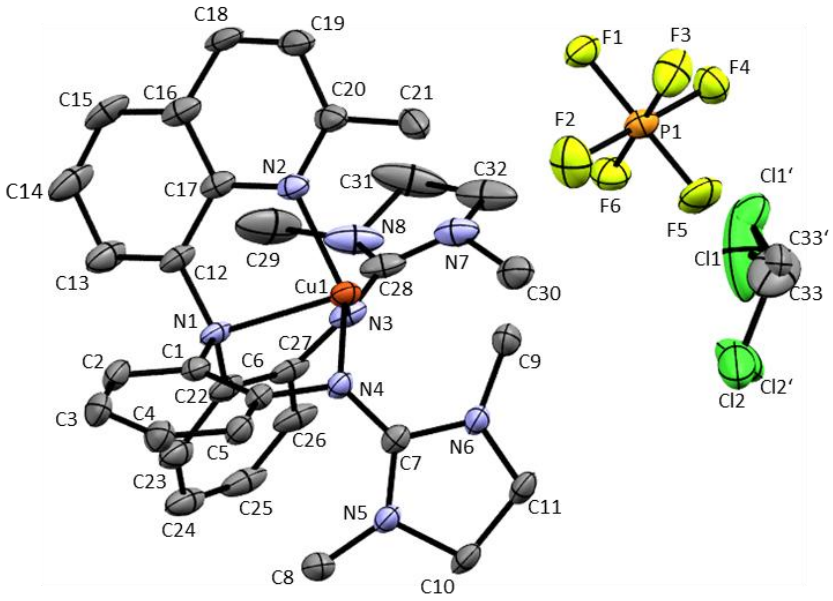

Figure 9.4: Molecular structure of [Cu{N(QuMe)(PhDMEG)$_2$}]PF_6 · DCM (**$C3_{DMEG}$–PF_6·DCM**) in the solid state (50 % probability, asymmetric unit, H atoms are omitted for clarity).

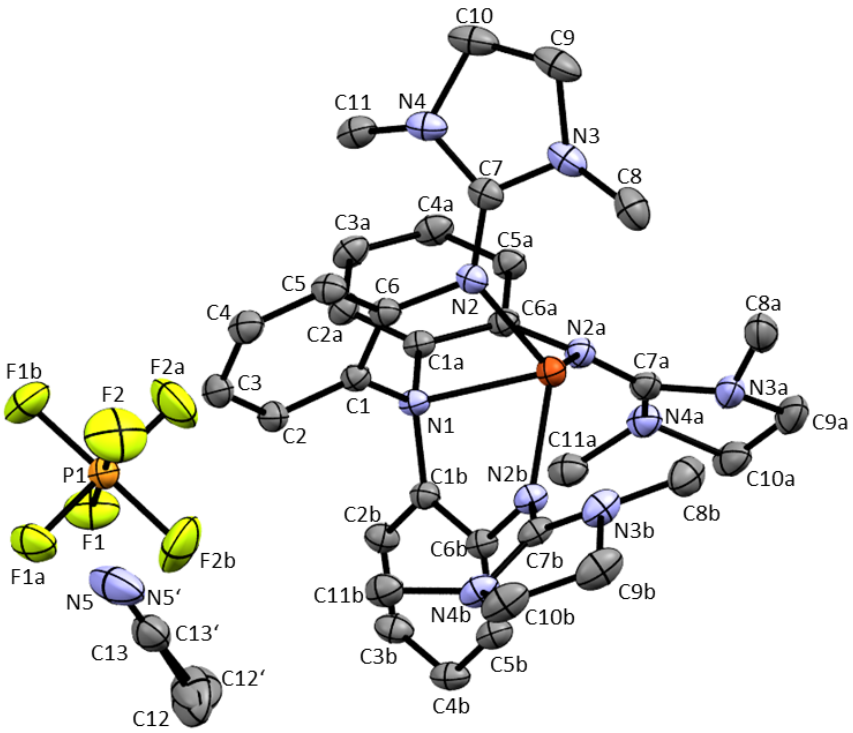

Figure 9.5: Molecular structure of [Cu(DMEG$_3$trphen)]PF_6 · MeCN (**$C5_{DMEG}$–PF_6·MeCN**) in the solid state (50 % probability, H atoms are omitted for clarity).

Table 9-2: Crystallographic data of [Cu{N(QuMe)$_2$(PhDMEG)}]PF_6 · MeCN (**$C1_{DMEG}$–PF_6·MeCN**), [Cu{N(QuMe)(PhDMEG)$_2$}]PF_6 · DCM (**$C3_{DMEG}$–PF_6·DCM**) and of [Cu(DMEG$_3$trphen)]PF_6 · MeCN (**$C5_{DMEG}$–PF_6·MeCN**).

	$C1_{DMEG}$–PF_6·MeCN	**$C3_{DMEG}$–PF_6·DCM**	**$C5_{DMEG}$–PF_6·MeCN**
Empirical formula	$C_{33}H_{33}CuF_6N_7P$	$C_{33}H_{38}CuF_6N_8P_1Cl_2$	$C_{72}H_{93}Cu_2F_{12}N_{23}P_2$
Formular weight [g mol^{-1}]	736.17	826.12	1697.71
Crystal size [mm]	0.220 x 0.200 x 0.110	0.147 x 0.073 x 0.060	0.230 x 0.150 x 0.120
Crystal system	triclinic	triclinic	trigonal
Space group	$P\bar{1}$	$P\bar{1}$	$R\bar{3}c$
a [Å]	10.893(2)	9.0207(18)	14.977(2)
b [Å]	12.015(2)	14.171(3)	14.977(2)
c [Å]	15.064(3)	15.375(3)	59.777(12)
α [°]	66.91(3)	69.15(3)	90
β [°]	85.07(3)	81.46(3)	90
γ [°]	63.15(3)	73.01(3)	120
V [Å^3]	1608.1(8)	1754.2(8)	11613(4)
Z	2	2	6
ρ [g cm^{-1}]	1.520	1.564	1.457
μ [mm^{-1}]	0.800	0.891	0.679
Wavelength[Å]	0.71073	0.71073	0.71073
T [K]	100	100	100
F(000)	756	848	5292
hkl range	-15 ≤ *h* ≤ 15, -17 ≤ *k* ≤ 11, -21 ≤ *l* ≤ 21	-12 ≤ *h* ≤ 12, - 19 ≤ *k* ≤ 19, -21 ≤ *l* ≤ 16	-22 ≤ *h* ≤ 22, -22 ≤ *k* ≤ 18, -88 ≤ *l* ≤ 88
Reflections collected	59631	53162	84855
Independent reflections	8712	9063	4459
$R_{int.}$	0.0536	0.1238	0.0874
Number of parameters	502	493	172
Goodness-of-fit für F^2	1.052	0.963	1.067
R_1 [$I > 2\sigma(I)$]	0.0325	0.0494	0.0359
wR_2 (all data)	0.0895	0.0882	0.1030
Largest diff. Peak, hole [e Å^{-3}]	0.486, -0.337	0.696, -0.616	0.435, -0.713

9.1.2 Crystallographic Data of TMGqu Complexes

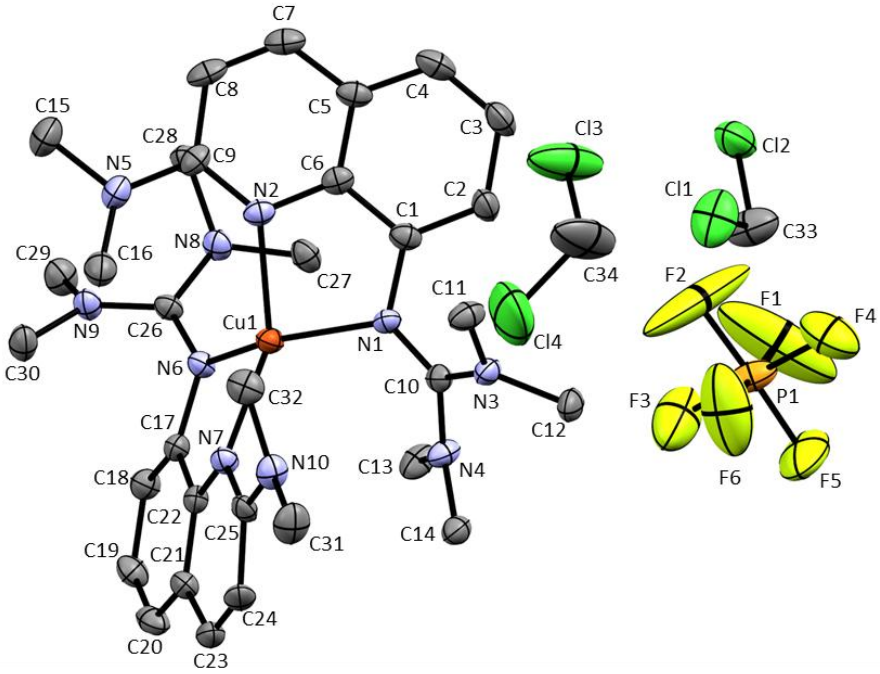

Figure 9.6: Molecular structure of $[Cu(TMG2NMe_2qu)_2]PF_6 \cdot 2$ DCM (**C7–PF$_6$·DCM**) in the solid state (50 % probability, asymmetric unit, H atoms are omitted for clarity). **C7–PF$_6$·DCM** is a twin and the data set was treated with the TwinRotMat routine as implemented in PLATON (rotation axis in reciprocal space (2 -1 0) and twin law 1 0 0 -1 -1 0 0 0 -1).

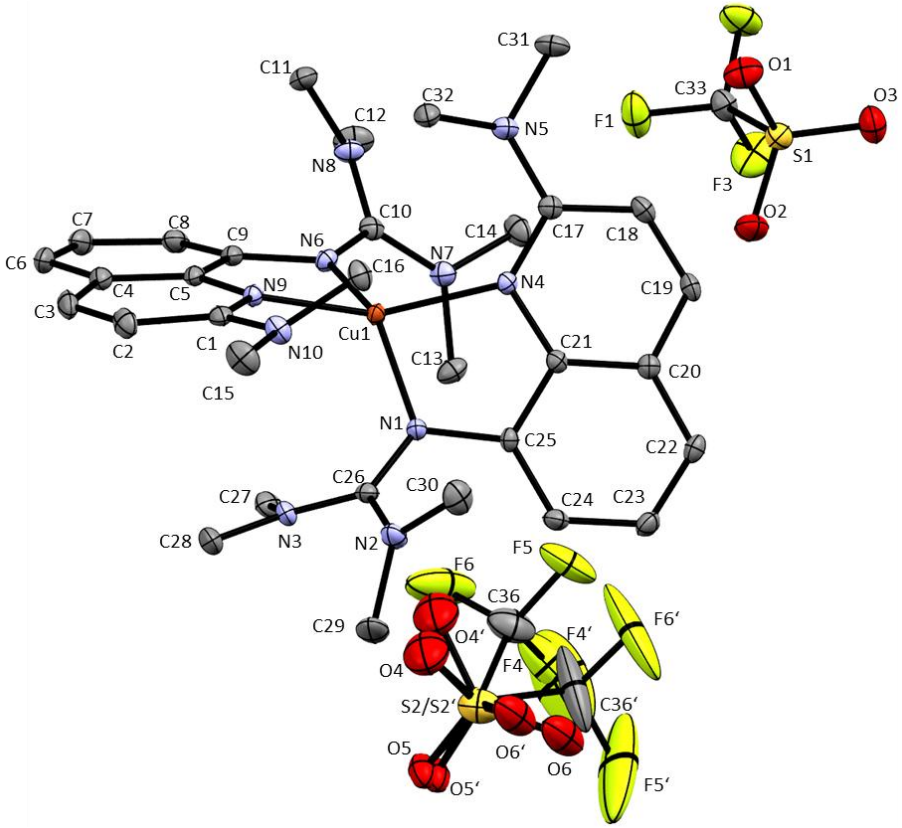

Figure 9.7: Molecular structure of $[Cu(TMG2NMe_2qu)_2](OTf)_2$ (**C8–OTf**) in the solid state (50 % probability, asymmetric unit, H atoms are omitted for clarity).

Table 9-3: Crystallographic data of $[Cu(TMG2NMe_2qu)_2]PF_6 \cdot 2$ DCM (**C7–PF_6·DCM**) and $[Cu(TMG2NMe_2qu)_2](OTf)_2$ (**C8–OTf**). **C7–PF_6·DCM** is a twin and the data set was treated with the TwinRotMat routine as implemented in PLATON (rotation axis in reciprocal space (2 -1 0) and twin law 1 0 0 -1 -1 0 0 0 -1).

	C7–PF_6·DCM	**C8–OTf**
Empirical formula	$C_{34}H_{50}Cl_4CuF_6N_{10}P \cdot 2\ CH_2Cl_2$	$C_{34}H_{46}CuF_6N_{10}O_6S_2$
Formular weight [g mol^{-1}]	949.15	932.47
Crystal size [mm]	0.113 x 0.100 x 0.057	0.170 x 0.160 x 0.085
Crystal system	trigonal	triclinic
Space group	$P3_2$	$P\bar{1}$
a [Å]	11.3244(16)	11.037(2)
b [Å]	11.3244(16)	12.206(2)
c [Å]	28.398(6)	16.663(3)
α [°]	90	98.57(3)
β [°]	90	104.20(3)
γ [°]	120	108.83(3)
V [Å^3]	3154.0(11)	1995.1(8)
Z	3	2
ρ [g cm^{-3}]	1.499	1.552
μ [mm^{-1}]	0.878	0.738
Wavelength[Å]	0.71073	0.71073
T [K]	100	100
F(000)	1470	966
hkl range	$-17 \leq h \leq 8$, $-17 \leq k \leq 17$, $-43 \leq l \leq 43$	$-14 \leq h \leq 14$, $-15 \leq k \leq 16$, $-22 \leq l \leq 22$
Reflections collected	15567	39575
Independent reflections	15567	9590
$R_{int.}$	twin	0.0385
Number of parameters	518	599
Goodness-of-fit für F^2	0.871	1.108
R_1 [$I > 2\sigma(I)$]	0.0464	0.044
wR_2 (all data)	0.1094	0.1389
Largest diff. Peak, hole [e Å^{-3}]	1.031, -0.692	3.455, -0.623

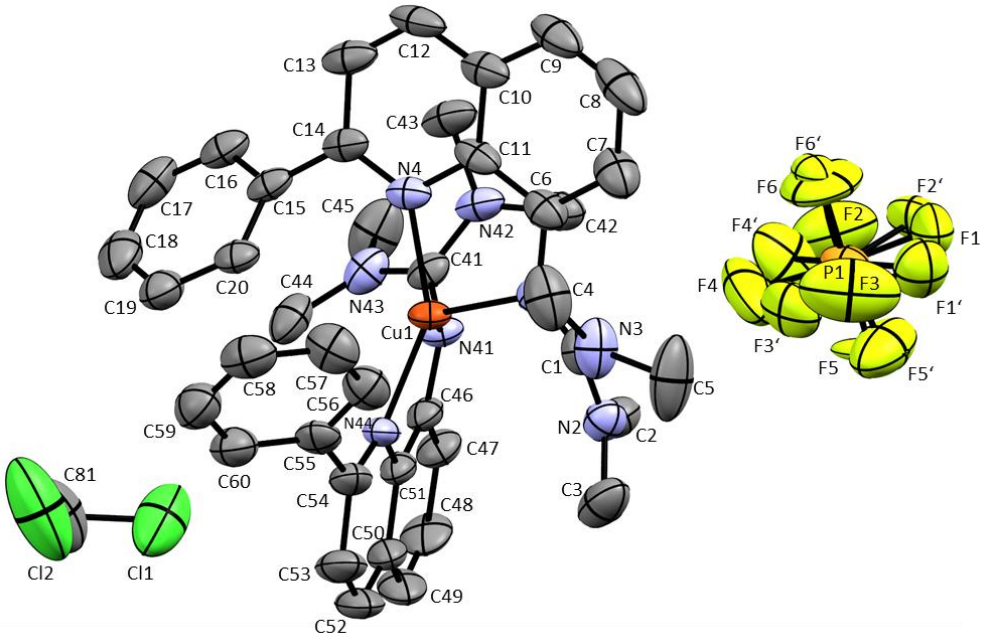

Figure 9.8: Molecular structure of $[Cu(TMG2Phqu)_2]PF_6 \cdot DCM$ (**C9–$PF_6 \cdot$ DCM**) in the solid state (50 % probability, asymmetric unit, H atoms are omitted for clarity).

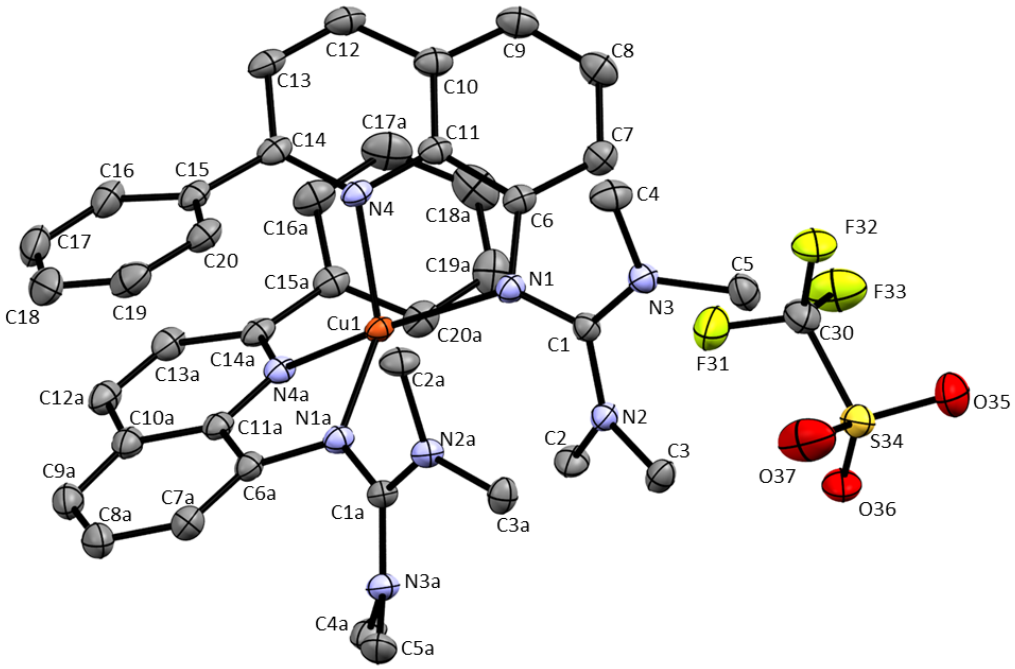

Figure 9.9: Molecular structure of $[Cu(TMG2Phqu)_2](OTf)_2 \cdot 0.5\ H_2O$ (**C10–OTf·H_2O**) in the solid state (50 % probability, H atoms are omitted for clarity, H_2O masked with SQUEEZE.

Table 9-4: Crystallographic data of $[Cu(TMG2Phqu)_2]PF_6 \cdot DCM$ (**C9–PF_6·DCM**) and $[Cu(TMG2Phqu)_2](OTf)_2 \cdot 0.5\ H_2O$ (**C10–OTf·H_2O**). In **C10–OTf·H_2O**, it was not possible to model the disordered solvent molecule (H_2O) in an adequate manner, and the data set was treated with the SQUEEZE routine as implemented in PLATON.

	C9–PF_6·DCM	**C10–OTf·H_2O**
Empirical formula	$C_{41}H_{46}Cl_2CuF_6N_8P$	$C_{42}H_{44}CuF_6N_8O_6S_2$ [+ 0.5 H_2O]
Formular weight [g mol^{-1}]	930.27	998.51
Crystal size [mm]	0.130 x 0.120 x 0.100	0.160 x 0.120 x 0.050
Crystal system	monoclinic	Orthorhombic
Space group	$P2_1/c$	*Pbcn*
a [Å]	15.993(3)	12.985(3)
b [Å]	16.367(3)	22.954(5)
c [Å]	16.176(3)	14.661(3)
α [°]	90	90
β [°]	91.43(3)	90
γ [°]	90	90
V [$Å^3$]	4232.9(15)	4370.0(15)
Z	4	4
ρ [g cm^{-3}]	1.460	1.518
μ [mm^{-1}]	0.748	0.679
Wavelength[Å]	0.71073	0.71073
T [K]	150	100
F(000)	1920	2060
hkl range	$-19 \leq h \leq 19$, $-19 \leq k \leq 19$, $-19 \leq l \leq 19$	$-16 \leq h \leq 16$, $-29 \leq k \leq 27$, $-18 \leq l \leq 18$
Reflections collected	90187	46030
Independent reflections	7880	4774
$R_{int.}$	0.0911	0.0414
Number of parameters	595	298
Goodness-of-fit für F^2	1.052	1.047
R_1 [$I > 2\sigma(I)$]	0.0686	0.0421
wR_2 (all data)	0.2139	0.1206
Largest diff. Peak, hole [e $Å^{-3}$]	2.139, -1.168	0.779, -0.424

9.1.3 Powder Diffraction Data of $[Cu(TMG2Phqu)_2](OTf)_2$

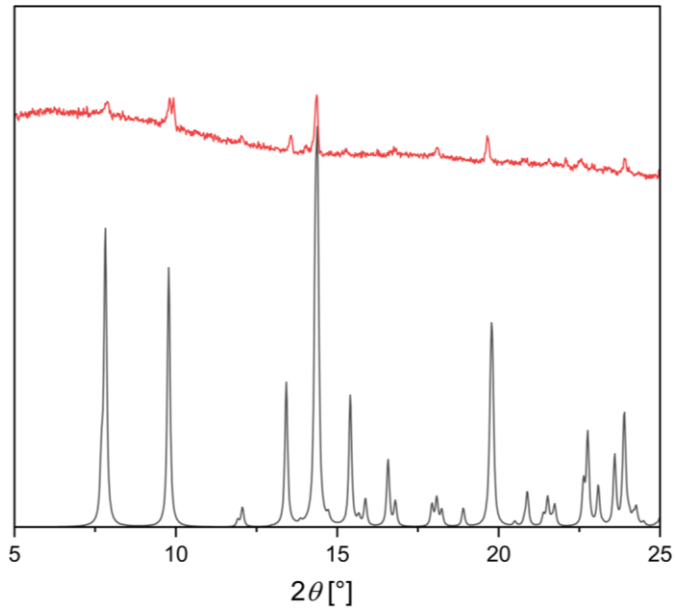

Figure 9.10: Experimental (red) and simulated (black) PXRD spectra of $[Cu(TMG2Phqu)_2](OTf)_2 \cdot 0.5\ H_2O$ (**C10–OTf·H₂O**).

9.2 Cyclic Voltammograms

9.2.1 Cyclic Voltammograms of Tripodal Model Systems

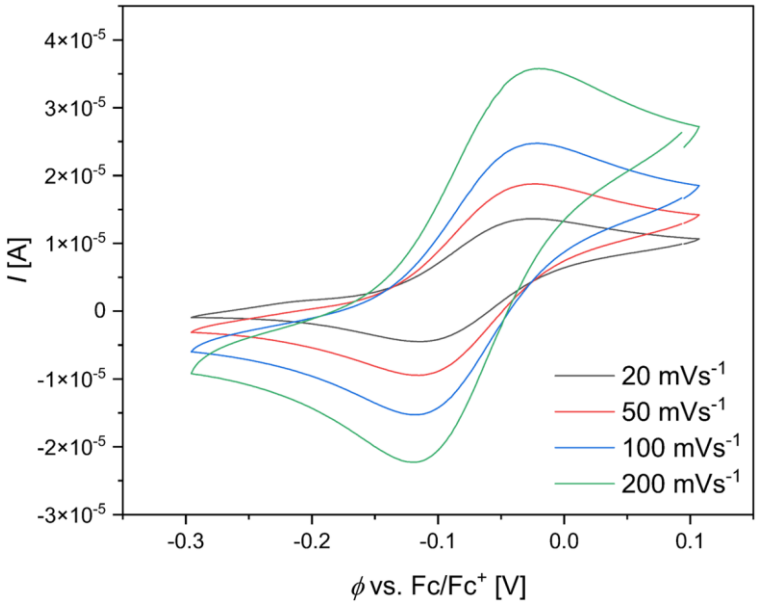

Figure 9.11: Cyclic voltammogram of $\mathbf{R1_{TMG}}$ starting from the corresponding Cu(I) complex $\mathbf{C1_{TMG}–PF_6}$ (c = 10^{-3} M) in MeCN with $[NBu_4][PF_6]$ (c = 0.1 M).

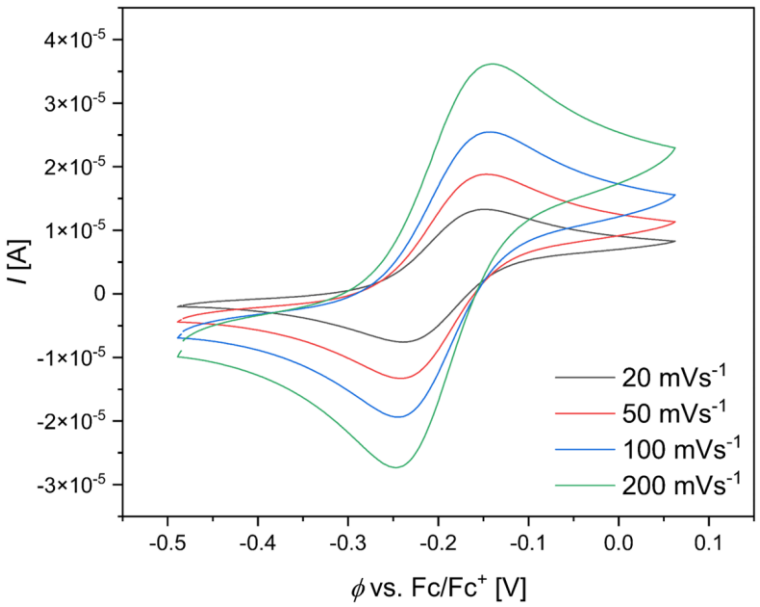

Figure 9.12: Cyclic voltammogram of **R2$_{TMG}$** starting from the corresponding Cu(I) complex **C3$_{TMG}$–PF$_6$** (c = 10^{-3} M) in MeCN with [NBu$_4$][PF$_6$] (c = 0.1 M).

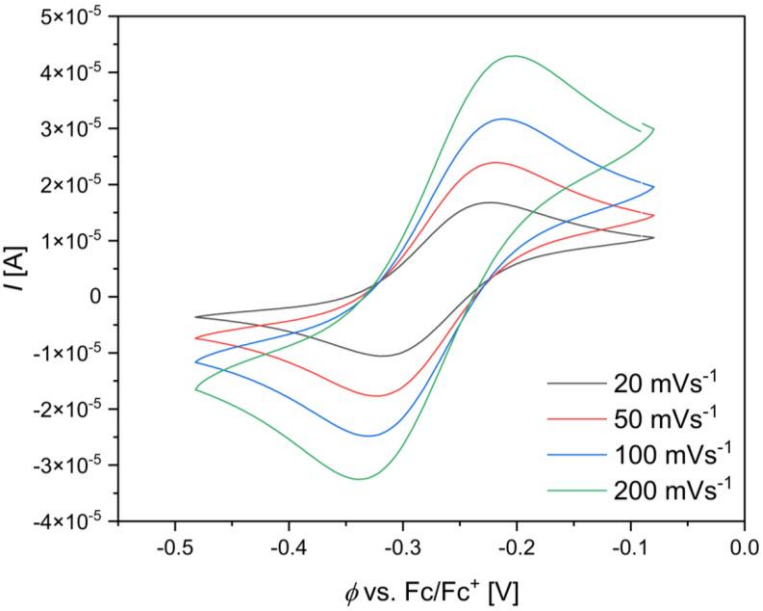

Figure 9.13: Cyclic voltammogram of **R3$_{TMG}$** starting from the corresponding Cu(I) complex **C5$_{TMG}$–PF$_6$** (c = 10^{-3} M) in MeCN with [NBu$_4$][PF$_6$] (c = 0.1 M).

9.2.2 Cyclic Voltammograms of $[Cu(TMG2NMe_2qu)_2]^{+/2+}$ (R4)

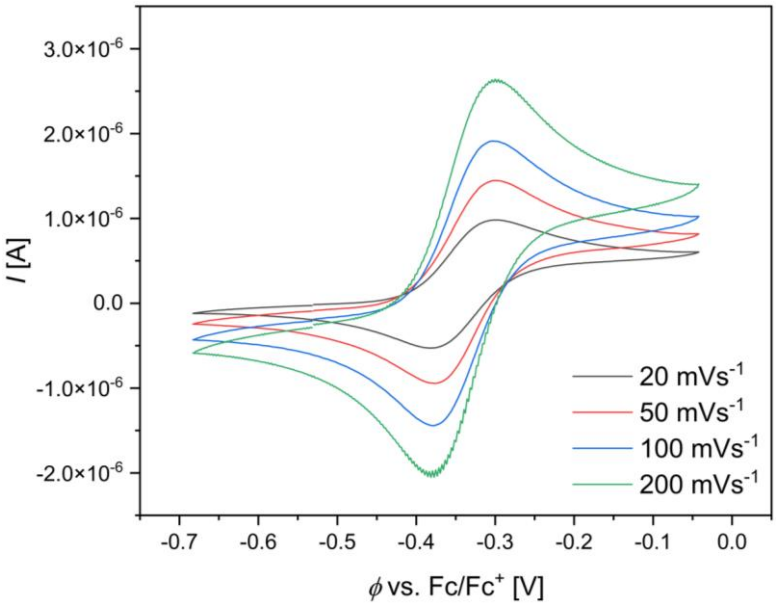

Figure 9.14: Cyclic voltammogram of **R4** starting from the corresponding Cu(I) complex **C7–PF_6** (c = 10^{-3} M) in MeCN with $[NBu_4][PF_6]$ (c = 0.1 M).

9.2.3 Extended Cyclic Voltammogram of $[Cu(TMGqu)_2]PF_6$ in MeCN

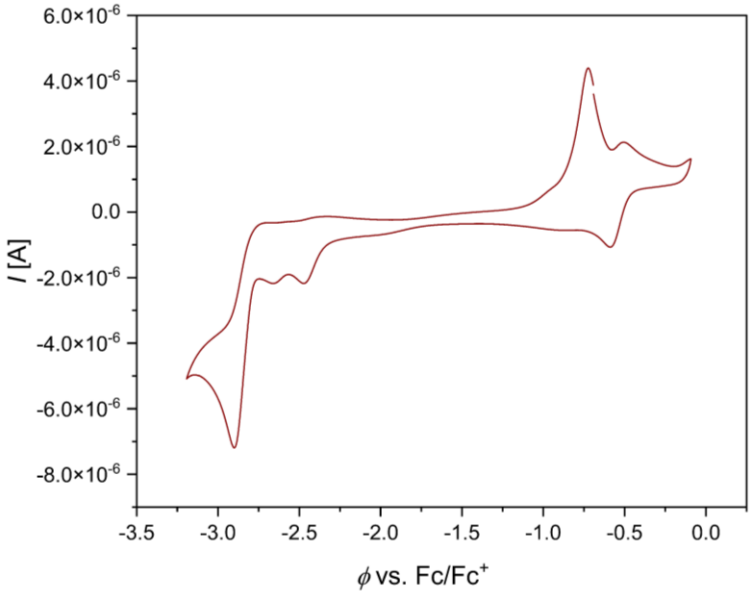

Figure 9.15: Extended cyclic voltammogram of **R6** starting from the corresponding Cu(I) complex **C11–PF_6** (c = 10^{-3} M) in MeCN with $[NBu_4][PF_6]$ (c = 0.1 M) under inert conditions. Scan rate was set to 100 mV s^{-1}.

Table 9-5: Key parameters of the E_{ox} redox waves of **C11–PF$_6$** and **C13–PF$_6$** obtained from the cyclic voltammograms in MeCN.

	E_{ox} *vs.* Fc/Fc$^+$ [V]	ΔE [mV]	I_{red}/I_{ox} [ ]
C11–PF$_6$	-0.44	71	0.99
C13–PF$_6$	-0.22	68	1.03

9.3 Kinetic Plots of Stopped-Flow UV/vis Spectroscopic Measurements

9.3.1 Kinetic Plots of Tripodal Model Systems

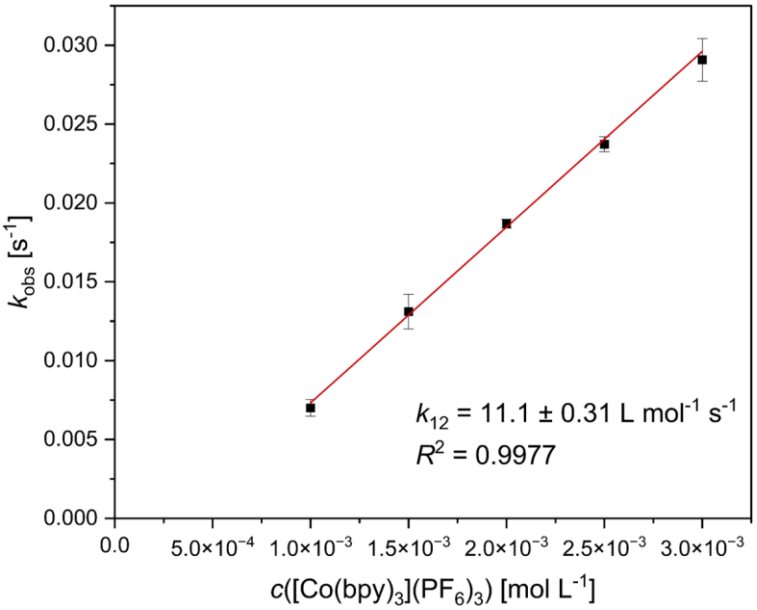

Figure 9.16: Plot of the reaction rate k_{obs} of the cross reaction between **C3$_{TMG}$–PF$_6$** and [Co(bpy)$_3$](PF$_6$)$_3$ in MeCN solution at 298 K against the concentration of [Co(bpy)$_3$](PF$_6$)$_3$ (some error bars are too small to be visualized properly).

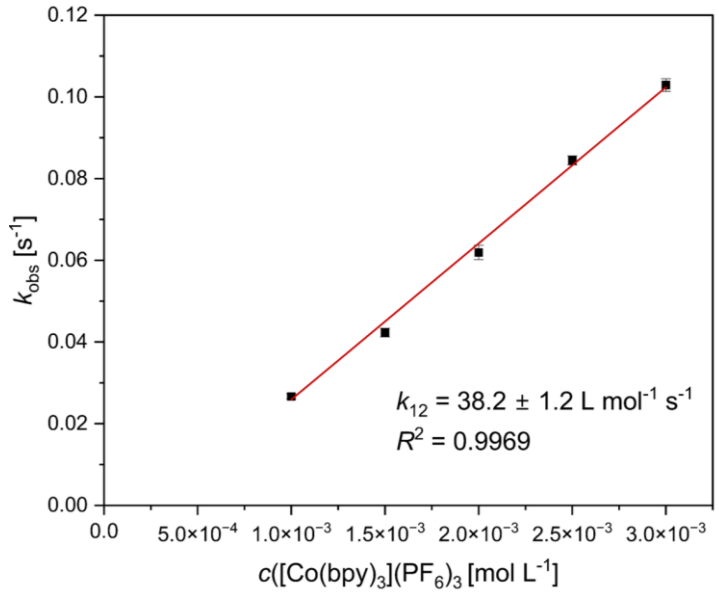

Figure 9.17: Plot of the reaction rate constants k_{obs} of the cross reaction between **C5$_{TMG}$–PF$_6$** and $[Co(bpy)_3](PF_6)_3$ in MeCN solution at 298 K against the concentration of $[Co(bpy)_3](PF_6)_3$ (some error bars are too small to be visualized properly).

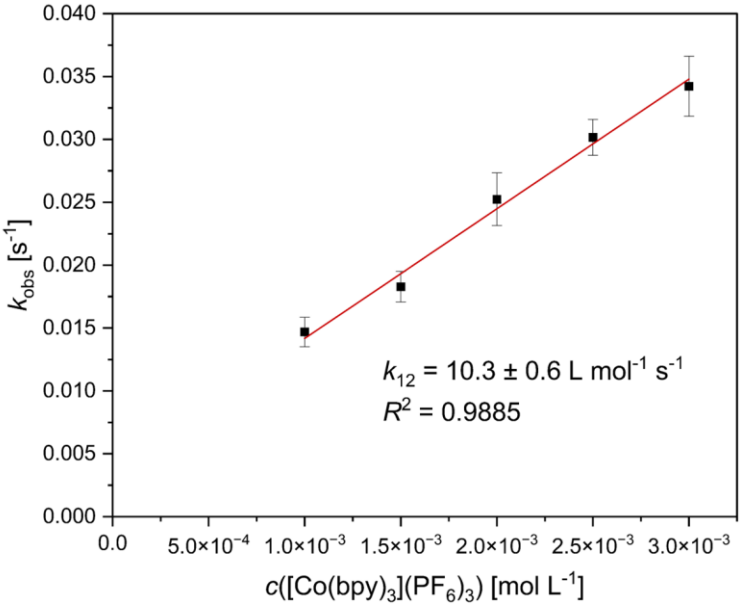

Figure 9.18: Plot of the reaction rate constants k_{obs} of the cross reaction between **C1$_{DMEG}$–PF$_6$** and $[Co(bpy)_3](PF_6)_3$ in MeCN solution at 298 K against the concentration of $[Co(bpy)_3](PF_6)_3$.

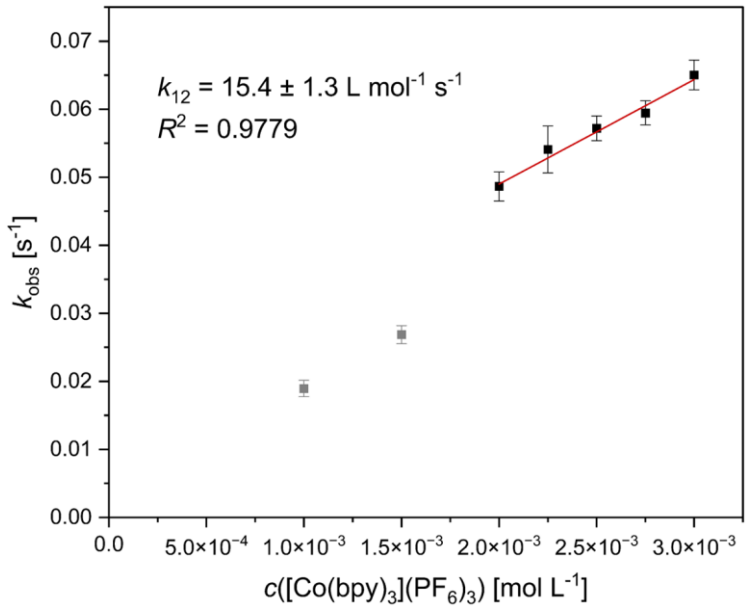

Figure 9.19: Plot of the reaction rate constants k_{obs} of the cross reaction between **C3$_{DMEG}$–PF$_6$** and [Co(bpy)$_3$](PF$_6$)$_3$ in MeCN solution at 298 K against the concentration of [Co(bpy)$_3$](PF$_6$)$_3$. The greyed-out data point are outliers due to interference of the counter complex in the observed wavelength of 400 nm (See Section 7.3.11).

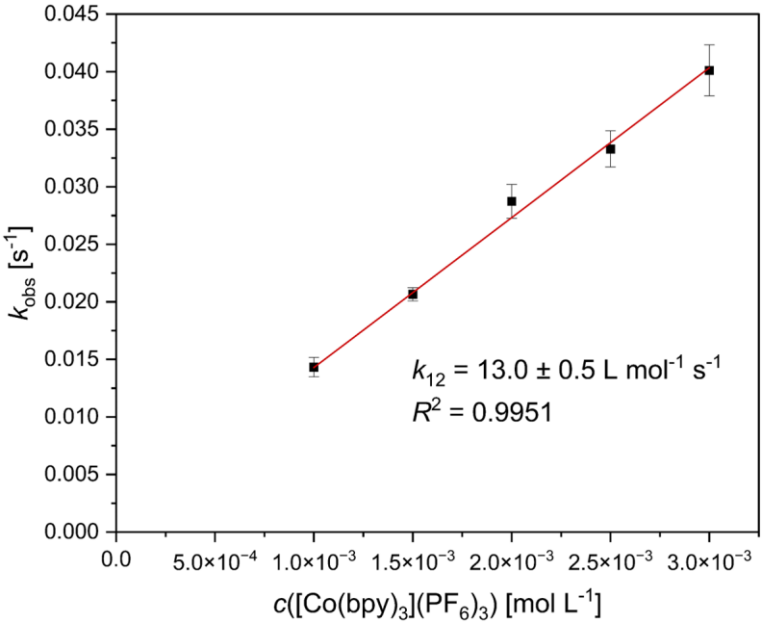

Figure 9.20: Plot of the reaction rate constants k_{obs} of the cross reaction between **C5$_{DMEG}$–PF$_6$** and [Co(bpy)$_3$](PF$_6$)$_3$ in MeCN solution at 298 K against the concentration of [Co(bpy)$_3$](PF$_6$)$_3$ (some error bars are too small to be visualized properly).

9.3.1.1 UV/vis Spectrum of $C2_{DMEG}$ and $[Co(bpy)_3]PF_6$

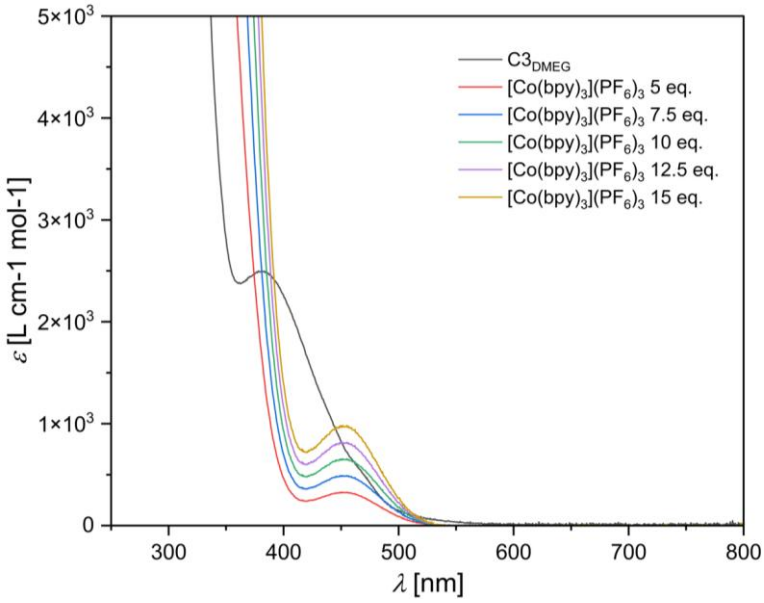

Figure 9.21: UV/Vis-spectra of **$C3_{DMEG}$** with different equivalents of the complex $[Co(bpy)_3](PF_6)_3$. The latter are adjusted to the corresponding equivalents employed in the stopped-flow spectroscopic measurements.

9.3.2 Kinetic Plots of $[Cu(TMG2Phqu)_2]^{+/2+}$

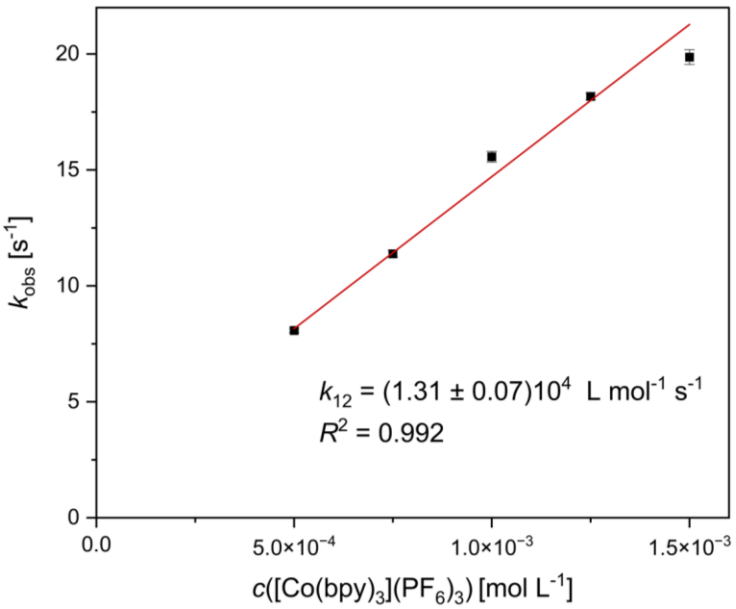

Figure 9.22: Plot of the reaction rate constants k_{obs} of the cross reaction between **C9−PF_6** and $[Co(bpy)_3](PF_6)_3$ in MeCN solution at 298 K against the concentration of $[Co(bpy)_3](PF_6)_3$ (some error bars are too small to be visualized properly).

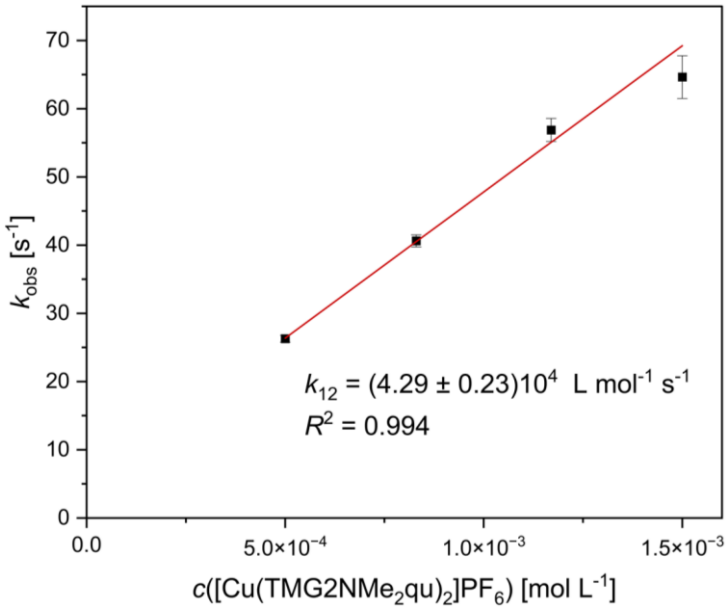

Figure 9.23: Plot of the reaction rate constants k_{obs} of the cross reaction between **C10−OTf** and [Cu(TMG2NMe$_2$qu)$_2$]PF$_6$ in MeCN solution at 298 K against the concentration of [Cu(TMG2NMe$_2$qu)$_2$]PF$_6$ (some error bars are too small to be visualized properly).

9.4 Fluorescence Emission Spectra

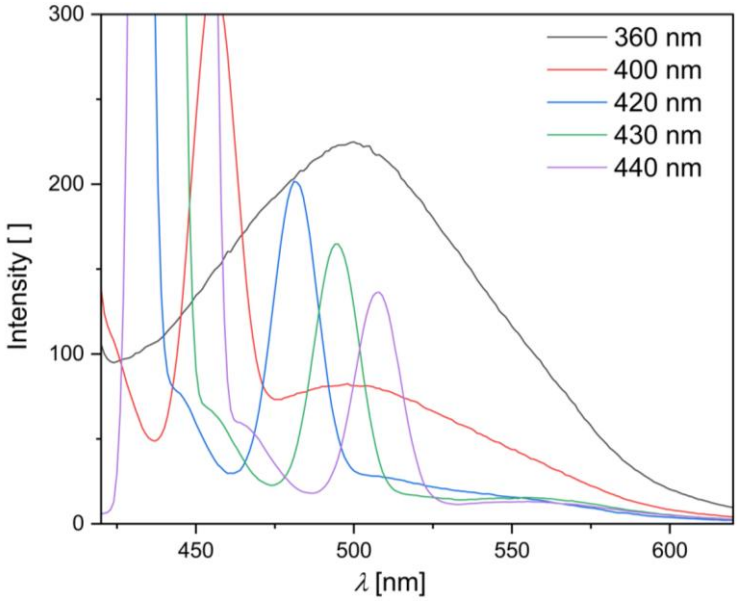

Figure 9.24: Fluorescence emission spectra of [Cu(TMGqu)$_2$]PF$_6$ (**C11–PF$_6$**, c = 10 µmol L^{-1}) in degassed THF for different excitation wavelengths.

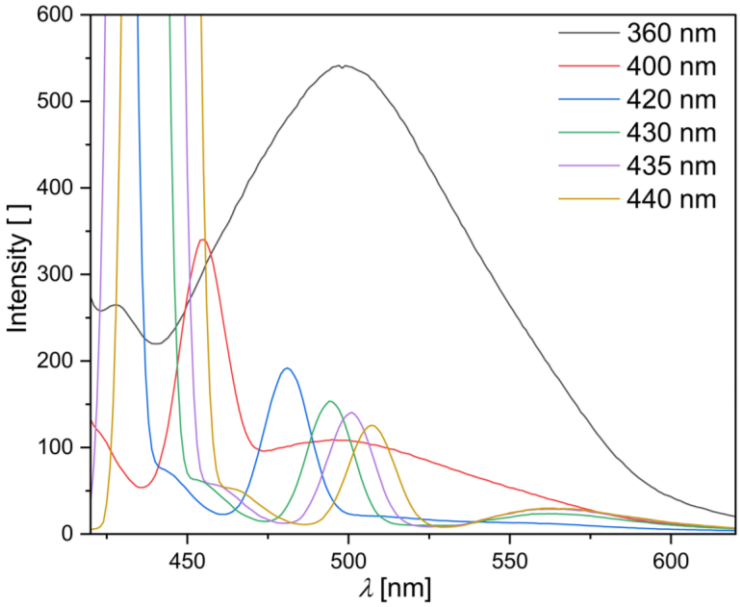

Figure 9.25: Fluorescence emission spectra of $[Cu(TMG2Mequ)_2]PF_6$ (**C13–PF$_6$**, *c* = 10 µmol L^{-1}) in degassed THF for different excitation wavelengths.

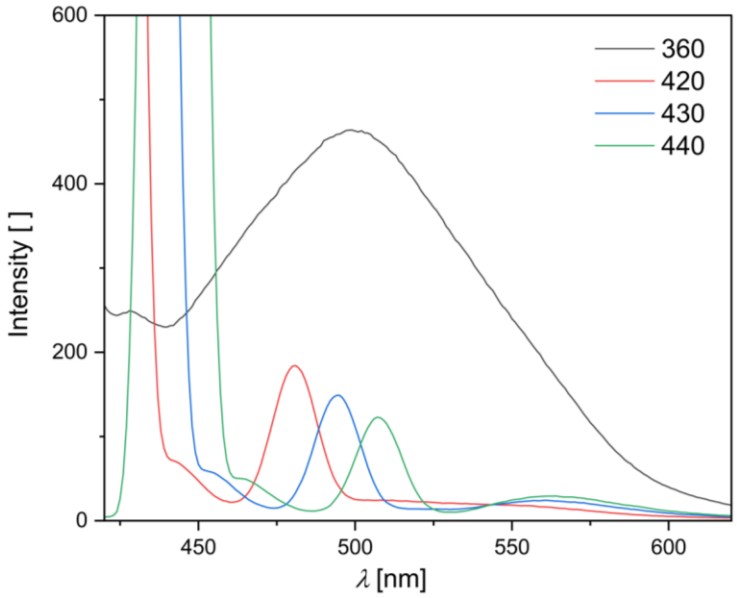

Figure 9.26: Fluorescence emission spectra of $[Cu(TMG2^cHexqu)_2]PF_6$ (**C15–PF$_6$**, *c* = 10 µmol L^{-1}) in degassed THF for different excitation wavelengths.

9.5 XAFS Delay Scans (Measured by Rübhausen Group)

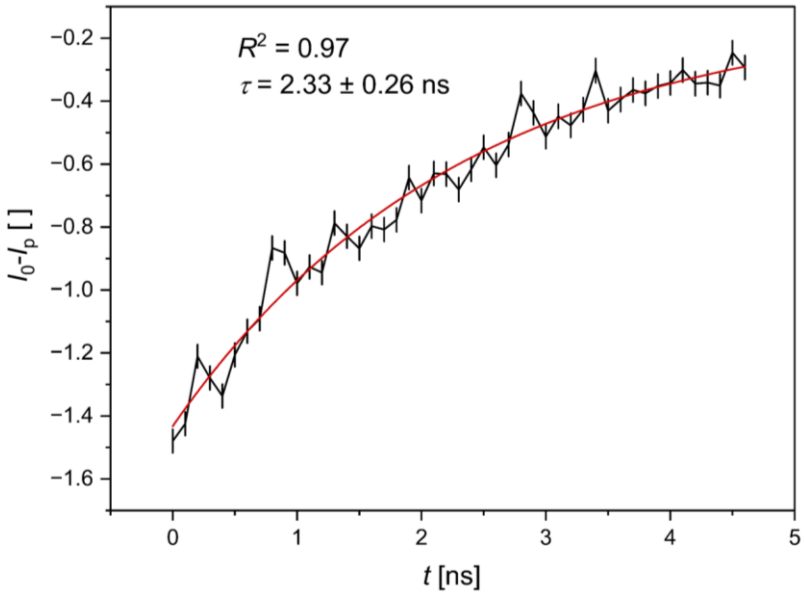

Figure 9.27: Baseline-corrected delay scan of **C13–PF$_6$** after pump at 435 nm at 3 mmol L^{-1} with first-order decay fit and time constant τ.

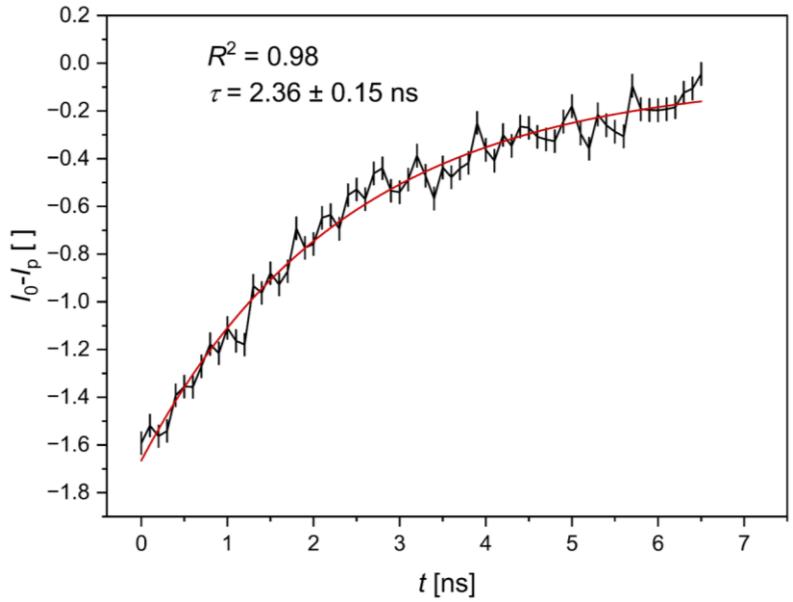

Figure 9.28: Baseline-corrected delay scan of **C13–PF$_6$** after pump at 435 nm at 2 mmol L^{-1} with first-order decay fit and time constant τ.

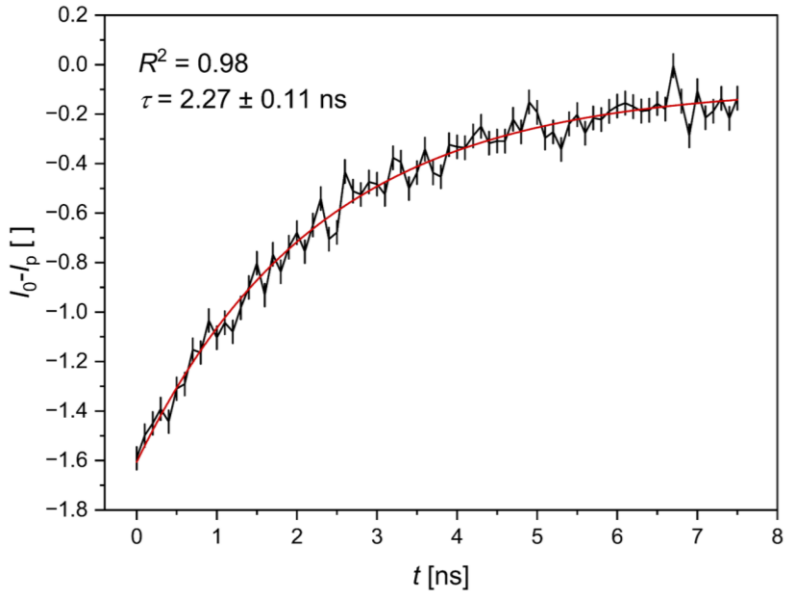

Figure 9.29: Baseline-corrected delay scan of **C13–PF_6** after pump at 435 nm at 1 mmol L^{-1} with first-order decay fit and time constant τ.

9.6 Structural Data of the Computationally Obtained Cu(II) Geometries of Complex Cations C2, C4 and C6.

Table 9-6: Key structural data of the computationally obtained geometries of the $\mathbf{C2_{TMG}}$ and $\mathbf{C2_{DMEG}}$ conformers (TPSSh-D3BJ/def2-TZVP+ PCM(MeCN) // TPSSh-D3BJ/def2-TZVP + PCM(MeCN)).

	$\mathbf{C2_{TMG}}$			$\mathbf{C2_{DMEG}}$		
	Apical A	Apical B	Basal B	Apical A	Apical B	Basal B
			Bond Lengths [Å]			
$Cu–N_{left}(1)$	2.020 (N_{Qu})	2.022 (N_{Qu})	2.125 (N_{Qu})	2.012 (N_{Qu})	2.020 (N_{Qu})	2.090 (N_{Qu})
$Cu–N_{apical}(2)$	2.254 (N_{Am})	2.226 (N_{Am})	2.164 (N_{Qu})	2.236 (N_{Am})	2.234 (N_{Am})	2.173 (N_{Qu})
$Cu–N_{right}(3)$	2.112 (N_{Qu})	2.021 (N_{Gua})	2.009 (N_{Gua})	2.084 (N_{Qu})	2.032 (N_{Gua})	1.998 (N_{Gua})
$Cu–N_{trans}(4)$	2.000 (N_{Gua})	2.045 (N_{Qu})	2.081 (N_{Am})	2.013 (N_{Gua})	2.038 (N_{Qu})	2.085 (N_{Am})
$Cu–N_{MeCN}(5)$	1.971	1.995	1.960	1.971	1.981	1.966
			Bond Angles [°]			
N(1)–Cu–N(2)	81.6	82.4	100.8	82.3	82.2	98.5
N(1)–Cu–N(3)	151.5	157.9	137.2	154.1	157.0	142.9
N(1)–Cu–N(4)	92.5	96.3	77.9	91.3	96.6	78.6
N(2)–Cu–N(3)	75.4	77.9	113.1	75.9	76.9	110.0
N(2)–Cu–N(4)	92.5	81.3	80.6	80.7	81.1	80.9
N(3)–Cu–N(4)	99.8	90.5	82.6	98.7	89.5	82.9
N(5)–Cu–N(1)	92.8	88.4	93.5	93.6	90.6	92.6
N(5)–Cu–N(2)	119.3	109.5	109.8	120.0	112.8	115.2
N(5)–Cu–N(3)	84.1	88.9	98.6	85.4	88.8	96.1
N(5)–Cu–N(4)	160.4	168.8	167.7	159.2	165.2	162.8
			Structural Parameters			
ρ [ ]	0.99	0.99	1.00	0.98	0.97	1.00
τ_5 [ ]	0.15	0.18	0.51	0.09	0.14	0.33

Table 9-7: Key structural data of the computationally obtained geometries of the **$C4_{DMEG}$, $C6_{TMG}$, $C6_{DMEG}$** conformers (TPSSh-D3BJ/def2-TZVP+ PCM(MeCN) // TPSSh-D3BJ/def2-TZVP + PCM(MeCN)).

	$C4_{DMEG}$				**$C6_{TMG}$**	**$C6_{DMEG}$**	
	Apical A	Apical B	Basal A	Basal B	Basal	Apical	Basal
Bond lengths [Å]							
Cu–N_{left}(1)	2.047 (N_{Gua})	2.036 (N_{Gua})	2.041 (N_{Gua})	2.003 (N_{Gua})	2.059 (N_{Gua})	2.010 (N_{Gua})	2.045 (N_{Gua})
Cu–N_{apical}(2)	2.276 (N_{Am})	2.252 (N_{Am})	2.126 (N_{Qu})	2.163 (N_{Gua})	2.153 (N_{Gua})	2.317 (N_{Am})	2.178 (N_{Gua})
Cu–N_{right}(3)	2.011 (N_{Gua})	2.016 (N_{Qu})	2.089 (N_{Gua})	2.081 (N_{Qu})	2.027 (N_{Gua})	2.056 (N_{Gua})	2.019 (N_{Gua})
Cu–N_{trans}(4)	2.060 (N_{Qu})	2.020 (N_{Gua})	2.061 (N_{Am})	2.098 (N_{Am})	2.080 (N_{Am})	2.027 (N_{Gua})	2.072 (N_{Am})
Cu–N_{MeCN}(5)	1.984	1.982	1.969	1.970	1.984	1.998	1.976
Bond Angles [°]							
N(1)–Cu–N(2)	75.5	76.6	117.4	101.1	112.2	80.6	110.5
N(1)–Cu–N(3)	150.6	156.6	126.4	144.1	135.2	149.2	139.6
N(1)–Cu–N(4)	90.2	94.2	82.0	82.9	78.2	97.6	78.8
N(2)–Cu–N(3)	80.9	81.9	108.5	105.0	103.6	74.7	101.4
N(2)–Cu–N(4)	79.0	80.7	81.3	79.5	80.0	77.8	79.5
N(3)–Cu–N(4)	102.4	91.2	78.9	78.1	82.5	94.9	83.4
N(5)–Cu–N(1)	88.5	89.3	99.4	96.3	92.5	89.0	93.6
N(5)–Cu–N(2)	125.7	112.0	105.3	118.6	111.1	118.2	111.6
N(5)–Cu–N(3)	91.2	90.4	93.6	92.5	99.1	86.7	97.3
N(5)–Cu–N(4)	153.8	167.3	171.4	161.5	167.8	163.7	168.4
Structural Parameters							
ρ [ ]	0.97, 1.00	0.97, 0.99	0.99, 0.99	1.00, 0.97	0.99, 0.99, 0.98	0.99, 0.99, 0.97	1.00, 0.97, 1.00
τ_5 [ ]	0.05	0.18	0.75	0.29	0.54	0.24	0.48

9.7 Charge Transfer Energies from the NBO calculations of C2, C4 and C6

Table 9-8: Charge transfer energies E_{CT} for the σ and π contributions of each donor in all conformers of **$C2_{TMG}$** (Population analysis was performed using the NBO 6.0 package, based on the DFT structures calculated with the TPSSh-D3BJ/def2-TZVP+ PCM(MeCN) // TPSSh-D3BJ/def2-TZVP + PCM(MeCN) method).

$C2_{TMG}$						
	Apical A		Apical B		Basal B	
	E_{CT} [kcal mol^{-1}]					
	σ	π	σ	π	σ	π
$N_{basal,left}(1)\rightarrow Cu$	51.8 (N_{Qu})	0.1	56.5 (N_{Qu})	0.8	34.0 (N_{Qu})	0.5
$N_{apical}(2)\rightarrow Cu$	7.8 (N_{Am})	-	7.7 (N_{Am})	-	23.3 (N_{Qu})	0.3
$N_{basal,right}(3)\rightarrow Cu$	43.2 (N_{Qu})	1.1	60.7 (N_{Gua})	-	46.0 (N_{Gua})	12.1
$N_{basal,trans}(4)\rightarrow Cu$	45.4 (N_{Gua})	11.7	46.2 (N_{Qu})	0.3	31.7 (N_{Am})	-
$N_{MeCN}(5)\rightarrow Cu$	53.0	0.4	48.3	1.0	53.7	-
Sum	214.3		221.6		201.6	

Table 9-9: Charge transfer energies E_{CT} for the σ and π contributions of each donor in all conformers of **$C2_{DMEG}$** (Population analysis was performed using the NBO 6.0 package, based on the DFT structures calculated with the TPSSh-D3BJ/def2-TZVP+ PCM(MeCN) // TPSSh-D3BJ/def2-TZVP + PCM(MeCN) method).

$C2_{DMEG}$						
	Apical A		Apical B		Basal B	
	E_{CT} [kcal mol^{-1}]					
	σ	π	σ	π	σ	π
$N_{basal,left}(1)\rightarrow Cu$	55.8 (N_{Qu})	0.1	58.4 (N_{Qu})	-	39.2 (N_{Qu})	0.7
$N_{apical}(2)\rightarrow Cu$	9.0 (N_{Am})	-	8.1 (N_{Am})	-	22.8 (N_{Qu})	0.3
$N_{basal,right}(3)\rightarrow Cu$	45.7 (N_{Qu})	1.7	62.3 (N_{Gua})	0.3	45.4 (N_{Gua})	21
$N_{basal,trans}(4)\rightarrow Cu$	37.1 (N_{Gua})	15.9	48.8 (N_{Qu})	0.3	37.9 (N_{Am})	-
$N_{MeCN}(5)\rightarrow Cu$	53.1	0.3	51.7	0.7	52.4	0.1
Sum	218.8		230.5		220.2	

Table 9-10: Charge transfer energies E_{CT} for the σ and π contributions of each donor in all conformers of **C4$_{DMEG}$** (Population analysis was performed using the NBO 6.0 package, based on the DFT structures calculated with the TPSSh-D3BJ/def2-TZVP+ PCM(MeCN) // TPSSh-D3BJ/def2-TZVP + PCM(MeCN) method).

	C4$_{DMEG}$							
	Apical A		Apical B		Basal A		Basal B	
	E_{CT} [kcal mol^{-1}]							
	σ	π	σ	π	σ	π	σ	π
$N_{basal,left}$(1)→Cu	56.8 (N_{Gua})	1.3	58.4 (N_{Gua})	0.2	35.7 (N_{Gua})	9.0	46.1 (N_{Gua})	19.3
N_{apical}(2)→Cu	8.8 (N_{Am})	-	7.1 (N_{Am})	-	26.5 (N_{Qu})	0.5	22.1 (N_{Gua})	1.0
$N_{basal,right}$(3)→Cu	46.3 (N_{Gua})	26.7	55.2 (N_{Qu})	1.0	26.5 (N_{Gua})	8.5	40.3 (N_{Qu})	0.8
$N_{basal,trans}$(4)→Cu	41.1 (N_{Qu})	0.3	36.8 (N_{Gua})	17.4	45.0 (N_{Am})	-	36.8 (N_{Am})	-
N_{MeCN}(5)→Cu	47.5	0.6	50.8	0.7	53.8	0.4	51.5	0.04
Sum	229.5		227.6		205.8		217.9	

Table 9-11: Charge transfer energies E_{CT} for the σ and π contributions of each donor in all conformers of **C6$_{TMG}$** and **C6$_{DMEG}$** (Population analysis was performed using the NBO 6.0 package, based on the DFT structures calculated with the TPSSh-D3BJ/def2-TZVP+ PCM(MeCN) // TPSSh-D3BJ/def2-TZVP + PCM(MeCN) method).

	C6$_{TMG}$		**C6$_{DMEG}$**			
	Basal		Apical		Basal	
	E_{CT} [kcal mol^{-1}]					
	σ	π	σ	π	σ	π
$N_{basal,left}$(1)→Cu	35.0 (N_{Gua})	7.1	46.5 (N_{Gua})	18.9	33.6 (N_{Gua})	13.5
N_{apical}(2)→Cu	21.3 (N_{Gua})	0.3	5.6 (N_{Am})	-	19.8 (N_{Gua})	1.2
$N_{basal,right}$(3)→Cu	40.7 (N_{Gua})	4.9	50.7 (N_{Gua})	2.4	40.0 (N_{Gua})	12.5
$N_{basal,trans}$(4)→Cu	39.0 (N_{Am})	-	35.6 (N_{Gua})	14.3	41.8 (N_{Am})	-
N_{MeCN}(5)→Cu	47.7	0.3	44.7	1.3	50.8	0.2
Sum	196.2		219.9		213.4	

9.8 Reorganization Energies

9.8.1 Inner Reorganization Energies for R1, R2 and R3

Table 9-12: Single point energies and their differences for the computationally obtained reorganization energies of **R1$_{TMG}$**, **R2$_{TMG}$** and **R3$_{TMG}$** (TPSSh-D3BJ/def2-TZVP+ PCM(MeCN) // TPSSh-D3BJ/def2-TZVP + PCM(MeCN).

	R1$_{TMG}$		**R2$_{TMG}$**		**R3$_{TMG}$**	
	C1$_{TMG}$	**C2$_{TMG}$**	**C3$_{TMG}$**	**C4$_{TMG}$**	**C5$_{TMG}$**	**C6$_{TMG}$**
$E_{Cu(X)L(1)}$ [Hartree]	-3170.35898	-3170.349473	-3322.844607	-3322.836079	-3475.329368	-3475.320234
$E_{Cu(X)L(2)}$ [Hartree]	-3170.168015	-3170.179012	-3322.662494	-3322.672287	-3475.150322	-3475.161893
$\lambda_{11,I,Cu(X)}$ [Hartree]	0.01099665	0.00950682	0.00979263	0.00852852	0.01157031	0.00913409
$\lambda_{11,I}$ [kJ mol^{-1}]	53.8		48.1		54.4	

All Cu(II) geometries are tetracoordinate species ($[Cu(II)(L)]^{2+}$).

Table 9-13: Single point energies and their differences for the computationally obtained reorganization energies of **R1$_{DMEG}$**, **R2$_{DMEG}$** and **R3$_{DMEG}$** (TPSSh-D3BJ/def2-TZVP+ PCM(MeCN) // TPSSh-D3BJ/def2-TZVP + PCM(MeCN).

	R1$_{DMEG}$		**R2$_{DMEG}$**		**R3$_{DMEG}$**	
	C1$_{TMG}$	**C2$_{TMG}$**	**C3$_{TMG}$**	**C4$_{TMG}$**	**C5$_{TMG}$**	**C6$_{TMG}$**
$E_{Cu(X)L(1)}$ [Hartree]	3169.16233	3169.149029	3320.450452	3320.439267	3471.738631	3471.726426
$E_{Cu(X)L(2)}$ [Hartree]	3168.96966	3168.981365	-3320.26432	3320.275529	3471.552714	3471.564994
$\lambda_{11,I,Cu(X)}$ [Hartree]	0.01170535	0.01330478	0.0112089	0.01118408	0.01227963	0.01220513
$\lambda_{11,I}$ [kJ mol^{-1}]	65.7		58.8		64.3	

All Cu(II) geometries are tetracoordinate species ($[Cu(II)(L)]^{2+}$).

9.8.2 Inner Reorganization Energies for R4 and R5

Table 9-14: Single point energies and their differences for the computationally obtained reorganization energies of **R4** for the relaxed and frozen Cu(I) geometry each (TPSSh-D3BJ/def2-TZVP+ PCM(MeCN) // TPSSh-D3BJ/def2-TZVP + PCM(MeCN).

	$R4_{Relaxed}$		**R4***	
	C7	**C8**	**C7***	**C8**
$E_{Cu(X)L(1)}$ [Hartree]	-3436.04884	-3630.313913	-3630.305609	-3630.313913
$E_{Cu(X)L(2)}$ [Hartree]	-3435.88481	-3630.138987	-3630.147258	-3630.138987
$\lambda_{11,I,Cu(X)}$ [Hartree]	0.0085633	0.00827122	0.0083041	0.00827122
$\lambda_{11,I}$ [kJ mol^{-1}]	45.0		68.4	

All Cu(II) geometries are tetracoordinate species ($[Cu(II)(L)]^{2+}$).

Table 9-15: Single point energies and their differences for the computationally obtained reorganization energies of the two most stable conformers of **R5** (TPSSh-D3BJ/def2-TZVP+ PCM(MeCN) // TPSSh-D3BJ/def2-TZVP + PCM(MeCN).

	$R5_{cis-1}$		**$R5_{trans-1}$**	
	$C9_{cis-1}$	**$C10_{cis-1}$**	**$C9_{trans-1}$**	**$C10_{trans-1}$**
$E_{Cu(X)L(1)}$ [Hartree]	-3630.316433	-3630.307391	-3630.313913	-3630.305609
$E_{Cu(X)L(2)}$ [Hartree]	-3630.146666	-3630.154974	-3630.138987	-3630.147258
$\lambda_{11,I,Cu(X)}$ [Hartree]	0.00830754	0.0090421	0.00827122	0.0083041
$\lambda_{11,I}$ [kJ mol^{-1}]	45.6		43.5	

9.9 Transition States of C1, C3 and C5

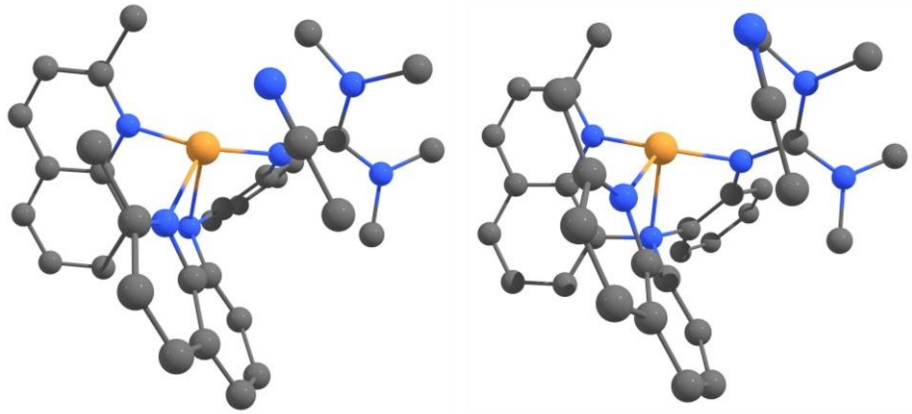

Cu(I)–N_{MeCN} = 2.937 Å Cu(I)–N_{MeCN} = 4.137 Å

Figure 9.30: Transition state geometry of **$C1_{TMG}$** showing the imaginary mode at a displacement scale of 0 (left) and 2 (right) (TPSSh-D3BJ/def2-TZVP+ PCM(MeCN) // TPSSh-D3BJ/def2-TZVP + PCM(MeCN).

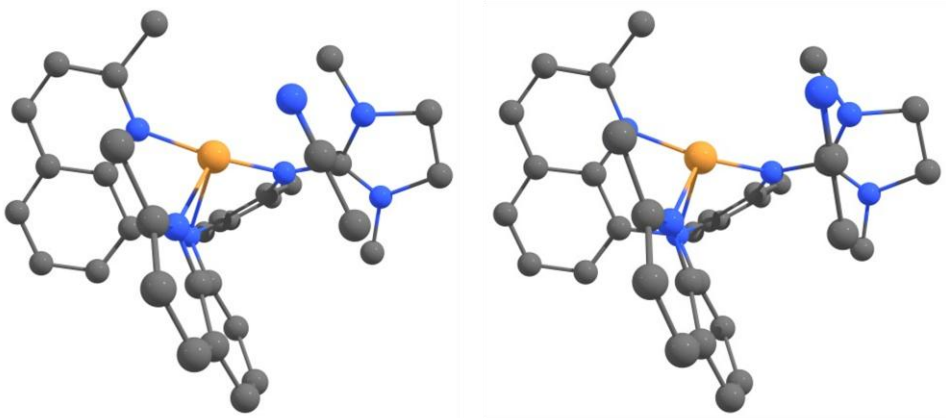

Cu(I)–N_{MeCN} = 3.009 Å Cu(I)–N_{MeCN} = 4.316 Å

Figure 9.31: Transition state geometry of **$C1_{DMEG}$** showing the imaginary mode at a displacement scale of 0 (left) and 2 (right) (TPSSh-D3BJ/def2-TZVP+ PCM(MeCN) // TPSSh-D3BJ/def2-TZVP + PCM(MeCN).

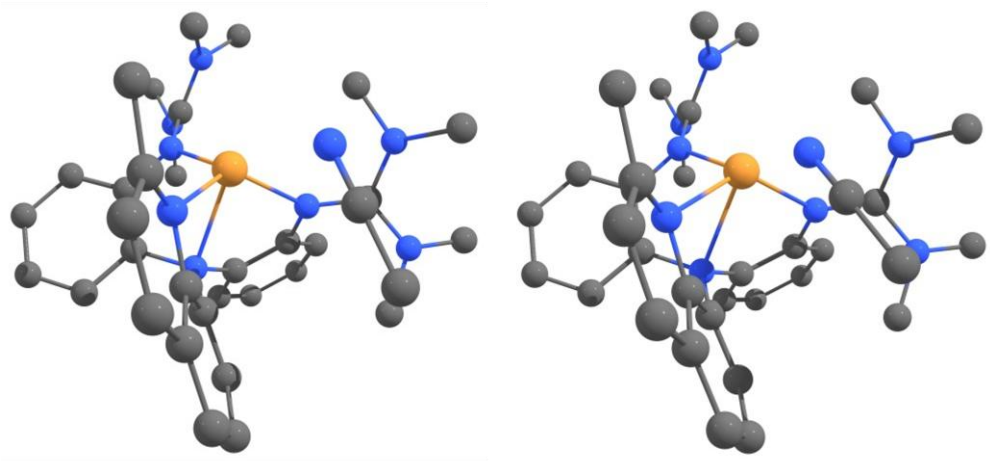

Cu(I)–N_{MeCN} = 2.786 Å Cu(I)–N_{MeCN} = 1.489 Å

Figure 9.32: Transition state geometry of **C3$_{TMG}$** showing the imaginary mode at a displacement scale of 0 (left) and 2 (right) (TPSSh-D3BJ/def2-TZVP+ PCM(MeCN) // TPSSh-D3BJ/def2-TZVP + PCM(MeCN).

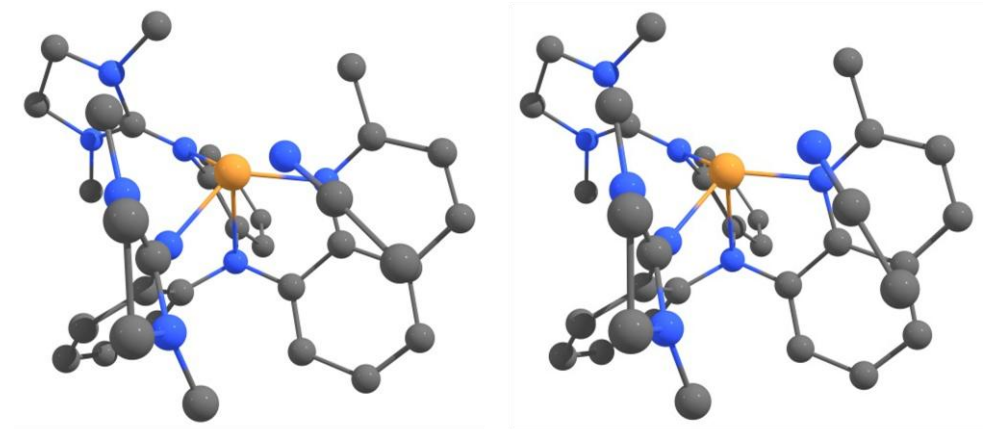

Cu(I)–N_{MeCN} = 2.717 Å Cu(I)–N_{MeCN} = 3.914 Å

Figure 9.33: Transition state geometry of **C3$_{DMEG}$** showing the imaginary mode at a displacement scale of 0 (left) and 2 (right) (TPSSh-D3BJ/def2-TZVP+ PCM(MeCN) // TPSSh-D3BJ/def2-TZVP + PCM(MeCN).

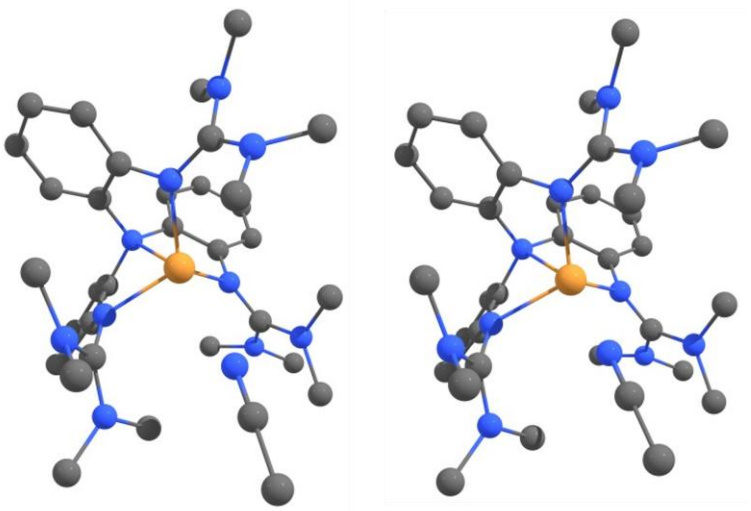

Figure 9.34: Transition state geometry of **C5$_{TMG}$** showing the imaginary mode at a displacement scale of 0 (left) and 2 (right) (TPSSh-D3BJ/def2-TZVP+ PCM(MeCN) // TPSSh-D3BJ/def2-TZVP + PCM(MeCN).

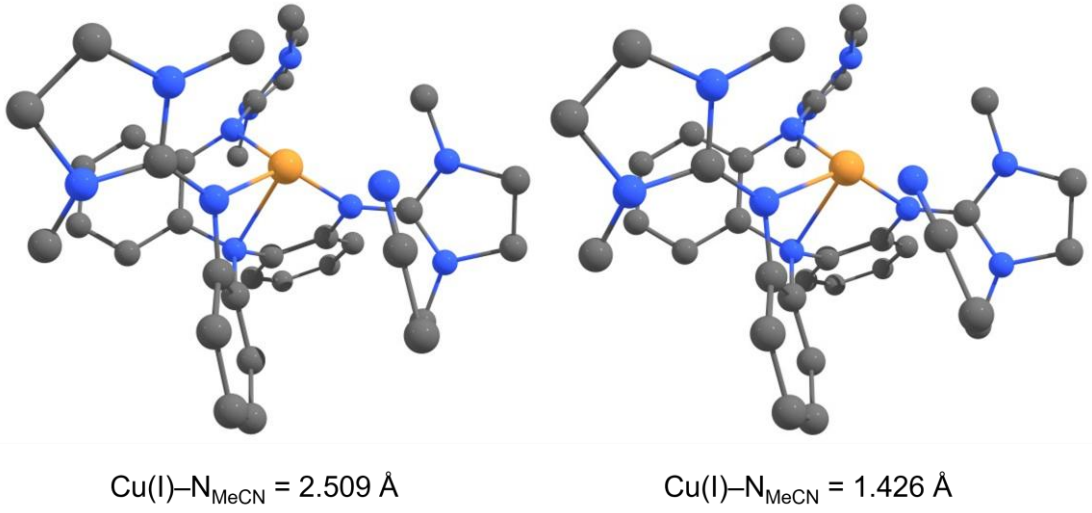

Figure 9.35: Transition state geometry of **C5$_{DMEG}$** showing the imaginary mode at a displacement scale of 0 (left) and 2 (right) (TPSSh-D3BJ/def2-TZVP+ PCM(MeCN) // TPSSh-D3BJ/def2-TZVP + PCM(MeCN).

Table 9-16: Gibbs energies for all computed transition states, the tetracoordinate complex with explicit solvent molecules and the activation barrier for the coordination-change for complex pairs **C1**, **C3**, **C5** (TPSSh-D3BJ/def2-TZVP+ PCM(MeCN) // TPSSh-D3BJ/def2-TZVP + PCM(MeCN).

	$C1_{TMG}$	**$C1_{DMEG}$**	**$C3_{TMG}$**	**$C3_{DMEG}$**	**$C5_{TMG}$**	**$C5_{DMEG}$**
$G_{[Cu(L)] + MeCN}$ [Hartree]	-3302.64876	-3301.47001	-3455.03665	-3452.68285	-3607.42399	-3603.88980
G_{TS} [Hartree]	-3302.63811	-3301.46004	-3455.02679	-3452.67209	-3607.40630	-3603.87920
$\Delta G^{‡}$ [kJ mol^{-1}]	27.98	26.17	25.88	28.26	46.45	27.82

9.10 Used DFT data for C11 to C16

Table 9-17: Structural data taken from literature of **R6** to **R8** used in Section 4.[22]

Redox Couple	**$[Cu(TMGqu)_2]^{+/2+}$ (R6)**		**$[Cu(TMG2Mequ)_2]^{+/2+}$ (R7)**		**$[Cu(TMG^cHexqu)_2]^{+/2+}$ (R8)**	
State	Cu(I)	Cu(II)	Cu(I)	Cu(II)	Cu(I)	Cu(II)
Bond Lengths [Å]						
Cu–N_{Gua}(1/2)	2.066	1.975	2.084	1.987	2.053	1.993
Cu–N_{Gua}(1/2)	1.997	1.979	2.001	1.987	2.035	1.991
Bond Angles [°]						
N_{Gua}(1)–Cu–N_{Gua}(2)	129.3	149.4	124.6	136.2	131.1	124.7
N_{Gua}(1)–Cu–N_{Qu}(2)	114.3	104.6	115.8	107.9	128.0	134.5
N_{Gua}(1)–Cu–N_{Qu}(1)	82.3	83.4	81.9	83.3	81.5	83.0
N_{Gua}(2)–Cu–N_{Qu}(1)	114.3	104.6	115.8	107.9	128.0	134.5
N_{Gua}(2)–Cu–N_{Qu}(2)	82.3	83.4	81.9	83.3	81.5	83.0
N_{Qu}(1)–Cu–N_{Qu}(2)	142.2	150.4	143.1	150.4	111.0	102.8
Structure Parameters						
τ_4 [ ]	0.63	0.43	0.65	0.52	0.72	0.65
$\Delta\tau_4$ [ ]	0.53		0.59		0.68	
$\varnothing\tau_4$ [ ]	0.20		0.13		0.07	
∢ [°]	70.3	46.5	74.4	57.3	81.5	68.2
Δ∢ [°]	23.8		17.1		13.3	
ρ [ ]	0.98	1.00	0.97	1.00	0.97	1.00
RMSD vs. SXCRD [Å]	0.207	0.192	0.194	0.100	0.216	0.229

9.11 Structural Data of the Conformers of C9 and C10 using Method M2

Table 9-18: Key bond lengths, bond angles and structural parameters of the DFT optimized geometries of the conformers of the complex cation $[Cu(TMG2Phqu)_2]^+$ **C9** and $[Cu(TMG2Phqu)_2]^{2+}$ **C10** (MN15/def2-TZVP+ PCM(MeCN) // MN15/def2-TZVP + PCM(MeCN)).

Conformer	**Cis-1**		**Cis-2**		**Cis-3**		**Trans-1**		**Trans-2**		**Trans-3**		**Trans-4**	
Oxidation state	Cu(I)[a]	Cu(II)[a]	Cu(I)[c]	Cu(II)[c,d]	Cu(I)[c]	Cu(II)[c]	Cu(I)[b]	Cu(II)[b]	Cu(I)[c]	Cu(II)[c]	Cu(I)[c]	Cu(II)[c]	Cu(II)[c]	Cu(II)[c,d]
	Bond Lengths [Å]													
$Cu–N_{Gua}(1)$	2.092	1.980	2.086	-	2.061	1.965	2.098	2.022	2.083	1.951	2.048	1.984	2.127	-
$Cu–N_{Gua}(2)$	2.092	1.980	2.067	-	2.061	1.965	2.092	1.988	2.136	2.001	2.117	1.950	2.068	-
$Cu–N_{Qu}(1)$	2.095	1.997	2.106	-	2.165	2.070	2.112	1.970	2.110	2.171	2.141	1.981	2.095	-
$Cu–N_{Qu}(2)$	2.095	1.997	2.124	-	2.165	2.070	2.111	2.009	2.068	1.965	2.058	2.193	2.156	-
	Bond Angles [°]													
$N_{Gua}(1)–Cu–N_{Gua}(2)$	116.8	113.3	122.1	-	126.4	132.8	120.1	123.7	118.6	114.6	122.0	112.2	119.7	-
$N_{Gua}(1)–Cu–N_{Qu}(2)$	138.5	143.6	129.1	-	127.0	118.1	126.8	113.6	143.9	153.5	142.3	112.9	119.0	-
$N_{Gua}(1)–Cu–N_{Qu}(1)$	80.9	83.5	80.3	-	79.5	83.0	79.6	82.5	80.2	80.9	80.0	83.5	79.8	-
$N_{Gua}(2)–Cu–N_{Qu}(1)$	138.5	143.6	135.7	-	127.0	118.1	111.3	105.5	106.7	103.7	102.4	146.5	134.5	-
$N_{Gua}(2)–Cu–N_{Qu}(2)$	80.9	83.5	80.0	-	79.5	83.0	80.8	83.3	80.5	83.4	81.4	80.0	79.5	-
$N_{Qu}(1)–Cu–N_{Qu}(2)$	111.3	102.0	117.1	-	124.6	128.5	142.0	153.8	126.2	115.0	127.1	122.3	129.5	-
	Structure Parameters													
τ_4 [ ]	0.59	0.52	0.68	-	0.75	0.70	0.65	0.59	0.64	0.65	0.64	0.65	0.68	-
$\Delta\tau_4$ [ ]	0.07		-		0.05		0.06		-0.01		-0.01		-	
$\varnothing\tau_4$ [ ]	0.56		-		0.73		0.62		0.65		0.65		-	
RMSD [Å]	0.293		-		0.381		0.281		0.163		0.629		-	
RMSD vs. SCXRD [Å]	-	0.464	-	-	-	-	0.231	-	-	-	-	-	-	-

a: Optimized beginning from **C9–PF_6·DCM**; b: Optimized from **C10–PF_6·H_2O**; c: Optimized starting from geometry obtained via CREST; d: Geometry always interconverted into cis-1 upon optimization. e: Geometry always interconverted into trans-3 upon optimization.

9.12 Boltzmann Distributions for the Conformational Isomers of C9 and C10

Table 9-19: Energies, Boltzmann factors and probabilities of the conformers of **C9** and **C10** using method **M1** (TPSSh-D3BJ/def2-TZVP+ PCM(MeCN) // TPSSh-D3BJ/def2-TZVP + PCM(MeCN).

TPSSh

Cu(I)	*E* [Hartree]	*G* [Hartree]	ΔE [kJ/mol]	ΔG [kJ/mol]	Boltzman Factors [ ]	Probability [%]
Cis-1	-3630.31643	-3629.62252	0	0	1	7.52
Cis-2	-3630.31054	-3629.62014	15.4710213	6.240813501	0.080659733	0.61
Cis-3	-3630.31136	-3629.62157	13.3140943	2.488974001	0.366395913	2.76
Trans-1	-3630.31391	-3629.62482	6.61749399	-6.05177750	11.48750061	86.39
Trans-2	-3630.30909	-3629.61967	19.2856628	7.474798501	0.049031136	0.37
Trans-3	-3630.31056	-3629.62003	15.4105035	6.52436750	0.071941629	0.54
Trans-4	-3630.31139	-3629.62118	13.2375084	3.51554450	0.24216047	1.82
						$\Sigma = 100.00$
CuII	*E* [Hartree]	*G* [Hartree]	ΔE [kJ/mol]	ΔG [kJ/mol]	Boltzman Factors [ ]	Probability [%]
Cis-1	-3630.15497	-3629.45682	0	0	1	99.63
Cis-2	-	-	-	-	-	-
Cis-3	-3630.14454	-3629.44859	27.3953859	21.623618	0.000162819	0.02
Trans-1	-3630.14726	-3629.45148	20.2577541	14.0175445	0.003501325	0.35
Trans-2	-3630.13991	-3629.44436	39.5602989	32.7058535	1.86287E-06	0.00
Trans-3	-3630.1435	-3629.44632	30.1273237	27.562499	1.4834E-05	0.00
Trans-4	-3630.14206	-3629.44651	33.9136623	27.0662795	1.81215E-05	0.00
						$\Sigma = 100.00$

Table 9-20: Energies, Boltzmann factors and probabilities of the conformers of **C9** and **C10** using method **M2** (MN15/def2-TZVP+ PCM(MeCN) // MN15/def2-TZVP + PCM(MeCN)).

			MN15			
Cu(I)	*E* [Hartree]	*G* [Hartree]	ΔE [kJ/mol]	ΔG [kJ/mol]	Boltzman Factors [ ]	Probability [%]
Cis-1	-3627.83826	-3627.13774	0.00	0.00	1	58.51
Cis-2	-3627.83289	-3627.13610	14.09	4.28	0.177554921	10.39
Cis-3	-3627.83224	-3627.13456	15.81	8.34	0.034568666	2.02
Trans-1	-3627.8339	-3627.13662	11.43	2.92	0.307975322	18.02
Trans-2	-3627.83203	-3627.13527	16.35	6.46	0.073793735	4.32
Trans-3	-3627.83206	-3627.13544	16.28	6.04	0.087606082	5.13
Trans-4	-3627.83004	-3627.13434	21.59	8.90	0.027558116	1.61
						$\Sigma = 100.00$
CuII	*E* [Hartree]	*G* [Hartree]	ΔE [kJ/mol]	ΔG [kJ/mol]	Boltzman Factors [ ]	Probability [%]
Cis-1	-3627.65539	-3626.95027	0.00	0.00	1	100.00
Cis-2	-	-	-	-	-	-
Cis-3	-3627.63743	-3626.93639	47.17	36.43	4.14027E-07	0.00
Trans-1	-3627.64360	-3626.94037	30.95	25.98	2.80944E-05	0.00
Trans-2	-3627.63817	-3626.93496	45.22	40.18	9.15323E-08	0.00
Trans-3	-3627.64143	-3626.93375	36.66	43.35	2.54105E-08	0.00
Trans-4	-	-	-	-	-	-
						$\Sigma = 100.00$

9.13 TD-DFT Transitions of $C10_{cis-1}$

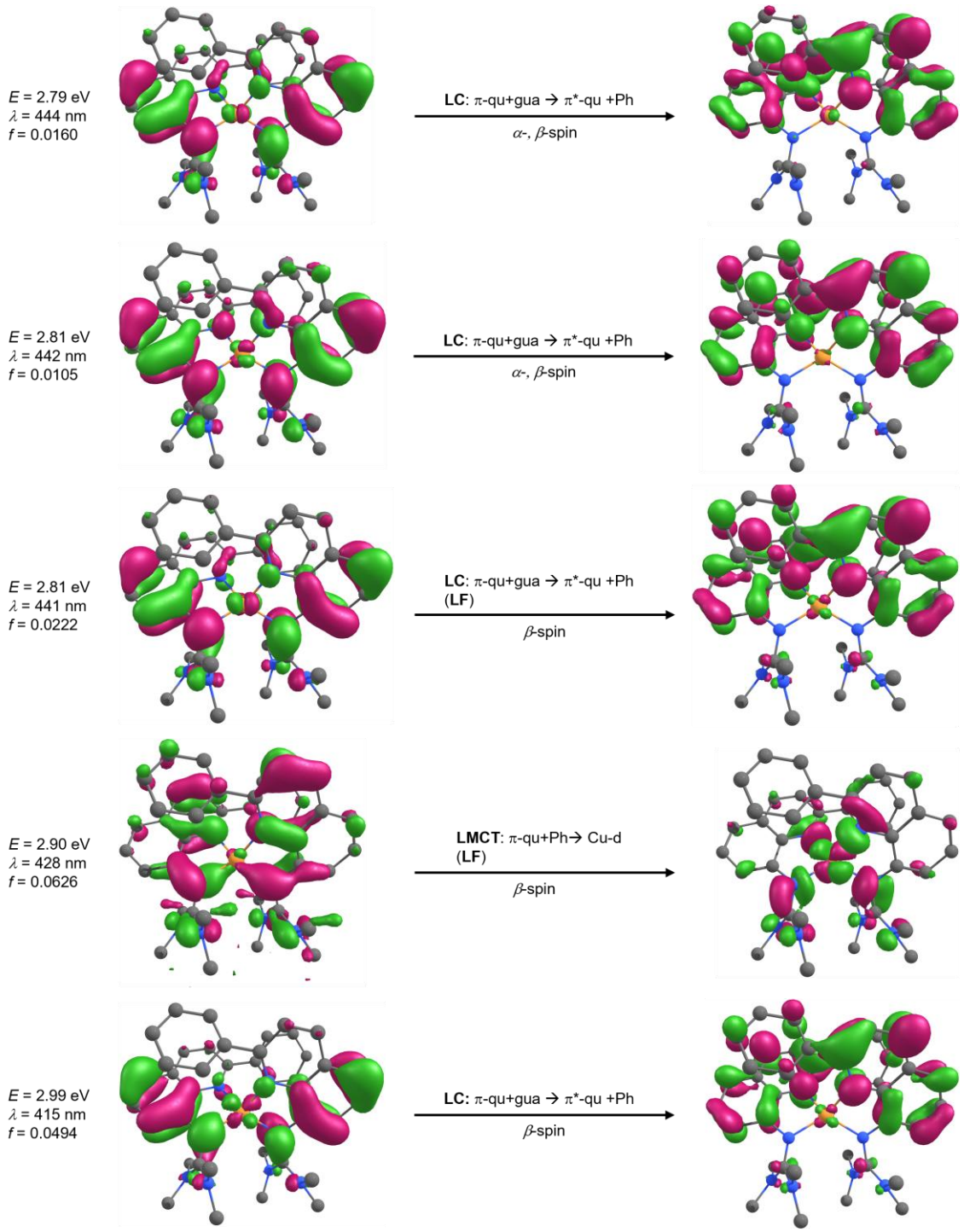

Figure 9.36: NTOs of the dominant transitions of the cis-1 conformer of $[Cu(TMG2Phqu)_2]^{2+}$ (**$C10_{cis-1}$**) causing the characteristic transitions at 328 to 378 nm (DFT: 430 nm) (TPSSh-D3BJ/def2-TZVP+ PCM(MeCN) // TPSSh-D3BJ/def2-TZVP + PCM(MeCN)).

9.14 Attempted Exciplex Computation of P2 and P3

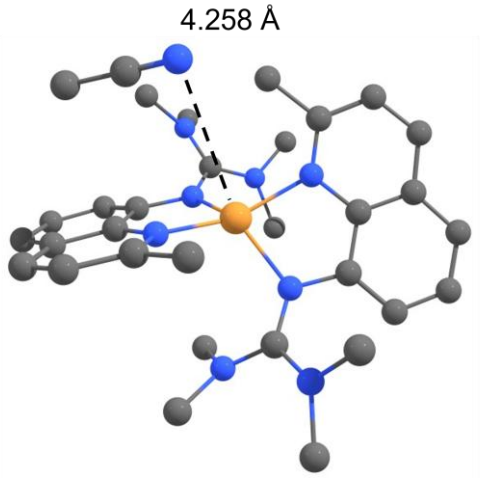

τ_4 „exciplex“ = 0.53 τ_4 triplet state= 0.54

Figure 9.37: Geometry and τ_4 parameter of the attempted exciplex computation of **C13** (TPSSh-D3BJ/def2-TZVP+ PCM(MeCN) // TPSSh-D3BJ/def2-TZVP + PCM(MeCN)).

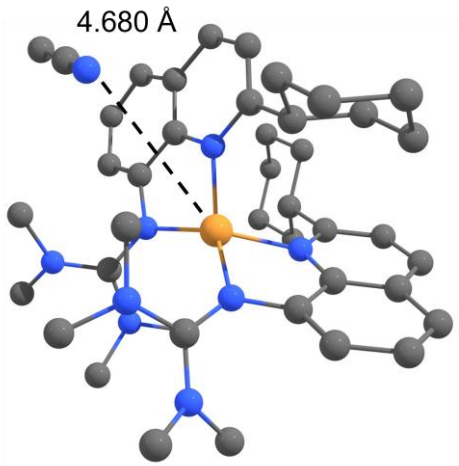

τ_4 „exciplex“ = 0.62 τ_4 triplet state= 0.65

Figure 9.38: Geometry and τ_4 parameter of the attempted exciplex computation of **C15** (TPSSh-D3BJ/def2-TZVP+ PCM(MeCN) // TPSSh-D3BJ/def2-TZVP + PCM(MeCN)).

9.15 Coordinates of Further Cu(I) and Cu(II) Structures of Tripodal Ligands

9.15.1 [Cu(I)L] + S Geometries

[Cu(I)(TMG$_3$trphen)]$^+$ (C5$_{TMG}$) + MeCN

Cu	-0.210323000	0.011878000	0.707563000
N	-0.455460000	-0.054486000	-1.604571000
C	-1.513990000	0.897724000	-1.767088000
C	-2.433366000	1.058309000	-0.708425000
C	-3.484888000	1.970160000	-0.883203000
H	-4.185697000	2.121612000	-0.070087000
C	-3.608673000	2.707106000	-2.054152000
H	-4.424777000	3.413516000	-2.155176000
C	-2.677508000	2.561775000	-3.081501000
H	-2.763045000	3.145737000	-3.989873000
C	-1.634878000	1.654234000	-2.929875000
H	-0.898569000	1.524137000	-3.714610000
N	-2.196156000	0.412347000	0.509322000
C	-3.204584000	-0.036412000	1.237461000
N	-4.336830000	-0.581435000	0.707583000
C	-4.330993000	-1.190620000	-0.611432000
H	-3.315753000	-1.476419000	-0.875871000
H	-4.720286000	-0.510315000	-1.376104000
H	-4.958159000	-2.084950000	-0.581868000
C	-5.649489000	-0.385387000	1.308418000
H	-5.561583000	0.253483000	2.183815000
H	-6.101140000	-1.338277000	1.598399000
H	-6.304697000	0.103369000	0.580336000
N	-3.116784000	-0.003439000	2.593624000
C	-2.228782000	0.940453000	3.246390000
H	-2.017022000	1.763041000	2.568341000
H	-1.285615000	0.465709000	3.537742000
H	-2.714824000	1.320584000	4.148398000
C	-3.638209000	-1.072592000	3.435039000
H	-4.051434000	-1.860744000	2.810405000
H	-4.411814000	-0.704547000	4.114264000
H	-2.821156000	-1.488223000	4.032161000
C	0.856266000	0.362403000	-1.994682000
C	1.553390000	1.243062000	-1.138017000
C	2.815501000	1.697205000	-1.546239000
H	3.369487000	2.360995000	-0.893269000
C	3.381073000	1.265963000	-2.740046000
H	4.365840000	1.621560000	-3.021184000
C	2.705571000	0.357940000	-3.553704000
H	3.152257000	0.005458000	-4.475475000
C	1.441966000	-0.084701000	-3.176061000
H	0.892991000	-0.781699000	-3.798591000
N	1.021526000	1.522001000	0.125270000
C	1.188370000	2.707498000	0.685000000
N	1.229558000	3.880799000	-0.010157000
C	0.580417000	4.016908000	-1.302274000
H	-0.173508000	3.241547000	-1.414921000
H	1.296181000	3.940479000	-2.127503000
H	0.095181000	4.995347000	-1.345048000
C	2.090402000	4.987079000	0.386250000
H	2.676824000	4.702220000	1.256438000
H	1.507155000	5.882645000	0.618948000
H	2.772502000	5.220620000	-0.437514000
N	1.292290000	2.792976000	2.038009000
C	1.661309000	1.614550000	2.800946000
H	2.382259000	1.026287000	2.240459000
H	0.786181000	0.991660000	3.024002000
H	2.109555000	1.936722000	3.742431000
C	0.669241000	3.874245000	2.793441000
H	0.154512000	4.547523000	2.112415000
H	1.411573000	4.435622000	3.366396000
H	-0.061854000	3.453389000	3.489690000
C	-0.798045000	-1.432376000	-1.789018000
C	-0.333795000	-2.365557000	-0.838471000
C	-0.673111000	-3.714606000	-1.017514000
H	-0.344862000	-4.438686000	-0.280502000
C	-1.452145000	-4.120828000	-2.093236000
H	-1.708305000	-5.168763000	-2.199776000
C	-1.922600000	-3.187596000	-3.016038000
H	-2.540376000	-3.499716000	-3.849332000
C	-1.591301000	-1.846802000	-2.856132000
H	-1.952123000	-1.102779000	-3.556675000
N	0.329834000	-1.904146000	0.303084000
C	1.313285000	-2.600049000	0.844057000
N	2.208269000	-3.343226000	0.132024000
C	2.462084000	-3.078612000	-1.274013000
H	2.189408000	-2.052072000	-1.508721000
H	1.895442000	-3.753411000	-1.923647000
H	3.527929000	-3.220608000	-1.466051000
C	2.778969000	-4.579615000	0.651631000
H	2.358755000	-4.794393000	1.631037000
H	3.867738000	-4.511231000	0.730777000
H	2.530183000	-5.400378000	-0.028285000
N	1.476382000	-2.563775000	2.195682000
C	0.352213000	-2.162906000	3.022789000
H	-0.566774000	-2.585941000	2.623274000
H	0.244423000	-1.070852000	3.059725000
H	0.517981000	-2.533996000	4.035243000
C	2.793793000	-2.452479000	2.812869000
H	3.563286000	-2.534492000	2.050388000
H	2.941594000	-3.235899000	3.559750000
H	2.888979000	-1.478210000	3.301678000
C	5.128344000	0.182429000	0.759049000
N	4.998631000	0.936208000	1.624051000
C	5.291470000	-0.762965000	-0.331630000
H	6.223489000	-0.557764000	-0.859964000
H	4.458358000	-0.659651000	-1.027259000
H	5.319998000	-1.780123000	0.060469000

E(RTPSSh) = -3608.16010812
Zero-point correction = 0.827088 (Hartree/Particle)
Thermal correction to Energy = 0.880738
Thermal correction to Enthalpy = 0.881682
Thermal correction to Gibbs Free Energy = 0.736117

[Cu(I)(DMEG$_3$trphen)]$^+$ (C5$_{DMEG}$) + MeCN

Cu	0.073421000	-0.025805000	0.705963000

Cu 0.073421000 -0.025805000 0.705963000

N	0.530112000	0.172449000	-1.596182000
N	-1.611469000	0.860828000	-0.021977000
N	-2.268833000	2.155688000	1.816704000
N	-2.901555000	2.894414000	-0.194846000
C	-0.781385000	-0.110876000	-2.072906000
C	-0.997709000	-0.822038000	-3.249444000
H	-0.140940000	-1.176180000	-3.810760000
C	-2.291491000	-1.065325000	-3.698236000
H	-2.452091000	-1.619565000	-4.615064000
C	-3.373566000	-0.576279000	-2.968559000
H	-4.386490000	-0.749754000	-3.313129000
C	-3.166249000	0.118117000	-1.782503000
H	-4.010321000	0.474171000	-1.204673000
C	-1.871335000	0.343506000	-1.299662000
C	-2.234455000	1.901673000	0.474856000
C	-2.083860000	1.132939000	2.823651000
H	-1.593862000	1.564871000	3.696648000
H	-1.450928000	0.341539000	2.413964000
H	-3.041479000	0.698128000	3.128886000
C	-3.196364000	3.249876000	2.097343000
H	-2.819289000	3.887714000	2.896416000
H	-4.170284000	2.843290000	2.392779000
C	-3.263945000	3.957766000	0.750980000
H	-4.252147000	4.357035000	0.525168000
H	-2.528999000	4.768830000	0.687423000
C	-2.515402000	3.346088000	-1.525549000
H	-3.351252000	3.898639000	-1.955631000
H	-2.288279000	2.500761000	-2.166720000
H	-1.639102000	4.001005000	-1.471866000
N	0.502737000	-1.940315000	0.190952000
N	-0.709867000	-3.165938000	1.779304000
N	-0.395216000	-4.144236000	-0.205786000
C	1.530331000	-0.838694000	-1.707147000
C	2.564244000	-0.735645000	-2.633531000
H	2.596199000	0.131392000	-3.283055000
C	3.536541000	-1.725033000	-2.721704000
H	4.336806000	-1.637728000	-3.446527000
C	3.470162000	-2.826265000	-1.868975000
H	4.225811000	-3.601635000	-1.921363000
C	2.450288000	-2.929936000	-0.931659000
H	2.417545000	-3.772689000	-0.251141000
C	1.462180000	-1.941044000	-0.829931000
C	-0.143469000	-3.025307000	0.544247000
C	-0.243996000	-2.422675000	2.931479000
H	-1.056760000	-2.326364000	3.651497000
H	0.063961000	-1.427589000	2.604304000
H	0.610191000	-2.915572000	3.409757000
C	-1.169339000	-4.541605000	1.963887000
H	-2.103638000	-4.573181000	2.523928000
H	-0.411271000	-5.118329000	2.506883000
C	-1.319178000	-5.020675000	0.525328000
H	-1.048685000	-6.067531000	0.392103000
H	-2.339874000	-4.868607000	0.155726000
C	-0.578441000	-4.090931000	-1.650825000
H	-0.495404000	-5.104261000	-2.043940000
H	0.187237000	-3.473935000	-2.110331000
H	-1.565223000	-3.686454000	-1.901734000
N	1.719242000	1.203118000	0.667357000
N	2.791157000	0.618390000	2.664344000
N	4.112686000	1.283236000	0.986105000
C	0.959966000	1.533708000	-1.605100000
C	0.708480000	2.371020000	-2.687942000
H	0.170705000	1.973995000	-3.541153000
C	1.142458000	3.692024000	-2.673512000
H	0.944102000	4.337661000	-3.520466000
C	1.836273000	4.173717000	-1.564153000
H	2.177613000	5.202252000	-1.540583000
C	2.076308000	3.348811000	-0.471902000
H	2.587369000	3.732968000	0.403365000
C	1.638243000	2.018342000	-0.467440000
C	2.814752000	1.064180000	1.369754000
C	1.634297000	0.820036000	3.513144000
H	1.622876000	0.062369000	4.296531000
H	0.733349000	0.724497000	2.906356000
H	1.644511000	1.815897000	3.972284000
C	4.119147000	0.758611000	3.259942000
H	4.337068000	-0.068835000	3.934525000
H	4.180162000	1.699735000	3.820058000
C	5.014368000	0.778840000	2.029344000
H	5.882660000	1.427652000	2.139273000
H	5.354015000	-0.229703000	1.764683000
C	4.572125000	1.105697000	-0.385133000
H	5.541684000	1.594217000	-0.485697000
H	3.877166000	1.561073000	-1.083509000
H	4.677018000	0.042456000	-0.625216000
C	-4.700076000	-0.627107000	1.209013000
N	-5.436853000	0.256265000	1.313584000
C	-3.755276000	-1.722599000	1.079704000
H	-2.767411000	-1.320947000	0.847734000
H	-4.068063000	-2.389615000	0.275818000
H	-3.708209000	-2.280121000	2.015453000

E(RTPSSh) = -3604.57184464
Zero-point correction = 0.766340 (Hartree/Particle)
Thermal correction to Energy = 0.814824
Thermal correction to Enthalpy = 0.815768
Thermal correction to Gibbs Free Energy = 0.682048

$[Cu(I)\{N(QuMe)(PhTMG)_2\}]^+$ ($C3_{TMG}$) + MeCN

N	0.070166000	0.374702000	1.447526000
C	0.882581000	-1.894156000	1.100178000
N	1.035396000	1.663111000	-0.849719000
N	-1.964885000	-0.256603000	-0.316591000
C	0.573742000	-3.578010000	2.820921000
H	0.705889000	-4.600093000	3.156872000
N	1.223275000	-1.502294000	-0.198173000
C	-0.090697000	-2.657193000	3.629528000
H	-0.473953000	-2.951738000	4.598866000
N	-2.898010000	-1.462523000	-2.058903000
C	-0.258879000	-1.351530000	3.180663000
H	-0.777456000	-0.620622000	3.790264000
N	-3.683443000	-1.832576000	0.091473000
C	0.228548000	-0.965799000	1.935445000
N	3.502804000	-2.154673000	-0.076287000
C	2.351411000	-1.889628000	-0.759387000
N	2.404308000	-2.007511000	-2.115813000
C	1.162436000	-2.091054000	-2.861986000
H	0.732241000	-1.094692000	-3.036939000
H	1.365486000	-2.556526000	-3.827765000
H	0.442069000	-2.690436000	-2.310193000
C	3.563591000	-1.547363000	-2.874974000
H	3.274830000	-0.694489000	-3.496813000
H	4.346877000	-1.229058000	-2.192052000

H	3.946429000	-2.339440000	-3.522626000
C	3.787953000	-1.536380000	1.207113000
H	4.839392000	-1.238148000	1.221419000
H	3.169573000	-0.651082000	1.332206000
H	3.602362000	-2.221417000	2.040581000
C	4.426513000	-3.201852000	-0.491912000
H	5.412610000	-2.792001000	-0.728914000
H	4.537417000	-3.923984000	0.323272000
H	4.030107000	-3.714762000	-1.364795000
C	0.743959000	2.003298000	-3.226226000
H	-0.164593000	1.429486000	-3.036539000
H	0.490976000	2.910030000	-3.779286000
H	1.408971000	1.407721000	-3.858647000
Cu	-0.049486000	-0.006740000	-0.829485000
C	1.416151000	2.334694000	-1.931823000
C	2.441582000	3.306533000	-1.882418000
H	2.703355000	3.839589000	-2.787679000
C	3.107567000	3.535963000	-0.710004000
H	3.919713000	4.251909000	-0.659076000
C	2.734895000	2.826088000	0.456340000
C	3.412366000	2.976399000	1.687870000
H	4.243673000	3.669437000	1.745766000
C	3.029083000	2.240529000	2.782462000
H	3.558231000	2.338799000	3.722262000
C	1.925752000	1.371164000	2.698417000
H	1.614363000	0.806789000	3.569169000
C	1.218851000	1.225424000	1.523623000
C	1.647134000	1.917248000	0.354609000
C	-2.260309000	0.582765000	0.764976000
C	-3.525662000	1.155303000	0.952064000
H	-4.328675000	0.879890000	0.278650000
C	-3.744290000	2.102948000	1.944036000
H	-4.729622000	2.540893000	2.053689000
C	-2.700697000	2.511938000	2.771829000
H	-2.864165000	3.262789000	3.535069000
C	-1.440192000	1.946356000	2.609320000
H	-0.616658000	2.252225000	3.243340000
C	-1.216226000	0.982585000	1.629384000
C	-2.841778000	-1.154784000	-0.738089000
C	-3.355706000	-2.050883000	1.490058000
H	-2.284838000	-1.933784000	1.636063000
H	-3.884357000	-1.350629000	2.144848000
H	-3.642700000	-3.070694000	1.758008000
C	-5.035260000	-2.202839000	-0.306616000
H	-5.745309000	-1.764601000	0.401542000
H	-5.245257000	-1.813725000	-1.299881000
H	-5.168038000	-3.288375000	-0.305862000
C	-2.425859000	-0.513952000	-3.052765000
H	-2.523130000	0.498404000	-2.669329000
H	-1.379729000	-0.699324000	-3.320947000
H	-3.035756000	-0.621322000	-3.952629000
C	-3.113915000	-2.825691000	-2.528503000
H	-2.266164000	-3.127269000	-3.150439000
H	-3.180849000	-3.499725000	-1.677994000
H	-4.026919000	-2.901403000	-3.124895000
C	1.051495000	-3.203022000	1.571148000
H	1.533898000	-3.932065000	0.930367000
C	-2.231550000	3.506895000	-1.545043000
N	-2.802916000	3.061733000	-2.444397000
C	-1.515478000	4.071852000	-0.415478000
H	-2.093009000	4.891982000	0.012511000
H	-0.545198000	4.447271000	-0.742742000
H	-1.368527000	3.303014000	0.343936000

E(RTPSSh) = -3455.67866029
Zero-point correction = 0.722372 (Hartree/Particle)
Thermal correction to Energy = 0.769338
Thermal correction to Enthalpy = 0.770282
Thermal correction to Gibbs Free Energy = 0.642009

$[Cu(I)\{N(QuMe)(PhDMEG)_2\}]^+$ ($C3_{DMEG}$) + MeCN

N	-0.098195000	0.314211000	1.482271000
C	1.124832000	1.018731000	1.710319000
N	-1.187425000	1.663412000	-0.729322000
C	1.252567000	1.994959000	2.692082000
H	0.391234000	2.249081000	3.298224000
N	-1.136552000	-1.483874000	-0.307997000
C	2.475241000	2.627466000	2.900153000
H	2.568558000	3.386125000	3.667543000
N	1.979035000	-0.124353000	-0.236985000
C	3.575738000	2.264732000	2.126485000
H	4.533763000	2.746592000	2.283450000
N	3.854252000	-1.602683000	0.000417000
C	3.449400000	1.309928000	1.123962000
H	4.293578000	1.072089000	0.488227000
N	2.839601000	-1.441492000	-1.980813000
C	2.219955000	0.686759000	0.879819000
N	-2.544323000	-1.567366000	-2.177495000
C	2.856119000	-0.988709000	-0.691146000
N	-3.418861000	-2.247561000	-0.238879000
C	3.824745000	-1.798120000	1.443191000
H	4.039439000	-2.847325000	1.653951000
H	2.836133000	-1.560498000	1.832279000
H	4.566603000	-1.173060000	1.944153000
C	2.279269000	-0.658619000	-3.064629000
H	1.963540000	-1.327032000	-3.865474000
H	3.004038000	0.065378000	-3.451844000
H	1.408687000	-0.112050000	-2.692489000
C	4.496008000	-2.618615000	-0.839821000
H	4.116717000	-3.609648000	-0.567769000
H	5.578316000	-2.607172000	-0.714297000
C	4.057215000	-2.211286000	-2.243039000
H	4.802734000	-1.570345000	-2.728362000
H	3.850868000	-3.064094000	-2.888919000
C	-1.336305000	1.020777000	1.600802000
C	-2.062665000	0.990420000	2.772008000
H	-1.682436000	0.414020000	3.606795000
Cu	0.078338000	0.131585000	-0.813256000
C	-3.273472000	1.696536000	2.898236000
H	-3.816624000	1.657903000	3.834321000
C	-3.746991000	2.445530000	1.849276000
H	-4.666213000	3.012471000	1.939646000
C	-3.045472000	2.476268000	0.622272000
C	-1.842066000	1.735076000	0.477422000
C	-3.502276000	3.210783000	-0.497713000
H	-4.408217000	3.799650000	-0.412529000
C	-2.796966000	3.168895000	-1.668666000
H	-3.120693000	3.727984000	-2.537260000
C	-1.641877000	2.360722000	-1.766007000
C	-0.906284000	2.240691000	-3.062960000
H	-0.806468000	3.214328000	-3.546409000

H	-1.450190000	1.586150000	-3.749908000
H	0.084838000	1.814511000	-2.895220000
C	-0.119213000	-1.074369000	1.840072000
C	0.454287000	-1.535163000	3.020540000
H	0.936250000	-0.824894000	3.682605000
C	0.405118000	-2.888036000	3.343063000
H	0.853379000	-3.242527000	4.263207000
C	-0.229490000	-3.776574000	2.477079000
H	-0.273350000	-4.832361000	2.718433000
C	-0.790250000	-3.324111000	1.288052000
H	-1.251128000	-4.022273000	0.598821000
C	-0.735744000	-1.968701000	0.941868000
C	-2.293918000	-1.769987000	-0.845086000
C	-1.469262000	-1.550335000	-3.148677000
H	-1.846048000	-1.134631000	-4.082524000
H	-1.065796000	-2.553138000	-3.332559000
H	-0.664276000	-0.911616000	-2.778361000
C	-3.717558000	-2.050549000	1.173544000
H	-4.745204000	-1.693870000	1.261056000
H	-3.053671000	-1.300598000	1.599513000
H	-3.612417000	-2.979696000	1.736897000
C	-3.803685000	-2.220482000	-2.536667000
H	-3.609298000	-3.227312000	-2.926140000
H	-4.341365000	-1.646541000	-3.290514000
C	-4.528701000	-2.271690000	-1.196656000
H	-5.163698000	-1.391012000	-1.046947000
H	-5.133787000	-3.169734000	-1.075457000
C	2.782776000	3.206920000	-1.654939000
N	3.602285000	2.837549000	-2.380141000
C	1.744964000	3.664260000	-0.748540000
H	2.188074000	3.953650000	0.205006000
H	1.037897000	2.850822000	-0.574381000
H	1.219463000	4.515170000	-1.183924000

E(RTPSSh) = -3453.28441718
Zero-point correction = 0.681277 (Hartree/Particle)
Thermal correction to Energy = 0.725264
Thermal correction to Enthalpy = 0.726208
Thermal correction to Gibbs Free Energy = 0.601566

$[Cu(I)\{N(QuMe)_2(PhTMG)\}]^+$ ($C1_{TMG}$) + MeCN

N	0.496767000	-0.310395000	1.174766000
C	2.066604000	0.305742000	-3.516442000
H	2.750583000	0.902683000	-4.121349000
H	1.198961000	0.908126000	-3.240232000
H	1.717305000	-0.527632000	-4.134433000
Cu	0.050524000	-0.178626000	-1.052347000
N	2.009814000	-0.320195000	-1.182779000
C	2.743404000	-0.211466000	-2.287264000
N	-0.952735000	-1.900562000	-0.608664000
C	4.099929000	-0.602181000	-2.318645000
H	4.660226000	-0.477531000	-3.236355000
N	-1.172880000	1.251507000	-0.327228000
C	4.675458000	-1.155226000	-1.207995000
H	5.706286000	-1.489556000	-1.220787000
N	-3.411623000	1.808465000	0.222466000
C	3.917929000	-1.292116000	-0.021581000
N	-2.778224000	1.419111000	-1.976579000
C	4.438812000	-1.889101000	1.148641000
H	5.460318000	-2.250978000	1.140353000
C	3.653219000	-2.018540000	2.267043000
H	4.042738000	-2.491289000	3.160069000
C	2.340755000	-1.509923000	2.272478000
H	1.737799000	-1.594420000	3.167927000
C	1.811565000	-0.889306000	1.162274000
C	2.579929000	-0.815302000	-0.034294000
C	-1.197232000	-2.577606000	-2.916865000
H	-0.941149000	-3.553865000	-3.335246000
H	-0.346809000	-1.903274000	-3.030734000
H	-2.038755000	-2.186374000	-3.495058000
C	-1.562273000	-2.701935000	-1.470634000
C	-2.544047000	-3.632948000	-1.053798000
H	-3.009227000	-4.273521000	-1.792362000
C	-2.910905000	-3.690526000	0.262025000
H	-3.683087000	-4.373663000	0.596557000
C	-2.276184000	-2.846454000	1.205095000
C	-2.629170000	-2.823612000	2.573395000
H	-3.412202000	-3.486125000	2.923534000
C	-1.997067000	-1.961335000	3.436119000
H	-2.277403000	-1.928246000	4.481554000
C	-0.964451000	-1.124919000	2.971964000
H	-0.466747000	-0.450455000	3.658403000
C	-0.573685000	-1.143555000	1.650493000
C	-1.258466000	-1.979309000	0.725241000
C	0.383960000	1.085555000	1.508104000
C	1.170435000	1.684383000	2.485656000
H	1.921062000	1.094400000	2.997161000
C	0.994382000	3.027962000	2.802825000
H	1.612064000	3.488908000	3.563686000
C	0.016025000	3.767475000	2.142043000
H	-0.131058000	4.813563000	2.384353000
C	-0.754548000	3.182921000	1.143686000
H	-1.474363000	3.776612000	0.592685000
C	-0.569424000	1.841444000	0.790712000
C	-2.424922000	1.501197000	-0.665303000
C	-1.748793000	1.490992000	-2.998457000
H	-1.273339000	0.514359000	-3.167162000
H	-0.986210000	2.207180000	-2.700245000
H	-2.209281000	1.817544000	-3.932210000
C	-4.042022000	0.815599000	-2.389765000
H	-3.838043000	-0.083961000	-2.977519000
H	-4.626847000	1.507760000	-3.000011000
H	-4.617075000	0.532682000	-1.511954000
C	-3.361196000	1.367317000	1.605952000
H	-2.649191000	0.552228000	1.703916000
H	-4.352901000	1.007819000	1.891746000
H	-3.069642000	2.178684000	2.280207000
C	-4.492536000	2.728602000	-0.107567000
H	-4.330683000	3.143727000	-1.099273000
H	-4.498037000	3.544412000	0.621673000
H	-5.464891000	2.228833000	-0.077323000
C	3.434138000	2.677722000	-0.169220000
N	4.379091000	2.323570000	0.392152000
C	2.246980000	3.125538000	-0.875489000
H	1.544735000	2.294902000	-0.971511000
H	2.520955000	3.484968000	-1.868210000
H	1.767615000	3.928615000	-0.315294000

E(RTPSSh) = -3303.19277966
Zero-point correction = 0.617340 (Hartree/Particle)
Thermal correction to Energy = 0.657901
Thermal correction to Enthalpy = 0.658845
Thermal correction to Gibbs Free Energy = 0.544017

[Cu(I){N(QuMe)$_2$(PhDMEG)}]$^+$ (C1$_{DMEG}$) + MeCN

Cu	0.916254000	1.012492000	-0.473990000
N	0.955832000	-1.029110000	0.548688000
N	-0.211865000	-0.032351000	-1.786491000
N	2.869416000	0.774408000	-0.366065000
N	-0.360502000	1.309592000	1.084810000
N	-2.705741000	1.443868000	1.651896000
N	-1.850174000	2.806936000	0.095433000
C	0.860164000	-0.596352000	1.916558000
C	1.498563000	-1.268713000	2.953149000
H	2.104406000	-2.137991000	2.726141000
C	1.353212000	-0.831556000	4.266246000
H	1.850249000	-1.360110000	5.070470000
C	0.559148000	0.281498000	4.536368000
H	0.437857000	0.627809000	5.556212000
C	-0.061082000	0.972647000	3.502182000
H	-0.647358000	1.860418000	3.708785000
C	0.089850000	0.556764000	2.174096000
C	-1.565326000	1.808665000	0.982377000
C	-0.826885000	3.704212000	-0.401814000
H	-1.218673000	4.235617000	-1.268112000
H	0.046323000	3.121751000	-0.712791000
H	-0.512569000	4.427537000	0.359067000
C	-2.943285000	0.064608000	2.064647000
H	-3.852881000	0.044464000	2.664231000
H	-2.119695000	-0.304039000	2.669232000
H	-3.071827000	-0.586944000	1.194090000
C	-3.195628000	3.321316000	0.347932000
H	-3.689386000	3.598186000	-0.582915000
H	-3.148416000	4.199593000	1.002964000
C	-3.852775000	2.134804000	1.040472000
H	-4.575579000	2.428112000	1.800885000
H	-4.338440000	1.471995000	0.316866000
C	2.232963000	-1.508285000	0.109584000
C	2.535374000	-2.850533000	0.050143000
H	1.771129000	-3.576907000	0.297568000
C	3.828434000	-3.287395000	-0.298369000
H	4.038340000	-4.349468000	-0.326605000
C	4.822145000	-2.376260000	-0.559254000
H	5.829775000	-2.701731000	-0.790080000
C	4.537544000	-0.990994000	-0.547785000
C	3.219815000	-0.548348000	-0.258029000
C	5.508876000	-0.003384000	-0.835060000
H	6.530179000	-0.305565000	-1.036209000
C	5.147900000	1.317104000	-0.856771000
H	5.875461000	2.091071000	-1.064610000
C	3.799335000	1.681989000	-0.647965000
C	3.347852000	3.101838000	-0.785097000
H	4.169629000	3.798212000	-0.617061000
H	2.542035000	3.307263000	-0.076890000
H	2.959210000	3.275533000	-1.794026000
C	-0.214258000	-1.655266000	0.002539000
C	-0.838504000	-2.699457000	0.648589000
H	-0.451714000	-3.033617000	1.603822000
C	-1.958602000	-3.336910000	0.082175000
H	-2.422298000	-4.162499000	0.607797000
C	-2.442095000	-2.929631000	-1.137406000
H	-3.286062000	-3.430290000	-1.597151000
C	-1.853382000	-1.833103000	-1.806729000
C	-0.746871000	-1.162822000	-1.221554000
C	-2.334509000	-1.342899000	-3.043917000
H	-3.171130000	-1.838932000	-3.521675000
C	-1.744507000	-0.249333000	-3.613736000
H	-2.091115000	0.142994000	-4.561339000
C	-0.686243000	0.409458000	-2.943804000
C	-0.089245000	1.658632000	-3.511349000
H	0.127687000	1.536501000	-4.574635000
H	0.830030000	1.910837000	-2.979347000
H	-0.790080000	2.492584000	-3.413922000
C	-5.640009000	-1.257702000	-0.572459000
N	-5.442487000	-0.374034000	-1.289013000
C	-5.886566000	-2.366891000	0.333908000
H	-6.031142000	-3.284969000	-0.237050000
H	-6.780924000	-2.167734000	0.925590000
H	-5.034141000	-2.493323000	1.002426000

E(RTPSSh) = -3301.99094760
Zero-point correction = 0.596324 (Hartree/Particle)
Thermal correction to Energy = 0.635801
Thermal correction to Enthalpy = 0.636745
Thermal correction to Gibbs Free Energy = 0.520943

9.15.2 [Cu(I)LS] Geometries

[Cu(I)(TMG$_3$trphen)(MeCN)]$^+$ (C5$_{TMG}$ + MeCN)

Cu	-0.054958000	-0.202739000	-0.733393000
N	0.575910000	0.108285000	1.701641000
N	1.803309000	-1.019621000	-0.496080000
N	-1.515242000	-1.483703000	1.003851000
N	0.104623000	1.840058000	-0.401799000
N	-3.695371000	-1.314737000	0.052354000
N	-2.402759000	-3.239500000	-0.181419000
N	2.516370000	-1.072456000	-2.709349000
N	4.091103000	-0.747914000	-1.044380000
N	-0.907123000	2.690556000	-2.308697000
N	-1.288028000	3.742988000	-0.274160000
N	-1.355838000	-0.589517000	-2.069993000
C	1.323849000	-1.097590000	1.871526000
C	2.016990000	-1.605923000	0.755714000
C	2.779364000	-2.770010000	0.922558000
H	3.295003000	-3.184916000	0.063752000
C	2.836654000	-3.421119000	2.149104000
H	3.424427000	-4.326939000	2.246694000
C	2.120182000	-2.928049000	3.238100000
H	2.149907000	-3.438581000	4.193488000
C	1.369042000	-1.765973000	3.091366000
H	0.808539000	-1.362522000	3.926840000
C	1.349437000	1.308099000	1.598081000
C	2.382817000	1.585877000	2.489043000
H	2.621547000	0.853343000	3.251673000
C	3.095214000	2.777254000	2.404290000
H	3.896863000	2.984902000	3.102761000
C	2.761621000	3.697713000	1.411276000

H	3.309266000	4.629764000	1.327077000
C	1.745865000	3.419208000	0.506177000
H	1.525282000	4.119252000	-0.291992000
C	1.022005000	2.216705000	0.573883000
C	-0.636143000	0.210188000	2.451248000
C	-0.764601000	1.088968000	3.522870000
H	0.068401000	1.734846000	3.772158000
C	-1.940457000	1.143403000	4.266564000
H	-2.027290000	1.834968000	5.096170000
C	-2.983102000	0.276985000	3.949014000
H	-3.894743000	0.280385000	4.536447000
C	-2.866438000	-0.597275000	2.874795000
H	-3.683761000	-1.268922000	2.640212000
C	-1.711313000	-0.627697000	2.072658000
C	2.786138000	-0.965562000	-1.380583000
C	4.450782000	-0.051798000	0.177726000
H	5.306698000	0.594831000	-0.031371000
H	4.720267000	-0.748416000	0.978812000
H	3.613891000	0.558058000	0.507034000
C	5.188376000	-1.411696000	-1.735340000
H	4.795648000	-2.072259000	-2.504322000
H	5.752375000	-2.011221000	-1.013492000
H	5.868127000	-0.686754000	-2.192050000
C	1.410680000	-1.877842000	-3.197215000
H	0.668226000	-1.255652000	-3.700980000
H	0.937185000	-2.381817000	-2.358991000
H	1.789511000	-2.617758000	-3.909888000
C	3.248344000	-0.322960000	-3.718617000
H	3.846674000	-0.979062000	-4.358179000
H	3.900978000	0.400018000	-3.234859000
H	2.532534000	0.211697000	-4.349664000
C	-2.530104000	-1.983263000	0.331070000
C	-1.313762000	-4.083147000	0.288104000
H	-1.614498000	-5.127355000	0.179765000
H	-1.106235000	-3.860898000	1.331017000
H	-0.400310000	-3.914695000	-0.293042000
C	-2.969240000	-3.640930000	-1.461061000
H	-2.162563000	-3.808009000	-2.182868000
H	-3.625220000	-2.864763000	-1.841483000
H	-3.539048000	-4.567544000	-1.356051000
C	-4.994201000	-1.971635000	0.021449000
H	-5.482689000	-1.844634000	-0.949670000
H	-5.638215000	-1.531407000	0.790766000
H	-4.877741000	-3.032405000	0.230374000
C	-3.734737000	0.136967000	0.036346000
H	-2.721150000	0.524143000	-0.047413000
H	-4.197824000	0.540181000	0.942985000
H	-4.315972000	0.462318000	-0.831171000
C	-0.664733000	2.754307000	-0.974599000
C	0.087571000	2.149823000	-3.221400000
H	-0.287726000	1.255720000	-3.722938000
H	0.980319000	1.891330000	-2.658457000
H	0.330482000	2.900599000	-3.979885000
C	-2.177452000	3.080803000	-2.899717000
H	-2.083839000	3.983870000	-3.510191000
H	-2.908548000	3.250923000	-2.112774000
H	-2.531832000	2.270150000	-3.541437000
C	-1.538737000	3.598300000	1.150179000
H	-2.507052000	4.049199000	1.379185000
H	-0.766869000	4.092816000	1.749099000
H	-1.561633000	2.542967000	1.410164000
C	-1.474848000	5.084086000	-0.813437000
H	-1.028681000	5.149570000	-1.802571000
H	-0.973878000	5.801444000	-0.156220000
H	-2.534538000	5.346554000	-0.873891000
C	-2.138178000	-0.720894000	-2.909824000
C	-3.115501000	-0.877224000	-3.968843000
H	-2.877323000	-0.202045000	-4.792685000
H	-4.111658000	-0.641552000	-3.590249000
H	-3.104515000	-1.903954000	-4.338084000

E(RTPSSh) = -3608.16051133
Zero-point correction = 0.828586 (Hartree/Particle)
Thermal correction to Energy = 0.880875
Thermal correction to Enthalpy = 0.881820
Thermal correction to Gibbs Free Energy = 0.744256

Cu(I)(DMEG$_3$trphen)(MeCN)]$^+$ (C5$_{DMEG}$ + MeCN)

Cu	-0.316291000	-0.095766000	-0.871751000
N	0.352803000	-0.043840000	1.451799000
N	-2.132836000	-0.373253000	0.240894000
N	-3.485681000	-1.239098000	-1.461482000
N	-3.763091000	-2.127139000	0.565741000
C	-0.839241000	0.383390000	2.131957000
C	-0.761273000	1.035465000	3.359463000
H	0.215869000	1.211094000	3.793437000
C	-1.909426000	1.458588000	4.018321000
H	-1.835367000	1.965341000	4.972769000
C	-3.152617000	1.223944000	3.431179000
H	-4.059431000	1.554840000	3.924980000
C	-3.240191000	0.584792000	2.203052000
H	-4.206784000	0.428230000	1.737993000
C	-2.088232000	0.148455000	1.523532000
C	-3.079865000	-1.186650000	-0.163799000
C	-3.368730000	-0.109687000	-2.360999000
H	-3.045547000	-0.445955000	-3.347110000
H	-2.633039000	0.582154000	-1.955280000
H	-4.333074000	0.402822000	-2.455706000
C	-4.597273000	-2.171432000	-1.617134000
H	-4.497664000	-2.757829000	-2.530978000
H	-5.543546000	-1.618442000	-1.654228000
C	-4.483168000	-3.017147000	-0.353395000
H	-5.449520000	-3.305001000	0.059182000
H	-3.888801000	-3.921597000	-0.530759000
C	-3.198447000	-2.742165000	1.757512000
H	-3.986639000	-3.310205000	2.251706000
H	-2.838868000	-1.978322000	2.440969000
H	-2.372424000	-3.415784000	1.504254000
N	0.183820000	1.839463000	-0.527759000
N	-1.260066000	2.852850000	-2.072555000
N	-0.915202000	3.953865000	-0.153110000
C	1.371760000	0.961419000	1.378473000
C	2.468821000	0.965846000	2.231048000
H	2.574161000	0.164054000	2.952763000
C	3.415000000	1.982645000	2.153124000
H	4.269883000	1.981313000	2.818698000
C	3.248464000	3.004555000	1.219270000
H	3.979681000	3.801766000	1.149349000
C	2.157479000	2.999086000	0.358041000
H	2.044819000	3.775789000	-0.389660000

C	1.204411000	1.975391000	0.419176000
C	-0.594456000	2.834191000	-0.876257000
C	-0.739274000	2.164300000	-3.240105000
H	-1.524204000	2.118609000	-3.994449000
H	-0.453857000	1.147862000	-2.964586000
H	0.133256000	2.681449000	-3.655439000
C	-1.890302000	4.159603000	-2.261731000
H	-2.851957000	4.062119000	-2.764688000
H	-1.238745000	4.807872000	-2.860221000
C	-2.011991000	4.658743000	-0.828938000
H	-1.896325000	5.738073000	-0.737305000
H	-2.969458000	4.362770000	-0.383484000
C	-0.961416000	3.946229000	1.304410000
H	-1.073183000	4.976041000	1.643603000
H	-0.040245000	3.541507000	1.712757000
H	-1.805850000	3.350660000	1.667472000
N	2.101375000	-1.065861000	-0.350985000
N	3.601515000	-0.129037000	-1.860694000
N	4.519299000	-1.301611000	-0.191800000
C	0.756434000	-1.399239000	1.601772000
C	0.216337000	-2.230534000	2.578668000
H	-0.489082000	-1.817688000	3.288970000
C	0.569827000	-3.576625000	2.638624000
H	0.134853000	-4.213145000	3.400132000
C	1.479386000	-4.092631000	1.719530000
H	1.755756000	-5.140465000	1.752044000
C	2.034220000	-3.263973000	0.748785000
H	2.734159000	-3.662163000	0.022633000
C	1.695857000	-1.906920000	0.671059000
C	3.319723000	-0.872241000	-0.737165000
C	2.599531000	0.119581000	-2.873453000
H	2.910226000	0.977121000	-3.471881000
H	1.655792000	0.343443000	-2.378628000
H	2.459036000	-0.746423000	-3.533176000
C	4.991370000	-0.321352000	-2.250246000
H	5.404099000	0.584407000	-2.694925000
H	5.084316000	-1.144726000	-2.971635000
C	5.628484000	-0.673671000	-0.914883000
H	6.471637000	-1.358940000	-1.005384000
H	5.959066000	0.227940000	-0.382383000
C	4.737368000	-1.486981000	1.234566000
H	5.539477000	-2.214024000	1.376064000
H	3.838538000	-1.861424000	1.712988000
H	5.029110000	-0.541845000	1.706175000
C	-0.594811000	-2.427922000	-2.794107000
N	-0.409415000	-1.481655000	-2.160725000
C	-0.848939000	-3.622169000	-3.574119000
H	-1.743286000	-4.120159000	-3.194887000
H	0.001199000	-4.301657000	-3.496848000
H	-1.002166000	-3.356346000	-4.621200000

E(RTPSSh) = -3604.57341730
Zero-point correction = 0.766312 (Hartree/Particle)
Thermal correction to Energy = 0.814518
Thermal correction to Enthalpy = 0.815462
Thermal correction to Gibbs Free Energy = 0.682926

$[Cu(I)\{N(QuMe)(PhTMG)_2\}(MeCN)]^+$ ($C3_{TMG}$ + MeCN)

N	-0.004718000	-0.782801000	1.420332000
C	0.125200000	1.654965000	1.601154000
N	-1.052174000	-2.385571000	-0.516613000
N	1.863149000	-0.507231000	-0.600269000
C	1.180453000	2.658448000	3.552342000
H	1.495323000	3.550018000	4.082838000
N	-0.396753000	1.739603000	0.316013000
C	1.443008000	1.396988000	4.085501000
H	1.954374000	1.293598000	5.034730000
N	2.927292000	0.534259000	-2.375700000
C	1.043773000	0.268714000	3.379193000
H	1.245958000	-0.722348000	3.767428000
N	4.017360000	0.433156000	-0.327373000
C	0.386788000	0.386347000	2.157065000
N	-2.097938000	3.324840000	0.774802000
C	-1.162718000	2.758285000	-0.040160000
N	-1.069996000	3.254253000	-1.300807000
C	0.155672000	3.107599000	-2.066347000
H	0.054029000	2.325520000	-2.824483000
H	0.379199000	4.053709000	-2.567023000
H	0.968383000	2.848977000	-1.392822000
C	-2.228680000	3.726667000	-2.045699000
H	-2.279475000	3.188054000	-2.996097000
H	-3.134895000	3.526439000	-1.478982000
H	-2.162352000	4.797297000	-2.258559000
C	-2.677122000	2.582995000	1.880721000
H	-3.738330000	2.833839000	1.949083000
H	-2.573788000	1.516985000	1.693803000
H	-2.193052000	2.827022000	2.832211000
C	-2.387564000	4.752977000	0.753450000
H	-3.429125000	4.945746000	0.481846000
H	-2.205210000	5.165824000	1.750483000
H	-1.731330000	5.251089000	0.044096000
C	-0.588427000	-3.430153000	-2.639202000
H	0.444286000	-3.462191000	-2.292270000
H	-0.839170000	-4.369814000	-3.133476000
H	-0.666737000	-2.628412000	-3.380891000
Cu	-0.026515000	0.086084000	-0.918489000
C	-1.512966000	-3.150298000	-1.490233000
C	-2.837140000	-3.654161000	-1.481871000
H	-3.173118000	-4.287697000	-2.294084000
C	-3.679868000	-3.324508000	-0.452093000
H	-4.702365000	-3.685834000	-0.432334000
C	-3.215646000	-2.501040000	0.600027000
C	-4.029063000	-2.083913000	1.681742000
H	-5.059829000	-2.416261000	1.729487000
C	-3.503953000	-1.260152000	2.646658000
H	-4.118703000	-0.932669000	3.476912000
C	-2.159898000	-0.835955000	2.587640000
H	-1.763313000	-0.195422000	3.365219000
C	-1.338281000	-1.226764000	1.550364000
C	-1.864242000	-2.068489000	0.521354000
C	2.021986000	-1.552289000	0.314209000
C	3.063949000	-2.485527000	0.221690000
H	3.828850000	-2.345596000	-0.533716000
C	3.098237000	-3.604588000	1.045134000
H	3.910987000	-4.315047000	0.944895000
C	2.082991000	-3.828660000	1.973649000
H	2.099242000	-4.707593000	2.606851000
C	1.049061000	-2.904825000	2.085623000
H	0.250992000	-3.052431000	2.804815000
C	1.023108000	-1.773463000	1.278497000
C	2.924825000	0.124545000	-1.081221000
C	3.917984000	0.563351000	1.117130000

H	2.888745000	0.780022000	1.393359000
H	4.239400000	-0.349299000	1.629670000
H	4.557616000	1.390626000	1.433438000
C	5.370909000	0.393528000	-0.865903000
H	5.960845000	-0.327406000	-0.291130000
H	5.345054000	0.073000000	-1.904456000
H	5.854761000	1.371854000	-0.799254000
C	2.083040000	-0.130809000	-3.355173000
H	1.892539000	-1.151280000	-3.033339000
H	1.122455000	0.381207000	-3.478454000
H	2.604921000	-0.138965000	-4.314576000
C	3.555050000	1.777142000	-2.805706000
H	2.820354000	2.379659000	-3.346096000
H	3.895349000	2.334376000	-1.935964000
H	4.402537000	1.589635000	-3.470589000
C	0.537167000	2.784722000	2.329504000
H	0.375864000	3.767793000	1.902374000
C	-2.424448000	0.035219000	-2.779370000
N	-1.431732000	0.076877000	-2.191163000
C	-3.677526000	-0.032807000	-3.503734000
H	-3.496025000	0.089677000	-4.572660000
H	-4.347366000	0.756948000	-3.159264000
H	-4.144319000	-1.003335000	-3.327013000

E(RTPSSh) = -3455.68193840
Zero-point correction = 0.722319 (Hartree/Particle)
Thermal correction to Energy = 0.769185
Thermal correction to Enthalpy = 0.770129
Thermal correction to Gibbs Free Energy = 0.641859

$[Cu(I)\{N(QuMe)(PhDMEG)_2\}(MeCN)]^+$ ($C3_{DMEG}$ + MeCN)

N	-0.009170000	-0.996608000	1.307485000
C	-0.880167000	-2.075382000	0.952474000
N	1.387789000	-2.099906000	-0.740106000
C	-0.791746000	-3.317632000	1.569642000
H	-0.014721000	-3.481825000	2.307889000
N	0.175446000	1.658070000	0.531094000
C	-1.692057000	-4.328655000	1.248397000
H	-1.620554000	-5.294804000	1.733348000
N	-1.789285000	-0.634494000	-0.755639000
C	-2.692301000	-4.079650000	0.309911000
H	-3.403759000	-4.856512000	0.053857000
N	-4.068854000	0.054905000	-0.477080000
C	-2.772582000	-2.844659000	-0.323161000
H	-3.525963000	-2.668726000	-1.082562000
N	-2.894468000	0.865353000	-2.196584000
C	-1.860567000	-1.824413000	-0.024163000
N	0.954373000	3.397406000	-0.845529000
C	-2.866184000	0.026206000	-1.112299000
N	1.669214000	3.388585000	1.263196000
C	-4.233813000	-0.273931000	0.931478000
H	-4.865702000	0.487339000	1.391293000
H	-3.266011000	-0.274462000	1.431239000
H	-4.701456000	-1.252354000	1.058988000
C	-2.062622000	0.618943000	-3.362582000
H	-1.979028000	1.541246000	-3.937339000
H	-2.493998000	-0.163717000	-3.998092000
H	-1.068246000	0.310318000	-3.039120000
C	-4.936932000	1.067557000	-1.083084000
H	-4.928264000	1.973267000	-0.466573000
H	-5.962496000	0.709230000	-1.169530000
C	-4.273387000	1.298224000	-2.436938000
H	-4.725545000	0.672873000	-3.215994000
H	-4.307791000	2.339152000	-2.757170000
C	1.360381000	-1.275394000	1.496932000
C	2.044059000	-0.942273000	2.648291000
H	1.509264000	-0.478380000	3.467812000
Cu	0.078080000	0.128223000	-0.929216000
C	3.422612000	-1.213777000	2.772816000
H	3.927688000	-0.941120000	3.692012000
C	4.116877000	-1.832311000	1.761585000
H	5.172954000	-2.054956000	1.862920000
C	3.448393000	-2.175844000	0.561590000
C	2.067698000	-1.879844000	0.413979000
C	4.088169000	-2.782844000	-0.545320000
H	5.140527000	-3.036326000	-0.477543000
C	3.376698000	-3.032911000	-1.689179000
H	3.848770000	-3.496689000	-2.547177000
C	2.011653000	-2.656726000	-1.762578000
C	1.223339000	-2.870152000	-3.021130000
H	0.976709000	-3.930028000	-3.140350000
H	1.797370000	-2.567942000	-3.900007000
H	0.297007000	-2.298928000	-2.977061000
C	-0.602688000	0.020375000	2.124160000
C	-1.341277000	-0.313499000	3.256009000
H	-1.463901000	-1.361024000	3.505558000
C	-1.911374000	0.674411000	4.050795000
H	-2.483968000	0.405116000	4.929850000
C	-1.731319000	2.012037000	3.699995000
H	-2.172103000	2.796808000	4.304546000
C	-1.008000000	2.353231000	2.565933000
H	-0.902265000	3.394251000	2.282893000
C	-0.430825000	1.367483000	1.745540000
C	0.877761000	2.756611000	0.354439000
C	-0.113309000	3.334782000	-1.825265000
H	0.304449000	3.275747000	-2.830820000
H	-0.749808000	4.224493000	-1.752411000
H	-0.714245000	2.447489000	-1.632656000
C	2.187553000	2.742967000	2.456655000
H	3.265390000	2.909714000	2.507255000
H	2.000800000	1.671731000	2.404665000
H	1.720280000	3.143126000	3.359198000
C	1.708477000	4.642443000	-0.708066000
H	1.012775000	5.488228000	-0.662113000
H	2.383469000	4.791522000	-1.551129000
C	2.447665000	4.446613000	0.615988000
H	3.475472000	4.100352000	0.461813000
H	2.469977000	5.350726000	1.224372000
C	2.353486000	0.727275000	-2.865255000
N	1.432099000	0.497284000	-2.210101000
C	3.520987000	1.007542000	-3.675927000
H	4.002137000	1.922012000	-3.324986000
H	3.227470000	1.132270000	-4.719356000
H	4.225034000	0.177334000	-3.597368000

E(RTPSSh) = -3453.28699691
Zero-point correction = 0.680989 (Hartree/Particle)
Thermal correction to Energy = 0.725040
Thermal correction to Enthalpy = 0.725984
Thermal correction to Gibbs Free Energy = 0.600603

[Cu(I){N(QuMe)$_2$(PhTMG)}(MeCN)]$^+$ (C1$_{TMG}$ + MeCN)

N	0.586471000	-0.763261000	-1.093694000
C	0.925605000	-0.896369000	3.867562000
H	1.412708000	-0.879589000	4.842156000
H	0.117073000	-1.632171000	3.899301000
H	0.476458000	0.080568000	3.669150000
Cu	-0.083070000	0.121106000	1.078212000
N	1.516824000	-1.003978000	1.526005000
C	1.894581000	-1.240831000	2.780627000
N	1.663180000	1.674283000	-0.547263000
C	3.164905000	-1.774287000	3.086578000
H	3.421777000	-1.956904000	4.122033000
N	-1.776397000	-0.766848000	0.363157000
C	4.066426000	-2.009045000	2.082751000
H	5.063082000	-2.375215000	2.301390000
N	-3.978557000	-0.299699000	-0.377410000
C	3.697689000	-1.758241000	0.742709000
N	-3.347005000	0.141634000	1.805734000
C	4.593859000	-1.922027000	-0.340199000
H	5.601019000	-2.267306000	-0.137619000
C	4.188892000	-1.633392000	-1.619417000
H	4.875735000	-1.741589000	-2.449952000
C	2.863332000	-1.226495000	-1.867807000
H	2.538642000	-1.028695000	-2.882628000
C	1.960051000	-1.087111000	-0.839605000
C	2.374200000	-1.298398000	0.501487000
C	2.987662000	2.901876000	1.052302000
H	4.027562000	3.170358000	0.844271000
H	2.962099000	1.935744000	1.554016000
H	2.585130000	3.666444000	1.722602000
C	2.192197000	2.837203000	-0.218852000
C	2.011530000	3.994352000	-1.019768000
H	2.466711000	4.930034000	-0.717102000
C	1.256259000	3.916421000	-2.159562000
H	1.095224000	4.790111000	-2.781673000
C	0.670844000	2.682642000	-2.532714000
C	-0.147431000	2.519576000	-3.676368000
H	-0.336567000	3.371479000	-4.319552000
C	-0.691725000	1.289370000	-3.952156000
H	-1.318357000	1.153838000	-4.825736000
C	-0.440428000	0.180079000	-3.117623000
H	-0.871222000	-0.783232000	-3.359103000
C	0.348127000	0.307143000	-1.993956000
C	0.921950000	1.575953000	-1.678600000
C	-0.298148000	-1.900518000	-1.174616000
C	0.049241000	-3.030641000	-1.908670000
H	1.005463000	-3.053540000	-2.416689000
C	-0.815953000	-4.115421000	-1.997059000
H	-0.535397000	-4.988755000	-2.572960000
C	-2.042412000	-4.062183000	-1.337653000
H	-2.725775000	-4.902159000	-1.389505000
C	-2.389311000	-2.946389000	-0.588913000
H	-3.324994000	-2.930935000	-0.042463000
C	-1.526616000	-1.843453000	-0.485059000
C	-3.011693000	-0.337779000	0.581332000
C	-2.660724000	-0.312963000	3.003167000
H	-1.967032000	0.446221000	3.374489000
H	-2.109720000	-1.221667000	2.775532000
H	-3.402594000	-0.519948000	3.779405000
C	-4.243044000	1.276093000	1.982213000
H	-3.732130000	2.038010000	2.577593000
H	-5.160512000	0.987691000	2.502688000
H	-4.494589000	1.698441000	1.012380000
C	-3.643496000	-0.219487000	-1.788032000
H	-2.637249000	0.176341000	-1.898459000
H	-4.349541000	0.457976000	-2.274082000
H	-3.698348000	-1.198461000	-2.275271000
C	-5.381974000	-0.554764000	-0.077069000
H	-5.490916000	-0.824344000	0.970464000
H	-5.727651000	-1.390276000	-0.693286000
H	-6.002573000	0.318818000	-0.294650000
C	-0.727577000	3.015380000	1.806069000
N	-0.466094000	1.906563000	1.623925000
C	-1.043229000	4.413177000	2.019279000
H	-1.027560000	4.636324000	3.087159000
H	-2.034452000	4.633189000	1.619581000
H	-0.302935000	5.033444000	1.510933000

E(RTPSSh) = -3303.19590183
Zero-point correction = 0.617247 (Hartree/Particle)
Thermal correction to Energy = 0.657817
Thermal correction to Enthalpy = 0.658761
Thermal correction to Gibbs Free Energy = 0.542715

[Cu(I){N(QuMe)$_2$(PhDMEG)}(MeCN)]$^+$ (C1$_{DMEG}$ + MeCN)

Cu	-0.058699000	0.045100000	1.095000000
N	0.614020000	-0.695334000	-1.116152000
N	1.457754000	1.831758000	-0.553352000
N	1.638923000	-0.965716000	1.446535000
N	-1.698512000	-0.975561000	0.384549000
N	-3.993498000	-0.668125000	-0.297439000
N	-3.357437000	-0.026482000	1.743414000
C	-0.131922000	-1.926036000	-1.186922000
C	0.331070000	-3.008993000	-1.928247000
H	1.273410000	-2.920435000	-2.454670000
C	-0.403736000	-4.187084000	-1.999238000
H	-0.034648000	-5.023150000	-2.580426000
C	-1.617243000	-4.274735000	-1.319036000
H	-2.200731000	-5.187360000	-1.361357000
C	-2.078311000	-3.205746000	-0.563889000
H	-3.006963000	-3.288284000	-0.011285000
C	-1.345309000	-2.011532000	-0.474937000
C	-2.944984000	-0.604014000	0.580006000
C	-2.718201000	-0.292658000	3.018141000
H	-2.749461000	0.602611000	3.639411000
H	-1.680364000	-0.568260000	2.842719000
H	-3.227496000	-1.111845000	3.538735000
C	-3.818454000	-0.642671000	-1.742133000
H	-4.770476000	-0.906561000	-2.202416000
H	-3.072590000	-1.370280000	-2.047044000
H	-3.516407000	0.352880000	-2.084536000
C	-4.805645000	0.171954000	1.724251000
H	-5.079059000	1.123532000	2.179670000

H	-5.295705000	-0.638541000	2.276540000
C	-5.118934000	0.110554000	0.234847000
H	-6.067729000	-0.377495000	0.015178000
H	-5.118832000	1.109163000	-0.217237000
C	2.023650000	-0.863353000	-0.924743000
C	2.904543000	-0.845054000	-1.980434000
H	2.529803000	-0.636228000	-2.975601000
C	4.274922000	-1.107295000	-1.782571000
H	4.946005000	-1.090786000	-2.632649000
C	4.747545000	-1.416687000	-0.531379000
H	5.792991000	-1.654249000	-0.372611000
C	3.869678000	-1.419615000	0.578984000
C	2.497990000	-1.099968000	0.391562000
C	4.295058000	-1.709111000	1.894204000
H	5.330961000	-1.973892000	2.073056000
C	3.395939000	-1.643979000	2.926127000
H	3.695802000	-1.865093000	3.942321000
C	2.067417000	-1.238271000	2.677024000
C	1.087549000	-1.069584000	3.795936000
H	1.569710000	-1.179354000	4.766716000
H	0.291780000	-1.815591000	3.715423000
H	0.622130000	-0.081236000	3.736648000
C	0.196786000	0.369312000	-1.955161000
C	-0.660162000	0.188961000	-3.019247000
H	-0.999412000	-0.808685000	-3.265957000
C	-1.095648000	1.287501000	-3.788857000
H	-1.770791000	1.109223000	-4.617471000
C	-0.667146000	2.561920000	-3.508803000
H	-0.997160000	3.406139000	-4.103352000
C	0.215667000	2.780809000	-2.424097000
C	0.650239000	1.684234000	-1.632877000
C	0.691306000	4.060253000	-2.048928000
H	0.389754000	4.928404000	-2.624940000
C	1.518341000	4.188479000	-0.964819000
H	1.892018000	5.159635000	-0.662298000
C	1.881595000	3.035998000	-0.221252000
C	2.760112000	3.150869000	0.990343000
H	3.753157000	3.516967000	0.713134000
H	2.860714000	2.177286000	1.467760000
H	2.342744000	3.863155000	1.707356000
C	-0.867503000	2.839999000	2.017263000
N	-0.542654000	1.769320000	1.738536000
C	-1.261543000	4.192745000	2.353712000
H	-0.748479000	4.893617000	1.692952000
H	-0.990696000	4.409248000	3.388252000
H	-2.339853000	4.305338000	2.231393000

E(RTPSSh) = -3301.99861826
Zero-point correction = 0.596793 (Hartree/Particle)
Thermal correction to Energy = 0.635832
Thermal correction to Enthalpy = 0.636776
Thermal correction to Gibbs Free Energy = 0.5237

9.15.3 [Cu(II)L] Geometries

[Cu(II)(TMG$_3$trphen)]$^{2+}$ (C6$_{TMG}$ - MeCN)

Cu	-0.018047000	-0.121928000	0.598894000
N	0.147089000	-0.405809000	-1.562333000
C	-1.237382000	-0.456268000	-1.990078000
C	-2.220092000	-0.668077000	-1.008978000
C	-3.561819000	-0.687026000	-1.406174000
H	-4.333222000	-0.814841000	-0.656447000
C	-3.906717000	-0.508004000	-2.740003000
H	-4.952364000	-0.517128000	-3.023398000
C	-2.924763000	-0.285163000	-3.701930000
H	-3.195292000	-0.123161000	-4.737576000
C	-1.587893000	-0.252878000	-3.318977000
H	-0.811482000	-0.056487000	-4.048102000
N	-1.831845000	-0.762426000	0.337715000
C	-2.468275000	-1.595271000	1.171474000
N	-2.915108000	-2.808105000	0.773074000
C	-2.295194000	-3.519201000	-0.338082000
H	-1.289368000	-3.139343000	-0.501068000
H	-2.876277000	-3.409895000	-1.257969000
H	-2.238619000	-4.577191000	-0.075687000
C	-4.150505000	-3.391319000	1.289390000
H	-4.652244000	-2.675802000	1.935792000
H	-3.953822000	-4.312309000	1.842765000
H	-4.803892000	-3.620673000	0.443612000
N	-2.630097000	-1.237797000	2.460194000
C	-2.659964000	0.164125000	2.849704000
H	-2.839765000	0.777211000	1.971153000
H	-1.717845000	0.460535000	3.318462000
H	-3.465545000	0.311739000	3.571646000
C	-2.606283000	-2.206301000	3.551845000
H	-2.288532000	-3.174691000	3.173602000
H	-3.586314000	-2.299853000	4.025104000
H	-1.887813000	-1.864621000	4.300131000
C	0.859623000	0.790350000	-1.950548000
C	0.691920000	1.943045000	-1.157706000
C	1.372168000	3.109130000	-1.541648000
H	1.276338000	3.998359000	-0.930126000
C	2.184672000	3.119548000	-2.665148000
H	2.699758000	4.032365000	-2.940051000
C	2.364444000	1.961671000	-3.423396000
H	3.010964000	1.967547000	-4.291777000
C	1.706190000	0.796004000	-3.055594000
H	1.840564000	-0.116339000	-3.623630000
N	-0.026169000	1.839543000	0.029848000
C	-0.713450000	2.881300000	0.498664000
N	-1.457534000	3.670777000	-0.314599000
C	-1.953755000	3.177088000	-1.592234000
H	-2.022430000	2.092435000	-1.562682000
H	-1.301481000	3.474862000	-2.418718000
H	-2.948112000	3.595868000	-1.756186000
C	-1.581495000	5.110588000	-0.105787000
H	-0.955022000	5.418559000	0.727099000
H	-2.617826000	5.396343000	0.088477000
H	-1.238645000	5.622151000	-1.009159000
N	-0.717267000	3.138134000	1.823806000
C	0.405195000	2.748673000	2.664634000
H	1.233779000	2.436041000	2.035709000
H	0.125669000	1.931766000	3.334832000
H	0.708701000	3.604010000	3.272866000
C	-1.853252000	3.738487000	2.513512000
H	-2.721006000	3.737583000	1.858505000
H	-1.636370000	4.760667000	2.833151000
H	-2.075514000	3.140883000	3.400314000
C	0.942461000	-1.605705000	-1.611908000
C	1.867293000	-1.765373000	-0.560807000

C	2.739929000	-2.857644000	-0.602058000
H	3.449119000	-3.009221000	0.201944000
C	2.651799000	-3.783158000	-1.634629000
H	3.322027000	-4.634319000	-1.639992000
C	1.691289000	-3.646486000	-2.635411000
H	1.616029000	-4.381666000	-3.426656000
C	0.833910000	-2.551498000	-2.622616000
H	0.090432000	-2.420979000	-3.398864000
N	1.745412000	-0.908404000	0.551200000
C	2.805903000	-0.630229000	1.333721000
N	4.040595000	-0.442782000	0.828436000
C	4.240870000	0.030820000	-0.536875000
H	3.316418000	0.455360000	-0.918245000
H	4.566164000	-0.782865000	-1.189759000
H	5.009951000	0.805179000	-0.519703000
C	5.253728000	-0.816902000	1.551502000
H	4.993857000	-1.403899000	2.428411000
H	5.829812000	0.061350000	1.850043000
H	5.866013000	-1.428959000	0.885363000
N	2.606707000	-0.503156000	2.658432000
C	1.510363000	-1.189771000	3.335260000
H	1.099675000	-1.956781000	2.684595000
H	0.724396000	-0.484838000	3.616512000
H	1.899170000	-1.653025000	4.244224000
C	3.395446000	0.401511000	3.490616000
H	3.960068000	1.081837000	2.858207000
H	4.075731000	-0.144569000	4.147492000
H	2.706880000	0.980503000	4.109041000

E(UTPSSh) = -3475.16189274
Zero-point correction = 0.785346 (Hartree/Particle)
Thermal correction to Energy = 0.831933
Thermal correction to Enthalpy = 0.832877
Thermal correction to Gibbs Free Energy = 0.708624

$Cu(II)(DMEG_3trphen)]^{2+}$ ($C6_{DMEG}$ - MeCN)

Cu	0.049319000	-0.204572000	-0.557485000
N	0.233558000	0.049901000	1.570314000
N	-0.322895000	1.822458000	-0.448113000
N	-1.553727000	2.339350000	-2.372821000
N	-2.192716000	3.323459000	-0.474072000
C	0.777969000	1.387841000	1.640481000
C	1.656643000	1.758448000	2.654371000
H	1.960899000	1.022422000	3.388497000
C	2.116450000	3.066450000	2.726938000
H	2.786803000	3.360109000	3.524645000
C	1.698527000	3.997300000	1.773622000
H	2.052464000	5.020070000	1.826179000
C	0.852406000	3.623482000	0.740576000
H	0.563498000	4.338728000	-0.020239000
C	0.381779000	2.305274000	0.644907000
C	-1.290676000	2.486094000	-1.048924000
C	-0.522630000	2.003243000	-3.341217000
H	-0.944353000	1.375539000	-4.125752000
H	0.279133000	1.467071000	-2.838918000
H	-0.113868000	2.913432000	-3.792490000
C	-2.625235000	3.255310000	-2.773564000
H	-3.317118000	2.772391000	-3.462515000
H	-2.188611000	4.132085000	-3.263710000
C	-3.266467000	3.613773000	-1.435308000
H	-3.571927000	4.657083000	-1.373308000
H	-4.128669000	2.974871000	-1.216557000
C	-2.558504000	3.241536000	0.934400000
H	-3.102828000	4.147854000	1.196720000
H	-1.668829000	3.179106000	1.554399000
H	-3.193446000	2.369628000	1.122270000
N	1.896391000	-0.756531000	-0.390436000
N	2.816231000	-0.740778000	-2.555875000
N	4.085666000	0.058751000	-0.926922000
C	1.173823000	-0.990457000	1.888729000
C	1.174537000	-1.677800000	3.094833000
H	0.400365000	-1.478632000	3.824956000
C	2.191095000	-2.587329000	3.362079000
H	2.208455000	-3.113515000	4.308029000
C	3.200717000	-2.798641000	2.420654000
H	3.997590000	-3.501120000	2.632895000
C	3.180710000	-2.147325000	1.195917000
H	3.935445000	-2.361999000	0.449161000
C	2.138489000	-1.261535000	0.893029000
C	2.909042000	-0.500322000	-1.240719000
C	1.844967000	-1.615417000	-3.186267000
H	1.302182000	-1.076076000	-3.963918000
H	1.147287000	-1.973380000	-2.432007000
H	2.358857000	-2.469593000	-3.633780000
C	4.064850000	-0.390754000	-3.240619000
H	3.868413000	0.270369000	-4.084636000
H	4.536836000	-1.303757000	-3.610453000
C	4.892156000	0.284131000	-2.133536000
H	5.883745000	-0.153490000	-2.020289000
H	4.996532000	1.359358000	-2.293035000
C	4.383662000	0.773938000	0.302173000
H	5.170010000	0.263983000	0.861481000
H	3.488880000	0.841413000	0.914944000
H	4.715744000	1.782810000	0.049439000
N	-1.659276000	-1.056720000	-0.108123000
N	-2.193930000	-2.284033000	-2.029734000
N	-2.464725000	-3.324970000	-0.080068000
C	-1.137854000	-0.066205000	2.034161000
C	-1.522507000	0.447574000	3.266050000
H	-0.786694000	0.942608000	3.887885000
C	-2.843241000	0.332620000	3.685615000
H	-3.143521000	0.733176000	4.645394000
C	-3.773174000	-0.286490000	2.853266000
H	-4.808418000	-0.367109000	3.162595000
C	-3.396281000	-0.776048000	1.609076000
H	-4.131234000	-1.223078000	0.950799000
C	-2.068145000	-0.676541000	1.177374000
C	-2.100514000	-2.167979000	-0.689642000
C	-2.302987000	-1.153451000	-2.932337000
H	-1.584945000	-1.251001000	-3.747269000
H	-2.109772000	-0.238056000	-2.376475000
H	-3.313008000	-1.108782000	-3.350279000
C	-2.774149000	-3.576175000	-2.398320000
H	-2.228093000	-4.031106000	-3.224019000
H	-3.815739000	-3.429023000	-2.700703000
C	-2.659192000	-4.371020000	-1.097380000
H	-3.546509000	-4.963072000	-0.878488000
H	-1.784420000	-5.028708000	-1.103415000
C	-1.919717000	-3.753728000	1.203464000
H	-2.531749000	-4.575770000	1.572211000
H	-1.955252000	-2.943448000	1.925137000
H	-0.885728000	-4.095809000	1.089332000

E(UTPSSh) = -3471.56499398
Zero-point correction = 0.722362 (Hartree/Particle)
Thermal correction to Energy = 0.765433
Thermal correction to Enthalpy = 0.766377
Thermal correction to Gibbs Free Energy = 0.645359

$[Cu(II)\{N(QuMe)(PhTMG)_2\}]^{2+}$ ($C4_{TMG}$ - MeCN)

N	-0.018371000	1.508130000	0.309833000
C	0.284918000	-0.315177000	1.921272000
N	1.557869000	0.355487000	-1.671964000
N	-1.989277000	-0.006680000	-0.747168000
C	-0.401754000	-0.020909000	4.228232000
H	-0.495227000	-0.423805000	5.229647000
N	0.712865000	-1.094667000	0.852361000
C	-0.860329000	1.267721000	3.950102000
H	-1.305152000	1.873659000	4.729012000
N	-2.996503000	-1.975692000	-1.446542000
C	-0.746850000	1.769089000	2.660939000
H	-1.113404000	2.759311000	2.420414000
N	-3.902388000	-0.829232000	0.361082000
C	-0.161428000	0.996190000	1.662660000
N	2.751425000	-1.804045000	1.795336000
C	1.672957000	-2.005722000	0.997160000
N	1.609107000	-3.153873000	0.290614000
C	0.331645000	-3.691416000	-0.153035000
H	0.207441000	-3.563768000	-1.231732000
H	0.298580000	-4.759818000	0.072290000
H	-0.473740000	-3.184792000	0.371076000
C	2.797469000	-3.841704000	-0.201635000
H	2.667101000	-4.038097000	-1.268227000
H	3.669398000	-3.207189000	-0.063671000
H	2.952200000	-4.794492000	0.310501000
C	3.215267000	-0.464193000	2.126467000
H	4.306516000	-0.461511000	2.097094000
H	2.839625000	0.245552000	1.394396000
H	2.884782000	-0.160085000	3.123962000
C	3.372629000	-2.887359000	2.551915000
H	4.403312000	-3.057171000	2.231321000
H	3.374375000	-2.613868000	3.610447000
H	2.796486000	-3.800679000	2.428582000
C	1.655719000	-1.384116000	-3.359423000
H	0.743165000	-1.720849000	-2.867760000
H	1.412256000	-1.119107000	-4.391615000
H	2.368765000	-2.209661000	-3.389545000
Cu	-0.094201000	-0.295644000	-0.858207000
C	2.244523000	-0.204142000	-2.658753000
C	3.504308000	0.306270000	-3.048945000
H	4.032923000	-0.177258000	-3.859761000
C	4.041278000	1.378226000	-2.393001000
H	5.015579000	1.765822000	-2.666233000
C	3.323351000	1.993010000	-1.339578000
C	3.828815000	3.078933000	-0.591576000
H	4.806387000	3.473744000	-0.840207000
C	3.098853000	3.605980000	0.446125000
H	3.493253000	4.424797000	1.033754000
C	1.827147000	3.089187000	0.754457000
H	1.265936000	3.501794000	1.583060000
C	1.291735000	2.056327000	0.018489000
C	2.048159000	1.461210000	-1.019337000
C	-2.261000000	1.362853000	-0.566743000
C	-3.478618000	1.956661000	-0.916541000
H	-4.305842000	1.336239000	-1.237425000
C	-3.602913000	3.339455000	-0.924029000
H	-4.545742000	3.784207000	-1.218462000
C	-2.520413000	4.154369000	-0.596375000
H	-2.618269000	5.232152000	-0.622740000
C	-1.311792000	3.579331000	-0.218922000
H	-0.470165000	4.202699000	0.053344000
C	-1.195895000	2.197169000	-0.170847000
C	-2.976065000	-0.924581000	-0.609314000
C	-3.631954000	-0.131490000	1.614522000
H	-2.561398000	0.000651000	1.739091000
H	-4.126559000	0.842458000	1.633092000
H	-4.013948000	-0.743416000	2.433273000
C	-5.274960000	-1.303039000	0.191005000
H	-5.944576000	-0.495150000	0.493403000
H	-5.457422000	-1.538494000	-0.853923000
H	-5.477652000	-2.178348000	0.811159000
C	-2.503237000	-1.880132000	-2.818197000
H	-2.213763000	-0.855382000	-3.031990000
H	-1.650054000	-2.545791000	-2.963957000
H	-3.300981000	-2.185000000	-3.499453000
C	-3.501685000	-3.287151000	-1.048651000
H	-2.783964000	-4.037757000	-1.384295000
H	-3.583304000	-3.333729000	0.034203000
H	-4.470056000	-3.504683000	-1.503981000
C	0.151322000	-0.806532000	3.228806000
H	0.464665000	-1.821422000	3.441522000

E(UTPSSh) = -3322.67228708
Zero-point correction = 0.679849 (Hartree/Particle)
Thermal correction to Energy = 0.720227
Thermal correction to Enthalpy = 0.721171
Thermal correction to Gibbs Free Energy = 0.60984

$[Cu(II)\{N(QuMe)(PhDMEG)_2\}]^{2+}$ ($C4_{DMEG}$ - MeCN)

N	0.042316000	1.528047000	0.246629000
C	1.194270000	2.217972000	-0.288337000
N	-1.601639000	0.282545000	-1.622028000
C	1.298170000	3.598376000	-0.382746000
H	0.453326000	4.224416000	-0.127464000
N	-0.626353000	-1.069384000	0.906966000
C	2.504768000	4.167868000	-0.775080000
H	2.595993000	5.244881000	-0.833978000
N	1.992124000	0.014887000	-0.830407000
C	3.599188000	3.351694000	-1.063612000
H	4.542020000	3.796608000	-1.357563000
N	3.867292000	-0.916156000	0.337816000
C	3.487301000	1.969534000	-1.016221000
H	4.323354000	1.341946000	-1.299697000
N	3.054456000	-2.005066000	-1.411131000
C	2.265582000	1.380967000	-0.669190000

N	-1.601051000	-3.118579000	0.308419000
C	2.954049000	-0.913644000	-0.639691000
N	-2.666530000	-1.899382000	1.836060000
C	3.836322000	-0.100240000	1.539819000
H	3.848847000	-0.757936000	2.410984000
H	2.927158000	0.493659000	1.560212000
H	4.703826000	0.560954000	1.572587000
C	2.487143000	-2.150478000	-2.740076000
H	1.903087000	-3.069748000	-2.799307000
H	3.291876000	-2.188206000	-3.478387000
H	1.850224000	-1.293914000	-2.949130000
C	4.668969000	-2.146557000	0.296493000
H	4.444365000	-2.742354000	1.183637000
H	5.732840000	-1.911282000	0.288586000
C	4.196899000	-2.828637000	-0.997934000
H	4.957166000	-2.798495000	-1.781483000
H	3.888877000	-3.862507000	-0.844869000
C	-1.287458000	2.050945000	-0.010758000
C	-1.802844000	3.105701000	0.707558000
H	-1.211018000	3.558833000	1.492630000
Cu	0.099352000	-0.294023000	-0.855244000
C	-3.095004000	3.593271000	0.437817000
H	-3.472914000	4.431808000	1.008223000
C	-3.866417000	3.010605000	-0.537996000
H	-4.861853000	3.379658000	-0.753377000
C	-3.381340000	1.899091000	-1.261847000
C	-2.081292000	1.402777000	-0.987551000
C	-4.142261000	1.225250000	-2.246066000
H	-5.135317000	1.586120000	-2.486333000
C	-3.622720000	0.129699000	-2.877622000
H	-4.185902000	-0.400738000	-3.633887000
C	-2.334298000	-0.341006000	-2.535431000
C	-1.783134000	-1.575248000	-3.172865000
H	-2.020309000	-1.596125000	-4.237074000
H	-2.232584000	-2.459878000	-2.712959000
H	-0.700961000	-1.633843000	-3.049550000
C	0.236297000	1.060241000	1.612318000
C	0.843234000	1.873930000	2.564017000
H	1.203674000	2.853416000	2.274643000
C	0.977303000	1.430674000	3.872572000
H	1.437874000	2.069220000	4.615373000
C	0.509585000	0.161632000	4.218108000
H	0.611620000	-0.192981000	5.236869000
C	-0.063640000	-0.666690000	3.266110000
H	-0.387374000	-1.665736000	3.531970000
C	-0.206296000	-0.239668000	1.936463000
C	-1.574218000	-1.978890000	1.043487000
C	-0.404810000	-3.736826000	-0.236074000
H	-0.607413000	-4.126738000	-1.233877000
H	-0.073031000	-4.557274000	0.408632000
H	0.386529000	-2.992360000	-0.291774000
C	-3.197602000	-0.655222000	2.371230000
H	-4.244563000	-0.564893000	2.075102000
H	-2.644876000	0.189347000	1.965965000
H	-3.128963000	-0.636973000	3.460404000
C	-2.702926000	-3.976658000	0.753081000
H	-2.303670000	-4.783138000	1.376598000
H	-3.226370000	-4.414394000	-0.096155000
C	-3.578388000	-3.015326000	1.560080000
H	-4.427278000	-2.646750000	0.976067000
H	-3.950376000	-3.457136000	2.483830000

E(UTPSSh) = -3320.27552869
Zero-point correction = 0.637476 (Hartree/Particle)
Thermal correction to Energy = 0.675727
Thermal correction to Enthalpy = 0.676671
Thermal correction to Gibbs Free Energy = 0.566411

[Cu(II){N(QuMe)$_2$(PhTMG)}]$^{2+}$ (C6$_{TMG}$ - MeCN)

N	0.774388000	1.087884000	0.123977000
C	1.980374000	-3.244640000	-1.930708000
H	2.614705000	-4.001259000	-2.387970000
H	1.319891000	-2.830755000	-2.696451000
H	1.359919000	-3.732792000	-1.176305000
Cu	0.261425000	-0.839962000	-0.549885000
N	2.180786000	-1.120410000	-0.774148000
C	2.807696000	-2.160823000	-1.316802000
N	-0.210253000	-1.165591000	1.461124000
C	4.216617000	-2.236948000	-1.318574000
H	4.688564000	-3.099081000	-1.769571000
N	-1.308495000	0.063864000	-1.191597000
C	4.961289000	-1.242594000	-0.743626000
H	6.042803000	-1.302135000	-0.718941000
N	-3.594980000	0.454119000	-0.730144000
C	4.316868000	-0.118837000	-0.180599000
N	-2.853030000	-1.638299000	-1.409910000
C	5.014974000	0.943415000	0.436708000
H	6.096074000	0.897961000	0.485955000
C	4.328887000	2.003547000	0.974758000
H	4.859073000	2.811570000	1.461607000
C	2.924709000	2.058706000	0.888373000
H	2.398402000	2.901647000	1.315972000
C	2.221885000	1.053698000	0.266820000
C	2.899986000	-0.078331000	-0.243418000
C	-0.445340000	-3.576618000	1.388425000
H	0.027314000	-4.303805000	2.051356000
H	0.163280000	-3.464036000	0.493941000
H	-1.420731000	-3.979265000	1.104308000
C	-0.610785000	-2.265309000	2.081546000
C	-1.204561000	-2.210379000	3.365575000
H	-1.499174000	-3.134321000	3.845756000
C	-1.424077000	-1.001711000	3.964260000
H	-1.907989000	-0.938756000	4.931820000
C	-1.022234000	0.188384000	3.313136000
C	-1.254243000	1.474856000	3.846855000
H	-1.747369000	1.561487000	4.807469000
C	-0.875360000	2.594268000	3.146178000
H	-1.070648000	3.582704000	3.541125000
C	-0.220413000	2.467202000	1.908086000
H	0.063190000	3.354803000	1.356829000
C	0.055723000	1.224269000	1.384496000
C	-0.375618000	0.052749000	2.056488000
C	0.204820000	1.907059000	-0.936290000
C	0.742583000	3.115268000	-1.353017000
H	1.672362000	3.473865000	-0.931708000
C	0.063948000	3.866945000	-2.307204000
H	0.471257000	4.816273000	-2.630531000
C	-1.138634000	3.400380000	-2.834422000
H	-1.663836000	3.983502000	-3.580977000
C	-1.659217000	2.172630000	-2.444392000
H	-2.561188000	1.790583000	-2.904808000
C	-0.977313000	1.397205000	-1.503921000
C	-2.588774000	-0.353490000	-1.115617000
C	-2.061928000	-2.388845000	-2.381326000
H	-1.490127000	-3.177304000	-1.887760000
H	-1.390238000	-1.712784000	-2.903013000
H	-2.741756000	-2.850383000	-3.100887000
C	-3.922087000	-2.383259000	-0.751292000
H	-3.521547000	-3.355097000	-0.458339000
H	-4.772921000	-2.544313000	-1.416627000
H	-4.244288000	-1.849248000	0.139082000
C	-3.396475000	1.566060000	0.193279000
H	-2.414811000	1.496689000	0.650972000
H	-4.157607000	1.503207000	0.973275000
H	-3.490583000	2.522784000	-0.325201000
C	-4.949428000	0.318693000	-1.264061000
H	-4.940277000	-0.342139000	-2.126764000
H	-5.283182000	1.309333000	-1.579555000
H	-5.642013000	-0.062313000	-0.510790000

E(UTPSSh) = -3170.17901200
Zero-point correction = 0.574910 (Hartree/Particle)
Thermal correction to Energy = 0.608909
Thermal correction to Enthalpy = 0.609853
Thermal correction to Gibbs Free Energy = 0.511599

[Cu(II){N(QuMe)$_2$(PhDMEG)}]$^{2+}$ (C6$_{DMEG}$ - MeCN)

Cu	0.166123000	-0.920280000	-0.365416000
N	0.808340000	1.097223000	-0.122340000
N	-0.193586000	-0.840406000	1.662282000
N	2.051555000	-1.338319000	-0.583786000
N	-1.349155000	-0.101451000	-1.206553000
N	-3.624918000	0.234176000	-0.516630000
N	-3.054107000	-1.711275000	-1.405802000
C	0.186600000	1.745584000	-1.261770000
C	0.697674000	2.871277000	-1.890302000
H	1.659694000	3.270187000	-1.597193000
C	-0.049482000	3.501081000	-2.880723000
H	0.339605000	4.389512000	-3.361275000
C	-1.305441000	3.004331000	-3.230157000
H	-1.890985000	3.503228000	-3.992583000
C	-1.802534000	1.853234000	-2.637398000
H	-2.752217000	1.438736000	-2.952895000
C	-1.039043000	1.181415000	-1.674565000
C	-2.639418000	-0.490095000	-1.059382000
C	-2.350611000	-2.621404000	-2.292266000
H	-2.200674000	-3.582146000	-1.797990000
H	-1.389061000	-2.186468000	-2.554191000
H	-2.940030000	-2.771043000	-3.199690000
C	-3.471200000	1.442543000	0.275395000
H	-4.120231000	2.225675000	-0.118224000
H	-2.440573000	1.781619000	0.239329000
H	-3.743943000	1.231715000	1.312146000
C	-4.492593000	-1.861078000	-1.155914000
H	-4.690041000	-2.766748000	-0.583581000
H	-5.014067000	-1.925854000	-2.113410000
C	-4.843756000	-0.577699000	-0.386286000
H	-5.700203000	-0.051272000	-0.805356000
H	-5.026906000	-0.767802000	0.673650000
C	2.260078000	1.012047000	-0.079729000
C	3.053805000	2.086505000	0.248508000
H	2.600083000	3.032294000	0.513525000
C	4.456477000	1.969662000	0.249091000
H	5.057410000	2.834218000	0.499465000
C	5.053432000	0.774881000	-0.069524000
H	6.132352000	0.677848000	-0.078662000
C	4.264640000	-0.357168000	-0.372008000
C	2.850818000	-0.243749000	-0.359792000
C	4.814860000	-1.624773000	-0.673317000
H	5.891601000	-1.742369000	-0.697321000

C	3.988803000	-2.685592000	-0.923244000
H	4.388242000	-3.663685000	-1.155384000
C	2.587001000	-2.520745000	-0.862853000
C	1.670135000	-3.669018000	-1.133959000
H	2.081958000	-4.596716000	-0.736200000
H	1.544462000	-3.792189000	-2.213787000
H	0.686664000	-3.500750000	-0.694645000
C	0.193576000	1.481242000	1.143894000
C	0.013817000	2.807288000	1.464371000
H	0.288055000	3.571087000	0.747849000
C	-0.522883000	3.183502000	2.709789000
H	-0.641011000	4.234893000	2.937577000
C	-0.877315000	2.225950000	3.627457000
H	-1.273235000	2.503931000	4.596830000
C	-0.749329000	0.855123000	3.310434000
C	-0.231964000	0.468385000	2.044559000
C	-1.140074000	-0.178245000	4.191311000
H	-1.523627000	0.078504000	5.171727000
C	-1.044889000	-1.485230000	3.795314000
H	-1.340073000	-2.290850000	4.454141000
C	-0.590161000	-1.795060000	2.494044000
C	-0.550901000	-3.208505000	2.004536000
H	-0.998086000	-3.887667000	2.728109000
H	0.483566000	-3.516246000	1.831532000
H	-1.093928000	-3.297286000	1.060275000

E(UTPSSh) = -3168.98136512
Zero-point correction = 0.553396 (Hartree/Particle)
Thermal correction to Energy = 0.586492
Thermal correction to Enthalpy = 0.587436
Thermal correction to Gibbs Free Energy = 0.489292